Laurentide Ice Sheet dynamics evolution in the inner-ice sheet region of northeastern Quebec, Canada

by

Jessey Rice

A thesis

presented to the University of Waterloo

in fulfillment of the

thesis requirement for the degree of

Doctor of Philosophy

in

Earth and Environmental Sciences

Waterloo, Ontario, Canada, 2020

Examining Committee Membership

The following served on the Examining Committee for this thesis. The decision of the Examining Committee is by majority vote.

External Examiner	Dr. Chris Clark
Supervisor	Dr. Martin Ross
Internal Member	Dr. John Johnston
	Dr. Brian Kendall
Internal-external Member	Dr. Christine Dow

Authors Declaration

This thesis consists of material all of which I authored or co-authored: see Statement of Contributions included in the thesis. This is a true copy of the thesis, including any required final revisions, as accepted by my examiners. I understand that my thesis may be electronically available to the public.

Statement of Contributions

Jessey Rice is the sole author for Chapters 1 and 5, which were written under the supervision of Dr. Martin Ross and were not written for publication. This thesis consists in part of three manuscripts written for publication. Exceptions to sole authorship of material is as follows:

Chapter 2 is published in the *Journal of Quaternary Science* (Rice et al., 2019). A large portion of the work was conducted by the author of this thesis with critical research design and recommendations by the thesis supervisor (Martin Ross, second author) and third author (Roger Paulen). The fourth (Samuel Kelley) and fifth (Jason Briner) authors assisted with the ^{10}Be analysis and interpretation. The final two authors (Olav Lian and Christina Neudorf) assisted with the analysis and interpretation of the optically stimulated luminescence data. As lead author, I was responsible for writing and revising the manuscript, but all co-authors provided useful comments and suggestions on the manuscript. Surficial geology maps (1:50 000 scale) of the study area have also been published (Appendices S1.1 and S1.2) by the Geological Survey of Canada (Rice et al., 2017a, 2017b) and are coauthored with Roger Paulen (GSC) and the thesis supervisor (Martin Ross). As principal mapper, I did all the air photo interpretation and related line work, but the co-authors provided guidance and recommendations at all stages, from fieldwork to final revisions of the maps. The maps bring critical surficial geology information that has been useful in addressing all the thesis objectives.

Citation: Rice, J.M., Ross, M., Paulen, R.C., Kelley, S.A., Briner, J.P., Neudorf, C.M., and Lian, O.B. 2019. Refining the ice-flow chronology and subglacial dynamics across the migrating Labrador Divide of the Laurentide Ice sheet with age constraints on deglaciation. Journal of Quaternary Science, 34(7): 519-535. doi: 10.1002/jqs.3138

Chapter 3 been submitted as a journal paper to *Earth Surface Processes and Landforms* (Rice et al., *submitted)*. Similar to Chapter 2, a large portion of the work was conducted by the author of this thesis with critical research design and recommendations by the thesis supervisor (Martin Ross, second author) and third author (Roger Paulen). The fourth (Samuel Kelley) and fifth (Jason Briner) authors assisted with the ^{10}Be analysis and interpretation. As lead author, I was responsible for writing and revising the manuscript, but all co-authors provided useful comments and suggestions on the manuscript.

Citation: Rice, J.M., Ross, M., Paulen, R.C., Kelley, S.E., and Briner, J.P. submitted. A GIS-based multi-proxy analysis of the evolution of subglacial dynamics of the Quebec-Labrador ice dome, northeastern Quebec, Canada. Earth Surfaces Processes and Landforms.

Chapter 4, at the time of writing, has not yet been submitted to an academic journal. The majority of the work was conducted by the author of this thesis with guidance from the thesis supervisor (Martin Ross) and colleagues at the Geological Survey of Canada (Roger Paulen and Beth McClenaghan).

Abstract

The study of past ice sheets, such as the Laurentide Ice Sheet (LIS), which covered most of northern North America during the last glaciation (last ~100-kyr), provides critical knowledge about the long-term behaviour of ice sheets, how they modified landscapes and the sedimentary record, and how they responded to external climate forcings. The LIS had a complex evolution including several changes in its configuration (e.g., ice sheet extent, its surface topography and its thickness). This is essentially known through multiple studies of ice-flow indicators and glacial landforms and sediments. However, conflicting ice flow reconstructions exist for many regions of the LIS, with implications for the overall understanding of the long-term evolution of ice sheets. One of these regions, within the Quebec-Labrador (Q-L) sector of the LIS, is located in northern Quebec and western Labrador. The Q-L sector is one of the largest 'inner-regions' of the LIS where the main ice divides formed with an unresolved ice-flow history. Specifically, a major landform boundary, commonly referred to as the horseshoe unconformity, has been the source of conflicting paleoglaciological reconstructions. Changes in the thermal regime at the base of the ice sheet have been invoked to explain this landscape, whereby relict fragments of the ice sheet imprint are partially preserved following a switch from warm-based to cold-based conditions. However, previous research has disagreed on the sequence of events, the relative timing/duration, and significance. Large areas within the former Q-L sector also lack field-based evidence and detailed data regarding ice-flow indicators, sediment transport, and other characteristics (e.g., weathering), which contributed to the uncertainties in ice sheet reconstructions. Therefore, a study area within the inner-region of the Q-L sector was selected to investigate its glacial evolution. The overall goal of this thesis is to characterize the glacial sediments and their distribution across the study area and develop a better understanding of the evolution of this inner-ice sheet region throughout glaciation. A specific focus is placed on establishing the ice-flow chronology, subglacial conditions associated with these ice-flow phases, and detailing the resulting dispersal of subglacial materials.

To achieve these research objectives, a multi-faceted approach is used, whereby ice-flow phases are reconstructed based on the glacial geomorphological evidence (e.g., landform and outcrop-scale ice-flow indicators), with new geochronology constraints on deglaciation (e.g., optical dating and cosmogenic isotope 'exposure' dating). Additionally, the evolution of subglacial dynamics was reconstructed using a number of different proxies (e.g., landform

density and elongation, lake abundance and area, and the presence of a till blanket). These proxies were then used to derive a subglacial dynamics index map to infer the mobility of the ice sheets bed/sediment layer, which is tested against a chemical index of alteration (from till matrix composition) as well as cosmogenic isotope (^{10}Be) inheritance from till and bedrock outcrops.

Results from this research have revealed a complex ice-flow history, detailing four ice-flow phases associated with complex spatiotemporal fluctuations in subglacial conditions that led to a fragmentary glacial landscape, as well as amoeboid type sediment dispersal patterns (i.e., dispersed in multiple directions around the source). Six distinct glacial terrain zones (GTZs) with varying degrees of overprinting and preservation are recognized. Together, these GTZs form a mosaic landscape with remarkable landscape preservation of older glacial terrains in some GTZs, and stronger overprinting by younger phases in others. Dispersal patterns across the study area provide additional insights into sediment entrainment and deposition in relation to the different ice-flow phases identified, allowing for a more holistic understanding of the glacial processes and history for the inner-regions of the Q-L sector.

The oldest flow recognized in the study area (Flow 1) was a regional northeast ice-flow event with predominantly warm-based conditions across the majority of the ice-bed interface; it is best preserved in the eastern portion of the study area (GTZ1). Flow 1 had a significant impact on the dispersal patterns across the study area, with evidence for long transport distance (>100 km) towards a general northeast direction. Following Flow 1, subglacial conditions transitioned to more cold-based conditions, likely relating to the formation of an ice-divide in the eastern portion of the study area, except in the northwest corner (GTZ2), where ice-flow indicators almost completely overprint the evidence of Flow 1. Flow 2 is associated with ice streaming events in Ungava Bay and its landscape imprint has produced high subglacial index, indicating highly dynamic basal ice. Following Flow 2 the ice stream catchment shifted west in Ungava Bay and evidence within the study area suggests the ice divide within the study area also shifted west, as indicated by multiple sites where an almost complete ice-flow reversal is recorded. Most of these sites are located along the edge of a central upland terrain, consisting of resistant bedrock (De Pas Batholith), characterized by an overall lower subglacial index (GTZ4) than elsewhere within the study area. The high angle crosscutting of Flow 2 and Flow 3 (near opposite flows) provides compelling evidence for westward ice divide migration across the study area, which probably happened in response to the changing configuration of the Ungava Bay ice

stream. Evidence of Flow 3 is discontinuous, but it is abundant on the eastern flank (GTZ3) of the central uplands (GTZ4), where Flow 3 indicators overprint Flow 1 indicators at a few key sites. Considering the broader glacial landscape from outside the study area, it appears that this flow phase was also influenced by ice streaming, specifically by a few ice streams operating on the eastern margin of the Quebec-Labrador sector. Again, high proxy values associated with mobile bed conditions are abundant within the inner regions of the two GTZs correlated to this ice-flow phase (GTZ3 and GTZ3b). Both GTZ3 and GTZ3b are surrounded by areas interpreted as inter-ice stream regions, which preserved most of the Flow 1 evidence (forming GTZ1), while producing undulating till blanket areas lacking streamlined landforms (GTZ5) due perhaps to basal meltout. East-trending eskers also crosscut Flow 1 features, suggesting Flow 3 occurred just prior to channelized meltwater drainage and final deglaciation. However, a fourth and final deglaciation ice-flow phase (Flow 4) is recognized in the striation record. This ice-flow phase was largely topographically controlled as the larger ice sheet began to fragment into smaller and thinner ice caps during deglaciation, which probably occupied the central upland area (GTZ4). Flow 4 had little if any impact on the landscape and has no discernable dispersal patterns. Geochronological results suggest the study area was deglaciated by about 8 ka. This deglacial timing is consistent with other regional deglacial ages, but it provides new additional constraints for the position of the retreating ice margin within the study area during this time.

Although this thesis focuses on a specific region of the Q-L sector, evidence indicates that the sector was characterized by transient polythermal conditions, similar to the other large inner region with ice divides of the LIS (the Keewatin sector over northcentral Canada). Specifically, the spatiotemporal subglacial fluctuations occurred predominantly at the onset of deglaciation, after spatially extensive warm-based conditions had covered the region. As the ice sheet thinned, a greater proportion of the bed became cold-based; however, ice streaming events began to drain ice further inland, keeping warm-based conditions along narrow corridors. Subglacial conditions thus changed relatively rapidly, highly influenced by both the thinning of the LIS and regional ice streaming. This suggests the Q-L sector of the ice sheet had more transient polythermal conditions than previously reconstructed and modelled, which highlight the need to further improve our knowledge of bed thermal properties of inner ice sheet regions and the effect of ice stream catchment processes far into ice sheets, close to ice divides.

Acknowledgements

First and foremost, I would like to sincerely thank my supervisor, Dr. Martin Ross for all of his advice and guidance over the years. Thank you for the countless lessons during our office discussions and guidance in the field, you have been an incredible supervisor and this thesis would not have been possible without you. I also would like to thank Roger Paulen for getting me addicted to the Quaternary, writing advice, comedic relief, and most of all your guidance and wisdom in the field. I would also like to thank Dr. Samuel Kelley for all is help with the written portions of the thesis, advice in interpreting the cosmogenic data, and carrying several of our soccer teams to intramural victories. I would also like to thank Beth McClenaghan for her life advice, lessons on writing, fieldwork, and the many delicious meals you over the years.

I would also like to thank Dr. Olav Lian and Dr. Christina Neudorf for their assistance with processing the Optically Stimulated Luminesces samples. Dr. Jason Briner is thanked for his handling of the bedrock and till samples collected for cosmogenic nuclide abundance analysis. Sincere thanks go out to my committee members Dr. John Johnston, Dr. Brian Kendall, Dr. Christine Dow, and Dr. Chris Clark. Additionally, I would like to thank Dr. Chris Yakymchuk for sitting in on my comprehensive exam. I would also like to thank the many people at the Geological Survey of Canada who have helped me in various ways throughout this process including Mary Sanborn-Barrie, Alan Plouffe, Isabelle McMartin, Janet Campbell, Matt Pyne, Wendy Spirito, and Mike Parkhill at the New Brunswick Survey. I would like to thank Grant Hagedorn for his help in the field, with GIS troubles, and the many, many, office visits and discussions! A big thank you also goes out to the rest of the many Quaternary Graduate students that I have had the pleasure of knowing during my time at Waterloo (Tyler, Aaron, Ying, Shawn, Amanda, Bob, Rebecca, Ameerah, and especially Thomas). A special thanks goes out the Graduate Studies at the University of Waterloo for ensuring the defense portion of this thesis could be completed during the Covid-19 pandemic. Financial support for this work was provided by Natural Resources Canada's Geo-mapping for Energy and Minerals (GEM II) program, the Ontario Graduate Scholarship, and the Northern Scientific Training Program.

Finally, I would like to thank my family, especially my mom and dad for all the love and support, I couldn't have done it without you! Most of all I would like to thank Dr. Hilary White, my best friend in the world, thank you for endless support and encouragement throughout this process, I can't imagine completing this without you at my side.

Table of contents

List of figures

List of tables

List of Abbreviations

LIS- Laurentide Ice Sheet

ka- kilo annum (1000 years)

Q-L- Quebec-Labrador

GTZ- Glacial Terrain Zone

LGM- Last glacial maxima

FIS- Fennoscandian Ice Sheet

QLD- Quebec-Labrador Dome

NRCan- Natural Resources Canada

GSC- Geological Survey of Canada

GEM- Geo-mapping for Energy and Minerals

DEM- Digital elevation model

SRTM- Shuttle Radar Topographic Mission

NTS- National Topographic System

m asl- meters above sea level

LT- Labrador Trough

Ga- giga annum (1 billion years)

NQO- New Quebec orogen

RL- Rachel-Laporte

GR- George River

MR-Mistinibi-Raude

UBLS- Ungava Bay landform swarm

UBIS- Ungava Bay ice stream

OSL- Optically stimulated luminescence

GPS- Global positioning system

CIA- Chemical index of alteration

MH- Moderately-high

ML- Moderately-low

WL- warm-low

GIS- Geographic information system

LREE- Light rare earth elements

ICPMS- Inductively coupled plasma mass spectrometry

ICPAES- Inductively coupled plasma atomic emission spectrometry

QA/QC- Quality Assurance/ Quality Control

PGM- Platinum group elements

MMSIM- metamorphic/magnetic massive sulphide indicator minerals

1 Chapter 1: Introduction

Ice sheets are critical components of the global climate, influencing atmospheric and oceanic circulation, as well as planetary albedo (Clark and Mix, 2002). Understanding the role that large Quaternary ice sheets played in global-scale climate fluctuations is important, as it can provide key insights into the long-term response of present-day ice sheets to changes in Earth systems (e.g., atmosphere and oceans). Numerical models are commonly used to reconstruct past ice sheets and predict future ice sheet behaviour (e.g., Marshall and Clark, 2002; Tarasov and Peltier, 2007; Stokes et al., 2012; Bakker et al., 2017, van den Broeke et al., 2017). These models require numerous parameters that need to be constrained (e.g., boundary conditions and ice margin positions at specific time steps). For the Laurentide Ice Sheet (LIS) the extent and timing of last glacial maxima (LGM) are reasonably well constrained (Dyke et al., 2003; Dalton et al., 2020), however, important uncertainties regarding ice sheet build-up (Kleman et al., 2002; Kleman et al., 2010; Stokes et al., 2012) ice sheet configuration (Clark et al., 2000; Jansson et al., 2003), subglacial dynamics change during the last glacial cycle (Veillette et al., 1999; Clarhäll and Jansson, 2003), and ice margin retreat configuration and timing (Dyke et al., 2003) persist. These uncertainties are greatest near the centres of the major ice-domes of the LIS. In addition, the subglacial thermomechanical conditions that evolved throughout glaciation in these inner-ice sheet regions remain poorly constrained.

There is widespread evidence now that the larger Quaternary ice sheets, such as the LIS and the Fenno-Scandian Ice Sheet (FIS), had polythermal bases, indicating that regions of their bed were below the pressure-melting point (cold-based) and were surrounded by regions above the pressure-melting point (warm-based). Past cold-based zones are recognized by several diagnostic features (e.g., Goodfellow, 2007), including the occurrence of old tors, pre-glacial saprolites, and/or regions with minimal evidence of glacial erosion (e.g., few scattered erratics and meltwater channels). Examples of cold-based terrains have been described on the high plateaus of Baffin Island (Davis et al., 2006), Somerset Island (Dyke, 1983), Cornwallis Island (Edlund, 1991), Boothia and Melville peninsulas (De Angelis and Kleman, 2005), and in central Sweden (Kleman and Stroeven, 1997). These cold-based zones are surrounded by glacial landscapes characterized by subglacial sediments and landforms indicative of warm-based ice (i.e., thick glacial deposits and streamlined landforms). Typically, the landform record suggests the transition between cold-based and warm-based zones is abrupt. In the cases listed above, it is assumed that the boundaries observed in once glaciated

landscapes are representative of stable thermal boundaries under an ice centre (ice dome) of the past ice sheet. These ice centres were thus relatively stationary and the surrounding evidence of warm-based ice includes ice flow features indicative of ice flow radiating out from the stable cold-based zones. However, some of the largest regions under the LIS where numerical ice sheet models predict low probability of warm-based conditions and thus very limited subglacial erosion (Tarasov and Peltier, 2007; Stokes et al., 2012; Melanson et al., 2013) contain abundant subglacial features typical of warm-based ice (Veillette et al., 1999; McMartin and Henderson, 2004; Trommelen et al., 2012; Hodder et al., 2016), or have not been extensively studied in the field.

The two largest regions of snow and ice accumulation of the LIS, from where ice flow generally propagates (i.e., ice domes), were the Keewatin and Quebec-Labrador ice domes (Figure 1.1A). In the Keewatin sector, there is extensive evidence of crosscutting ice-flow indicators which suggests a lateral migration of the ice divide over a 500 km distance (McMartin and Henderson, 2004). Additionally, surficial drill cores collected within the Keewatin sector contain subglacial till produced in thick sequences (~ 5-30 m) with contrasting lithological (provenance) indicators (Hodder et al., 2016). This evidence suggests warm-based subglacial conditions and a dynamic mobile ice centre (Boulton and Clark, 1990) within regions that have been modelled as having low probabilities of warm-based conditions and low cumulative erosion (Figures 1.1B and 1.1C; Tarasov and Peltier, 2007; Melanson et al., 2013).

The nomenclature used to describe the other large sector of the LIS has varied widely over the last several decades (e.g., *New Québec Dome*- Roy et al., 2015; -or- *Labrador Sector*- Andrews, 1994; Ullman et al., 2016; -or- *Labrador-Québec Dome*-Roy et al., 2009; -or- *Quebec-Labrador Dome*- Veillette et al., 1999; Clark et al., 2000; Occhietti et al., 2011; Dubé-Loubert et al., 2018). The majority of the research cited within this thesis refers to this region as the Quebec-Labrador Dome and, as the sector did cover the majority of Quebec and Labrador, Quebec-Labrador Dome (QLD) will be used throughout this thesis.

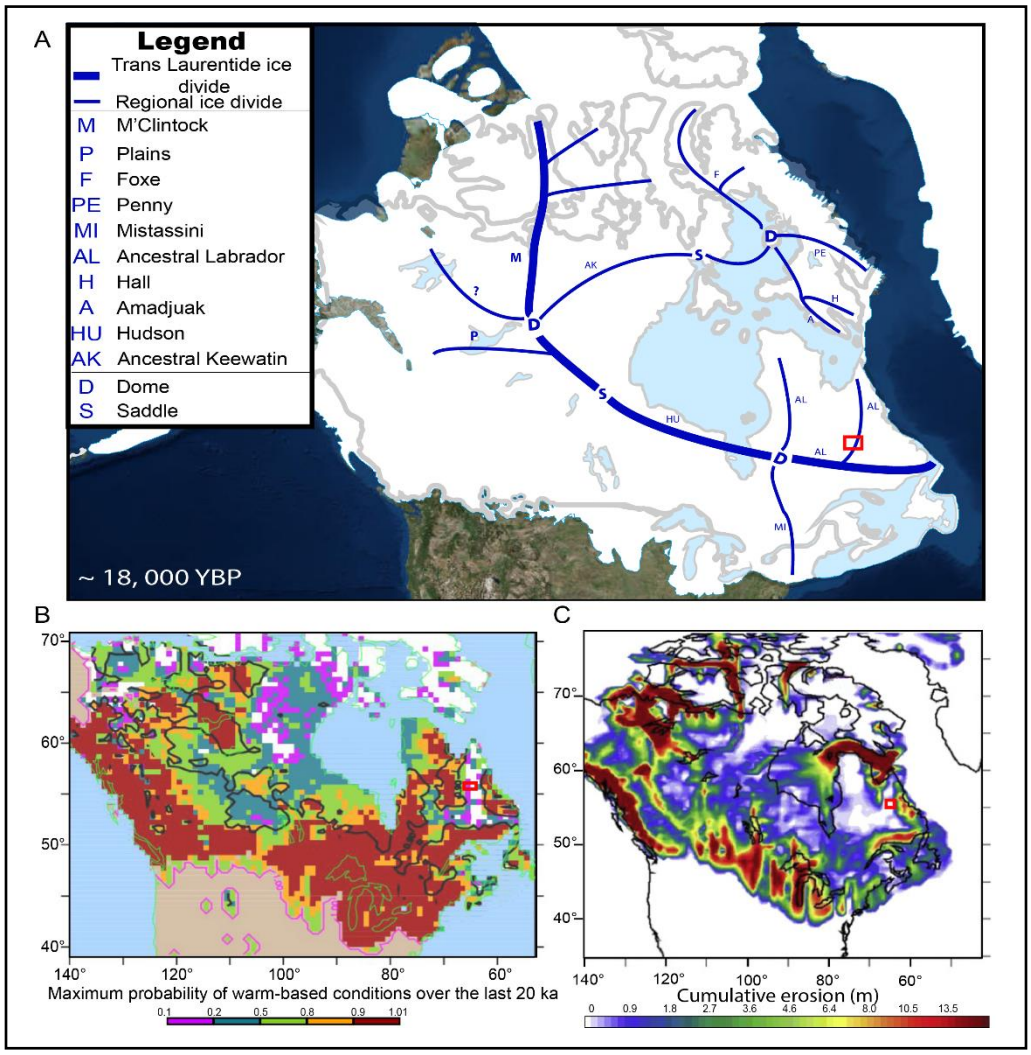

Figure 1.1. **(A)** Map of Canada with the location of the study area (red box) in northcentral Quebec with the LIS ice margins of Dyke and Prest (1987) at LGM (~18 ka) with the locations of the Dyke and Prest's (1987) two major ice centres of the LIS (the Keewatin and the Quebec-Labrador - Ds on figure) and proposed ice divide and ice saddle locations. **(B)** Numerical model showing the probability of warm-based conditions over the last 20 ka (Tarasov and Peltier, 2007), showing that the study area (red box) has a low probability of warm-based conditions (white cells). **(C)** Numerical model indicating the cumulative subglacial erosion predicted to occur over the last glacial cycle (Melanson et al., 2013). The study area (red box) was predicted to have some of the lowest erosion within the LIS (white cells).

The QLD has a subglacial organization equally as complex as the Keewatin, with field-based evidence of only localized, sustained cold-based conditions (Dubé-Loubert and Roy, 2017) and overall, dynamic ice-divide migration (Veillette et al., 1999). Conversely, numerical models predict a low probability of extensive warm-based conditions under the QLD (Figures 1.1B and 1.1C; Tarasov and Peltier, 2007; Stokes et al., 2012) and geomorphological reconstructions have indicated vast regions of predominantly frozen bed during LGM for the entire inner-region of the QLD (Kleman and Glasser, 2007). The discrepancies between numerical models and field-observations suggest

numerical models may overestimate the surface area covered by cold-based conditions (e.g., Hodder et al., 2016), perhaps because of important simplifications in the parameterization (e.g., constant bedrock thermal conductivity, changing air temperature, and/or subglacial hydrology). Numerical models are also limited by the available geoscience data used to constrain the models and a major barrier to understanding the thermal conditions under the QLD is that the ice-flow history and associated subglacial conditions of this region remain unresolved (Veillette et al., 1999; Clark et al., 2000; Jansson et al., 2003). Thus, there is a need for detailed, field-verified, geoscience data in order to characterize and understand the subglacial evolution of these inner-ice sheet regions throughout glaciation.

To address these major issues with ice sheet modelling of the LIS, robust, field-verified studies are needed to reconstruct the evolution of the interior regions of the LIS. This thesis focuses on the QLD, one of the largest domes (inner regions) of the LIS. The research is threefold: 1) establishment of the ice flow history for the study area, 2) analysis of the relative changes in subglacial conditions associated with each ice-flow phase, and 3) analysis of subglacial erosion, as well as till entrainment and deposition across the study area. Understanding how past ice sheets evolved throughout glaciation and into deglaciation will also provide important insights into how future ice sheet changes may occur with continued global climate change. However, modern analogues also offer important insights into how past ice sheets may have behaved as well. Specifically, examining the organization of ice streams within the Antarctic and Greenland ice sheets could provide important insights into how ice streams of the LIS may have been organized, the landforms associated with them, and the rate ice of ice flow. Correlations between past and present ice sheets cannot be directly compared due to difference in their terminal positions (land vs sea) and differences between their bed morphology, but generalized ice sheet behaviour does provide important correlations to how past ice-sheets may have operated.

The impetus for this study is the multi-disciplinary field-based research project carried out in the remote region of northcentral Quebec and western Newfoundland and Labrador by Natural Resources Canada's (NRCan) Geological Survey of Canada (GSC) under its Geo-mapping for Energy and Minerals (GEM II) program. The aim of the overall GSC project is to generate new high-quality geoscience data for northern Quebec and Newfoundland and Labrador to support mineral exploration in the region through a better understanding of how sediments are dispersed in inner ice

sheet regions. This improved understanding will assist mineral exploration programs within these inner ice sheet regions. This thesis describes the detailed geoscience fieldwork and research of a ~ 7000 km^2 region in northern Quebec undertaken to characterize the effects of multiple ice-flow phases and changing subglacial conditions on the landscape to elucidate the enigmatic nature of a part of the LIS' interior regions.

1.1 Study location

1.1.1 Study area

This thesis encompasses a region in northeastern Quebec between 55°30' and 56°00'W latitude and 64°00' and 66°00'N longitude (Figure 1.2) and covers eight 1:50 000 scale National Topographic System (NTS) Maps (NTS 23P/9-16) within the larger 1:250 000 scale NTS 23P Map sheet: Lac Resolution. This ~ 7 000 km^2 region is northeast of Schefferville, Quebec and is typical of most Canadian Shield terrain with undulating uplands and low to moderate relief. This terrain is characterized by windswept uplands (525-659 m asl) with abundant large and small lakes, especially within the lowlands (300 – 425 m asl). It is similar to the *knock-and-lochan* landscape of northwest Scotland (Linton, 1963), whereby topographic variations largely reflect bedrock hardness and structure. The lowest elevation is located in the George River valley (398 m asl) and the highest point is found within the central upland (659 m asl). The study area lies within the Lake Plateau division within the James Region physiographic region and the George Plateau and Whale lowland divisions of the larger Davis region within the Canadian Shield (Bostock, 2014). The tree line trends east to west across the study area, with trees abundant in the lowlands but scarcer on the uplands (Figures 1.3A and 1.3B) where small shrubs and bushes are more common (Figure 1.3C). Larger shrubs and small trees are more common in the lowland areas (Figure 1.3D). Extensive discontinuous permafrost covers 50-90% of the study area (Smith, 2010). Due to the lack of infrastructure in the region, the study area is only accessible by helicopter.

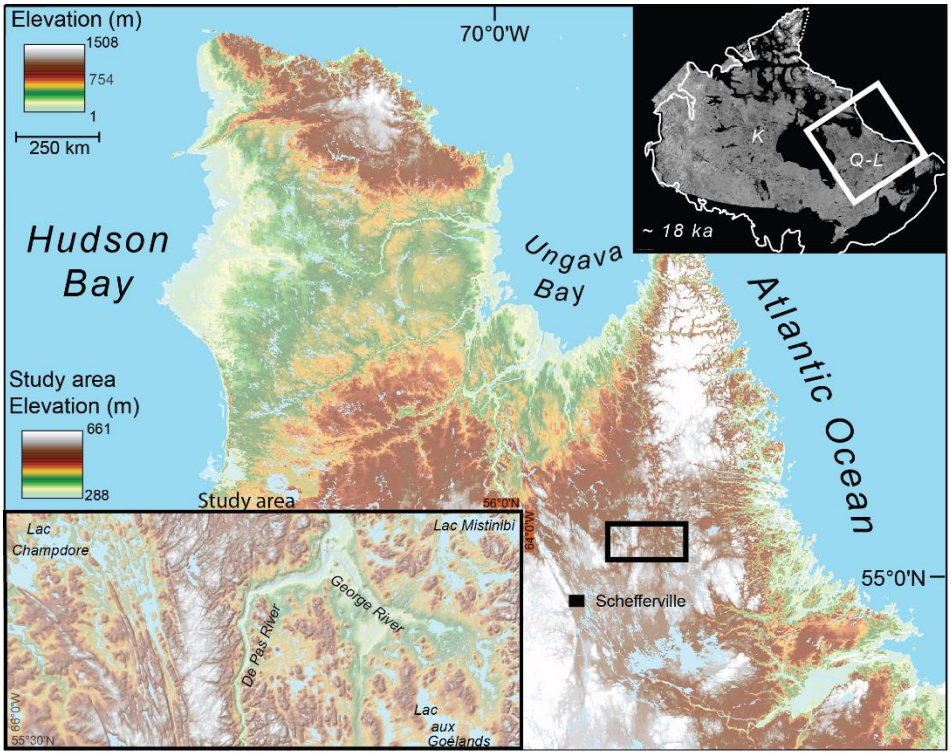

Figure 1.2. Location of the study area within a regional context of the larger Quebec/Labrador region annotated over a digital elevation model (DEM) created using Satellite Radar Topography Mission (SRTM) data (30 m vertical and horizontal resolution, United States Geological Survey, 2014). **(Top inset)** Extent of the LIS during LGM (~18 ka) with the general locations of the two major ice divides indicated in bold letters (Keewatin= K; Quebec/Labrador=Q-L). **(Bottom inset)** detailed DEM of the study with major rivers and lakes indicated.

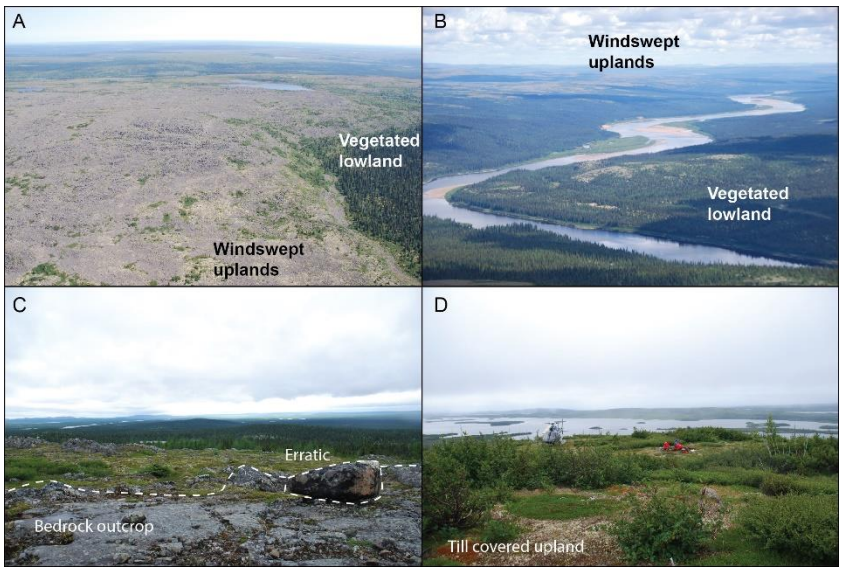

Figure 1.3. **(A)** Photograph taken from a helicopter showing the tree-line boundary between the windswept uplands and more vegetated lowlands. **(B)** Photograph taken from a helicopter of the De Pas River, showing the increased vegetation density, especially large trees in the lowland valleys, with treeless windswept uplands that can be seen in the distance. **(C)** Photograph from the ground showing the lack of vegetation, perched erratics, and bedrock outcrops typical of the upland clearings. **(D)** Photograph taken from the ground showing increased vegetation, lack of erratics, and till cover more prominent in the lowlands. A large lake, typical of the lowland regions can be observed in the background.

1.1.2 Bedrock Geology

The study area is just east of the Schefferville iron-ore district within the Labrador Trough (LT), a Paleoproterozoic (2.17 -1.87 Ga) belt of metamorphosed volcano-sedimentary rocks folded onto the Superior Craton during the New Quebec Orogen (NQO). The study area lies between the NQO and the Torngat orogen (Figure 1.4) and consists of three major domains: Rachel-Laporte (RL) in the west, George River (GR) centering the study area, and Mistinibi-Raude (MR) domain in the east (Sanborn-Barrie, 2016; Corrigan et al., 2018; Figures 1.4 and 1.5). The RL domain is a Paleoproterozoic (2.17 to 1.87 Ga) group of metasedimentary rocks, with interlocking blocks associated with Archean structural complexes belonging to the Superior Province (Wardle et al., 2002). The RL is bounded to the east by the Lac Tudor shear zone which separates the RL from the GR. The GR domain is dominated by the De Pas Batholith, which forms the topographic high north to south through the entire study area. The GR is comprised of Paleoproterozoic (1.837- 1.820 Ga) rocks and is considered to be a transition zone between the NQO to the west and the Torngat Orogen to the east (Lafrance et al., 2018). The GR domain is bounded to the east by the George River shear zone, which also marks the western boundary of the MR domain. The MR domain is a Neoarchean and Paleoproterozoic (2.3-2.5 Ga) suite of rocks largely composed of paragneiss and diatexite sequences, metavolcanic rocks, and gneisses (van der Leeden et al., 1990; Lafrance et al., 2018). The MR also contains numerous Mesoproterozoic intrusions, which form the eastern boundary of the study area (Figure 1.5).

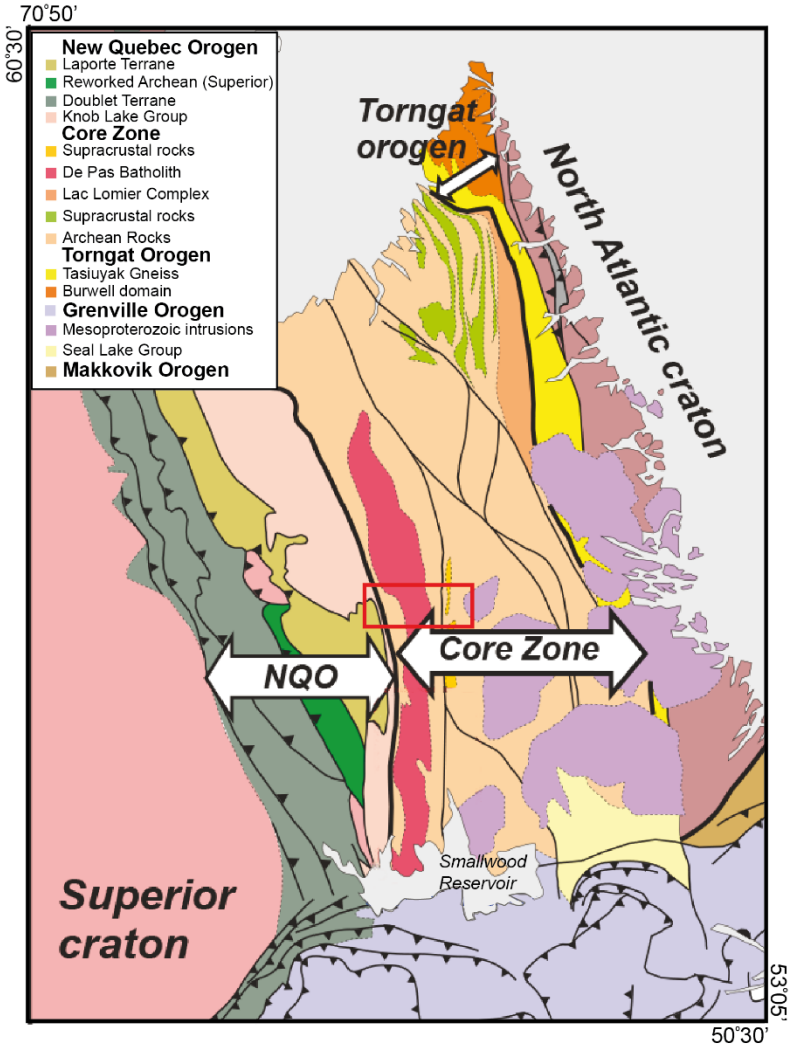

Figure 1.4. Regional bedrock units and major regional orogens. The study area (red box) straddles the border of the New Quebec Orogen (NQO) and the Core Zone. Modified from Sanborn-Barrie (2016).

1.2 **Previous work**

1.2.1 Surficial sediment mapping

Surficial sediments were previously only mapped at a scale of 1:1 000 000 for the region prior to this research project (Klassen et al., 1992; Fulton, 1995). This provincial scale map was produced using aerial photographs and was verified through fieldwork exercises (~1 to 5 sites per 100 km^2; Klassen and Thompson, 1993). Klassen and Thompson's (1993) sample density was highly influenced by the economic potential of the regions, with higher sampling densities around potential economic interests (i.e., Labrador Trough) and lower densities elsewhere, especially within Quebec. Landform mapping has been a greater focus in the region, specifically

targeting the ‘horseshoe divide’ and the Ungava Bay ice stream (Clark et al., 2000; Jansson, 2005). The horseshoe divide (or horseshoe unconformity; Clark et al., 2000) is the boundary between a group of radially southward oriented glacial and glaciofluvial landforms and a separate group of glacial and glaciofluvial landforms converging northward toward Ungava Bay (Figure 1.6). Detailed surficial landform mapping conducted by Jansson (2005) shows a paucity of landforms within the study area just west of the horseshoe divide, referred to as a ‘driftless region’ (red box- Figure 1.6). An explanation for the lack of landform formation and till production in the region was not proposed by Jansson (2005), however, its proximity to Dyke and Prest’s (1987) Ancestral Labrador Ice Divide, suggest a possible region of sustained cold-based conditions.

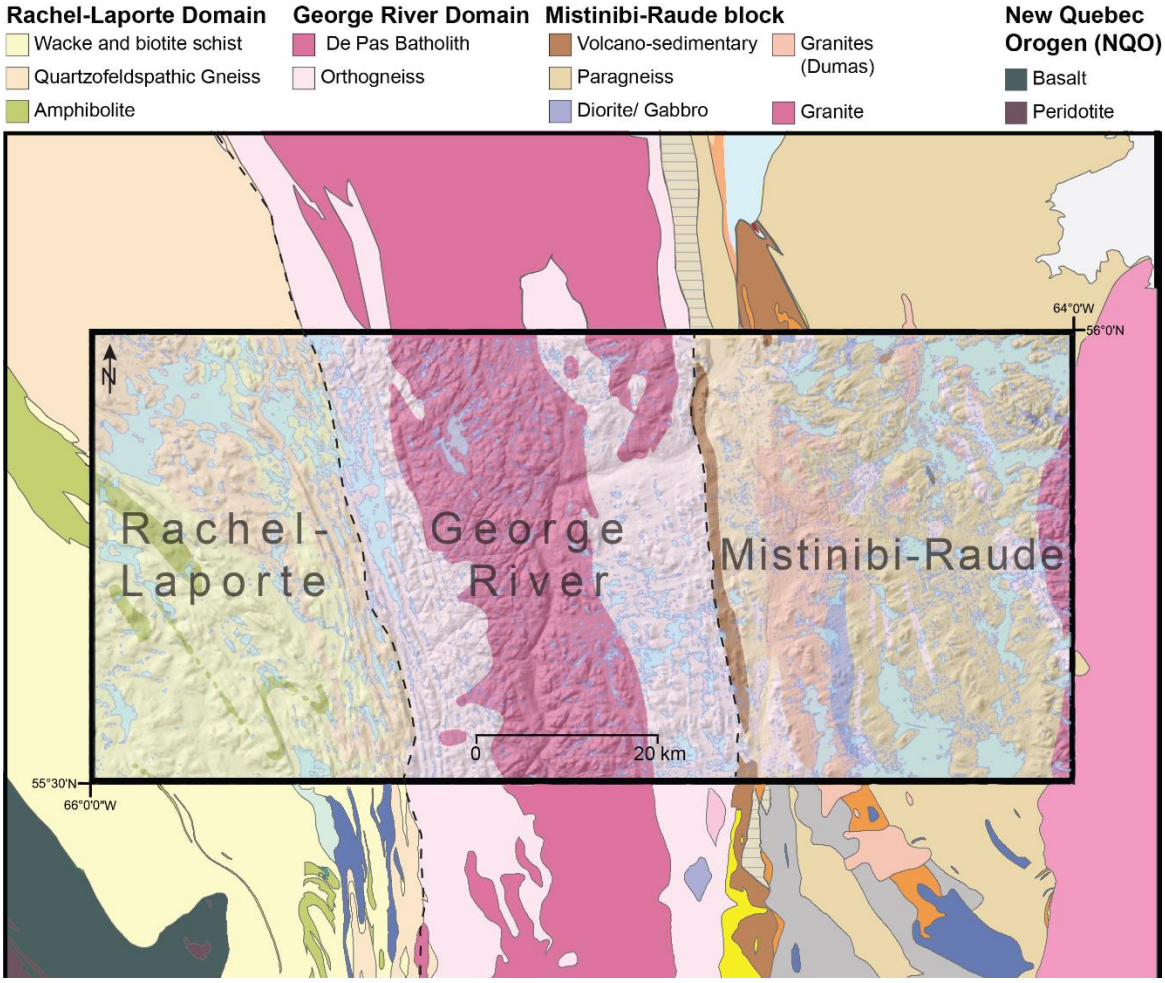

Figure 1.5. A more detailed bedrock geology map of the study area outlined (red box) in Figure 1.4, with surrounding bedrock units also shown. The study area contains three major bedrock domains, the Rachel-Laporte of the NQO in the west, and the George River (centre) and Mistinibi-Raude (east) of the Core Zone. The bedrock geology within the study area is underlain by hillshade DEM using SRTM data (30 m vertical and horizontal resolution, United States Geological Survey, 2014).

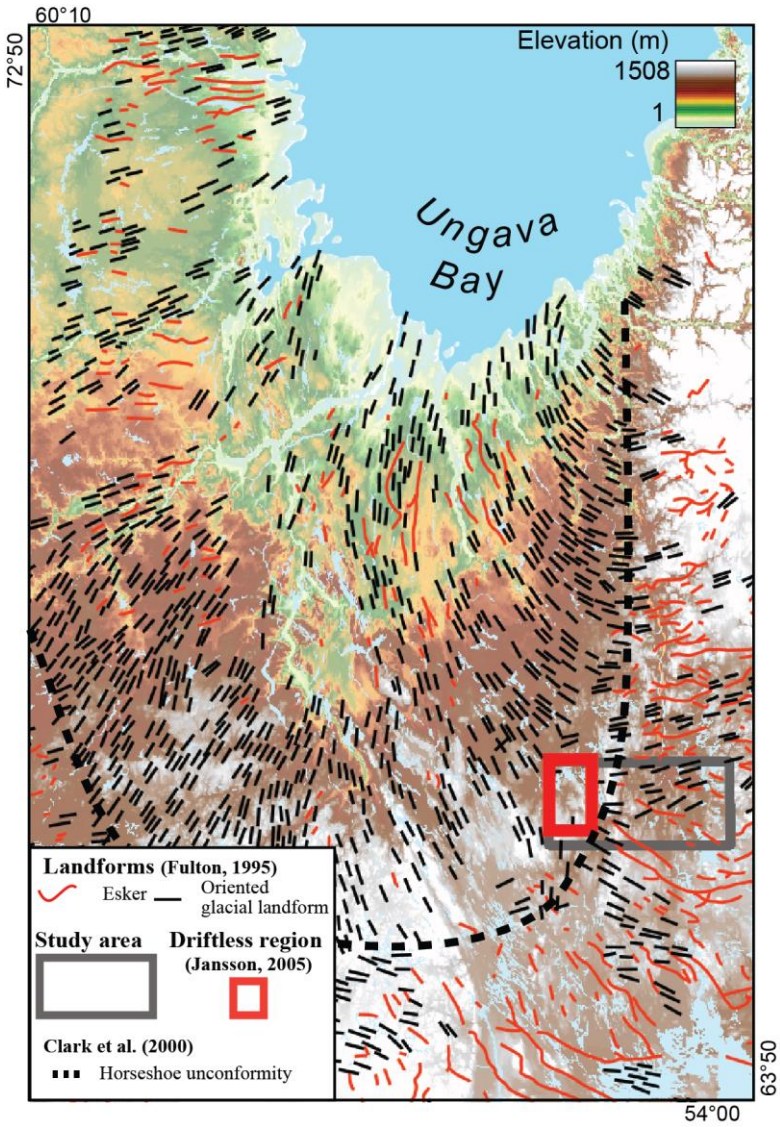

Figure 1.6. Regional landforms as mapped by Fulton (1995), showing a funneling of landform trending toward Ungava Bay and landforms fanning away from Ungava Bay. The transition between these landform orientations has been labelled the "horseshoe unconformity" (Clark et al., 2000). A region largely devoid of landforms and glacial sediment is also indicated (red box) as identified by Jansson (2005). The study area is outlined with a grey box.

1.2.2 Ice flow chronology

Striation measurements were first used as evidence of the existence of a dispersal centre that shifted from east of James Bay to northwest of the modern-day Caniapiscau Reservoir by Low (1896). Little work was done in the region until the first regional ice-reconstruction was done by Henderson (1959) who used aerial photographs and striation measurements around the town of Schefferville, Henderson (1959) to identify multiple ice-flow phases with unestablished chronologies. This complex ice-flow history was used as evidence by Ives (1960a) to suggest

that the region had been the location of a major ice dispersal centre. Hughes (1964) followed up on this work and conducted systematic mapping of landforms and striations around the Schefferville region. Through this work, Hughes (1964) interpreted the glacial record to indicate there was an ice-divide located somewhere over the LT, as erratics from the LT were observed more than 100 km west of their source (Hughes, 1964). More extensive landform mapping, striation measurements, and erratic dispersal train analysis was conducted in western Labrador by Klassen and Thompson (1987; 1993), Klassen et al. (1992) and Klassen and Paradis (1990) building on Hughes' (1964) ice-flow chronology.

Striation-based relative ice-flow chronology reconstruction by Veillette et al. (1999) around the Caniapiscau Reservoir expanded on earlier work by Klassen and Thompson (1993). When combining the two works, Veillette et al. (1999) identified an old ice flow trending northeast, that had a large geographical extent and originated somewhere in the highlands north of the St. Lawrence River with evidence of this ice flow found across Quebec and Labrador (covering ~ 700 km east to west- Veillette et al., 1999 their Figure 13). Veillette et al. (1999) also concluded the Ungava Bay swarm of the northward converging landforms was the youngest subglacial bed in the region, having formed during the onset of deglaciation around 10 ka. Further investigation by Clark et al. (2000) identified multiple palaeo-ice streams within the Ungava Bay "landform swarm", indicating a much more complex glacial history associated with the converging landforms than previously recognized. The complex landforms identified by Clark et al. (2000) were refined by Jansson et al. (2003) who interpreted the "Ungava Bay Landform Swarm" (UBLS) as the imprint of the dynamic Ungava Bay ice streams (UBIS) that is comprised of nine separate, although partially overlapping, converging flowsets.

Southeast of the Ungava swarm in the Lac aux Goélands (Whitegull Lake) region (Figure 1.2), Clarhäll and Jansson (2003) documented east-trending ice-flow indicators within a zone they interpreted to have been preserved under subsequent cold-based ice conditions. In their reconstruction, the ice-divide migrated north and occupied the region south of the UBLS, preserving relic glacial landscapes in that area. In stark contrast to previous reconstructions of a highly mobile ice divide, under mostly warm-based conditions, Clarhäll and Jansson (2003) attributed the landforms in the region to brief events within otherwise long periods of cold-based

conditions until final deglaciation. Detailed discussion and figures regarding ice-flow chronology for the QLD area is presented in Chapter 2.0.

1.2.3 Till sampling surveys

Klassen and Thompson (1993) conducted a large till sampling project using an irregular sampling grid largely focusing on economic bedrock targets across central Labrador, including the current study area. Their till sampling was focused on the western portion of Labrador, with only a few samples (n=5) collected within the current study area. This till sampling program was intended to act as a broad framework for future exploration and, as such, had a low sampling density (tens to hundreds of kilometers). Klassen and Thompson (1993) identified five ice-flow phases and suggested glacial processes re-entrained erratics during several of these ice-flow phases. Klassen and Thompson's (1993) research yielded significant insights into the dispersal patterns of specific bedrock lithologies using geochemistry and clast lithology dispersals. Numerical quantities were not published, and only qualitative descriptions of abundances were used (i.e., not found, rare, present, common, and abundant). Clasts were also classified using the same qualitative scale, however only ~50 clasts were analyzed for each till sample with a cumulative weight of only 10 g. Follow up work by Klassen (1999) identified the best elemental targets for geochemical dispersal mapping from the LT and indicated dispersal distance in excess of 120 km from the source. A detailed discussion of previous till sediment sampling surveys is presented in Chapter 4.

1.3 Current understandings and outstanding knowledge gaps

Although the general location of the Quebec-Labrador ice-centre has been established, large uncertainties surrounding its migration and subglacial thermal conditions persist. This problem largely stems from the issues outlined below:

1. Discrepancies remain unresolved between different regional ice flow reconstructions and their associated subglacial conditions, with important implications for the study area (Veillette et al., 1999; Clark et al., 2000; Jansson et al., 2003).

2. The driftless region identified as lacking glacial landforms by Jansson (2005), was previously mapped by Fulton (1995) and Klassen et al. (1992) as till covered.

3. A discrepancy also exists between numerical models and field observations in core regions of the LIS. In some of these regions, numerical models predict low probabilities of warm-based conditions (Fig. 1.1B; Tarasov and Peltier, 2007; Stokes et al., 2012), whereby basal sliding and erosion in the models are suppressed (Hildes et al., 2004; Melanson et al., 2013). In contrast, field research and surficial mapping have revealed widespread evidence of warm-based conditions and sliding from these same inner-ice sheet regions, especially in the Keewatin sector (e.g., McMartin and Henderson, 2004; Hodder et al., 2016). For the QLD, the area of very low probability of warm-based conditions is smaller than for the Keewatin (Fig. 1.1B) and lies within an understudied region which includes the study area of this thesis. There is thus limited documented evidence to support either warm-based/sliding or cold-based conditions.

4. The effect of recently identified paleo-ice streams (Margold et al., 2015; Paulen et al., 2017; Rice et al., 2020) on inner-ice sheet regions, particularly the influence on the position of local ice-divides, remains unknown.

5. All of the above points have implications for till provenance/dispersion in the region, which in turn, limits the ability to link subglacial processes from the landform record to the sedimentary evidence.

1.4 Aims of the thesis

A lack of robust geoscience data within the study area has created contradicting ice-flow chronologies and conflicting models of subglacial conditions throughout glaciation. This lack of data has resulted in paleoglaciological models that oversimplify glacial conditions making them difficult to implement for more detailed geoscience studies. Additionally, several palaeo-ice streams have been recognized and are now considered critical components of the evolution of the LIS (Clark et al., 2000; Greenwood and Clark, 2009; Ross et al., 2009; Margold et al., 2018). However, it is still unclear how far paleo-ice streams propagate into the ice sheet and how their

catchment zones affect the interior regions, such as the configuration of ice divides and their stability over time (e.g., Hodder et al., 2016).

This thesis uses detailed field observations and measurements in conjunction with remote-sensing data and till compositional data to reconstruct the paleo glaciology of northeastern Quebec, which is thought to have been influenced by ice-divide conditions. Although this thesis focuses on a relatively small portion of the interior region of the QLD, it still allows important insights into the overall evolution of the QLD, with implications for other similar regions, offering a unique window into the dynamic record of the much larger QLD. This thesis has multiple objectives with the end goal of providing a robust understanding of how an inner-ice sheet region within the QLD evolved throughout glaciation. Specifically, this thesis will:

1. Resolve the conflicting ice flow chronologies, which have previously mainly been extrapolated for the study area from surrounding regions, by refining surficial mapping, documenting and interpreting outcrop-scale ice flow measurements across the study area, and by using remote sensing data. Additionally, the timing of deglaciation within the study area will be confined and placed in a regional deglacial context using in situ cosmogenic nuclide analysis and luminescence methods.
2. Characterize the subglacial regime that evolved during each ice-flow phase through its surficial signature (e.g., landscape analysis, till weathering).
3. Characterize the dispersal patterns associated with the established ice flow chronology and the associated subglacial conditions across the study area.

1.5 Research design and methods overview

To develop an understanding of the complex glacial history of the inner ice sheet region of the QLD, its subglacial evolution, and the resulting sediment dispersal patterns, a multi-faceted investigation using different proxy data from the erosional and depositional records were required. This thesis used a combination of remote sensing, field-based, and laboratory methods

that allowed for a more robust analysis of the study area. Each of these methodologies is outlined below

1.5.1 Establishing the ice flow chronology and glacial evolution

Surficial mapping, including outcrop-scale ice-flow measurements conducted during fieldwork, is an effective way of producing geoscience data can be used during ice-flow reconstructions. However, within many inner-ice sheet regions, only low-resolution surficial maps exist, and striation measurements exist only for a few locations and are usually uncorrelated to larger ice-flow reconstructions (i.e., landforms-based reconstructions). Therefore, higher resolution surficial maps and outcrop-scale ice flow measurements were required for this thesis.

1.5.1.1 Surficial Mapping

Detailed surficial maps were unavailable for the study area, with only regional-scale (1: 1 000 000) maps published prior to this study. Surficial maps allow for a more holistic evaluation of the glacial evolution of an area, in that the maps identify features from not only glacial periods but post-glacial processes as well (i.e., glacial lake beaches and lateral meltwater channels). Additionally, the identification of post-glacial features can highlight regions that might be suitable for collecting samples that can be used to constrain the timing of ice-margin retreat (i.e., optically stimulated luminescence (OSL) or ^{10}Be exposure). Surficial maps were created using black and white aerial photographs (1:60 000 scale) obtained from the National air photo library in Ottawa, Canada. Glacial features were identified through stereoscope visualization that allows for a three-dimensional examination of the landscape. Three-dimensional visualization enhances the accuracy of surficial unit separation based on vegetation, topography, reflectivity, and texture of the surface (Mollard and James, 1984). This new mapping effort increases the resolution of the surficial geology of the study area by ~ 17 times.

1.5.1.2 Relative ice-flow chronology

Ice-flow directions were first determined using oriented glacial landforms (e.g., crag-and-tail forms, drumlins, and large-scale glacial lineations) identified through both aerial photographs and remote sensing examination. Landsat 8 satellite image mosaics were coupled with digital elevation models (DEM) from Canadian Digital Elevation Data (www.geobase.ca- 30 m vertical and horizontal resolution) following procedures outlined by Clark et al. (2000) and Stokes and

Clark (2001). These landform features often form flowsets that crosscut each other allowing for the development of relative age chronology at the landscape scale (e.g., Kleman et al., 1997; Clark et al., 2000). However, flowsets do not always clearly overlap and some ice-flow phases are not always preserved at the landscape scale. Therefore, remote sensing analysis was supplemented with outcrop-scale ice-flow indicator measurements, including striations, grooves, rat tails, and mini roches moutonnées (e.g., McMartin and Paulen, 2009). Following the methodology of Klassen and Bolduc (1984), Parent et al. (1995), Veillette and Roy (1995), Veillette et al. (1999) and Paulen et al. (2013) the ice-flow chronology was determined through lee side preservation, where ice-flow indicators on the lee side position are assumed to indicate earlier (older) ice-flow events. The azimuths of the striae and grooves were determined from outcrop shape and lee side plucking features (Rea et al., 2000). The relative chronology established from outcrop-scale indicator analysis is then compared with the surrounding landform record to establish a more relative age chronology of all observed multi-scale ice-flow indicators.

1.5.1.3 Constraining ice-margin retreat

Understanding the pattern of ice margin retreat for large ice sheets provide important details in reconstructing the complete glacial history of the region. Additionally, having robust data for ice margin retreat provides a framework for how large ice sheets behave during deglaciation. One method for constraining the timing and pattern of ice margin retreat is to determine the timing of deglaciation in different location. Prior to this research, no such constraints existed for the study area. The lack of useable material for ^{14}C data within the study area requires the use of optically stimulated luminescence (OSL) or ^{10}Be exposure age dating. OSL and ^{10}Be have proven to be effective methods in determining deglacial ages in a large variety of previously glaciated landscapes (Atkin, 1998 and references therein, and Dunai, 2010 and references therein, respectively).

1.5.1.4 OSL age determination

OSL, hereafter referred to as optical dating, has been used successfully to date the formation of glaciolacustrine beaches (e.g., Lepper et al., 2013; Hickin et al., 2015). The utility of this method depends on sampling littoral facies with depositional settings that expose feldspar grains to sufficient sunlight before final deposition and subsequent burial. Therefore, to

further constrain the timing of deglaciation coarse-to-fine-grained sandy-beach sediments were targeted for optical dating as they contain sand-sized particles that are more likely to have experienced complete resetting prior to burial (Fuchs and Owen, 2008). Samples were collected by digging vertically into the beach sediments, taking note of the stratigraphy and facies, to access sediment suitable for optical dating. Elevation data for each site was collected with a hand-held GPS. Samples were collected following procedures outlined by Aitken (1998) and Lian (2013). Glaciofluvial outwash sediments have a lower bleaching potential than beach or dune deposits (Fuchs and Owen, 2008), but have been used successfully in other studies (e.g., Klasen et al., 2006; Alexanderson and Murray, 2007; Bøe et al., 2007).

Samples were submitted to the Luminescence Dating Laboratory, University of the Fraser Valley, Abbotsford, British Columbia, where optical dating analysis was conducted on sand-sized K-feldspar grains. The equivalent dose (D_e) of each sample was measured using the single-aliquot regenerative-dose (SAR) protocol (Wintle and Murray, 2006). All ages were corrected for anomalous fading using the correction model of Huntley and Lamothe (2001). Ages were calculated using the Central Age Model (CAM) weighted mean D_e value (Galbraith et al., 1999) and the environmental dose rates ('total' dose rates). Where over dispersion values were high, the Minimum Age Model (MAM) of Galbraith et al. (1999) was also used to obtain age estimates from the most thoroughly bleached grains.

1.5.1.5 ^{10}Be exposure ages

Glacially eroded, well-polished, bedrock and perched glacial erratics have proven to be good targets for determining cosmogenic ^{10}Be exposure ages in determining when a landscape became ice free (Dunai, 2010 and references therein). Therefore, ^{10}Be exposure age determination was selected as an appropriate methodology for constraining ice margin retreat within this study area. Samples collected from 2015 were submitted to the PRIME Lab at Purdue University for physical processing, chemical processing, and ^{10}Be measurement. Samples collected in 2016 were submitted to the Paleoclimate Lab at University at Buffalo for physical and chemical processing, while ^{10}Be measurement was carried out at Lawrence Livermore National Laboratory. Samples were crushed, sieved, and then subjected to a chemical treatment designed to isolate quartz following procedures outlined by Kohl and Nishiizumi (1992).

The results were blank corrected and the $^{9}Be/^{10}Be$ ratios from AMS measurements were used to calculate ^{10}Be concentrations. The ^{10}Be concentrations were used with the University of Washington's CRONUS-Earth online calculator (V.3) (https://hess.ess.washington.edu/) for exposure age determination (Balco et al., 2008), using the Baffin Bay/Arctic ^{10}Be production rate (Young et al., 2013) and the nuclide and time-dependent LSDn scaling scheme (Lifton et al., 2014). For each sample, the latitude, longitude, thickness of the sample, and density of the sample were entered as reported from field observations. Densities of the granitic outcrops were approximated to the density of the rock's most common mineral, quartz (2.65 g/cm^3). No shielding corrections were required as the samples were collected from topographically unobstructed bedrock outcrops. Elevation data for the samples were adjusted to reflect the local isostatic rebound following procedures outlined by Ullman et al. (2016) and Cuzzone et al. (2016). Isostatic rebound data were obtained from the ICE-6G (VM5a) model (Argus *et al*., 2014; Peltier et al., 2015). Uplift rates from the estimated timing of local deglaciation (7.5 ka) to present day were averaged, yielding a correction of 61 meters, which was subtracted from each sample location elevation. Cuzzone et al. (2016) and Ullman et al. (2016) demonstrated that the atmospheric effects created by a retreating ice margin had little to no impact on the local air pressure, and thus atmospheric effects were not accounted for in this study. In this thesis all ^{10}Be results as "apparent ages" due to uncertain amounts of cosmogenic nuclide inheritance (e.g., Nishiizumi et al., 1989; Davis et al., 1999; Briner et al., 2003, 2006; Ullman et al., 2016). The level of inheritance for each sample has been estimated based on its variation from regional deglacial ages (Dubé-Loubert et al., 2018) and by our OSL ages.

1.5.2 Reconstructing the evolution of subglacial conditions

Basal ice/sediment mobility has been estimated in Canadian Shield terrain through the analysis of subglacial erosional and depositional proxies. A commonly used erosional proxy for this type of analysis is lake density across bedrock and till veneer regions. However, within the study area, surficial maps indicate that bedrock and till veneer covers only about 46% of the study area. The remaining 54% of the study area is covered with till blanket and other surficial sediments that mask the underlying scoured bedrock surface. Lakes at the surface in these areas of thicker sediments occur in depressions that formed through a variety of processes (e.g., kettle lakes or thermokarst lakes) and are thus not reliable indicators of subglacial erosion due to a mobile basal ice/sediment layer. Therefore, proxies other than bedrock erosion, such as till blanket and elongated landforms (e.g., drumlins) on till blanket need to be used across these areas of thicker subglacial sediments.

To conduct a uniform analysis across the study area, 2.5 x 2.5 km cells were created in ArcGIS (v.10.3.1) to create a grid overlay that would allow for a comparison between the lake and landform proxies. This grid size has proven effective in other studies with similar geospatial resolution (e.g., Ebert, 2015). It is important to note that about 26% of the study area still needed to be excluded from our analysis because it dominantly consists of proglacial and postglacial surficial sediments (Rice et al., 2017a, 2017b) that do not reflect subglacial processes. Grid-cells containing >50% of proglacial and postglacial surficial sediments were thus masked and not considered further in the analysis. The remaining cells were then categorized based on lake spatial density, lake area, streamlined landform spatial density, streamlined landform elongation, and till blanket. The ggplot2 package (Wickham, 2009) within the R statistical environment (R Core Team, 2015) which is commonly used for geoscience data analysis (Grunsky, 2002), was also used to plot results for further analysis and interpretation of the data. The following subsections describe in more detail how these different proxies of subglacial dynamics that were mapped and analyzed

1.5.2.1 Lake density and lake area

Lake spatial density was measured using two different methods: 1) Calculation of each lake's central point and totaling the number of centroids per 6.25 km^2 cell, and 2) calculation of the total area of each cell covered by a lake (i.e., % of the 6.25 km^2 cell occupied by a lake). The

two techniques were applied together because they may reveal patterns associated with different types of subglacial bedrock erosion, different bedrock lithology, or structural effects (Phillips et al., 2010; Alley et al., 2019; Cook et al., 2020).

1.5.2.2 Landform density and elongation

In this study area, elongated features of glacial origin occur over bedrock, till veneer, and till blanket areas. Therefore, an analysis that considers not only bedrock-controlled lakes, but also the elongated bedrock and bedrock-cored features (e.g., whalebacks or rock drumlins), as well as till-cored drumlinoid landforms and till blanket areas (28% of the study area) is likely to provide more complete and thus more useful information about subglacial conditions and overall dynamics across a larger proportion of the study area. It is particularly useful for subdividing till blanket areas between 'low-warm' and higher classes.

Landform density was calculated using the same regular 2.5 km raster grid used for lake analysis, to allow for an equal comparison between the methods. The represented values correspond to the number of landforms per each cell (i.e., landforms per 6.25 km^2). To obtain landform elongation measurements, polygons first needed to be created. Polygons were outlined manually using a multi-directional hill-shade with a vertical exaggeration of 4X from the source DEM. The ArcGIS (v.10.3.1)'s "minimum bounding geometry" tool was used to fit each polygon with a minimum bounding rectangle to calculate the elongation of the landform (elongation = length of minimum bounding rectangle divided by the width of minimum bounding rectangle). The average elongation value was then calculated for each cell of the same raster grid used for landform density.

1.5.2.3 Constraining the GIS analysis/interpolation with the chemical index of alteration and ^{10}Be abundance data

It is assumed that areas of limited net glacial erosion/deposition (low to no ice/bed mobility) related to the last glaciation will have a higher degree of weathering (higher chemical index of alteration (CIA) value) and higher cosmogenic isotope abundance than the warm-based zones of higher ice/bed mobility and erosion (e.g., Staiger et al., 2006; Refsnider and Miller, 2010; Corbett et al., 2016). The bedrock and till across the different zones are further examined using a weathering index (CIA) and cosmogenic inheritance as proxies for the erosional vigour exerted on the landscape.

The CIA of till/regolith matrix has been used on Baffin Island to characterize areas affected by sustained cold-based conditions (Refsnider and Miller, 2010). When employed in concert with other proxies, regions of high CIA values (>70) on Baffin Island correlate to regions of low lake spatial density and high cosmogenic exposure inheritance (elevated ^{10}Be abundances beyond postglacial exposure) in regolith and these were interpreted as zones of low erosion or inherited CIA values associated with sustained cold-based (low erosion) conditions (Refsnider and Miller, 2010). ^{10}Be abundances have also been successfully used as a proxy for estimating subglacial in the Cordilleran (Stroeven et al., 2010), Fennoscandian (Fabel et al., 2002; Linge et al., 2006), and Greenland (Beel et al., 2016; Corbett et al., 2016). ^{10}Be accumulates within quartz at the surface of the Earth during periods of exposure to cosmic radiation primarily through the spallation reaction with oxygen within quartz (Lal, 1991; Gosse and Phillips, 2001). The rate at which ^{10}Be accumulates (the production rate) largely depends on latitude, elevation, shielding from cosmic rays, and radioactive decay of ^{10}Be (Dunai, 2010). During glaciation, subglacial bedrock surfaces are shielded from cosmic radiation and are exposed during interglacial or non-glacial periods. Therefore, without any type of shielding (e.g., ice, snow, or sediment), shallow (<2 m) quartz grains within a glaciated outcropping bedrock surface are exposed to cosmic radiation and ^{10}Be is produced. If glacial erosion was limited throughout the last glaciation and thus did not remove pre-glacial ^{10}Be, the bedrock surface would contain an amount of ^{10}Be inherited from a previous interglacial in addition to the recent post-glacial accumulation. Therefore, if all other production factors remain constant, the only major effect on ^{10}Be abundance will be the erosion of the bedrock surface during glaciation, which provides a qualitative proxy to assess the vigour of glacial erosion, and thus the net effect of the subglacial thermomechanical regime throughout glaciation.

For this thesis both bedrock and till samples were collected, as the till has been sourced from a wider area than is represented by a bedrock outcrop; therefore, the bedrock gives local information whereas the till should provide insights into inheritance from the surrounding region (e.g., Staiger et al., 2006). Areas that have experienced less overall erosion and whose till is immature (short-transport) should thus have a high paired inheritance. Areas of local low bedrock erosion but with relatively long-transport (englacial) till deposited by meltout should show more discrepancy between bedrock and till results.

1.5.3 Characterizing dispersal

The composition of till dispersed throughout glaciation (i.e., till matrix geochemistry, indicator minerals, and clasts) provide important constraints on models of subglacial processes and sediment transport (Melanson et al., 2013). Additionally, characterizing the dispersal of glacial sediments provides important insights into how ice sheets, erode, entrain, and disperse glacial materials, which remains largely uncharacterized, especially within inner-ice sheet regions. Improved understanding of these mechanisms will help mineral exploration exercises in such terrains.

1.5.3.1 Sample collection

To characterize the dispersal of glacial sediments across the study area, till samples were collected from across the study area. Till samples were collected from frost boils (within regions of active permafrost); otherwise, samples were collected from hand-dug pits through the naturally developed soil profile to collect C-horizon (unoxidized) till. Samples were collected from *in situ* till assumed to be the direct result of glacial processes and not by other secondary processes (e.g., slumping). The results used in this manuscript are a portion of a larger database collected as part of Natural Resource Canada's Geo-mapping for Energy and Mineral (GEM 2) Hudson-Ungava Surficial program (McClenaghan et al., 2017).

1.5.3.2 Geochemical analysis

Numerous studies have used till-matrix geochemistry in order to evaluate ice-flow chronology and its effect on glacial dispersal (McClenaghan et al., 2002; Plouffe et al., 2016; Kelley et al., 2019), which has indicated it can produce useful data in glacial reconstructions. For this thesis, till matrix geochemistry samples were shipped to the Sedimentology Lab at the Geological Survey of Canada (Ottawa) for sample preparation. The samples were then split into multiple aliquots for grain size analysis, Munsell colour determination, and till matrix geochemistry analysis. Another aliquot of <0.063 mm was submitted to Bureau Veritas Minerals Canada Limited (Vancouver) for analysis of a suite of major, minor, and trace elements through total digestion (lithium metaborate/tetraborate fusion followed by nitric acid total digestion; BV LF200 package on 0.2 g) followed by Inductively Coupled Plasma-Mass Spectrometry (ICP-MS) and Inductively Coupled Plasma Emission Spectrometer (ICP-ES) determination. The <0.063 mm was selected as it allows for relatively quick, inexpensive separation (Levson, 2001) and is a

size fraction that ore minerals are easily comminuted to over relatively short glacial transport and this fraction contains phyllosilicates that will scavenge cations released during weathering (Shilts, 1995). These laboratory procedures are summarized in Figure 1.6.

1.5.3.3 Indicator mineral identification

Unfortunately, geochemical data can become diluted to background levels quite rapidly with continued down-ice commutation, or, may be indistinguishable from similar surrounding bedrock lithologies. Because of this, indicator minerals have been used to supplement drift prospecting exercises (McClenaghan and Paulen, 2018). Therefore, for this thesis, the two methods were combined, to allow for a more robust characterization of dispersal patterns from the different bedrock lithologies in and around the study area (Figure 1.4). Till samples collected for indicator mineral analysis and were shipped to Overburden Drilling Management Limited (ODM), Ottawa for indicator mineral separation and analysis. The minerals separated during processing were examined by trained personnel using binocular microscopes to identify sulphide minerals, gold grains, platinum group minerals (PGMs), and silicate minerals as well as ODM's suite of magmatic or metamorphosed massive sulphide indicator minerals (MMSIM®, Averill, 2001). A limited number of identified minerals were verified with a scanning electron microscope.

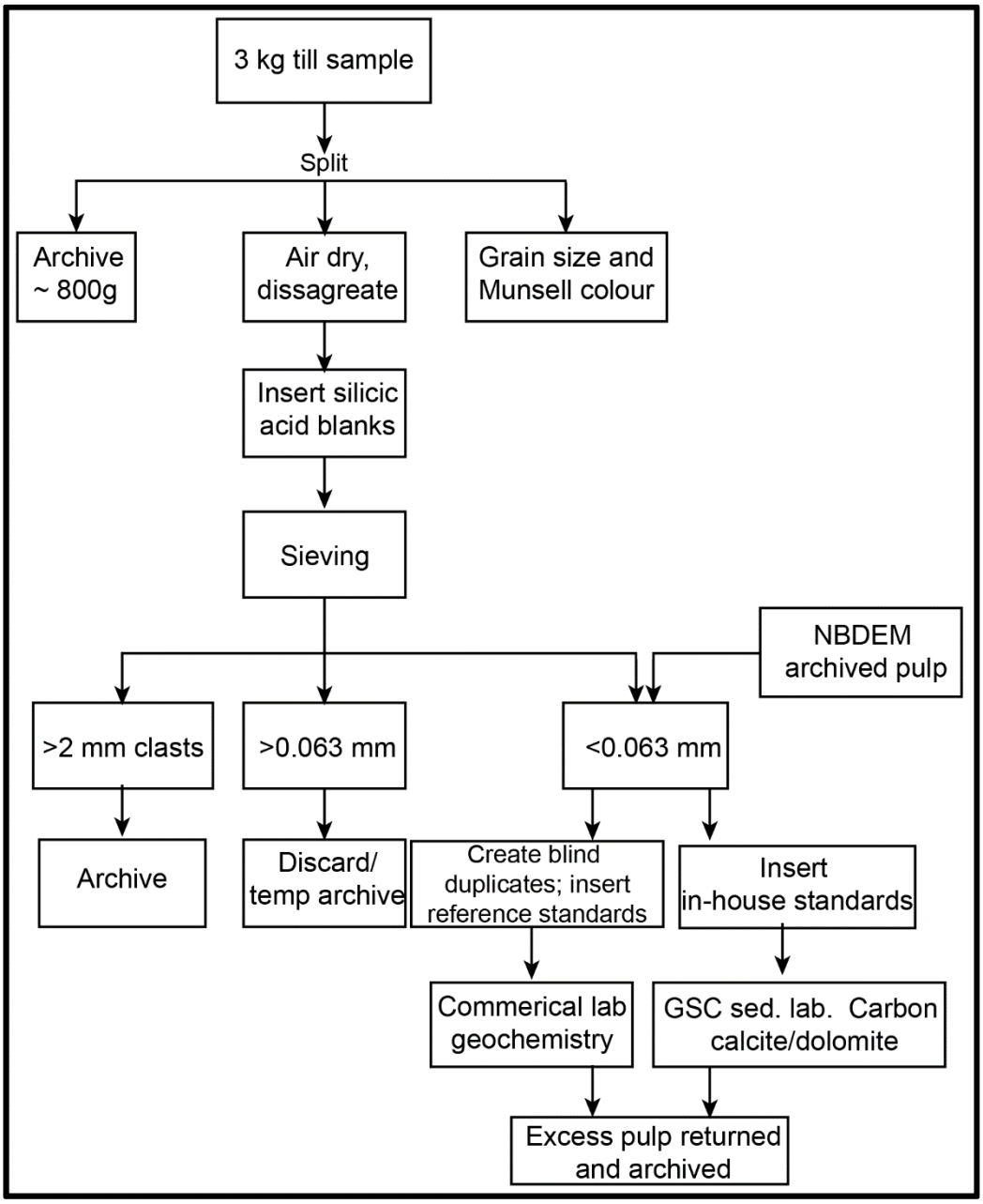

Figure 1.7. Flowchart outlining sample processing and preparation of collected till samples at the Geological Survey of Canada Sedimentology Lab, Ottawa. Modified from McClenaghan et al. (2013).

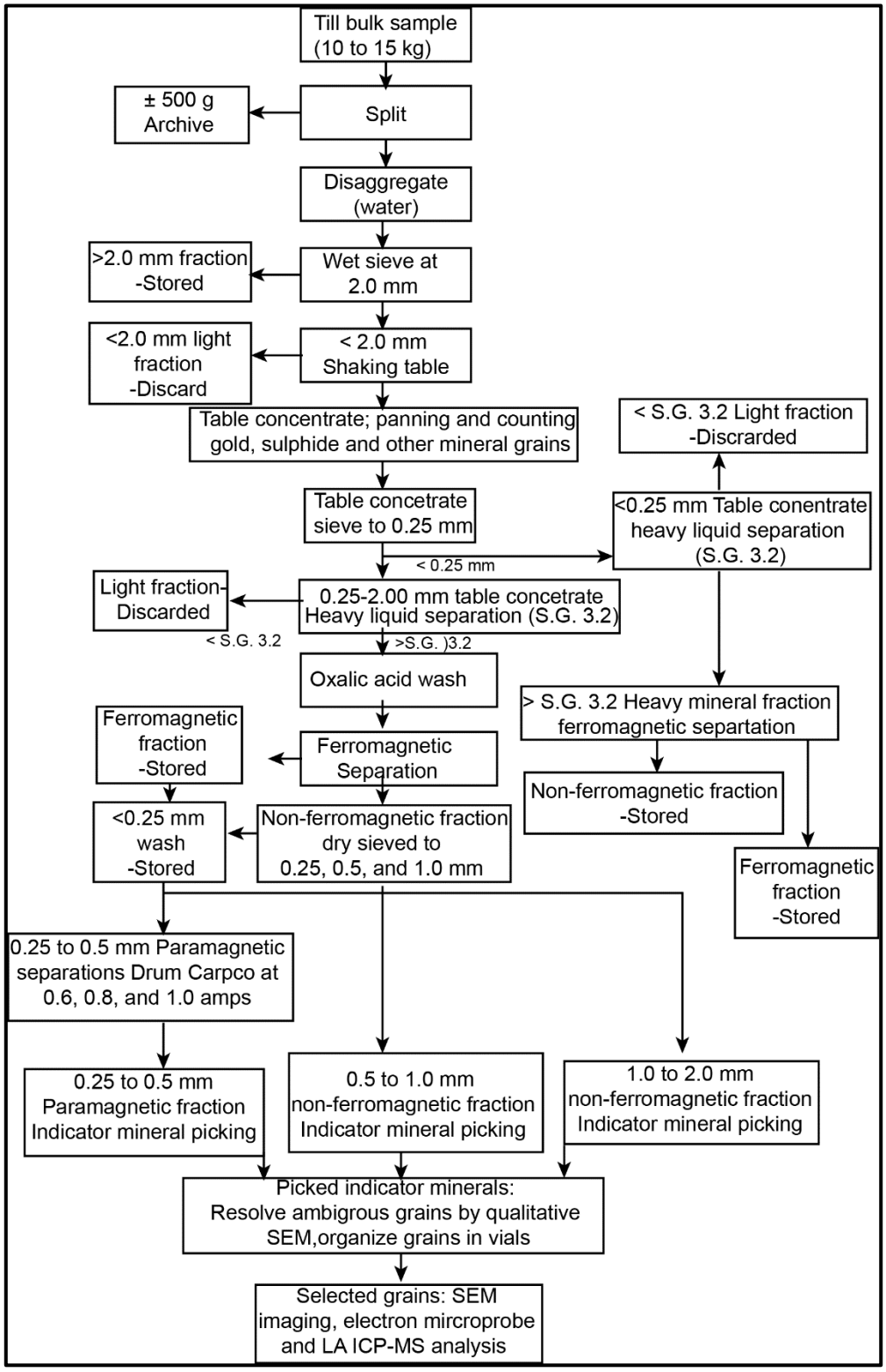

Figure 1.8 Flowchart outlining sample processing and preparation of collected till samples at the Geological Survey of Canada Sedimentology Lab, Ottawa. Modified from McClenaghan et al. (2013).

1.5.3.4 Clast lithologies

Clasts identified from subglacial tills have been utilized to determine dispersal patterns in regions across Canada, as they identify dispersal from a single known bedrock lithologies (Klassen and Thompson, 1993; McClenaghan et al., 1996; Trommelen et al., 2013). Therefore, clast identification was included to enhance the dispersal patterns identified through geochemical and indicator mineral analysis. The > 2.0 mm fraction separated during indicator mineral preparation was washed in a light acid bath and retained for clast lithology analysis. Clasts were grouped into one of 13 lithological categories using a binary microscope. To simplify the spatial organization of the interpretation, the 13 lithologies were grouped by their larger domains and classified as either RL (metasedimentary, Laporte (leucogranites with pink weathering), leucogranite, and quartzites), GR (felsic intrusive and vein quartz), MR (mafic intrusive, intermediate intrusive, ultramafic, and Mistinibi (multiple lithologies from the Mistinibi unit, including paragneiss, volcano-sedimentary, and gabbro) or Labrador Trough (LT; iron formation and metavolcanic); See Figure 1.5 for bedrock domains. The latter does not outcrop in our study area, but glacial clasts of that lithology were observed in till near our study area (Klassen and Thompson, 1993). All clasts that could not be associated with a known bedrock unit were placed under the “other” classification.

1.6 Thesis format

This thesis is comprised of three journal manuscripts (Chapters 2, 3, 4; summarized below) with an introductory chapter (this chapter) and a concluding chapter (Chapter 5) summarizing the findings of all three manuscripts.

Chapter 2 presents the analysis of ice-flow indicators both at landscape and outcrop-scales, with new deglacial age data that further confines the retreat of the regional ice-margin during deglaciation. Through this analysis, an ice-flow chronology is developed that resolves the conflicting ice flow hypotheses that were previously proposed (Veillette et al., 1999; Clark et al., 2000; Clarhäll and Jansson, 2003). The age data are used in conjunction with other regional age data to confine the timing of deglaciation within the region. Chapter 2 is published in the *Journal of Quaternary Science* (Rice et al., 2019). A large portion of the work was conducted by the author of this thesis with critical research design and recommendations by the thesis supervisor (Martin Ross, second author) and third author (Roger Paulen). The fourth (Samuel Kelley) and fifth (Jason Briner) authors assisted with the ^{10}Be analysis and interpretation. The final two authors (Olav Lian and Christina Neudorf) assisted with the analysis and interpretation of the optically stimulated luminescence data. As lead author, I was responsible for writing and revising the manuscript, but all co-authors provided useful comments and suggestions on the manuscript. Surficial geology maps (1:100 000 scale) of the study area have also been published (Appendices S1.1 and S1.2) by the Geological Survey of Canada (Rice et al., 2017a, 2017b) and are coauthored with Roger Paulen (GSC) and the thesis supervisor (Martin Ross). As principal mapper, I did all the aerial photography interpretation and related line work, but the co-authors provided guidance and recommendations at all stages, from fieldwork to final revisions of the maps. The maps bring critical surficial geology information that has been useful in addressing all the thesis objectives.

Chapter 3 uses a number of landscape proxies of glacial dynamics (e.g., lake density and surface area, glacial landform density and elongation) from remote sensing data and the newly produced surficial geology maps to map spatial patterns of relative subglacial dynamics. Results are then compared to the ice flow record analyzed in Chapter 2, as well as to CIA values from till matrix geochemistry data and *in situ* cosmogenic isotope data from bedrock outcrops and till. The latter two datasets are also considered proxies of subglacial erosion and are used as an independent measure of subglacial dynamics that are then compared to the GIS-based analysis. This chapter has been

submitted as a journal paper to *Earth Surface Processes and Landforms* (Rice et al., *submitted)*. Similar to Chapter 2, a large portion of the work was conducted by the author of this thesis with critical research design and recommendations by the thesis supervisor (Martin Ross, second author) and third author (Roger Paulen). The fourth (Samuel Kelley) and fifth (Jason Briner) authors assisted with the ^{10}Be analysis and interpretation. As lead author, I was responsible for writing and revising the manuscript, but all co-authors provided useful comments and suggestions on the manuscript.

Chapter 4 builds on the findings of Chapter 2 and Chapter 3, using till compositional data from till samples collected across the study area to characterize sediment dispersal patterns and analyze them within the context of the ice-flow and glacial dynamics reconstructions of Chapters 2 and 3. The data presented in this chapter are a subset of the Geological Survey of Canada's publicly available data (Rice et al., 2017c; McClenaghan et al., 2017). Again, the majority of the work was conducted by the author of this thesis with guidance from the thesis supervisor (Martin Ross) and colleagues at the Geological Survey of Canada (Roger Paulen and Beth McClenaghan). At the time of writing, this manuscript had not yet been submitted to an academic journal.

Chapter 5 summarizes the findings of the three preceding chapters, placing the results within the larger context of the Q-L sector of the LIS. This chapter highlights the main contributions of the thesis and insights into how the findings have improved the overall understanding of how an inner region of the QLD developed.

2 Chapter 2: Refining the ice-flow chronology and subglacial dynamics across the migrating Labrador Divide of the Laurentide Ice Sheet with constraints on deglaciation

2.1 Overview

It is now recognized that the Laurentide Ice Sheet was characterized by a dynamic and complex polythermal base. However, important data and knowledge gaps have led to multiple contrasting reconstructions in certain areas such as the Labrador Ice Divide. In this study, detailed fieldwork was conducted at the southeastern edge of a major landform boundary, referred to as the horseshoe unconformity, to resolve the relative ice-flow chronology and further constrain the evolution of the subglacial dynamics including the migration and collapse of the Labrador Ice Divide. Specifically, regional surficial mapping and the analysis of 94 new outcrop-scale ice-flow indicators were used to develop a relative ice-flow chronology. ^{10}Be exposure ages were used with optical ages to constrain the timing of deglaciation within the study area. Locally, four phases of ice-flow were identified. The oldest ice-flow phase was a regional flow to the northeast (Flow 1) and is well-preserved in the eastern portion of the study area. The preservation of this older flowset requires a shift to non-erosive subglacial conditions over the area associated with the development of an ice divide. Flow 1 was followed by a spatially restricted ice-flow phase (Flow 2) towards the northwest which is correlated to the UBIS. The drawdown associated with the inland propagation of the palaeo-ice stream catchment likely pulled the ice divide towards the west. The new ice divide location preserved Flow 2 features in the northwest part of the study area and is associated with Flow 3's east-trending indicators and eskers. Finally, the youngest flow phase (Flow 4) is limited to sparse fine striations within and around the regional uplands. The new optical ages and ^{10}Be exposure ages add to the regional geochronology dataset, which further constrains the timing of ice margin retreat in the area to around 8.0 ka.

2.2 Introduction

Reconstructing past ice sheets, including their thickness, the extent of land they covered at different times, and the dynamic evolution of their dispersal centres is critical to understanding how ice sheets evolve and how they shape glacial landscapes. Both empirical and numerical reconstructions can help predict how current ice sheet melting may influence global temperatures, how global temperatures might affect melting rates, and their influence on global sea levels

(Napieralski et al., 2007; Löfverström et al., 2014). However, large uncertainties remain concerning the configuration, subglacial regimes, and ice-flow chronology of large portions of the LIS, especially in remote regions of northern Canada (e.g., Margold et al., 2018).

The QLD, a major ice dispersal centre in the eastern sector of the Laurentide Ice Sheet, persisted throughout the last glacial cycle (Dyke, 2004) and covered an area of about 3,000,000 km^2. At LGM the QLD was up to 2.5 km thick (Figure 2.1A) and likely had several dynamic saddles or secondary ice-divides extending across northcentral Quebec and northwest Labrador (Dyke and Prest, 1987; Vincent, 1989; Veillette et al., 1999; Dyke, 2004; Parent et al., 2004) including the Labrador Divide. Reconstructing such a large feature of the LIS has been a challenging task, especially due to the complexity of ice-flow directional indicators across the region. As a result, the location, migration, and subglacial regime of the QLD have long been debated and are still uncertain (Hughes, 1964; Klassen and Thompson, 1993; Clark et al., 2000; Jansson et al., 2002). The retreat of the ice margin has been constrained by glacial lake reconstructions (Clark et al., 2000), ^{10}Be cosmogenic ages (Carlson et al., 2007; Ullman et al., 2016: Dubé-Loubert et al., 2018), and widely spaced radiocarbon minimum ages which are largely restricted to coastal regions (compiled by Dyke et al., 2003). The ice margin retreat is known to have occurred rapidly (Ullman et al., 2016); however, the configuration of ice margin retreat is poorly confined within the interior Quebec region (Figure 2.1B). The understanding of the style, timing, and rate of ice margin retreat for this core region would improve with an increased density of chronologic constraints.

The goals of this study are to characterize the surficial geology, determine the local ice-flow chronology, gain insights into subglacial dynamics, and constrain the timing of deglaciation for the region north of the Quebec-Newfoundland and Labrador provincial border, an area that experienced a complex, yet unresolved ice-flow history (Figure 2.2). This investigation included air photo-based surficial mapping coupled with field observations and outcrop-scale ice-flow measurements to determine local ice-flow chronologies, which were then integrated into the broader regional context. To constrain the timing of deglaciation within the study area, ^{10}Be exposure age dating was applied to bedrock and perched erratics and optical dating methods were applied to glaciolacustrine beach sediments and proglacial outwash sands to constrain the local timing of ice margin retreat.

The patterns of glacial sediment distribution, in conjunction with ice-flow indicators, and deglacial ages, have allowed for a robust local reconstruction that contributes to understanding how the LIS operated in one of its core regions. The constraints on ice-flow chronology will also be useful for future ice-sheet reconstructions.

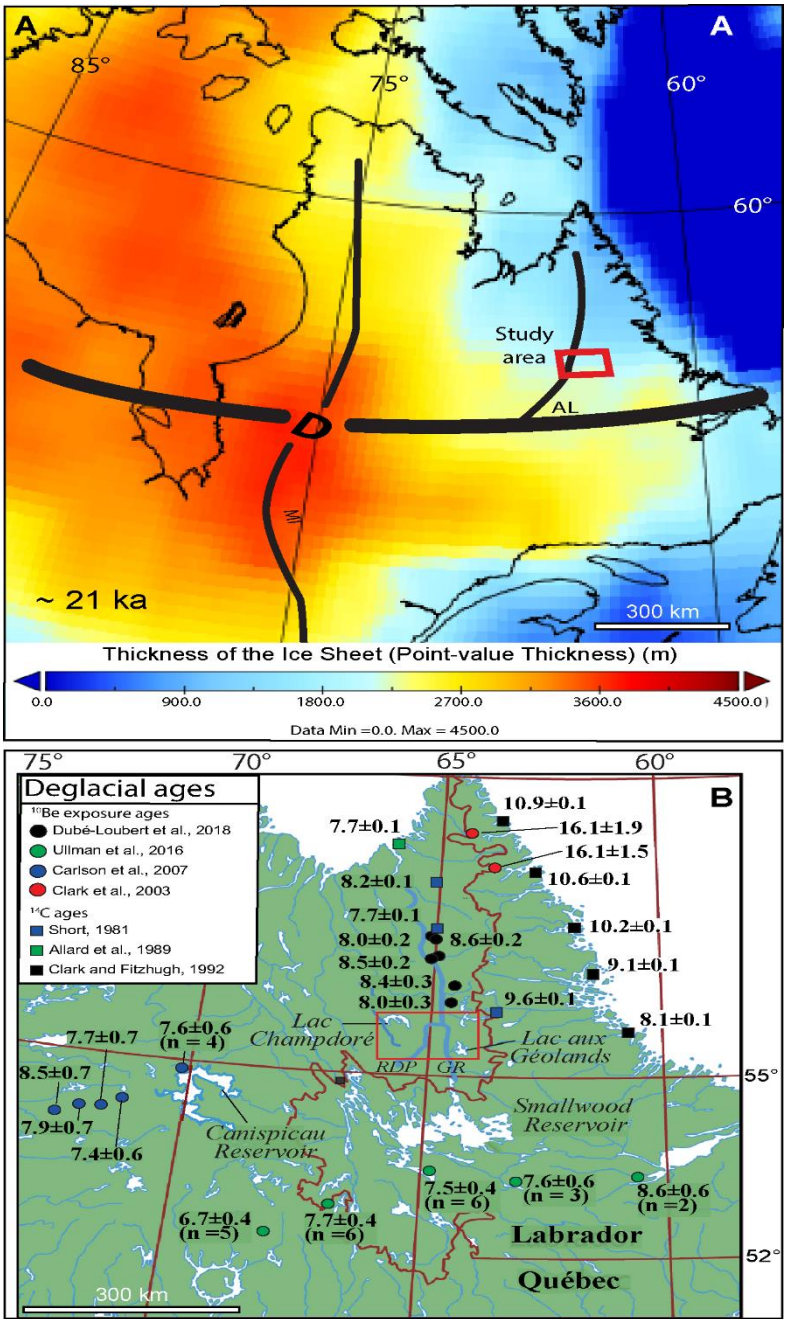

Figure 2.1. **(A)** Location of the study area within a context of the Laurentide Ice Sheet with ice thickness as modelled by ICE-6G (VM5a) dataset (Argus et al., 2014; Peltier et al., 2015) with major ice dome (QLD) and regional ice-divides Mistassini (MI) Ancestral Labrador Ice divide (a.k.a. Labrador Divide) (AL) annotated on top (Dyke and Prest, 1987). **(B)** The study area with major geographical locations identified and previously reported deglacial ages (^{14}C ages are reported in cal a BP and ^{10}Be ages have been calculated using the Baffin Bay production rate of Young et al. (2013)). RDP is the Rivière De Pas and GR is the George River.

2.2.1 Previous work

Striation measurements that suggested a dispersal centre shifted from east of James Bay to northwest of the modern-day Caniapiscau Reservoir were first reported by Low (1896). One of the first regional ice-flow chronologies was created through air photo landform mapping and ice-flow measurements by Henderson (1959) indicating an old flow to the south-southwest followed by a northeast flow, with topographically controlled flows later flowing to the northwest, north and southeast. This complex ice-flow history was used as evidence by Ives (1960a) to suggest that the region had been the location of an ice dispersal centre. Hughes (1964) conducted systematic mapping of landforms and striations around the Labrador Trough and indicated the ice-divide was located somewhere on the Labrador Trough as erratics from the trough were observed more than 100 km west of their source. Hughes (1964) also recognized a boundary between a southward radial pattern of glaciofluvial landforms and glacial landforms converging northward into Ungava Bay and radially oriented southward away from Ungava Bay (Figure 2.2A), subsequently referred to as the horseshoe unconformity (Clark et al., 2000; Jansson et al., 2002; Jansson et al., 2003; Dubé-Loubert and Roy, 2017). More extensive landform mapping, striation measurements, and erratic dispersal train analysis in western Labrador have brought additional evidence largely consistent with Hughes (1964) ice-flow chronology (Figure 2.2B-Klassen and Thompson, 1987, 1993; Klassen and Paradis, 1990).

Chronological striation-based reconstruction by Veillette et al. (1999) around the Caniapiscau Reservoir aligned with earlier work by Hughes (1964) and Klassen and Thompson (1993) with the oldest northeast-trending flow having a large geographical extent and having originated somewhere in the highlands north of the St. Lawrence River (Figure 2.2B). Veillette et al. (1999) also concluded the Ungava Bay swarm was the youngest subglacial bed in the region having formed during the onset of deglaciation around 10 ka.

Clark et al. (2000) identified multiple palaeo-ice streams within the Ungava Bay “landform swarm”, indicating a much more complex glacial history associated with the converging landforms. Through this work, Clark et al. (2000) were unable to establish an age relationship between Klassen and Thompson (1993) and Veillette et al. (2000)’s Flow II and Flow III.

Nonetheless, Clark et al. (2000) were able to conclude that ice margin retreat was rapid along the southern margin but slower along the northern margin. In addition, they interpreted a shift in ice sheet thermal regime from cold-centred to entirely cold-based associated with ice sheet thinning

before it fragmented into smaller ice caps. The complex landforms identified by Clark et al. (2000) were further analyzed by Jansson et al. (2003) who interpreted the UBLS as the imprint of the dynamic UBIS that formed during deglaciation.

Southeast of the Ungava swarm in the Lac aux Goélands (Whitegull Lake) region (Figure 2.2-inset) Clarhäll and Jansson (2003) documented east-trending ice-flow indicators within a zone they interpreted to have been preserved under cold-based conditions. In their reconstruction, the ice-divide migrated north and occupied the region south of the UBLS, preserving relict glacial landscapes in that area (Figure 2.2B). They also attributed the landforms in the region to brief warm-based events within otherwise long periods of cold-based conditions until final deglaciation (Figure 2.2- inset). In summary, they attribute the landforms in the Lac aux Goélands area to brief events interspersed between long periods of cold-based conditions until final deglaciation.

Deglaciation has been constrained by proglacial lakes features (Clark et al., 2000; Dubé-Loubert and Roy, 2017). The timing of deglaciation in the region is based on several ages (Figure 2.1B) from the Torngat Mountains to the George River (Clark et al., 2003; Marquette et al., 2004; Staiger et al., 2005; Carlson et al., 2008; Ullman et al., 2016; Dubé-Loubert et al., 2018). Work by Clark et al. (2003), Carlson et al. (2008), Ullman et al. (2015), and Ullman et al. (2016) showed evidence that the region west of the Caniapiscau Reservoir was ice free by 8.2 ± 0.5 ka and the region to the south of the Smallwood Reservoir deglaciated later at 6.7 ± 0.4 ka, which led to the conclusion that the ice margin in that sector of the LIS retreated rapidly. North of 56° N, within the George River Basin, Dubé-Loubert et al. (2018) analyzed and dated shorelines and outburst-flood related landforms and concluded glacial Lake Naskaupi drained catastrophically at 8.3 ± 0.3 ka. Glacial Lake Naskaupi and glacial Lake McLean were two proglacial lakes that formed during ice margin retreat within the study area (Ives, 1960a, 1960b; Dubé-Loubert and Roy, 2017). The pathway and timing of drainage of Lake Naskaupi have been well-defined (Dubé-Loubert and Roy, 2017; Dubé-Loubert et al., 2018), however, its southern extent has not been verified through field investigation. There are also no age constraints on Lake McLean and its extent has been defined only through air photo investigation (Ives, 1960b). Finally, there is a large spatial gap between the geochronological transects in the regions, including this study area (Figure 2.1B).

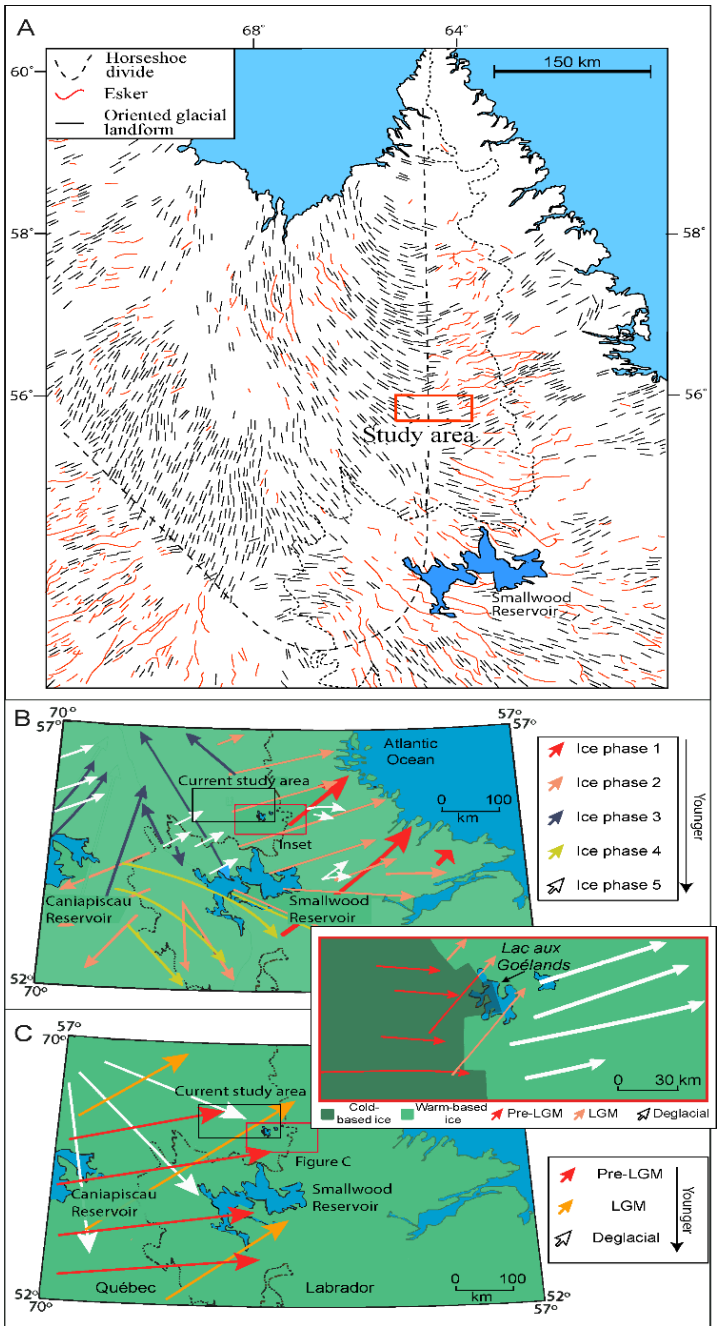

Figure 2.2. (**A)** Regional distribution and orientation of eskers and glacial landforms across Quebec and Labrador. The dotted line represents the horseshoe divide marking the transition from landforms converging toward Ungava Bay to landforms radiating away from Ungava Bay. Landforms have been redrawn from Fulton (1995). (**B)** Regional ice flow reconstruction by Klassen and Thompson (1993) and Veillette et al. (1999) showing five phases of ice flow. The study area is outlined in black, and *Inset* location is also outlined in red. (**Inset)** Contrasting ice flow reconstruction by Clarhäll and Jansson (2003) indicating the oldest flow of Klassen and Thompson (1993) and Veillette et al. (1999) (Fig. 2B, ice phase 1, red arrow) was a Late Wisconsin ice-flow phase (Figure 2C, LGM flow, orange arrow). Consequently, their ice flow three (Fig. 2B, purple arrow) was a deglacial divergent flow away from Ungava Bay (Fig. 2C, white arrow). (**C)** Regional ice flow of Clarhäll and Jansson (2003) and Jansson et al. (2002).

2.3 Methodology

2.3.1.1 Surficial mapping

For this work, two 1:100 000 scale surficial geology maps (Rice et al., 2017a, 2017b) were created using black and white aerial photographs (1:60 000 scale). The photographs provide a stereoscopic three-dimensional visualization of the landscape which enhances the accuracy of surficial unit separation based on vegetation, topography, reflectivity, and texture of the surface (Mollard and James, 1984). Field verification of mapped surficial units was completed during three summer field seasons (2014-2016). A total of 142 sites were investigated to validate mapped surficial units.

2.3.1.2 Relative ice-flow chronology

Ice-flow directions were first determined using oriented glacial landforms (e.g., crag-and-tail forms, drumlins, and large-scale glacial lineations) identified through both air photo and satellite imagery interpretation. Landsat 8 satellite image mosaics were coupled with digital elevation models (DEM) from Canadian Digital Elevation Data (www.geobase.ca- 30 m vertical and horizontal resolution) following procedures outlined by Clark et al. (2000) and Stokes and Clark (2001). These landform features often form flowsets that crosscut each other allowing for the development of relative age chronology at the landscape scale (e.g., Kleman et al., 1997; Clark et al., 2000). However, flowsets do not always clearly overlap and some ice-flow phases are not always preserved at the landscape scale. Remote sensing analysis was supplemented with a total of 94 outcrop-scale ice-flow indicator measurements, including striations, grooves, rat tails, and mini *roches moutonnées* (e.g., McMartin and Paulen, 2009). Following the methodology of Klassen and Bolduc (1984), Parent et al. (1995), Veillette and Roy (1995), Veillette et al. (1999) and Paulen et al. (2013) the ice-flow chronology was determined through lee side preservation, where ice-flow indicators on the lee side position are assumed to indicate earlier (older) ice-flow events. The azimuths of the striae and grooves were determined from outcrop shape and lee side plucking features (Rea et al., 2000). The relative chronology established from outcrop-scale indicator analysis is then compared with the surrounding landform record to establish a more relative age chronology of all observed multi-scale ice-flow indicators. This methodology follows several other researchers (e.g., Parent et al., 1995; Veillette et al., 1999; McMartin and Henderson, 2004; Trommelen et al.,

2012; Gauthier et al., 2019) in adopting an approach whereby the pattern and orientation of subglacial streamlined landforms are correlated to the different ice flow directions identified in outcrop striation measurements. Furthermore, because glacial landsystems are typically fragmented near core regions of ice sheets (e.g., Gauthier et al., 2019), patterns of ice-flow indicators (both landform flowsets and outcrop-scale records) are also analyzed across the study area to determine whether disjointed zones with internally coherent records can be identified. This is an important step in the identification and characterization of different palimpsest glacial beds (e.g., Kleman and Glasser, 2007). In this conceptual model, unmodified older subglacial landsystems are preserved due to a shift from warm-based active ice to cold-based, non-erosive ice. Typically, these relict unmodified terrains are identified next to an area where they are variably overprinted by younger ice-flow events.

The evolution of ice sheet dynamics can thus be deciphered, to an extent, in a large study area based on all the above concepts and methods. There are inherent uncertainties associated with these type of landscape analyses and an ice sheet reconstruction is always incomplete and fragmentary due to the erosion of older flows by younger flows and the resultant incomplete preservation of the full record at any location. Nonetheless, it provides useful insights into the long-term behaviour of ice sheets and is critical to understanding glacial landscapes and their evolution.

2.3.2 Geochronological constraints

Previously reported deglacial ages from the surrounding region (Carlson et al., 2007, 2008; Ullman et al., 2016; Dubé-Loubert et al., 2018) are used in conjunction with deglacial chronology developed as part of this study.

2.3.2.1 Cosmogenic ^{10}Be exposure dating

Glacially eroded, well-polished, bedrock and perched glacial erratics have proven to be good targets for determining cosmogenic ^{10}Be exposure ages, hereafter simply "^{10}Be ages" (see Appendix S2.1 for detailed methodology). For this study, eight locations were selected to collect bedrock samples for ^{10}Be chronology (Figure 2.3). At each site, a single bedrock sample was collected from the highest windswept bedrock outcrops with high quartz content. At two of the bedrock sites (15-PTA-081E and 15-PTA-077E), erratic boulders were also sampled. Boulders were selected based on quartz content (quartz > 35%), size (>1 m^3), stability (no evidence of post-depositional movement),

and absence of topographic shielding. Samples were collected along an east-west transect, perpendicular to the regional ice margin retreat direction of Dyke and Prest (1987) to capture the timing of deglaciation across the study area. Ages were calculated using the online exposure age calculator v.3 (http://hess.ess.Washington.edu) using the Baffin Bay/Arctic ^{10}Be production rate (Young et al., 2013) and the nuclide -and-time-dependent scaling scheme (Lifton et al., 2014). All ^{10}Be results are treated as "apparent ages" due to the potentially added uncertainty caused by cosmogenic nuclide inheritance (*see* Appendix S2.1). A detailed description of cosmogenic ^{10}Be exposures sample sites are shown in the Supplementary Material (Figure S2.1) and detailed dating methods can also be found in the Supplementary Material (Appendix S2.1; Table S2.1). Field and lab chemistry data are presented in Table 2.1.

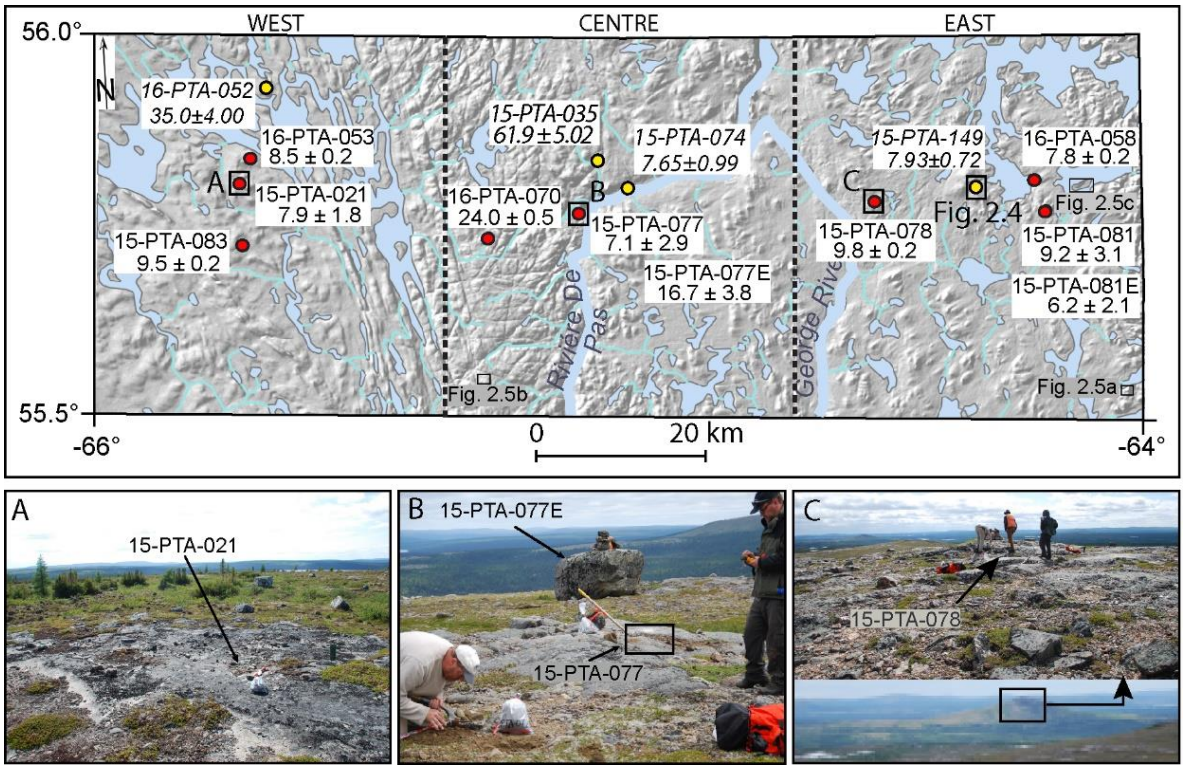

Figure 2.3. Sample location of ^{10}Be cosmogenic exposure samples (red) and OSL samples (yellow) with calculated ages. Ages are reported in thousands of years before present (ka). **(A)** Sample site 15-PTA-021 from the western portion of the map sheet. The sample was collected from exposed bedrock on an upland clearing. Location of Figure 2.5 photographs are also indicated**. (B)** Sample site 15-PTA-077 (foreground) and 15-PTA-077E (background) collected from an exposed bedrock outcrop and perched erratic on a windswept upland near the Rivière De Pas. **(C)** Sample 15-PTA- 078 collected from bedrock outcrop (top image) located on the knob of a large crag-and-tail (bottom image).

Table 2.1. ^{10}Be sample data

Sample	Latitude (°N)	Longitude (°W)	Elev. (masl)	Corr. Elev. (masl) [a]	Thick (cm)	Topo. shielding correction	[Be-10] atoms/g	± atoms /g	Exposure age (LSDn ± 1 σ (yrs)) [b]	1 σ (%)
EAST										
16-PTA-058	55.843	-64.207	494	433	3.0	1	4.80E+04	1.23E+03	7800 ± 200	2.6%
15-PTA-078	55.821	-64.515	517	456	2.5	1	6.28E+04	1.24E+03	9800 ± 200	2.0%
15PTA-081*	55.810	-64.189	559	498	2.0	1	6.10E+04	2.03E+04	9200 ± 3100	33.7%
15PTA-081E*	55.810	-64.189	559	498	1.5	1	4.13E+04	1.37E+04	6200 ± 2100	33.9%
CENTRE										
15PTA-077*	55.810	-65.080	495	434	3.0	1	4.35E+04	1.78E+04	7100 ± 2900	40.8%
15PTA-077E*	55.810	-65.080	495	434	2.0	1	4.35E+04	1.78E+04	16700 ± 3800[c]	22.8%
16-PTA-070	55.784	-65.251	623	562	1.0	1	1.03E+05	2.35E+04	24000 ± 500[c]	2.1%
WEST										
16-PTA-053	55.867	-65.709	517	456	3.0	1	5.36E+04	1.19E+03	8500 ± 200	2.4%
15-PTA-083	55.772	-65.721	509	448	1.0	1	5.95E+04	1.14E+03	9500 ± 200	2.1%
15PTA-021*	55.838	-65.729	529	468	2.0	1	5.07E+04	1.14E+04	7900 ± 1800	22.8%

[a] Elevation were corrected to isostatic uplift by averaging the uplift from modern elevation using data from ICE-6G(VM5a) (Argus et al., 2014; Peltier et al., 2015)

[b] Error is reported to 1σ of internal uncertainty. Values have been rounded to nearest 10s value.

[c] Outlier samples

*Sample analyzed by PRIME lab.

LSDn = Nuclide and time-dependent scaling theme (Lifton et al., 2014)

2.3.2.2 Optical dating

Optically stimulated luminescence (OSL), hereafter referred to as optical dating has been used successfully to date the formation of glaciolacustrine beaches (e.g., Lepper et al., 2013; Hickin et al., 2015). The utility of this method depends on sampling littoral facies with depositional settings that exposed feldspar grains to sufficient sunlight prior to final burial. Therefore, to further constrain the timing of deglaciation coarse-to-fine-grained sandy-beach sediments associated with the two identified glacial lakes were targeted for optical dating as they contain sand-sized particles that are more likely to have experienced complete resetting prior to burial (Fuchs and Owen, 2008).

Samples were collected by digging vertically into the sediments, taking note of the stratigraphy, to access sediment suitable for optical dating. Elevation data for each site was collected with a hand-held GPS. Samples were collected following procedures outlined by Aitken (1998) and Lian (2013). A total of four samples were collected for optical dating. Three ages were determined from the analysis of coarse-to-fine-grained littoral sediments and a third age was calculated from fine-grained subaqueous outwash sediments. Samples 15-PTA-035 (elev: 464 ± 5 m) and 15-PTA-149 (elev: 486 ± 5 m) (Figure 2.3 and 2.4) are from the littoral sediments of Lake Naskaupi in the northeastern section of the study area. Sample 16-PTA-052 (elev: 426 ± 5 m) was collected from a coarse-to-medium grained sand facies associated with littoral sediments of Lake McLean on an upland peninsula in the northwest region of the study area (Figure 2.3). Sample 15-PTA-074 (elev: 314 ± 5 m) was collected from a fine-grained, subaqueous, outwash fan deposited into Lake Naskaupi likely near its lowest level in the region, providing an age for the late stages of Lake Naskaupi. Glaciofluvial outwash sediments have a lower bleaching probability than beach or dune deposits (Fuchs and Owen, 2008); however, they have been used successfully in other studies (e.g., Klasen et al., 2006; Alexanderson and Murray, 2007; Bøe et al., 2007). Samples were submitted to the Luminescence Dating Laboratory, University of the Fraser Valley, Abbotsford, British Columbia, where optical dating analysis was conducted on sand-sized K-feldspar grains, as the optical signal from quartz was found to be unsuitable because it lacked the desired so-called “fast component” (Bailey et al., 1997). Experimental procedures specific to this study are found in the Supplementary Material (Appendix S2.2). Detailed sample site figures are shown in the Supplementary Material (Figure S2.2). Field and laboratory data are described in Table 2.2.

2.4 **Results**

2.4.1 Bedrock and till landscapes

The highlands are characterized by bedrock outcrops draped by a discontinuous thin till veneer (Figure 2.5A), often with large perched erratics and thicker deposits of till in the lower relief areas which mask the underlying bedrock topography. Bedrock outcrops are also observed where glaciofluvial outwash or proglacial lake wave erosion has removed the glacial sediments (Figure 2.6). Streamlined landforms occur in the east of the study area (Figure 2.7), with steep stoss and gradual lee side slopes characteristic of drumlins (a-axes up to 3 km long) and more elongated

smaller glacial lineations with less steep stoss edges (a-axes 1.5 km long) oriented to the northeast. Large drumlins (a-axes 4 km long) oriented to the northwest are also observed, but in lower quantities in the most northwestern portion of the study area. Till of varying thickness is the most abundant surficial sediment across the study area (Figure 2.6). There were no exposures showing glacial stratigraphy within the study area.

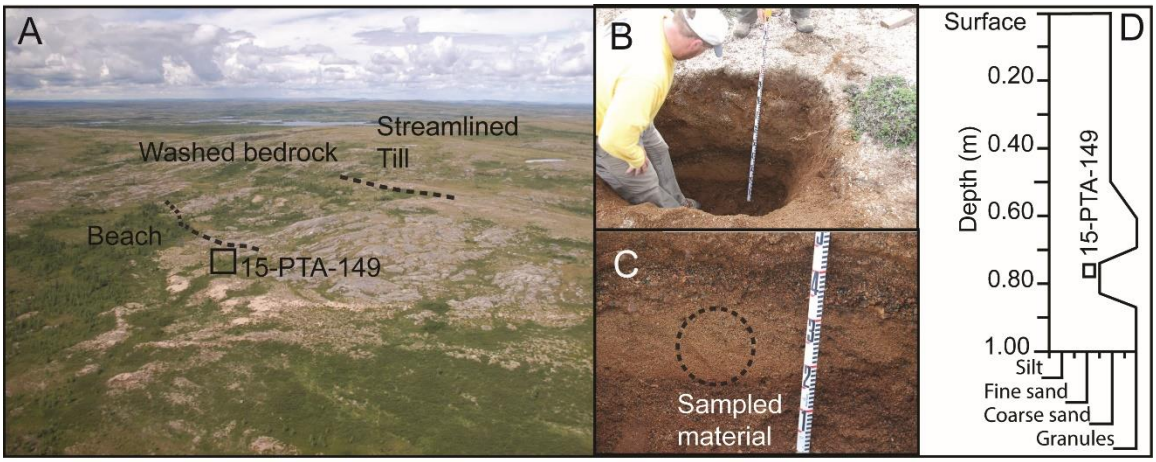

Figure 2. 4. **(A)** Location of optical dating sample 15-PTA-149 collected from littoral sediments below the washing limit of glacial Lake Naskaupi (elev. 486 ± 5 m a.s.l.). **(B)** Sample pit of optical dating sample collected from a depth of ~0.8 m. **(C)** Close up of fine sand collected for optical dating. **(D)** Lithofacies of grain sizes changes within the optical dating sampling pit.

2.4.2 Meltwater features

Glaciofluvial deposits are common within the central portions of the map sheet, where subglacial drainage channels are abundant (Figure 2.5B). These channels typically are incised into the glacial sediments but are also found as V-shaped channels eroded into bedrock up to 8 m deep. The smaller channels usually lead to larger meltwater systems that eventually drain to the east and west of the central upland. In the eastern portion of the study area, these meltwater channels transition into depositional systems, forming large sinusoidal eskers fanning eastward toward the Labrador coast. The generally parallel (~10-12 km between eskers) eastward organization of the eskers indicates a local drainage pattern oriented east-southeast associated with meltwater drainage during deglaciation. These eskers are associated with the large radial pattern of eskers in the region correlated with the retreat of the QLD ice margin toward central Quebec (Occhietti et al., 2004, 2011). These large eskers systems are oblique to subglacial lineations in the region, which is a key observation indicating the northeast ice-flow indicators in the study area (*see below*) predate the establishment of the channelized draining system that deposited the eskers.

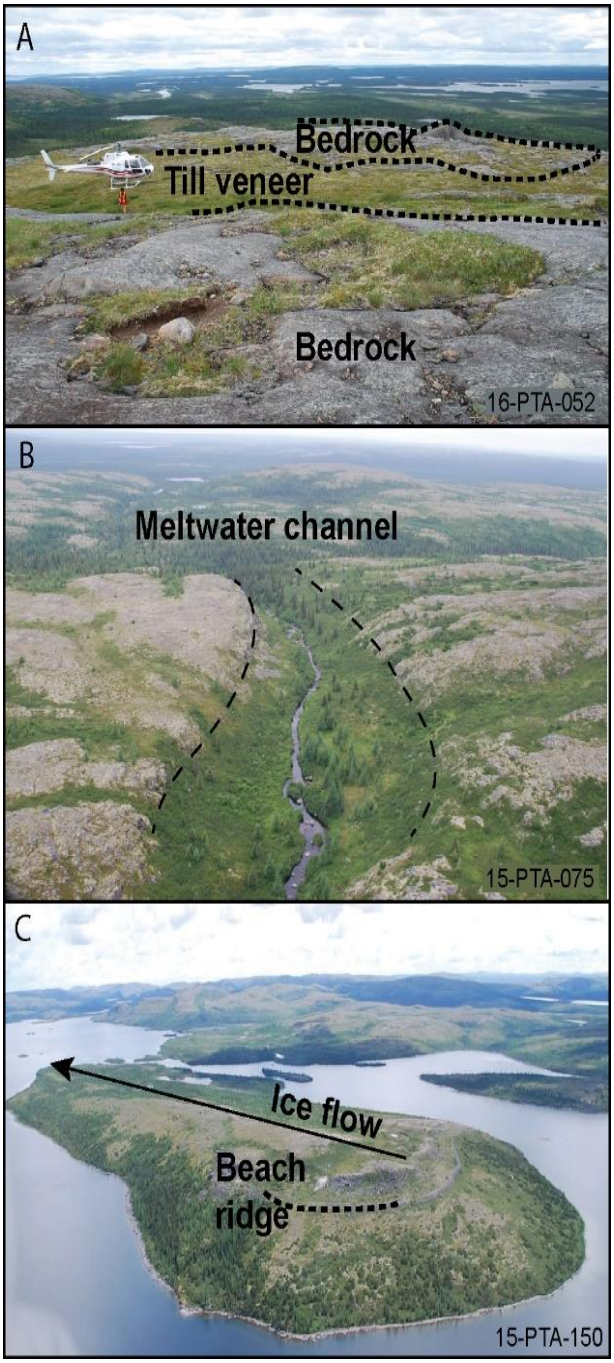

Figure 2.5. Location of features are indicated on Figure 2.3. **(A)** An example of bedrock uplands with a thin till veneer and thicker till blanket in the valley in the background. **(B)** An example of a deep meltwater channel (~ 8 m). **(C)** An example of a large streamlined landform winnowed by Glacial Lake Naskaupi, leaving a cobble beach near the top of the landform.

2.4.3 Glaciolacustrine features

The two glacial lakes that inundated the study area, Naskaupi and McLean, occupied the general basins of present-day *Lac Mistinibi* in the east and *Lac Champdoré/Lac Tudor* in the west, respectively (Figure 2.6-purple). Although no fine-grained, ice-distal, glacial-lake deposits were identified within the study area, well-developed beach ridges associated with each lake were mapped (Figure 2.5C). Fieldwork from this thesis confirms that Lake McLean extended south of 56° N and the highest elevation inundated at 426 m a.s.l. (±5 m) with a second level of well-developed beaches approximately 15 m lower in elevation. In the eastern portion of the study area, multiple beach ridges associated with Lake Naskaupi were identified. The maximum modern elevation of Lake Naskaupi within the study area was 486 ± 5 m a.s.l., with well-developed lower shorelines at 462 ± 5 m a.s.l.

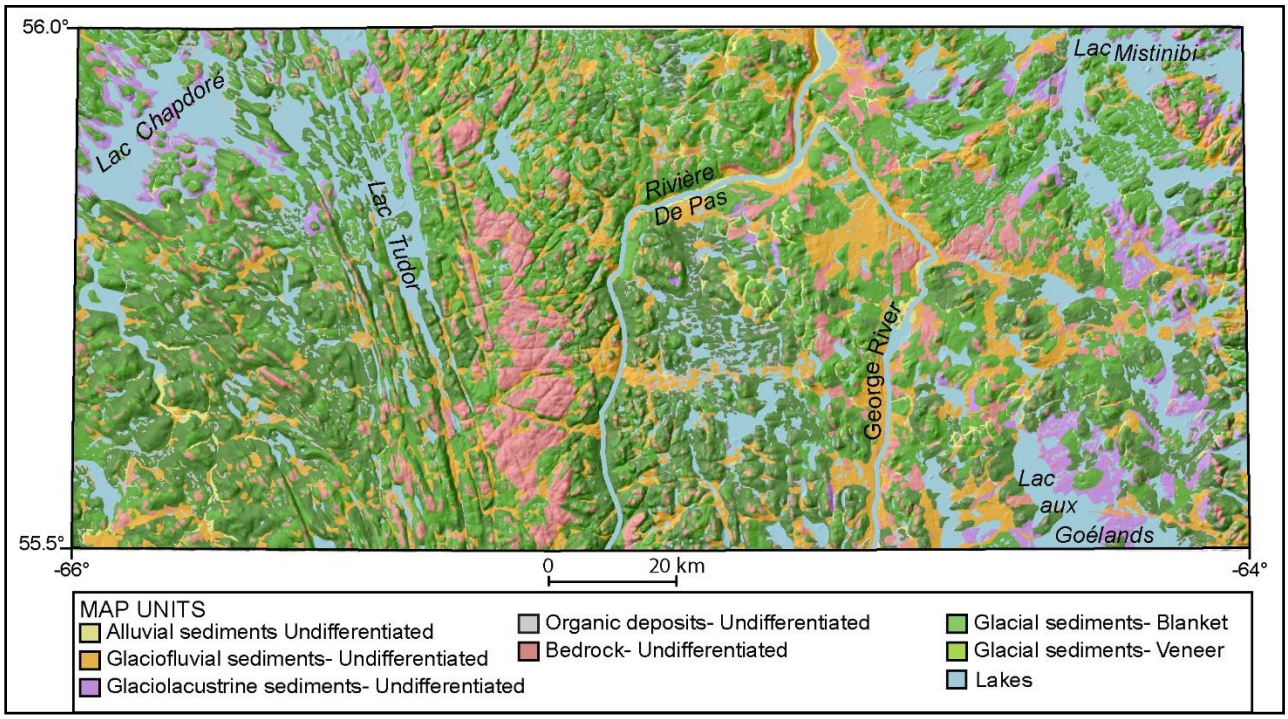

Figure 2.6. A simplified surficial map compiled from two 1:100 000 surficial geology maps (Rice et al., 2017a, 2017b). The large north-to-south trending bedrock outcrop (red) in the centre of the map is the De Pas Batholith. Surficial deposits have been draped over a 30 m resolution Shuttle Radar Topography Mission imagery derived hillshade (www.earthexplorer.usgs.gov).

2.4.3.1 Ice-flow indicators and relative chronology

A total of 306 glacial streamlined landforms have been mapped in the study area (Figure 2.7). They consist of rock and till drumlins, roches moutonées and small streamlined till ridges. They are concentrated in three zones across the study area: 1) northeast trending landforms in the northeast (n=165, average azimuth = 70°), 2) northwest trending landforms in the northwest (n=60, average azimuth = 288°), and 3) east-trending landforms on the eastern flank of the central highlands (n=81, average azimuth = 87°). Only a few (n=3) crosscutting landforms were identified within the study area, with large Flow 1 landforms crosscut by small Flow 3 landforms. Striations were also observed and analyzed at 94 sites across the study area (Supplementary data Table S2.2). At 41 of these sites multiple ice-flow phases were identified (Figure 2.7). The striation sites with multiple phases of ice-flow were critical in developing a relative ice-flow chronology, which was used to establish which singular striations sites were associated with which ice-flow phase. Most striations and grooves preserved in the lee side of numerous outcrops sculpted by later flows indicate ice flow toward the northeast (Figure 2.8). Notably, the majority of these observations were made at sites located in the eastern portion of the study area where a number of streamlined landforms trending in the same general direction were also mapped (Figure 2.7). Based on this, sites with northeast-trending indicators across the study area were correlated to Flow 1 (Figure 2.8). A total of 76 sites with striations and grooves associated with the oldest ice-flow to the northeast. The orientation of these outcrop-scale ice-flow indicators range in direction from 20 to 90° with a mean azimuth of 55° (σ^1=12.5°).

The second phase of ice-flow (Flow 2) was identified from outcrop-scale microforms measured at 19 sites across the study area (Figure 2.8). These ice-flow measurements were constrained to the western portion of the study area (Figure 2.8). Microforms measured in the study area indicated a west-northwest ice-flow ranging in direction between 286 to 332° with a mean azimuth of 305° (σ^1=10.4°). Three sites were critical in establishing this flow as younger than Flow 1 (Figure 2.7; Figure 2.8).

At 12 key sites, features associated with older flows (Flow 1 and 2) are crosscut by younger east-trending ice-flow indicators (Figure 2.7) and three landforms associated with Flow 3 have slightly reworked older, larger landforms from Flow 1. Additionally, the eskers mapped in the study area also trend eastward. Based on these relationships, all the east-trending ice flow features are correlated to the third phase of ice-flow (Flow 3-Figure 2.8). Outcrop-scale ice-flow measurements

associated with Flow 3 indicate a southeast-to-eastward flow ranging in direction between 52-140° with a mean azimuth of 83° (σ^1= 16.1°).

Finally, ice-flow features indicating flow to the west-southwest, ranging between 229-270° with a mean azimuth of 248° (σ^1=14.1°) have also been observed at 13 sites. These ice-flow indicators were the youngest flow at each site where they were identified (Figure 2.8). These ice-flow measurements were restricted to the central and western portion of the study area. They are correlated to the youngest ice-flow phase (Flow 4-Figure 2.8).

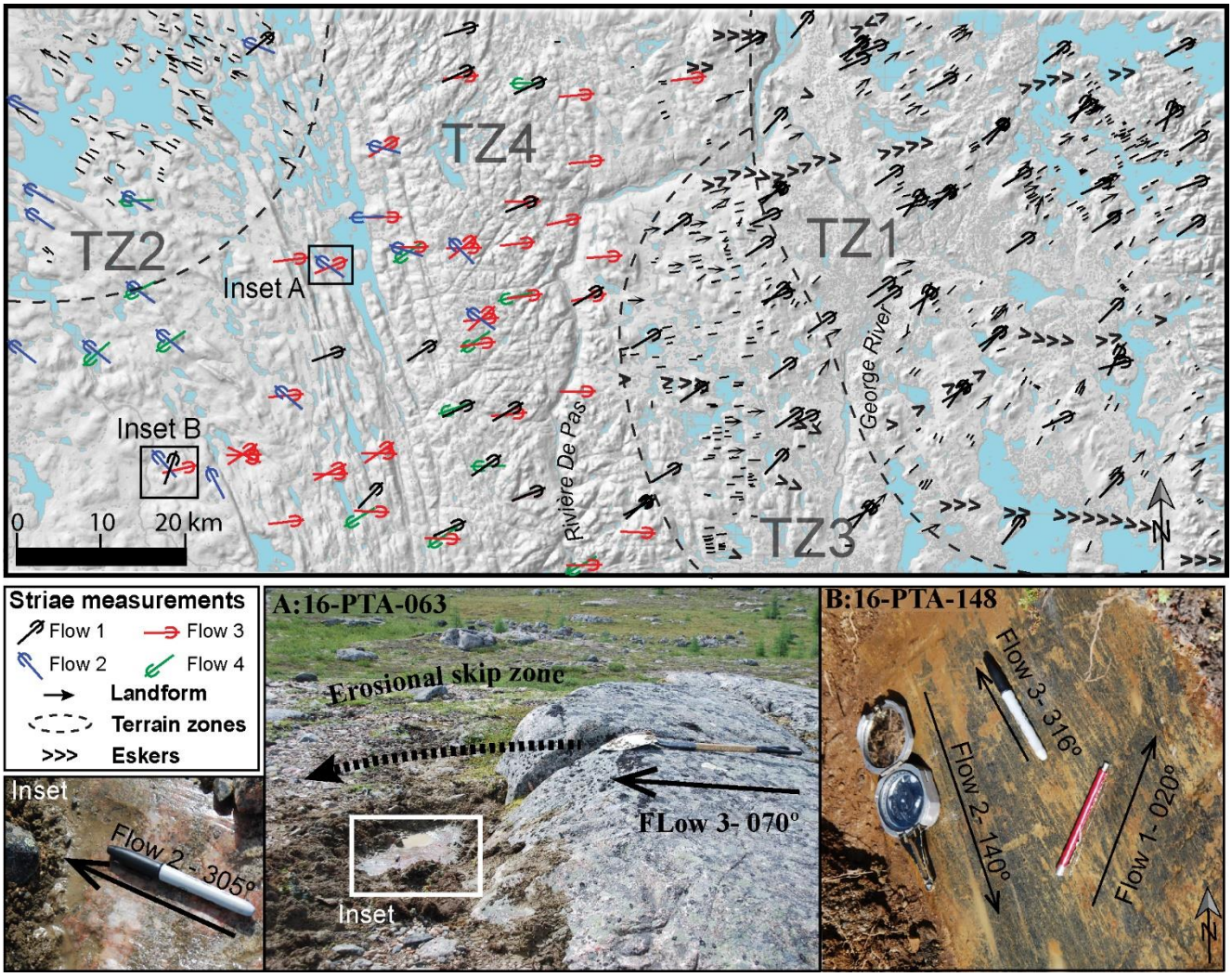

Figure 2.7. Hillshade DEM of the study area with outcrop-scale ice-flow indicators and mapped oriented glacial landforms. **(A)** Sample site 16-PTA- 063 gives an example of the lee-side protection of Flow 2 from Flow 3, indicating that Flow 2 is younger in age. **(Inset)** closer view of Flow 2 in lee- side protected surface. **(B)** Three phases of ice flow exemplified by deep grooves associated with the oldest ice flow, with finer and more abundant striations from later ice-flow phases (sample 16-PTA-148).

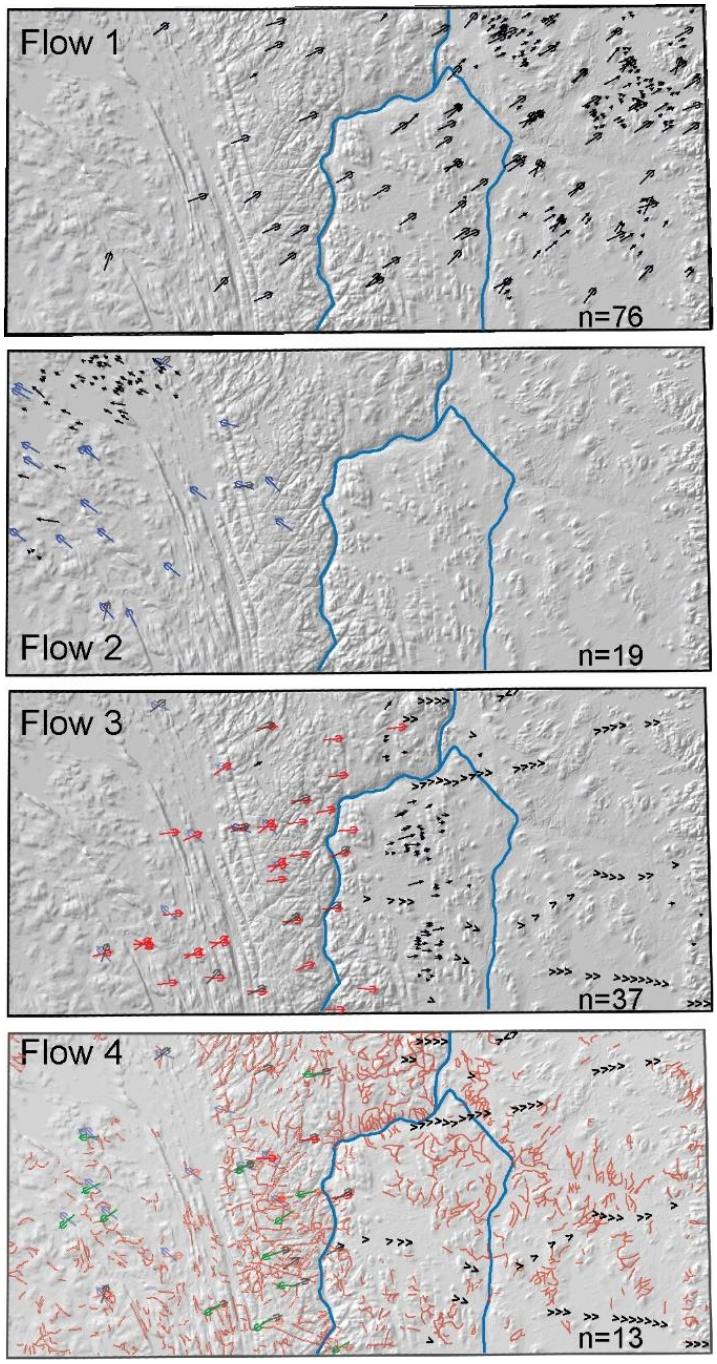

Figure 2.8. Ice flow diagrams with supporting striae and landforms. Where multiple ice-flow phases were recorded at one site, the ice-flow indicators from previous flow were left on younger ice flow figures to aid in interpreting the relative ages of each flow: (Flow 1) the oldest ice-flow phase in the study area to the northeast as identified by landforms and striations. (Flow 2) The second phase of ice-flow to the northwest as identified by striations and landforms. (Flow 3) The third phase of ice flow, following a westward migration of the ice-divide, characterized by flow to the east as evident from striations and landforms. Eskers (>>) have been included on this diagram to indicate the ice margin retreated from the east-southeast to north-northwest at least until the Rivière De Pas. (Flow 4) The final phase of ice flow is associated with a late-deglaciation flow of an independent ice-cap, with local ice flow largely resulting from the local topography. Evidence of this flow is only observed in the striation record. Meltwater channels (red) have also been overlain Ice flow chronology symbols are the same as indicated in Figure 2.7.

2.4.4 Deglacial chronology

2.4.4.1 ^{10}Be ages

^{10}Be ages are summarized in Figure 2.3, with detailed site information in the Supplementary Material (Figure S2.1). Samples were grouped based on their spatial proximity (eastern group, central group, and western group- Figure 2.3). Summed probabilities were created for each group using ^{10}Be ages to evaluate the approximate timing of deglaciation for each group (Figure 2.9). The ^{10}Be ages in the eastern group (n=4) range from 6.2 ± 2.1 to 9.8 ± 0.2 ka. The central group (n=3) had the largest variance in ^{10}Be ages, ranging from 7.1 ± 2.9 to 24.0 ± 0.5 ka (Figure 2.9). The western group (n=3) reveals the tightest clustering of ages ranging from 7.9 ±1.8 to 9.5 ± 0.2 ka (Figure 2.9). Two ^{10}Be ages of 24.0 ± 0.5 ka (16-PTA-070) and 16.7 ± 3.8 ka (15-PTA-077E), which are significantly older than the others, are considered outliers. These two samples, one from bedrock (16-PTA-070) and the other from an erratic (15-PTA-077E), likely experienced insignificant glacial erosion and thus contain inherited ^{10}Be (Briner et al., 2005). Because of this, samples 16-PTA-070 and 15-PTA-077E have been removed from this thesis' deglacial age discussion and figures.

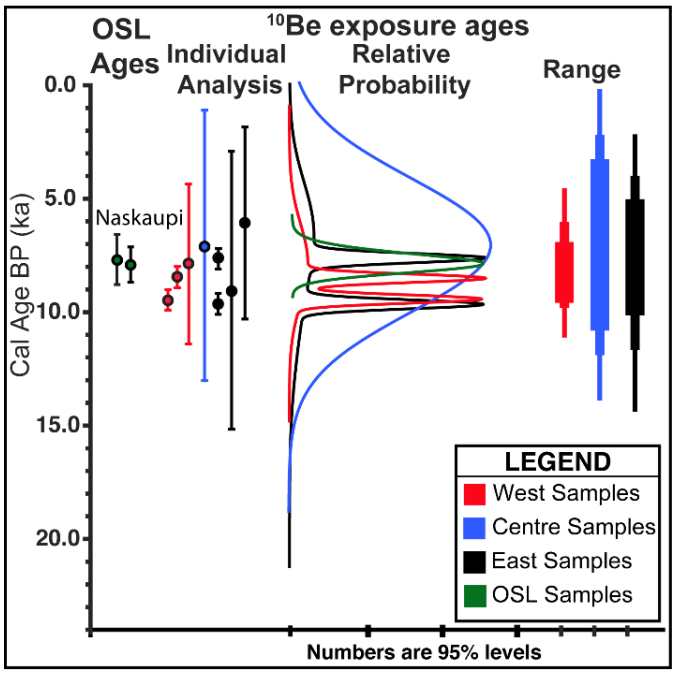

Figure 2.9. Plot showing the individual calculation of each ^{10}Be exposure age and optical age sample, the relative probability of the age for each group of samples, and the range of ages for each group (east (black), centre (blue), west (red), and glacial lakes (green)). The ages included on the matchstick figures (Range) indicate the 5th percentile, the peak probability of the sample, and the 95th percentiles of the samples. Note: ^{10}Be exposure samples 16-PTA-070 and 15-PTA-077E and Optical ages 15-PTA-035 and 16-PTA-052 not included in this figure (*see* Section 2.4.5).

2.4.4.2 Optical dating

Two samples, 15-PTA-149 (elev. 486 ± 5 m) and 15-PTA-035 (450 ± 5 m) were collected for optical dating from proglacial littoral sediments associated with Lake Naskaupi. They yielded ages of 7.93 ± 0.72 and 61.9 ka ± 5.02 ka BP, respectively (Figure 2.10; Table 2.2). A third sample 15-PTA-074 (314 ± 5 m), was collected from an outwash fan deposit associated with Lake Naskaupi. These outwash sediments formed during the late stages of the proglacial lake and yielded an age of 7.65 ± 0.99 ka BP (Figure 2.10; Table 2.2). Data from the only sample collected from Lake McLean (16-PTA-052) indicate a minimum age of 35.5 ± 4.0 ka. Given what is known about the regional deglacial history, this result, and that from sample 15-PTA-035 are clearly anomalous. It is likely that these age values result from poor bleaching prior to deposition, which can be common in advanced-phase glacial outwash environments that are typically turbid (Fuchs and Owen, 2008), or that were deposited as an outwash delta into the lake (see Supplementary Material for more details). Because of this, these two samples were omitted from the discussion of the deglacial ages. Laboratory results from the optical dating experiments are reported in the Supplementary Material (Appendix S2.2, Figure S2.3, and Tables S2.3, S2.4, S2.5).

Table 2.2 OSL sample details

Sample ID	Elev. (± 5 m.a.s.l)	Depth (cm)	H_2O[1] (Δ^w)	K (%)	Rb (ppm)	Th (ppm)	U (ppm)	D_e (CAM) (Gy)	Uncorr. CAM age (ka)	Fading-corrected CAM[2] age estimate (ka)[3]	Fading-corrected MAM[2] age estimate (ka)[3]
15-PTA-035	464	100	0.0088 ± 0.001	2.50 ± 0.13	52.5 ± 2.77	3.00 ± 2.77	0.39 ± 0.08	23.0 ± 4.0	40.0 ± 3.2	61.9 ± 5.02	29.9 ± 3.10
15-PTA-074	314	370	0.185 ± 0.002	1.80 ± 0.1	61.8 ± 3.31	5.50 ± 0.28	2.13 ± 1.69	7.0 ± 1.0	6.13 ± 0.79	7.65 ± 0.99	n/a
15-PTA-149	486	75	0.0329 ± 0.003	2.40 ± 0.1	108 ± 5.50	5.50 ± 0.28	1.30 ± 0.11	33.0 ± 5.0	6.59 ± 0.60	7.93 ± 0.72	4.59 ± 0.45
16-PTA-052	426	140	0.021 ± 0.010	2.9 ± 0.1	80 ± 5	20.6 ± 0.5	1.3 ± 0.1	120.8 ± 10.8	21.6 ± 3.6	35.0 ± 4.0	15.5 ± 2.7 (20.5 ± 3.5)

[1] Water contents are "as collected" values and are defined as (mass water)/(mass minerals).

[2] Fading corrections were applied using the method of Hunley and Lamothe (2001). Because the natural signal (Ln/Tn) falls in the non-linear part of the dose response curves of samples (Fig. 8), this correction method may underestimate the true age by ~15-20% (*cf.* Mathewes et al., 2015).

[3] MAM (Minimum age model) age in brackets excludes two lowest outlying D_e values (Supp. Fig. S3). CAM=Central age model

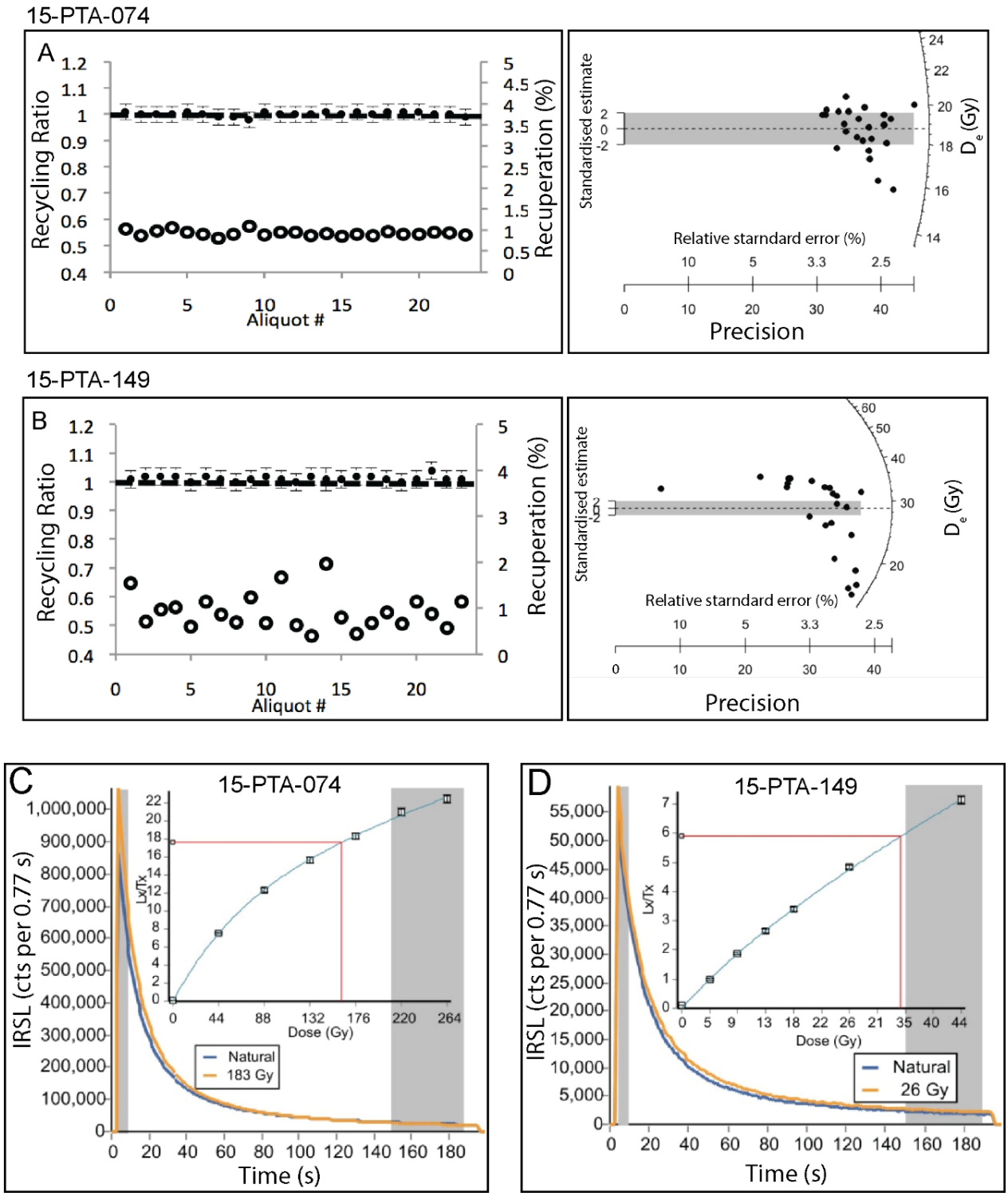

Figure 2.10. Recuperation values, recycling ratios, and De distributions for samples 15-PTA-074 **(A)** and 15-PTA-149. **(B)** The shaded region on the decay curves marks the initial and final parts of the optical signal used to calculate the equivalent dose (De) value. Optical decay curves and dose-response curves (inset) for optical samples 15-PTA-0174 **(C)** and 15-PTA-149. **(D)** See Supplementary appendix S2.2 for graphs from all collected samples.

2.5 Interpretation and discussion

2.5.1 Ice-flow reconstruction

Flow 1: The earliest ice-flow indicators identified in the study area provide evidence of ice-flow to the northeast. Evidence for this oldest northeastern ice-flow event is found across the central and eastern portions of the study area (Figure 2.8). This ice-flow event was also reported in recent surficial maps to the south (Paulen et al., 2017; Campbell et al., 2018), indicating that the ice sheet flowed in a generally uniform northeast pattern across the study area with only slight deviations, as recorded in striae azimuths (Figure 2.8). This investigation extends Klassen and Thompson (1993)'s E1 ice-flow phase (Figure 2.2B, red arrow) further northwest than previously reported. However, it is lacking in the northwest part of the study area and it is not known whether this is due to local cold-based conditions during Flow 1, or if the record of this flow were eroded during subsequent ice-flow phases (e.g., Flow 2).

An abundance of large glacially scoured landforms was also identified in the northeastern portion of the study area, parallel to striation measurements associated with Flow 1 and are presumed to have been created during the same ice-flow event (Figure 2.8). Altogether, these observations suggest that Flow 1 was an erosive flow that was sustained for a considerable period (Clark, 1993). In addition, the degree of preservation of old northeast-trending features in the eastern portion of the study area and lack of overprinting by younger features, suggest a shift from warm-based to cold-based subglacial conditions in the eastern portion of the study area (Figure 2.7, Figure 2.8). Only the eskers seem to crosscut the features associated with Flow 1 in that area. Notably, orientations of the eskers to east-southeast differ from the landforms and striations associated with Flow 1 by ~ 50°, which indicates that Flow 1 must have occurred prior to the formation of the eskers, at a time when the ice sheet had a different configuration. These northeast-trending landforms were not included in Clark et al. (2000)'s reconstruction of the QLD but are presumed to predate their flowsets (or group of similar oriented landforms) 19 through 23, as landforms within this study area with similar orientation to Clark et al. (2000)'s flowset 19 formed during a later ice-flow event (see below).

Flow 1 represents a large-scale glacial flow from an ice-mass somewhere to the south-southwest likely centred in the Quebec Highlands (Klassen and Thompson, 1993; Veillette et al., 1999; Parent et al., 2004). The timing of this ice-flow event, how long this flow was sustained, its possible duration, or if there were any earlier glacial events, is currently unclear. Veillette et al. (1999)

reported outcrops striated by a northeast flow with a ferromanganese varnish, which was considered evidence of long exposure to weathering from an interglacial period (striated bedrock surfaces do not typically show this kind of weathering in northern Canada). Additionally, Klassen et al. (1988) reported inter-till stratified units at a single site in the Labrador Trough, indicating an ice-flow event followed by an ice-free period. However, no evidence of ferromanganese staining or inter-till (non-glacial) units was observed in this study area. In addition, three bedrock outcrops in the eastern portion of the study area, where the northeast-trending flowset is dominant, yielded apparent ^{10}Be ages that are considered close to the deglacial age (Figure 2.3) suggesting that the amount of inheritance (little to no inheritance) over this landscape is not indicative of a relict glacial landscape from pre-Wisconsin glaciation (Briner et al., 2006). Nonetheless, a more detailed investigation would be required in order to more completely test the pre-Wisconsin interpretation of that flowset, including an analysis of weathering across the flowset area. Therefore, it is likely Flow 1 is the oldest preserved flow phase in the study area, and it likely occurred at a time of extensive and thick ice due to the overall record of a uniform regional flow. Findings related to Flow 1 corroborate Klassen and Thompson (1993) and Veillette et al. (1999) earliest flow phase (Figure 2.2B, red arrow) and add new evidence which now extends this flow's influence further north into the study area.

Flow 2: Following Flow 1, an ice-flow switch is recorded in the western half of the study area. Flow 2 represents flow toward the northwest that initiated somewhere over the highlands in the central portion of the study area (Figure 2.8). The age relationship between these two flows was established from outcrop-scale ice-flow indicators from Flow 1 that are crosscut or preserved in the lee side of outcrop sculpted by Flow 2 at three locations (Figure 2.8). The landforms in the northwestern portion of the study area also trend to the northwest (Figure 2.8). The abundance of streamlined bedrock landforms in the western region suggests a highly erosive flow. This may explain the lack of older features within that flowset.

Thompson and Klassen (1993) reported ice-flow indicators of similar orientation to Flow 2, which they associated with the swarm of landforms toward Ungava Bay, but associated them with their third flow phase (Figure 2.2B, purple arrow). Flow 2 is also correlated to Clark et al. (2000) Flowset 19 and Jansson et al. (2003) Fan D. These flowsets were suggested to have formed during deglaciation. In their reconstruction of the UBIS, Jansson et al. (2003), suggested Fan D was a relatively early phase in the evolution of the palaeo-ice stream catchment. These findings suggest

Flow 2 features also formed at a relatively early stage of deglaciation as they are locally overprinted by younger phases. Therefore, Flow 2 can be constrained as occurring sometime before the formation of Flow 3 features and associated east-trending eskers. Based on the reconstruction of the UBIS by Jansson et al. (2003), Flow 2 would have shut down and the catchment would have moved further west. One possible scenario is this evolution led to a progressive shift of the ice divide toward the west over Flow 2 flowset. This shift would have preserved Flow 2 under the ice divide and start forming Flow 3 features to the east.

Flow 3: Outcrop-scale ice-flow indicators from Flow 2 are crosscut or preserved in the lee side of outcrop sculpted by Flow 3 at seven key locations (Figure 2.8). As indicated above, this shift suggests the dispersal centre migrated westward, across the study area, likely influenced by the UBIS (Clark et al., 2000; Jansson et al., 2003). This change in dynamics caused ice to flow east (Flow 3), possibly pulled by palaeo-ice streams to the east (ice stream #187- Margold et al., 2018) although Flow 3 appears to be restricted to the central portion of the study area and could thus have developed later; coeval to the eskers. As these landforms could not have formed directly under the ice-divide, it is unlikely the landforms of Flow 2 and Flow 3 formed isochronous and therefore likely formed time-transgressive, as the ice-divide migrated west across the study area. However, it is possible that Flow 2 and Flow 3 operated coevally for some time during ice divide migration. These two flows were likely separated by the eastern arm of the horseshoe divide that was being influenced by the changing dynamics of surrounding palaeo-ice streams, however, more detailed work would be required to confirm this. The preservation of ice-flow indicators from Flow 1 and Flow 2 in the western portion of the study area (Figure 2.7) suggest that subglacial conditions in that part of the study area shifted to a cold-based thermal regime during Flow 3, preserving the older ice-flow indicators. Furthermore, the erosive intensity of the ice sheet was minimal within the central highlands of the study area, as evident from the lack of glacially sculpted landforms in this region, and from crosscutting, opposing, striations associated with numerous double stoss-and-lee outcrops (Figure 2.11). Additionally, the landforms associated with Flow 3 are the same general orientation of elongate eskers in the eastern part of the study area (Figure 2.8) and likely formed at the late stages of Flow 3 when the ice-bed conditions switched to warm-based as eskers typically form during late-stage meltwater flow (Shilts et al., 1987; Boulton et al., 2009).

Klassen and Thompson (1993)'s deglacial ice-flow (Figure 2.2A- phase 2, orange arrows) and Clarhäll and Jansson (2003)'s deglacial phase (Figure 2.2, white arrow) all have a similar orientation

with this thesis' deglacial Flow 3. Landforms from this flow were not identified by Clark et al. (2000). Dubé-Loubert and Roy (2017) reported a similar pattern of eskers that shows a general retreat from east to west which stops at the George River valley area, ~ 135 km north of the study area. These eskers transition to frost-shattered bedrock and oxidized glacial deposits with multiple instances of lateral meltwater channels east of the George River associated with sustained cold-based conditions. Dubé-Loubert and Roy (2017) indicated the ice retreat was irregular and fragmented caused by changes in the basal thermal regime of the melting ice sheet. These findings lend additional support to this reconstruction, although evidence of sustained cold-based conditions, such as felsenmeer or other types of weathered *in-situ* regolith is lacking in the study area. It is possible the ice divide in thesis' study area was more sensitive and responded more to changes taking place in Ungava Bay than the area located to the north where Dubé-Loubert and Roy (2017) completed their work.

Flow 4: Following Flow 3 there was late-deglacial flow (Flow 4) to the east-southeast (Figure 2.8). Flow 4 overprints striations of all previous flows and was identified at 13 locations. There are no landforms associated with this ice-flow phase, suggesting it was likely short-lived and not highly erosive (Stokes and Clark, 2001), most likely due to thinner ice. This ice-flow event was not identified by Clarhäll and Jansson (2003) but was identified by Klassen and Thompson (1993) and Veillette et al. (1999) and was associated with both reconstruction's divergent phase 2 (Figure 2.2, orange arrow). Striation evidence firmly constrains Flow 4 to have occurred after Flow 3 and the formation of elongate eskers. It is still unclear as to how the ice margin and overall retreat of the LIS evolved from Flow 3 to Flow 4.

Ives (1958) and Kirby (1961) reported multiple sets of lateral meltwater channels and discordant striation measurements that indicated small ice caps in the Schefferville and Kivivic Lake regions. These findings support the scenario of multiple retreating ice centres proposed by Clark et al. (2000), whereby small ice caps formed during deglaciation, turned cold-based, and retreated toward the central highlands. Therefore, either the ice thinned to a point the bedrock topography became the predominant control on ice flow direction (Flow 4), and/or similar to other observations in the region (Ives, 1958; Clark et al., 2000), a small ice-cap formed somewhere on the De Pas upland before the final disappearance of the ice-mass.

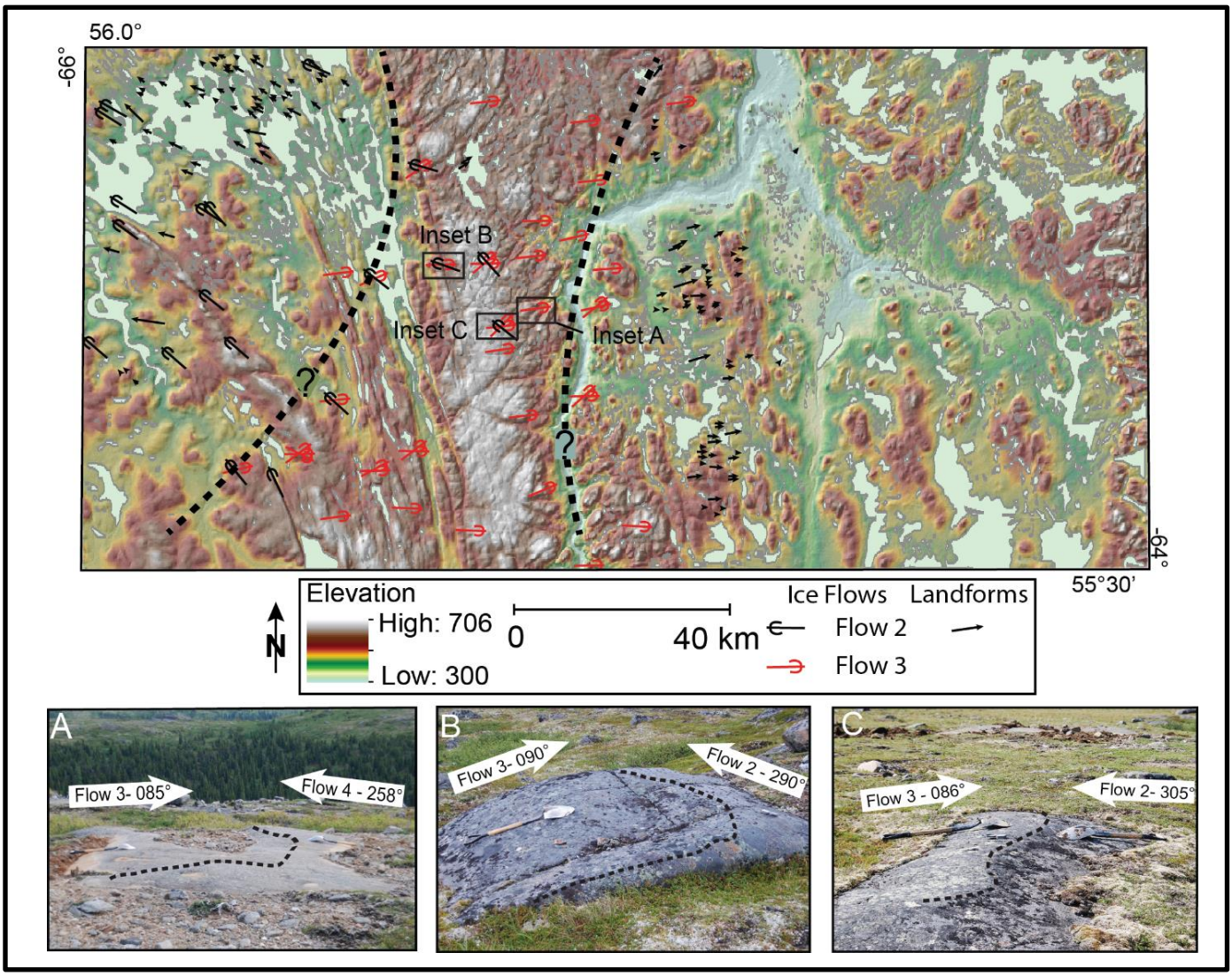

Figure 2.11. Hillshaded and elevation classed regional DEM with striations from ice-flow phase 2 (black) and phase 3 (red). The region of substrate protection is highlighted with dashed lines. The De Pas Batholith is evident as the elevated ridge (white colour on the DEM) bisecting the map sheet just west of the Rivière De Pas. **(A)** Outcrop from sample site 15-PTA-024 with evidence of ice flow reversal. **(B)** Bevelled outcrop at sample site 15-PTA-058 formed by two near opposing ice flow directions. **(C)** Double stoss-and-lee outcrop at sample site 16-PTA-069 again created by two near opposing ice-flow phases.

2.5.2 Timing of deglaciation

Following a deglacial flow to the east (Flow 3), the ice sheet began to significantly melt, and meltwater flowed to the central upland cutting large meltwater channels. These channels fed meltwater drainage systems toward the east which deposited large eastward trending eskers. At some point following the formation of the eskers, proglacial Lake Naskaupi formed in the upper George River valley (Dubé-Loubert and Roy, 2017) and presumably, Lake McLean formed in the general basin of modern-day *Lac Champdoré*. During deglaciation, a late stage, short-lived ice cap developed on the central upland (Flow 4), followed by final melting under cold-based conditions which formed abundant lateral meltwater channels (Figure 2.8).

The ^{10}Be results lack a clear separation in ages between the east, centre, and west groups. The large spread in ages within the centre spatial group (Figure 2.9 – blue) is indicative of inheritance within the samples. This inheritance is presumably the result of insufficient glacial erosion required to remove all previous accumulations of ^{10}Be (Fabel et al., 2004; Briner et al., 2005). This supports this thesis' ice-flow reconstruction model where sluggish, less erosive ice occupied the central portions of the map sheet with limited subglacial erosion throughout ice-divide migration. A more detailed investigation of the cosmogenic inheritance across the landscape and of related glacial erosion would significantly improve a discussion on the changing subglacial conditions across the region.

^{10}Be ages from perched erratics to the south and west of this study by Carlson et al. (2007; 2008), indicated that the LIS began retreating rapidly from the Hudson Bay coast at 8.2 ka and the entire region was completely ice-free by 6.8 ± 0.2 ka. Additionally, Ullman et al. (2016) suggested that the dominant loss of ice from the LIS occurred by 7.6 ± 0.6 ka following a rapid retreat of ice margins. Optical and ^{10}Be results range from 9.8 to 6.2 ka (Figure 2.9; Table 2.1). This relatively broad range is mostly due to the uncertainty or minor inheritance of some of the ^{10}Be ages. The two OSL results that were considered reliable cluster within a slightly narrower range of 7.7 - 7.9 ka. These results are consistent with Ullman et al. (2016)'s reconstruction considering the distance between the two study areas and the general deglaciation pattern. Results also correlate reasonably well with the more local ^{10}Be ages from Lake Naskaupi shoreline, which indicate Lake Naskaupi must have reached its largest extent before draining catastrophically at 8.3 ± 0.3 ka (Dubé-Loubert et al., 2018). This event is further confined by the optical dating of Lake Naskaupi highest (sample 15-PTA-149; 7.93 ± 0.72 ka) and lowest (sample 15-PTA-074; 7.65 ± 0.99 ka) levels in the study

area (Figure 2.3), which matches Dubé-Loubert et al. (2018)'s findings well. Unfortunately, samples from Lake McLean yielded no usable results, therefore a discussion on its formation and drainage is not possible without further investigation.

2.5.3 Paleoglaciological implications

Records indicating ice flow reversals have been documented elsewhere and interpreted as evidence of ice-divide migration, most notably, within the Keewatin ice-divide region (McMartin and Henderson, 2004) and in the Canadian Arctic (Dyke et al., 1992) but also just west of the current study area (Parent et al., 2004). In this study, the ice-flow shift between Flow 1 and Flow 2 may not necessarily require ice-divide migration, as it may have been caused by the development of the UBIS. However, the degree of preservation of Flow 1 features to the east suggest that an ice-divide developed over that zone separating the UBIS from the ice flow dynamics further to the east toward the Labrador coast. Furthermore, an ice-divide migration appears to best explain both the preservation of Flow 2 in the northwest and the development of Flow 3 features to the east. This type of ice divide migration is not of the same magnitude as the one documented in the Keewatin (~ 500km – McMartin and Henderson, 2004) and does not require a large ice sheet reorganization. Nonetheless, it influenced the study area's landscape evolution and it shows the impact an ice stream catchment zone has on the glacial dynamics far inland (e.g., Rignot et al., 2011).

It appears that subglacial conditions also evolved from regionally widespread warm-based conditions during Flow 1 to a polythermal base, which led to the preservation of Flow 1 features in the eastern portion, partial overprinting in the central portion by subsequent flows, and more intense overprinting during Flow 2 in the northwest. The net effect of this evolution is a mosaic terrain at the landscape-scale somewhat similar to the fragmented landscape described in the outer zone of the Keewatin (Trommelen et al., 2012; Gauthier et al., 2019). This is best shown in the landform record, where Flow 1, Flow 2, and Flow 3 are limited to their own spatial zone, with only minor crosscutting of the flows evident in the striation record (Figure 2.8). Long intervals in which the base of the ice is near or below the pressure melting point (limited net erosion) are needed to generate the landscape fragments or zones containing multiple ice-flow indicators of highly variable directions.

These two ice domes (Keewatin and Labrador) were the largest and probably thickest mid-latitude ice sheet domes of the last glaciation (e.g., Dyke and Prest, 1987; Tarasov et al., 2012).

These ice domes have left a unique record that contrasts other ice-divide areas. For example, smaller and thinner ice domes over Baffin Island (Davis et al., 2006), the Boothia and Melville peninsulas (De Angelis and Kleman, 2005), and in central Sweden (Kleman and Stroeven, 1997), have widespread evidence of sustained cold-based conditions and lack evidence for major ice-divide translocation. These other smaller ice-divides at higher latitudes appear to have remained relatively stationary throughout glaciation. The LIS thus had polythermal ice-divide regions that migrated throughout glaciation, preserving ice-flow mosaics from different ice-flow directions. This complex mosaic is recognizable at multiple scales, not just at the large landform-scale (e.g., Boulton and Clark, 1990), such as within the regional striation record and by small-scale landforms. This approach, where landform mapping is supplemented with outcrop-scale observations, is key in the reconstruction of ice-flow dynamics and resolving existing, and conflicting ice-flow reconstructions. The multiple sites where different ice-flow events are recorded in the striation record were critical in resolving the ice-flow history of the study area, for which conflicting ice flow reconstructions existed. Additional research on glacial erosion and till transport, and further investigation into cosmogenic radionuclide inheritance in both bedrock and till (e.g., Staiger et al., 2006), should help further test and improve these reconstructions and add to the overall understanding of ice-sheet and landscape evolution of ice-divide regions.

2.6 Conclusions

The purpose of this research was to constrain the relative ice-flow chronology in a debated region that had insufficient field observations and to establish the local timing of deglaciation. This work builds on regional glacial reconstructions conducted nearby which intended to elucidate the complex ice-flow chronology through extensive field-based investigations. The conflicting ice-flow chronologies within the study area (Veillette et al., 1999; Jansson et al., 2002) have been resolved, with four ice-flow phases identified from striae measurements and landform analysis. The first ice-flow phase was uniform to the northeast across most of the study area, which was followed by the propagation of the UBIS within the western portion of the study area, which dispersed ice to the northwest and formed large oriented landforms. A change in subglacial thermal regime took place in the eastern portion which favoured the preservation of Flow 1 features. Flow 3 marks an important shift toward the deglaciation of the region, as the UBIS influence became weaker in the study area.

Ice then stagnated or was sluggish in most areas, eskers developed, and the ice margin retreated from the east to the west toward the George River. A short-lived late-deglacial phase from the central highlands to the west-southwest occurred during deglaciation as recorded by weak and discontinuous late-stage ice-flow indicators (Flow 4). The exact timing of these ice-flow events remains unknown. Optical ages from Lake Naskaupi indicate beach ridges associated with the lake were formed around 7.9 ± 0.7 ka and is consistent with detailed deglacial work by Dubé-Loubert et al. (2018) north of this thesis' study area, which provides additional constraints south of their study area to constrain the timing of local deglaciation.

Future work on constraining the subglacial conditions across the region should help further elucidate the complex evolution of the QLD throughout glaciation providing important constraining parameters for future ice sheet scale reconstructions (e.g., Clark et al., 2000; Dyke et al., 2003; Margold et al., 2018).

3 Chapter 3: A GIS-based multi-proxy analysis of the evolution of subglacial dynamics of the Quebec-Labrador ice dome, northeastern Quebec, Canada

3.1 Overview

The glacial records of the inner regions of the Laurentide Ice Sheet (LIS) document complex, yet coherent patterns of ice sheet change (e.g., ice-divide migration). This study develops a conceptual model of the evolution of subglacial dynamics within a major ice-dispersal centre of the LIS in northeastern Quebec, Canada using a GIS-based analysis of the surficial geologic record. Three proxies of subglacial ice/bed mobility (subglacial streamlined landforms, lake density, and lake surface area on bedrock), were analyzed through grid-overlay techniques, then classified based on different relative subglacial bed mobility levels: High (widespread bedrock erosion and/or streamlined landform development), Low (no indication of subglacial ice/bed mobility) and two 'transitional' zones that separate the end-member classifications (Moderate-high (MH) and Moderate-low (ML)). An additional proxy (till blanket) was also used to identify areas of till deposition lacking streamlined landforms as a warm-low (WL) category (low ice/bed mobility but net will deposition). Based on local ice flow reconstructions, the most 'relict' glacial terrain is defined as High or MH over 66% of its area (~ 1730 km^2) suggesting laterally extensive subglacial ice/bed mobility during the oldest identified ice-flow phase. This relict terrain is partially overprinted in two main regions of high ice/bed mobility (41% and 73% defined as High or HM). Another narrower landscape zone associated with the eastern catchment of the Ungava Bay ice streams is classified as High or MH over 32% of its area (~1890 km^2). These three zones are separated by a central zone of reduced subglacial ice/bed mobility (53% ML), within an upland area where all proxies are low but crosscutting striations are more common. The age of the 'relict' glacial landscape is unknown, however, till across all zones have consistently low chemical index of alteration values (mean =50.3, σ = 3.5) and cosmogenic nuclide abundances (bedrock and till) reveal limited ^{10}Be inheritance, including the central zone of reduced subglacial mobility. This landscape represents the net effect of spatio-temporal shifts in ice flow, ice-divide position, and thermal regime, over the last glacial cycle. The landscape shows that, despite being a core region of the LIS where models indicate low probability of warm-based conditions, the region experienced extensive transient conditions during the last glaciation. No clear evidence of sustained cold-based conditions throughout glaciation

was found in the study area through this analysis. Instead, results suggest subglacial warm-based conditions (active erosion and/or deposition) were uniformly widespread during an early phase of subglacial landscape development and later became more focused along specific corridors dur to the influence of different late-glacial ice stream catchments.

3.2 Introduction

Interior regions of the LIS show crosscutting subglacial landforms indicative of multiple ice-flow phases that several studies have interpreted to reflect ice divide migration caused by internal ice dynamic shifts and/or other processes that take place far from the ice margins, as well as closer to ice margins during the final stages of deglaciation (Boulton and Clark, 1990; Clark et al., 2000; McMartin and Henderson, 2004; Trommelen et al., 2012; Hodder et al., 2016; Gauthier et al., 2019). Portions of the glacial landscape in these regions thus contain subglacial landforms correlated to old ice-flow phases. In some places, these old features form extensive coherent landscapes that were largely preserved under unmodified "frozen-bed" and "ephemeral" patches (Kleman and Glasser, 2007). Their occurrence indicates a shift in thermo-mechanical conditions from warm-based flowing ice to cold-based (frozen at the bed-not moving) at some point during the last, or a preceding glaciation. Despite their fragmentary nature, these patches of relict glacial terrains offer a window into previous ice sheet configurations and subglacial conditions (Kleman and Glasser, 2007; Gauthier et al., 2019). In addition, the distribution, and degree of overprinting of these relict glacial beds by younger phases provide key information about how glacial dynamics evolved over time. These interior regions also contain evidence of more sustained cold-based ice, where subglacial landscape features are lacking (Dyke, 1983; Edmund, 1991; Kleman and Stroeven, 1997; De Angelis and Kleman, 2005; Davis et al., 2006). Therefore, inner core regions of the ice sheets often form subglacial mosaics of different Glacial Terrain Zones (GTZ; Trommelen et al., 2012) and investigating these records can improve the understanding of the long-term subglacial conditions and overall ice sheet dynamics of the LIS (e.g., Gauthier et al., 2019).

One of the largest ice dispersal centres of the LIS occupied northern Quebec and is commonly referred to as the New Quebec-Dome (Hillaire-Marcel et al.,1981; Vincent, 1989; Roy et al., 2015), or, the QLD (Kleman et al., 2002; Jansson et al., 2003; Occhietti et al., 2011; Stokes et al., 2012). The QLD has been estimated to be 2-3 km thick at the Last Glacial Maximum (e.g., Ganopolski et al., 2010; Peltier et al., 2015), with ice-flow dispersal patterns spreading across and

west of Hudson Bay during various phases (Prest et al., 2000; Trommelen and Ross, 2014), and left evidence of its important influence on the overall behaviour of the LIS. The QLD is characterized by a complex ice-flow record (Veillette et al., 1999). At the landscape-scale (Figure 3.1), crosscutting flow sets indicate a partially preserved, long temporal record that has been overprinted locally by late-glacial features associated with dynamic adjustments in regional ice-flow configuration (Clark et al., 2000; Jansson et al., 2003; Margold et al., 2015, 2018). The landform record of the QLD is also characterized by a horseshoe-shaped unconformity (Clark et al., 2000) separating landforms converging toward Ungava Bay from landforms radially oriented away from Ungava Bay (Figure 3.1).

The southeastern branch of this horseshoe unconformity was recently the focus of ice-flow reconstruction and deglacial studies (Dubé-Loubert and Roy, 2017; Dubé-Loubert et al., 2018; Chapter 2). The subglacial record of this thesis' 7000 km^2 study area is thought to reflect ice divide migration, as well as changes in palaeo-ice stream catchment, which together suggests a complex evolution characterized by transient polythermal subglacial conditions

This investigation analyzes the subglacial record of an inner region of the QLD that experienced a complex ice-flow history and, to improve our understanding of the net effect of the changing ice sheet dynamics on the glacial landscape. This investigation combines various proxies typically used to analyze patterns and intensity of bedrock erosion and/or glacial landform (e.g., drumlin) development related to actively flowing ice. By placing this spatial analysis within the context of the ice flow history and related fragmented GTZs (Trommelen et al., 2012), insights into the relative strength of subglacial activity related to the older flowsets and younger overprinting phases can be obtained. These GTZs are then further assessed using independent proxies of glacial erosion, specifically the chemical index of alteration (CIA) and abundance of ^{10}Be in till and bedrock, to determine whether there is evidence of weathering and/or inherited exposure in areas where the other proxies indicate limited net glacial imprint on the landscape or where 'relict glacial beds of unknown age are particularly well-preserved. This is then used to interpret changes in subglacial ice-flow dynamics and related thermo-mechanical conditions throughout the established ice-flow history including an ice divide migration within the study area. This work builds on the understanding of how the interior regions of ice sheets evolve from a subglacial landscape perspective throughout one or more glaciation(s).

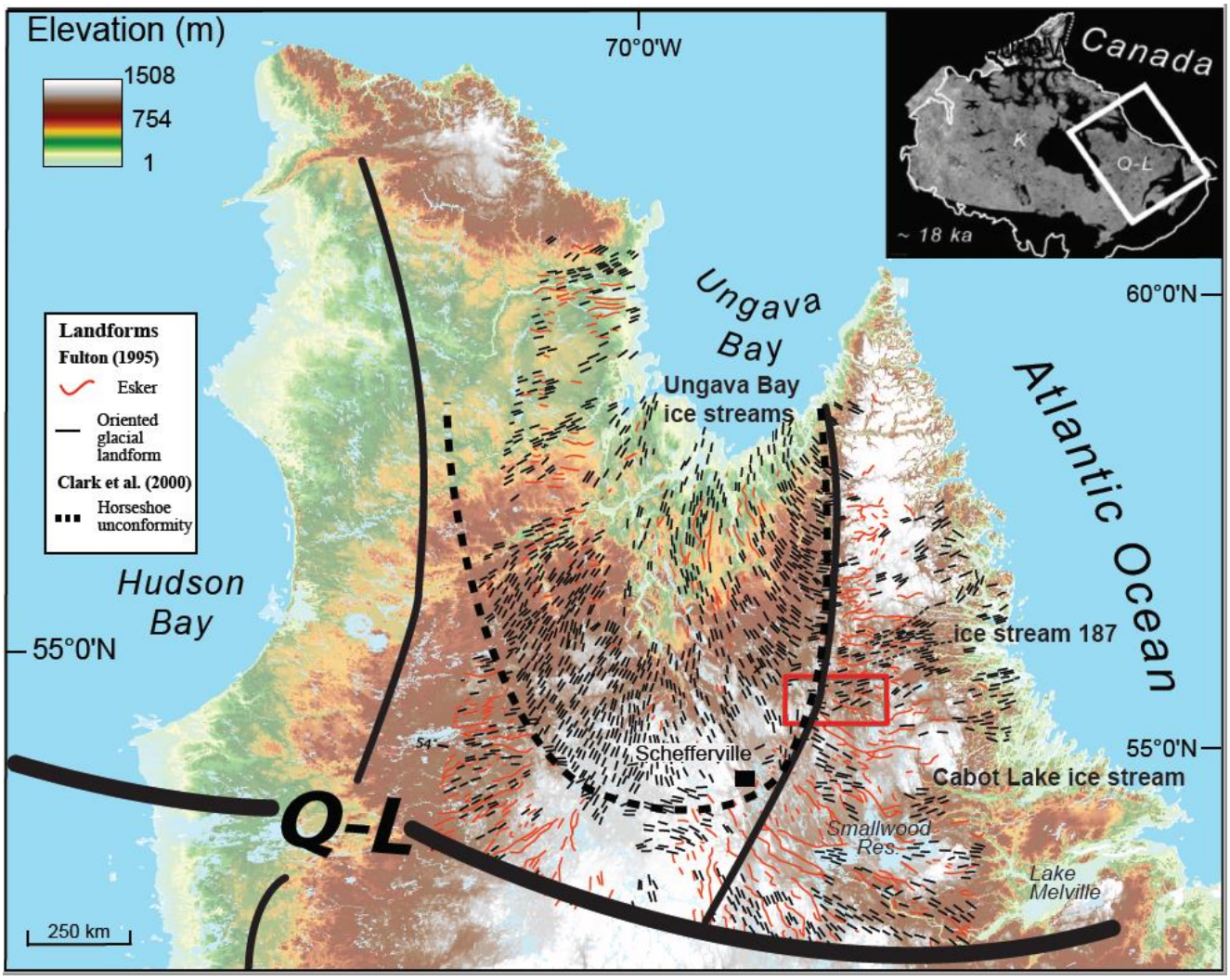

Figure 3.1. A digital elevation model of northern Quebec and Labrador with select regional landforms annotated from Fulton (1995) and the horseshoe unconformity of Clark et al. (2000). The approximate locations of the ice divide identified by Dyke and Prest (1987) are also annotated. Several notable ice streams are also identified (Margold et al., 2015; Rice et al., 2020). The current study area is outlined in red. **(Inset)** The approximate extent of the LIS at 18 ka (Dyke 2004), with the approximate centres of the Keewatin (K) and the Quebec-Labrador (Q-L) sectors, thick lines represent large ice divides and thinner lines represent smaller divides (see Dyke and Prest, 1987).

3.2.1 Study Area

The study area is located in northcentral Quebec, Canada (Figure 3.1) and encompasses the border region between two large lithotectonic blocks: the Core Zone (CZ) in the east and the NQO in the west (Figure 3.2A). The CZ is a 300 km wide suite of Archean rocks reworked during the

collision of the Superior and Nain cratons which forms the eastern edge of the Canadian Shield (Figure 3.2A) that has been identified as a regional of mineral potential with recent bedrock mapping projects (Corrigan et al., 2018). Different bedrock lithologies can have significant controls on landscape evolution (Phillips et al., 2010), glacial erosion rates (Dühnforth et al., 2010), and glacial sediment properties (McClenaghan and Paulen, 2018), therefore considering the lithological variation across the study area is essential. Bedrock within the study area is subdivided into three general domains: the RL of the larger NQO in the west, the GR in the centre, and the MR in the east, both part of the larger CZ block (Figure 3.2A).

The Paleoproterozoic RL domain is comprised of metasedimentary and felsic plutonic rocks (Sanborn-Barrie, 2016; Corrigan et al., 2018). The metasedimentary bedrock of the RL domain are highly metamorphosed, with well-developed folding structures. Less structural control on the topography is evident in the quartzofeldspathic gneiss lithologies in the north of the domain (Figure 3.2B). The Lac Tudor Shear Zone defines the eastern border of the RL domain with the western orthogneiss and GR lithologies. The De Pas upland is a felsic batholith within the GR Domain that strikes north/south through the middle of the study area (Sanborn-Barrie, 2016). This resistant lithology forms a highland region that roughly bisects the study area (Figure 3.2C). The GR valley within this domain has the lowest elevations within the study area (290 m -Figure 3.2). The De Pas batholith is flanked on both sides by ~ 12 km wide bands of Archean orthogneiss. East of the De Pas batholith and its associated eastern orthogneiss lies the high-grade magmatic MR domain, which is composed of paragneiss, granitoids, diorites, and mafic-ultramafic plutonic rocks (van der Leeden et al., 1990). The MR is within the larger CZ and marks its eastern boundary.

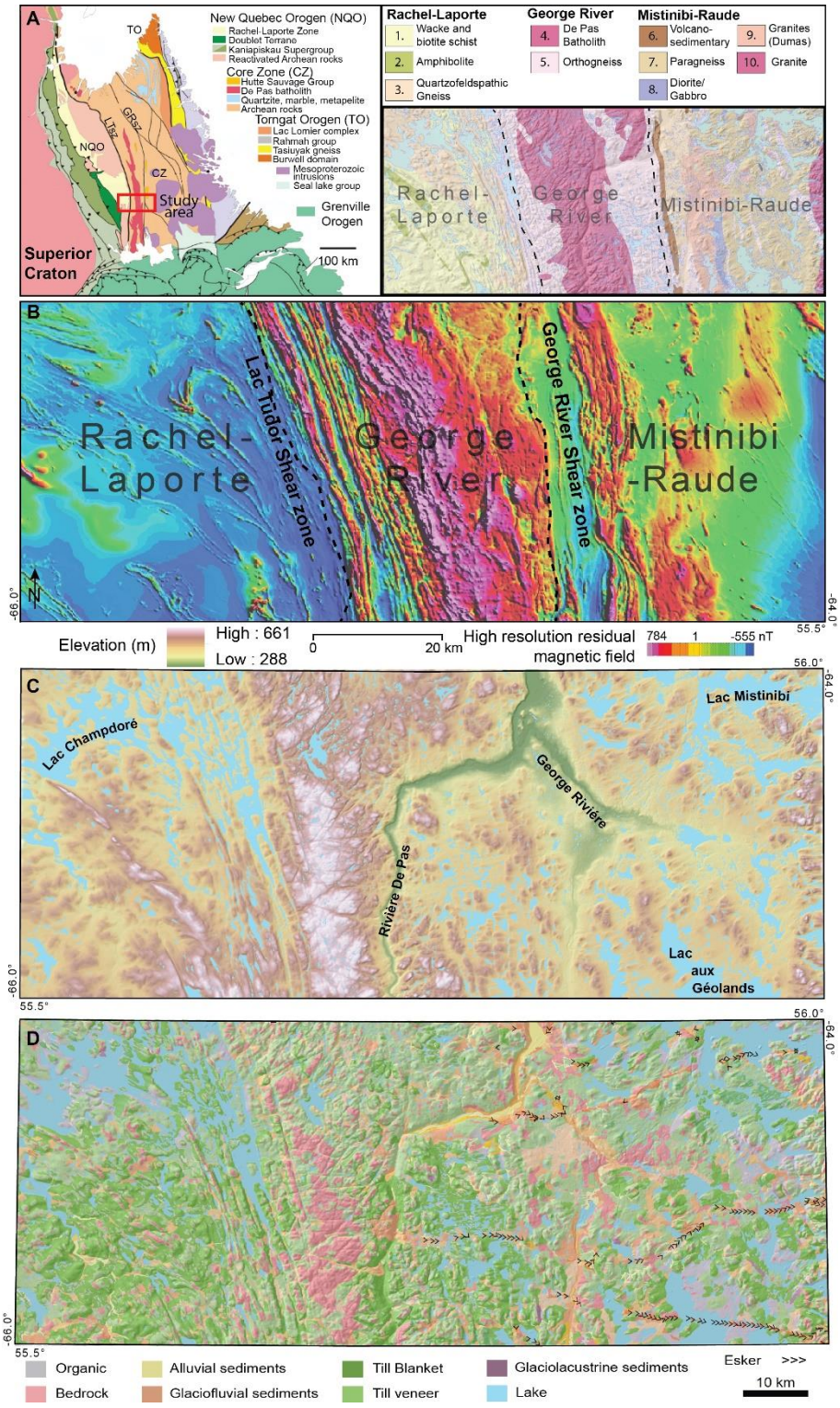

Figure 3.2 **(A** Simplified regional bedrock geology of Quebec-Labrador (modified from James et al., 2003). (Top inset) Simplified local bedrock geology of the study area (modified after Wardle et al., 1997; Sanborn-Barrie, 2016; Corrigan et al., 2018). **(B)** High-resolution residual magnetic field data for the study area, highlight bedrock structures (MERN, 2019). **(C)** Digital elevation model of the study area with major rivers and lakes labelled (data source: USGS). **(D)** Simplified surficial geology of the study area (modified from Rice et al., 2017a, 2017b**).**

3.2.2 Surficial geology and ice flow history

The study area is characterized by bedrock uplands that are glacially sculpted and flanked by discontinuous till veneers, with thicker till deposits in the valleys (Figure 3.2D; Rice et al., 2017a, 2017b). Glaciofluvial erosional and depositional features (e.g., meltwater channels, eskers, kames, and kettles) are common within the central and eastern parts of the study area with abundant meltwater channels cut into the bedrock of the central highland. Eskers occur in the eastern part of the study area and are radially oriented toward the east-northeast. Two glacial lakes briefly inundated the study area during ice margin retreat; Lake Naskaupi in the east and Lake McLean in the west (Ives et al., 1976; Jansson, 2003; Dubé-Loubert et al., 2018). Shoreline and littoral features represent the main evidence for the existence of these short-lived lakes as fine-grained ice distal lake deposits were not observed in the study area.

Within the study area, four ice-flow phases were identified (Figure 3.3; Chapter 2). The earliest ice-flow phase (Flow 1) was to the northeast and covered most of the study area; it has been documented in other regions of Quebec and Labrador (Klassen and Thompson, 1993; Veillette et al., 1999). Flow 1 was followed by the development of an ice divide within the eastern portion of the study area, which resulted in a northwest-trending ice-flow phase (Flow 2) in the western sector of the study area. This ice-flow phase was likely caused by a shift in ice dynamics associated with ice streaming occurring in Ungava Bay (Clark et al., 2000; Jansson et al., 2003; Margold et al., 2015). A later westward shift in the dynamics of the UBIS (Jansson et al., 2003) led to a westward migration of the dispersal divide, commonly referred to as the Ancestral Labrador ice divide (Dyke and Prest, 1987), and a concomitant eastward shift of ice flow. This westward shift is recorded by younger east-trending ice flow features (Flow 3) across the central portion of the study area (Figure 3.3; Chapter 2). Flow 3 likely occurred sometime during deglaciation as the eskers in the study area are parallel to the trend of this ice-flow phase. Following Flow 3, there was a minor late-deglacial ice-flow phase, with ice flow mainly trending to the west, likely sourced from a smaller localized ice centre located on the central upland (Chapter 2). Palaeo-ice streams also developed during this phase, such as the Strange Lake palaeo-ice stream (McClenaghan et al., 2019), Kogaluk River ice stream (Margold et al., 2015), and the Cabot Lake ice stream (Paulen et al., 2019; Rice et al., 2020), but their footprints are mostly located outside of the study area, with the exception of the northeast corner (Lake Mistinibi region) where subglacial lineations appear to be part of the converging catchment of the

Kogaluk River ice stream. Evidence of Flow 4 is limited to striations, which suggests it was short-lived and associated with thinner, less erosive ice. In contrast to areas further north (Dubé-Loubert and Roy, 2017), frost-shattered bedrock or regions of oxidized glacial deposits were not identified during fieldwork within the study area (Chapter 2*)*.

Previous studies of complex glacial landscapes have identified spatially distinct subglacial zones (Stea and Fink, 2001), glaciodynamic zones (Tremblay et al., 2013) or GTZs (Trommelen et al., 2012) that provide important insights into changing subglacial dynamics across glaciated terrains. The separation of different regions based on their surficial characteristics was conducted southwest of Hudson Bay where ice sheet reconfiguration and other factors led to multiple ice-flow shifts and transient subglacial conditions which together, resulted in spatially coherent, yet distinct, GTZs (Trommelen et al., 2012; Gauthier et al., 2019). Using these principles, four glacial terrain zones were identified in the study area (Chapter 2, Figure 3.3).

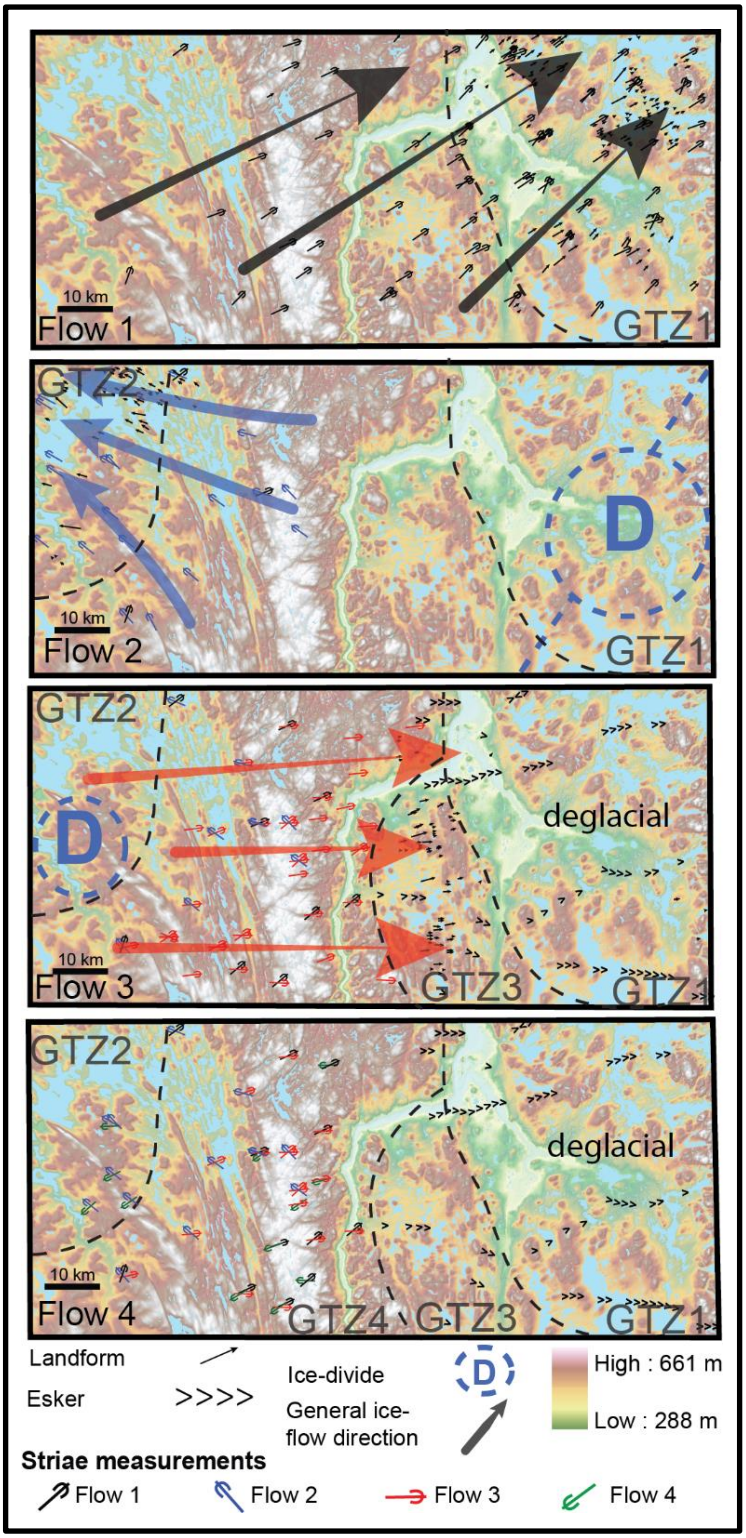

Figure 3.3. Ice flow history of the study area with identified glacial terrain zones (GTZs) identified in Chapter 2. Crosscutting striations are annotated on later ice-flow events.

GTZ1 contains numerous northeast-trending ice-flow indicators associated with Flow 1. Several streamlined landforms oriented within that same range typically consist of large rock drumlins and crag-and-tails; it is interpreted as a relict flowset preserved under later cold-based conditions (Chapter 2*).* In the northeast corner of the study area, around the Lake Mistinibi region (Figure 3.2), numerous smaller and more elongated drumlins occur within a slightly oblique orientation relative to Flow 1 features; they trend toward 65°. This area was initially included within GTZ1 (Chapter 2), but here have now divided it to amend these boundaries, as the degree of overprinting by late-stage ice flow appears to be stronger in that area than elsewhere within GTZ1. This overprinting is likely part of the converging catchment of the Kogaluk palaeo-ice stream located further to the northeast (Figure 3.1). Elsewhere, however, GTZ1 remains the same as in Chapter 2 as it is clearly associated with the oldest regional northeast ice-flow phase. It is characterized by abundant streamlined landforms and striations of similar northeast orientation that are only locally crosscut at a high angle (~45°) by eskers interpreted to have formed during deglaciation. These eskers could have formed as efficient drainage corridors lowering water pressure, raising effective pressure and inhibiting ice flow (Boulton et al., 2007), or as time-transgressively in short segments close behind a retreating ice mass of limited erosive power (Livingston et al., 2015). It is important to note that GTZ1, as delineated within the current study area, lies approximately in-between two late-stage paleo-ice streams: the Kogaluk ice stream to the northeast (#187; Margold et al., 2015) and the Cabot Lake ice stream to the south (Rice et al., 2020). Cold-based inter-ice stream conditions could thus have contributed to preserving the relict (Flow 1) features of GTZ1.

GTZ2 is dominated by landforms and striations associated with Flow 2 to the northwest with some striation evidence from Flow 3. GTZ3 is characterized by smaller, east-trending subglacial lineations (rock drumlins, crag-and-tails, and till drumlins) overprinted on northeast-trending features associated with Flow 1 (Figure 3.3) as well as by short segments of generally east-trending eskers. This GTZ is thus defined by relatively strong overprinting of Flow 1 landscape by Flow 3 features, although a palimpsest Flow 1 landscape is still evident in the outcrop and landform records. GTZ4 is the largest zone within the study area and has multiple outcrops with crosscutting striations, double-stoss-and-lee outcrops, and few landforms (Figure 3.3). The internal features of these GTZs show variability that has yet to be characterized. Determining the variation of subglacial proxies within each GTZ and the contrasting assemblages between them will offer insights into how subglacial dynamics varied during the different relative ice-flow phases.

3.2.3 Timing of ice-flow phases

The age of the ice-flow phases identified within the study area is unknown. However, by examining the ages of ice-flow events from surrounding regions where crosscutting landforms and organic material suitable for dating have provided relatively well-established ice flow "ages", an approximation can be made. No age correlation can be made for Flow 1 (Figure 3.4A), likely due to its heavy overprinting by subsequent ice-flow phases in regions where ^{14}C dating can be conducted (i.e., coastal regions), however, given its widespread warm-based conditions (Chapter 3), it likely occurred close to LGM when insulation was greatest and ice-sheet models have indicated higher probabilities of more broad warm-based conditions (Tarasov and Peltier, 2007).

Recent work by Stokes et al. (2016) and Margold et al. (2018) focused on the dating of crosscutting palaeo-ice streams and available ^{14}C data to develop a preliminary understanding of the timing of palaeo-ice streams operation across the LIS. This work has indicated the earliest activated palaeo-ice stream (#17- Margold et al., 2018) to penetrate the QLD was the Ungava Bay Fans 1 that formed around 11.5 cal ka BP (Figure 3.4B). The Ungava Bay Fans 1 correlates to this thesis' Flow 2 and indicates palaeo-ice streams propagated a significant distance up ice, close to the hypothesized ice divide location. Similar palaeo-ice stream propagation has been documented in the Keewatin sector during LGM (Hodder et al., 2016) and in northern Hudson Bay (Ross et al., 2011). Following the establishment of the Ungava Bay Fan 1 (#17- Margold et al., 2018), a shift in ice sheet dynamics resulted in the westward shift in the position of the Ungava Bay catchment (#16-Ungava Bay Fans 2-Margold et al., 2018), creating an entirely different palaeo-ice stream flowset that crosscuts the older one. This second phase is suggested to have occurred around 10.1 cal ka BP (Margold et al., 2018; Figure 3.4C). This westward migration of the palaeo-ice streams in Ungava Bay is consistent with the westward migration of the ice divide and the development of east-trending ice flow (Flow 3 of this study) in the study area and thus, correlates to transient events. Following the palaeo-ice streaming events into Ungava Bay, multiple ice streams developed on the eastern margin of the QLD at around 8.9 cal ka BP (#186- Happy Valley-Goose Bay-Margold et al., 2018; Figure 3.4C). Palaeo-ice streams not identified by Margold et al. (2018) but have been identified through more recent mapping are along the same longitude (Smallwood ice stream - Paulen et al., 2017; Cabot Lake ice stream- Rice et al., 2020; Paulen et al., 2020). These paleo-ice streams are of a similar orientation to Margold et al.'s (2018) ice stream #186 and #187 suggesting it also formed during this time. The relatively short time between these palaeo-ice stream operations (~2.6 cal ka BP between Ungava Bay fan 1 and Happy Valley-Goose Bay) suggest relatively rapid changes to the overall organization of the QLD, prior to deglaciation (Figure 3.4D).

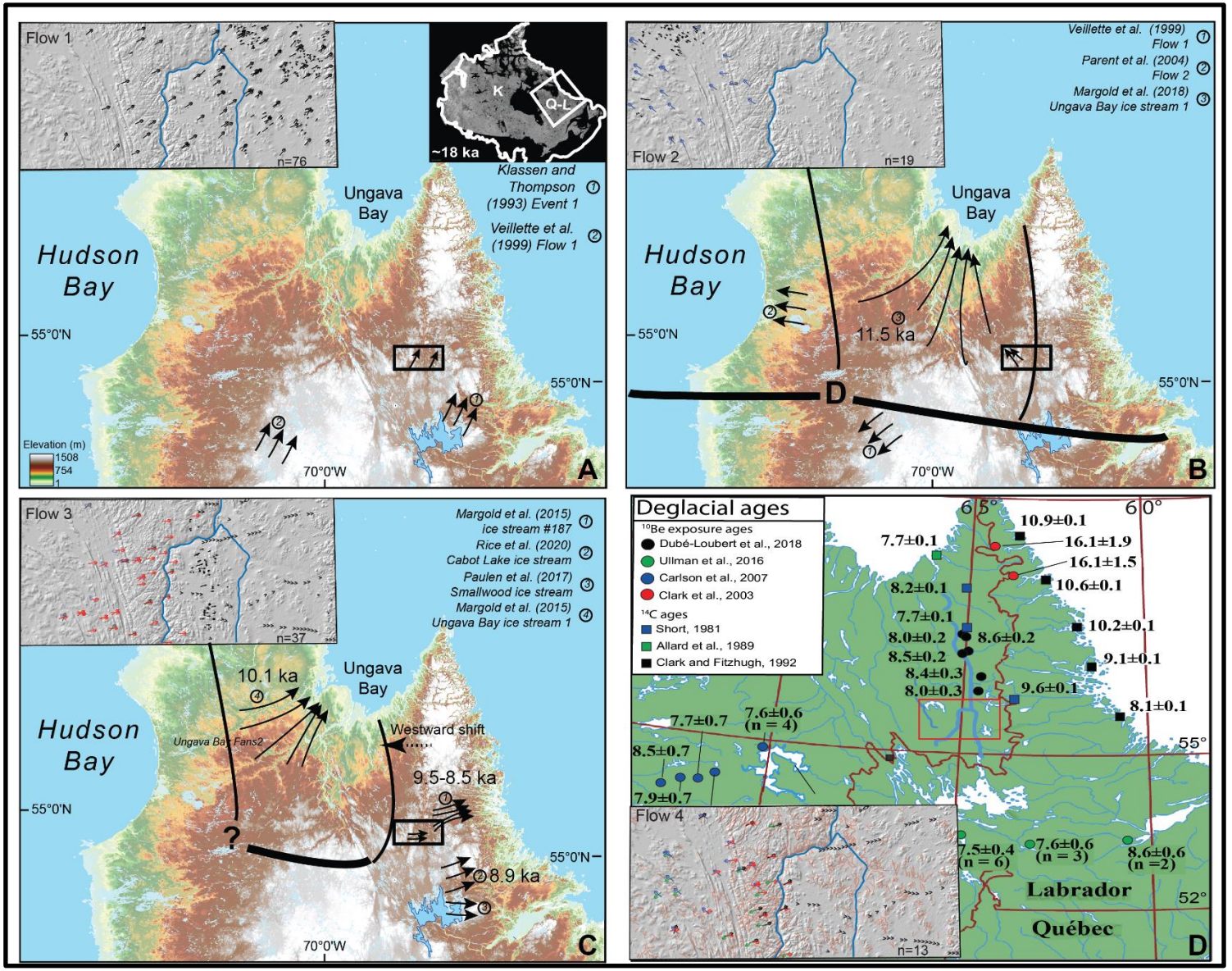

Figure 3.4. **(A)** Regional northwest flow observed in several locations across Quebec/Labrador. **(B)** Establishment of an ice saddle in the eastern half of the study area, with ice flowing toward Ungava Bay. **(C)** A westward shift in ice streaming within the Ungava Bay ice stream causes the ice divide to migrate westward across in the study area, leading to east flowing ice which also influenced by multiple other east-trending ice streams during deglaciation. **(D)** Flow 4 occurs during late deglaciation. Regional ^{10}Be exposure ages and ^{14}C ages suggest deglaciation occurred rapidly across the entire region. Ages are reported in thousands of calibrated years before present (cal ka BP).

3.3 Methods

For this investigation, multiple analytical methods were collectively used to assess the mobility of the subglacial ice/bed across the study area. This collective assessment was completed through an analysis of the surficial signature (i.e., surficial geology), lake density, lake area, streamlined landform density, and streamlined landform elongation, which have all been independently used to assess the changes in subglacial conditions across other glaciated terrains. The cumulative changes between all these proxies were then used with a grid-overlay to classify the study area into different cells based on the relative differences in the proxies. Additionally, the CIA from collected till samples and cosmogenic nuclides abundances from bedrock and till samples were examined to further constrain subglacial erosional vigour. The detailed methodologies of each of these analytical methods can be found below.

3.3.1 Surficial signature of the study area

Net subglacial erosion and other effects of actively flowing basal ice have been inferred from the spatial density of bedrock-controlled lakes across the Canadian Shield (Sugden, 1978; Andrews et al., 1985), on Baffin Island (Briner et al., 2008; Ebert et al., 2015), and over Iceland (Principato and Johnson, 2009). The general approach analyzes the abundance of lakes within terrains characterized by thin discontinuous veneer and bedrock outcrops and thus, provides insights into variable spatial erosion from basal sliding across a hard bed. However, within the current study area, surficial maps indicate that bedrock and till veneer covers only about 46% of the study area (Figure 3.2D). The abundance of striations and other outcrop-scale glacial erosional indicators (Chapter 2) supports the glacial erosion formation of lake-filled depressions within these terrains. In these regions, spatial lake density can be used to assess the degree and pattern of spatial erosion by abrasion and quarrying from basal sliding across a hard bed. However, the remaining 54% of the study area is covered with till blanket and other surficial sediments that mask the underlying scoured bedrock surface. Lakes at the surface in these areas of thicker sediments occur in depressions that formed through a variety of processes (e.g., kettle lakes, thermokarst lakes) and are thus not reliable indicators of subglacial erosion. However, areas of till blanket are interpreted as subglacial traction tills (Rice et al., 2017a, 2017b) which also represents areas of actively flowing warm-based ice. Proxies other than bedrock erosion proxies therefore need to be used across these areas of thicker subglacial sediments.

Areas of till blanket provide evidence of bed mobility, as basal meltout and/or active lodgment is required to deposit the till. Cells containing >50% till blanket, but lacking landforms, were thus automatically categorized as till blanket and used as a proxy of active bed mobility (i.e., warm-based).

Elongated subglacial landforms have been used as a proxy for basal ice flow velocity through measurement of landform elongation (Stokes and Clark, 2002; Bradwell et al., 2007; Stokes et al., 2007; Clark et al., 2009; King et al., 2009; Ross et al., 2009, 2011; Stokes et al., 2013), and landform spatial density (Hart and Smith, 1997; Stokes and Clark, 2001; Briner, 2007; Dowdeswell et al., 2010; Principato and Johnson, 2009). In this study area, elongated features of glacial origin occur over bedrock, till veneer, as well as parts of till blanket areas. Therefore, an analysis that considers not only bedrock-controlled lakes, but also the elongated bedrock and bedrock-cored features (e.g., whalebacks, rock drumlins), as well as till-cored drumlinoid landforms and till blanket areas (28% of study area) is likely to provide more complete and thus more useful information about subglacial conditions and overall dynamics across a larger proportion of the study area.

To conduct a uniform analysis across the study area, 2.5 x 2.5 km cells was created in ArcGIS (v.10.3.1) to create a grid overlay that would allow for a comparison between proxies. This grid size has proven effective in other studies with similar geospatial resolution (e.g., Ebert, 2015). It is important to note that about 26% of the study area needed to be excluded from this thesis' analysis because it dominantly consists of proglacial and postglacial surficial sediments (Rice et al., 2017a, 2017b) that do not reflect subglacial processes. Grid-cells containing >50% of proglacial and postglacial surficial sediments were thus masked and not considered further in the analysis. The remaining cells were then categorized based on lake spatial density, lake area, streamlined landform spatial density, streamlined landform elongation, and till blanket. The ggplot2 package (Wickham, 2009) within the R statistical environment (R Core Team, 2015) which is commonly used for geoscience data analysis (Grunsky, 2002), was also used to plot results for further analysis and interpretation of the data. The following subsections describe in more detail how these different proxies of subglacial dynamics were mapped and analyzed.

3.3.2 GIS analysis

3.3.2.1 Lake analysis

Waterbodies data (1:50 000 scale) were obtained from the Canadian Geogratis website (www.geogratis.gc.ca). Lakes within identified masked regions were removed from the analysis, as their formation could not be associated with subglacial ice/bed mobility (Sugden, 1978; Andrews et al., 1985; Ebert, 2015). Within the ~ 7000 km^2 study area, there are 27,169 lakes; 6738 lakes (24.8%) were within masked units and not used, leaving 20,431 lakes for this analysis.

Lake spatial density was measured by first computing the centroid of each lake, using the point density function within ArcGIS. Then the number of centroids per grid cell was calculated to derive a lake spatial density per grid cell. This technique has been used in other glaciated regions (Principato and Johnson, 2009; Ebert, 2015). A potential problem with this technique is that the results are sensitive to the aerial extent of the lake relative to the grid cell size. Within the study area, there are numerous small lakes, as well as a few large lakes (Figures 3.5A and 3.5B). The mean lake surface area is 0.18 km^2, but 16 large lakes exceed the regular cell size of 6.25 km^2 and have a combined surface area of 743.6 km^2. The point density function provides only a single centroid for a lake that covers several cells. To address this, a second technique was used, which consists of calculating the area of each cell that is covered by a lake polygon. With this technique, numerous small lakes or few larger lakes will both give a high value. However, the two techniques were applied together because they may reveal patterns associated with different types of subglacial bedrock erosion, different bedrock lithology, or structural effects. For instance, characteristics of the underlying bedrock (i.e., lithology and/or structure) and irregular depth of pre-glacial weathering profiles have modulated the style of bedrock erosion and final shape and size of lakes in regions of areal scouring resulting from a mobile bed (e.g., Krabbendam and Bradwell, 2014). During the onset of deglaciation (e.g., Flow 2) low effective pressure and related faster flowing basal ice (warm-based conditions) favour the development of longer lee side cavities down-ice of bedrock obstructions. Frequent water pressure fluctuations within these cavities can lead to large stress variations in the down-ice edge of the bedrock obstruction, creating conditions that favour quarrying and greater subglacial erosion, especially in the presence of pre-existing sub-vertical fractures in bedrock (Iverson, 2012; Alley et al., 2019). Quarrying can excavate greater volumes of bedrock than abrasion but requires a relatively rough bedrock surface to be effective (Cook et al., 2020). The up-ice side of the bedrock obstacles is dominated by abrasion due to the sliding and pressing of debris-rich ice

along the stoss side. Therefore, the two processes tend to operate together in areas of irregular hard, but jointed bedrock. This can be preserved and form an irregular bedrock landscape with numerous small rock knobs and depressions, which have since ponded with water, creating small lakes; a characteristic of areal scouring landscapes (Sugden, 1978; Andrews et al., 1985). However, in the presence of a more spatially focused network of steeply dipping faults and fractures (weathered bedrock), with some extensive lineaments oriented parallel (anisotropic bedrock) to ice flow, these glacial erosion processes of abrasion and quarrying can be more effective at excavating large volumes of rock along specific narrow corridors. Under the right glaciological conditions, these areas will thus be affected by higher overall erosion rates, which will produce more elongated and deeper bedrock depressions. Therefore, by analyzing both lake density and lake surface areas, the spatial distribution of these different situations (i.e., numerous small lakes and few elongated lakes oriented with paleo-ice flow) can be more accurately captured. This should give insights into the overall style and intensity of bedrock erosion, as opposed to focusing on mapping the spatially well-distributed abrasion-quarrying process of the areal scouring landscape. Additionally, erosion rates from modern glacial environments are positively correlated to sliding velocities, indicating faster ice flow is more erosive and provides further evidence that high erosion rates correlate to warm-based highly dynamic ice (Cook et al., 2020).

The lake spatial density and the lake area results were grouped into five classes using Jenks natural breaks. The average elevation for each cell was also calculated and plotted against the lake area within the same cell. This was done specifically to evaluate whether the lakes are organized in a pattern consistent with or independent of topographic controls, which has been shown to have a correlation in other ice divide regions (e.g., Sugden, 1978; Andrews et al., 1985; Briner and Swanson, 1998; Ebert, 2015).

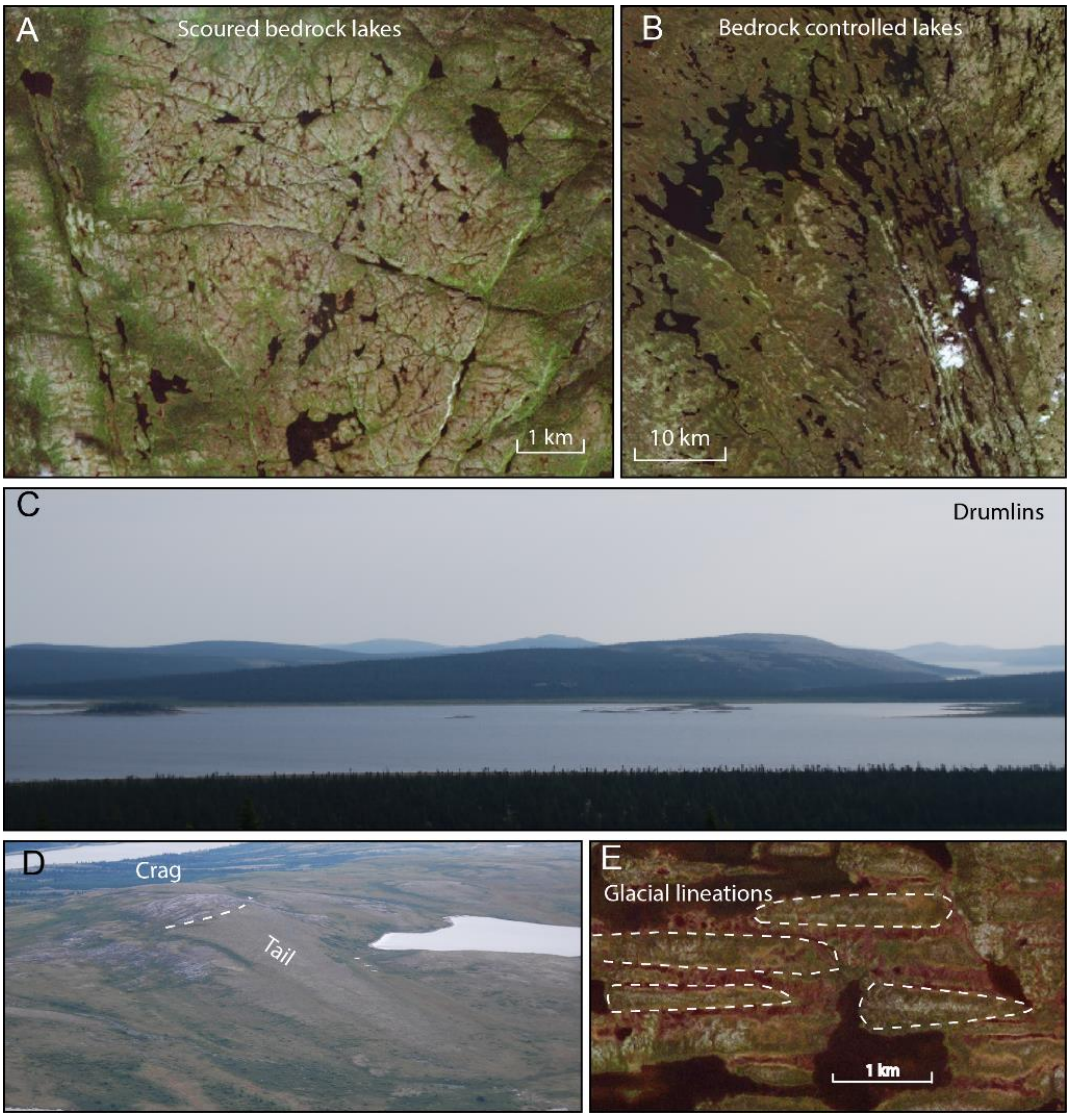

Figure 3.5. Examples of the GIS proxies examined across the study area including **(A)** scoured bedrock lakes atop the De Pas Batholith (Landsat imagery), **(B)** Bedrock controlled lake (Lac Champadoré) with larger lake coverage (Landsat imagery), **(C)** drumlins (a-axis ~ 3 km; Field photo), **(D)** crag-and-tails (a-axis ~1.5 km; Field photo), and **(E)** glacial lineations (Landsat imagery).

3.3.2.2 Landform analysis

Glacial landform data were obtained from the Geological Survey of Canada surficial geology maps (1:100 000 scale - Rice et al., 2017a, 2017b) that were produced by aerial photograph interpretation and contain detailed identification of glacial landforms. To supplement the surficial geology maps, Shuttle Radar Topography Mission (SRTM) DEM (30 m vertical and horizontal resolution, United States Geological Survey, 2014) data were coupled with Landsat 7 Enhanced Thematic Mapper+ satellite imagery (Panchromatic band 8) with a resolution of 15 m, which was

obtained from the United States Geological Survey's Earth Explorer website (earthexplorer.usgs.gov). The DEM and satellite imagery were used to confirm the correct location and extent of the landforms. For this analysis, all types of elongated oriented subglacial bedforms were analyzed (Figure 3.5C-E).

Subglacial landforms have been identified under active warm-based palaeo-ice streams resulting from rapid rates of erosion and deposition (e.g., King et al., 2009; King et al., 2016). Although some debate regarding the formational process of subglacial landform persists, they appear to be the result of a complex interplay of several subglacial processes but are associated with subglacial ice/bed mobility (Hindmarsh et al., 1989; Hindmarsh, 1999; Fowler, 2009, 2010; Stokes et al., 2013; Fowler and Chapwanya, 2014). Therefore, subglacial landform distribution and elongation data offer significant insights into ice/bed mobility (e.g., thermal regime) that would have persisted at least during their formation.

Landform density was calculated using the same regular 2.5 km raster grid used for lake analysis, to allow for an equal comparison between the methods. The represented values correspond to the number of landforms per each cell (i.e., landforms per 6.25 km^2). To obtain landform elongation measurements, polygons first needed to be created. Polygons were outlined manually using a multi-directional hill-shade with a vertical exaggeration of 4X from the source DEM. Although automated estimation of glacial landforms length, width, and height has been used successfully with high-resolution LiDAR data (e.g., Yu et al., 2015; Sookhan et al., 2016, 2018), the lower resolution of any DEM currently available for the study area made the automation process ineffective. Jorge and Brennand (2017) performed an analysis of five different methodologies for estimating landform elongation and concluded that drumlin elongation was best estimated using the minimum bounding rectangle. Therefore, ArcGIS (v.10.3.1)'s "minimum bounding geometry" tool was used to fit each polygon with a minimum bounding rectangle to calculate the elongation of the landform (elongation = length of minimum bounding rectangle divided by the width of minimum bounding rectangle). The average elongation value was then calculated for each cell of the same raster grid used for landform density. The landform spatial density and the elongation results were grouped into five classes using Jenks natural breaks to allow for a similar comparison to lake spatial density distribution.

3.3.3 Classification of cells

Results from all the proxies described above (i.e., lake spatial density and surface area, landform spatial density and elongation, and till blanket) were then combined and interpreted in terms of ice/bed mobility (Figure 3.6). Each proxy was given equal weight during cell classification, but it was also evaluated independently (Figures 3.7-3.10) in order to assess if a single proxy had the greatest effect on cell classification. Because both cold- (no basal ice flow and no erosion) and warm-based (considered here to represent active ice/bed mobility) conditions are effectively endmembers of the subglacial thermomechanical spectrum, with complex transitional zones, two transitional classes were created to represent the subglacial conditions (e.g., moderately active bed conditions) between these two endmember environments. In total, five categories were used for this classification: High, transitional Moderate-High (HM), transitional Moderate-Low (ML), warm-based-low (WL), and Low. 'High' cells indicate cells with till blankets and/or high proxy values (i.e., high density of landforms or lakes) or cells without till blanket and high proxy values, requiring warm-based conditions to create the proxies measured. WL indicates cells with till blanket but otherwise low proxy values, again requiring warm-based conditions for till production and deposition, but low dynamics that did not create subglacial landforms or erode bedrock depressions. Cells with moderate proxy values cells are classified as MH indicative of transitioning away from 'High' dynamic conditions; Or as ML if characterized by low proxy values, indicative of transitioning away from end-member cold-based conditions. The last category (Low) was added to include cells with lowest proxies and no till blanket. These cells would be considered representative of sustained cold-based conditions. However, end-member cold-based zones characterized by weathered non-glacial regolith were not observed in the study area; these types of conditions were documented well north of the study area by Dubé-Loubert and Roy (2017).

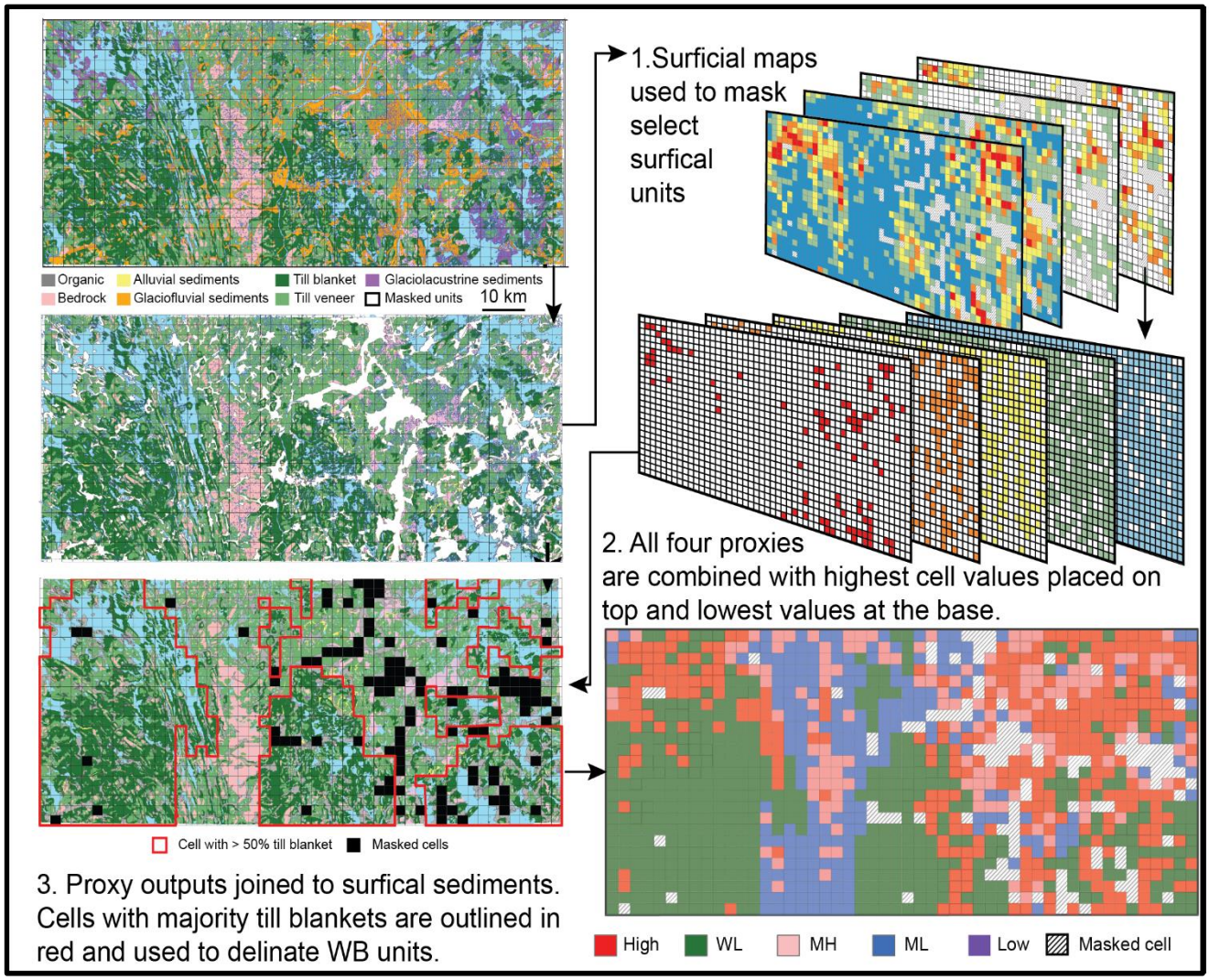

Figure 3.6. Summary of the process used to classify ice/bed mobility using a grid overlay and proxy results. First, the surficial map was used to mask surficial sediments not suitable for analysis. Second, the landforms and lake proxies were classified, then combined. Finally, the proxy values were used in conjunction with the surficial map to classify zones based on whether the cell was mostly characterized by till blanket and the relative value of proxies within that cell. Note: High= high proxies; WL= warm-based, low proxies; MH= Moderately-high proxies; ML=Moderately-low proxies; Low=low proxies, no till blanket.

3.3.4 Till weathering and cosmogenic exposure

In principle, areas classified as 'High' or 'MH', indicative of a highly mobile bed should be characterized by relatively fresh bedrock and till containing similarly fresh clasts. In contrast, areas classified as ML and Low, indicative of lower ice/bed mobility, would be expected to show a comparable, higher degree of surface weathering and cosmogenic exposure inheritance (from previous interglaciations) due to lower overall erosion of these zones during the last glaciation (e.g.,

Refsnider and Miller, 2010). Within inner-ice sheet regions, there is also the additional possibility that relict glacial sediments and surfaces from a previous glaciation were preserved during the last glaciation under a sustained 'frozen patch' (Kleman and Glasser, 2007). For example, areas of relict Flow 1 glacial landscape (GTZ1), with minimal overprint by younger phases could, in theory, have a higher weathering signature and cosmogenic exposure inheritance if Flow 1 was produced during a previous glaciation (Veillette et al., 1999), as opposed to the most recent glacial event.

In summary, an area of limited net glacial erosion would have a higher degree of weathering and higher cosmogenic isotope abundance than the warm-based zones of higher erosion (Staiger et al., 2006; Refsnider and Miller, 2010; Corbett et al., 2016), with the possible exception of zones corresponding to an old glacial bed or "frozen patch" that would have been exposed to cosmic radiation and weathering during the last interglacial. Bedrock and till proxies were examined across the different zones using a weathering index and cosmogenic inheritance as proxies for the erosional vigour exerted on the landscape during the last glaciation and to test for the possibility that 'relict; zones (e.g., GTZ1) have higher weathering and exposure inheritance than expected based on their glacial landform record (i.e., are preserved from a previous glaciation).

3.3.4.1 Chemical Index of Alteration

The CIA of till/regolith matrix has been used on Baffin Island to characterize areas affected by sustained cold-based conditions (Refsnider and Miller, 2010). When employed in concert with other proxies, regions of high CIA values (>70) on Baffin Island correlate to regions of low lake spatial density and high cosmogenic exposure inheritance (elevated ^{10}Be abundances beyond postglacial exposure) in regolith and these were interpreted as zones of low erosion or inherited CIA values associated with sustained cold-based conditions (Refsnider and Miller, 2010).

In contrast, low CIA values of till that are similar to the local fresh bedrock reflect widespread glacial erosion of fresh bedrock and depositions of unweathered glacial debris during the last glaciation. In essence, the CIA values calculated from till matrix geochemistry reflect the glacial erosion during the last glaciation and, as previously stated, the residence time of till on the landscape. High CIA values thus indicate immature till/regolith produced from old weathered bedrock or a relict till surface from a previous glaciation that was preserved under a 'frozen patch' throughout the last glaciation.

The CIA is a measure of the proportion of primary minerals to chemically weathered minerals as defined by Nesbitt and Young (1982):

$$CIA = \left[\frac{Al_2O_3}{Al_2O_3 + CaO^* + NaO + K_2O}\right] x\ 100$$

Minerals used in this calculation have been reported according to their molar proportions (weight % / molecular mass). CaO* is assumed to be derived from silicate-bearing minerals. It is important to note, however, that the CIA formula is based on the removal of Na and Ca during the chemical breakdown of feldspar from felsic rocks to clay minerals, which results in the enrichment of Al and the depletion of Ca, Na, and K (Fedo et al., 1995). Fresh felsic rocks typically have CIA ranging from 40-55, whereas weathered felsic rocks and derived sediments have higher index values > 70 (Nesbitt and Young, 1982). For this study, the CaO* is derived from silicate-bearing minerals, as there are no known carbonate lithologies in the region (Sanborn-Barrie, 2016). However, the southern Rachel-Laporte is characterized by a medium-grade metamorphic quartz-biotite metasedimentary sequence with small bands of amphibolite and ultramafic rocks containing fewer feldspars (0-40%; Sanborn-Barrie, 2016). The metasedimentary rocks of the Rachel-Laporte domain within this thesis' study area could thus exhibit higher 'fresh rock' CIA values or greater CIA variability, which would limit the use of the CIA index in that portion of the study area (e.g., Refsnider and Miller, 2010). However, the bedrock geology underlying the remainder of the study area dominantly contains felsic rocks that have an average fresh bedrock CIA of 51 (Énergie et Ressources naturelles Québec Report, 2010).

CIA calculations were conducted on till-matrix geochemistry results from 74 till samples collected across the study area from hand-dug pits (depths which range between 0.2 and 0.7 m) into active frost boils or the naturally developed soil horizon to collect unoxidized till. At each sample site, a ~ 3 kg sample was collected for geochemical analysis (for detailed collection and analytical methodology see Rice et al., 2017c). Standard reference material (CANMET standard Till 4, n=12) and silica blanks (n=13) were added to the collected till samples to assess the accuracy of the analysis and possible cross-contamination between samples, following procedures of Plouffe et al. (2013). The < 0.063 mm fraction was submitted to Bureau Veritas Commodities Canada Limited Vancouver for analysis. Samples underwent lithium metaborate/tetraborate fusion and nitric acid total digestion followed by ICP-MS (Inductively Coupled Plasma Mass Spectrometry) determination

(BV LF200 package) on 0.2 g aliquots. Quality assurance and quality control (QA/QC) procedures outlined by Piercey (2014) were applied to the geochemical data before CIA calculations. Specifically, precision was evaluated using the relative standard deviation method (Jenner, 1996) for reference material using the major oxides used in the CIA formula; a value of 0.47% was obtained, which is 'excellent'. The precision of the analytical method was also evaluated by plotting results of duplicates on scatterplots and Thompson-Howarth plots, which yielded results with better than 5% precision. QA/QC methods yielded acceptable quality data, confirming that results are suitable for further analysis and interpretation. The full results of the QA/QC can be found in Supplementary Appendix S3.1. Detailed CIA calculations are reported in Supplementary Table T3.1.

3.3.4.2 Cosmogenic ^{10}Be abundances

^{10}Be abundances have been successfully used as a proxy for estimating subglacial erosion on Baffin Island (Miller et al., 2006; Briner et al., 2014), in the Cordilleran (Stroeven et al., 2010), Fennoscandia (Fabel et al., 2002; Linge et al., 2006), and Greenland (Beel et al., 2016; Corbett et al., 2016). ^{10}Be accumulates within quartz at the surface of the Earth during periods of exposure to cosmic radiation primarily through a spallation reaction with oxygen within the quartz (Lal, 1991; Gosse and Phillips, 2001). The rate at which ^{10}Be accumulates (the production rate) largely depends on latitude, elevation, shielding from cosmic rays, and radioactive decay of ^{10}Be(Dunai, 2010). During glaciation, subglacial bedrock surfaces are shielded from cosmic radiation and are exposed during interglacial or non-glacial periods. Therefore, without any type of shielding (e.g., ice, snow, or sediment), shallow (<2 m) quartz grains within a glaciated outcropping bedrock surface are exposed to cosmic radiation and ^{10}Be is produced. If glacial erosion was limited throughout the last glaciation and thus did not remove pre-glacial ^{10}Be, the bedrock surface would contain an amount of ^{10}Be inherited from a previous interglacial in addition to the recent post-glacial accumulation. Therefore, if all other production factors remain constant, the only major effect on ^{10}Be abundance will be the erosion of the bedrock surface during glaciation, which provides a qualitative proxy to assess the vigour of glacial erosion, and thus the net effect of the subglacial thermomechanical regime throughout glaciation.

Available ^{10}Be concentrations from bedrock and glacial erratics were previously used to constrain the timing of ice-margin retreat across the study area along a sampling transect perpendicular to inferred ice margin retreat (Chapter 2). The sample transects also crossed the

identified glacial terrain zones, which were hypothesized to have discernible differences in ^{10}Be abundances (e.g., Staiger et al., 2006; Briner et al., 2006, 2008). For this thesis' analysis herein, ^{10}Be abundances from bedrock were used in combination with ^{10}Be abundances from till samples collected within a few meters of the bedrock samples. The analysis of bedrock and till pairs is useful, as the till has been sourced from a wider area than is represented by a bedrock outcrop; therefore, the bedrock gives local information whereas the till should provide insights into inheritance from the surrounding region (Staiger et al., 2006). Areas that have experienced less overall erosion and whose till is immature (short-transport) should thus have a high paired inheritance. Areas of local low bedrock erosion but with relatively long-transport (englacial) till deposited by meltout should show more discrepancy between bedrock and till results. Finally, the hypothetical situation of a relict glacial bed from a previous glaciation (e.g., possibly GTZ1), should yield higher paired inheritance than expected from a glacially scoured landscape.

The till samples were collected from hand-dug pits that exposed the entire till profile from the surface to bedrock to a maximum depth of 0.35 m; having sampled the entire profile as a single bulk sample. This method of sample collection ensures homogenous mixing of quartz, given that cryoturbation affects the surficial till in the region. The eight bedrock samples were collected from windswept bedrock outcrops that had high quartz content (>35%) and were free from present-day shielding such as boulders, surrounding topography, or vegetation. ^{10}Be abundances were normalized based on production rates and scaling (calculated using Cronus online calculator (V.3) https://hess.ess.washington.edu/), to limit any bias in elevation difference between the samples. Elevation values were corrected for isostatic rebound using data from ICE-6G_C database (Argus et al., 2014; Peltier et al., 2015). Details of the methodology used for ^{10}Be abundance determination are described in the Supplementary Material (Appendix S3.2).

3.4 **Results**

3.4.1 GIS analysis

3.4.1.1 Lake spatial density and lake area

Lake spatial density based on the centroid method shows a low density of lakes in the central and western part of the study area, with a higher density of lakes in the east and northwest (Figure 3.7A). The highest density of lakes occurs between 400 and 500 m asl (Figure 3.7B), particularly in the MR domain (Figure 3.7C). Lake area coverage per cell shows a very different spatial distribution than the lake spatial density map (Figure 3.8A). The cells with the greatest lake area coverage also occur between 400 and 500 m, but in different areas and bedrock domains (Figure 3.8B). Lake area is greatest in the northwest (quartzofeldspathic gneiss-Unit 3), in the northeast, and the southeast (paragneiss-Unit 7; Diorite/Gabbro-Unit 8; Figure 3.8C).

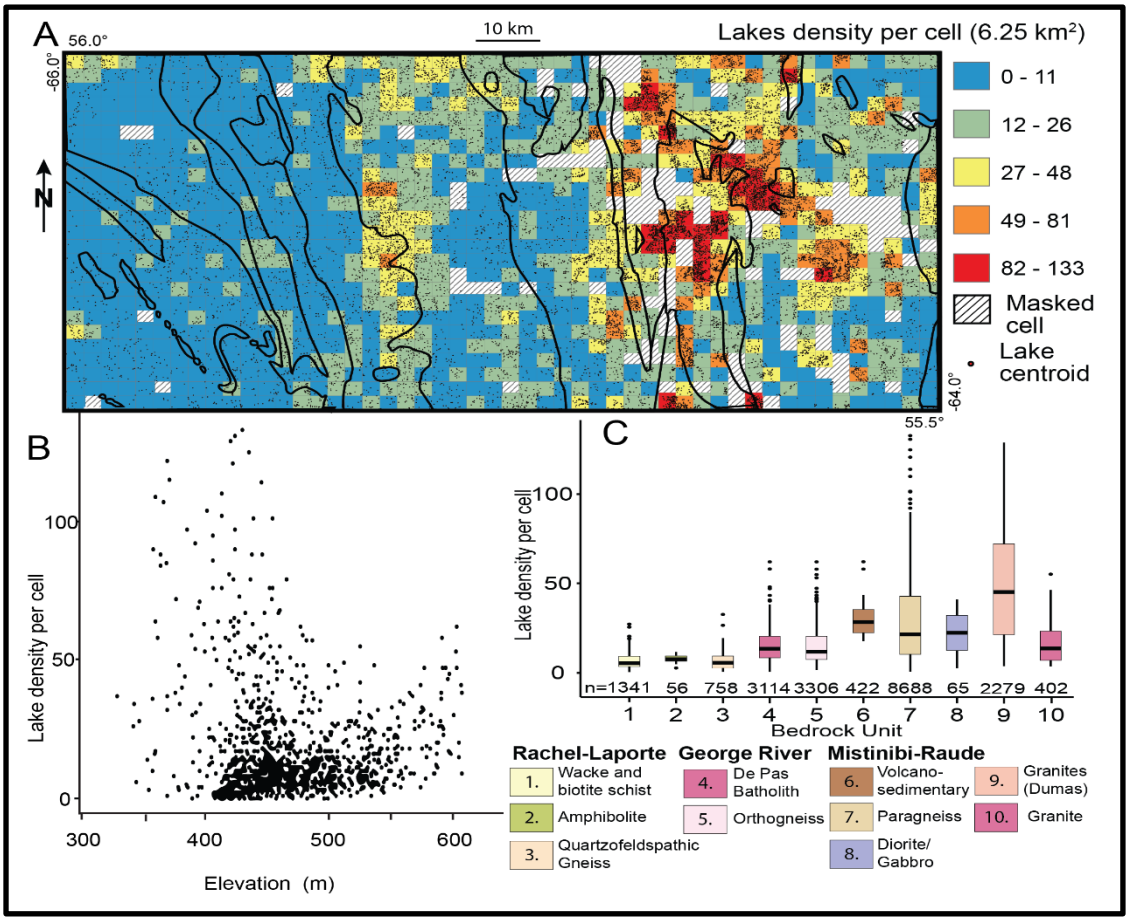

Figure 3.7. **(A)** The sum of the number of lakes within each cell across the study area. The outline of bedrock units indicated in Figure 3.2 is overlain. The legend is the same as Figure 3.2. **(B)** Scatterplot showing the average elevation of each cell plotted against the number of lakes within that cell. **(C)** Boxplots showing the range in the number of lakes within each cell underlain by each of the bedrock lithologies. The number of each cell with lakes analyzed is reported underneath the boxplot.

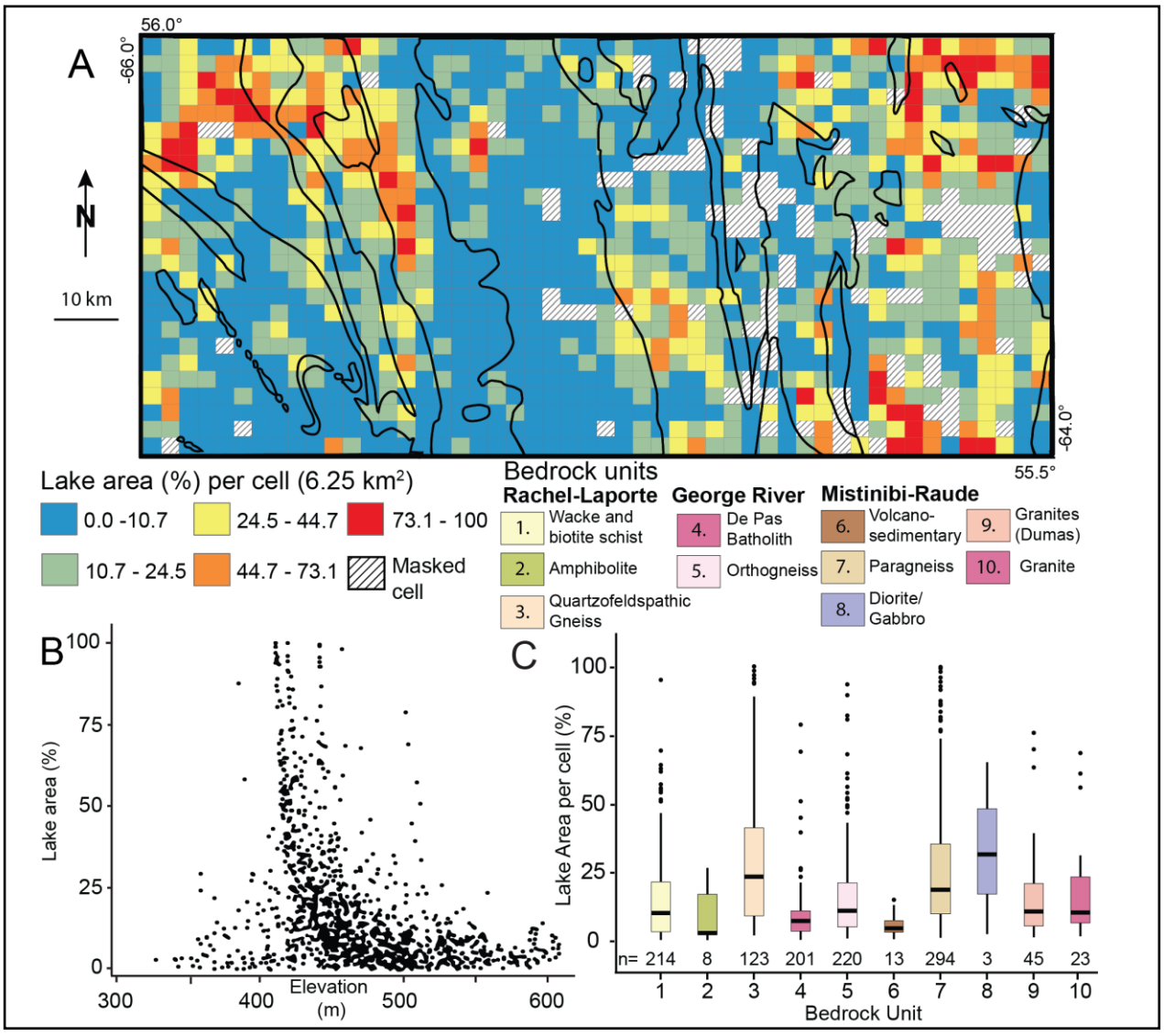

Figure 3.8. **(A)** Percent of each cell that is covered by a lake (%) across the study area. The outline of bedrock units indicated in Figure 3.2 is overlain. **(B)** Scatterplot showing the average elevation of each cell against the percentage of that cell that is covered by a lake. **(C)** Boxplots showing the range in percentage of each cell's lake coverage within each bedrock unit. The number of cells analyzed within each cell is reported below the boxplot. Bedrock units are the same as reported in Figure 3.2.

3.4.1.2 Landform spatial density and elongation

A total of 683 streamlined glacial landforms were identified and outlined in the study area (Table 3.1; Figure 3.9A). Cells containing only a single landform are the most common (Figure 3.9B); likely due to landform size and spacing relative to cell size. However, similar patterns were obtained using other grids (e.g., cell area of 1 km^2, and 25 km^2). The maximum number of landforms within a cell is twelve. Few landforms occur in the southwest and west-central part of the study area. Conversely, the highest density of landforms occurs in the northwest (quartzofeldspathic gneiss-Unit 3), east-central (orthogneiss-Unit 5) and northeast (paragneiss–Unit 7) part of the study area (Figure 3.9C). Landform elongation is limited to cells containing landforms (Figure 3.10A). Landforms with elongation ratios between 2.0 and 6.0 are most common (Figure 3.10B) with the highest elongation ratios in the northeast lithologies (Figure 3.10C). However, plotting of the length and width of the landforms against the elongation value shows no clear difference between the six newly (see discussion) defined GTZs (Figure 3.10D-F).

Table 3.1 Landform characteristics

GTZ	Count	Variable	Range	Median	10^{th} percentile	90^{th} percentile	Coefficient of variance
1	168	a-axis (m)	2998.2	1283.3	662.3	2142.6	43.9
		b-axis (m)	1311.6	335.5	140.4	761.4	63.3
		Elongation	8.3	3.5	2.3	6.6	41.6
2	168	a-axis (m)	3794.0	1331.1	785.5	2038.5	39.0
		b-axis (m)	1535.9	391.6	144.5	748.1	61.8
		Elongation	10.0	3.6	2.2	6.5	47.8
3	175	a-axis (m)	2870.3	1138.1	728.3	1903.9	40.5
		b-axis (m)	1355.6	282.9	139.2	592.4	61.1
		Elongation	12.7	4.0	2.3	6.9	46.3
3b	163	a-axis (m)	3364.7	960.7	495.1	1848.9	54.4
		b-axis (m)	1761.0	201.2	115.3	568.4	78.3
		Elongation	10.1	4.1	2.4	7.7	44.6
4	9	a-axis (m)	868.5	1398.1	722.1	1590.6	19.4
		b-axis (m)	552.5	789.4	415.5	1588.7	48.0
		Elongation	1.1	2.4	1.9	2.9	15.2
5	N/A						

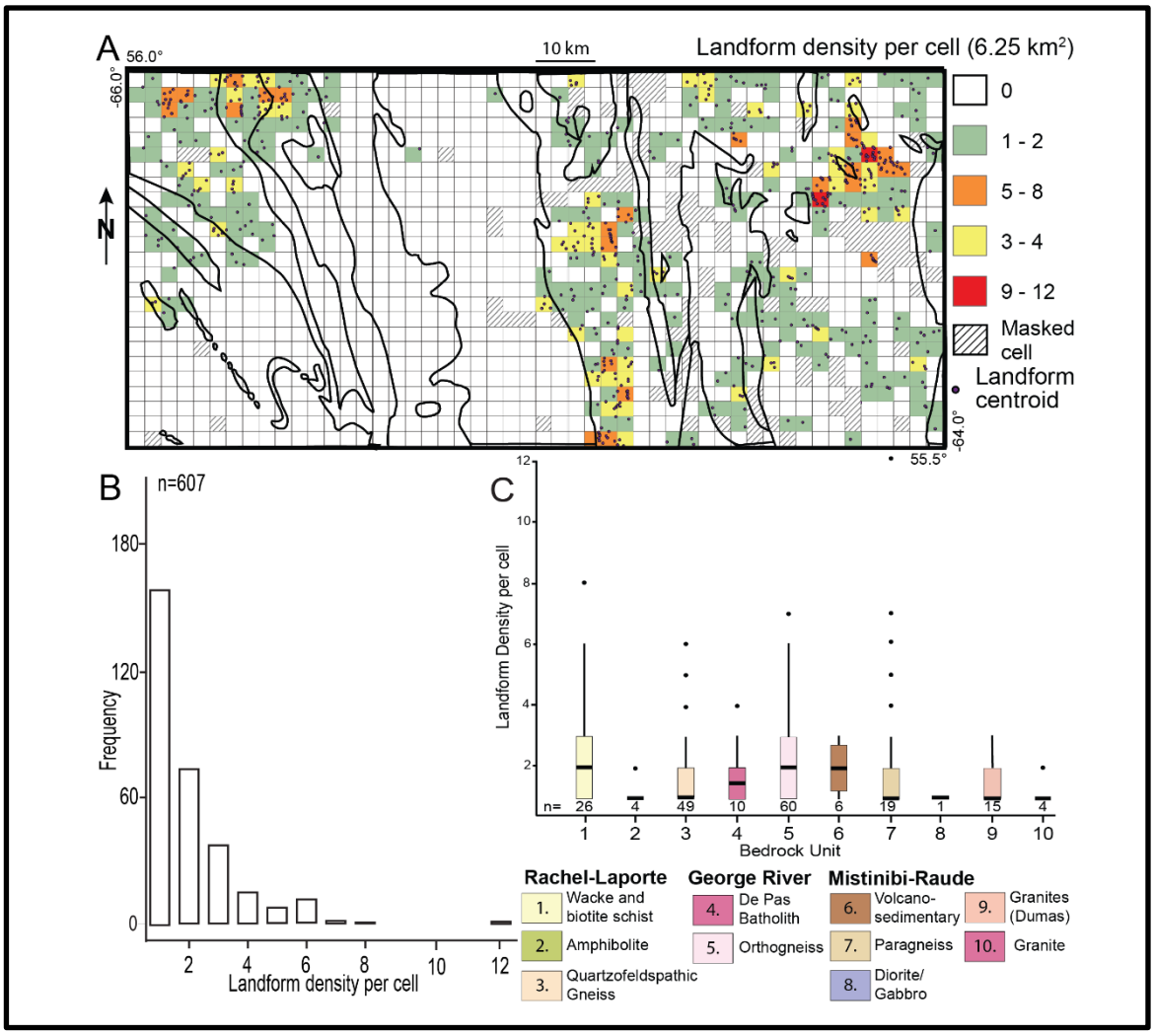

Figure 3.9. **(A)** Total number of landforms within each cell across the study area. The outline of bedrock units indicated in Figure 3.2 is overlain. **(B)** Frequency of landforms per cell within the study area. **(C)** Boxplots of landform density per cell across each bedrock unit, the number of landforms analyzed within each bedrock unit are reported below each boxplot.

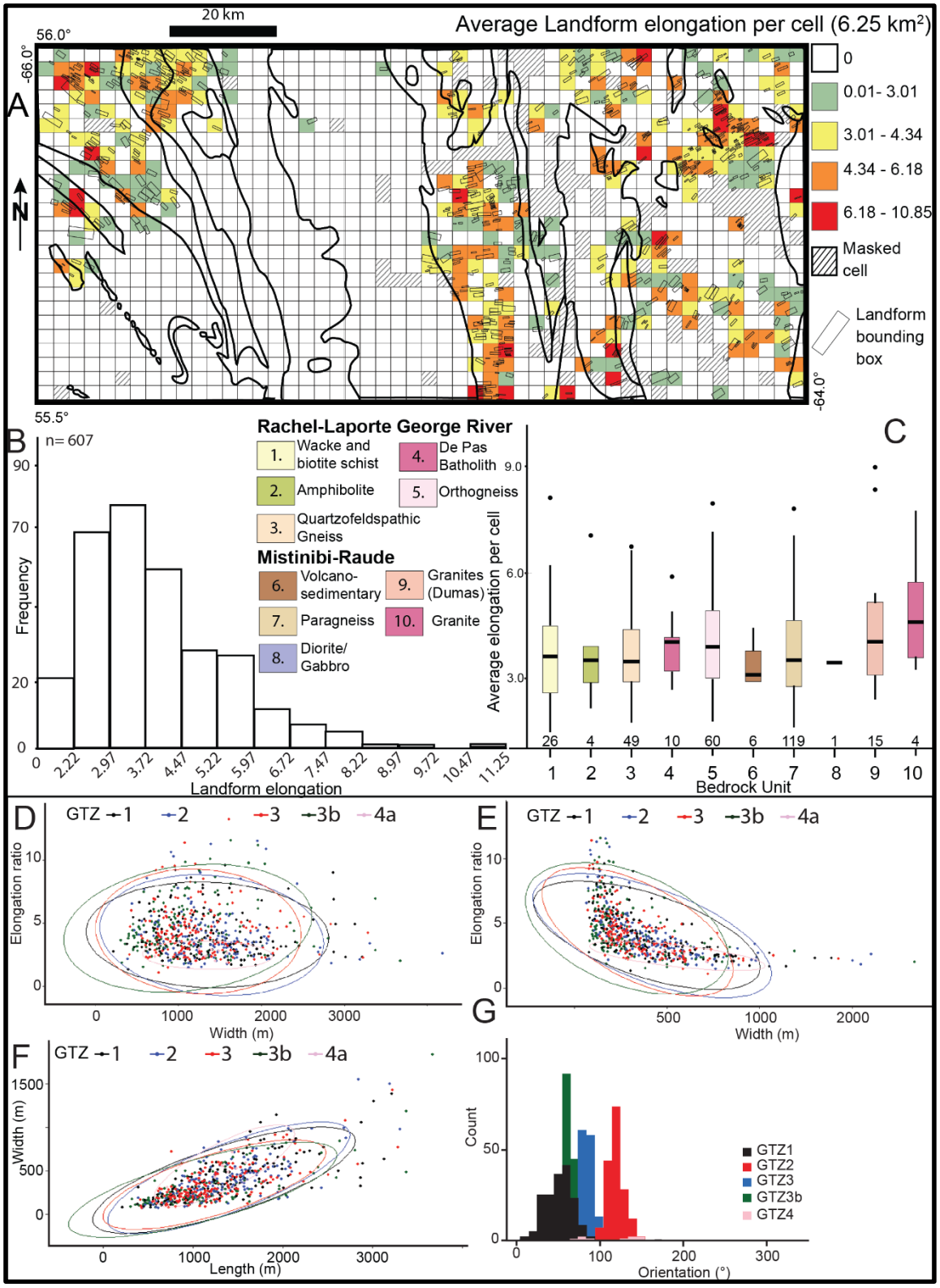

Figure 3.10. **(A)** Average elongation ratios of landforms from within each cell across the study area. The outline of bedrock units indicated in Figure 3.2 is overlain. **(B)** Frequency of cells containing different amounts of landforms. **(C)** Boxplots of the abundance of landforms within each of the 10 bedrock units within the study area. The number of cells with each landform is indicated below the boxplot. **(D-F)** Elongation ratios against width and length data from all landforms, the colour of the dot represents which landform it is located within. Coloured ellipses encircle 99% of the points within each GTZ. **(G)** Frequency plot (10° bins) for orientation of landforms from each GTZ.

3.4.2 Classification of cells

A total of 1300 cells were created as an overlay for the assessment of the outlined proxies with 155 (12%) cells having been masked. This left a total of 1145 unmasked cells that were analyzed based on all the GIS-based proxies and surficial maps. From this overlay and the combined results of the proxies, 311 (27%) cells are classified as 'High', 474 (41%) as WL, 143 (13%) as MH, and 217 (19%) as ML (Figure 3.11). No cells were classified as Low (i.e., no till blanket, few lakes, no landforms).

3.4.3 Additional testing

3.4.3.1 Chemical Index of Alteration

The CIA results are limited to the 74 cells (6.5% of the total grid) in which till samples were collected for geochemical analysis (Figure 3.12A). Values range from 46.4 to 64.7 with an average CIA of 50.2 (σ= 0.03). The highest CIA values are from samples in the southwestern part of the study area within the RL domain (Bedrock Unit 1-Figure 3.2A) where they range from 49.1 to 64.7 (Figure 3.12B) with an average of 56.1. A scatterplot of CIA values and elevation shows no clear correlation but does show clustering of samples from the RL domain with the highest CIA values, even when compared to samples from similar elevations (Figure 3.12C).

3.4.3.2 ^{10}Be abundances

Table 3.2 shows ^{10}Be abundances in bedrock and till samples, along with elevation corrections and normalized values. The normalized values are used during the discussion of ^{10}Be abundances. ^{10}Be abundances fluctuate across the east to west transect of collected till and bedrock samples (Figure 3.11A). ^{10}Be values from bedrock samples are lower in the eastern and western ends of the transect (4.0×10^4 to 6.1×10^4 atoms/g), except for one sample (15-PTA-081B) which has a relatively elevated concentration of ^{10}Be (9.1×10^4 atoms/g). Bedrock samples collected from the centre of the study area have the highest abundances of ^{10}Be (7.4×10^4 to 1.9×10^5 atoms/g; Figure 3.11B). The abundance of ^{10}Be in till has similar spatial patterns to bedrock results with lower abundances in the east and west (3.8×10^4 to 7.9×10^4 atoms/g) and higher abundances in the central part of the study area (8.2 to 9.0×10^4 atoms/g). When these abundances are plotted against the longitudinal position from which the sample was collected a general arc in abundance can be seen, with higher abundances in the middle and lower

abundances in the east and west (Figure 3.11A). Although there is some overlap between the centre portion and eastern and western portions, this overall pattern can still be observed (Figure 3.11B).

3.4.4 Preservation of old ice-flow indicators

Preserved outcrop-scale ice-flow indicators were identified at 15 locations within the study area (Figure 3.11A). Outcrops with multiple crosscutting older ice-flow indicators are limited to the central part of the study area. These outcrops are located mainly within ML cells (7 of 15), over the most elevated portion of the region (Figure 3.2C). More uniform ice-flow indicators of consistent direction and relative age are observed in the eastern and western parts of the study area. Flow 4 (green arrows, Figure 3.11) was not considered in this assessment due to its lack of inferred erosional vigour within the study area

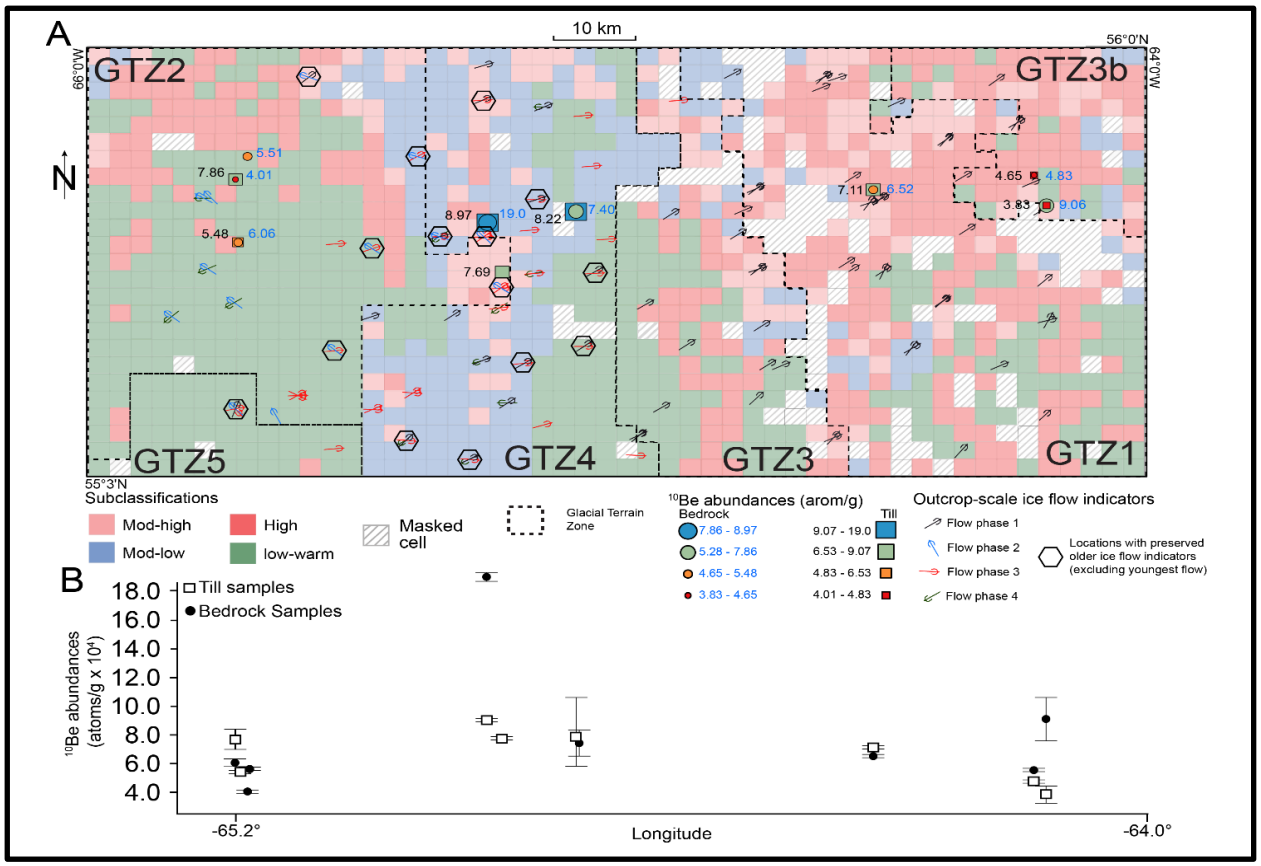

Figure 3.11. **(A)** Results of the classification processes showing the distribution of the different zones. ^{10}Be results have been overlaid with bedrock (circles) abundances reported in blue and till (squares) abundances reported in black beside the given sample. Striation measurements, with colours indicating the relative age of the ice flow, have also been overlain. Outcrops with evidence of preserved older flows (excluding Flow 4 (green arrow)) are also indicated. **(B)** Scatter plot of ^{10}Be results for till and bedrock samples plotted against the longitude from which it was collected, error bars are reported to 1σ.

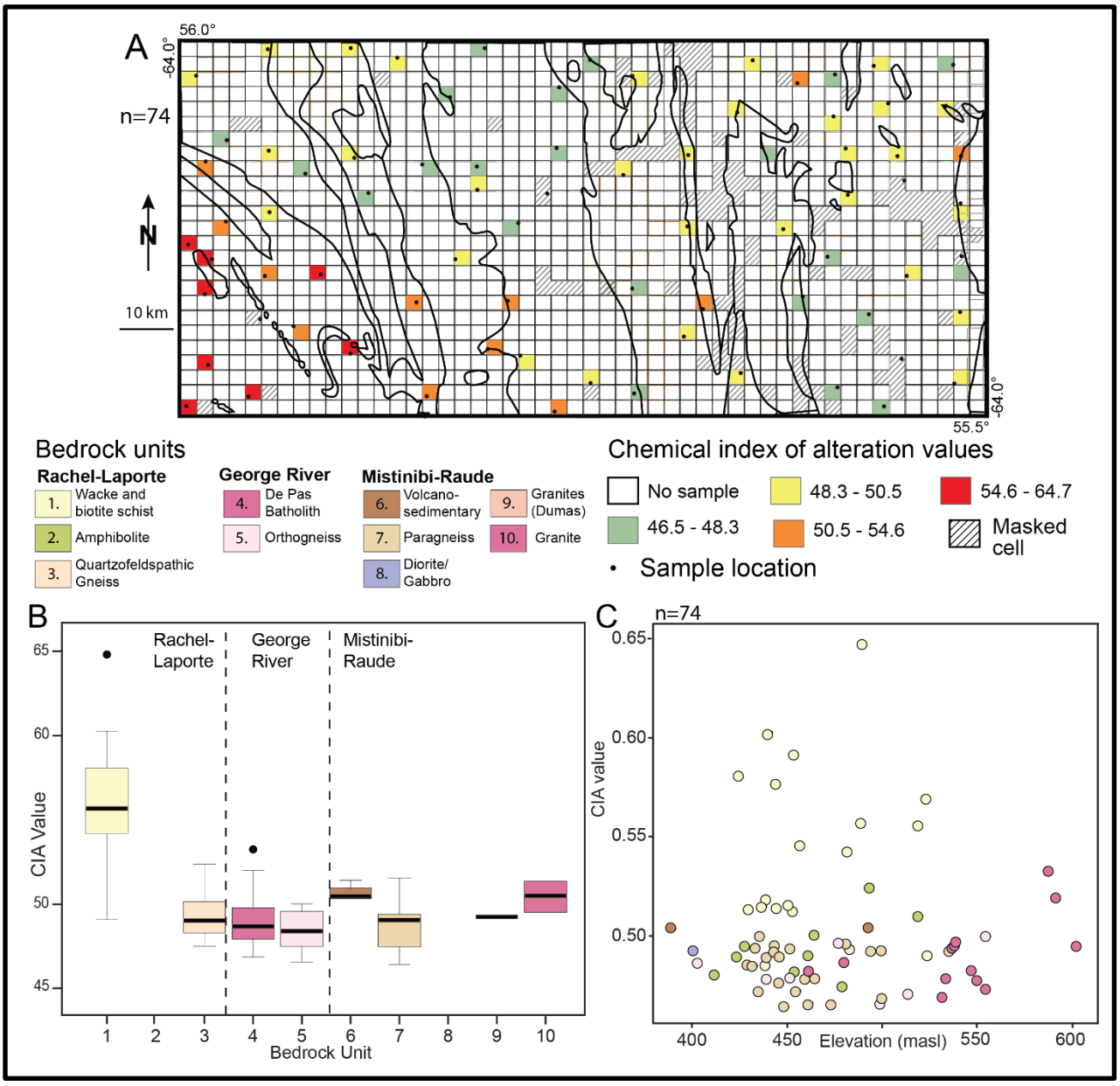

Figure 3.12. **(A)** Chemical Index of Alteration (CIA) values from samples collected across the study area. The outline of bedrock units indicated in Figure 3.2 is overlain. **(B)** Boxplot showing the range in CIA values collected from till samples separated by the underlying bedrock lithology. **(C)** Scatterplot showing the distribution of CIA values in relationship to the elevation from which they were collected. The colours of the dots represent the bedrock unit from which they were collected; Colour references are to study area bedrock and are the same legend as **(B)** and Figure 3.2.

Table 3.2. ^{10}Be abundance data

Field ID[a]	Lat (°N)	Long (°W)	Elev. (m asl)[b]	Production rate (atom/g/a)	Measured ^{10}Be (10^4 atoms/g)	Uncertainty (10^4 atoms/g)	Precision	Normalized values (10^4 atoms/g)
16-PTA-058T	55.843	-64.207	433	5.18	4.65	0.12	3%	4.65
16-PTA-069T	55.721	-65.218	542	5.83	6.80	0.13	2%	7.69
16-PTA-070T	55.784	-65.251	562	6.44	7.19	0.16	2%	8.97
15-PTA-078T	55.821	-64.515	454	5.42	6.76	0.13	2%	7.11
15-PTA-083T	55.772	-65.721	468	6.18	4.57	0.09	2%	5.48
15-PTA-021T	55.838	-65.729	468	6.23	6.51	1.97	30%	7.86
15-PTA-077T	55.810	-65.080	434	5.15	8.22	2.35	29%	8.22
15-PTA-081T	55.810	-64.189	498	5.59	3.53	0.68	19%	3.83
16-PTA-053B	55.867	-65.709	456	6.63	5.63	0.02	2%	5.51
16-PTA-058B	55.843	-64.207	433	6.49	4.80	0.12	3%	4.83
16-PTA-070B	55.784	-65.251	562	7.36	16.66	0.31	2%	19.00
15-PTA-078B	55.821	-64.515	456	6.69	6.28	0.12	2%	6.52
15-PTA-083B	55.772	-65.721	488	6.57	5.95	0.11	2%	6.06
15-PTA-021B	55.838	-65.729	468	6.7	3.85	0.73	19%	4.01
15-PTA-077B	55.810	-65.080	434	6.44	7.40	0.86	12%	7.40
15-PTA-081B	55.810	-64.189	498	6.91	7.21	1.50	21%	9.06

[a] T= till sample, B=bedrock sample
[b] Corrected for isostatic rebound

3.5 **Discussion**

3.5.1 Variation of proxies across the study area

The combination of subglacial erosional proxies such as streamlined landform density and elongation ratio, lake area and lake density, and surficial sediment classification using a grid-cell analysis suggests a complex mosaic of subglacial conditions across the study area. As a result of this analysis, the GTZs proposed in Chapter 2 were slightly modified to better reflect changing ice/bed mobility inferred from the grid-based analysis across the study area (see Figure 3.11 compared to Figure 3.3). Specifically, GTZ2 was slightly expanded, GTZ3b was recognized, and GTZ5 was added. GTZ2 is partially characterized by structurally controlled lakes, which is evident in the southern extent of the study area, hence its expansion to include this region. The extent of the northeast GTZ1 has been reduced, changing it to GTZ3b because a strong overprint by late-stage flow in the northeast corner is now recognized (Lac Mistinibi;

Figure 3.2C); possibly associated to the southern catchment of the Kogaluk palaeo-ice stream during the Flow 3 ice-flow phase, hence its relation to GTZ3. The streamlined ridges in that GTZ also have a different shape (i.e., smaller subdued, and more elongated). They are also aligned in a slightly more eastern direction than the Flow 1 indicators. The creation of GTZ5 represents its unique surficial signature having abundant till blankets, but low proxy values creating a large patch of WL cells with very few lakes and landforms and no striations associated with Flow 2 (Figure 3.11).

The complexity of the mosaic is partially due to the required simplification of the analytical methods, as changes in the subglacial regime are likely not consistent over 2.5 km^2 but needed to be unscaled to a grid that fits the resolution of the available data. However, some patterns between the zones are discernible (Figure 3. 11), notably, the concentration of 'High' (red) cells in GTZ1, GTZ2, GTZ3, and GTZ3b which are generally surrounded by WL (green) and MH (pink) cells. Conversely, GTZ4 is characterized by a central region of more abundant ML (blue) cells (53.2%), indicating less ice/bed mobility in comparison to surrounding GTZs (Figure 3.11). GTZ5 is almost entirely WL (green) cells (95.9%). Collectively, GTZ1, GTZ2, GTZ3, GTZ3b and GTZ5 have the highest percentages of warm-based cells ('High', WL, MH) with the central GTZ4 having the highest percentage of ML cells (Figure 3.13A).

Lake area coverage is greatest in GTZ3b, GTZ2 and GTZ1, with lake density being the greatest in GTZ1 with significantly fewer lakes in GTZ2 (Figure 3.13A). The underlying bedrock structure within GTZ2, in the northern portion of the RL domain (Figure 3.2B), has a similar orientation to Flow 2's ice-flow direction (northwest), which suggests the bedrock structure may have played a role in subglacial erosion and geometry of the upstream portion of the UBIS (e.g., Phillips et al., 2010; Krabbendam and Glasser, 2011). These results indicate that spatially, subglacial conditions transitioned rapidly from these warm-based zones toward the central upland, as evidenced by the lack of elongated landforms and large lakes on the De Pas batholith, with few exceptions (Figures 3.7 and 3.9). However, the lake density has led to small groupings of MH cells on the upland, which is evidence that suggests these zones experienced areal scouring (Figures 3.5A and 3.8). Observations of evidence indicative of warm-based ice streams with their onset zone at the edge of cold-based terrains have been documented in other

ice stream regions within the northeastern LIS (e.g., Dyke et al., 1992; De Angelis and Kleman, 2005, 2008).

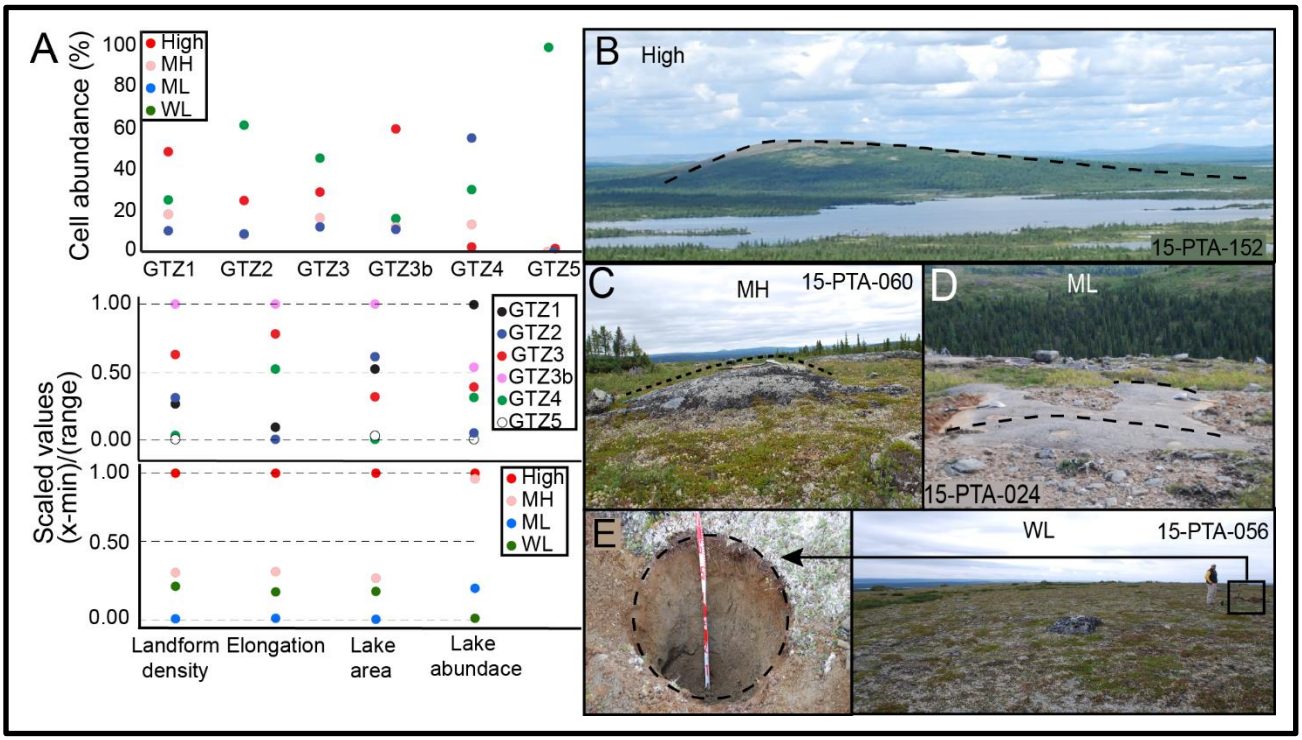

Figure 3.13 **(A-Top)** Percentage cell coverage of each of the four cell classifications per GTZ. **(A-Middle)** Scaled averages ((x- min)/(range)), of each proxy from within each GTZ and **(A-Bottom)** classified cell, with 1.00 being the zone with the highest average value of that proxy and 0.00 being the lowest, the x-axis is the same for both scaled value graphs. **(B)** Example of landscapes from locations observed within the zone defined as High, showing a large drumlinized landscape. **(C)** Example of MH landscape showing small bedrock moulding. **(D)** Example of ML landscape showing double stoss-and-lee outcrop indicative of sluggish erosion caused by opposing ice-flow events. **(E)** Example of WL landscape with thick till deposits, but lacking landforms and lakes.

Streamlined landforms are abundant in GTZ1, GTZ2, GTZ3, and GTZ3b with few landforms within GTZ4 and no landforms in GTZ5 (Figure 3.9). GTZ3 has the highest density of landforms (n=175), followed by GTZ1 and GTZ2 (both n=168), then GTZ3b (n=163), with only a few in GTZ4 (n=9) and no landforms in GTZ5 (Figure 3.10G; Table 3.1). Areas of higher landform abundance tend to cluster together in patches that occur in the centre of GTZ2, GTZ3, and GTZ3b indicating conditions for landform formation (active ice/bed mobility) are optimal in the middle of the GTZs, with less favourable conditions toward the exterior, possibly due to slower-moving ice toward the lateral margins of the confined ice flow where the margins imposes side drag (Stokes and Clark, 2002). Interestingly, GTZ1 has a more evenly distributed

high density of landforms, suggesting more uniform subglacial conditions. Elongation values vary throughout GTZ1, GTZ2, GTZ3, GTZ3b, and GTZ4, with the scaled elongation values indicating that GTZ2 has lowest elongation values (Figure 3.13A). However, overall the variation between landform elongations is minimal between all of the GTZs (Table 3.1 and Figure 3.10). This could indicate that similar processes produced most of the landforms within the study area (e.g., Ely et al., 2016). Although elongation ratios in other ice stream corridors are highest in the centre (e.g., Briner, 2007; Stokes and Clark, 2002), elongation ratios across identified GTZs show no clear organization. This is likely due to slight variations in subglacial conditions throughout each ice-flow phase that resulted from ice-flowing at slower speeds than those required for such streamlined landform organization (i.e., warm-based, but not ice streaming), or a limitation of the data resolution. More likely, the study area does not capture the full footprint of the ice streams and therefore does not have the same pattern (i.e., the study area only captures the catchment zone of the ice stream where typical ice stream organization has not occurred).

Till and bedrock samples collected for cosmogenic analysis are limited in both number and spatial distribution; nonetheless, they do suggest differences across GTZs, which correlate well with subglacial conditions inferred from the categorized cells. GTZ3b, GTZ2, and GTZ1 have the lowest ^{10}Be abundances (Figure 3.11), suggesting relatively 'High' net subglacial erosion over the last glaciation and are located near high concentrations of 'High' cells within those zones. The only high ^{10}Be abundance within GTZ1 (9.06×10^5 atoms/g) is from a bedrock sample and lies near a cluster of WL, MH, and ML cells indicating relatively lower local net subglacial erosion during the last glaciation. Although most samples collected from GTZ4 are only marginally higher than samples collected to the east and west, the highest ^{10}Be value is within GTZ4 (Figure 3.11). This sample (16-PTA-070B), collected from the centre of GTZ4 has nearly double the ^{10}Be abundances of the surrounding samples (1.9×10^5 atoms/gram) which could indicate there was insufficient bedrock material (2-3 m) eroded following pre-glacial cosmic exposure (interglacial) leaving an inherited ^{10}Be signal (e.g., Staiger et al., 2006; Briner et al., 2006, 2008). Generally, it appears that subglacial erosion removed most (if not all) preglacial inheritance in GTZ3b and GTZ2 (predominantly 'High' and MH cells). However, in GTZ4 where ML cells are abundant, higher ^{10}Be abundances are reported, indicating some ^{10}Be inheritance and thus lower net erosion during the last glaciation.

The CIA results show little variation across the entire study area with the highest values residing in till collected over the metasedimentary rocks of the RL domain, which have a higher fresh CIA (59.2). This pattern indicates an influence of the underlying bedrock lithology on the CIA, therefore, this portion of the study area is thus considered not suitable for the evaluation of weathering and glacial erosion through CIA analysis. Nonetheless, results from the remaining study area suggest that the till analyzed was sourced from relatively fresh till and bedrock indicating that sufficient glacial erosion occurred in the study area during the last glaciation to remove or dilute any inherited CIA index values. Although this does not assist in evaluating changing subglacial erosional conditions between GTZ, it does support field observations that this region did not experience widespread sustained cold-based conditions during the full duration of the last glaciation; otherwise, some preserved evidence of pre-existing weathered regolith in the form of higher inherited CIA values and ^{10}Be would have been found, similar to those observed on Baffin Island (Refsnider and Miller, 2010). Interestingly, CIA values surrounding the highest levels within the RL domain are elevated as well, possibly indicating geochemical dispersal patterns observable through CIA calculations.

Sites where multiple crosscutting outcrop-scale ice-flow indicators have been documented are concentrated within the central portion of the study area. The majority (8 of 15) are within GTZ4, with six sets near the edges of GTZ2, and a single set in GTZ5 (Figure 3.11). Although striation measurements were largely restricted to regions of till veneer or bedrock, the partial overprinting of older ice-flow indicators by younger indicators at these locations suggests these areas experienced enough subglacial erosion to sculpt, striate, and/or polish the bedrock surface during multiple ice-flow phases, but never sufficiently to completely remove evidence of older ice-flows. The abundance of these preserved striations suggests limited overall subglacial erosion, possibly due to low basal ice velocity and bedrock hardness. Because the De Pas Batholith is a local topographic high this region is more likely to have acted as an area of basal drag and this would have slowed down basal ice of that area. The other sites of crosscutting ice-flow indicators are located around the edge of GTZ2 and could therefore be near the onset zone of the UBIS catchment where erosion was more limited than down-ice, in the zone of basal ice flow acceleration (toward the northwest of the study area within the centre of GTZ2).

The large WL zone within GTZ5 presents a more complex subglacial history. The large spatial distribution of the till blankets were likely produced during Flow 1, during wide-spread

warm-based conditions across the study area. It is unknown how deep these till deposits are, however, as the till shows signs of subglacial origin (e.g., faceted striated clast), it was produced and entrained by actively flowing basal ice and may have been deposited later by sluggish ice, or meltout processes following late-stage ice sheet stagnation, possibly during Flow 3 or Flow 4. This created terrain with no landforms and few lakes at the surface, exemplified by the prominently WL cells within this GTZ, as warm-based conditions were needed to produce the till blanket, but low dynamics must have been involved (at least during subsequent ice-flow phases) to not produce any subglacial landforms or lakes, or bury any existing landforms or lakes with meltout sediments.

3.5.2 Polythermal subglacial conditions relating to ice flow history

GTZ1 has subglacial landforms associated only with Flow 1 suggesting the northeast ice-flow phase was largely warm-based (active ice/bed-mobility) across at least the eastern portion of the map sheet (Figure 3.14). In the centre of the study area, ice/bed mobility seems to have been minimal. Given that there are still small lakes across most of the upland, it suggests abrasion was more pervasive across the hard bedrock upland, with some, but not extensive quarrying. In the southwestern portion of the study area, actively flowing warm-based ice produced till, possibly during Flow 1, but as previously stated, the lack of drumlins and somewhat hummocky or rolling topography suggests a later shift to more stagnant conditions as it transitioned to colder-based conditions between the active palaeo-ice stream in the region (see below). Following Flow 1, an ice-divide formed somewhere within, or just beyond the southeast corner of the study area (Figure 3.14) resulting in a change from active ice/bed mobility to limited or no ice/bed mobility. This change in the subglacial regime in the eastern portion of the study area preserved Flow 1 features. West of the divide, in the northwest of the study area, warm-based conditions developed in association with ice-flow to the northwest, with landforms from Flow 2 restricted to GTZ2. Flow 2 has been associated with palaeo-ice streaming events funneling into Ungava Bay (Clark et al., 2000; Jansson et al., 2003; Chapter 2), which suggest the warm-based conditions associated with this ice-flow phase propagated up-ice toward the central upland. On the upland, Flow 2 transitioned from highly erosive active flowing ice with warm-based conditions (GTZ2) to less erosive less mobile bed conditions resulting in more areal

scouring, locally producing abundant small lakes (GTZ4), although these lakes are probably the net effect of both Flow 2 and Flow 3 (Figure 3.2).

A change in dynamics of the UBIS catchment led to the stoppage of northwest-trending fast ice flow in the northwest portion of the study area, and a western shift of active palaeo-ice stream catchment (Margold et al., 2018). The stoppage of fast flow over GTZ2 and shift to cold-based conditions is required to preserve the Flow 2 landscape, which is only weakly overprinted by Flow 3 features along the eastern edge of GTZ2. This reconstruction is further supported by the occurrence of long strips of ribbed moraines that have developed onto and deformed northwest-trending drumlins northwest of the current study area (Jansson, 2005). The westward shift of the UBIS catchment is thought to have also caused the ice divide (over GTZ1 and GTZ4) to migrate westward (Chapter 2). The ice divide migrated to, or just beyond, the western edge of the study area, resulting in ice flowing to the east (Flow 3) over part of the study area. The westward migration of the divide likely caused a transient shift from warm-based to cold-based conditions across the western portion of the study area. This type of thermal migration has been shown in older glaciations (> 1 Ma) on Baffin Island (Refsnider and Miller, 2010; Briner et al., 2014). GTZ3 contains a small band of 'High' cells that have abundant small, but elongate landforms. Interestingly, GTZ3 contains landforms indicative of eastward ice flow, but no striation evidence for Flow 3 was observed at the accessible outcrops in GTZ1 (n=12). Striation evidence of Flow 3 is limited to the central highlands (Figure 3.11). This suggests that subglacial abrasion of bedrock was locally limited in GTZ3 during Flow 3, especially on the more elevated outcrops that were accessible in this study. The higher density of small lakes on the central upland may have been formed as transient abrasive conditions occurred on the upland during the transition from Flow 2 to Flow 3. The east-trending landforms at lower elevation could have formed through deformation of the till (e.g., Menzies et al., 2016), with the highlands acting as "sticky spots" preserving Flow 1 striations (Stokes et al., 2007). Down-ice (east) from the cluster of 'High' cells in GTZ3 (Figure 3.14), a lack of landforms or striations associated with Flow 3 (marking the eastern boundary of GTZ3) suggests an abrupt change in subglacial conditions. Similarly, GTZ3b is thought to have occurred during the third ice-flow phase, as it contains landforms of a similar size and orientation and represents the catchment region of the Kogaluk ice stream to the northeast (Margold et al., 2015; Paulen et al., 2017). In GTZ3, a strong overprinting of Flow 1 is recognized. Large subglacial landforms with a more northeastern

orientation are surrounded by smaller, more easterly landforms associated with Flow 3. There is also another east-trending flowset, the Cabot Lake ice stream, just south of the study area that likely formed contemporaneously to Flow 3 (Rice et al., 2020). Cell classification within GTZ3b shows highly dynamic subglacial conditions with decreasing dynamic conditions along its southern limit, indicative of palaeo-ice stream catchment regions and similar to GTZ2. Flow 3 is associated with deglaciation, as evident from the near parallel eskers to the east of Flow 3 landforms. Following Flow 3, there was a late-deglacial flow away from the central highland to the southwest (Flow 4), which had no significant impact on the surficial signature (as defined by the proxies); it only left sporadic outcrop-scale ice-flow indicators (Figure 3.14). It is currently still unclear whether Flow 2 or Flow 3 removed landforms associated with Flow 1 within GTZ5, but this zone appears to be in-between large 'competing' regions of fast flow; UBIS catchment (Flow 2) and ice flowing southeast into the Smallwood Reservoir area and Lake Melville (Figure 3.1).

Overall, the migration of the Labrador Divide across the study area and palaeo-ice stream catchment dynamics caused transient polythermal and changing subglacial erosional conditions, which ultimately created a fragmented mosaic of subglacial features. Some cold-based regions may have been overprinted after a switch to warm-based conditions, but extensive preservation of relict landforms in the east and northwest of the study area requires the opposite situation (i.e., a switch from warm-based to cold-based conditions). This is exemplified by the landforms associated with Flow 1, which formed under warm-based conditions but were preserved under cold-based conditions following the formation and migration of the ice divide (Figure 3.14). This work supports the observation by Clarhäll and Jansson (2003) in the southern Lac aux Goélands area (Figure 3.2) that also proposed a shift from warm to cold-based conditions, preserving older glacial landscapes and subglacial landforms. They further suggested that these changes occurred in restricted subglacial zones during restricted time periods. These transient subglacial conditions and the resulting mosaic of subglacial thermal zones created a fragmented landscape similar in many ways to the outer zone of the Keewatin Dome, such as in the Shield terrain of northeastern Manitoba (Trommelen et al., 2012).

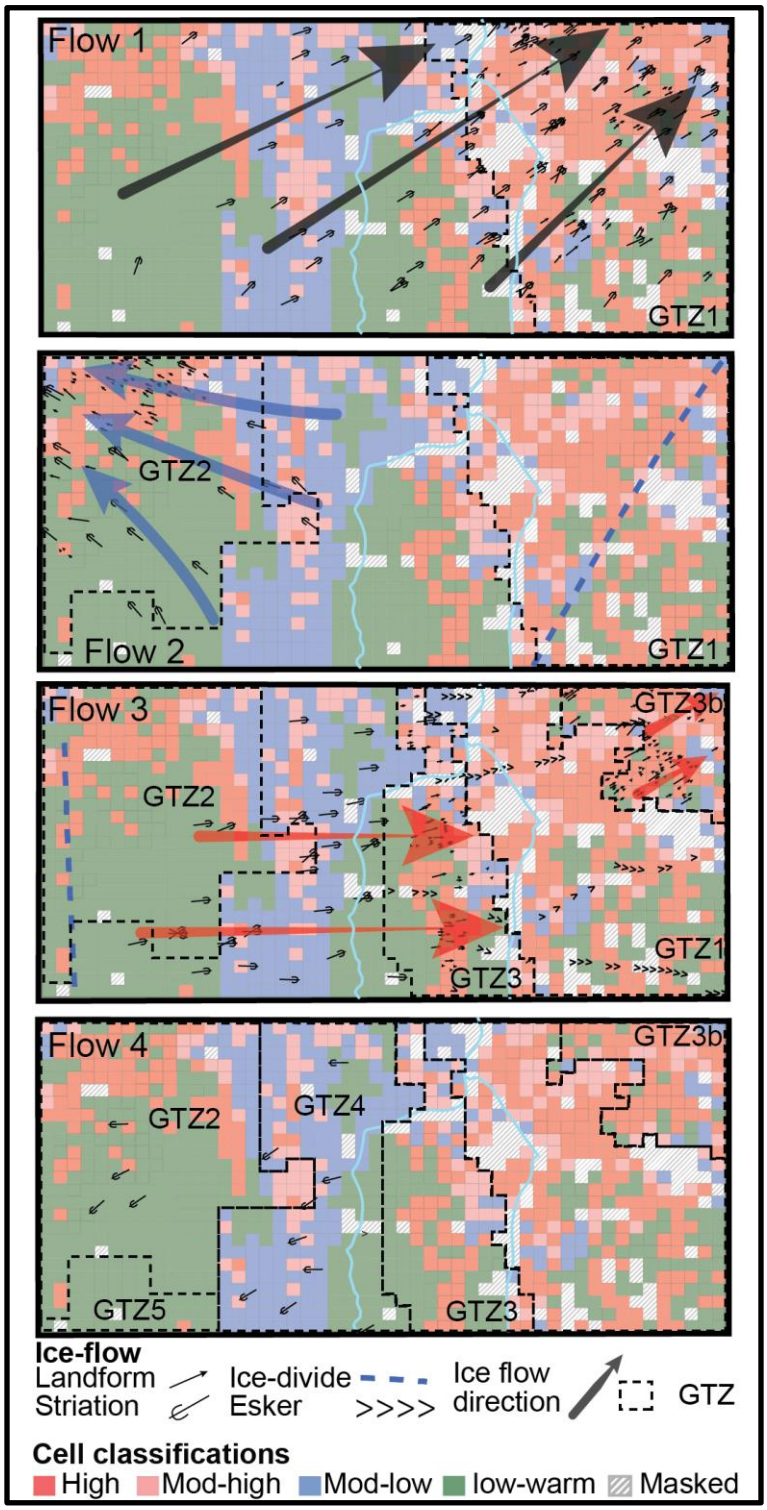

Figure 3.14. GTZ formation and cell classification within the context of the local ice-flow history showing the preservation of relict warm-based High conditions created during the migration of the ice divide across the study area. The cells are classified the same as in Figure 3.7.

3.5.3 Evaluation of study area within a larger glaciological context

The patterns of subglacial conditions identified in this study do not match the symmetrical subglacial thermal regimes observed in other ice-divide regions (e.g., Kleman and Stroeven, 1997; De Angelis and Kleman, 2005; Davis et al., 2006; Staiger et al., 2006; Briner et al., 2008; Refsnider and Miller, 2010), which were affected by sustained cold-based subglacial conditions near an inferred stable ice-divide centre. In studies that examine ^{10}Be abundances from different subglacial regimes, it was reported that results with 10 times the abundance of ^{10}Be (when compared to nearby samples over glacially eroded terrain) are typically interpreted to reflect regions of sustained cold-based conditions (Marquette et al., 2004; Staiger et al., 2006; Briner et al., 2008; Fu et al., 2018). Other studies utilizing the same methodology reported samples as low as 4 times the abundance of ^{10}Be to be indicative of sustained cold-based regimes (Fabel et al., 2002; Briner et al., 2014). Intermediate or transition zones, between warm and cold-based end-member categories, yield ^{10}Be abundances 1.4 to 4.2 times higher than surrounding warm-based terrains (Li et al., 2005; Staiger et al., 2006; Fu et al., 2018).

The highest ^{10}Be abundances from the study are 2.1 to 2.6 times greater than what would be expected from post-glacial exposure, an order of magnitude lower than those used to infer sustained cold-based conditions in other studies (see above). The highest ^{10}Be abundances within the current study area are thus comparable to those interpreted to reflect intermediate conditions in other studies. Similarly, the CIA values from this study (excluding samples from the RL Domain) ranged from 46.4 to 53.2, significantly lower than 70.0 - 90.0 reported by Refsnider and Miller (2010) from a region with high ^{10}Be abundances and inferred cold-based landscape. Taken together, these results are interpreted to reflect transient subglacial conditions associated with the ice-divide migration across the study area with no zone indicative of sustained, stable, cold-based conditions for the full Laurentide glaciation. This is best explained by the migration of the ice-divide eroding enough bedrock material to remove inherited CIA values and remove some, but not all, of the pre-glacial ^{10}Be build-up over the central upland area where cold-based conditions were likely the most pervasive. Shattered bedrock and felsenmeer were observed by Dubé-Loubert and Roy (2018) approximately 140 km to the north of the current study area but occur over small upland areas only. Those sustained cold-based conditions either did not extend into this study area or were eroded during warm-based conditions during subsequent ice-flow phases (Figure 3.14). These results suggest that the current study area was more sensitive or

susceptible to larger ice-sheet dynamics, possibly due to its proximity to palaeo-ice stream catchments.

Interestingly, GTZ1 has a high abundance of 'High' cells (47.7%) whose features were largely (if not solely) created during Flow 1. Ice-flow phases with similar orientations to Flow 1 have been identified across southern and central Quebec and in eastern Labrador (Klassen and Thompson, 1993; Veillette et al., 1999; Parent et al., 2004). The exact age of this extensive, yet discontinuous and 'old' flowset is unknown. However, the CIA and the more limited cosmogenic results (in GTZ1) do not show evidence that would support a pre-Late Pleistocene age for GTZ1 landscape, due to the low inheritance in both bedrock and till (6.5×10^4 and 7.1×10^4 atoms/g respectively; Figure 3.11). Uncertainties, persist, however, because Flow 3, although its imprint lies outside of GTZ1, could have sufficiently trimmed the Flow 1 landscape surface to remove most of the cosmogenic inheritance. No erosional evidence related to Flow 3 across GTZ1 was identified, but the possibility of some Flow 3 erosion cannot be completely ruled out. In addition, it is unclear whether weathering during the last interglacial would have been enough to create a distinctly higher CIA across GTZ1. Nonetheless, the interpretation, as based on the currently available data, suggests the regional northeast Flow 1 formed at an early stage of the last glaciation rather than a previous glaciation (*cf.* Veillette et al., 1999). If correct, this would indicate that during the earliest glacial phase, the bed was more broadly warm-based than during subsequent ice-flow phases with later ice-flow events being more localized and highly influenced by ice streaming events. Ground temperature reconstruction from several borehole temperature profiles collected across the Canadian Shield indicates that the coldest ground surface temperatures (near the pressure melting point for most boreholes) were not reached before the LGM, suggesting wide-spread warm-based conditions (Pickler et al., 2016); the closest deep borehole site to this study area is in Sept-Iles (~ 500 km south), where minimum reconstructed ground temperatures reached -1.4°C shortly after LGM (Pickler et al., 2016). This may not be representative of the conditions within this thesis' study area, but it does provide some evidence that some core regions of the LIS on the Canadian Shield were mostly warm-based throughout the last glaciation, except perhaps for a relatively short time around LGM and shortly thereafter. Ice sheet models also provide useful insights into this question, and low 'warm-based' probabilities for the entire last glaciation are only predicted for a few small regions (e.g., Tarasov and Peltier, 2007). Interestingly, one of these probable 'sustained cold-based' zones is located

quite close to the study area (Tarasov and Peltier, 2007; their Figure 3.11). Progress in numerical modelling and the future development of geothermal energy in remote northern communities, which necessitates deep boreholes, may soon increase the resolution and accuracy of basal LIS temperature reconstructions for the last glaciation.

3.6 Conclusions

This research spatially analyzed a glacial landscape of mosaic GTZs of a core region of the LIS that represents the net effect of multiple ice-flow phases and complex interactions between palaeo-ice stream catchment dynamics and local ice divide migration (Chapter 2). Five different glacial landscape features considered to be proxies of subglacial dynamics were used, namely bedrock-controlled lake density and surface area, glacial landforms density and elongation, and till blanket. The results were classified into different relative subglacial dynamic intensities ('High', MH, ML, WL, and Low). The 'High' class represents warm-based areas indicative of actively flowing basal ice, the low class represents cold-based (non-sliding) ice, with the moderate classes representing intermediate thermomechanical conditions. Results distinctly different characteristics between the GTZs. Through these analyses, it has been established that the study area did not experience sustained cold-based conditions, but rather polythermal subglacial evolution associated with a transient ice-divide migration. A grid-cell classification of the subglacial dynamics proxies identifies regions of erosive warm-based conditions in all GTZs. Interestingly, the most relict GTZ1 shows evidence of 'High' subglacial dynamics conditions over 47.7% of its area and is well preserved. GTZ2 is associated with the onset of the UBIS and is classified as 'High' subglacial dynamics over 24.4% of its area. GTZ3 is associated with a short deglacial flow is now classified as having 'High' subglacial dynamics over 30.8% of its area. The related GTZ3b, which represents a portion of the catchment zone of the Kogaluk ice stream, is classified as having 'High' subglacial dynamics over 58.9% of its area. Local eskers abruptly end at the eastern edge of GTZ3, and the change in elevation associated with the western boundary of GTZ3 and the formation of eskers may be a partial control on the confinement of GTZ3 and onset of esker formation. GTZ4 is the largest GTZ and centres the study area with a classification of 'High' subglacial dynamics over only 3% of its area. GTZ4 represents an area that evolved under less erosive ice conditions that removed pre-glacial

weathering but did not erode deeply into the bedrock as indicated by ^{10}Be abundances, abundant cross-cutting striations, and CIA results from across the GTZ. CIA and ^{10}Be abundance analysis also indicate that the oldest ice-flow phase (Flow 1 to the northeast) recorded within the study area (and regionally) most likely belong to the last glaciation as opposed to being the result of ice flow from a previous glaciation and preserved due to limited glacial erosion (*cf.* Veillette et al., 1999). GTZ5 is classified as having WL conditions over 95.9% of its area, indicating warm-based conditions at some point in order to deposit till blankets, but 'low' dynamics that did not produce any measurable proxies during subsequent conditions that deposited meltout till over GTZ5.

Overall, this work has shown the subglacial dynamics of northeastern Quebec and adjacent Newfoundland and Labrador, a core region of the northeastern sector of the LIS, varied throughout the last glaciation and was subject to time-transgressive changes associated with ice divide migration. How rapidly these changes occurred remains uncertain, but they seem to have all taken place during the last glaciation. Although more information may be required, specifically concerning the physical properties of the bedrock, such as hardness and thermal conductivities, the findings of this research provide useful constraints or a testable reconstruction for future numerical ice sheet modelling efforts. Understanding how the reconstructed subglacial conditions relate to sediment erosion and transport would further improve the understanding of how these complex regions of the LIS evolved through the last glacial cycle.

4 Chapter 4: Glacial sediment dispersal from ice divide migration and evolving polythermal subglacial conditions in the Quebec-Labrador sector of the Laurentide Ice Sheet

4.1 Overview

There is growing evidence that suggests the LIS had a dynamic polythermal base. However, the subglacial thermal organization of the LIS and its evolution throughout glaciation are poorly constrained, especially within the inner regions of the ice sheet. Specifically, the processes of subglacial erosion, transportation, and deposition in relation to changing subglacial conditions remain poorly constrained. In this chapter, the results of a regional-based till sampling program that was conducted in a region within the interior of the Q-L sector of the LIS is was known to have experienced ice divide migration and polythermal subglacial conditions are presented. This research will improve the overall understanding of how glacial dispersal patterns in these inner ice sheet regions evolve throughout glaciation. The collected till samples were subjected to till matrix geochemistry analysis, indicator mineral identification, and clasts lithology classification. These results were then evaluated within the context of the relative ice flow chronology and subglacial thermal evolution. Dispersal patterns suggest the earliest flow phase was the most influential, with widespread warm-based conditions turning to patchier dispersal patterns, as a result of changes in subglacial conditions that varied spatiotemporally during subsequent ice-flow phases. These conditions were likely created as the ice sheet thinned and reduced driving stresses that led to an overall reduction in erosion, till production, and dispersal. However, where warm-based conditions existed, predominantly in regions influenced by nearby palaeo-ice streams, dispersal of fresh and/or re-entrained glacial material is identifiable, creating complex dispersal patterns across the study area. These results provide important insights for future mineral exploration programs in inner ice sheet regions and demonstrates the importance of a robust understanding of ice-flow history and subglacial conditions during mineral exploration programs.

4.2 Introduction

Subglacial conditions in the inner regions of the LIS (e.g., ice divides) are considered to have changed spatially and temporally throughout the last glaciation, not just as a result of ice

sheet growth and retreat phases, but also because of ice divide migration and associated changing subglacial conditions (i.e., thermal regime and/or basal shear stress). This is supported by several glacial geology and geomorphology studies in northern Canada (Boulton and Clark, 1990; Kleman et al., 1997; Kleman and Hättestrand, 1999; Veillette et al., 1999; Kleman and Glasser, 2007; Greenwood and Clark, 2009; Smith and Knight, 2011; Trommelen et al., 2013; Hodder et al., 2016; Gauthier et al., 2019; Chapter 2), numerical ice sheet studies (Hildes et al., 2004; Tarasov and Peltier, 2004, 2007; Stokes et al., 2012; Melanson et al., 2013), and to some extent, by analyses of deep borehole temperature profiles (Pickler et al., 2016). The detailed reconstructions differ from one study to the next, however, most of them indicate that core-regions of the LIS were affected by transient subglacial conditions in response to changes in ice sheet configuration and overall dynamics (e.g., from internal and external forcings). The geological record of these inner regions may thus reflect the net effect of ice-marginal processes when the ice sheet was small, as well as processes that took place close to ice divides when the ice sheet was extensive and thick. One characteristic that has been documented in these regions, and is considered as evidence of ice flow reversal, are double-stoss and lee bedrock outcrops with ice-flow indicators on two opposing abraded surfaces (e.g., McMartin and Henderson, 2004). These regions also tend to have complex 'amoeboid' till dispersal patterns radiating away from their source locations (e.g., Stea and Fink, 2001; Trommelen et al., 2013), or till stratigraphy recording provenance reversal (e.g., Hodder et al., 2016). These features are therefore, considered characteristics of regions that have experienced ice divide migration. Reconstructing ice divide migration and/or rotation and the associated subglacial process over time therefore has repercussions across vast areas in every down-ice direction, not just the region experiencing ice-divide migration.

A comprehensive investigation of the glacial record within core regions must include an analysis of the geomorphological evidence, as well as an analysis of the spatial variations in till composition, as this allows a linkage between basal ice-flow records (e.g., outcrop-scale and landform-scale records) with glacial erosion and entrainment/deposition processes (e.g., Hodder et al., 2016; Gauthier et al., 2019). This is critical for understanding long-term paleo-ice sheets and glacial landscape evolution (e.g., Melanson et al., 2013) and has important implications for mineral exploration (McClenaghan et al., 2001; Paulen and McMartin, 2009).

One of the largest interior regions of the LIS was the Q-L sector. Significant advances have been made in the understanding of the ice flow history of the Q-L sector, both in terms of regional ice-flow phases and glacial sediment dispersal (e.g., Klassen and Thompson, 1993; Veillette et al., 1999; Clark et al., 2000; Jansson et al., 2003; Clarhäll and Jansson, 2003). Nonetheless, the size of the Q-L sector is such (3,000,000 km^2; Dyke, 2004) that important data and knowledge gaps remain. Recent progress has been made with respect to ice-flow phases, ice divide migration, and subglacial dynamics for a portion of the Q-L sector (Chapters 2 and Chapter 3), however uncertainties persist. The purpose of this chapter is to enhance this reconstruction by adding dispersal (provenance) analysis and place it within the broader regional context.

More specifically, the use of till compositional data (i.e., till matrix geochemistry, indicator minerals, and clast lithology abundances) to compare with, and enhance, the latest glacial reconstructions, which is currently based on ice-flow indicators (Chapter 2), and erosional/weathering proxies from till and bedrock (Chapter 3). These results are then placed within the broader regional till dispersal context (Klassen and Thompson, 1993) and ice sheet evolution context (e.g., Veillette et al., 1999; Clark et al., 2000; Clarhäll and Jansson, 2003; Chapter 2). This analysis will provide important constraints for glacial systems-models that include subglacial process models of erosion and sediment transport (e.g., Melanson et al., 2013). Furthermore, it will provide valuable insights into net glacial dispersal resulting from ice sheet growth, ice divide migration, and ice sheet retreat, which will be helpful for mineral exploration in such terrain.

4.2.1 Bedrock Geology and related indicators for till provenance

An understanding of the regional bedrock geology is critical for till compositional and related provenance analyses as glacial sediments are composed of the bedrock they erode and entrain. This section thus provides an overview of important bedrock geology features within and surrounding the study area. The study area is located approximately 90 km northeast of Schefferville, Quebec under what would have been the Q-L sector of the LIS (Figure 4.1). Recent bedrock mapping by Sanborn-Barrie (2016) and Corrigan et al. (2018) have provided updated lithotectonic understanding of the region, allowing for more detailed provenance studies of glacial sediments. The regional bedrock geology broadly represents an assemblage of various

Archean continental masses onto the Superior Craton and along sutures that are thought to have been modified by the Torngat and New Quebec orogens (Hoffman, 1988; Wardle et al., 2002; Charette et al., 2016). A suite of metamorphosed volcano-sedimentary rocks of Paleoproterozoic age, including the Doublet metavolcanics and the iron-ore producing LT, were over-thrusted and folded on top of the Superior Craton during the New Quebec Orogeny and outcrop southwest of the study area (Figure 4.2A; Sanborn-Barrie, 2016). Within the study area, three main bedrock domains are recognized, the RL, GR, and MR (Figure 4.2B). The RL domain is in the western part of the study area and is dominated by Paleoproterozoic (1.87-1.85 Ga) metasedimentary rocks and amphibolite in the south, and felsic plutonic rocks in the north, with blocks of Archean structural complexes belonging to the Superior province cut by small ultramafic belts (Wardle et al., 2002; Sanborn-Barrie, 2016). The RL is bounded by the Lac Tudor Shear Zone to the east which separates the RL domain from the GR domain. The GR domain exposes the De Pas Batholith, a suite of 1.84 -1.82 Ga porphyritic monzogranite-granodiorite-syenogranite rocks that roughly bisects the study area and forms a topographical highland. The De Pas Batholith is bounded to the east and west by thin (5-10 km wide) bands of orthogneiss. The GR also includes 2.79 -2.6 Ga plutonic rocks into which the De Pas Batholith intruded. The De Pas batholith is considered to be a transition zone between two regional orogens: The New Quebec Orogen to the west and the Torngat Orogen to the east (Lafrance et al., 2018; Figure 4.2A). The GR is bounded to the east by the George River shear zone that marks the western boundary of the MR domain (Figure 4.2B). The MR domain is comprised of paragneiss and diatexite and migmatite sequences, metavolcanic rocks, and gneisses of Neoarchean and Paleoproterozoic age (2.3-2.5 Ga) (van der Leeden et al., 1990). The MR domain also contains numerous Mesoproterozoic intrusions that mark the eastern boundary of the study area (Figure 4.2A).

Till is a complex sediment that is produced through a variety of glacial erosion and entrainment/depositional processes (Turner and Stea, 1990, Evans et al., 2006). Regardless of the exact origin of the sediments (e.g., direct abrasion/quarrying of bedrock or pre-existing sediments), the mechanisms of entrainment (e.g., englacial or subglacial deformation) and deposition (e.g., lodgment, deformation, meltout) depends on the spatiotemporal fluctuations of thermomechanical conditions across the ice-bed interface (Boulton, 1978; Iverson et al., 1995; Piotrowski et al., 2006; Melanson et al., 2013). Till typically consists of material that originated from multiple bedrock sources and, as such, is considered to have mixed provenance. There is

also a certain degree of compositional fractionation based on particle size (Shilts, 1995). Therefore, for a more comprehensive analysis, multiple indicators most indicative of each major bedrock domain within the study area were selected (Table 4.1) and are summarized below.

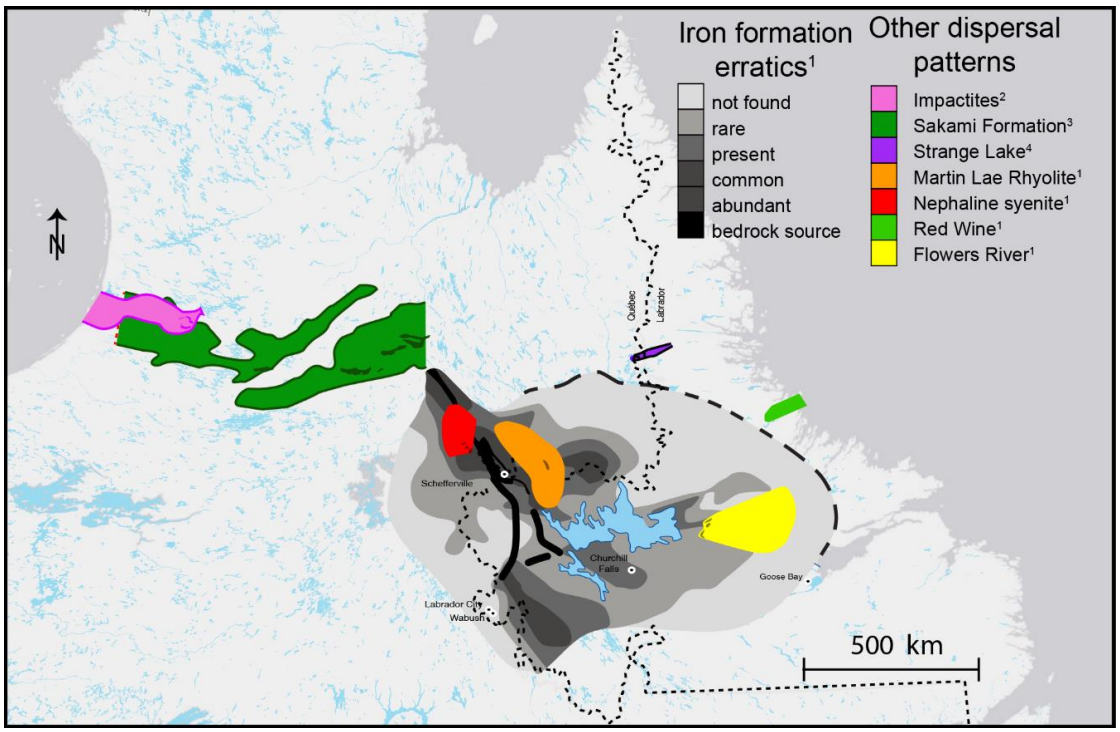

Figure 4.1. Dispersal patterns from across central Quebec and Labrador showing more linear dispersal near the coasts, with more complex dispersal within the inner regions of the ice sheet. Dark colours represent the source of the dispersal fan. Note: [1]Klassen and Thompson (1993) [2]Parent et al. (2005) [3]Parent et al. (1995) [4]McClenaghan et al. (2019).

Klassen and Thompson (1993) identified both Fe_2O_3 and MgO as geochemical indicators of the LT, as these lithologies are relatively enriched in these major oxides compared to other domains within the region (Table 4.2). Additionally, red rutile and Mn-epidote, which are commonly associated with metamorphosed massive sulphide deposits are likely to have originated within the Doublet mafic volcanic zone of the LT (Averill, 2001), therefore making good indicators of dispersal from the LT bedrock unit. Within the study area, Girard (1995) indicated elevated concentrations of Al_2O_3 in bedrock samples collected from over the RL, with lower values of SiO_2 compared to surrounding bedrock units (Table 4.2). Additionally, available lake sediment data from within the RL domain show elevated concentrations of U, especially close to the RL and LT contact (Clark and Wares, 2004; Amor et al., 2019). In the centre of the study area, within the GR domain, bedrock geochemistry data indicate elevated levels of light

rare earth elements (LREEs) and Zr (Kerr et al., 1994; Table 4.2). In addition, bedrock samples from the GR domain yielded relatively elevated values of Ba (Martelain et al., 1998; Table 4.2). Sanborn-Barrie (2016) documented a compositional change from hornblende-biotite assemblages in the east of the GR domain to more orthopyroxene-bearing assemblages in the western half of the De Pas Batholith. Further east, within the MR domain, leucogranite intrusions are characterized by relatively elevated U concentrations (Collins and Cashin, 2010). Finally, bedrock samples collected from the Mistinibi paragneiss, one of the largest units within the larger MR domain have elevated percentages of SiO_2 in comparison to surrounding bedrock units (Danis, 1988). Similar to the RL domain, no minerals are likely to be reliable indicators of the MR domain. However, clasts from collected till samples were used as lithological indicators of each bedrock domain (Table 4.1). Each bedrock domain thus has one or more indicator mineral(s) and pathfinder element(s), which are also summarized in Table 4.1.

Table 4.1. Indicators for each bedrock domain used

Domain	Indicators			References	
	Geochemical	Indicator Mineral	Clasts	Geochemical	Mineral
Labrador Trough	•Fe_2O_3+MgO	•Red rutile •Mn-epidote	•Iron fm. •Metavolcanics	•Klassen and Thompson (1993)	•Averill (2001)
Rachel-Laporte	•Al_2O_3/SiO_2 •U	n/a	•Metasediments •Laporte •Leucogranite •Quartzite	•Girard (1995) •Clark and Wares (2004), Amor et al. (2019)	n/a
George River	•Zr +LREEs •Ba	•Orthopyroxene	•Felsic Intrusive •Vein quartz	•Kerr et al. (1994) •Matelain et al. (1998) •Dickson and Kerr (2007)	•Sanborn-Barrie (2016)
Mistinibi-Raude	•SiO_2 •U	n/a	•Mafic intrusive •Intermediate intrusive •Ultramafic •Mistinibi paragneiss •Zeni •Syenite •Michikamau	•Danis (1988) •Collins and Cashins (2010)	n/a

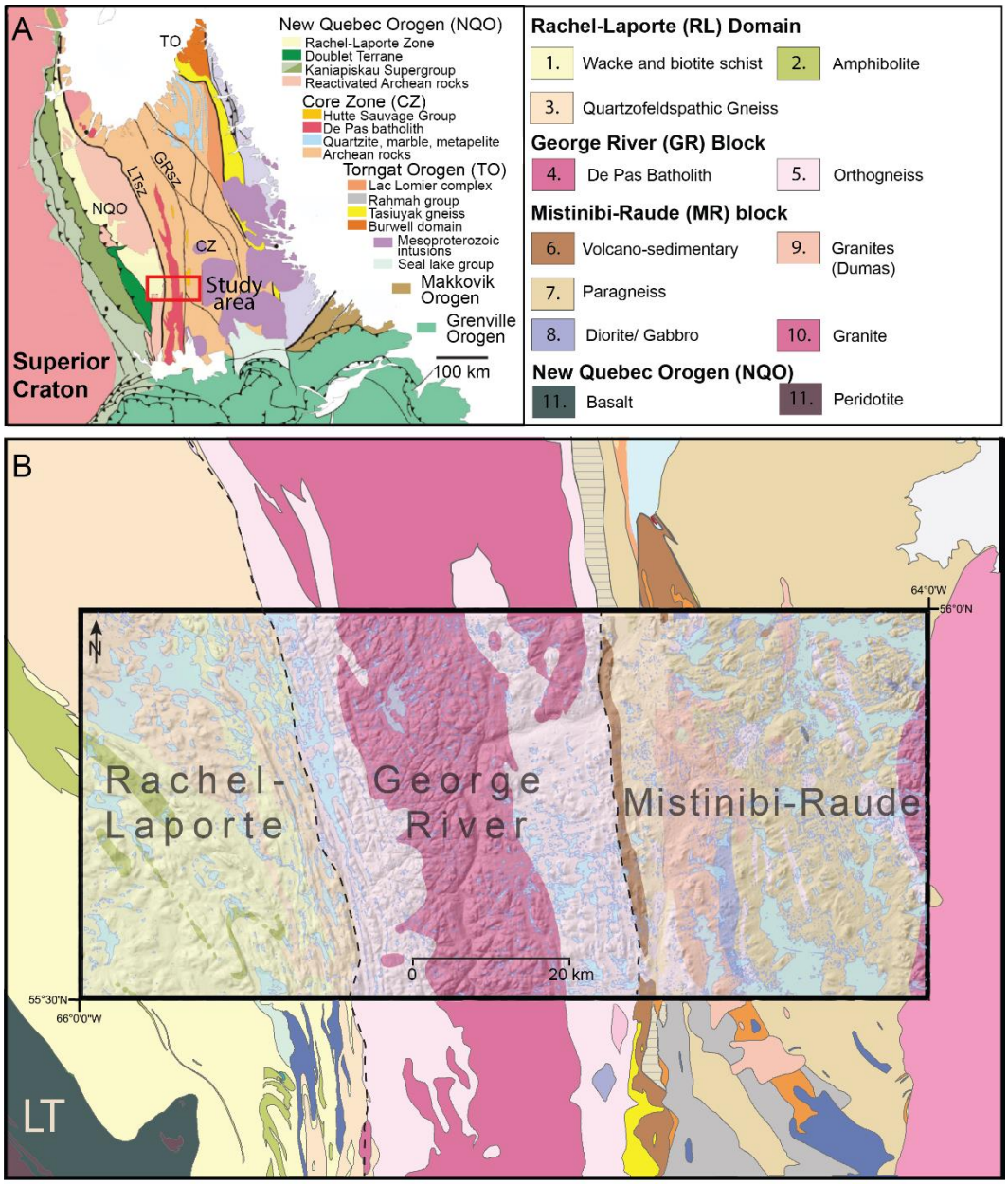

Figure 4.2. **(A)** Regional bedrock geology of Quebec and Labrador identifying major orogens, zones, and cratons. **(B)** Local bedrock of the study area and surrounding region simplified into three domains. Detailed bedrock units are indicated in the upper right, the study area is underlain with a hillshade DEM (SRTM, 30 m resolution, United States Geological Survey, 2014).

Table 4.2. Bedrock geochemical averages for geochemical pathfinders from each domain. Bold values indicate highest values for each column.

Domain	Geochemical Indicator	Domain average			
		Labrador Trough	Rachel-Laporte	George River	Mistinibi-Raude
Labrador Trough	•Fe_2O_3+MgO	•**34.82%**	•17.32%	•6.62%	•6.4%
Rachel- Laporte	•Al_2O_3/SiO_2 •U	•0.178% •5.15 ppm	•**0.32%** •**0.65 ppm**	•0.25% •1.9 ppm	•0.22% •7.79ppm
George River	•Zr +LREEs •Ba	•166.81 ppm •47.6 ppm	•179.16 ppm •376 ppm	•**1199ppm** •**1666 ppm**	•373.2 ppm •681 ppm
Mistinibi-Raude	•SiO_2 •U	•43.3% •5.15 ppm	•51.8 % •0.65 ppm	•64.5% •1.9 ppm	•**68.10%** •**7.79 ppm**

4.2.2 Ice flow history

The study area is located within the Q-L sector, which was one of the largest sectors of the LIS and is also considered to have been continuously covered by ice during the last glaciation (Dyke and Prest, 1987; Dyke et al., 2003). Within the study area, the Ancestral Labrador Ice divide, one of several ice divides of the larger Q-L sector, migrated from east to west across the study area (Dyke and Prest, 1987; Chapter 2; Chapter 3). This ice divide migration is associated with multiple ice-flow phases that have been identified within the study area (Chapter 2). The oldest ice-flow phase, Flow 1, was to the northeast (Figure 4.3) and is interpreted to have originated in the Quebec highlands (Klassen and Thompson, 1993; Veillette et al., 1999; Parent et al., 2004). The landscape associated to Flow 1 is only partially preserved at the regional-scale due to erosion and overprinting by subsequent ice-flow phases. Nonetheless, a relatively large and well-preserved "fragment" of the subglacial bed associated to Flow 1, shows limited (if any) overprinting in the eastern portion of the study area (Figure 2.7). Widespread warm-based conditions are inferred for this ice-flow phase (Chapter 3) because consistent northeast-trending ice-flow evidence of similar relative chronology (i.e., oldest flow) has been observed in other regions of northern Quebec and Labrador (Klassen and Thompson, 1993; Veillette et al., 1999) and have thus been correlated to form one regional ice-flow phase.

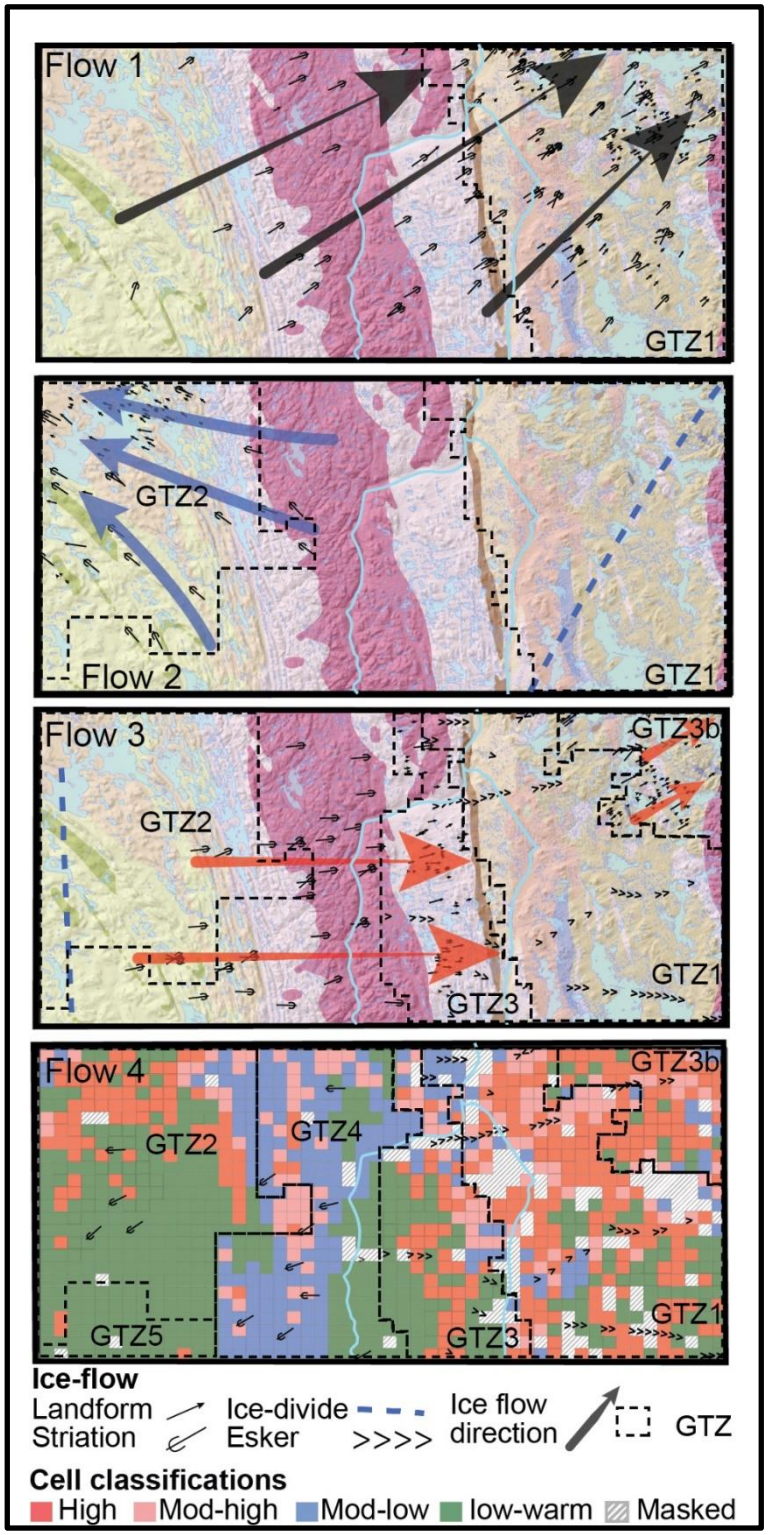

Figure 4.3. Ice flow chronology and associated Glacial Terrain Zones (GTZs) with annotated ice-flow indicators identified in Chapter 2 annotated over bedrock units described in Figure 3.2. Flow 4 has the estimated subglacial conditions identified in Chapter 3 for each GTZ.

Flow 1 was followed by the development of an ice divide in the east of the study area, and is related to a northwest ice-flow phase in the west of the study area (Flow 2), which resulted in the preservation of Flow 1 landscape in the east (under the inferred ice divide). The degree of preservation of the Flow 1 landscape indicates the eastern portion of the study area transitioned to sluggish subglacial conditions during Flow 2 (Chapter 3). Flow 2 is associated with the palaeo-ice streaming events in the Ungava Bay region (Clark et al., 2000; Jansson et al., 2003; Margold et al., 2015, 2018). Following Flow 2, the UBIS shifted westward (Jansson et al., 2003; Margold et al., 2018) and as a result, the ice divide migrated west as well (Chapter 2; Chapter 3). Subglacial conditions are thought to have shifted spatially in association with the westward migration of the ice divide, thus bringing cold-based conditions over the Flow 2 flowset. This shift from warm-based to cold-based over the Flow 2 flowset favoured its preservation and greatly limited erosion/overprinting by subsequent glacial events (Chapter 3). Another consequence of the westward ice divide migration is that ice eventually began to flow eastward away from the new western position of the divide. This is evidenced by a narrow corridor of east-trending features (e.g., striations, roches-moutonnées, crag-and-tails, and eskers) in the east-central (GTZ3) and northeast parts of the study area (GTZ3b) in the catchment zone of the Kogaluk ice stream (Figure 4.3). In the centre of the study area there was minimal subglacial erosion (mainly ML cells; Chapter 3), and a near-complete reversal of ice flow is recorded in the form of double stoss-and-lee outcrops (Chapter 2). Flow 3 likely occurred at a relatively late stage of deglaciation, as eskers within the region are generally parallel to landforms associated with Flow 3. Following Flow 3, a late resurgence ice-flow phase occurred (Flow 4). Flow 4 was largely topographically controlled, with ice flowing away from the topographic high in the centre of the study area to the southwest (Figure 4.3). The only evidence of Flow 4 are fine and shallow striae on a few polished bedrock surfaces. It is likely that a remnant ice cap reverted to cold-based conditions around this time, as evident by the abundance of topographically controlled meltwater channels within the study area (Chapter 2). The study area was deglaciated sometime following the catastrophic drainage of glacial Lake Naskaupi around 8.2 ka (Dubé-Loubert and Roy, 2017) with final ice likely disappearing shortly thereafter (Chapter 2).

This complex ice-flow history left a fragmented subglacial landscape of disjoint glacier bed ‘pieces’ each with a unique inheritance/overprint record. These pieces have been characterized as distinct GTZs, similar to the approach used by Trommelen et al. (2012) that

have each evolved differently throughout glaciation based on the changing subglacial conditions across the study area (Chapter 3). GTZ1 is a relict warm-based landscape formed during Flow 1 that was largely preserved under cold-based conditions during later ice-flow phases, but locally crosscut by east-trending eskers (Figure 4.3). GTZ2 is characterized by northwest-trending landforms (Flow 2) from the onset zone of the UBIS. Striations within this GTZ are predominantly from Flow 2, with two cross-cutting striation sites near the eastern margin of GTZ2 (Figure 4.3). GTZ3 is a smaller GTZ that is distinct from any other because it is the only GTZ characterized by east-oriented streamlined landforms associated with Flow 3 with striation evidence from only Flow 1. East trending eskers also cut across the eastern half of GTZ3 (Figure 4.3). GTZ3b although disconnected from GTZ3 is very similar to GTZ3 in that it has largely overprinted landforms from Flow 1 and is related to the catchment zone of the Kogaluk ice stream. GTZ4 is the centre of the study area and is characterized by an overall lack of landforms, and striation evidence from all four ice-flow phases. Multiple outcrops recording multiple phases of ice flow are preserved within GTZ4 (Figure 4.3; Chapter 3). Finally, GTZ5 is characterized by abundant till blankets but no subglacial landforms and few lakes or depression (Chapter 3). The relationship between these GTZs and dispersal patterns has remained undefined and thus is one aspect that is examined herein.

4.2.3 Previous glacial dispersal studies

The most spatially extensive glacial dispersal analysis in the region was conducted by Klassen and Thompson (1993). Their investigation focused mainly within Labrador but also covered portions of Quebec, providing a geological framework for mineral exploration in the region. Klassen and Thompson (1993) collected five samples within the study area, using only partial digestion analytical techniques and therefore could not be used in conjunction with the complete digestion results used in this thesis. Klassen and Thompson (1993) did conduct more extensive sample collection outside of the current study area and identified multiple key indicators of glacial dispersal in the region, such as clasts from the Flowers Rivers Igneous Suite, Snegamook Granite, Bruce River Group, Red Wine Complex, Martin Lake Formation, and Labrador Trough (Figure 4.1). Additionally, Klassen and Thompson (1993) identified multiple geochemical indicators from various bedrock units in Labrador that were ideal for drift exploration including: Fe_2O_3, MgO, Cu, Mn, Pb, Zn, Cr, U, and Ni. Some of these indicators are

applicable to this study (Table 4.1). Specifically, Klassen and Thompson (1993) identified dispersal patterns originating from older ice-flow phases that had been partially or completely overprinted during later ice-flow phases (Figure 4.1), depending on the location of the dispersal train in reference to the large regional ice-centre. This created a general pattern, from inland to the coast, of fan-like dispersal trains becoming increasingly overprinted by younger and more linear eastward dispersal patterns near the Labrador coast. Even further inland, close to the ice divide region, dispersal patterns are patchy, centred about the source, with dispersal generally to the west/northwest on the western side of the divide and east/northeast to the east of the divide. However, the extent of their dispersal patterns into the current study area remained uncharacterized. Lithological analysis of glacially transported clasts was also undertaken by Klassen and Thompson (1993), but was only qualitatively described (absent, rare, present, common, or abundant). Additionally, approximately 50 small clasts weighing only an average of 10 g were classified, making a detailed analysis of dispersal patterns difficult. Similar to the geochemical results, clast lithology analysis also indicated dispersal from the LT near the southern edge of the study area. No other unique bedrock unit (i.e., Snegamook granite, Bruce River group, Red Wine complex, Martin Lake formation) identified by Klassen and Thompson (1993) has been documented in the till close to or within the study area.

On the western side of the divide, working inland from the east coast of Hudson Bay, Parent et al. (2004) documented somewhat similar patterns to those identified by Klassen and Thompson (1993). Parent et al. (1995) and Parent et al. (2004) identified linear dispersal patterns that have been reworked by later ice-flow phases, which created palimpsest dispersal trains inland from the eastern coast of Hudson Bay. These dispersal investigations lead to significant insights into how subglacial sediments are dispersed as a result of shifting ice flow, highlighting that older glacial movements have residual effects on dispersal patterns due to re-entrainment of pre-existing till and incomplete mixing with newly-produced till during subsequent glacial movements (Parent et al., 1996). This work, although regional in scale, was nonetheless limited to western Quebec, and other till dispersal data from the more interior regions, closer to Labrador are undocumented.

Taken together, the dispersal studies surrounding the current study area to the southwest and southeast have shown increasingly more complex dispersal patterns towards the interior of the Q-L sector. More recent advances in paleoglaciology, especially those that focus on the

processes related to shifting polythermal conditions in response to ice stream or ice divide evolution (Jansson et al., 2002; Clarhäll and Jansson, 2003), provide an opportunity to further constrain, and possibly revisit, regional dispersal patterns within updated conceptual ice dynamic models and till compositional data. By using multiple characteristics of dispersal (e.g., geochemical, mineral, and clast lithology) across a region with evidence of ice divide migration and a fragmented landscape of GTZs inferred to record shifting polythermal conditions, a better understanding of subglacial erosion, sediment transport, sediment deposition, and overall ice-sheet dynamics can be developed.

4.3 Methodology

To characterize the dispersal of glacial sediments across the study area, the strategy was to identify massive matrix-supported diamicton and collect surficial samples of that material (Figure 4.4). The collected diamicton was determined to be subglacial till based on an abundance of sub-angular faceted and striated clasts within the sediment. Internal structures commonly associated with subglacial tills, such as fissility (Evans et al., 2006), were only rarely preserved within the till profile due to widespread periglacial processes that have mixed material within the active layer creating features such as frost boils (McMartin and Campbell, 2009). Frost boils are abundant across most of the study area where till is the surficial material. Till samples were collected from frost boils (n=64) within regions of active permafrost; otherwise, samples were collected from hand-dug pits through the naturally developed soil profile (n=12) to collect C-horizon (unoxidized) till (depth range: 0.1 – 0.8 m). Samples were collected from *in situ* till assumed to be the direct result of glacial processes and not by other secondary processes (e.g., slumping). During sample collection, cobbles and boulders (> 64 mm) were removed from the sample to minimize the weight of the sample during helicopter transport. At each location (n=76) a ~ 3 kg bag was collected for till-matrix geochemistry analysis. At 74 of these locations, an additional ~ 10 kg sample was collected for indicator mineral recovery and clast (> 2mm) separation. During indicator mineral separation, two samples (15-PTA-139 and 15-PTA-140) were inadvertently mixed in the lab during preparation and had to be removed from the analysis. Blanks were inserted into the sample batches to monitor carry-over contamination. Additionally, duplicates and certified standards (Till 1 and Till 4) were inserted into the batch of analyzed samples to monitor the precision/accuracy of the analysis, following protocols outlined by the

Geological Survey of Canada (McClenaghan et al., 2013; Plouffe et al., 2013). The results used in this manuscript are a portion of a larger database collected as part of Natural Resources Canada's Geo-mapping for Energy and Mineral (GEM 2) Hudson-Ungava Surficial program (McClenaghan et al., 2017).

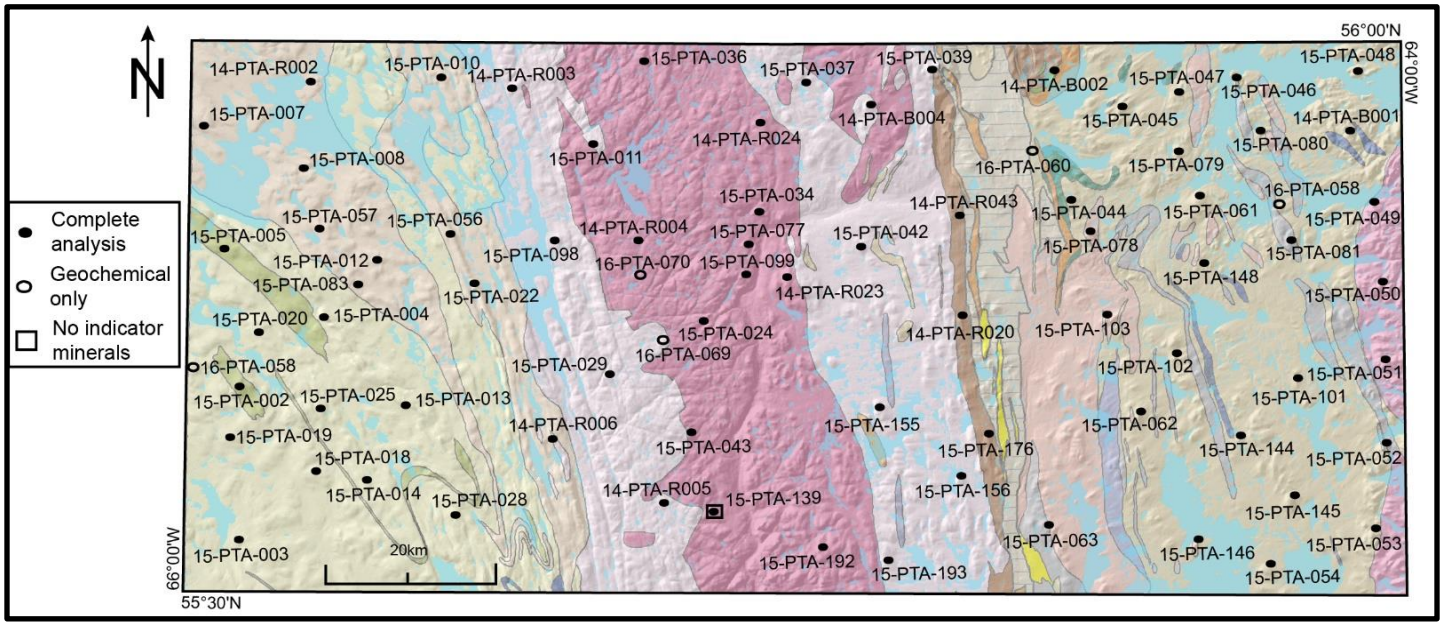

Figure 4.4. Distribution of samples collected across the study for grain size, geochemical, heavy mineral, and clast lithology analysis.

4.3.1 Till matrix characterization and till matrix geochemistry

Most studies using geochemistry have utilized anomalous values relative to local or regional background when discussing dispersal patterns (e.g., Levson and Giles, 1997; Klassen, 1999; McClenaghan, 2001; McClenaghan et al., 2002; Plouffe et al., 2016; Kelley et al., 2019). However, discriminating tills and identifying specific bedrock sources signatures can be difficult, as there is not always a strong geochemical contrast between bedrock units, especially if bedrock units are defined more on the basis of their age and tectonic history than their lithogeochemistry. Nonetheless, the pathfinder elements used in this study (Table 4.1) were selected based on regionally reported bedrock geochemistry data (Danis, 1988; Clark and Wares, 2004; Dickson and Kerr, 2007), existing bedrock maps (Sanborne-Barrie, 2016) and previous geochemical dispersal studies (Klassen and Thompson, 1993). These pathfinder elements are thus considered useful for the study area and should provide valuable insights into till dispersion.

For this study, the 3 kg samples collected at each sample site were shipped to the Sedimentology Lab at the Geological Survey of Canada (Ottawa) for sample preparation. Each sample was dried at 105°C for 15 to 30 minutes and then disaggregated using a rubber mallet following the procedures of Girard et al. (2004). The sample was then split into multiple aliquots for grain size analysis, Munsell colour determination, and till matrix geochemistry analysis. Grain size analysis was determined through a stack of sieves for material > 0.063 mm. For the remaining material (<0.063 mm) grain size was determined using a Leotrac LT-100 Particle Size Analyzer. Results are reported based on the Shepard (1954) system for determining sand-silt-clay ratios. Once dried aliquot was analyzed using a Spectrophotometer linked to IQC colour software for Munsell colour determination. Another aliquot of <0.063 mm fraction was submitted to Bureau Veritas Minerals Canada Limited (Vancouver) for analysis of a suite of major, minor, and trace elements through total digestion (lithium metaborate/tetraborate fusion followed by nitric acid total digestion; BV LF200 package on 0.2 g) followed by Inductively Coupled Plasma-Mass Spectrometry (ICP-MS) and Inductively Coupled Plasma Emission Spectrometer (ICP-ES) determination. The <0.063 mm was selected as it allows for relatively quick, inexpensive separation (Levson, 2001) and is a size fraction that ore minerals are easily comminuted to over relatively short glacial transport and this fraction contains phyllosilicates that will scavenge cations released during weathering (Shilts, 1995). Common QA/QC procedures were applied, and no issues were found, confirming that results are suitable for further analysis and interpretation (Piercy, 2014). Specifically, precision and accuracy were evaluated using the relative standard deviation method for reference material and a value of 4.81% was obtained, which is ‘very good’ (Jenner, 1996). The quality of the analytical method was also evaluated by plotting duplicate samples on scatterplots and Thompson-Howarth plots (See Appendix S4.1), which yielded results with better than 90% precision for all samples. Blanks were evaluated using Shewart plots to assess any contamination during the analytical process (Abzalov, 2008; Piercy, 2014; Scrucca, 2004) and no issues were detected. The full results of the QA/QC can be found in Supplementary Appendix S4.1. Complete laboratory results for till-matrix geochemistry are presented in Supplementary Table T4.1.

The low spatial density of the regional sampling (~ 1 sample/ 90 km^2), the variability of the underlying bedrock, and the complexity of the ice-flow patterns, which together affect the length and direction of spatial data continuity/correlation, made contouring or interpolation of

results impractical. However, discernible patterns are still evident in the data. Results focus on the pathfinder elements discussed in the bedrock section and listed in Table 4.1 and are presented as proportional dot maps. A full description of thresholds used for the proportional dot maps is described in Supplementary Appendix S4.2.

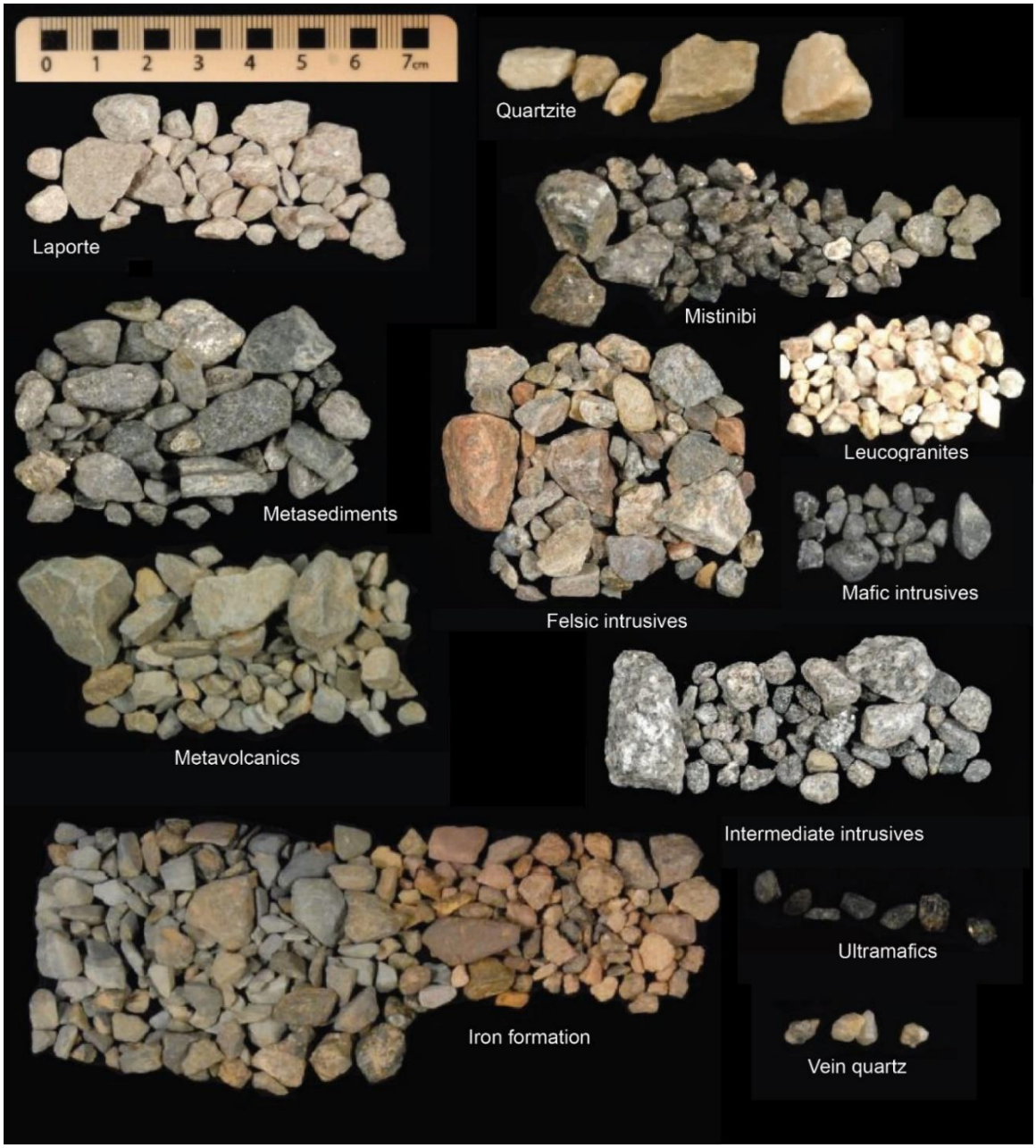

Figure 4.5. Examples of clasts taken from multiple till samples showing the difference in lithology classification used to analyze clasts.

4.3.2 Indicator mineral identifications

The use of indicator minerals in drift exploration has become an increasingly important method over the last several decades (e.g., McClenaghan and Paulen, 2018 and references therein) highlighting the benefit of using indicator minerals as a tracer for glacial dispersal and as such were used for this study. All till samples collected for indicator mineral analysis were shipped to Overburden Drilling Management Limited (ODM), Ottawa for indicator mineral separation and analysis. The < 2.0 mm fraction of each sample was sieve-separated from the bulk ~ 10 kg samples and retained for clast lithology analysis. The remaining < 2.0 mm fraction was processed by ODM following procedures outlined in McClenaghan et al. (2015). The minerals separated during processing were examined by trained personnel using binocular microscopes to identify sulphide minerals, gold grains, platinum group minerals (PGMs), and silicate minerals as well as ODM's suite of magmatic or metamorphosed massive sulphide indicator minerals (MMSIM®, Averill, 2001). A limited number of identified minerals were verified with a scanning electron microscope. Select indicator mineral results are presented as proportional dot maps and have been normalized to a 10 kg (wet) sample weight of the < 2.00 mm fraction. Detailed results of all identified indicator minerals are presented in Supplementary Table T4.2.

4.3.3 Clast lithologies

Clasts identified from subglacial tills have been utilized to determine dispersal patterns in regions across Canada, as they identify dispersal from a single known bedrock source (Klassen and Thompson, 1993; McClenaghan et al., 1996; Trommelen et al., 2013). The > 2.0 mm fraction separated during indicator mineral preparation was washed in a light acid bath and retained for clast lithology analysis (n=72). An average of 700 clasts was recovered from each sample, which was coned and quartered to randomly select 300- 400 clasts for interpretation (average = 384). Clasts were grouped into one of 13 categories (Figure 4.5) using a binary microscope. To simplify the spatial organization of the interpretation, the 13 lithologies were grouped by their larger domains and classified as either RL (metasedimentary, Laporte (leucogranites with pink weathering streaks), leucogranite, and quartzites), GR (felsic intrusive and vein quartz), MR (mafic intrusive, intermediate intrusive, ultramafic, and Mistinibi (multiple lithologies from the Mistinibi unit, including paragneiss, volcano-sedimentary, and gabbro)) or Labrador Trough (LT) (iron formation and metavolcanic). The latter does not outcrop in the

study area, but glacial clasts of that lithology were observed in till near the current study area (Klassen and Thompson, 1993). All clasts that could not be associated with a known bedrock unit were placed under the "other" classification. Results of these classifications are presented as proportional dot maps indicating percentage of clasts within each sample. Detailed results of the clast lithology analysis are presented in Supplementary Table T4.3. Photographic results of clast separation from each sample are presented in Supplementary Figure S4.1.

4.4 **Results**

4.4.1 Till matrix characteristics

Till texture range from sandy-till to siltier, less sandy-till. The sand:silt ratio is somewhat higher over the RL domain (mean ratio: 1.65, σ= 0.61) than over the MR domain (mean ratio: 1.07, σ= 0.37), but till texture from the GR domain overlaps across the full range (Figure 4.6). Till across the study area is clay poor, with clay content having little variation across all bedrock units. The latter is particularly important because clay content variation is known to sometimes control geochemical variation of certain metals, which in this case can produce spatial geochemical patterns that have more to do with grain size distribution than glacial dispersion (Shilts, 1996). Complete grain-size results are presented in Supplementary Table T4.4.

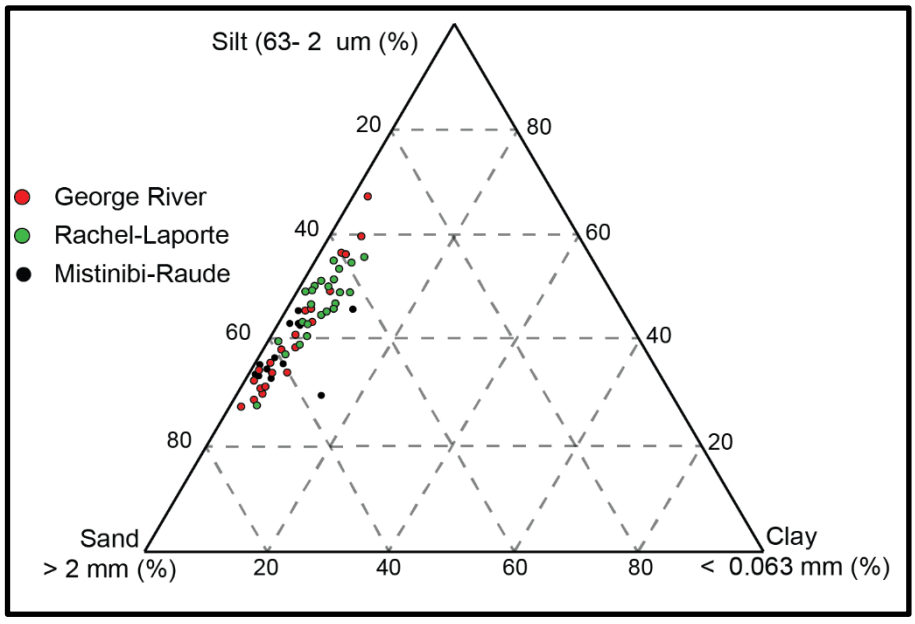

Figure 4.6. Grain size results from each sample categorized based on the underlying major bedrock unit from which they were collected (Figure 4.2).

4.4.2 Till matrix geochemistry

Till matrix geochemistry results indicate the LT signature (Table 4.1; $(Fe_2O_3+MgO)/SiO_2$)) are highest in the southwest corner of the study area, with intermediate values in the centre and northwest parts of the study area, and the lowest values in the eastern half of the study area (Figure 4.7A). Geochemical signature of the RL domain (Table 4.1; Al_2O_3/SiO_2) is highest in the southwest/southcentral portion of the study area, with intermediate values in the northwest and the lowest values in the eastern half of the study area (Figure 4.7B). Geochemical indicators associated with the GR domain (Table 4.1; Ba and Zr+LREE) display a more complex, patchy distribution with less clustering of higher values than the other bedrock domains. Specifically, the distribution of Zr + LREEs (Figure 4.8A) is highest in the northern portion of the study area, over the GR domain, as well as in the northwest part of the study area (Figure 4.8A). Ba (Figure 4.8B) is also generally highest in the northcentral part of the study area (Figure 4.8B). The main geochemical pathfinders of the MR domain (SiO_2) has its highest values clustered within the MR domain (Figures 4.9A). Uranium (U) is the other useful pathfinder for the MR domain, and the highest concentrations of U occur around the sites of known uranium mineralization within the MR domain. However, U is also relatively elevated within the RL domain, especially in the southwest corner of the study area. The sources of U within the RL domain are likely located near the RL/LT contact, close to elevated U measured in lake sediments (Clark and Wares, 2004; Amor et al., 2018), which is southwest of the study area.

4.4.3 Indicator minerals

Indicator minerals associated with the LT (Table 4.1; red rutile and Mn epidote) are highest in the southwest corner of the study area (Figures 4.10A and 4.10B). Red rutile abundance (Figure 4.10A) is also highest in the northwest of the study area, with intermediate values surrounding these regions and a single sample with high abundances in the southern GR domain. Abundance of Mn epidote is highest within the RL domain (Figure 4.10B), but the mineral is observed almost everywhere across the study area, except for a few samples (n=6). Orthopyroxene, the main indicator for the western GR (Table 4.1), has a discontinuous and irregular dispersal pattern similar to the GR geochemical pathfinder pattern (Figure 4.8) with high abundances occurring in the northwest and south-central portions of the study area (Figure 4.11). Intermediate mineral counts generally surround the highest counts, however, with low

values being the most common in the eastern half of the study area and only two sites with no orthopyroxene minerals identified (Figure 4.11). No specific indicator minerals are associated with the RL or MR bedrock domains.

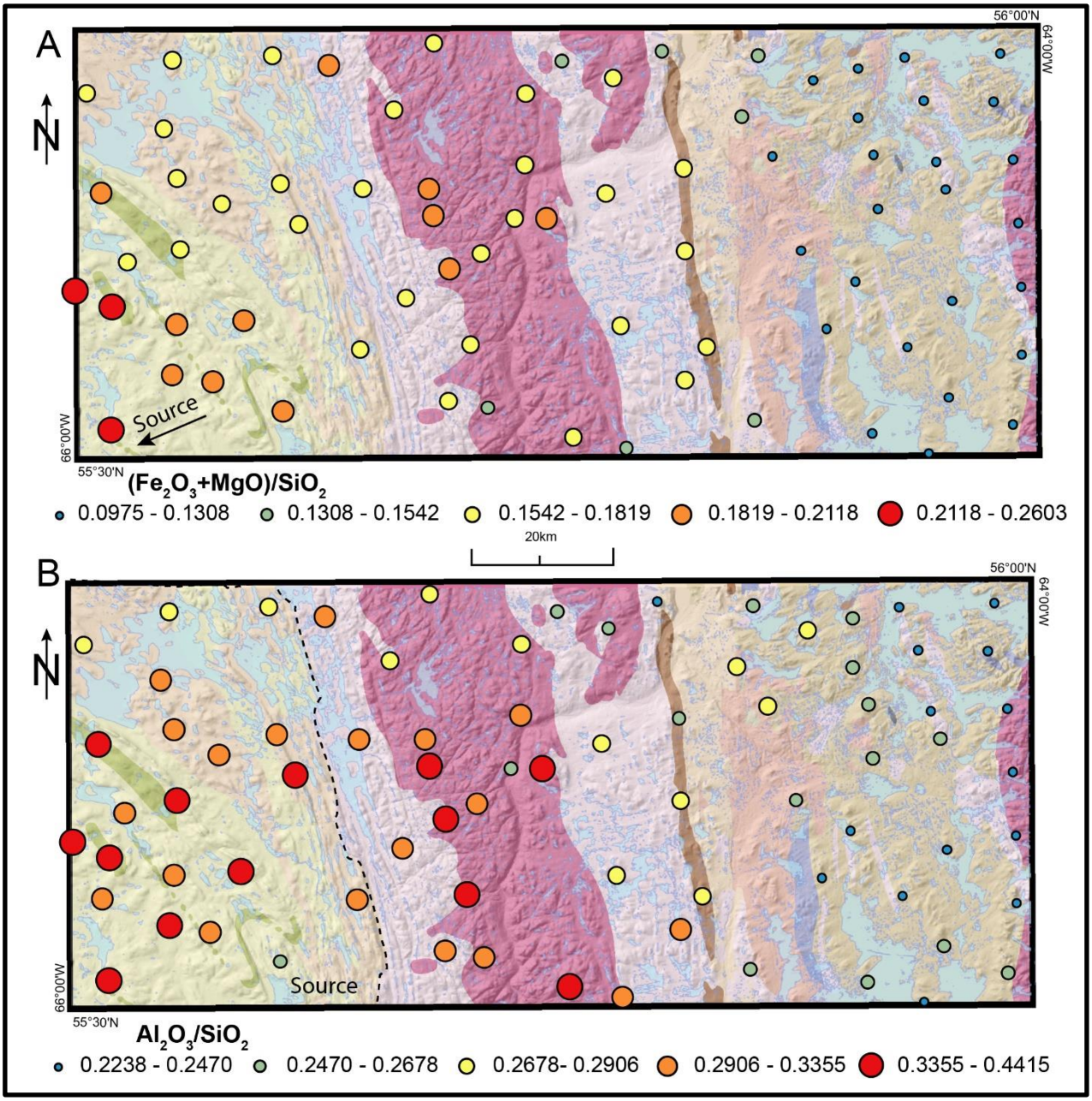

Figure 4.7. **(A)** Proportional dot symbol map showing the ratio of Fe_2O_3+MgO/SiO_2 as representing geochemical dispersal from the Labrador Trough and Doublet mafic volcanic units (southwest of current study area). **(B)** Proportional dot symbol map showing the ratio of Al_2O_3/SiO_2 as representing geochemical dispersal from the RL domain (dotted outline).

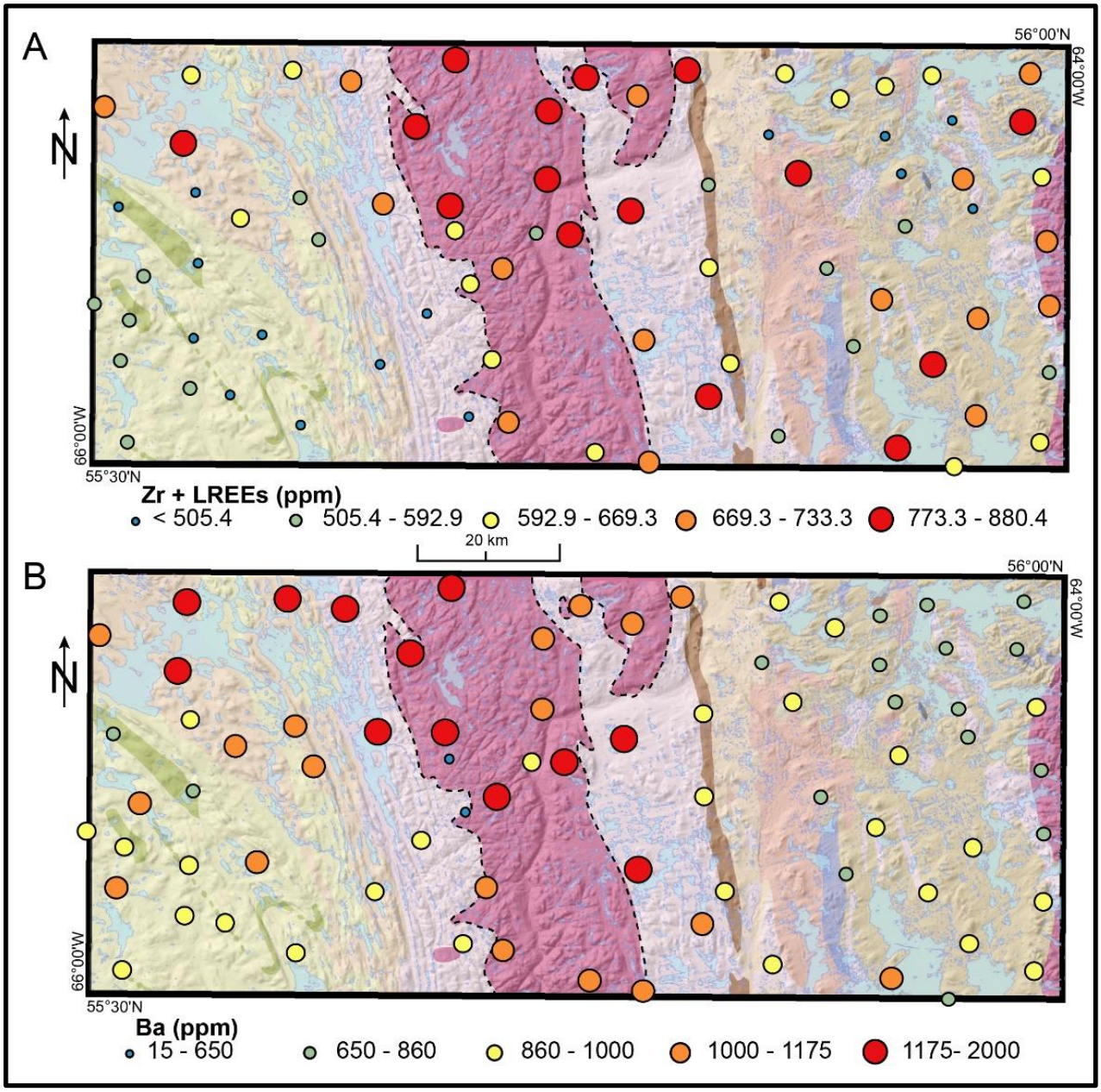

Figure 4.8. **(A)** Proportional dot symbol map showing Zr + LREE (all in ppm) as representing geochemical dispersal from the De Pas Batholith. **(B)** Proportional dot symbol map showing the distribution of Ba (ppm) as an indication of geochemical dispersal from the De Pas Batholith within the GR domain.

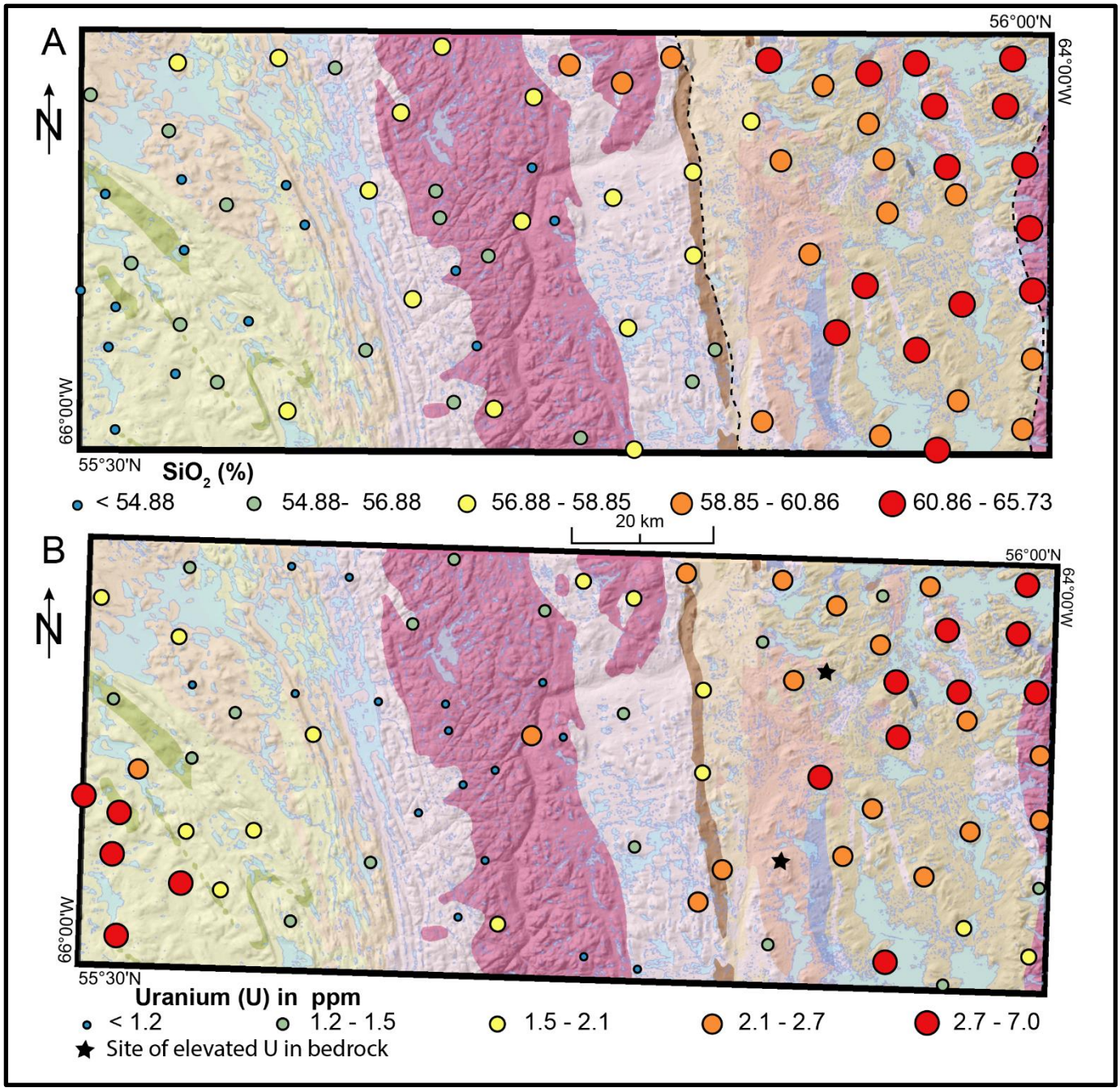

Figure 4.9. **(A)** Proportional dot symbol map showing the abundance of SiO_2 (%) as an indication of geochemical dispersal from the MR domain. **(B)** Proportional dot symbol map showing abundance of U (ppm) as representing geochemical dispersal from the known U mineralization (Collins and Cashin, 2010). An additional source of mineralization has been identified southwest of the study area where lake geochemistry studies have indicated elevated abundances of U at the margin between the RL and LT domains (Clark and Wares, 2004; Amor et al., 2016).

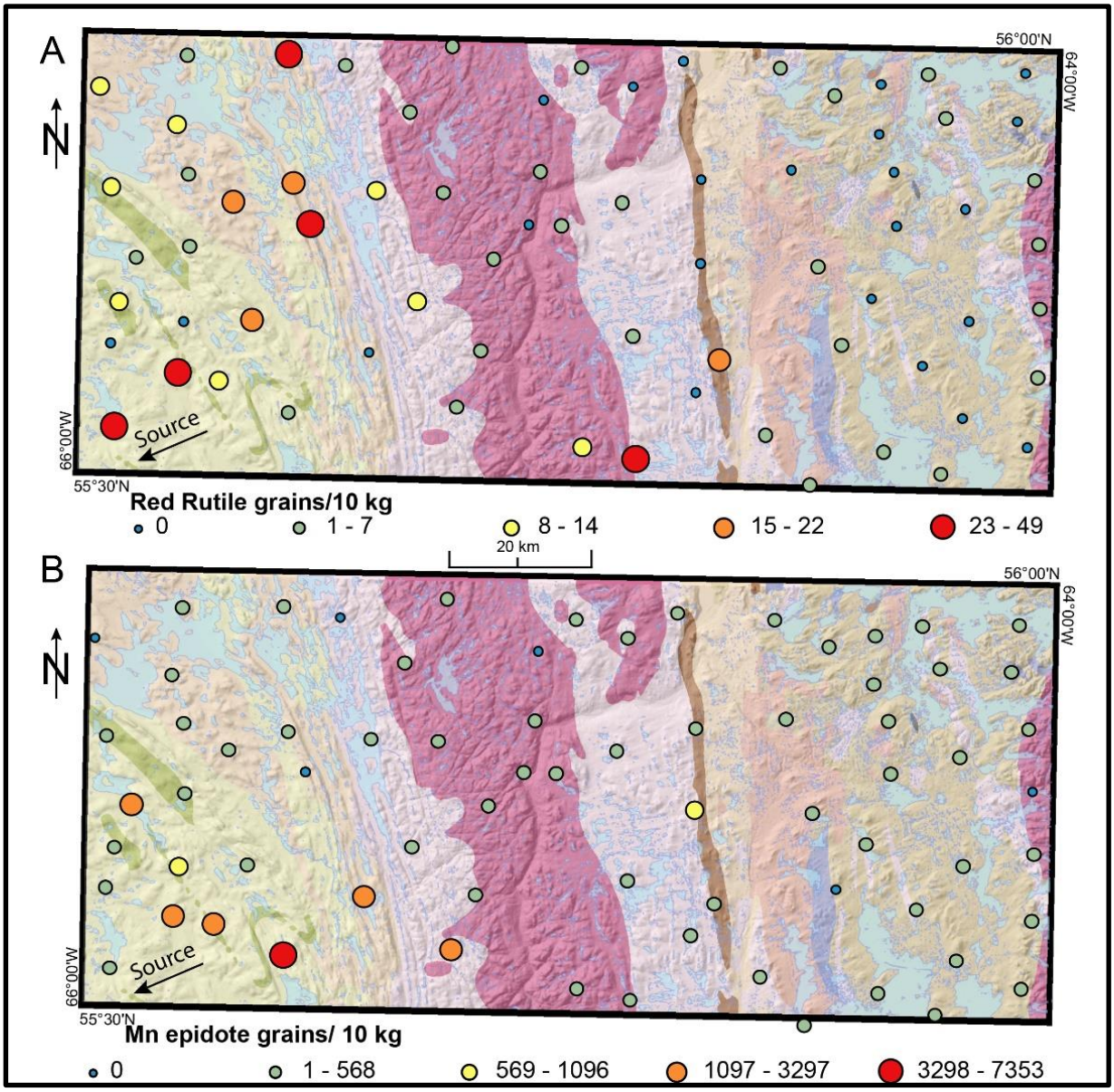

Figure 4.10 **(A)** Proportional dot symbol map showing the abundance of red rutile grains normalized to a 10 kg sample as an indication of dispersal from the LT domain. **(B)** Proportional dot symbol map showing the abundance of Mn-epidote grains per sample normalized to a 10 kg sample as an indication of dispersal from the LT domain.

4.4.4 Clast lithologies

Clasts of metavolcanics and metasedimentary rocks associated to the LT domain are identified in the majority of samples across the study area, although in low abundances up to 120 km from the eastern edge of the bedrock source (Figure 4.12A). The proportion of RL domain clasts is highest in the southern RL domain where the metasedimentary bedrock unit outcrops (Figure 4.12B). Percentages of RL derived clasts are much lower in the northern

quartzofeldspathic gneiss lithologies. Clasts derived from the GR domain (largely felsic intrusive rocks) are found across the study area, but with overall lower percentages in the RL and patches of low percentages within the MR domain (Figure 4.13A). The abundance of MR derived clasts (high-grade metamorphic rocks) is highest within the MR domain (Figure 4.13B), with lower abundances on the western half of the study area. Exotic clasts were identified across the study area, which suggests transport from regions well outside of the study area, or from a bedrock unit not identified during regional bedrock mapping. High percentages of GR clasts in the north of the RL domain suggests northwest dispersal from the upland region of the De Pas batholith, however, recent detailed bedrock mapping indicated that the quartzofeldspathic gneiss and De Pas Batholith were visually indistinguishable (Corrigan et al., 2018) meaning that some of the clasts identified as GR clasts could be sourced from the RL domain.

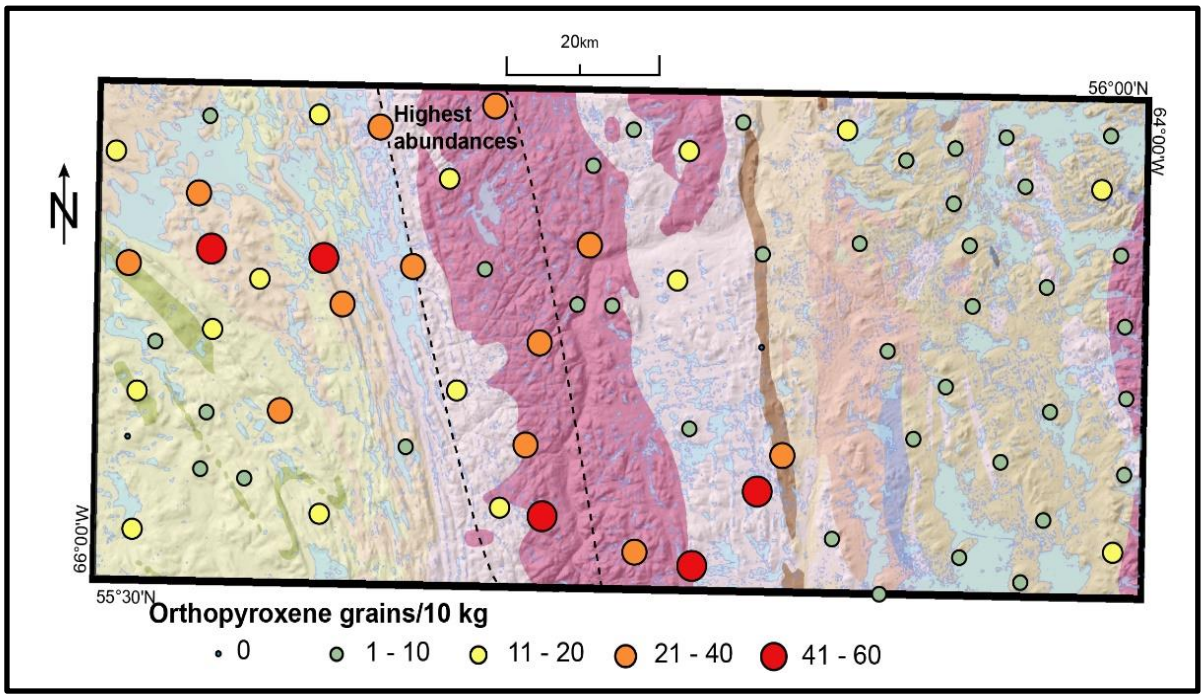

Figure 4.11. Proportional dot symbol map showing the ratio of Orthopyroxene grains across the study area normalized to a 10 kg sample likely to occur in the highest abundances on the western half of the De Pas Batholith (Sanborn-Barrie, 2016).

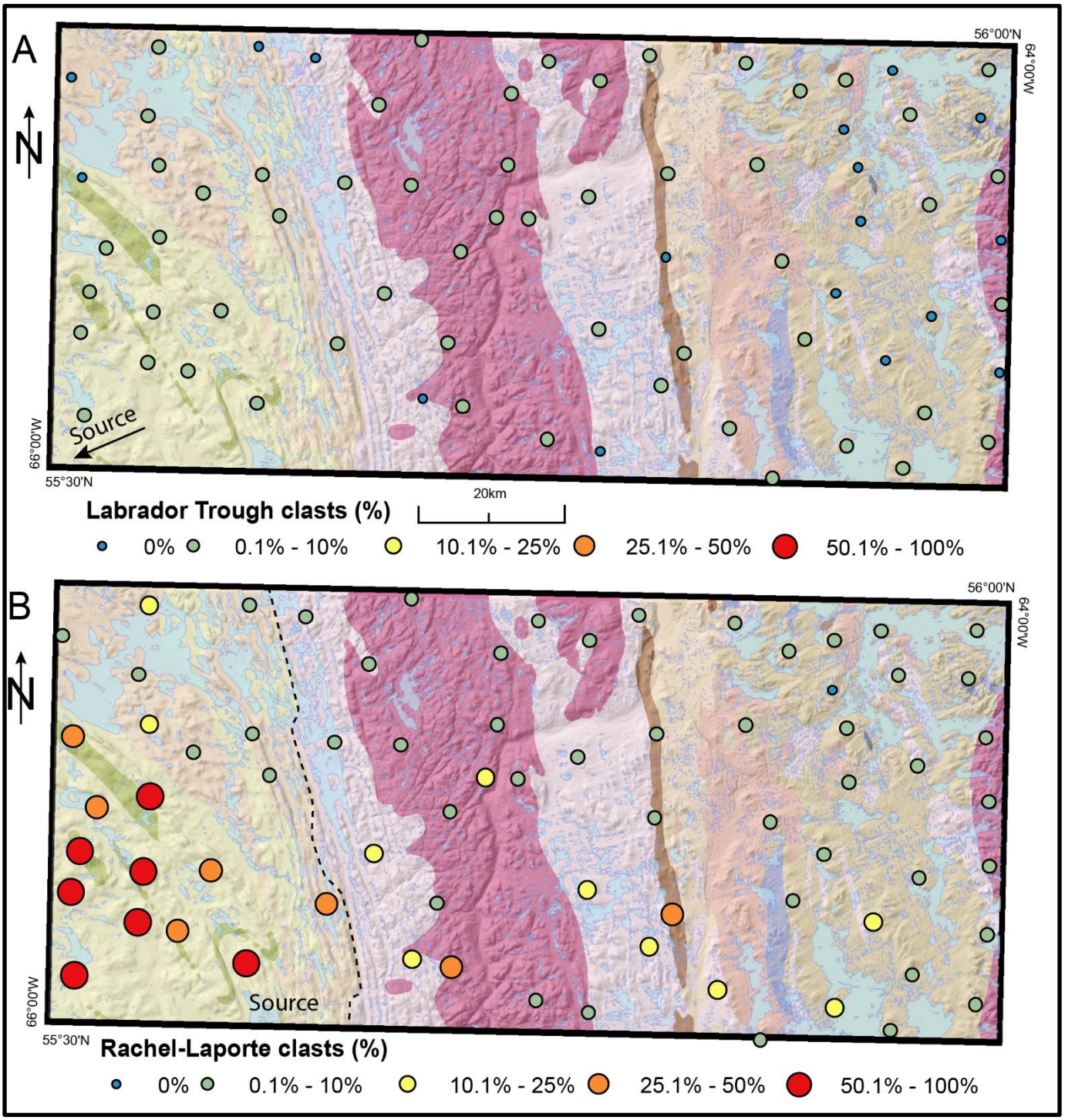

Figure 4.12. **(A)** Proportional dot symbol map showing the percentage of LT clasts from all clasts identified within each sample. **(B)** Proportional dot symbol map showing the percentage of RL clasts from all clasts identified within each sample (source is indicated by the dotted line).

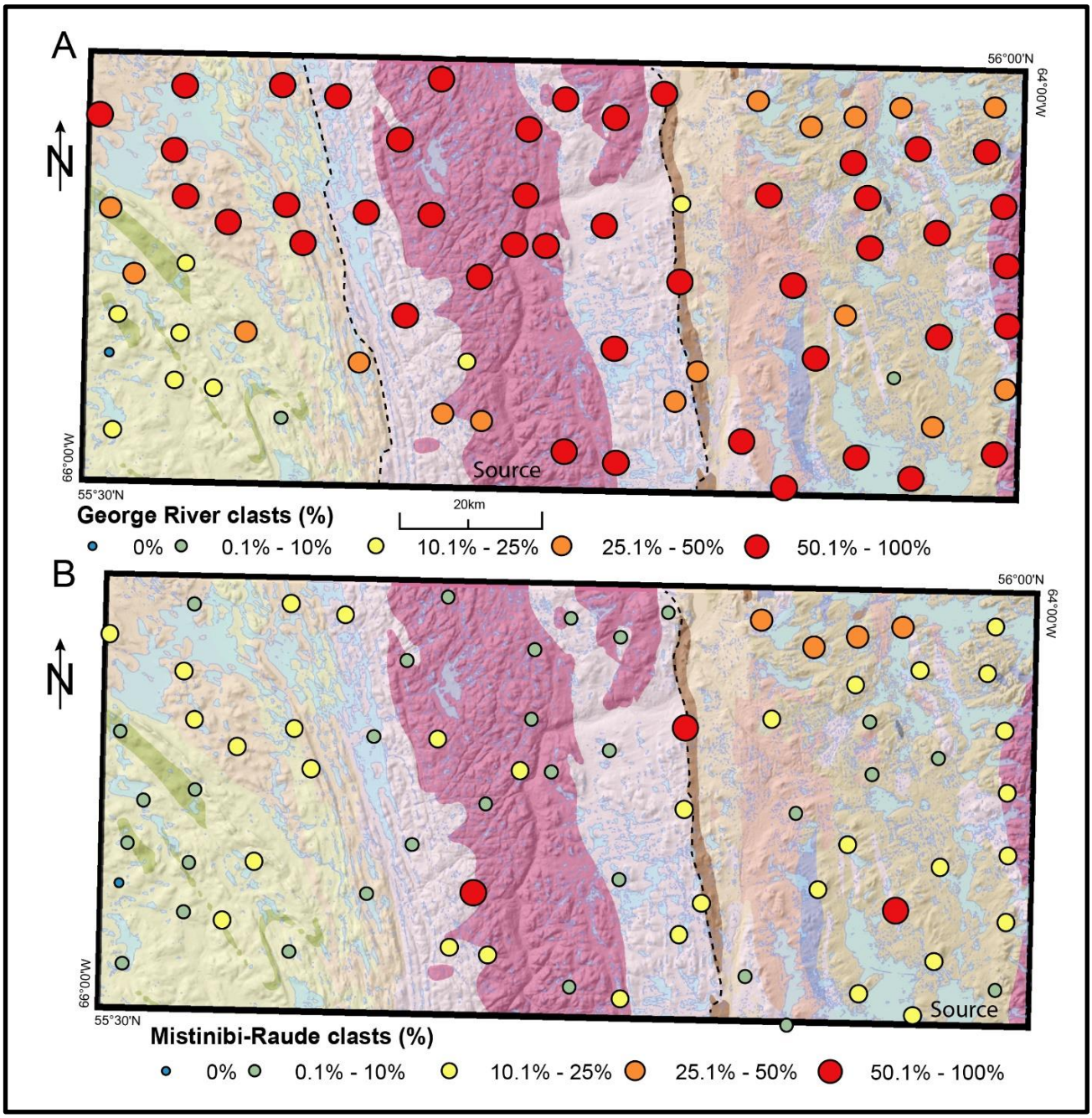

Figure 4.13. **(A)** Proportional dot symbol map showing the percentage of GR clasts from all clasts identified within each sample (source is indicated by the dotted line). **(B)** Proportional dot symbol map showing the percentage of MR clasts from all clasts identified within each sample (source is indicated by the dotted line).

4.5 Interpretation and discussion

The patterns described above are the result of the net evolution of glacial clastic dispersal in the study area; they thus provide important insights into past glacial erosion, entrainment, and deposition. In this section, the results of this thesis are analyze and interpreted within the context of the most recent reconstructions of regional ice-flow phases and associated subglacial dynamics (Chapter 2 and Chapter 3).

4.5.1 Dispersal patterns and ice flow history

Indicators associated to the LT (Table 4.1) are all higher in the southwest corner of the study area with decreasing abundance to the north and east across the study area (Figures 4.7A, 4.10A, and 4.10B). LT derived clasts are observed across the study area, although not at high abundances (Figure 4.12A). Given the LT bedrock domain is located 70 km outside the study area to the southwest, these patterns are interpreted as recording primarily the sedimentary clastic dispersal by regional northeast-trending Flow 1 (Klassen and Thompson, 1993; Veillette et al., 1999; Chapter 2). The landscape analysis revealed that the eastern portion of the study area (GTZ1) has the best-preserved geomorphological evidence of Flow 1 (with minimal overprinting by other ice-flow phases) and northeast trending dispersal patterns extend into GTZ1, especially Mn-epidote (Figure 4.10B). This is interesting because GTZ1 is separated from the LT source by at least one inferred low glacial erosion zone (GTZ4), as well as GTZ3, which has a stronger landform overprint related to younger ice-flow phases and only have a few outcrop-scale ice-flow indicators associated with Flow 1 (Figure 4.3). It was thus unclear whether till in GTZ1 would have distal debris from beyond GTZ4 and as far up-ice to the southwest as the LT domain. This shows that despite limited glacial erosion over the central highlands (GTZ4), subglacial and/or basal (englacial debris) were transported to the northeast across GTZ4 and into GTZ1. The till compositional data also clearly show that over the RL domain (GTZ5), the till has a relatively strong LT provenance indicative of northeast dispersal transport. The till in GTZ5 thus have a relatively high inheritance from the Flow 1 phase; this was not possible to decipher based on the landform analysis alone (Chapter 3). Overall, LT and RL clasts and LT and RL associated major oxides are more reliable indicators of northeast transport across the study area than trace elements. This may be due to trace elements (e.g., U) being more rapidly diluted in the down-ice

direction. That is to say, trace elements generated shorter recognizable dispersal patterns than lithological clasts and major oxides.

The question is how to reconcile the landscape interpretation of limited erosion across GTZ4 (Chapter 3) with the seemingly uninterrupted regional northeast, and perhaps later eastward re-entrainment, dispersal of LT and RL indicators across the study area? According to the landscape analysis, basal ice velocity and overall erosion were reduced across GTZ4 relative to GTZ1. Based on these findings, it would be expected that quarrying was reduced or suppressed across the uplands of GTZ4 (e.g., Iverson, 2012), due to lower sliding velocities (Alley et al., 2019; Cook et al., 2020), which would have limited excavation of bedrock in that region. The low lake density in that area (Chapter 3) support this hypothesis of reduced quarrying over GTZ4. However, Figure 4.13A shows that GR clasts are quite abundant and even dominant in till across most of the study area. Clearly, quarrying happened over at least parts of the GR domain during one or more ice-flow phases, probably along the edges of GTZ4 and adjacent portions of the other GTZs that partly overlie the GR domain (Figure 4.3). Nonetheless, LT and RL debris were transported northeast during Flow 1, across GTZ4, either englacial, or subglacially with minimal erosion. This may explain the relatively strong LT and RL footprint in till across the GR upland (i.e., limited dilution in the dispersal area). Interestingly, the LT and RL footprint decrease sharply over GTZ1. The latter extends further down-ice (Flow 1) relative to GTZ4 and RL sources, but GTZ1 has a much stronger subglacial erosional footprint. Indeed, *roches-moutonnées* and crag-and-tail landforms (i.e., evidence of glacial quarrying) related to Flow 1 are relatively abundant across GTZ1 (Rice et al., 2017a, 2017b). The effect of bedrock hardness and how it can limit the development of a strong erosional imprint is important. Hard bedrock reduces local erosion, which reduces basal sediment concentrations, which can further reduce abrasion (e.g., Alley et al., 2019). This would also explain the higher ^{10}Be inheritance over the uplands. However, GTZ4 also contains the highest abundance of ML cells, indicative of overall lower ice/bed mobility. Taken together, these results suggest the central upland was characterized by polythermal conditions with sufficient ice/bed mobility to allow subglacial and/or basal (englacial) debris to be entrained and discontinuously deposited over and beyond the highlands. Subglacial conditions were thus clearly different between GTZ1 and GTZ4 during the regional northeast ice-flow phase, and the landscape analysis suggests that more locally derived till was likely produced across GTZ1 due to high erosion. This could explain the sharp

decrease in LT and RL indicators across the GTZ4 and GTZ1 boundary, as well as the relatively strong relationship between MR domain indicators (Figure 4.8) and GTZ1. Nonetheless, the results show that widespread northeast till dispersion occurred during Flow 1 phase across most of the study area.

However, clasts from the central GR not only were dispersed to the northeast, they were also clearly dispersed to the northwest, across GTZ2 during Flow 2 (Figure 4.12A). Additionally, the MR domain is located in the eastern portion of the study area (Figure 4.12B) and data show that MR clasts were dispersed toward the west and northwest (Figure 4.12B). Indicators for these two domains include orthopyroxene, Zr+ LREEs and Ba (GR domain) which all show northwest dispersal into GTZ2 (Figures 4.8 and 4.9). The occurrence of red rutile grains within GTZ2 could be inheritance from regional Flow 1, either because Flow 1 extended across GTZ2, or because Flow 2's northwest ice flow re-entrained red rutile from the other adjacent GTZs due to a larger catchment zone than what the landform record suggests, or a combination of both. In any case, the occurrence of MR indicators within GTZ2 is evidence of western and/or northwestern sediment transport across a more extensive portion of the study area than just GTZ2. However, it is important to highlight that northwest ice-flow indicators have only been identified within the boundary of GTZ2, well outside the MR domain. There are several plausible explanations for this discrepancy. One is that MR clasts west of the MR were transported by an older ice-flow phase that is not preserved in the landform record, much like the Omar clasts sourced in southeastern Hudson Bay and found across the western Canadian prairies to the west (Prest et al., 2000). In this scenario, the occurrence of MR within GTZ2 would thus be inherited from a previous glaciation. Another explanation is that the catchment of Flow 2 extended further up-ice and into the MR domain without forming a recognizable landform footprint beyond GTZ2. A third possibility is that the MR clasts identified in the west of the study area are from unidentified lithologies, as the MR classification was broad and included mafic and ultramafic units that may occur as small bands within other larger lithological domains (i.e., the high concentration of MR clast in the middle of the De Pas Batholith). Finally, it is possible that during the last ice-flow phase (Flow 4) some MR clasts were dispersed to the west/southwest.

Northwest transport (Flow 2) of LT erratics were also reported by Klassen and Thompson (1993) from samples collected southwest of the current study area (Figure 4.1). Additionally, the Martin Lake Rhyolite located southwest of the study area and Nepheline Syenite located west of

the study area both show clear evidence of northwest transport (Klassen and Thompson, 1993; Figure 4.1). Klassen and Thompson (1993) associated the northwest dispersal of this material with the UBIS, which indicates GTZ2 likely would extend some distance to the west and southwest of the study area.

The subglacial streamlined landscape associated to Flow 3 is not particularly strong in the study area. Nonetheless, the overall dispersal patterns of LT clasts, orthopyroxene, red rutile, Mn-epidote, Ba, Zr+ LREEs, and pathfinder ratios associated with the RL domain (Al_2O_3/SiO_2) are perhaps best explained when considering both Flow 1 and Flow 3. Specifically, GTZ3 is associated with Flow 1 but is heavily overprinted by Flow 3. This crosscutting flowset landscape is restricted to a small region between the two main river valleys (Figure 4.3), even though the regional landform record shows that Flow 3 extended well outside of GTZ3. A close look at dispersal patterns within and around GTZ3 shows a greater influence of Flow 3 on the dispersal patterns within the study area. The most predominant example of this dispersal pattern is the dispersal of orthopyroxene grains across the southern GR domain (Figure 4.10). Despite limited data, the length of orthopyroxene dispersion from the GR is more extensive across GTZ3, where Flow 3 indicators are more abundant than outside of it. The dispersal of RL clasts also crosses multiple other GTZs (Figure 4.3) with intermediate values more common in the southern half of the study area (i.e., in GTZ3; Figure 4.12B). It is thus likely that Flow 3 reworked and re-entrained material that was first dispersed to the northeast during Flow 1 and "fanned" these dispersal patterns more to the east. However, these results suggest subglacial erosional and entrainment processes were reduced during the Flow 3 phase relative to previous phases. This is consistent with the glacial reconstruction that associate the more dynamic subglacial processes with Flow 1 and Flow 2 (Chapter 3) and a thinning of the ice sheet and less dynamic ice during Flow 3, which is also when most of the eskers crosscutting the older glacial landforms were formed. GTZ3b occurs at the onset of the Flow 3 flowset and, given that its source is within the same bedrock domain as GTZ1, dispersal is difficult to assess. However, there does appear to be a stronger northeast dispersal of U in the till matrix geochemistry to the northeast in GTZ3b, suggesting higher subglacial dynamics continued to disperse material to the northeast even after the more wide-spread Flow 1 dispersal.

Flow 4 (southwest) occurred as a late-deglacial resurgence likely from a highly fragmented ice cap (Chapter 2). This flow was topographically controlled, with no correlated

landforms and only a few striations that are limited to the western part of the study area (Figure 4.3). There are no clear dispersal patterns associated with this ice-flow phase, it is possible that some of the MR and GR clasts within the RL domain were transported during this late stage flow, but the lower abundances, in comparison to the other dispersal patterns, suggests the dispersal was not as pervasive.

4.5.2 Implications for glacial evolution

The dispersal patterns identified through the analysis of clast lithologies, indicator minerals, and till matrix geochemistry are broadly consistent with the reconstruction of glacial dynamics based on the geomorphological record and other, more limited, proxies (e.g., ^{10}Be data; Chapter 3). However, the analysis of till compositional data brings important additional insights into subglacial erosion and sediment entrainment/deposition processes across the region. Firstly, relatively long-distance northeast transport from the LT and the RL domains took place across the entire study area, during Flow 1, something that was previously undocumented (Figure 4.1). Specifically, previous work had documented rare occurrences of LT clasts in the surrounding region (Klassen and Thompson, 1993; Figure 4.1). Now it is clear that LT and RL debris were entrained across the study area, even in the central upland, where the landscape evidence shows limited glacial erosion, as well as further down-ice to the northeast (GTZ1). This confirms that Flow 1 was a widespread warm-based ice-flow phase that affected a large region. Nevertheless, subglacial erosion of the central upland (GTZ4) must have been limited during the last glaciation despite some basal and/or englacial sediment entrainment from more distal sources (LT and RL). The stronger erosion down-ice of the uplands (GTZ1) probably explains the more abrupt decline (by dilution) of LT and RL indicators in that area. The most reliable indicator of transportation from the MR domain across the central upland lies with the dispersal of MR clasts. However, the classification scheme used may have oversimplified the lithological units, constraining certain lithologies solely to the MR, even though they likely exist in other granitic lithologies to a lesser degree (i.e., intermediate intrusive and mafic intrusive clasts). These clast lithology classifications, in conjunction with limited geochemical tracers and lack of commonly associated indicator minerals, makes the assessment of dispersal from this unit difficult. The best dispersal indicators from the MR domain are elevated concentrations of U (black stars (Figure 4.9B)) and generally higher concentrations of SiO_2 in MR lithologies. Both U and SiO_2 lack a identifiable

westward dispersal pattern, but do display northeastern dispersal near the top of the study area within GTZ3b. This coupled with a lack of ice-flow indicators associated to a westward or northwestward phase over the MR domain, suggests erosion associated to a possible northwest Flow 2 phase in this region was limited if not non-existent in the MR domain.

The dispersal patterns of GR domain indicators also show that subglacial erosion took place in the central portion of the study area, perhaps more than the geomorphological record would suggest. However, most indicators may be sourced from near the onset zone of the surrounding flowsets on the edges of the GR domain, rather than its centres (i.e., centre of GTZ4). This could be the result of higher degrees of quarrying along sub-vertical fractures along the shear zones that mark the boundaries of the GR domain (e.g., Iverson, 2012; Alley et al., 2019) that allowed for more quarrying and dispersal from the edges of the domain, with more abrasive erosion in the middle of the GR (Chapter 3). In any case, the dispersal patterns associated to the GR domain are consistent with the classification of the central region (GTZ4) as a region of transitional subglacial conditions (i.e., predominantly MH and ML; Chapter 3), rather than Low (cold-based) end member type zone (e.g., Tremblay, 2017).

In some regions, there are relatively sharp boundaries between certain till compositional assemblages and remnant fragments of glacial beds or GTZs (e.g., Ross et al., 2009). That is to be expected when a GTZ is preserved following complete suppression of subglacial erosion and till production over that GTZ. The till can still have a hybrid signature, but one that only reflects ice-flow phases up to the point of GTZ preservation. In other regions, GTZs can have hybrid tills with variable degrees of inheritance and overprinting by subsequent ice-flow phases (e.g., Trommelen et al., 2013). In this study area, the GTZ boundaries are somewhat diffuse and the till dispersal patterns do not have sharp boundaries. The overall record (i.e., geomorphological and sedimentological records) are interpreted to reflect a complex sequence of ice-flow events that is summarized below and on Figure 4.14.

The geomorphological and till dispersal patterns associated to Flow 1 (to the northeast) are considered to form the oldest preserved glacial record in the study area. They provide evidence for a laterally extensive warm-based northeast trending ice-flow phase across the region (Figure 4.14). There is also clear sediment dispersion associated with Flow 2 (to the northwest) in the northwest portion of the study area (GTZ2) and this is associated to the development of the UBIS (Clark et al., 2000; Jansson et al., 2003; Chapter 2). The catchment appears to have

propagated far enough into the centre of the study area to erode at least the edges of the western GR domain as it clearly eroded and entrained GR indicators to the northwest into GTZ2. During that time, a switch from warm-based to cold-based conditions developed over GTZ1, which prevented overprinting of the Flow 1 geomorphological record and is associated this shift to the development of an ice divide over GTZ1 (Figure 4.14). Jansson et al. (2003) have proposed that the catchment zone of the UBIS was unstable, and its position shifted west at some point during its evolution. The westward shift of the catchment is thought to have forced the ice divide over GTZ1 to shift westward. The westward shift of the ice divide would explain the change in subglacial thermal regime over GTZ2 and the excellent preservation of the Flow 2 record. A third phase of ice flow (Flow 3) developed around this time, with ice flowing to the east. It is unclear how much of this Flow 3 phase contributed to dispersal patterns across GTZ1, GTZ3, and GTZ4. However, some patterns do appear to be more strongly aligned in an eastward direction where the geomorphological record associated to Flow 3 (GTZ3) is better developed. This could indicate more discrete (linear) erosion during that phase than during early ice-flow phases. No evidence of palaeo-ice streaming associated to Flow 3 has been identified within the study area; however, this phase is associated to palaeo-ice streaming identified just outside the study area. A number of palaeo-ice streams were operating during early stages of the LIS deglaciation, such as the Kogaluk River ice stream (Margold et al., 2015), located just 20 km north of the study area. Specifically, the Strange Lake dispersal train, which is characterized by a 50 km down-ice ribbon dispersal of REEs and associated indicator minerals, represents dispersal from the Kogaluk River ice stream (McConnell and Batterson, 1987; Batterson and Liverman, 2001; McClenaghan et al., 2019). GTZ3b also shows some evidence of northeast dispersal (Figure 4.9), and given the strong linear dispersal associated with the Strange Lake dispersal train (Figure 4.1), GTZ3b likely transported material a considerable distance outside the study area. Dispersal trains associated to Flow 3 within the study area are not expected to be as long, but the discontinuous geomorphological footprint of Flow 3 phase (e.g., GTZ3) suggests some re-entrainment in an eastward direction most likely took place. The last ice-flow phase (Flow 4) may have also contributed to the final shape of dispersal patterns, however, its impact was likely minimal. The ice sheet was probably very thin if not fragmented into multiple smaller ice caps (Clark et al., 2000; Chapter 2) during the late stage ice-flow phase and would thus not have had the erosional power to erode and entrain much till. This overall integrated reconstruction

indicates that the ice sheet in the region experienced more widespread warm-based conditions at an earlier stage of the glaciation and gradually shifted to more polythermal conditions with discrete (linear) subglacial dynamics (palaeo-ice stream catchment during Flow 2 and Flow 3). These findings provide useful constraints for future ice sheet and sediment transport modelling, as well as new knowledge regarding till provenance for drift prospecting applications.

Given the deglacial ages reported with the study area (~8.0 ka; Chapter 2) and ages reported by Dubé-Loubert et al. (2018) on the timing of the catastrophic draining of glacial Lake Naskaupi (8.2 ka), the glacial dynamics of the region changed rapidly following Flow 2 (11.5 ka-Figure 14.1B). Ullman et al. (2016) reported similar findings of a rapidly retreating ice margin following the Younger Dryas (~8 ka) with the entire QLD disappearing around 6.7 ka. These ages also correlate relatively with relative sea-level curves that indicate Ungava Bay was ice-free at 7.6 ± 0.2 ka (Clark and Fitzhugh, 1990). If Flow 2 did occur at the same time as Margold et al. (2018)'s palaeo-ice stream #17 at 11.5 ka, it would mean the entire ice mass disappeared in less than 4 ka, indicating relatively rapid switch in ice sheet dynamics led to the catastrophic collapse of the QLD, during which time subglacial conditions were cold-based (period between Flow 1 and Flow 2) with patchy mosaics of warm-based regions influenced by nearby palaeo-ice streams. These findings largely agree with Clark et al. (2000) who attributed the destabilization of the LIS to palaeo-ice streaming and mass loss of the ice sheet through Hudson Strait, presumably fed by streaming ice from Ungava Bay.

4.6 **Conclusions**

Till sediment sample collection and analysis of glacially transported clasts, indicator minerals, and till matrix geochemistry were used to identify the provenance of glacial sediments for a region that experienced a complex glacial history in northeastern Quebec (see Chapter 1 and Chapter 2) in order to gain insights into the regional glacial dynamics and their evolution in a core region of the LIS. Through this research, evidence from the sediment record and provenance analysis for widespread, relatively uniform, warm-based conditions and subglacial dynamics associated to an early northeast ice-flow phase (Flow 1) were identified. These results also support previously proposed westward shifts of the Ungava Bay catchment zone and which

is supported by further evidence of an associated westward ice divide migration, resulting in ice flow reversal.

The net effect of this complex evolution within a core region of the LIS is recorded in till compositional patterns in the form of amoeboid shaped dispersal patterns centred over the central uplands, which clearly overprinted the more laterally extensive northeast-trending dispersal patterns associated with Flow 1. Increasing evidence suggests that this core region of the LIS experienced widespread warm-based conditions and laterally uniform northeast ice flow during an early phase of glaciation. Following this ice-flow phase a more complex polythermal subglacial organization developed and were influenced by nearby palaeo-ice streams, which created patches of highly dynamic subglacial conditions that migrated in relation to changing ice sheet dynamics. Outside of these dynamic patches, subglacial conditions were sluggish. These sluggish conditions also migrated with changing ice-flow phases and preserved older ice-flow landscapes. This ultimately created a mosaic of GTZs that record multiple ice-flow phases that experienced polythermal subglacial conditions throughout glaciation.

5 Chapter 5: Discussion

This chapter highlights the importance of using a multi-proxy analysis for a more holistic understanding of ice sheet evolution within inner-ice sheet regions and highlights specific insights gained using each analytical method. Therefore, a novel aspect of the thesis is the way results from multiple methods (e.g., field observations, surficial mapping, remote sensing analysis, sediment compositional data analysis, cosmogenic isotope analysis, and luminescence dating), were combined to analyze a single glaciated region. Overall, this research has improved the understanding of how an inner-region of the LIS, and more specifically the Q-L sector, evolved throughout glaciation.

5.1 Key findings

The aim of this research project was to resolve discrepancies between regional ice-flow reconstructions and their inferred subglacial conditions, discrepancies between existing surficial maps, and apparent discrepancies between numerical ice sheet models and observation from within inner-ice sheet regions of the LIS (*see* Chapter 1). Furthermore, these results were evaluated with an updated understanding of the influence of ice streams on the position of ice divides and overall ice sheet dynamics. The cumulative effect of ice divide migration and subsequent polythermal subglacial conditions on the dispersal of glacial sediments was also investigated. The integrated findings are summarized below and the new contributions to knowledge (advances, new knowledge, and improvements over previous reconstructions) are detailed in section 5.2.

This research adds several new observations and constraints to the regional glaciological understanding, which lead to several improvements of previous glacial reconstructions and the overall understanding of the evolution of an inner-ice sheet region of the Q-L sector of the LIS:

- Evidence of four ice-flow phases is documented and placed within a relative ice-flow chronology. The oldest phase was to the northeast (Flow 1), followed by a more spatially restricted flow to the northwest (Flow 2), which appears to have only affected the northwest part of the study area. Flow 2 is related to ice streaming events in Ungava Bay. This was followed by an ice divide migration westward across the study area and a subsequent, or time-transgressive eastward ice-flow phase (Flow 3). Finally, a minor late-

deglacial ice-flow phase (Flow 4) that was largely topographically controlled, is recognized. This is the youngest ice-flow phase identified in the study area.

- Broad warm-based conditions are associated with Flow 1 due to the relatively strong subglacial landform imprint associated with that flow. However, these warm-based conditions switched following Flow 1 to more sluggish conditions, with warm-based regions spatially restricted to regions influenced by ice streaming events. These broad-warm-based conditions must not have extended north of the study area, where evidence of sustained cold-based conditions is evident (Dubé-Loubert et al., 2018).
- The cumulative results of this complex ice-flow history and associated subglacial evolution are also reflected in dispersal patterns identified across the study area. Dispersal was most pervasive during Flow 1 as recorded by the widespread distribution of material derived from the LT. It is now established that the regional dispersal train of LT material extends across and beyond the central upland region, which brings important information regarding glacial processes, especially over the uplands. The sediment record clearly indicates that basal and/or englacial sediment transport occurred across the entire study area including the central uplands, which has otherwise low subglacial dynamic indicators. Subsequent ice-flow phases re-entrained subglacial sediments creating palimpsest dispersal patterns across the study area. Some patterns are fan-shaped, reflecting ice flows in a limited range of directions (e.g., northeast and east), whereas others are amoeboid-shapes, reflecting dispersal radiating out of the centre of the study area.
- Taken together, the results indicate a complex mosaic of GTZs that record multiple ice-flow phases that experienced polythermal subglacial conditions and resulted in the partial preservation of relict ice-flow landscapes. These conditions allowed for an assessment of early ice-flow conditions and provide a more complete understanding of how inner-ice sheet regions evolved throughout glaciations.

5.2 Glacial dynamics relating to ice-flow phases

This section places the established ice-flow chronology of the study area into the regional context of the Q-L sector, presents possible timing of the four ice-flow phases, and the subglacial evolution throughout each ice-flow phase.

5.2.1 Flow 1

Four ice-flow phases were identified from outcrop-scale and landform-scale ice-flow indicators. The earliest ice-flow phase was to the northeast (Flow 1) and is believed to have influenced the majority of central Quebec and Labrador (Figure 5.1A). A similar northeast flow has been identified as the oldest ice-flow phase in multiple other regions within Quebec and Labrador (Klassen and Thompson, 1993; Veillette et al., 1999; Figure 5.1B). Prior to this study, it was unclear or unknown whether this flow phase was recorded in the study area, especially over the central uplands where sustained cold-based terrains have been documented further to the north (Dubé-Loubert et al., 2017). Now, it is clear that this old northeast ice-flow phase was also extensive within the study area. Subglacial conditions were likely broadly warm-based, as GIS investigations indicated dynamic ice/bed mobility over 47.7% of GTZ1, which was formed during Flow 1. There was limited (if any) overprinting by younger ice-flow phases over GTZ1 (Figure 5.1C). Additionally, multiple geochemical, mineral, and clast dispersal patterns into GTZ1 suggest significant (> 100 km) northeast transport, providing further evidence of widespread warm-based subglacial conditions, which would be required for widespread erosion and dispersal (Figure 5.1D). Overall, these findings agree with portions of all of the previous research in the area. Klassen and Thompson (1993) and Veillette et al. (1999) suggested there were widespread warm-based conditions associated with the earliest ice-flow phase, however, Veillette et al. (1999) attributed this phase to an older glaciation citing ferromanganese staining on the Flow 1 surfaces as evidence of an interglacial weathering varnish. No such weathering surfaces were identified in this study. This could be due to the fact that the ferromanganese stained bedrock outcrops reported by Veillette et al. (1999) are all from low elevation sites, whereas the striation sites in this study are largely from upland clearings (for helicopter access and more regional flow measurements that minimize topographical effects in valleys). It is worth noting here that oxidation on bedrock surfaces at low elevations may be recent and caused by seepage of surrounding wet moss and soils during the summer. The CIA results in this study

indicate the surface till that was collected across the study area lacks a weathering signature, and ^{10}Be abundances from bedrock and till samples have very limited exposure inheritance from the previous interglacial. Subsequent erosion (e.g., Flow 2 or Flow 3) could have removed weathered till and cosmogenic inheritance; however, it is important to note that GTZ1 is defined by Flow 1 features lacking overprinting by Flow 3 indicators. In this context, higher weathering and exposure inheritance would be expected from such a 'relict' landscape. Overall, and while recognizing some uncertainties, the results from this research support assigning Flow 1 to the last glaciation.

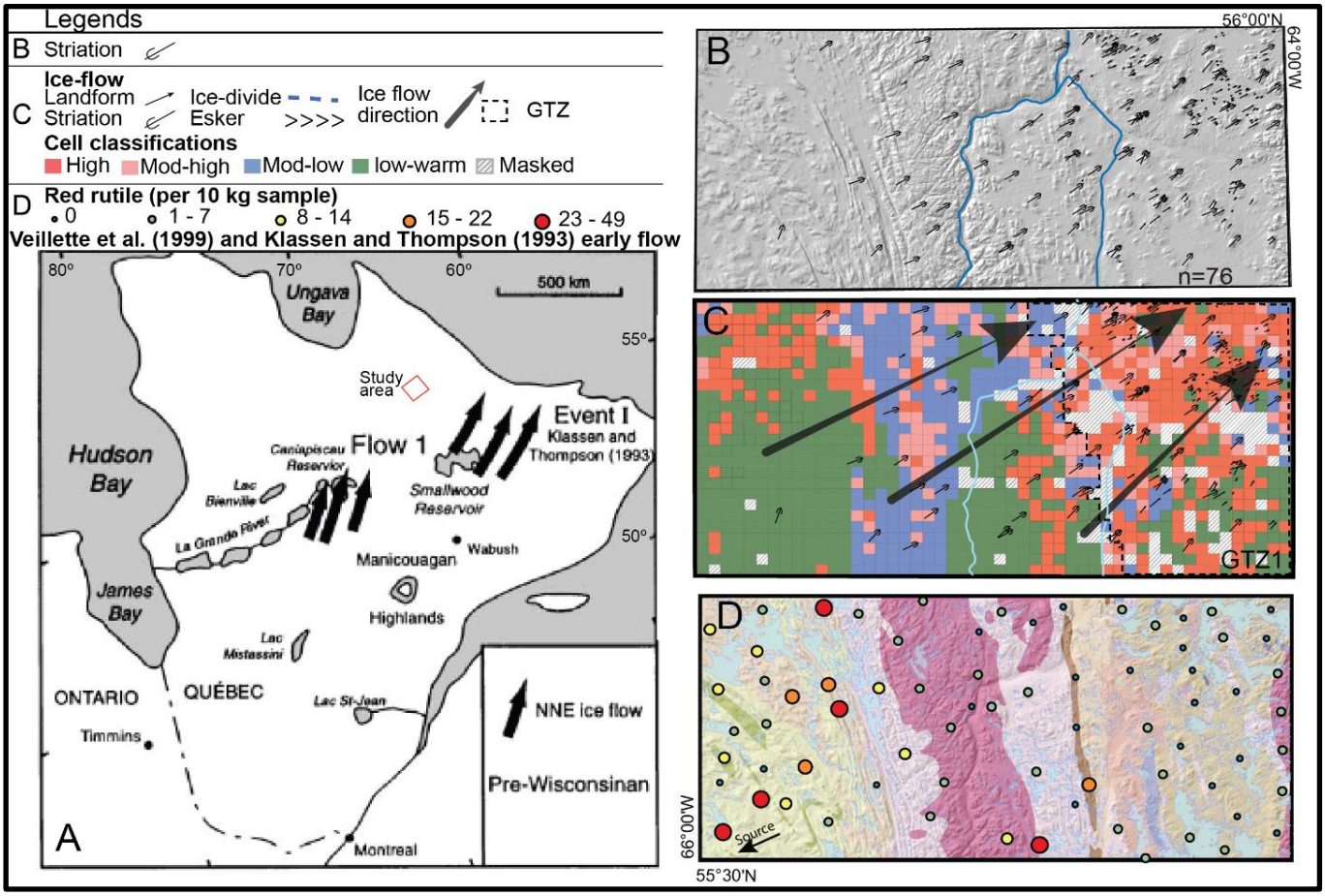

Figure 5.1. Summary of Flow 1 events **(A)** Early northeast ice flows identified across Labrador and Quebec by Klassen and Thompson (1993) and Veillette et al. (1999). **(B)** Striation and landforms associated with Flow 1 to the northeast within the study area. **(C)** Subglacial proxy values for GTZ indicating high proxy values within GTZ1. **(D)** Dispersal patterns for LT material completely across the entire study area, indicating broad-based warm-based conditions.

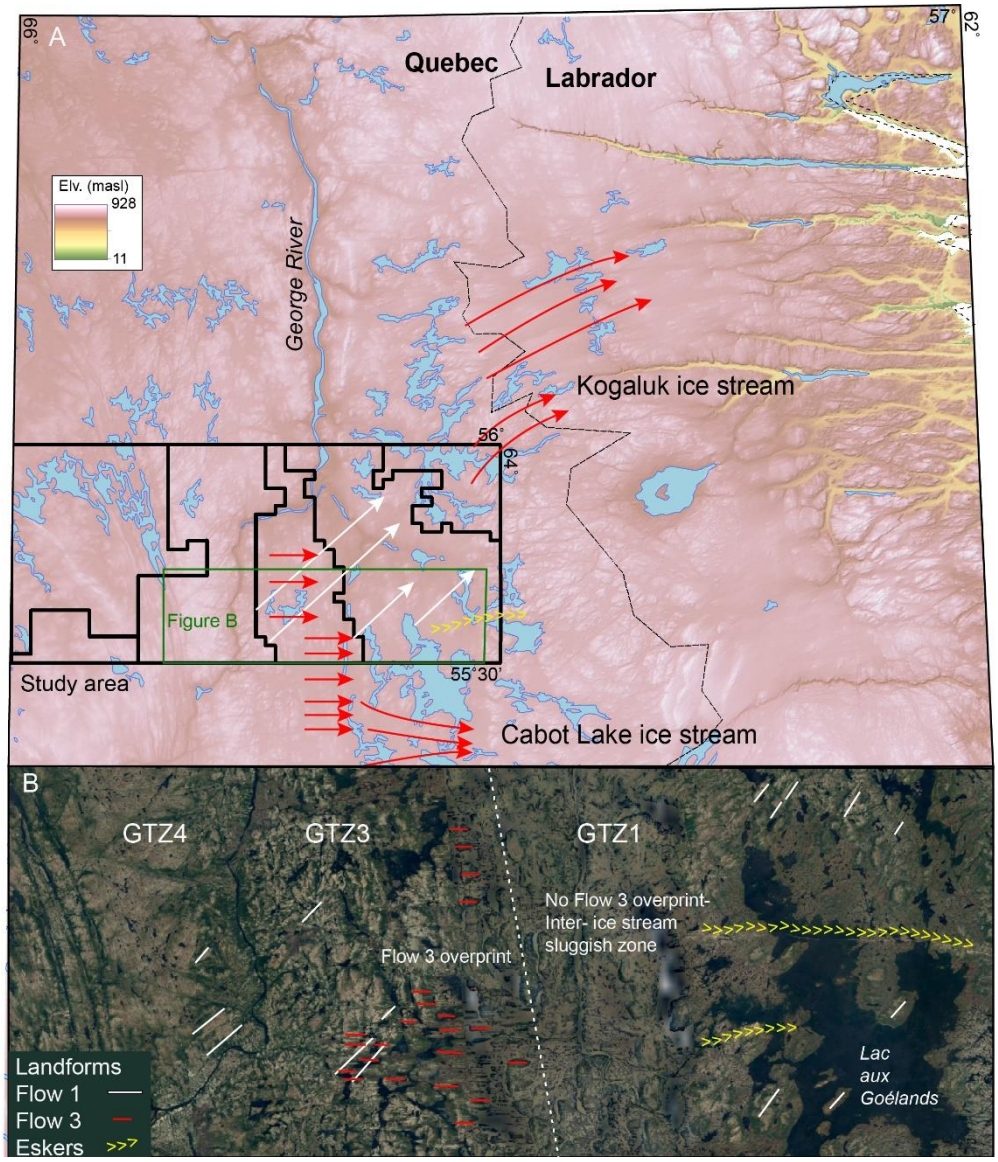

Figure 5.2. **(A)** Regional DEM (SRTM data from www.earthexplorer.usgs.gov), with the study area (outlined in black) and GTZs outlined. Flow 1 as identified within the study area (white lines), Flow 3 (red lines) within the study area correlated outside of the study area to the Kogaluk ice stream to the northeast (Batterson and Liverman, 2001; Margold et al., 2015) and the Cabot Lake ice stream to the south (Paulen et al., 2017; Rice et al., 2020). **(B)** Google earth imagery of a portion of the study area, where the change between GTZ4, GTZ3 and GTZ1 are clearly evident with GTZ4 lacking abundant landforms, GTZ3 having Flow 1 landforms crosscut by Flow 3 landforms, and GTZ1 having no Flow 3 overprint.

The remarkable preservation of the Flow 1 landscape within GTZ1 is indicative of switch in subglacial conditions from widespread warm-based conditions to widespread cold-based conditions. Therefore, despite the similar ice-flow chronology to Veillette et al. (1999), this research has provided evidence of landform preservation and therefore no evidence of continuous wide-spread warm-based subglacial conditions following LGM. These findings do

generally agree with the conclusions of Clarhäll and Jansson (2003) who indicated the region around Lac aux Goélands was a fragmented landscape resulting from a switch to widespread cold-based conditions in the region. However, the ice-flow chronology proposed by Clarhäll and Jansson (2003) is inconsistent with observations made in this study. Specifically, they proposed that eastward ice flow features west of Lac aux Goélands form a relict (pre-LGM) flowset that was preserved by cold-based ice. In this study, evidence within the same area clearly shows that eastward ice flow features are younger than the northeast features and are parallel to late-stage eskers. There were seven key sites where Flow 1 striations were established as older than Flow 3 striations through lee side preservation on upland bedrock clearings (Chapter 2). In addition, several small drumlins within GTZ3 are superimposed on larger southwest/northeast ridges that resemble large drumlinoid or other elongated landforms (Figure 5.2). Therefore, their eastward flow (Fan C) is re-interpreted herein as a late-stage deglacial flow and integrated to Flow 3, whereas their northeast flow (Fan B) is integrated in Flow 1.

Numerical models have indicated few intervals when the fraction of LIS ice (≤ 50%) was warm-based prior to LGM with little to no glacial erosion within the study area over the last glacial cycle (Melanson et al., 2013: Figure 5.3A). Other numerical models indicate a very low probability of warm-based ice within the study area during LGM (Tarasov and Peltier, 2007; Figure 5.3B). This could indicate that Flow 1 would have occurred before LGM when warm-based conditions could have been widespread. Tarasov and Peltier (2007) numerical model also suggests low basal velocities for the study area and surrounding area around LGM as well (Stokes et al., 2012; Figure 5.3C), again further suggesting Flow 1 must have occurred pre-LGM. However, the thermal regimes in these models are sensitive to bedrock thermal properties, which were either represented as constant values and other poorly-constrained parameters. For example, heat flow measurement sites are lacking for all of northern Quebec and Labrador (Pollack et al., 1993; Figure 5.3D). It is therefore possible that the probabilities of warm-based ice at the LGM in the region were underestimated. The poorly-constrained parameters constraining bed thermodynamics (the bed thermal model) in ice sheet models has been suggested to explain the discrepancies between model outputs and field observations in the Keewatin sector of the LIS, where thick till sequences (~5-30 m) with contrasting provenance indicators suggest warm-based subglacial conditions and mobile dispersal centres (Hodder et al., 2016). Regardless of its timing, Flow 1 must have occurred when ice was thick and would have

created enough thermal insulation to allow for warm-based conditions over a broad region of the QLD, which likely occurred around LGM.

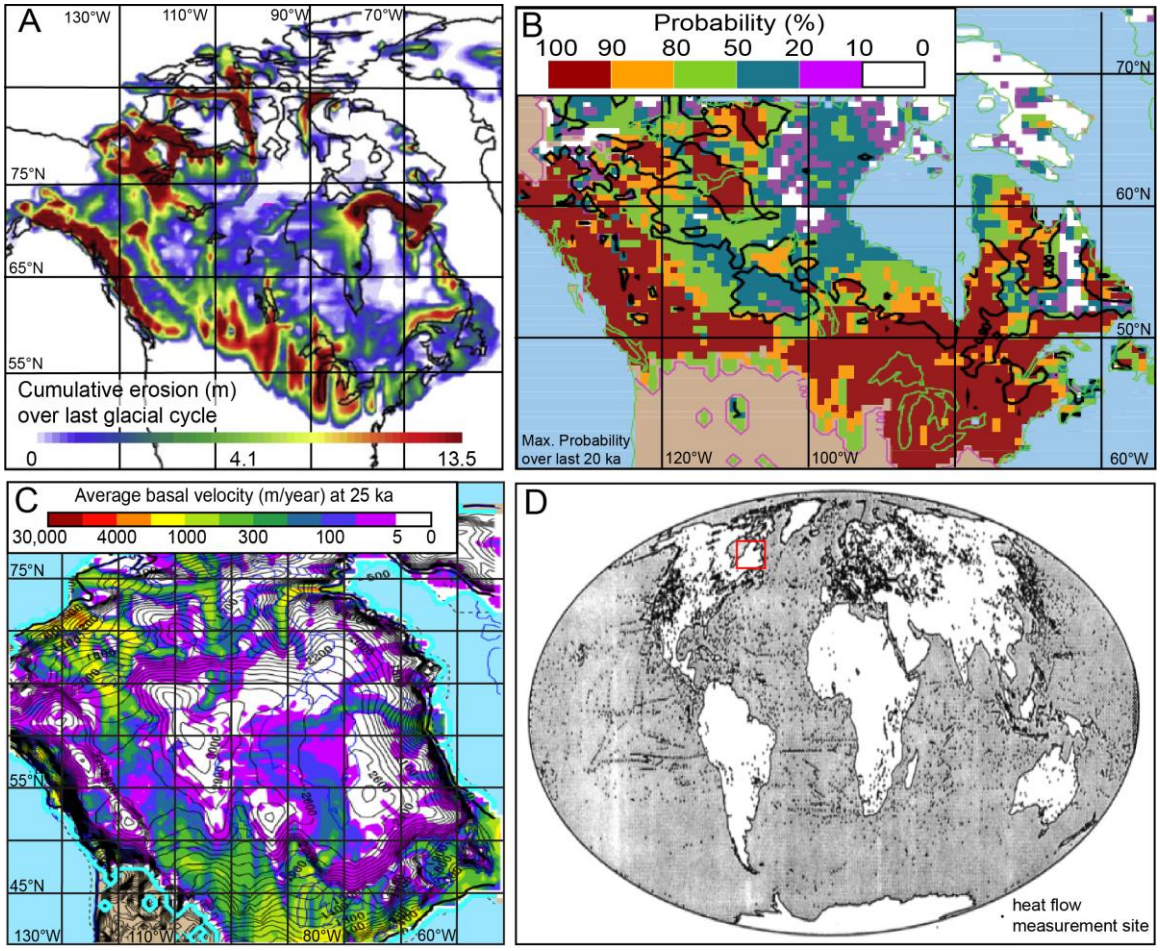

Figure 5.3. **(A)** Cumulative erosion over the last glacial cycle as indicated by Melanson et al. (2013), with the study area have very low (white) cumulative erosion. **(B)** Modelled maximum probability of warm-based conditions over the last 20 ka by Tarasov and Peltier (2007), the study area being in the white region of Q-L showing very low probability of being warm-based. **(C)** Modelled basal velocity of the LIS near LGM (~25 ka) by Stokes et al., 2012), again the study area shows very low average basal velocity at this time. **(D)** Heat flow measurement sites used by Pollack et al. (1993) and used in subsequent numerical models. Note the lack of available data within the entire Q-L sector.

Dispersal patterns associated with Flow 1 extend the dispersal distance of LT material identified by Klassen and Thompson (1993) by an additional ~125 km to the northeast. Of specific note, is the fact that this dispersal pattern crosses the entire study area, including across GTZ4, a GTZ characterized by predominantly low subglacial dynamics proxies and thus by inferred low subglacial erosion rates. The depositional record thus provides key insights into subglacial processes that could have been overlooked by focusing exclusively on the landscape

record, as it is clear that till was entrained across the uplands despite low glacial erosion indicators. A number of key parameters need to be considered to understand and reconcile the erosional and depositional records of the uplands 1) bedrock hardness of the De Pas batholith, 2) basal melting rates over the batholith, 3) basal debris concentration over hard bedrock. The effect of bedrock hardness and how it can limit the development of a strong erosional imprint is important. Hard bedrock reduces local erosion, which reduces basal sediment concentrations, which can further reduce abrasion (e.g., Alley et al., 2019). This would also explain the higher ^{10}Be inheritance over the uplands. However, GTZ4 also contains zones classified as MH for subglacial dynamics (Figures 5.4 and 5.5). Taken together, these results suggest the central upland was characterized by polythermal conditions with sufficient warm-based zones to allow subglacial and/or basal (englacial) debris to be entrained and discontinuously deposited over and beyond the highlands. These results also show the importance of incorporating till compositional data into glacial dynamic reconstruction.

5.2.2 Flow 2

Following Flow 1, a relatively narrow corridor of ice began to flow to the northwest in association with ice streaming events into Ungava Bay (Figures 5.4A, 5.4B). Flow 2 resulted in a switch to a mobile bed within GTZ2 (over 24%) that resulted in numerous landforms and large bedrock controlled lakes (Figure 5.4C). Dispersal patterns for Flow 2 are difficult to discern as it represents the most southeastern extent of the northwest flow, so dispersal was likely largely outside of the study area, however, some dispersal patterns to the northwest are recognizable (Figure 5.4D). The catchment area of Flow 2 is similar to Fan D outlined by Jansson et al. (2003), extending it ~ 10 km to the east. Margold et al. (2018) proposed that the onset of ice streaming into Ungava Bay occurred around 11.5 ka, which would suggest Flow 2 was operating around this time and may have initiated an acceleration in deglaciation of the Q-L sector (Ullman et al., 2016).

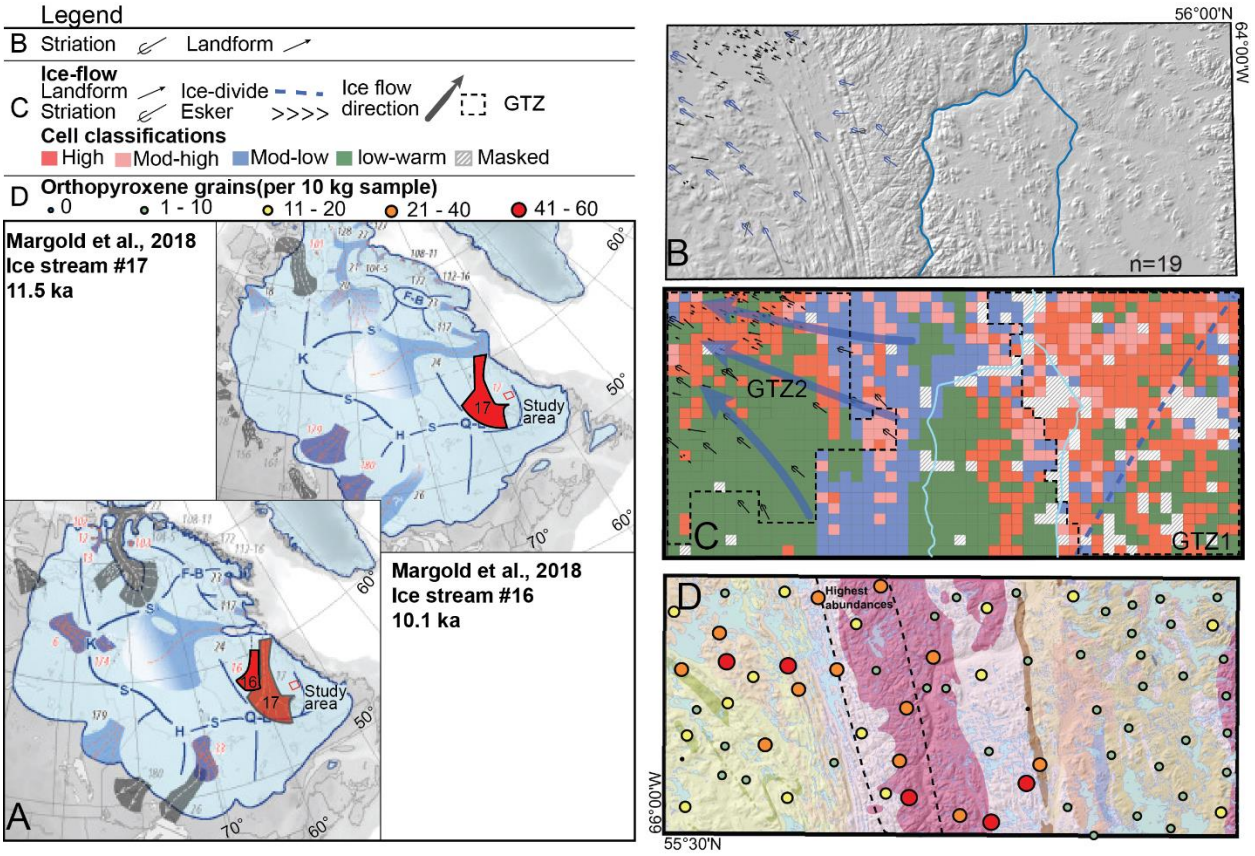

Figure 5.4. Summary of Flow 2 events **(A)** Ice streaming events into Ungava Bay, initiating in the east of the USIB catchment (#17) and migrating west shortly after (#16) **(B)** Striation and landforms associated with Flow 2 to the northwest within the study area (blue arrows), extending the catchment of ice stream #17 to the east. **(C)** Subglacial proxy values for GTZ2 indicating high proxy values within the central landform region, transitioning to less dynamic conditions near the central upland and low dynamics to the south. **(D)** Dispersal patterns for orthopyroxene being dispersed to the northwest.

5.2.3 Flow 3

Analysis of ice stream records by Jansson et al. (2003) suggests a westward shift in ice streaming events in Ungava Bay, which Margold et al. (2018) indicate as occurring sometime between 11.5 ka (ice stream #16) and 10.1 ka (ice stream #17; Figure 5.4A). This westward migration of ice streams likely influenced the migration of the ice divide across the study area resulting in Flow 3 (Figure 5.4B). Jansson et al. (2003) noted that eskers within Ungava Bay are in the same direction as Fan D, indicating it was a deglacial ice flow. This suggests the westward ice divide migration and Flow 3 happened prior to the esker formation, as eskers within the study

area are oriented to the east, aligned to this study's Flow 3. The relationship between these eskers and ice flow directions suggests Flow 2 and Flow 3 could have operated contemporaneously.

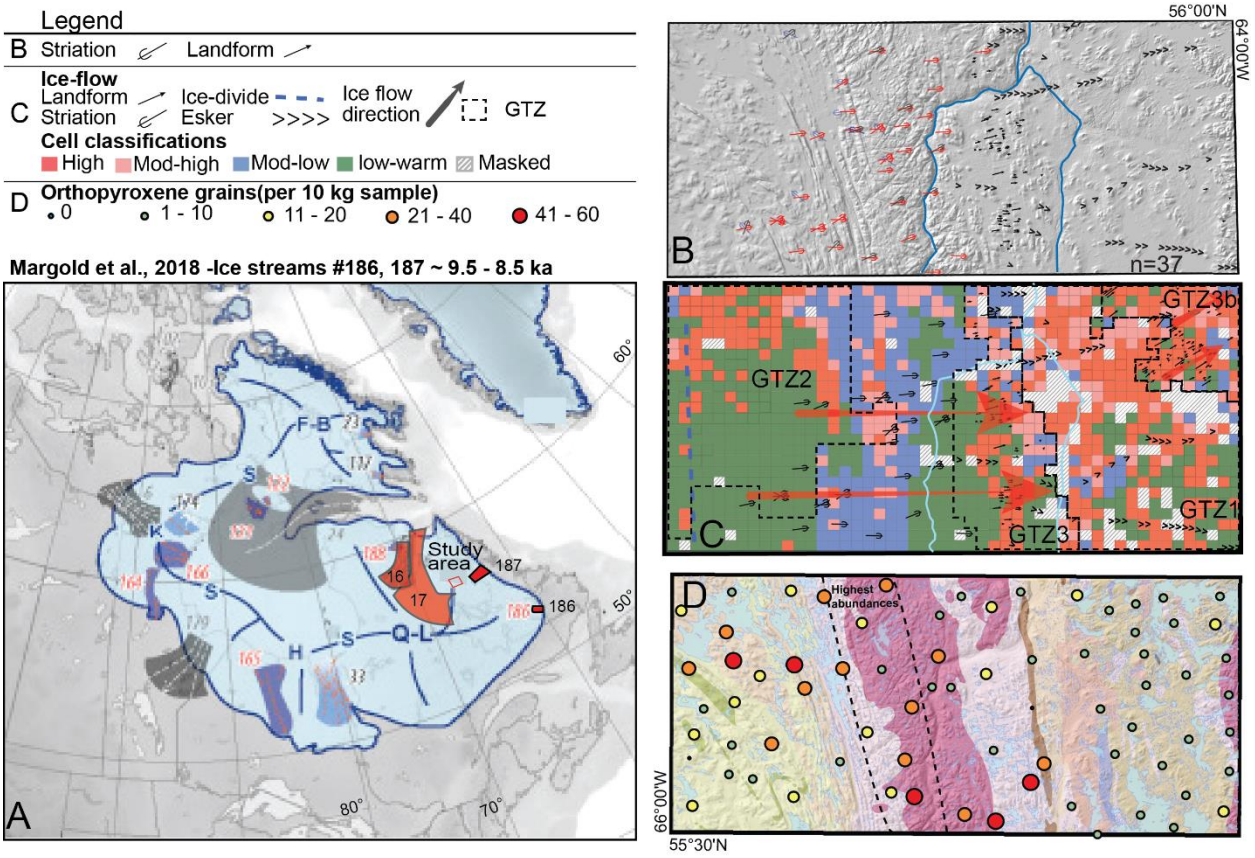

Figure 5.5. Summary of Flow 3 events **(A)** Following the migration west of ice streams in the UBIS, and ice divide migration, ice began streaming to the east as the ice margin retreated (#186 and #187). **(B)** Striation and landforms associated with Flow 3 to the east (red arrows) within the study area, note the similar orientation of the eskers to this ice-flow phase. **(C)** Subglacial proxy values for GTZ3 and GTZ3b indicating high proxy values within the central portion of the study area. **(D)** Dispersal patterns for orthopyroxene, which show a slight eastward dispersal, especially in the central-southern portion of the study area.

Flow 3 is characterized in GTZ3 and GTZ3b with elevated concentrations of high proxies, indicative of mobile bed conditions (30.8% and 58.9% of the area covered by each GTZ respectively; Figure 5.4C). ^{10}Be samples collected from bedrock uplands in GTZ3b had the lowest ^{10}Be abundances from all the collected samples, further suggesting significant subglacial erosion had occurred. Interestingly, these two GTZs are separated by GTZ1, which must have been a sluggish inter ice stream zone, protecting GTZ1 and the Flow 1 landscape (Figure 5.2). Dispersal patterns are difficult to attribute solely to dispersal from Flow 3, due to its overprinting of the Flow 1 landscape in GTZ3 and GTZ3b, however, a greater eastward influence on the

dispersal pattern of orthopyroxene in GTZ3 and U geochemistry in GTZ3b suggests some influence of the overall northeast dispersal patterns observed (Figure 5.4D).

Flow 3 landforms within GTZ3b are associated with the Kogaluk ice stream (#187 – Margold et al., 2018), which operated between 9.5 and 8.5 ka (Figure 5.4A and, south of the study area, the Happy Valley-Goose Bay ice stream (#186-Margold et al., 2018) was operating within this same timeframe (~8.9 ka; Figure 5.4A). That being said, Flow 3 is probably time-transgressive, with some flowsets indicative of general eastward ice flow in the region are clearly related to late-stage, topographical streaming. Other eastward ice-flow indicators could have developed at a later time or in an inter-ice stream position (slower ice flow), but all of these flows occurred after LGM (*cf.* Clarhäll and Jansson, 2003). Finally, a fan of eskers roughly oriented in this direction, which Lewington et al. (2020), through an analysis of meltwater features in the Keewatin, indicated the final depositional imprint of channelized drainage, forming close to the ice margin. Taken together, these findings provide strong evidence that suggests Flow 3 operated closer to deglaciation than to pre-LGM as suggested by Clarhäll and Jansson (2003).

5.2.4 Flow 4

Following the ice-streaming events of Flow 2 and Flow 3, the ice sheet had likely thinned considerably, and likely split into multiple smaller ice caps (Clark et al., 2000; Figure 5.6A). During this time ice flow was largely topographically controlled and predominantly flowed to the southwest (Figure 5.6B), off of the local topographic high (i.e., the De Pas Batholith). Dispersal patterns show no clear impact from Flow 4 (Figure 5.6C) and GTZ4 is not associated with a highly mobile bed (Figure 5.6D).

Collectively, it is now clear that wide-spread warm-based (Flow 1) conditions transitioned to more sluggish cold-based conditions with warm-based highly dynamic ice restricted to regions influenced by ice streaming events (Flow 2 and Flow 3) before the ice sheet likely fragmented to smaller ice caps (Flow 4) before final deglaciation. The various observations documented by previous researchers, including the ones that seemed conflicting or contradictory, have been integrated and reconciled with new observations from this study in order to produce a regionally coherent and consistent subglacial evolution model.

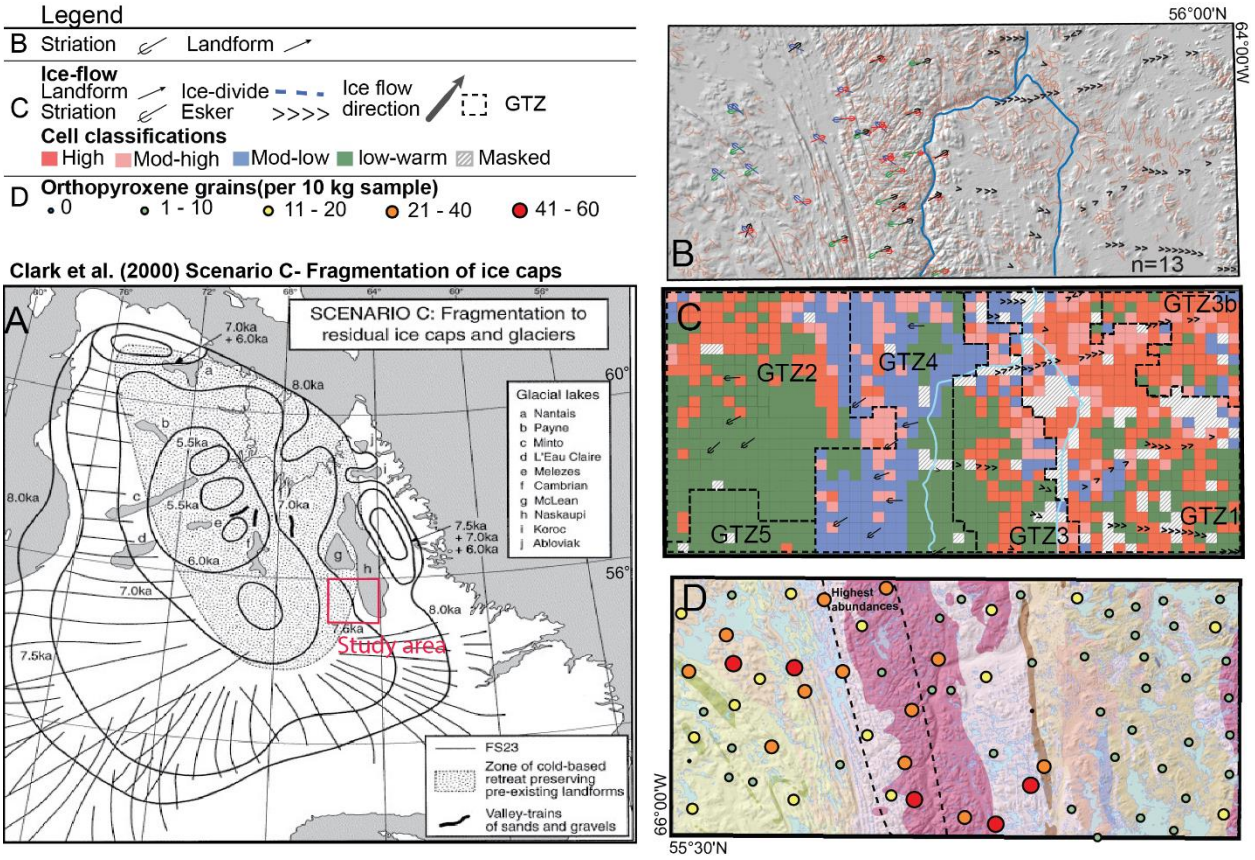

Figure 5.6 Summary of Flow 4 events **(A)** Scenario C of Clark et al. (2000) showing the fragmentation of the Q-L sector into smaller icecaps and a switch to cold-based conditions that would have preserved existing landscapes. **(B)** Striations of Flow 4 generally to the southwest (green arrows) within the study area. **(C)** Summary of all proxy analysis and subsequent GTZs for the entire study area **(D)** Dispersal patterns for orthopyroxene, which may have been influenced by Flow 4, however the lack of erosional proxies attributed to this Flow suggest this was unlikely.

5.3 Implications for glacial dispersal

Previous glacial dispersal research in the region had established significant dispersal distances in multiple directions creating large amoeboid dispersal patterns, notably around the LT region (Klassen and Thompson, 1993). These findings suggested active warm-based ice and considerable ice divide migration. However, only an average of 50 clasts weighing on average only 10 g were counted, making a detailed analysis of dispersal patterns difficult. Additionally, it was unknown how far the dispersed material was transported to the northeast, the chronology of ice flows that led to the observed dispersal patterns, or whether this sector of the QLD was

continuously warm-based with continuous dispersal (Klassen and Thompson, 1993; Veillette et al., 1999), or, had polythermal subglacial conditions throughout glaciation (Clarhäll and Jansson, 2003). Through this research, it was established that it was prominently Flow 1 that was responsible for the majority of northeast dispersal of LT material across the study area, which may have been later accentuated by Flow 3. It has also been shown that GTZs with high percentages of high dynamic proxies show evidence of re-entrainment such as amoeboid dispersal patterns. GTZ2 and GTZ3 have their own distinct dispersal patterns aligned in their respective ice-flow directions, highlighting the importance of understanding fragmented glacial landscapes and the complete ice-flow history of a region for drift prospecting activities. In fact, the dispersal patterns were able to add significant insights into the ice flow reconstruction and allowed further inferences on the widespread warm-based subglacial conditions that persisted during Flow 1. Dispersal of LT and RL pathfinders are now recognized to the northeast across the characteristically low proxy GTZ4, which was classified as 'low' subglacial dynamics based on the GIS analysis.

5.3.1 Implications for mineral exploration

This research was able to demonstrate the effectiveness of using geochemical, indicator, and clasts from collected till samples to understand dispersal patterns. Previous research (e.g., McClenaghan et al., 2000; McClenaghan et al., 2001; Paulen and McMartin, 2004; McClenaghan and Paulen, 2018) had found indicator minerals to be the best targets for long-distance glacial transport, as geochemical pathfinders may rapidly dilute or form complex assemblages that are difficult to fingerprint to a single source. Results from this study are consistent with this general finding. This is likely because: 1) the geochemical signature is diluted more easily through the incorporation of new till in the down ice-direction and 2) many of the bedrock lithologies within the bedrock unit are geochemically too similar to effectively separate based on till-matrix geochemistry data.

Additionally, the dispersal patterns, in the context of the ice/bed mobility analysis, indicate that bedrock also play an important role in glacial dispersal. While it has been previously documented that bedrock hardness, topography, (Parent et al., 1996) and weathering (Kettles and Shilts, 1989) plays an important role in determining how much bedrock is removed during

glacial erosion, the influence of bedrock structure (i.e., joints and folds) is not as well understood and could play an important role in dispersal patterns.

Finally, this research has shown the importance of establishing a robust ice-flow plays an important role in determining how much bedrock is removed during glacial erosion reconstruction for a study area, specifically in developing a relative understanding of the changing subglacial dynamics across an exploration region. Of significant note is the dispersal of glacial a considerable distance (> 100 km) across the study area including across a region with a low ice/bed-mobility signature during Flow 1. This highlights the importance of striae measurements as part of any exploration program. Without the striation evidence, it would not have been clear that Flow 1 was as widespread as its landform flowset suggests. The striation evidence was also critical in establishing the ice-flow chronology within the study area, which, in turn, critical for reconstructing dispersal patterns. Although the sampling resolution did not allow for the clear influence of Flow 3 on the Flow 1 dispersal pattern, the influence of ice-streams on dispersal patterns is likely to be significant. This influence is more evident outside of the study area, where the influence of ice streaming is more evident (e.g., Strange Lake- Batterson, 1989; McClenaghan et al. 2020). Despite this, the influence of Flow 2 on dispersal patterns within the study area is clearer, showing that even outside of the main ice-stream corridor, and indeed outside of the ice stream flowset, glacial dispersal still occurs, further justifying the importance of detailed striation measurements during exploration exercises.

5.3.2 Other implications

This thesis has shown that subglacial within an inner region of the Q-L sector changed from broad warm-based conditions with a highly mobile bed, to more sluggish ice conditions, with spatially constricted regions of mobile bed conditions highly influenced by regional ice streams. Given the abundance of ice streams with the Antarctic and Greenland ice sheets, some insights from this investigation may be applicable to modern ice sheet changes. Specifically, the relatively rapid ice-divide migration that occurred suggests that large-scale ice configurations can occur over short relatively short periods of time. The ice-divide migration could have occurred coevally, but regardless, show that these changes happened relatively rapidly leading up to deglaciation of the region. The deglacial ages from this and surrounding studies suggest that overall deglaciation occurred relatively quickly as well.

5.4 **Future work**

5.4.1 Glacial dynamics and subglacial evolution

This thesis has resolved conflicting ice-flow chronologies and associated subglacial dynamics for an inner region of the Q-L sector of the LIS. Through this research, insights into the subglacial organization of these inner regions have been recognized. However, given the overall size of the Q-L sector, more work is required to fully understand how these inner-ice sheet regions evolved. Additionally, it has been demonstrated that these inner-ice sheet regions can have regions of relict terrain, preserved from overprinting of subsequent ice-flow phases. These preserved landscapes offer a unique window into how early stages of the ice sheet evolved. These types of landscapes are often overprinted outside of these inner regions as exemplified by this thesis. Therefore, these inner ice sheet regions offer valuable insights into relict ice flow directions and subglacial conditions during periods when the ice-sheet was extensively thicker. These types of insights are rare outside these inner-ice sheet regions and highlights the value of future research within this region.

Future work should aim at expanding the GTZ classification outside of this region, specifically to the southwest, which would allow for a better understanding of the evolution of GTZ5. A denser sampling strategy may help refine dispersal patterns within the region, with a focus on fingerprinting MR clast and their potential northwest dispersal. If more GTZs are created for these inner-ice sheet regions, additional insights into early ice-flow phases could be discovered. This thesis has created an effective suite of methodologies that would be useful in other inner-ice sheet regions but may need additional methods to constrain some uncertainties discovered during this research (see below).

5.4.2 Methodologies and reconstructions

Through this research project, certain methodologies provided more useful data than others. Specifically, CIA results were able to constrain the residency time of the surficial till but were restricted to certain regions of the study area (Chapter 3). ^{10}Be abundances did provide valuable insights into erosional vigour and changes across the study area. However, these results must be considered in conjunction with a well-constrained ice-flow reconstruction, as one erosional event can remove inheritance within the bedrock and attributing these erosive

conditions to a single ice-flow phase can be difficult. Future work utilizing ^{10}Be abundances to infer erosion should aim at defining specific ranges of inheritance indicative of true cold-based conditions (i.e., 10 times the expected abundance?). From this work, it appears that despite this limitation ^{10}Be abundances are a great tool that is best utilized with multiple methods and interpreted together. Future work using ^{10}Be should use a higher density of samples with multiple samples from within each established GTZ. More ^{10}Be samples from inner-ice sheet regions that lack datable organic materials and fine-grained beach sediments for OSL dating would significantly improve the ability to constrain the timing and pattern of ice margin retreat in these regions, which are currently very poorly constrained. Additional sampling along the two glacial lakes within the study area would also improve margin retreat patterns and glacial lake formation in the region. Specifically, recent research has shown promising new methods in luminescence dating of cobbles in glacial sediments (Jenkins et al., 2018; Duller et al., 2019) which may be a more accurate optical dating method for the coarse beach deposits of glacial Lake McLean and Naskaupi.

Given the rapid accessibility of high-resolution geospatial data over the last several years, it is highly likely that more accurate landform analysis will be possible in the near future. Specifically, the use of automated landform mapping (Sookhan et al., 2019) will allow for quicker classification of landforms and their characteristics (i.e., elongation, azimuth). This would allow for improved GTZ separation and overall understanding of ice-sheet evolution, especially when correlating various ice stream phases east of the study area. However, as indicated in Chapter 2, landform analysis is best accompanied by field-based outcrop-scale ice flow measurements. These outcrop-scale ice flow measurements were critical in developing a relative ice-flow chronology for the region that otherwise would have made age-relationships between Flow 2 and Flow 3 impossible. It was these field-based measurements that allowed for the conflicting ice-flow reconstructions to be resolved. Therefore, it is highly recommended to conduct outcrop-scale ice-flow measurements when possible, but especially in inner-ice sheet regions where landform production is minimal to non-existent.

Overall, this thesis has shown the benefits of using multiple methodologies during ice-flow reconstructions. Chapter 2, Chapter 3, and Chapter 4 used distinctly different methodologies that each offered a unique insight into the subglacial evolution of the inner-ice

sheet region. However, each of the chapters build off of the previous chapter showing the importance of the initial establishment of the ice-flow chronology from which the subsequent chapters built from. Future ice-flow reconstructions should aim to incorporate multiple methodologies in investigating changings glacial conditions throughout glaciation, but should first strive to create a robust ice-flow chronology, being sure to incorporate striation data where landform reconstructions cannot confine ice-flow chronology.

Although significant progress has been made regarding the evolution of a portion of the Q-L sector, large uncertainties regarding the evolution of the LIS and its impact on other Earth systems persist. The need for similar detailed investigations into inner-sheet regions is strongly encouraged. Additionally, improved geochronology methods (i.e., ^{10}Be exposure ages and OSL ages) should allow for additional constraints on the timing of deglaciation across the Q-L sector and higher resolution geospatial data should allow for additional insights into ice-flow evolution. Future numerical models should account for switches from warm-based to cold-based conditions, following LGM, even for inner-ice sheet regions. Continued iterations between numerical models and constraints from field-based studies will improve the overall understanding of the LIS and its evolution. Understanding how the LIS evolved throughout glaciation and during deglaciation will provide important insights into how future ice sheet changes may occur.

6 References

Abzalov, M. 2008. Quality Control of Assay Data: A Review of Procedures for Measuring and Monitoring Precision and Accuracy. Exploration and Mining Geology, 17: 131–144, http://dx.doi.org/10.2113/gsemg.17.3

Aitken, M.J. 1998. An Introduction to Optical dating. Oxford University Press, Oxford, 267 p.

Alexanderson, H. and Murray, A.S. 2007. Was southern Sweden ice free at 19-25 ka, or were the post LGM glaciofluvial sediments incompletely bleached? Quaternary Geochronology, 2: 229-236.

Alley, R.B., Cuffey, K.M., and Zoet, L.K. 2019. Glacial erosion: status and outlook. Annals of Glaciology 1-13. doi: 10.1017/aog.2019.38

Amor, S., McCurdy, M., and Garrett, R. 2018. Creation of an atlas of lake-sediment geochemistry of Western Labrador and Northeastern Québec. Geochemistry: Exploration, Environment, Analysis, 19:339-393. doi 10.1144/geochem2018-061

Andrews, J.T. 1994. Wisconsinan Late-glacial environmental change on the southeast Baffin shelf, southeast Baffin Island and northern Labrador. Journal of Quaternary Science, 9(2): 179-183.

Andrews, J.T., Clark, P.U., and Stravers, J.A. 1985. The pattern of glacial erosion across the eastern Canadian Arctic. In: Quaternary Environments: Eastern Canadian Arctic, Baffin Bay, West Greenland. Edited by Andrews, J.T. and Unwin, E., London, UK, 69-92.

Argus, D.F., Peltier, W.R., Drummond, R., and Moore, A.Q. 2014. The Antarctica component of postglacial rebound model ICE- 6G_C (VM5a) based upon GPS positioning, exposure age dating of ice thicknesses, and relative sea level histories. Geophysics Journal International, 198: 537-563.

Averill, S.A. 2001. The application of heavy indicator mineralogy in mineral exploration with emphasis on base metal indicators in glaciated metamorphic and plutonic terrains. In Drift exploration in Glaciated Terrain, McClenaghan, M.B., Bobrowsky, P.T., Hall, G.E.M., and Cook, S.J. (eds), Geological Society of London. doi: doi.org/10.1144/GSL.SP.2001.185.01.04

Bailey, R.M., Smith, B.W., and Rhodes, E.J. 1997. Partial bleaching and the decay form characteristics of quartz OSL. Radiation Measurements, 27: 123-136.

Bakker, P., Clark, P.U., Golledge, N.R., Schmittner, A., and Weber, E. 2017. Centennial-scale Holocene climate variations amplified by Antarctic Ice Sheet discharge. Nature, 541:72-76.

Bardwell, T., Stoker, M., and Larter, R. 2007. Geomorphological signature and flow dynamics of the Minch palae-ice stream, northwest Scotland. Journal of Quaternary Science, 22: 609-617.

Batterson, M.J., and Liverman, D.G.E. 2001. Contrasting styles of glacial dispersal in Newfoundland and Labrador: methods and case studies. Geological Society of London, Special Publications, 185:267-285.

Beel, C.R., Lifton, N.A., Briner, J.P., and Goehring, B.M. 2016. Quaternary evolution and ice sheet history of contrasting landscapes in Uummannaq and Sukkertoppen, western Greenland. Quaternary Science Reviews, 149, 248-258.

Bøe, A-G., Murray, A., and Dahl, S.O. 2007. Resetting of sediments mobilized by the LGM ice-sheet in southern Norway. Quaternary Geochronology, 2: 1-4.

Bostock, H.S. 2014. Geology, Physiographic Regions of Canada. Geological Survey of Canada, Map 1254A (2nd edition), scale 1: 5 000 000. doi: 10.4095/293408

Boulton, G.S. 1987. Progress in glacial geology during the last fifty years. Journal of Glaciology, 33: 25-32.

Boulton, G.S. and Clark, C.D. 1990. A highly mobile Laurentide ice sheet revealed by satellite images of glacial lineations. Nature, 346: 813-817.

Boulton, G.S., Lunn, R., Vidstrand, P., and Zatsepin, S. 2007. Subglacial drainage by groundwater-channel coupling and the origin of esker systems: Part 1- glaciological observations. Quaternary Science Reviews, 26(7-8), 1067-1090.

Boulton, G.S., Hagdorn, M., Mailot, P.B., and Zatsepin, S. 2009. Drainage beneath ice sheets: groundwater-channel coupling, and the origin of esker systems from former ice sheets. Quaternary Science Reviews, 28: 621-638.

Bradwell, T., Stoker, M.S., Golledge, N.R., Wilson, C.K., Merrit, J.W., Long D., Everest, J.D., Hestvik, O.B., Stevenson, A.G., Hubbard, A.L., Finlayson, A.G., and Mathers, H.E. 2008. The northern sector of the last British Ice Sheet: Maximum extent and demise. Earth-Science Reviews, 88:207-226.

Briner, J.P. 2007. Supporting evidence from the New York drumlin field that elongate subglacial bedforms indicate fast ice flow. Boreas, 362: 143:147.

Briner, J.P., and Swanson, T.W. 1998. Using inherited cosmogenic 36Cl to constrain glacial erosion rates of the Cordilleran ice sheet. Geology, 26: 3-6.

Briner, J.P., Kaufman, D.S., Manley, W.F., Finkel, R.C., and Caffee, M.W. 2005. Cosmogenic exposure dating of late Pleistocene moraine stabilization in Alaska. Geological Society of America Bulletin, 117: 1108-1120.

Briner, J.P., Miller, G.H., Davis, P.T., and Finkel, R.C. 2006. Cosmogenic radionuclides from fiord landscapes support differential erosion by overriding ice sheets. Geological Society of America Bulletin, 118: 406-420.

Briner, J.P., Miller, G.H., Finkel, R., and Hess, D.P. 2008. Glacial erosion at the fjord onset zone and implications for the organization of ice flow on Baffin Island, Arctic Canada. Geomorphology, 97: 126-134.

Briner, J.P., Lifton, N.A., Miller, G.H., Refsnider, K., Anderson, R., and Finkel, R. 2014. Using in situ cosmogenic 10Be, 14C, and 26Al to decipher the history of polythermal ice sheets on Baffin Island, Arctic Canada. Quaternary Geochronology, 19: 4-13.

Campbell, H.E., Paulen, R.C., and Rice, J.M. 2018. Surficial geology, Ashuanipi River, Newfoundland and Labrador, NTS 23-I southwest. Geological Survey of Canada, Canadian Geoscience Map, 346. Scale 1:100 000. Open File 7771. doi: 10.4095/297563

Carlson, A.E., Clark, P.U., Raisbeck, G.M., and Brook, E.J. 2007. Rapid Holocene deglaciation of the Labrador sector of the Laurentide Ice Sheet. Journal of Climate, 20: 5126-5133.

Carlson, A.E., LeGrande, A.N., Oppo, D.W., Came, R.E., Schmidt, G.A., Anslow, F.S., Licciardi, J.M., and Obbink, E.A. 2008. Rapid early Holocene deglaciation of the Laurentide Ice Sheet. Nature Geoscience, 1: 620-624.

Charette, B., Lafrance, I., and Mathieu, G. 2016. Géologie de la region du Lac Jeannin (NTS 23B). Ministry of Energy and Natural Resources, Quebec.

Clarhäll, A. and Jansson, K.N. 2003. Time perspectives on glacial landscape formation-glacial flow chronology at Lac aux Goélands, northeastern Québec, Canada. Journal of Quaternary Science, 18: 441-452.

Clark, C.D. 1993. Mega-scale glacial lineations and cross-cutting ice-flow landforms. Earth surface Processes and Landforms, 18: 1-29.

Clark, C.D. and Stokes, C.R. 2001. Extent and basal characteristics of the M'Clinock Channel Ice Stream. Quaternary International, 86: 81-101.

Clark, C.D., Knight, J.K., and Gray, J.T. 2000. Geomorphological reconstruction of the Labrador sector of the Laurentide Ice Sheet. Quaternary Science Reviews 19: 1343-1366. doi:10.1016/S0277-3791(99)00098-0

Clark, C.D., Hughes, A.L., Greenwood, S.L., Spagnolo, M., and Ng, F.S. 2009. Size and shape characteristics of drumlins, derived from a large sample and associated scaling laws. Quaternary Science Reviews, 28: 677-692.

Clark, P.U. and Fitzhugh, W.W. 1990. Late Deglaciation of the Central Labrador Coast and its implications for the Age of Glacial Lakes Naskaupi and McLean for Prehistory. Quaternary Research, 34(3): 296-305.

Clark, P.U. and Mix, A.C. 2002. Ice sheets and sea level of the Last Glacial Maximum. Quaternary Science Reviews, 21 (1-3): 1-7.

Clark, P.U., Brook, E.J., Raisbeck, G.M., Yiou, F., and Clark, J. 2003. Cosmogenic 10Be ages of the Saglek Moraines, Torngat Mountains, Labrador. Geology, 31: 617-620.

Clark, P.U. and Mix, A.C. 2002. Ice sheets and sea level of the Last Glacial Maximum. Quaternary Science Reviews, 21(1-3): 1-7. doi: 10.1016/S0277-3791(01)00118-4

Clark, T. and Wares, R. 2004. Synthèse lithotectonique et métallogénique de l'Orogène du Nouvequ-Québec (Fosse du Labrador). Ministère des Ressources naturelles et de la Faune, Québec Report MM 2004-01, 182p.

Collins, P. and Cashin, P.J. 2010. Summary Report on the Mineral exploration Program July to August 2009. Quest Rare Minerals George River Project Nanuk claims NTS area 23P/16. Énergie et Ressources naturelles Québec Report GM 65368. Available online: http://gq.mines.gouv.qc.ca/documents/EXAMINE/GM65368/GM65368.pdf

Cook, S.J., Swift, D.A., Kirkbride, M.P., Knight, P.G., and Waller, R.I. 2020. The empirical basis for modelling glacial erosion rates. Nature Communications. doi: 10.1038/s41467-020-14583-8

Corbett, L.B., Bierman, P.R., and Davis, P.T. 2016. Glacial history and landscape evolution of southern Cumberland Peninsula, Baffin Island, Canada, constrained by cosmogenic 10Be and 26Al. Geological Society of America Bulletin, 128 (7-8), 1173-1192.

Corrigan, D., Wodicka, N., McFarlane, C., Lafrance, I., van Rooyen, D., Bandyayera, D., and Bilodeau, C. 2018. Lithotectonic Framework of the Core Zone, Southeastern Churchill Province, Canada. Geoscience Canada, 45: 1-24. doi: 10.12789/geocanj2018.45.128

Dalton, A., Margole, M. Stokes, C.R., Tarasov, L., Dyke, A.S. et al. 2020. An updated radiocarbon-based ice margin chronology for the last deglaciation of the North American Ice Sheet Complex. Quaternary Science Reviews, 234. doi: 10.1016/j.quascirev.2020.106223

Danis, D. 1988. Géologie de la region du lac Recouet (Territoire-du-Nouveau-Québec). Ministere de l'Énergie et des Ressources Québec; ET 86-11, 60p.

Davis, P.T., Briner, J.P., Coulthard, R.D., Finkel, R.W., and Miller, G.H. 2006. Preservation of Arctic landscapes overridden by cold-based ice sheets. Quaternary Research, 65: 156-163.

De Angelis, H. and Kleman, J. 2005. Paleo-ice streams in the norther Keewatin sector of the Laurentide ice sheet. Annals of Glaciology, 42: 135-144.

De Angelis, H. and Kleman, J. 2008. Palaeo-ice-stream onsets: examples from the north-eastern Laurentide Ice Sheet. Earth Surface Processes and Landforms, 33(4), 560-572.

Dickson, W.L. and Kerr, A. 2007. An updated database of historic geochemical data for granitoid plutonic suites of Newfoundland. Newfound and Labrador Geological Survey, Open File NFLD/2957

Dowdswell, J.A., Hogan, K.A., Evans, J., Noormets, R., Ó Cofaigh, C., and Ottesen, D. 2010. Past ice-sheet flow east of Svalbard inferred from streamlined subglacial landforms, Geology, 38(2) 163-166.

Dubé-Loubert, H. and Roy, M. 2017. Development, evolution and drainage of glacial Lake Naskaupi during the deglaciation of north-central Quebec and Labrador. Journal of Quaternary Science, 32: 1121-1137.

Dubé-Loubert, H., Roy, M., Schaefer, J.M., and Clark, P.U. 2018. 10Be dating of former glacial Lake Naskaupi (Québec-Labrador) and timing of its discharge during the last deglaciation. Quaternary Science Reviews, 191: 31-40.

Dühnforth, M., Anderson, R.S., Ward, Dylan, and Stock, G.M. 2010. Bedrock fracture control of glacial erosion processes and rates. Geology, 38(5): 423-246.

Duller, G.A.T., Robert, H.M., Jekins, G.T.G., Chiverrell, R.C., Ou, X., and Glasser, N.F. 2019. Luminescence isochron dating of glacial sediments using cobbles. 20th Congress of the International Union for Quaternary Research (INQUA), Abstract P-4611.

Dunai, T.J. 2010. Cosmogenic nuclides, Principles, concepts, and applications in the Earth Surface Sciences. Cambridge University Press, UK.

Dyke, A. 1983. Quaternary geology of Summerset Island, District of Franklin. Geological Survey of Canada Memoire, 403.

Dyke, A. 2004. An outline of North American deglaciation with emphasis on central and northern Canada. Developments in Quaternary Science, 2(Part B): 373-424.

Dyke, A.S. and Prest, V.K. 1987. Late Wisconsinan and Holocene history of the Laurentide Ice Sheet. Geographie Physique et Quaternaire, 41: 237-263.

Dyke, A.S., Morris, T.F., Green, D.E.C., and England, J. 1992. Quaternary Geology of Prince of Wales Island, Arctic Canada. Geological Survey of Canada Memoir, 433. doi: 10.4095/134058

Dyke, A.S., Moore, A., and Robertson, L. 2003. Deglaciation of Canada. Geological Survey of Canada, Open File 1574. Thirty-two maps at 1: 7 000 000 scale.

Ebert, K. 2015. GIS analysis of ice-sheet erosional impacts on the exposed shield of Baffin Island, eastern Canadian Arctic. Canadian Journal of Earth Science, 52: 966-979.

Ebert, K., Hall, A.M., Kleman, J., and Andersson, J. 2015. Unequal ice-sheet erosional impacts across low-relief shield terrain in northern Fennoscandia. Geomorphology, 233: 64-74.

Edlund, S.A. 1991. Preliminary surficial geology of Cornwallis and adjacent islands, Northwest Territories, Geological Survey of Canada, Paper 89-12.

Ely, C.J., Clark, C.D., Spagnolo, M., Stokes, C.R., Greenwood, S.L., Hughes, A.L.C., and Elyes, N. 2006. The role of meltwater in glacial processes. Sedimentary Geology, 190: 257-268.

Ely, C.J., Clark, C.D., Spagnolo, M., Stokes, C.R., Greenwood, S.L., Hughes, A.L.C., Dunlop, P., and Hess, D. 2016. Do subglacial bedforms comprise a size and shape continuum? Geomorphology, 257, 108-119.

Énergie et Ressources naturelles Québec. 2010. Summary on the Report on the mineral exploration July to August 2009, Quest Rare Minerals, George River Project, Nanuk Claims NTS 23P/16, Collins, P. and Cashin, J. Report GM 65368, available online: http://gq.mines.gouv.qc.ca/documents/EXAMINE/GM65368/GM65368.pdf

Evans, D.J.A., Phillips, E.R., Hiemstra, J.F., and Auton, C.A. 2006. Subglacial till: formation, sedimentary characteristics and classification. Earth-Science Reviews, 78(1-22): 115-176.

Fabel, D., Stoeven, A.P., Harbor, J., Kleman, J., Elmore, D., and Fink, D. 2002. Landscape preservation under Fennoscandian ice sheet determined from in situ produced 10Be and 26Al. Earth and Planetary Science letters, 201: 397-406.

Fabel, D., Harbor, J., Dahms, D., James, A., Elmore, D., Horn, L., Daley, K., and Steele, C. 2004. Spatial patterns of Glacial erosion at a valley scale derived from Terrestrial Cosmogenic 10Be and 26Al concentration in Rock. Annals of the Association of American Geographer, 94: 241-255.

Fedo, C.M., Nesbitt, H.W., and Young, G.M. 1995. Unraveling the effects of potassium metasomatism in sedimentary rocks and paleosols, with implications for paleoweathering conditions and provenance. Geology, 23: 921-924.

Fowler, A.C. 2009. Instability modelling of drumlin formation incorporating lee-side cavity growth. Proceedings of the Royal Society of London, Series A, 466(2121): 2673-2694.

Fowler, A.C. 2010. The formation of subglacial streams and mega-scale glacial lineations. Proceedings of the Royal Society of London, Series A, 466(2123):3181-3201.

Fowler, A.C. and Chapwanya, M. 2014. An instability theory for the formation of ribbed moraine, drumlins and mega-scale glacial lineations. Proceedings of the Royal Society A, 470. doi: 10.1098/rspa.2014.0185

Fu, P., Stroeven, A.P, Harbor, J.M., Heyman, J., Hätterstrand, C., and Caffee, M.M. 2018. Ice cap erosion patterns from bedrock 10Be and 26Al, southeastern Tibetan Plateau. Earth Surface Processes and Landforms, 44: 918-932. doi: 10.1002/esp.4544

Fuchs, M. and Owen, L.A. 2008. Luminescence dating of glacial and associated sediment: review, recommendations and future directions. Boreas, 37: 636-659.

Fulton, R.J. 1995. Surficial materials of Canada. Geological Survey of Canada, "A" Series, Map 1880A. 1: 5 000 000 scale.

Ganopolski, A., Calov, R., and Claussen, M. 2010. Simulation of the last glacial cycle with a coupled climate ice-sheet model of intermediate complexity. Climate of the Past, 6, 229-244.

Gauthier, M.S., Hodder, T.J., Ross, M., Kelley, S.E., Rochester, A., and McCausland, P. 2019. The subglacial mosaic of the Laurentide Ice Sheet; a study of the interior region of southwestern Hudson Bay. Quaternary Science Reviews, 214: 1-27.

Girard, R. 1995. Geologie de la region du lac Deborah, territoriore du Nouveau-Quebec. Ministere des Ressources naturelles, Quebec. MB 95-20: 185 p.

Girard, I., Klassen, R.A., and Laframboise, R.R. 2004. Laboratory Manual, Terrain Sciences Division. Geological Survey of Canada, Open File 4823. doi: 10.4095/216141

Goodfellow, B.W. 2007. Relict non-glacial surfaces in formally glaciated terrain. Earth-Science Reviews, 80 (1-2): 47-73.

Gosse, J.C. and Phillips, F.M. 2001. Terrestrial in situ cosmogenic nuclides: theory and application, Quaternary Science Reviews, 20: 1475-1560.

Greenwood, S.L. and Clark, C.D. 2009. Reconstructing the last Irish Ice Sheet 2: a geomorphologically-driven model of ice sheet growth, retreat and dynamics. Quaternary Science Reviews 28: 3101-3123.

Grunsky, E. 2002. R: a data analysis and statistical programming environment – an emerging tool for the geoscience, Computers and Geosciences, 28: 225-235.

Hart, J.K. and Smith, B. 1997. Subglacial deformation associated with fast ice flow, from the Columbia Glacier, Alaska, Sedimentary Geology, 111: 177-197.

Henderson, E.P. 1959. A glacial study of central-Labrador Quebec. Geological Survey of Canada, Bulletin, 40: 1-94.

Hickin, A.S., Lian, O.V., Levson, V.M., and Cui, Y. 2015. Pattern and chronology of glacial Lake Peace Shorelines and implications for isostacy and ice-sheet configuration in northeastern British Columbia, Canada. Boreas, 44: 228-304.

Hildes, D.H.D., Clarke, G.K.C., Flowers, G.E., and Marshall, S.J. 2004. Subglacial erosion and englacial sediment transport modelled for North American ice sheets. Quaternary Science Reviews, 23: 409-430.

Hillarie-Marcel, C., Occhietti, S., and Vincent, J-S. 1981. Sakami moraine, Quebec: A 500 km-long moraine without climatic control. Geology 9: 210-214, doi: 10.1130/0091-7613(1981)9<210:SMQAKM>2.0.CO;2

Hindmarsh, R.C.A. 1999. Coupled ice-till dynamics and the seeding of drumlins and bedrock forms. Annals of Glaciology, 28:221-230.

Hindmarsh, R.C.A., Boulton, G.S., and Hutter, K. 1989. Modes of operation of thermos-mechanically coupled ice sheets. Annals of Glaciology, 12:57-69.

Hodder, T.J., Ross, M.A., and Menzies, J. 2016. Sedimentary record of ice divide migration and ice streams in the Keewatin core region of the Laurentide Ice Sheet. Sedimentary Geology, 338: 97-114.

Hoffman, P.F. 1988. United plates of America, the birth of a craton: Early Proterozoic assembly and growth of Laurentia. Annual Review of Earth and Planetary Sciences, 16: 543-603.

Hughes, O.L. 1964. Surficial geology, Nichicun-Kaniapiscau Map-area. Geological Survey of Canada Bulletin, 106: 1-20.

Iverson, N.R. 2012. A theory of glacial quarrying for landscape evolution models. Geology, 40(8):679-682.

Iverson, N.R., Hanson, B., Hooke, R.L., and Jansson, P. 1995. Flow mechanism of Glaciers on Soft Beds. Science, 267 (5194): 80-81.

Ives, J.D. 1958. Glacial Drainage Channels as Indicators of Late-glacial Conditions in Labrador-Ungava: a Discussion. Cahiers de Geographie de Québec, 3: 57-72.

Ives, J.D. 1960a. The deglaciation of Labrador-Ungava- an outline. Cahiers de Geographie de Québec, 4: 323-343.

Ives, J.D. 1960b. Former ice-dammed lakes and the deglaciation of the middle reaches of the George River, Labrador-Ungava. Geographical Bulletin, 14: 44-69.

Ives, J., Nichols, H., and Short, S. 1976. Glacial history and palaeoecology of north eastern Nouveau-Quebec and northern Labrador. Arctic, 29: 48-52.

James, D.T., Nunn, G.A.G., Kamo, S., & Kwok, K. 2003. The southeastern Churchill Province revisited: U-Pb geochronology, regional correlations, and enigmatic Orman Domain. Newfoundland Department of Mines and Energy, Current Research 03-1, pp. 35-45.

Jansson, K.N. 2003. Early Holocene glacial lakes and ice marginal retreat pattern in Labrador/Ungava, Canada. Palaeogeography, Palaeoclimatology, Palaeoecology, 193(3-4), 473-501.

Jansson, K.N. 2005. Map of the glacial geomorphology of north-central Québec-Labrador, Canada. Jounral of Maps 1(1): 46-55.

Jansson, K.N., Kleman, J., and Marchant, D.R. 2002. The succession of ice-flow pattern in north central Quebec-Labrador, Canada. Quaternary Science Review, 21: 503-523.

Jansson, K.N., Stroeven, A.P., and Kleman, J. 2003. Configuration and timing of Ungava Bay ice streams, Labrador-Ungava, Canada. Boreas, 32: 256-262.

Jenner, G.A. 1996, Trace element geochemistry of igneous rocks: Geochemical nomenclature and analytical geochemistry, In Wyman, D.A., (ed.) Trace Element Geochemistry of Volcanic Rocks:

Applications for Massive Sulfide Exploration, 12, Geological Association of Canada, Short Course Notes: 51–77.

Jenskins, G.T.H., Duller, G.A.T., Roberts, H.M., Chiverell, R.C., and Glasser, N.F. 2018. A new approach to luminescence dating glaciofluvial deposits-high precision optical dating of cobbles. Quaternary Science Reviews, 192: 263-273.

Jorge, M.C. and Brennand, T.A. 2017. Measuring (subglacial) bedform orientation, length, and longitudinal asymmetry-Method assessment. PLoS ONE, 12. doi: 10.1371/journal.pone.0174312

Kelley, S.E., Ross, M., Elliot, B. and Normandeau, P.X. 2019. Effect of shifting ice flow and basal topography in shaping three-dimensional dispersal patterns, Lac de Gras region, Northwest Territories, Canada. Journal of Geochemical Exploration, 199: 105-127.

Kerr, A., James, D.T., and Fryer, B.J. 1994. Nd isotopic and geochemical studies in the Labrador Shield: a progress report and preliminary data from the Churchill (Rae) Province. In Eastern Canadian Shield Onshore- Offshore Transect (ECSCOOT), Wardle, R.J., and Hall, J. (eds.) Report of the transect meeting (Dec. 1994), The University of British Columbia, Lithoprobe Secretrait, Report 45: 51-62.

Kettles, I.M. and Shilts, W.W. 1989. Geochemistry of drift cover over the Precambrain Grenville Province, southeaster Ontario and southwestern Quebec. In: Drift Prospecting. R.N.W. DiLabrio and Coker, W.B. (eds) Geological Survey of Canada Paper 89-20, p. 97-112.

King, E.C., Hindmarsh, R.C.A., and Stokes, C.R. 2009. Formation of mega-scale glacial lineations observed beneath a west Antarctic ice stream. Nature geoscience, 2: 585-588.

King, E.C., Pritchard, H.D., and Smith, A.M. 2016. Subglacial landforms beneath Rutford Ice Stream, Antarctica: detailed bed topography from ice-penetrating radar. Earth Systems Science Data, 8, 151-158.

Kirby, R.P. 1961. Movements of ice in Central Labrador-Ungava. Cahiers de géographie du Québec, 5: 205-218.

Klasen, N., Fiebig, M., Preusser, F., and Radtke, U. 2006. Luminescence properties of glaciofluvial sediments from the Bavarian Alpine Foreland. Radiation Measurements, 41: 866-870.

Klassen, R.A. 1999. The application of glacial dispersal models to the interpretation of till geochemistry in Labrador, Canada. Journal of Geochemical Exploration, 67: 245-269.

Klassen, R.A. and Bolduc, A.M. 1984. Ice flow directions and drift composition, Churchill Falls, Labrador. Current Research. Geological Survey of Canada. Part A, 84-1A: 255-258.

Klassen, R.A. and Thompson, F.J. 1987. Ice flow history and glacial dispersal in the Labrador Trough. In Exploration technology and glacial dispersal studies, Geological Survey of Canada, Paper no. 87-1A: 61-710.

Klassen, R.A. and Thompson, F.J. 1993. Glacial history, drift composition, and mineral exploration, central Labrador, Geological Survey of Canada, Bulletin 435.

Klassen, R.A. and Paradis, S.J. 1990. Surficial geology, western Labrador (NTS 23 A, B, C, G, I, J and parts if 13 C, 22P, and 23 H. Geological Survey of Canada, Open File 2198.

Klassen, R.A., Matthews, J.V.J., Mott, R.J., and Thompson, F.J. 1988. The stratigraphic and paleobotanical record of Interglaciation in the Wabush region of western Labrador (abstract). In Climatic Fluctuations and Man 3, Annual Meeting of the Canadian Committee on Climatic Fluctuations. Jan. 18-19, Ottawa: 22-26.

Klassen, R.A., Paradis, S., Bolduc, A.M., and Thomas, R.D. 1992. Glacial landforms and deposits, Labrador, Newfoundland and eastern Quebec. Geological Survey of Canada, Map 1814A, scale 1:1000 000

Kleman, J. and Stroeven, A.P. 1997. Preglacial surface remnants and Quaternary glacial regimes in northwestern Sweden. Geomorphology, 19: 35-54.

Kleman, J. and Hatterstrand, C. 1999. Frozen-bed Fennoscandian and Laurentide ice sheets during the Last Glacial Maximum. Nature, 402 (6757): 63 – 66.

Kleman, J. and Glasser, N.F. 2007. The subglacial thermal organisation (STO) of ice sheets. Quaternary Science Reviews, 26: 585-597.

Kleman, J., Hätterstrand, C., Borgström, I., and Stroeven, A. 1997. Fennoscandian palaeoglaciology reconstructed using a glacial geological inversion model. Journal of Glaciology, 43 (144): 283-299.

Kleman, J., Fastook, J., and Stroeven, A.P. 2002. Geologically and geomorphologically constrained numerical model of Laurentide Ice Sheet inception and build-up. Quaternary International, 95: 87-98.

Kleman, J., Jansson, K., De Angelis, H., Stroeven, A.P., Hätterstrand, C., Alm, G. and Glasser, N. 2010. North American Ice Sheet build-up during the last glacial cycle, 115- 21 kyr. Quaternary Science Reviews, 29 (17-18): 2036-2051.

Krabbendam, M., and Glasser, N.F. 2011. Glacial erosion and bedrock properties in NW Scotland: abrasion and plucking, hardness and joint spacing. Geomorphology, 130: 374 - 383.

Krabbendam, M. and Bradwell, T. 2014. Quaternary evolution of glaciated gneiss terrains: pre-glacial weathering vs. glacial erosion. Quaternary Science Reviews, 95: 20-42.

Lafrance, I., Charette, B., and Vanier, M-A. 2018. Sud-est de la Province de Churchill, Nunavik, Québec Canada: synthèse de la géologie. Ministère de l'Énergie et des Ressources naturelles, Québec. http://gq.mines.gouv.qc.ca/bulletins-geologiques/churchill/#carto

Lal, D. 1991. Cosmic ray labeling of erosion surfaces: in situ production rates and erosion models. Earth and Planetary Science Letters, 104: 424-439.

Lepper, K., Buell, A.W., Fisher, T.G., and Lowell, T.V. 2013. A chronology for glacial Lake Agassiz along Upham's namesake transect. Quaternary Research, 80: 88-98.

Levson, V.M. 2001. Quaternary geology of the Babine porphyry copper district: implications for geochemical exploration. Canadian Journal of Earth Sciences, 38: 733-749.

Levson, V.M. and Giles, T.R. 1997. Quaternary geology and till geochemistry studies in the Nechako and Fraser Plateaus, central British Columbia. In Interior Plateau Geoscience Project: Summary of Geological, Geochemical and Geophysical Studies, Diakow, L.J., and Newell, J.M. (eds.) Geological Survey of Canada, Open File 3448.

Lewington, E.L.M., Livingstone, S.J., Clark, C.D., Sole, A.J., and Storrar, R.D. 2020. Large-scale integrated subglacial drainage around the former Keewatin Ice Divide, Canada reveals interaction between distributed and channelized systems. The Cryosphere. doi: 10.5194/tc-2020-10

Li, Y., Harbor, J., Stroeven, A.P., Fabel, D., Kleman, J., Fink, D., Caffee, M., and Elmore, D. 2005. Ice sheet erosion patterns in valley systems in northern Sweden investigated using cosmogenic nuclides. Earth Surface Processes and Landforms, 30: 1039-1049.

Lian, O.B. 2013. Luminescence dating: optical dating. In Encyclopedia of Quaternary Science, Elias, S.A. (ed). Elsevier, Amsterdam: 653-666.

Lifton, N., Beel, C., Hätterstrand, C., Kassab, C., Rogozhina, I., Heermance, R., Oskin, M., Burbank, D., Blomdin, R., Gribenski, N., Caffe, M., Goehring, B.M., Heyman, J., Ivanov, M., Li, Y., Li, Y., Petrakov, D., Usualiev, R., and Stroeve, A.P. 2014. Constraints on the late Quaternary glacial history of the Inylcheck and Sary-Dzaz valleys from in situ cosmogenic 10Be and 26Al, eastern Kyrgyz Tian Shan. Quaternary Science Reviews, 101: 77-90.

Linge, H., Brook, E.J., Nesje, A., Raisbeck, G.M., Yiou, F., and Clark, H. 2006. In situ 10Be exposure ages from southeastern Norway: implications for the geometry of the Weichselian Scandinavian ice sheet. Quaternary Science Reviews, 25(9-10), 1097-1109.

Linton, D.L. 1963. The forms of Glacial Erosion. Transactions and papers (Institute of British Geographers), No. 33: 1-22. doi: 10.2307/620998

Livingston, S.J., Storrar, R.D., Hilier, J.K., Stokes, C.R., Clark, C.D., and Tarasov, L. 2015. An ice-sheet scale comparison of eskers with modelled subglacial drainage routes. Geomorphology, 246, 104-112.

Löfverström, M., Caballero, R., Nilsson, J., and Kleman, J. 2014. Evolution of the large-scale atmospheric circulation in response to changing ice sheets over the last glacial cycle. Climate of the past, 10: 1453-1471

Low, A.P. 1896. Report on exploration in the Labrador Peninsula along the Eastmain, Koksoak, Hamilton, Manikuagan and portions of other rivers in 1982-93-94-95. Geological Survey of Canada, Annual Report, 8: Part L.

Margold, M., Stokes, C.R., and Clark, C.D. 2015. Ice streams in the Laurentide Ice Sheet: Identification, characteristics and comparisons to modern ice sheets. Earth Science Reviews, 143: 117-146.

Margold. M., Stokes, C.R., and Clark, C.D. 2018. Reconciling records of ice streaming and ice margin retreat to produce a paleographic reconstruction of the deglaciation of the Laurentide Ice Sheet. Quaternary Science Reviews, 189: 1-30.

Marquette, G.C., Gray, J.T., Gosse, J.C., Courchesne, F., Stockli, L., Macpherson, G., and Finkel, R. 2004. Felsenmeer persistence under non-erosive ice in the Torngat and Kaumejet mountains, Quebec and Labrador, as determined by weathering and cosmogenic nuclide exposure dating. Canadian Journal of Earth Sciences, 41: 19-38.

Marshall, S.J. and Clark, P.U. 2002. Basal temperature evolution of North American ice sheets and implications for the 100-kyr cycle. Geophysical Research Letters, 29: 67-1-67-4.

Martelain, J., Chenevoy, M., and Bélanger, M. 1998. Le Batholite de De Pas, Noveau-Québec: infratstructure composite d'arc magmatique protéroïque. Canadian Journal of Earth Sciences, 35: 1-15.

Mathewes, R.W., Lian, O.B., Claguem J,J., and Huntleym M,J,W. 2015. Early Wisconsinan (MIS 4) glaciation on Haida Gwaii, British Columbia, and implications for biological refugia. Canadian Journal of Earth Science, 52: 939-951.

McClenaghan, M.B. 2001. Regional and local-scale gold grain and till geochemical signatures of lode Au deposits in the western Abitibi Greenstone Belt, central Canada. In: McClenaghan, M.B., Bobrowsky, P.T., Hall, G.E.M. and Cook, S.J. (eds), Drift Exploration in Glaciated Terrain, Geological Society Special Publication 185: 201-223

McClenaghan, M.B. 2005. Indicator mineral methods in mineral exploration. Geochemistry: Exploration, Environment, Analysis, v 5: 233–245.

McClenaghan, M.B. and Paulen. R.C. 2018. Application of till mineralogy and geochemistry to mineral exploration. In Past Glacial Environments 2nd Edition, Menzies, J. van der Meer, J. (eds), Elsevier.

McClenaghan, M.B., Kjarsgaard, I.M., Schulze, D.J., Stirling, J.A.R., Pringle, G., and Berger, B.R. 1996. Mineralogy and geochemistry of the B30 kimberlite and overlying glacial sediments, Kirkland Lake, Ontario. Geological Survey of Canada, Open File 3295, 245 p.

McClenaghan, M.B., Thorleifson, L.H., and DiLabio, R.N.W. 2000. Till geochemical and indicator mineral methods in mineral exploration. Ore Geology Reviews, 16:145-166.

McClenaghan, M.B., Ward, B.C., Kjarsgaard, I.M., Kjarsgaard, B.A., Kerr, D.E., and Dredge, L.A. 2002. Indicator mineral and till geochemical dispersal patterns associated with the Ranch Lake Kimberlite, Lac de Gras region, NET, Canada. Geochemistry: Exploration, Environment, Analysis, 2: 299-319.

McClenaghan, M.B., Plouffe, A., McMartin, I., Campbell, J.E., Spirito, W.A., Paulen, R.C., Garrett, R.G., and Hall, G.E.M. 2013. Till sampling and geochemical analytical protocols used by the Geological Survey of Canada. Geochemistry: Exploration, Environment, Analysis, 13: 285-301.

McClenaghan, M.B., Plouffe, A., Paulen, R.C., Houlé, M.G., Jackson, S.E., and Peter, J.M. 2015. Overview of Indicator mineral Research at the Geological Survey of Canada- An Update. Explore, 170.

McClenaghan, M.B., Paulen, R.C., Rice, J.M., McCurdy, M.W., Amor, S.D., Garrett, R.G., Solgadi, F., Fortin, R., Spirito, W.A., Adcock, S.W., Ross, M., Campbell, H.E., Pyne, M., Hagedorn, G.Q., and Arnaud, E. 2017. GEM 2 Hudson-Ungava project 2017 report of activities for the Core Zone: surficial geology, geochemistry, and gamma-ray spectrometry studies in northern Quebec and Labrador. Geological Survey of Canada, Open File 8331.

McClenaghan, M.B., Paulen, R.C., and Kjarsgaard, I.M. 2019. Rare metal indicator minerals in bedrock and till at the Strange Lake peralkaline complex, Quebec and Labrador, Canada. Canadian Journal of Earth Sciences, 56(8): 857-869.

McMartin, I. and Henderson, P. 2004. Evidence from Keewatin (Central Nunavut) for paleo-ice divide migration. Geographie Physique et Quaternaire, 58: 163-186.

McMartin, I. and Campbell, J.E. 2009. Near surface till sampling protocols in shield terrain, with examples from western and northern Canada. In: Paulen, R.C., McMartin, I. (eds.), Application of till and stream sediment heavy mineral and geochemical methods to Mineral Exploration in Western and Northern Canada. Geological Association of Canada, Canada, Short Course Notes 18: 75-79.

McMartin, I. and Paulen, R.C. 2009. Ice-flow indicators and the importance of ice-flow mapping for drift prospecting. In Application of Till and Stream Sediment Heavy Mineral and Geochemical Methods to Mineral Exploration in Western and Northern Canada, Paulen RC, McMartin I (eds). Geological Association of Canada, Short Course Notes, 18:15-34.

Melanson, A., Bell, T., and Tarasov, L. 2013. Numerical modelling of subglacial erosion and sediment transport and its application the North American ice sheets over the Last Glacial cycle. Quaternary Science Reviews, 68: 154-174. doi: 10.1016/j.quascirev.2013.02.017

Menzies, J., Hess, D.P., Rice, J.M., Wagner, K.G., and Ravier, E. 2016. A case study in the New York Drumlin Field, an investigation using microsedimentology, resulting in the refinement of a theory of drumlin formation. Sedimentary Geology, 338: 84-96.

Miller, G.H., Briner, J.P., Lifton, N.A., and Finkel, R.C. 2006. Limited ice-sheet erosion and complex exposure histories derived from in situ cosmogenic 10Be, 26Al, and 14C on Baffin Island, Arctic Canada. Quaternary geochronology, 1(1), 74-85.

Mollard, J.O. and James, R. 1984. Air photo interpretation and the Canadian landscape. Canadian Government Publishing Centre, Hull, Canada, p.415.

Napieralksi, J., Hubbard, A., Li, Y., Harbor, J., Stroeven, A.P., Kleman, J., Alm, G., and Jansson, K.N. 2007. Toward a GIS assessment of numerical ice-sheet model performance using geomorphological data. Journal of Glaciology, 53: 71-83.

Nesbitt, H.W. and Young, G.M. 1982. Early Proterozoic climates and plate motions inferred from major element chemistry of lutites. Nature, 299: 715-717.

Occhietti, S., Govare, É., Klassen, R., Parent, M., and Vincent, J-S. 2004. Late Wisconsinan –Early Holocene deglaciation of Québec-Labrador. In Quaternary glaciations, Extent and chronology Part II: North America, Ehlers J, Gibbard PL (eds). Elsevier, New York.

Occhietti, S., Parent, M., Lajeunesse, P., Robert, F., and Govare, É. 2011. Chapter 47- Late Pleistocene-Early Holocene Decay of the Laurentide Ice Sheet in Quebec-Labrador. Developments in Quaternary Science, 15: 601-630.

Parent, M., Paradis, S.J., and Boisvert, É. 1995. Ice-flow patterns and glacial transport in the eastern Hudson Bay region: implications for the Late Quaternary dynamics of the Laurentide Ice Sheet. Canadian Journal of Earth Sciences, 32: 2057-2070.

Parent, M., Paradis, S., and Doiron, A. 1996. Palimpsest glacial dispersion trains and their significance to drift prospecting. Journal Geochemical Exploration, 56: 123-140.

Parent, M., Beaumier, M., Girrard, R., and Paradis, S.J. 2004. Diamond exploration in the Archean craton of northern Québec Kimberlite indicator minerals in eskers of the Saindon-Cambrian corridor. Quebec Ministry of Natural Resources, Fauna and Parks, Manuscript 2004-02.

Paulen, R.C. and McMartin, I. 2009. Application of Till and Stream Sediment Heavy Mineral and Geochemical Methods to Mineral Exploration in Western and Northern Canada. Geological Association of Canada, Shor Course Notes 18.

Paulen, R.C., McClenaghan, M.B., and Hicken, A.K. 2013. Regional and local ice-flow history in the vicinity of the Izok Lake Zn-Cu-Pb-Ag deposit, Nunavut. Canadian Journal of Earth Sciences, 50: 1209-1222.

Paulen, R.C., Rice, J.M., and McClenaghan, M.B. 2017. Surficial geology northwest Smallwood Reservoir, Newfoundland and Labrador NTS 23-I southeast. Geological Survey of Canada Geoscience Map 315, scale: 1: 100 000.

Peltier, W.R., Argus, D.F., and Drummond, R. 2015. Space geodesy constrains ice age terminal deglaciation: The global Ice-6G_C (VM5a) model, Journal of Geophysical Research: Solid Earth, 120: 450-487.

Phillips, E., Everest, J., and Diaz-Doce, D. 2010. Bedrock controls on subglacial landform distribution and geomorphological process: evidence from the Late Devensian Irish Sea Ice Stream. Sedimentary Geology, 232: 98-118.

Pickler, C., Beltrami, H., and Mareschal, J-C. 2016. Laurentide Ice Sheet basal temperatures during the last glacial cycle as inferred from borehole data. Climate of the Past, 12(10): 115-127.

Piercey, S.J. 2014. Modern Analytical Facilities 2. A review of Quality Assurance and Quality Control (QA/QC) Procedures for lithogeochemical Data. Geoscience Canada, 42: 75-88.

Piotrowski, J.A., Larsen, N.K., Menzies, J., and Wysota, W. 2006. Formation of subglacial till under transient bed conditions: deposition, deformation, and basal decoupling under Weichselian ice sheet lobe, Poland. Sedimentology, 53(1): 83-106.

Plouffe, A., McClenaghan, M.B., Paulen, R.C., McMartin, I., Campbell, J.E., and Spirito, W.A. 2013. Processing of unconsolidated glacial sediments for the recovery of indicator minerals: Protocols used at the Geological Survey of Canada. Geochemistry: Exploration, Environment, Analysis, 13: 303-316.

Plouffe, A., Ferebey, T., Hashmi, S., and Ward, B.C. 2016. Till geochemistry and mineralogy: vectoring towards Cu porphyry deposits in British Columbia, Canada. Geochemistry: Exploration, Environment, Analysis, 16: 213-232.

Prest, V.K., Donaldson, J.A., and Mooers, H.D. 2000. The omar story: the role of omars in assessing glacial history of west-central North America. Géographie Physique et Quaternaire, 54(3):257-270.

Principato, S.M. and Johnson, J.S. 2009. Using a GIS to quantify patterns of glacial erosion on northwest Iceland: Implications for independent ice sheets. Arctic, Antarctic, and Alpine Research, 41: 128-137.

R Core Team. 2015. R: A language and environment for statistical computing. R Foundation for Statistical Computing, Vienna, Austria. URL www.R-project.org.

Rea, B.R., Evans, D.J.A., Dixon, T.S., and Whalley, W.B. 2000. Contemporaneous, localized, basal ice-flow variations: implications for bedrock erosion and the origin of p-forms. Journal of Glaciology, 46: 470-476.

Refsnider, K.A. and Miller, G.H. 2010. Reorganization of ice sheet flow patterns in Arctic Canada and the mid-Pleistocene transition. Geophysical Research Letter, 37: 1-5.

Rice, J.M., Paulen, R.C., and Ross, M. 2017a. Surficial geology, Lac Mistinibi, Quebec, NTS 23-P northeast. Geological Survey of Canada. Canadian Geoscience Map 316.

Rice, J.M., Paulen, R.C., and Ross M. 2017b. Surficial geology, Rivière De Pas, Quebec, NTS 23-P northwest. Geological Survey of Canada, Canadian Geoscience Map 333.

Rice, J.M., McClenaghan, M.B., Paulen, R.C., Pyne, M.D., and Ross, M. 2017c. Till geochemical data for the southern Core Zone, Quebec and Newfoundland and Labrador (NTS 23-P and 23-I): samples collected in 2015 and 2016. Geological Survey of Canada, Open File 8219, doi: 10.4095/304280

Rice, J.M., Ross, M., Paulen, R.C., Kelley, S.A., Briner, J.P., Neudorf, C.M., and Lian, O.B. 2019. Refining the ice-flow chronology and subglacial dynamics across the migrating Labrador Divide of the Laurentide Ice sheet with age constraints on deglaciation. Quaternary Science Reviews, 10.1002/jqs.3138

Rice, J.M., Ross, M., Paulen, R.C., Kelley, S.E., and Briner, J.P. *submitted.* A GIS-based multi-proxy analysis of the evolution of subglacial dynamics of the Quebec-Labrador ice dome, northeastern Quebec, Canada. Earth Surfaces Processes and Landforms.

Rice, J.M., Ross, M., and Paulen, R.C. 2020. The Cabot Lake ice stream: a Paleo-ice stream near the Ancestral Labrador Ice Divide of the Laurentide Ice Sheet's Quebec-Labrador Dome. Geological Survey of Canada Scientific Presentation 109. doi: 10.4095/321077

Ringnot, E., Mouginot, J., and Scheuchl, B. 2011. Ice Flow of the Antarctic Ice Sheet. Science, 333: 1427-1430.

Ross, M., Campbell, J.E., Parent, M., and Adams, R.S. 2009. Palaeo-ice streams and the subglacial landscape mosaic of the North American mid-continental prairies. Boreas, 38(3): 421-239.

Ross, M., Lajeunesse, P., and Kosar, K.G.A. 2011. The subglacial record of northern Hudson Bay: insights into the Hudson Strait Ice Stream catchment. Boreas, 40: 73-91.

Roy, M., Hemming, S.R., and Parent, M. 2009. Sediment sources of northern Québec and Labrador glacial deposits and the northeastern sector of the Laurentide Ice Sheet during ice-rafting events of the last glacial cycle. Quaternary Science Reviews, 28(27-28): 3236-3245.

Roy, M., Veillette, J.J., Daubois, V., and Ménard, M. 2015. Late-stage phases of glacial Lake Ojibway in the central Abitibi region, eastern Canada, Geomorphology, 248: 14-23, doi: 10.1016/j.geomorph.2015.07.026

Sanborn-Barrie, M. 2016. Refining lithological and structural understanding of the southern Core Zone, northern Quebec and Labrador in support of mineral resource assessment. Geological Survey of Canada, Open File 7956. doi: 10.4095/297560

Scrucca, L. 2004. qcc: an R package for quality control charting and statistical process control. R News 4/1, 11-17.

Shepard, F.P. 1954. Nomenclature based on sand-silt-clay ratios. Journal of Sedimentary Research, 24(3):151-158.

Shilts, W.W. 1995. Geochemical partitioning in till. In Bobrowsky, P.T., Sibbick, J.M., Newell, J.M., and Maysek, P.F (Eds.), Drift Exploration in the Canadian Cordillera. British Columbian Ministry of Energy, Mines and Petroleum resources, Paper 1995-2, p. 149-163.

Shilts, W.W. 1996. Drift Exploration. In: J. Menzies (Ed.) Glacial Environments, Sediment Forms and Techniques, Butterword Hienemann, pp. 411-439.

Shilts, W.W., Aylsworth, J.M., Kaszycki, C.A., and Klassen, R.A. 1987. Canadian Shield. In Geomorphic systems in North America, Graf WL (ed). Geological Society of America, centennial Special Volume 2: 119-161.

Smith, M.J. and Knight, J. 2011. Palaeoglciology of the last Irish ice sheet reconstructed from striae evidence. Quaternary Science Reviews 30:147-160

Smith, S. 2010. Trends in permafrost conditions and the ecology in northern Canada. Canadian Biodiversity: Ecosystems status and Trends 2010, Canadian Councils of Resource Ministers Technical Thematic Report No. 9.

Sookhan, S., Eyles, N., and Putkinen, N. 2016. LiDAR- based volume assessment of the origin of the Wadena drumlin field, Minnesota, USA. Sedimentary Geology, 338: 72-83.

Sookhan, S., Eyles, N., and Arbelaez-Moreno, L. 2018. Converging ice streams: a new paradigm for reconstructions of the Laurentide Ice Sheet in southern Ontario and deposition of the Oak Ridges Moraine. Canadian Journal of Earth Science, 55: 373-396.

Staiger, J.K.W., Gosse, J.C., Johnson, J.V., Fastook, J., Gray, J.R., Stockli, D.F., Stockli, L., and Finkel, R. 2005. Quaternary relief generation by polythermal glacier ice. Earth Surface processes and Landforms, 30: 1145-1159.

Staiger, J.W., Gosse, J., Little, E.C., Utting, D.J., Finkel, R., Johnson, J.V., and Fastook, J. 2006. Glacial erosion and sediment dispersion from detrital cosmogenic nuclide analyses of till. Quaternary Geochronology, 1: 29-42.

Stea, R.R., 1994. Relict and palimpsest glacial landforms in Nova Scotia, Canada. In Warren, W.P. and Croot, D.G. (Eds.), Formation and Deformation of Glacial Deposits. A.A. Balkema, Rotterdam, 141-158.

Stea, R.R., and Finck, P.W. 2001. An evolutionary model of glacial dispersal and till genesis in Maritime Canada. In: McClenaghan, M.B., Bobrowsky, P.T., Hall, G.E.M., and Cook, S.J. (eds) Drift exploration in Glaciated Terrain. Geological Society Special Publication 185: 237-265.

Stokes, C.R. and Clark, C.D. 2001. Paleo-ice streams. Quaternary Science Reviews, 20: 1437-1457.

Stokes, C.R. and Clark, C.D. 2002. Are long subglacial bedforms indicative of fast ice flow? Boreas, 31: 239-249.

Stokes, C.R., Clark, C.D., Lian, O.B., and Tulaczyk, S. 2007. Ice stream sticky sort: a review of their identification and influence beneath contemporary and palaeo-ice streams. Earth-Science Reviews, 81: 217-249.

Stokes, C.R., Tarasov, L., and Dyke, A.S. 2012. Dynamics of the North American Ice Sheet Complex during its inception and build-up to the Last Glacial Maximum. Quaternary Science Reviews, 50: 86-104.

Stokes, C.R., Spagnolo, M., Clark, C.D., Ó Cofaigh, C., Lian, O.B., and Dunstone, R.B. 2013. Formation of mega-scale glacial lineations on the Dubawnt Lake Ice Stream bed: 1. Size, shape and spacing from a large remote sensing dataset. Quaternary Science Review, 77:190-209.

Stroeven, A.P., Fabel, D., Codilean, A.T., Kleman, J., Clague, J.J., Miguens-Rodriguez, M., and Xu, S. 2010. Investigating the glacial history of the northern sector of the Cordilleran Ice Sheet with cosmogenic 10Be concentrations in quartz. Quaternary Science Reviews, 29(25-26), 3630-3643.

Sugden, D.E. 1978. Glacial Erosion by the Laurentide Ice Sheet. Journal of Glaciology, 20: 367-391.

Tarasov, L. and Peltier, W.R. 2004. A geophysically constrained large ensemble analysis of the deglacial history of the North American ice-sheet complex. Quaternary Science Reviews, 23 (3-4): 359-388.

Tarasov, L., Dyke, A.S., Neal, R.M., and Peltier, W.R. 2012. A data-calibrated distribution of deglacial chronologies for the North American ice complex from glaciological modeling. Earth and Planetary Science Letters, 15: 30-40.

Tremblay, T. 2017. Advances in the surficial geology of the Boothia Peninsula, central Nunavut. Canada-Nunavut Geoscience office, Summary of Activities. NRCan Contribution #20170272

Tremblay, T., Leblanc-Dumas, J., Allard, M., Ross, M., and Johnson, C. 2013. Surficial geology of central Hall Peninsula, Baffin Island, Nunavut: summary of 2013 field season. In: Summary of Activities 2013, Canada-Nunavut Geoscience Office, pp. 109-120.

Trommelen, M.S. and Ross, M. 2014. Distribution and type of sticky spots at the centre of a deglacial streamlined lobe in northeaster Manitoba, Canada. Boreas, 43: 557-576.

Trommelen, M.S., Ross, M., and Campbell, J.E. 2012. Glacial terrain zone analysis of a fragmented paleoglacioloic record, southeast Keewatin sector of the Laurentide Ice Sheet. Quaternary Science Reviews, 40: 1-20.

Trommelen, M.S., Ross, M., and Campbell, J.E. 2013. Inherited clast dispersal patterns: Implications for palaeoglaciology of the SE Keewatin Sector of the Laurentide Ice Sheet. Boreas, 42: 693-713.

Trommelen, M.S., Hodder, T.J., Ross, M. Kelley, S.E., Rochester, A., and McCaulsand, P. 2019. The subglacial mosaic of the Laurentide Ice Sheet; a study of the interior region of southwestern Hudson Bay. Quaternary Science Reviews, 214: 1-27.

Turner, R.G. and Stea, R.R. 1990. Interpretation of till geochemical data in Nova Scotia, Canada using mapped till units, multi-element anomaly patterns, and the relationship of till clast geology to matrix geochemistry. Journal of Geochemical Exploration, 37: 225-254.

Ullman, D.J., Carlson, A.E., Anslow, F.S., LeGrande, A.N., and Licciardi, J.M. 2015. Laurentide ice-sheet instability during the last deglaciation. Nature Geoscience, 8: 534-537.

Ullman, D.J., Carlson, A.E., Hostetler, S.W., Clark, P.U., Cuzzone, J., Milne, G.A., Winsor, K., and Caffee, M. 2016. Final Laurentide ice-sheet deglaciation and Holocene climate-sea level change. Quaternary Science Reviews, 152: 49-59.

United States Geological Survey. (2014). Shuttle Radar Topography Mission, 1 arc second scene SRTM1N55W065V3, SRTM1N55W066V3, 23 September, 2014.

van den Broeke, M., Box, J., Fettweis, X., Hanna, E., Noël, B., Tedesco, M., van de Berg, W. and van Kampenhout L. 2017. Greenland Ice sheet surface Mass Loss: Recent Developments in Observation and Modeling. Glaciology and Climate Change, 3: 345-356.

van der Leeeden, J., Belanger, M., Danis, D., Girad, R., and Martelain, J. 1990. Lithotectonic domains in the high-grade terrain east of the Labrador Trough (Quebec). In Lewry, J.F., and Stauffer, M.R. (eds.) The Early Proterozoic Trans-Hudson Orogen of North America. Geological Association of Canada, Special Paper, 37: 371-386.

Veillette, J.J. and Roy, M. 1995. The spectacular cross-striated outcrops of James Bay, Quebec. In Current Research 1995-C. Geological survey of Canada: 243-248.

Veillette, J.J., Dyke, A.S., and Roy, M. 1999. Ice-flow evolution of the Labrador Sector of the Laurentide Ice Sheet: a review, with new evidence from northern Quebec. Quaternary Science Reviews, 18: 993-1019.

Vincent, J-S. 1989. Quaternary geology of the southeastern Canadian Shield: In Chapter 3 of Quaternary Geology of Canada and Greenland, Fulton RJ (ed). Geological Survey of Canada, Geology of Canada, no.1.

Wardle, R.J., James, D.T., and Hall, J. 2002. The southeastern Churchill Province: synthesis of a Paleoproterozoic transpressional orogen. Canadian Journal of Earth Sciences, 39: 369-366.

Wickham, H. 2009. Ggplot2: elegant graphics for data analysis. Springer New York, 2009.

Young, N.E., Schaefer, J.M., Briner, J.P., and Goehring, B.M. 2013. A Be-10 production rate calibration for the Arctic. Journal of Quaternary Science, 28: 515-526.

Yu, P., Eyles, N., and Sookhan, S. 2015. Automated drumlin shape and volume estimation using high resolution LiDAR imagery (Curvature Based Relief Separation): A test from the Wadena Drumlin Field, Minnesota. Geomorphology, 246: 589-601.

Ullman, D.J., Carlson, A.E., Anslow, F.S., LeGrande, A.N., and Licciardi, J.M. 2015. Laurentide ice-sheet instability during the last deglaciation. Nature Geoscience, 8: 534-537.

Ullman, D.J., Carlson, A.E., Hostetler, S.W., Clark, P.U., Cuzzone, J., Milne, G.A., Winsor, K., and Caffee, M. 2016. Final Laurentide ice-sheet deglaciation and Holocene climate-sea level change. Quaternary Science Reviews, 152: 49-59.

United States Geological Survey. (2014). Shuttle Radar Topography Mission, 1 arc second scene SRTM1N55W065V3, SRTM1N55W066V3, 23 September, 2014.

van den Broeke, M., Box, J., Fettweis, X., Hanna, E., Noël, B., Tedesco, M., van de Berg, W. and van Kampenhout L. 2017. Greenland Ice sheet surface Mass Loss: Recent Developments in Observation and Modeling. Glaciology and Climate Change, 3: 345-356.

van der Leeeden, J., Belanger, M., Danis, D., Girad, R., and Martelain, J. 1990. Lithotectonic domains in the high-grade terrain east of the Labrador Trough (Quebec). In Lewry, J.F., and Stauffer, M.R. (eds.) The Early Proterozoic Trans-Hudson Orogen of North America. Geological Association of Canada, Special Paper, 37: 371-386.

Veillette, J.J. and Roy, M. 1995. The spectacular cross-striated outcrops of James Bay, Quebec. In Current Research 1995-C. Geological survey of Canada: 243-248.

Veillette, J.J., Dyke, A.S., and Roy, M. 1999. Ice-flow evolution of the Labrador Sector of the Laurentide Ice Sheet: a review, with new evidence from northern Quebec. Quaternary Science Reviews, 18: 993-1019.

Vincent, J-S. 1989. Quaternary geology of the southeastern Canadian Shield: In Chapter 3 of Quaternary Geology of Canada and Greenland, Fulton RJ (ed). Geological Survey of Canada, Geology of Canada, no.1.

Wardle, R.J., James, D.T., and Hall, J. 2002. The southeastern Churchill Province: synthesis of a Paleoproterozoic transpressional orogen. Canadian Journal of Earth Sciences, 39: 369-366.

Wickham, H. 2009. Ggplot2: elegant graphics for data analysis. Springer New York, 2009.

Young, N.E., Schaefer, J.M., Briner, J.P., and Goehring, B.M. 2013. A Be-10 production rate calibration for the Arctic. Journal of Quaternary Science, 28: 515-526.

Yu, P., Eyles, N., and Sookhan, S. 2015. Automated drumlin shape and volume estimation using high resolution LiDAR imagery (Curvature Based Relief Separation): A test from the Wadena Drumlin Field, Minnesota. Geomorphology, 246: 589-601.

Acknowledgments

Surficial mapping was undertaken under the Geomapping for Energy and Minerals (GEM) in collaboration with Ministère de l'Énergie et des Ressources naturelles du Québec (MERNQ), the Geological Survey of Newfoundland and Labrador (GSNL), and the University of Waterloo. This research benefitted from the support of the Polar Continental Shelf Program. Financial assistance, as part of J. Rice's Ph.D. thesis, was also provided through the Northern Scientific Training Program on behalf of the Canadian Polar Commission. A. Lion (University of Ottawa), E. Rufiange (University of Ottawa), and M.B. McClenghan (GSC Ottawa) are thanked for their support and assistance in the field. M. Pyne (GSC Ottawa) and G. Huot-Vézina (GSC Quebec) are thanked for GIS and database support. C. Neudorf and O. Lian (University of the Fraser Valley) analyzed the glaciolacustrine beach sediments for Optically Stimulated Luminescence (OSL) dates.

References

Clark, P.U. and Fitzhugh, W.W., 1990. Late deglaciation of the central Labrador coast and its implications for the age of glacial lakes Naskaupi and McLean and for prehistory; Quaternary Research, 34, p. 296–305.

Ives, J.D. 1958. Glacial drainage channels as indicators of late-glacial conditions in Labrador-Ungava: a discussion; Cahiers de géographie du Québec 3, no. 5, p. 57–72.

Ives, J.D. 1960. Former ice-dammed lakes and the deglaciation of the middle reaches of the George River, Labrador-Ungava; Geographical Branch, Department of Mines and Technical Surveys, Geographical Bulletin, 14, p. 44–70.

Jansson, K.N., 2003. Early Holocene glacial lakes and ice marginal retreat pattern in Labrador/Ungava, Canada; Palaeogeography, Palaeoclimatology, Palaeoecology, 193, p. 473–501.

Jansson, K.N., Kleman, J., and Marchant, D.R., 2002. The succession of ice-flow patterns in north-central Québec-Labrador; Quaternary Science Reviews, 21, p. 503–523.

Klassen, R.A. and Thompson, F.J., 1993. Glacial history, drift composition, and mineral exploration, central Labrador; Geological Survey of Canada, Bulletin 435, 82 p. doi:10.4095/183906

Klassen, R.A., Paradis, S., Bolduc, A.M., and Thomas, R.D., 1992. Glacial landforms and deposits, Labrador, Newfoundland and eastern Québec; Geological Survey of Canada, Map 1814A, scale 1:1 000 000. doi:10.4095/183872

Occhietti, S., Govare, É., Klassen, R., Parent, M., and Vincent, J.S., 2004. Late Wisconsinan—Early holocene deglaciation of Québec-Labrador; in Quaternary glaciations — extent and chronology, Part II: North America, (ed.) J.J. Ehlers and P.L. Gibbard, Elsevier B.V., Amsterdam, Development in Quaternary Science Series, v. 2, p. 237–267.

Veillette, J.J., Dyke, A.S., and Roy, M., 1999. Ice-flow evolution of the Labrador Sector of the Laurentide Ice Sheet: a review, with new evidence from northern Quebec; Quaternary Science Reviews, 18, p. 993–1019.

Map no.	Station	Latitude	Longitude	Elevation (m)	Corrected Age
1	15PTA-149	55.8384	-64.3245	486	7.93 ± 0.72 ka
2	15PTA-074	55.8387	-64.9888	314	7.65 ± 0.99 ka

Table 1. Corrected ages by Optical Stimulated Luminescence (OSL) from fine-grained glaciolacustrine littoral sediments of glacial Lake Naskaupi.

Abstract

The Lac Mistinibi area is of moderate relief characterized by extensive till blankets and at higher elevations, till veneers and bedrock outcrops. The region was glaciated by the Laurentide Ice Sheet throughout Wisconsin time, east of the Quebec-Labrador ice centre. Two general phases of glacial landform development have occurred in the map-area, with northeast-trending large crag-and-tail landforms and streamlined eastward-trending landforms. These two orientations represent two phases of radial ice flow that have affected the region. Large eskers and related glaciofluvial deposits also transect the map sheet along west to east direction, indicative of the westward deglaciation of the region. Abundant, small meltwater channels in the upland areas of the region are evidence of late-phase ice ablation during final deglaciation. Below 488 m elevation, the region was inundated by glacial Lake Naskaupi, which occupied the George River basin and its tributaries and winnowed till surfaces.

Résumé

La région cartographique de Lac Mistinibi est une région au relief modéré, caractérisée par des nappes de till étendues et, aux altitudes plus élevées, par des placages de till et des affleurements du substratum rocheux. La région a été couverte par les glaces de l'Inlandsis laurentidien au cours du Wisconsinien, à l'est du centre glaciaire Québec-Labrador. Deux phases générales de formation de reliefs glaciaires ont eu lieu dans la région cartographique, produisant de vastes structures en crag-and-tail de direction nord est et des reliefs profilés de direction est. Ces deux directions rendent compte de deux phases d'écoulement glaciaire radial ayant touché la région. De grands eskers et des dépôts fluvioglaciaires connexes s'étirent aussi de l'ouest vers l'est dans la région cartographique, ce qui témoigne d'une progression vers l'ouest de la déglaciation de la région. De petits chenaux d'eau de fonte en abondance dans les secteurs élevés de la région sont des preuves d'une ablation glaciaire de phase tardive lors de la déglaciation finale. En deçà d'une altitude de 488 m, la région a été inondée par le Lac glaciaire Naskaupi, qui occupait le bassin de la rivière George et ses affluents et qui a vanné les surfaces de till.

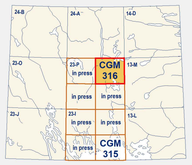

National Topographic System reference and index to adjoining published Geological Survey of Canada maps

Catalogue No. M183-1/316-2017E-PDF
ISBN 978-0-660-08105-2
doi:10.4095/300656

Natural Resources Canada | Ressources naturelles Canada

CANADIAN GEOSCIENCE MAP 316

SURFICIAL GEOLOGY

LAC MISTINIBI

Quebec

NTS 23-P northeast

1:100 000

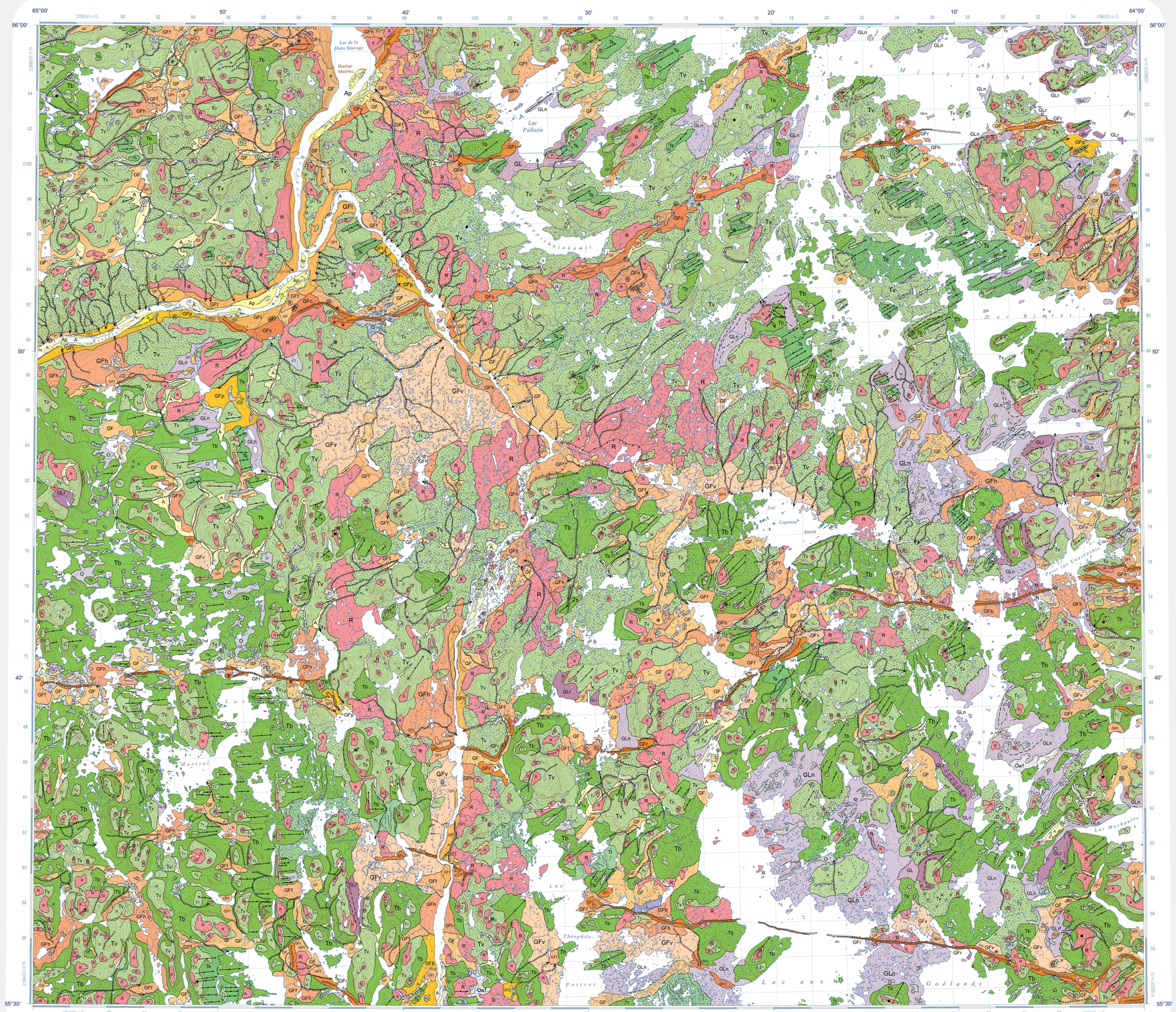

QUATERNARY

POST LAST GLACIATION

NON-GLACIAL ENVIRONMENT

ORGANIC DEPOSITS: peat and muck, 1 to 2 m thick on average; formed by the accumulation of plant material in various stage of decomposition; generally occurs as low relief, wet terrain (swamps, bogs and fens).

Owf — **Organic deposits, fen:** derived from sedges and partially decayed shrubs in a eutrophic environment; commonly forms a ribbed pattern of low shrubs transverse to drainage with ponds of open water.

O — **Organic deposits, undifferentiated:** undifferentiated bog and fen deposits, area may be locally mixed or underlain with alluvial sediments; often associated with minor alluvial channels established for surface drainage.

ALLUVIAL SEDIMENTS: undifferentiated deposits of sorted gravel, sand, silt, and organic detritus; commonly stratified, variable thickness; deposited by streams and rivers.

Ap — **Floodplain sediments:** sorted gravel, sand, and silt, possibly containing varying amount of organics, variable thickness. Deposited within the floodplain of active rivers and streams, including meander channels and scroll bars.

At — **Alluvial terrace sediments:** sorted sands and fine gravels; elongated, inactive terraces above floodplain of active rivers and streams.

A — **Alluvial sediments, undifferentiated:** gravel to silt and organic detritus, variable thickness.

LACUSTRINE SEDIMENTS: cobble to pebble gravel, sand, silt, and minor organic detritus; >1 m thick, consisting of beach and storm deposits, ice rafted debris or formed during recent fluctuations in lake levels, deposited along the shorelines of larger lakes.

L — **Lacustrine sediments, undifferentiated:** gravel, sand, silt, and organic detritus; variable thickness.

POSTGLACIAL OR LATE WISCONSIN

GLACIAL ENVIRONMENTS

GLACIOLACUSTRINE SEDIMENTS: coarse gravel, sand, silt, and minor clay; commonly massive to portly stratified; >1 m; derived from winnowing of till in relatively shallow water; formed in proglacial Lake Naskaupi.

GLr — **Ridged beach sediments:** pebbly to coarse granular sand; moderate to well sorted, with stratification and open framework of clasts. Deposited during glacial lake inundation limited to elevations approximately at 485 m for glacial Lake Naskaupi.

GLn — **Littoral and nearshore sediments:** sand and gravel, moderately sorted, not more than 1 m thick, commonly produced by glaciolacustrine winnowing of till deposits.

GL — **Glaciolacustrine sediments, undifferentiated:** sand silt, and minor clay; commonly overlain by organic deposits; low relief terrain.

GLACIOFLUVIAL SEDIMENTS: sand, gravel with minor silt and diamicton; well to poorly sorted, massive to stratified; deposited by glacial meltwater streams from, or in contact with, glacial ice in a subglacial, subaqueous or proglacial subaerial environment.

GFp — **Outwash plain sediments:** sand and rounded gravel, minor silt; moderately to well sorted; planar and cross-stratified; from low relief plains commonly with kettle lakes, channel scars, and minor kettle lakes; ice-contact stratified drift deposited in a proglacial, subaerial environment within meltwater corridors.

GFt — **Glaciofluvial terrace:** well sorted, subrounded to rounded cobbly-pebbly gravel to fine-sand; terraced sediments that were formed along former floodplain of glaciofluvial channels.

GFf — **Outwash fan sediments:** fine sand to well rounded gravel, minor silt, moderately sorted; cross-stratified, with foreset bedding; sediments fine toward distal edge of fan; deposited at the terminous of subglacial and subaerial meltwater corridors.

GFh — **Hummocky sediments:** gravel to fine-sand, with minor silt, and isolated boulders; massive to crudely stratified, moderate to poor sorting; commonly formed in ice-contact meltwater environments, local relief is 2 to 4 m.

GFc — **Ice-contact sediments:** moderately to poorly sorted, massive to crudely stratified often occurring as small hummocks and ridges (1 to 4 m high); deposits usually are restricted in morphology due to overlying ice, often associated with subglacial meltwater corridors and esker networks.

GFr — **Esker:** sinuous ridges of moderate to well sorted sand and gravel, cross-stratified to massive; characterized by pronounced ridges with crested peaks, or flat topped and winnowed by proglacial lakes; associated deposits often flank each side, deposited as ice-contact glaciofluvial sediments in larger subglacial meltwater corridors; can be associated with kame deposits, other ice-contact sediments and outwash fan deposits with kettle depressions and lakes.

GFv — **Glaciofluvial veneer:** glacial meltwater sediments, gravels to fine-sand with minor silt; cross-stratified to massive; <1 m thick, often draping the underlying till or bedrock morphology.

GF — **Glaciofluvial sediments, undifferentiated:** sand, gravel with minor silt; well to poorly sorted massive to stratified; deposited by glacial meltwater streams from or in contact with glacial ice in a subglacial, subaqueous or proglacial subaerial environment.

GLACIAL SEDIMENTS (TILL): silty-sand to sandy diamicton; with striated and faceted clasts of various lithologies; clast content ranges from 15 to 25%; thickness ranges from 1 to >5 m thick; till sheets and ridges have been exposed to varying degrees of washing and winnowing from meltwater channel systems and proglacial Lake Naskaupi; generally thicker in the lowland regions and also as lee-side tails of streamlined glacial landforms; deposited directly by the Laurentide Ice Sheet.

Tr — **Ridged till:** bouldery, silty-sand diamicton of varying thickness, characterized generally by subparallel low-relief ridges, often tranverse to regional ice flow indicators as ribbed moraine.

Ts — **Streamlined till:** silty-sand diamicton, deposited by active flowing ice, associated with larger landforms and former ice stream corridors; geomorphology includes mega scale glacial lineations (fluted forms with high length:width ratios), drumlinoid features, and larger crag-and-tail forms.

Tv — **Till veneer:** bouldery, sandy diamicton; generally less than 1 m but up to 2 m thick locally; forms a discontinuous cover over bedrock and interspersed with many small outcrops of bedrock; geomorphology commonly mimics the underlying bedrock structure; local regions of frost heaved bedrock and boulders are frequent at higher elevations.

Tb — **Till blanket:** silty-sand diamicton; >2 m thick; forms continuous cover that generally masks underlying bedrock topography and structure; frost boils and solifluction stripes are common.

PRE-QUATERNARY

R — **Bedrock:** Core Zone bedrock, a composite Precambrian lithotectonic terrane of undifferentiated Archean rocks, Paleoproterozoic supracrustal rocks and variable age plutons extensively reworked during ca. 1.8–1.9 Ga collision of the Superior and North Atlantic (or Nain) cratons.

Winnowed sediments and localized thin (<1 m) sorted sediments of sand, gravel and cobble lag deposits; surface may exhibit meltwater channels or minor littoral features.

- Kettle
- Geological boundary, defined
- Terrace scarp
- Beach crest
- Meltwater channel:
  - *Minor, sense unknown*
  - *Minor, sense known*
  - *Major scarp*
- Other moraine ridge, minor
- Esker ridge:
  - *Direction unknown or unspecified*
  - *Direction known or inferred*
- Drumlinoid ridge
- Crag-and-tail ridge
- Kame
- Striations:
  - *Direction known*
  - *Crossed, relative ages given (1 = oldest)*
- Small outcrop
- Station location (ground observation or stratigraphic section)
- Dated sample location, corrected age by Optical Stimulated Luminescence (OSL) (*see* Table 1)
- Till sample location

Recommended citation

Rice, J.M., Paulen, R.C., and Ross, M., 2017. Surficial geology, Lac Mistinibi, Quebec, NTS 23-P northeast; Geological Survey of Canada, Canadian Geoscience Map 316 (preliminary), scale 1:100 000. doi:10.4095/300656

Preliminary Preliminary Preliminary

Celebrating 175 yrs

Geological Survey of Canada
Canadian Geoscience Maps

Canada

Authors: J.M. Rice, R.C. Paulen, and M. Ross

Geology based on air photo interpretation and fieldwork by J.M. Rice, R.C. Paulen, and M. Ross, 2014–2016

Geological compilation by J.M. Rice and R.C. Paulen, 2014–2016

Geology conforms to Surficial Data Model v. 2.2

Geomatics by L. Robertson

Cartography by E. Everett

Initiative of the Geological Survey of Canada, conducted under the auspices of the GEM-2 Hudson-Ungava Core Zone Project as part of Natural Resources Canada's Geo-mapping for Energy and Minerals (GEM) program.

Logistical support provided by the Polar Continental Shelf Program as part of its mandate to promote scientific research in the Canadian north. PCSP 05915 (2015) and 06016 (2016)

Map projection Universal Transverse Mercator, zone 20. North American Datum 1983

Base map at the scale of 1:50 000 from Natural Resources Canada, with modifications.
Elevations in metres above mean sea level

CANADIAN GEOSCIENCE MAP 316

SURFICIAL GEOLOGY

LAC MISTINIBI

Quebec

NTS 23-P northeast

1:100 000

2 0 2 4 6 8 km

Mean magnetic declination 2017, 22°08'W, decreasing 14.4' annually. Readings vary from 21°54'W in the SW corner to 22°21'W in the NE corner of the map.

This map is not to be used for navigational purposes.

Title photograph: Photo of perched erratics that sit atop glacially scoured bedrock, looking to the southwest, a distant esker emerges out of Lac aux Goélands, NTS 23-P/09 (55°57'28"N / 65°28'09"W), Quebec. Photograph by J.M. Rice. 2017-039

The Geological Survey of Canada welcomes corrections or additional information from users.

Data may include additional observations not portrayed on this map. See map info document accompanying the downloaded data for more information about this publication.

This publication is available for free download through GEOSCAN (http://geoscan.nrcan.gc.ca/).

Preliminary publications in this series have not been scientifically edited.

CANADIAN GEOSCIENCE MAP 316

SURFICIAL GEOLOGY

LAC MISTINIBI

Quebec

NTS 23-P northeast

Descriptive Notes

This surficial map represents a complex ice-flow history associated with the migration of the Ancestral Labrador ice divide (Vincent, 1989). Three phases of glacial erosion consistently were observed throughout the map area. The oldest ice flow recorded in the striation record was to the northeast. The second flow phase was a radial flow situated somewhere near the eastern edge of the map sheet on the higher relief terrain of the De Pas batholith (a major bedrock unit associated with the Core Zone). A westward migration of that ice divide caused an offset in the radial ice flow directions, for the final ice-flow phase. Evidence of this ice divide shift across the region is best exemplified by numerous double-stoss outcrops (Figure 1) that were documented within the divide migration areas.

The presence of the Ancestral Labrador ice divide resulted in a relict landscape impacted by minor glacial erosion and landforms. The northwestern region of the map, furthest away from the former ice divide, has large crag-and-tail landforms, and are the only large-scale ice-erosional features mapped in this area. During the latter stages of deglaciation, the northwest lowlands was inundated by glacial Lake McLean (Ives, 1960). Proglacial Lake McLean covered the general region of present day Lac Champdoré and Lac Tudor. These regions are characterized by washed bedrock surfaces, winnowed till surfaces, and littoral beach deposits.

Acknowledgments

Surficial mapping was undertaken under the Geo-mapping for Energy and Minerals (GEM) program in collaboration with Ministère de l'Énergie et des Ressources Naturelles du Québec (MERNQ), the Geological Survey of Newfoundland and Labrador (GSNL), and the University of Waterloo. This research benefitted from the support of the Polar Continental Shelf Program. Financial assistance, as part of J.M. Rice's Ph.D. thesis, was also provided through the Northern Scientific Training Program on behalf of the Canadian Polar Commission. A. Lion (University of Ottawa), G. Hagedorn (University of Guelph), and M.B. McClenaghan (GSC Ottawa) are thanked for their support and assistance in the field. M. Pyne (GSC Ottawa) and G. Huot-Vézina (GSC Quebec) are thanked for GIS and database support.

References

Clark, P.U. and Fitzhugh, W.W., 1990. Late deglaciation of the central Labrador coast and its implications for the age of glacial lakes Naskaupi and McLean and for prehistory; Quaternary Research, 34, p. 296–305.

Ives, J.D., 1958. Glacial drainage channels as indicators of late-glacial conditions in Labrador-Ungava: a discussion; Cahiers de géographie du Québec 3, no. 5, p. 57–72.

Ives, J.D., 1960. Former ice-dammed lakes and the deglaciation of the middle reaches of the George River, Labrador-Ungava; Geographical Branch, Department of Mines and Technical Surveys, Geographical Bulletin, 14, p. 44–70.

Jansson, K.N., 2003. Early Holocene glacial lakes and ice marginal retreat pattern in Labrador/Ungava, Canada; Palaeogeography, Palaeoclimatology, Palaeoecology, 193, p. 473–501.

Jansson, K.N., Kleman, J., and Marchant, D.R., 2002. The succession of ice-flow patterns in north-central Québec-Labrador; Quaternary Science Reviews, v. 21, Issues 4–6, p. 503–523. https://doi.org/10.1016/S0277-3791(01)00013-0

Klassen, R.A. and Thompson, F.J., 1993. Glacial history, drift composition, and mineral exploration, central Labrador; Geological Survey of Canada, Bulletin 435, 82 p. https://doi.org/10.4095/183906

Klassen, R.A., Paradis, S., Bolduc, A.M., and Thomas, R.D., 1992. Glacial landforms and deposits, Labrador, Newfoundland and eastern Québec; Geological Survey of Canada, Map 1814A, scale 1:1 000 000, 1 .zip file. https://doi.org/10.4095/183872

Occhietti, S., Govare, É., Klassen, R., Parent, M., and Vincent, J.S., 2004. Late Wisconsinan—Early holocene deglaciation of Québec-Labrador; *in* Quaternary glaciations — extent and chronology, Part II: North America, (ed.) J. Ehlers and P.L. Gibbard, Development in Quaternary Science Series, v. 2, Part B, p. 243–273. https://doi.org/10.1016/S1571-0866(04)80202-1

Veillette, J.J., Dyke, A.S., and Roy, M., 1999. Ice-flow evolution of the Labrador Sector of the Laurentide Ice Sheet: a review, with new evidence from northern Quebec; Quaternary Science Reviews, v. 18, Issues 8–9, p. 993–1019. https://doi.org/10.1016/S0277-3791(98)00076-6

Vincent, J.S., 1989. Quaternary geology of the southeastern Canadian Shield: *in* Chapter 3 of Quaternary Geology of Canada and Greenland, (ed.) R.J. Fulton; Geological Survey of Canada, Geology of Canada, no. 1, p. 249–275 (also Geological Society of America, The Geology of North America, v. K-1). https://doi.org/10.4095/127905

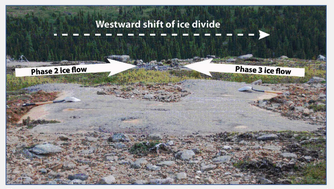

Figure 1. A bedrock outcrop sculpted by opposing ice flows, which resulted from the migration of the Ancestral Labrador ice divide. The outcrop was initially eroded by a westward flow (phase 2 flow) then, following the westward shift of the ice dispersal center, it was eroded by an eastward flow (phase 3 flow). Field station 15-PTA-024, with photo looking to the south.

Abstract

The Rivière De Pas area is of moderate relief, characterized by extensive till blanket units in lowlands and till veneer units and bedrock outcrops at higher elevations. The region was differentially eroded by the Laurentide Ice Sheet throughout Wisconsin time, largely influenced by the migration of the Ancestral Labrador Ice Divide, originally from east of the De Pas batholith to west of the map area. Phases of radial ice flow from the migrating ice divide imparted discordant erosional ice-flow landforms and flow indicators on the landscape. Significant regions of bedrock at higher elevations have been washed of till from late-phase ablation of the ice sheet during deglaciation, with associated small meltwater channels. Below 425 m elevation, the region was inundated by glacial Lake McLean, a proglacial lake that occupied the lowlands in the northwest. Sediments from glacial Lake McLean are limited to littoral beach deposits and winnowed till surfaces.

Résumé

La région de la rivière De Pas montre un relief modéré et est caractérisée par la présence de nappes de till étendues dans les basses terres et de placages de till et d'affleurements rocheux à des altitudes plus élevées. La région a été soumise à une érosion différentielle par l'inlandsis laurentidien au cours du Wisconsinien, en grande partie sous l'influence de la migration de la protoligne de partage glaciaire du Labrador, d'une position située à l'est du batholithe de De Pas jusqu'à l'ouest de la région cartographique. Les phases d'écoulement glaciaire radial à partir de la ligne de partage glaciaire en déplacement ont laissé dans le paysage des formes de relief et des indicateurs d'écoulement discordants. D'importantes zones de substrat rocheux à de plus hautes altitudes ont été dépouillées de leur couverture de till par les eaux de fonte libérées dans les derniers stades d'ablation de la nappe glaciaire lors de la déglaciation et auxquelles sont associés de petits chenaux. Au-dessous de 425 m d'altitude, la région a été inondée par le Lac glaciaire McLean, un lac proglaciaire qui occupait les basses terres dans le nord-ouest. Les sédiments du Lac glaciaire McLean sont limités à des dépôts de plage littoraux et à des surfaces de till vanné.

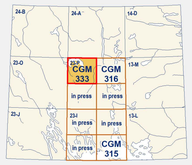

National Topographic System reference and index to adjoining published Geological Survey of Canada maps

Catalogue No. M183-1/333-2017E-PDF
ISBN 978-0-660-09982-7
https://doi.org/10.4095/306166

Natural Resources Canada | Ressources naturelles Canada

CANADIAN GEOSCIENCE MAP 333

SURFICIAL GEOLOGY

RIVIÈRE DE PAS

Quebec

NTS 23-P northwest

1:100 000

QUATERNARY

POST LAST GLACIATION

ORGANIC DEPOSITS: peat and muck, 1 to 2 m thick on average; formed by the accumulation of plant material in various stage of decomposition; occurs as low relief, wet terrain (swamps, bogs, and fens).

Owf — **Organic deposits:** Fen: derived from sedges and partially decayed shrubs in a eutrophic environment; commonly forms a ribbed pattern of small shrubs transverse to drainage with ponds of open water.

O — **Organic deposits, undifferentiated:** undifferentiated bog and fen deposits, the area may be locally mixed or underlain with alluvial sediments; often associated with minor alluvial channels established for surface drainage.

ALLUVIAL SEDIMENTS: Undifferentiated deposits of sorted gravel, sand, silt, and organic detritus; commonly stratified, variable thickness; deposited by streams and rivers.

Ap — **Floodplain sediments:** sorted gravel, sand, and silt, possibly containing varying amount of organics, variable thickness. Deposited within the floodplain of active rivers and streams, including meander channels and scroll bars.

Af — **Alluvial fan sediments:** sorted gravels and sands of varying thickness at the apex, fining to silts on the outer edge of the fan.

At — **Alluvial terrace sediments:** sorted sands and fine gravels; elongated, inactive terraces above the floodplain of active rivers.

A — **Alluvial sediments, undifferentiated:** gravel to silt and organic detritus, variable thickness.

LACUSTRINE SEDIMENTS: cobble to pebble gravel, sand, silt, and minor organic detritus; >1 m thick, consisting of beach and storm deposits, ice rafted debris or formed during recent fluctuations in lake levels, deposited along the shorelines of larger lakes.

Ln — **Littoral and nearshore sediments:** fine to coarse sand beaches with minor gravel and ice-rafted debris, relief is typically <1 m, sediments formed in the nearshore environment of larger lakes.

POSTGLACIAL OR LATE WISCONSIN

PREGLACIAL AND GLACIAL ENVIRONMENTS

GLACIOLACUSTRINE SEDIMENTS: coarse gravel, sand silt, and minor clay; commonly massive to portly stratified, >1 m; derived from winnowing of till in relatively shallow water; formed during various stages of proglacial Lake McLean.

GLr — **Ridged beach sediments:** pebbly to coarse granular sand; moderate to well sorted, with stratification and open framework of clasts. Deposited during glacial Lake McLean inundation limited to elevations approximately at 425 m.

GLn — **Littoral and nearshore sediments:** sand and gravel, moderately sorted, not more than 1 m thick, commonly produced by glaciolacustrine winnowing of till deposits.

GLACIOFLUVIAL SEDIMENTS: sand, gravel with minor silt and diamicton; well to poorly sorted, massive to stratified; deposited by glacial meltwater streams from, or in contact with, glacial ice in a subglacial, subaqueous or proglacial subaerial environment.

GFl — **Glaciofluvial terrace:** well-sorted, subrounded to rounded cobbly-pebbly gravel to fine-sand; terraced deposits that were formed along former floodplain of glaciofluvial channels.

GFf — **Outwash fan sediments:** fine sand to well-rounded gravel, minor silt, moderately sorted; cross-stratified, with foreset bedding; sediments fine toward distal edge of fan; deposited at the terminus of subglacial and subaerial meltwater corridors.

GFh — **Hummocky sediments:** gravel to fine-sand, with minor silt, and isolated boulders; massive to crudely stratified, moderate to poor sorting; commonly formed in ice-contact meltwater environments, local relief is 2 to 4 m.

GFc — **Ice-contact sediments:** moderately to poorly sorted, massive to crudely stratified often occurring as small hummocks and ridges (1 to 3 m high); deposits usually are restricted in morphology due to overlying ice, often associated with subglacial meltwater corridors and esker networks.

GFr — **Esker:** sinuous ridges of moderate to well-sorted sand and gravel, cross-stratified to massive; characterized by pronounced ridges with crested peaks, or flat topped and winnowed by proglacial lakes; associated deposits often flank each side; deposited as ice-contact glaciofluvial sediments in larger subglacial meltwater corridors; can be associated with kame deposits, other ice-contact sediments and outwash fan deposits with kettle depressions and lakes.

GFv — **Glaciofluvial veneer:** glacial meltwater sediments, gravels to fine-sand with minor silt; cross-stratified to massive; <1 m thick, often draping the underlying till or bedrock morphology.

GFb — **Outwash blanket:** moderately to poorly sorted with isolated boulders, massive to crudely stratified >2 m thick; forms a continuous cover that masks underlying bedrock topography and structure.

GF — **Glaciofluvial sediments, undifferentiated:** sand, gravel with minor silt; well to poorly-sorted massive to stratified; deposited by glacial meltwater streams from or in contact with glacial ice in a subglacial, subaqueous or proglacial subaerial environment.

GLACIAL SEDIMENTS (TILL): silty-sand to sandy diamicton; with striated and faceted clasts of various lithologies; clast content ranges from 15 to 25%; thickness ranges from 1 to >3 m thick; till sheets and ridges have been exposed to varying degrees of washing and winnowing from meltwater channel systems and proglacial Lake McLean; generally thicker in the lowland regions and also as lee-side tails of streamlined glacial landforms; deposited directly by the Laurentide Ice Sheet.

Ts — **Streamlined till:** silty-sand diamicton, deposited by active flowing ice, associated with larger oriented landforms; geomorphology includes drumlinoid features, and larger crag-and-tail forms.

Tv — **Till veneer:** bouldery, sandy diamicton; less than 1 m but up to 2 m thick locally; forms a discontinuous cover over bedrock and interspersed with many small outcrops of bedrock; geomorphology commonly resembles the underlying bedrock structure; local regions of frost heaved bedrock and boulders are frequent at higher elevations.

Tb — **Till blanket:** silty-sand diamicton; >2 m thick; forms continuous cover that masks underlying bedrock topography and structure; frost boils and solifluction stripes are frequent.

PRE-QUATERNARY

R — **Bedrock:** Core Zone bedrock, a composite Precambrian lithotectonic terrane of undifferentiated Archean rocks, and Paleoproterozoic supracrustal rocks. Dominated in the upland eastern half of the map sheet by the De Pas Batholith. Metasedimentary, amphibole, and felsic plutonic rocks of the Laporte Domain and metavolcanic rocks of the Doublet Zone associated with the New Quebec Orogen occur in the western half of the map sheet.

Winnowed sediments and localized thin (<1 m) sorted sediments of sand, gravel and cobble lag deposits; surface may exhibit meltwater channels or minor littoral feature.

Kettle

Geological boundary, defined

Beach crest

Meltwater channel:

Minor, sense unknown

Minor, sense known

Major scarp

Drumlinoid ridge

Crag-and-tail ridge, sense known

Kame

Striations:

Direction known

Crossed, relative ages given (1 = oldest)

Small outcrop

Station location

Till sample location

Recommended citation
Rice, J.M., Paulen, R.C., and Ross, M., 2017. Surficial geology, Rivière De Pas, Quebec, NTS 23-P northwest; Geological Survey of Canada, Canadian Geoscience Map 333 (preliminary), scale 1:100 000. https://doi.org/10.4095/306166

Celebrating 175 yrs

Geological Survey of Canada
Canadian Geoscience Maps

Authors: J.M. Rice, R.C. Paulen, and M. Ross

Geology based on air photo interpretation and fieldwork by J.M. Rice, R.C. Paulen, and M. Ross, 2014–2016

Geological compilation by J.M. Rice and R.C. Paulen, 2017

Geology conforms to Surficial Data Model v. 2.3

Geomatics by L. Robertson

Cartography by E. Everett

Initiative of the Geological Survey of Canada, conducted under the auspices of the GEM-2 Hudson-Ungava Core Zone Project as part of Natural Resources Canada's Geo-mapping for Energy and Minerals (GEM) program.

Logistical support provided by the Polar Continental Shelf Program as part of its mandate to promote scientific research in the Canadian north. PCSP 05915 (2015) and 06016 (2016)

Map projection Universal Transverse Mercator, zone 20. North American Datum 1983

CANADIAN GEOSCIENCE MAP 333

SURFICIAL GEOLOGY

RIVIÈRE DE PAS

Quebec

NTS 23-P northwest

1:100 000

2 0 2 4 6 8 km

Base map at the scale of 1:50 000 from Natural Resources Canada, with modifications.
Elevations in metres above mean sea level

Mean magnetic declination 2017, 21°50'W, decreasing 14.2' annually. Readings vary from 21°35'W in the SW corner to 22°04'W in the NE corner of the map.

This map is not to be used for navigational purposes.

Title photograph: Washed bedrock overlooking the Rivière De Pas, glacial fluvial deposits can be observed as exposed by the river along its banks, Quebec. Photograph by J.M. Rice. 2017-040

The Geological Survey of Canada welcomes corrections or additional information from users.

Data may include additional observations not portrayed on this map. See map info document accompanying the downloaded data for more information about this publication.

This publication is available for free download through GEOSCAN (http://geoscan.nrcan.gc.ca/).

This publication has been scientifically reviewed, but it has not undergone a formal edit.

CANADIAN GEOSCIENCE MAP 333

SURFICIAL GEOLOGY

RIVIÈRE DE PAS

Quebec

NTS 23-P northwest

Appendix S2.1 ^{10}Be dating methods

Samples collected from 2015 were submitted to the PRIME Lab at Purdue University for physical processing, chemical processing, and ^{10}Be measurement. Samples collected in 2016 were submitted to the Paleoclimate Lab at University at Buffalo for physical and chemical processing, while ^{10}Be measurement was carried out at Lawrence Livermore National Laboratory. At both locations, samples were crushed, sieved, and then subjected to chemical treatment designed to isolate quartz following procedures outlined by Kohl and Nishiizumi (1992). As part of the quartz isolation, the samples are placed in a series of acid baths, starting with an Aqua Regia treatment, followed by an HF bath in order to dissolve any non-quartz minerals that are within the crushed portion. Next, the outer portion of the quartz grain, which may be contaminated by meteoric but not cosmogenic ^{10}Be, is removed using an ultra-sonic HF bath. The quartz grains are then optically verified and then a small sample aliquot is dissolved and the cation load is measured via ICP-AES to ensure an adequate level of purity has been reached. After the sample has achieved adequate purity (low cation load), the quartz samples are dissolved with a spike of a known mass of BeCl (^{9}Be atoms) to provide sufficient atomic amounts of BeO to be detected by accelerator mass spectrometry (AMS). Finally, the dissolved sample is subjected to precipitation controlled, cation and anion chromatography to isolate the Be in solution. This process utilizes the physical precipitation of Be from BCl using pure ammonia gas to create BeOH. The precipitate is then oxidized at 850^{o} C in order to remove any liquid or gas phases of the sample.

S2.1.1 Age calculation

The results were blank corrected and the ^{9}Be/^{10}Be ratios from AMS measurements were used to calculate ^{10}Be concentrations. The ^{10}Be concentrations were used with the University of Washington's CRONUS-Earth online calculator (V.3) (https://hess.ess.washington.edu/) for exposure age determination (Balco et al., 2008), using the Baffin Bay/Arctic ^{10}Be production rate (Young et al., 2013) and the nuclide and time dependant LSDn scaling scheme (Lifton et al., 2014). For each sample, the latitude, longitude, thickness of the sample, and density of the sample were entered as reported from field observations. Densities of the granitic outcrops were approximated to the density of the rocks most common mineral, quartz (2.65 g/cm^{3}). No shielding corrections were required as the samples were collected from topographically unobstructed bedrock outcrops. Elevation data for the samples were adjusted to reflect the local isostatic rebound following procedures outlined by Ullman et al. (2016) and Cuzzone et

al. (2016). Isostatic rebound data were obtained from the ICE-6G (VM5a) model (Argus et al., 2014; Peltier et al., 2015). Uplift rates from the estimated timing of local deglaciation (7.5 ka) to present day were averaged, yielding a correction of 61 meters, which was subtracted from each sample location elevation (see supplementary Table S1). Cuzzone et al. (2016) and Ullman et al. (2016) demonstrated that the atmospheric effects created by a retreating ice margin had little to no impact on the local air pressure, and thus atmospheric effects were not accounted for in this study. We treat all ^{10}Be results as "apparent ages" due to uncertain amounts of cosmogenic nuclide inheritance *(*e.g., Nishiizumi et al*.*, 1989; Davis et al., 1999; Briner et al., 2003, 2006; Ullman et al., 2016). The level of inheritance for each sample has been estimated based on its variation from previously reported deglacial ages (Dubé-Loubert et al., 2018) and also as constrained by our OSL ages.

References

Argus, D.F., Peltier, W.R., Drummond, R. and Moore, A.W. 2014 The Antarctica component of postglacial rebound model ICE-6G_C (VM5a) based upon GPS positioning, exposure age dating of ice thicknesses, and relative sea level histories. Geophysics Journal International, 198: 537-563.

Balco, G., Stone, J.O., Lifton, N.A., and Dunai, T.J. 2008. A complete and easily accessible means of calculating surface exposure ages or erosion rates from ^{10}Be and ^{26}Al measurements. Quaternary Geochronology, 3: 174-195.

Borchers, B., Marrenro, S., Balco, G., Caffeee, M., Goerhring, B., Lifron, N., Nishiizumi, K., Phillios, F., Schaefer, J., and Stone, J. 2016. Geological calibration of spallation production rates in the CRONUS-Earth project. Quaternary Geochronology, **31**: 188-198.

Briner, J.P., Miller, G.H., Davis, P.T., Bierman, and P.R., Caffee, M. 2003. Last Glacial Maximum ice sheet dynamics in Arctic Canada inferred from young erratics perched on ancient tors. Quaternary Science Reviews, 22: 437-444.

Briner, J.P., Miller, G.H., Davis, P.T., and Finkel, R.C. 2006. Cosmogenic radionuclides from fiord landscapes support differential erosion by overriding ice sheets. Geological Society of America Bulletin, 118: 406-420.

Cuzzone, J.K., Clark, P.U., Carlson, A.E., Ullman, D.J., Rinterknecht, V.R., Milne, G.A., Lunkka, J-P., Wohlfarth, B., Marcot,t S.A., and Caffee, M. 2016.Final deglaciation of the Scandinavian Ice Sheet and implications for the Holocene global sea-level budget. Earth and Planetary Science Letters, 448: 34-41.

Davis, P.T., Bierman, P.R., Marsella, K.A., Caffee, M.W., and Southon, J.R. 1999. Cosmogenic analysis of glacial terrains in the eastern Canadian Arctic: a test for inheritance nuclides and the effectiveness of glacial erosion. Annals of Glaciology, 28: 181-188.

Dubé-Loubert, H., Roy, M., Schaefer, J.M., and Clark, P.U. 2018. ^{10}Be dating of former glacial Lake Naskaupi (Québec-Labrador) and timing of its discharge during the last deglaciation. Quaternary Science Reviews, 191: 31-40.

Kohl, C.P., and Nishiizumi, K. 1992. Chemical isolation of quartz for measurement of in-situ produced cosmogenic nuclides. Geochimica et Cosmochimica Acta, 9: 3583-3587.

Lifton, N., Sat, T., and Dunai, T.J. 2014. Scaling in situ cosmogenic nuclide production rates using analytical approximations to atmospheric cosmic-ray fluxes. Earth and Planetary Science Letters, 386: 149-160.

Nishiizumi, K., Winterer, E.L., Kohl, C.P., Klein, J., Middleton, R., Lal, D,, Arnold, J.R. 1989. Cosmic ray production of ^{10}Be and ^{26}Al in quartz from glacially polished rocks. Journal of Geophysical Research, 94: 17 907-17 915.

Peltier, W.R., Argus, D.F., and Drummond, R. (2015) Space geodesy constrains ice-age terminal deglaciation: The global ICE-6G_C (VM5a) model. Journal of Geophysics Solid Earth, 120: 450-487,

Ullman, D.J., Carlson, A.E., Hostetler, S.W., Clark, P.U., Cuzzone, J., Milne, G.A., Winsor, K., and Caffee, M. 2016. Final Laurentide ice-sheet deglaciation and Holocene climate-sea level change. Quaternary Science Reviews, 152: 49-59.

Young, N., Schaefer, J.M., Briner, J.P., Goehring, B.M. 2013. A ^{10}Be production-rate calibration for the Arctic. Journal of Quaternary Science, 28: 515-526.

Appendix S2.1 Optical dating methods

Samples collected for optical dating, more broadly referred to as luminescence dating, were extracted from the sample tubes under dim orange light. The outermost (light-exposed) scrapings of each tube sample was retained for dosimetry. Water contents were also measured from these scrapings for samples 15-PTA-035 and 16-PTA-052, and from separate bags of sediment collected adjacent to the sample sites of 15-PTA-074 and 15-PTA-149. The concentrations of radioisotopes ^{40}K, Th, U and Rb (Table S2.3) were determined from the dosimetry samples using neutron activation analysis at a commercial laboratory. A component of the bulk material was treated with HCl acid (10%) and H_2O_2 solution (10%) to remove any traces of carbonates and organic material, respectively. Potassium-rich (K) feldspar was extracted using wet sieving and heavy liquid separation; the size fractions dated depended on available material. Separated K-feldspar grains were then subjected to standard HF acid treatments to remove the outermost part of the grains that would have been exposed to α radiation, washed in HCl to remove fluoride precipitate, rinsed and dried, and mounted on aluminum discs using silicone oil. All measurements were made using a Risø TL/OSL DA-20 reader equipped with a calibrated ^{90}Sr/^{90}Y β source that delivered β particles to the sample at a rate of ~5–6 Gy/min (Bøtter-Jensen et al., 2010). The luminescence signal from K-feldspar grains was measured at 50°C with infrared (IR) (880 nm) light-emitting diodes and the blue-violet (~400 nm) emissions were detected using an Electron Tubes Ltd. 9235QA photomultiplier tube (PMT) fitted with Schott BG-39 and Corning 7-59 filters.

The equivalent dose (D_e) of each sample was measured using the single-aliquot regenerative-dose (SAR) protocol (Wintle and Murray, 2006) shown in Table S3.4. The relatively low (160°C) preheat temperature and 180°C hotwash in this protocol have been applied successfully to K-rich feldspar on the coast of British Columbia (Neudorf et al., 2015, 2017) as well as in the Northwest Territories (Wolfe et al., 2018). Due to unusually bright infrared-stimulated luminescence (IRSL) signals of these samples, the D_e was measured using aliquots prepared using a 1 mm mask (70-100 grains per aliquot for sample 15-PTA-074, 10-20 grains for sample 15-PTA-149, and ~60 grains for samples 15-PTA-035 and 16-PTA-052, Table S2.5) and a reduced stimulation power (20% or ~29 mW/cm^2). Aliquots were rejected from analysis if their recuperation value was greater than 5% of the natural signal and if their

recycling ratio deviated from unity by more than 10%. The recycling ratios, recuperation values, D_e distributions of accepted aliquots, typical IRSL signals, and dose response curves are shown in Figure 2.10. The rate of anomalous fading of the IRSL signal (Table S2.5) was measured from 12 aliquots of each sample using the SAR protocol of Auclair et al. (2003) and the same preheat and stimulation temperatures and durations shown in Table S4. The IRSL signal from feldspar fades linearly with the logarithm of time since irradiation (Huntley and Lamothe, 2001) and only aliquots showing a clear linear relationship (as indicated by an R^2 value ≥ 0.70) were used to calculate a weighted mean fading rate for each sample. All ages were corrected for anomalous fading using the correction model of Huntley and Lamothe (2001). Because the natural signal (Ln/Tn, Table S2.4) falls in the non-linear part of the dose response curves of samples 15-PTA-035 and 16-PTA-052 this correction method may underestimate the true age by ~15-20% (c.f. Mathewes et al., 2015). An alternative correction method (the DRC method) proposed by Lamothe et al. (2003) is purported to be immune to the effects of non-linearity and may thus provide more accurate ages, but the applicability of this model has yet to be demonstrated generally.

Research elsewhere has shown that overdispersion (OD) values for small multi-grain aliquots of quartz known or thought to have been fully bleached at burial and not affected by post-depositional disturbance (or by significant differences in β dose rate among grains buried at the same time) commonly have values of ~10–20%, with some reported examples exceeding 30% (Galbraith et al., 2005; Jacobs and Roberts, 2007; Arnold and Roberts, 2009, their Table 5). Here we assume this applies to K-feldspar as well. Ages were calculated using the Central Age Model (CAM) weighted mean D_e value (Galbraith et al., 1999) (Table S2.5) and the environmental dose rates ('total' dose rates listed in Table S5). Where OD values were high (sample 16-PTA-052), the Minimum Age Model (MAM) of Galbraith et al. (1999) was also used to obtain age estimates from the most thoroughly bleached grains (Table S2.5).

The OD values of samples 15-PTA-035 (23%) and 15-PTA-149 (33%), along with the lack of skewness in the D_e distributions, suggests that most grains were well bleached prior to deposition. The much lower OD value (7%) of sample 15-PTA-074 may be a consequence of complete bleaching of grains; if any partially bleached grains in this sample exist they are probably masked by averaging effects of the IRSL signal measured from a moderate number of

grains (70-100) in each aliquot. Nonetheless, these results suggest that the subaqueous outwash fan sands of sample 15-PTA-074 were transported and rapidly deposited by a subaerial proglacial river.

The OD value of sample 16-PTA-052 (48%) is substantially larger than that of the other two samples suggesting either partial bleaching of the sample, and/or mixing of younger grains with older (perhaps glacial or pre-glacial) material. The high OD value and anomalously old age are suggestive of either subglacially deposited sediment, or advance phase glacial outwash sediments that are typically transported in turbid water and thus prone to partial bleaching (Fuchs and Owen, 2008).

References

Arnold, L.J. and Roberts, R.G. 2009. Stochastic modelling of multi-grain equivalent dose (De) distributions: Implications for OSL dating of sediment mixtures. Quaternary Geochronology, 4: 204–230.

Auclair, M., Lamothe, M., and Huot, S. 2003. Measurement of anomalous fading for feldspar IRSL using SAR. Radiation Measurements, 37: 487–492.

Bøtter-Jensen, L., Thomsen. K.J., and Jain, M. 2010. Review of optically stimulated luminescence (OSL) instrumental developments for retrospective dosimetry. Radiation Measurements, 45: 253–257.

Fuchs, M., and Owen, L.A. 2008. Luminescence dating of glacial and associated sediment: review, recommendations and future directions. Boreas, 37: 636–659.

Galbraith, R.F., Roberts, R.G., Laslett, G.M., Yoshida, H., and Olley, J.M. 1999. Optical dating of single and multiple grains of quartz from Jinmium rock shelter, northern Australia: Part I, experimental design and statistical models. Archaeometry, 41: 339–364.

Galbraith, R.F., Roberts, R.G., and Yoshida, H. 2005. Error variation in OSL palaeodose estimates from single aliquots of quartz: a factorial experiment. Radiation Measurements, 39: 289–307.

Huntley, D.J., and Lamothe, M. 2001. Ubiquity of anomalous fading in K-feldspars and the measurement and correction for it in optical dating. Canadian Journal of Earth Sciences, 38: 1093–1106.

Jacobs Z, Roberts RG. 2007. Advances in optically stimulated luminescence dating of individual grains of quartz from archaeological deposits. Evolutionary Anthropology, 16: 210–223.

Lamothe, M., Auclair, M., Hamzaoui, C., and Huot, S. 2003. Towards a prediction of long-term anomalous fading of feldspar IRSL. Radiation Measurements, 37: 493–498.

Mathewes, R.W., Lian, O.B., Clague, J.J., Huntley, M.J.W. 2015. Early Wisconsinan (MIS 4) glaciation on Haida Gwaii, British Columbia, and implications for biological refugia. Canadian Journal of Earth Science, 52: 939–951.

Neudorf, C.M., Lian, O.B., Walker, I.J., Shugar, D.H., Eamer, J.B.R., and Griffin, L.C.M. 2015. Toward a luminescence chronology for coastal dune and beach deposits on Calvert Island, British Columbia central coast. Canada. Quaternary Geochronology, 30: 275–281.

Neudorf, C.M., Smith, N.F., Lepofsky, D., Toniello, G., and Lian, O.B. 2017. Between a rock and a soft place: Using optical ages to date ancient clam gardens on the Pacific Northwest. PLoS ONE, 12: e0171775.

Wintle, A.G. and Murray, A.S. 2006. A review of quartz optically stimulated luminescence characteristics and their relevance in single-aliquot regeneration dating protocols. Radiation Measurements, 41: 369–391.

Wolfe, S.A., Morse, P.D., Neudorf, C.M., Kokelj, S.V., Lian, O.B., and O'Neill, H.B. 2018. Contemporary sand wedge development in seasonally-frozen ground and paleoenvironmental implications. Geomorphology, 308: 215–229.

Appendix S3.1 Quality assurance and quality control methodology for CIA elements

Quality Assurance and Quality Control (QA/QC) was conducted for till matrix geochemistry data following the till sample collection methodology of Plouffe et al. (2013). Samples used for this study area subset of samples collected as part of the Geo-mapping for Energy and Minerals (GEM2) Hudson-Ungava Surficial program (Rice et al., 2017). Silicic acid (silica sand) blanks were inserted into the analytical batches to monitor potential cross contamination between samples during sample processing and analysis (n=13). Additionally, CANMET certified standards Till-1 and Till-4 were inserted to monitor analytical accuracy. Precision of the reference material were evaluated using relative standard deviation Garrett (1969), yielding an average value of 0.48% for the major oxides and is well within the threshold of 15% recommended by Abzalov (2008) for geological interpretation (Table 3.1.1).

Table 3.1.1. Major oxide results from analyzed standards.

	Method	LF200	LF200	LF200	LF200	
	Analyte	Al2O3	CaO	Na2O	K2O	
	Unit	%	%	%	%	
	MDL	0.01	0.01	0.01	0.01	
CANMET standard Till-1						
15-MPB-010-A		13.47	2.72	2.76	2.15	
15-PTA-055-A		13.58	2.72	2.77	2.15	
15-PTA-182-A		13.63	2.71	2.76	2.15	
	Stnd. deviation	0.08	0.01	0.01	0.00	Till-1
	Average	13.56	2.72	2.76	2.15	$\%RSD_i$
	RSD_i	0.01	0.00	0.00	0.00	0.26%
CANMET standard Till-4						
14PTA-R059A		14.31	1.26	2.50	3.22	
14PTA-B024A		14.38	1.26	2.49	3.22	
14-MPB-1014A		14.39	1.25	2.47	3.22	
15-MPB-022-A		14.38	1.26	2.49	3.25	**Total averaged $\%RSD_i$**
15-PTA-089-A		14.45	1.27	2.47	3.18	**0.47%**
15-PTA-128-A		14.31	1.25	2.50	3.20	
16-PTA-175		14.46	1.25	2.47	3.24	
16-PTA-176		14.25	1.24	2.47	3.18	
16-PTA-177		14.60	1.26	2.50	3.21	
	Stnd. deviation	0.10	0.01	0.01	0.02	Till-4
	Average	14.39	1.26	2.48	3.21	$\%RSD_i$
	RSD_i	0.01	0.01	0.01	0.01	0.68%

Duplicate samples were also collected every minimum of 40 samples (8 duplicates for 276 total samples). The precision of the analytical process was evaluated for the major oxides used in the CIA analysis using Thompson-Howarth plots for each of the duplicates (Piercy, 2014). Thompson-Howarth

plots were created using the R Statistical package (Garrett and Grunsky, 2003), including ggplot2 (Wickham, 2016). Results from these plots indicate all of the samples yield better than 95% precision within a 99% confidence level (Figure 1). Scatterplots for each of the major oxides used for CIA calculations also show high precision, falling within 5% variance (Figure 3.1.2. The silica blank samples show no evidence of cross-contamination (Table 3.1.2).

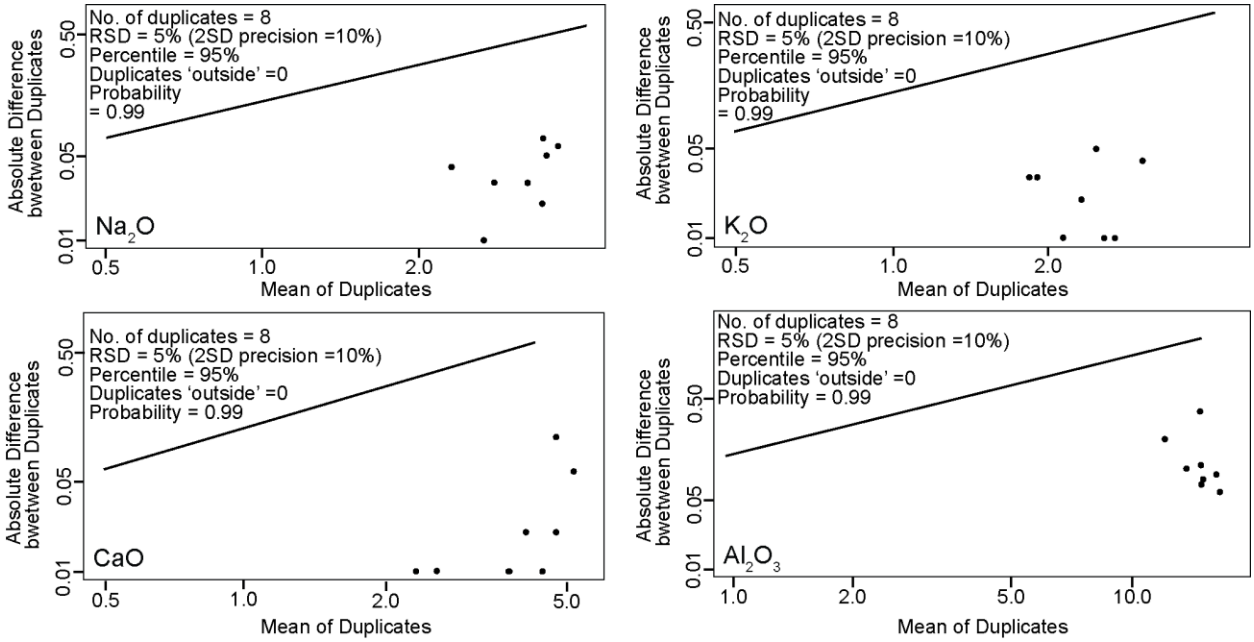

Figure 3.2.1. Thompson-Howarth plots for each of the major oxides used in the Chemical Index of Alteration (CIA) calculation. All points lie well below the control point line indicating greater than 5% precision (n=8).

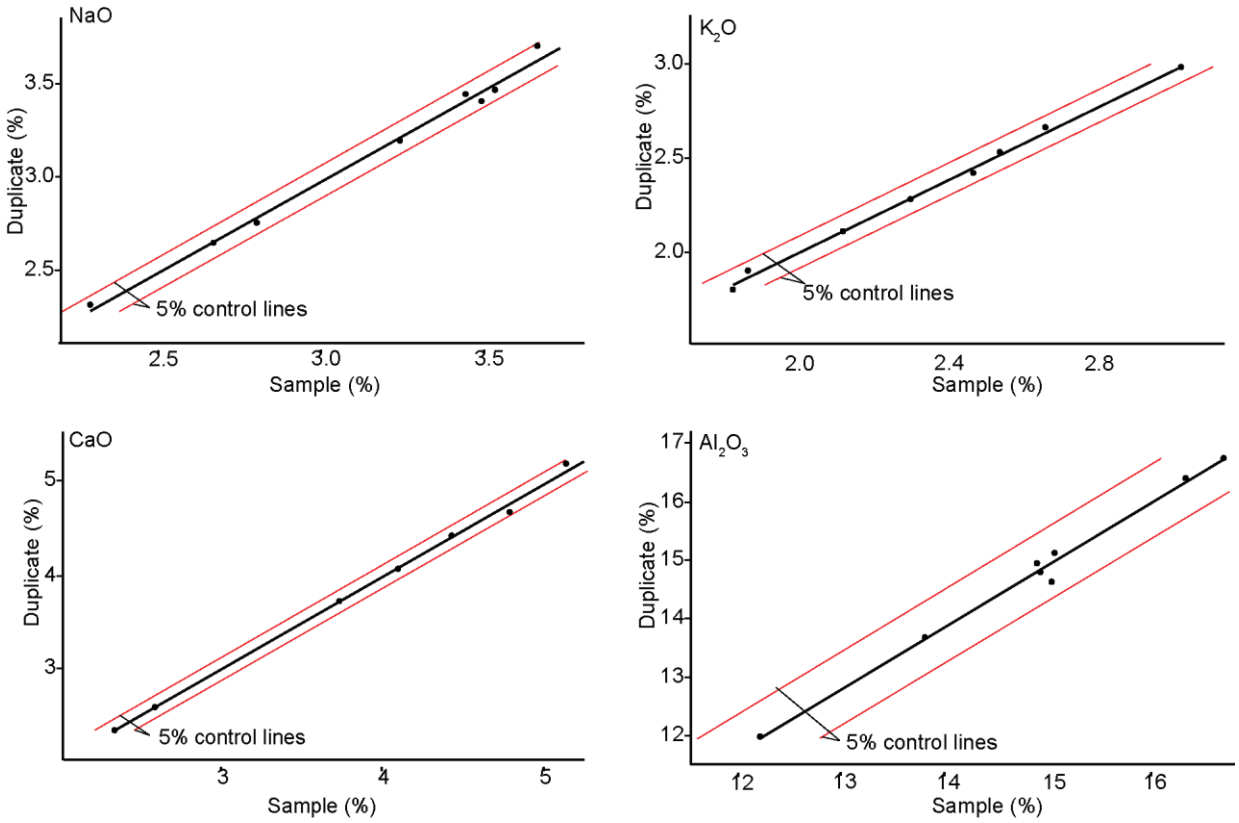

Figure 3.1.2. Precision scatterplots for each of the four major oxides used in CIA calculations. All the duplicates (n=8) fall within the 5% precision for each of the samples.

Table 3.1.2. Analytical values for blank samples

Method	LF200	LF200	LF200	LF200
Analyte	Al2O3	CaO	Na2O	K2O
Unit	%	%	%	%
MDL	0.01	0.01	0.01	0.01
Sample				
14PTA-R001	<0.01	0.09	0.01	<0.01
14PTA-R012	<0.01	0.09	0.01	0.01
14PTA-B043	<0.01	0.09	0.01	<0.01
15-PTA-001-A	<0.01	0.08	<0.01	<0.01
15-PTA-025-A-C	<0.01	0.08	<0.01	<0.01
15-PTA-090-A-C	0.02	0.08	0.01	<0.01
15-PTA-157-A-C	0.02	0.09	<0.01	<0.01
16-PTA-001-A	0.02	0.09	0.01	<0.01
16-PTA-111-A	<0.01	0.08	<0.01	<0.01
16-PTA-172-A	<0.01	0.09	<0.01	<0.01
16-PTA-100-A	<0.01	0.09	<0.01	<0.01
16-PTA-173-A	<0.01	0.09	<0.01	<0.01
16-PTA-174-A	<0.01	0.09	<0.01	<0.01

References

Abzalov, M. 2008. Quality control of assay data: a review of procedures for measuring and monitoring precision and accuracy. Exploration and Mining Geology, 17(3-4):131-144.

Garret, R.G. 1969. The determination of sampling and analytical errors in exploration geochemistry. Economic Geology, 64: 568-569.

Garrett, R.G. and Grunsky, E.C. 2003. S and R functions for the display of Thompson-Howarth plots. Computers and Geosciences, 29: 239-242.

Piercey, S.J. 2014. Modern analytical facilities 2. A review of quality assurance and quality control (QA/QC) procedures for lithogeochemical data. Geoscience Canada, 41(1): 75-88.

Plouffe, A., McClenaghan, M.B., Paulen, R.C., McMartin, I., Campbell, J.E., and Spirito, W.A. 2013. Quality assurance and quality control measures applied to indicator mineral studies of glacial sediments at the Geological Survey of Canada. IN: McClenaghan, M.B., Plouffe, A., Layton-Matthews, D., (eds.), Application of indicator mineral methods to mineral exploration. Geological Survey of Canada, Open File 7553.

Rice, J.M., McClenaghan, M.B., Paulen, R.C., Pyne, M.D., and Ross, M. 2017. Till geochemical data for the southern Core Zone, Quebec and Newfoundland and Labrador (NTS 23P and 23I): samples collected in 2015 and 2016. Geological Survey of Canada, Open File 8219.

Wickham, H. 2016. Ggplot2: Elegant Graphics for Data Analysis. Springer-Verlag, New York.

Appendix 3.2 ^{10}Abundance methodology

Samples collected for ^{10}Be abundance analysis, were collected from windswept uplands free from vegetation or other obstructions that would affect the level of cosmogenic bombardment and under the assumption each location was continuously exposed to cosmic radiation following deglaciation. In total, eight bedrock and eight till samples were collected for ^{10}Be abundance analysis. Till samples were collected from hand-dug pits sampling the entire till profile from surface to bedrock with a maximum depth of 0.35 m. Two till samples and three bedrock samples were submitted to the Purdue Rare Isotope Measurement Laboratory (PRIME Lab) at Purdue University for mineral separation, ^{10}Be isolation from quartz, and ^{10}Be measurement. Six till samples and five bedrock samples were submitted to the Paleoclimate Lab, University at Buffalo for mineral separation and ^{10}Be isolation, and then sent to the Lawrence Livermore National Laboratory Center for Mass Spectrometry for ^{10}Be measurement. At both labs, all bedrock samples were crushed and sieved (retaining the 850- 425 μm fraction), then acid-washed to remove organic and carbonate material. Quartz was isolated via froth flotation and when necessary, heavy mineral separation. Once isolated, meteoric ^{10}Be was removed by etching the quartz with hydrofluoric acid, the quartz was then dissolved with a "spike" containing a known quantity of ^{9}Be before anion and cation column chromatographys were used to purify the ^{10}Be. The purified beryllium was converted to BeO and packed into targets for measurements.

The abundance of ^{10}Be was then normalized to the production rate of each sample location. The production rates of cosmogenic nuclides are a direct function of a samples location and altitude (Lal, 1991; Desilets and Zreda, 2001; Dunai, 2010). Due to the isostatic rebound of the study area, the elevation of the sample sites must be adjusted to account for post glacial uplift. For our study area, it was assumed that the region experienced a steady-state uplift with continuous exposure, negligible erosion, and no burial (Gosse and Stone, 2001; Dunai, 2010). An estimate of isostatic rebound for the study area was obtained from the ICE-6G (VM5a) model (Argus et al., 2014; Peltier et al., 2015) and uplift rates were averaged from the inferred timing of deglaciation (7.5 ka- as indicated by the ICE-6G/VM5a model) to present day. This data yielded an average correction of 61 m, which was added to each sample location's elevation (Table 3.2.1). Cuzzone et al. (2016) and Ullman et al. (2016) conducted sensitivity tests on the effect of changes in atmospheric pressure created by a retreating localized ice mass and found the ice mass had little impact on the local air pressure and therefore minimal atmospheric effects on the incoming cosmogenic radiation received at the sample sties. Due to the rapid retreat of the ice margin (Ullman et al., 2016; Dubé-Loubert et al., 2018;

Rice et al., 2019) and minimal effect on cosmogenic bombardment, we choose not to adjustment our data to reflect these effects.

Table 3.2.1. Uplift corrections to account for isostatic rebound since deglaciation.

Data source: Argus et al. 2014, Peltier et al. 2015 (https://www.atmosp.physics.utoronto.ca/~peltier/data.php)

Time (ka)	Topo	Topo Diff	Uplift		
					Cells: Lat: 55; Long 295.5
8	951.7	517.6	-517.6	<- modelled ice sheet occupation of cell	
7.5	206.5	-151	151		
7	231.5	-146	146		
6.5	253.6	-129.8	129.8		
6	274.3	-109.2	109.2		
5.5	291.1	-92.4	92.4		
5	305.8	-77.8	77.8		
4.5	318.5	-65.2	65.2		
4	329.6	-54.2	54.2		
3.5	339.5	-44.3	44.3		
3	348.3	-35.5	35.5		
2.5	356.1	-27.8	27.8		
2	362.9	-21	21		
1.5	369	-14.9	14.9		
1	374.6	-9.4	9.4		
0.5	379.5	-4.4	4.4		
0	384	0	0		
	Average uplift		61.43125		

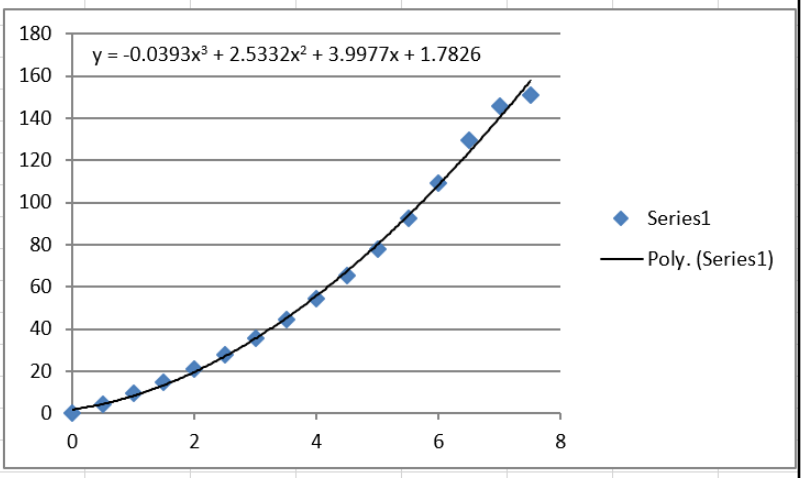

References

Argus, D.F., Peltier, W.R., Drummond, R. and Moore, A.W. 2014 The Antarctica component of postglacial rebound model ICE-6G_C (VM5a) based upon GPS positioning, exposure age dating of ice thicknesses, and relative sea level histories. Geophysics Journal International, 198: 537-563.

Cuzzone, J.K., Clark, P.U., Carlson, A.E., Ullman, D.J., Rinterknecht, V.R., Milne, G.A., Lunkka, J-P., Wohlfarth, B., Marcott, S.A., and Caffee, M. 2016.Final deglaciation of the Scandinavian Ice Sheet and implications for the Holocene global sea-level budget. Earth and Planetary Science Letters, 448: 34-41.

Dresilets, D. and Zreda, M. 2001. On scaling cosmogenic nuclide production rates for altitude and latitude using cosmic-ray measurements. Earth and Planetary Science Letters, 193(1-2): 213-225.

Dubé-Loubert, H., Roy, M., Schaefer, J.M., and Clark, P.U. 2018. ^{10}Be dating of former glacial Lake Naskaupi (Québec-Labrador) and timing of its discharge during the last deglaciation. Quaternary Science Reviews, 191: 31-40.

Dunai, T.J. 2010. Cosmogenic nuclides: Principals, concepts and applications in the Earth Surface Sciences, Cambridge University Press, UK.

Gosse, J.C. and Stone, J.O. 2001. Terrestrial cosmogenic nuclide methods passing milestones toward paleo-altimetry. Eos, Transactions American Geophysical Union, 82(7): 82-89.

Lal, D. 1991. Cosmic ray labelling of erosion surfaces: in situ nuclide production rates and erosion models. Earth and Planetary Science Letters, 104: 429-439.

Peltier, W.R., Argus, D.F. and Drummond, R. (2015) Space geodesy constrains ice-age terminal deglaciation: The global ICE-6G_C (VM5a) model. Journal of Geophysics Solid Earth, 120, 450-487.

Rice, J.M., Ross, M., Paulen, R.C., Kelley, S.A., Briner, J.P., Neudorf, C.M., and Lian, O.B. 2019. Refining the ice-flow chronology and subglacial dynamics across the Labrador Divide of the Laurentide Ice Sheet with age constraints on deglaciation. Quaternary Science Reviews, 34(7): 519-535.

Ullman, D.J., Carlson, A.E., Hostetler, S.W., Clark, P.U., Cuzzone, J., Milne, G.A., Winsor, K., Caffee, M. 2016. Final Laurentide ice-sheet deglaciation and Holocene climate-sea level change. Quaternary Science Reviews, 152: 49-59.

Appendix S4.1 Quality control and quality assurance methodology for geochemical data

Quality Assurance and Quality Control (QA/QC) was conducted for till matrix geochemistry data following the till sample collection methodology of Plouffe et al. (2013). Samples used for this study area subset of samples collected as part of the Geo-mapping for Energy and Minerals (GEM2) Hudson-Ungava Surficial program (Rice et al., 2017).

S4.1.1 Certified Standards

Two types of CANET certified standards were included in the analysis (n=12), including both CANMET standard Till 1 and Till 4. The certificate of analysis for this reference material is available at: https://www.nrcan.gc.ca/mining-materials/certified-reference-materials/certificate-price-list/8137 Precision of the reference material were evaluated using relative standard deviation Garrett (1969), yielding an average value of 4.81% for all samples (Table 4.1.1), which is deemed "very good" (Jenner, 1996).

S4.1.2 Blanks

Silicic acid (silica blanks, n=13) were inserted into the sample batch and analyzed along with collected samples to monitor any potential cross-contamination or instrumental memory affect during analytical procedures. For this analysis values that were below the detection limit were assigned values of one half of the lower detection limit, following procedures of Dinse et al. (2014). Shewart control plots were constructed to evaluate element abundances of blanks and to evaluate potential drift or bias in the analysis (Croakin and Tobais, 2006). The x-axis represents the order in which samples were analyzed and blanks are marked by red circles, with the dotted lines representing 2 standard deviations above and below the control line (Figure 4.1.1). The control charts were constructed using the qcc package within the R statistical environment (Scrucca, 2004). Results indicate no carryover or drift in any of the elements during the analytical process, with generally uniform composition of the blank samples.

S4.1.3 Duplicates

Duplicate samples were also collected every minimum of 30 samples (9 duplicates for 276 total samples). The precision of the analytical process was evaluated for all samples used in geochemical dispersals using Thompson-Howarth plots for each of the duplicates (Piercy, 2014). Thompson-Howarth plots were created using the R Statistical package (Garrett and Grunsky, 2003), including ggplot2 (Wickham, 2016). Results from these plots indicate all of the samples yield better than 95% precision

within a 99% confidence level (Figure 4.1.2). Scatterplots for elements used also show high precision, falling within 10% variance (Figure 4.1.3).

Table 4.1.1. Results from inserted Till standards to monitor QA/QC

Method	LF200	LF200	LF200	LF200	LF200	LF200	LF200	LF200	LF200	LF200	LF200	LF200
Analyte	SiO2	Al2O3	Fe2O3	MgO	U	Zr	La	Ce	Pr	Nd	Sm	Eu
Unit	%	%	%	%	PPM	PPM	PPM	PPM	PPM	PPM	PPM	PPM
MDL	0.01	0.01	0.04	0.01	0.10	0.10	0.10	0.10	0.02	0.30	0.05	0.02
CANMET standard Till-1												
15-MPB-010-A	60.80	13.47	7.07	2.17	2.10	488.50	27.60	66.60	7.05	27.80	5.74	1.50
15-PTA-055-A	60.99	13.58	6.89	2.17	1.90	437.60	23.50	61.40	6.33	25.70	4.97	1.34
15-PTA-182-A	60.63	13.63	6.94	2.17	2.10	532.00	27.60	70.80	7.03	28.80	5.77	1.38
Std. Dev.	0.18	0.08	0.09	0.00	0.12	47.25	2.37	4.71	0.41	1.58	0.45	0.08
Average	60.81	13.56	6.97	2.17	2.03	486.03	26.23	66.27	6.80	27.43	5.49	1.41
RSD_i	0.00	0.01	0.01	0.00	0.06	0.10	0.09	0.07	0.06	0.06	0.08	0.06
											$\%RSD_i$	**4.98%**
CANMET standard Till-4												
14PTA-R059A	64.79	14.31	5.62	1.25	4.00	385.10	37.20	72.50	8.49	31.70	6.59	1.14
14PTA-B024A	64.85	14.38	5.65	1.26	4.40	393.50	39.70	74.10	8.79	32.30	6.34	1.14
14-MPB-1014A	64.68	14.39	5.69	1.26	4.30	386.20	39.50	75.20	8.93	33.00	6.28	1.06
15-MPB-022-A	64.39	14.38	5.67	1.24	4.50	401.60	43.30	83.40	9.15	34.10	6.83	1.12
15-PTA-089-A	64.80	14.45	5.80	1.26	4.40	367.00	38.10	73.10	8.08	29.40	5.63	0.98
15-PTA-128-A	64.37	14.31	5.71	1.25	5.50	450.80	44.80	87.00	9.47	35.10	6.70	1.22
16-PTA-175	64.60	14.46	5.71	1.27	4.50	384.30	41.00	72.70	8.50	30.80	6.47	1.11
16-PTA-176	65.04	14.25	5.69	1.25	4.40	424.60	43.00	77.70	9.26	34.50	7.09	1.17
16-PTA-177	64.57	14.60	5.78	1.27	4.30	381.50	38.50	69.60	8.64	31.20	6.20	1.14
Std. Dev.	0.22	0.10	0.06	0.01	0.41	25.62	2.62	5.65	0.44	1.88	0.42	0.07
Average	64.68	14.39	5.70	1.26	4.48	397.18	40.57	76.14	8.81	32.46	6.46	1.12
RSD_i	0.00	0.01	0.01	0.01	0.09	0.06	0.06	0.07	0.05	0.06	0.07	0.06
	Total averaged $\%RSD_i$			**4.81%**							**$\%RSD_i$**	**4.64%**

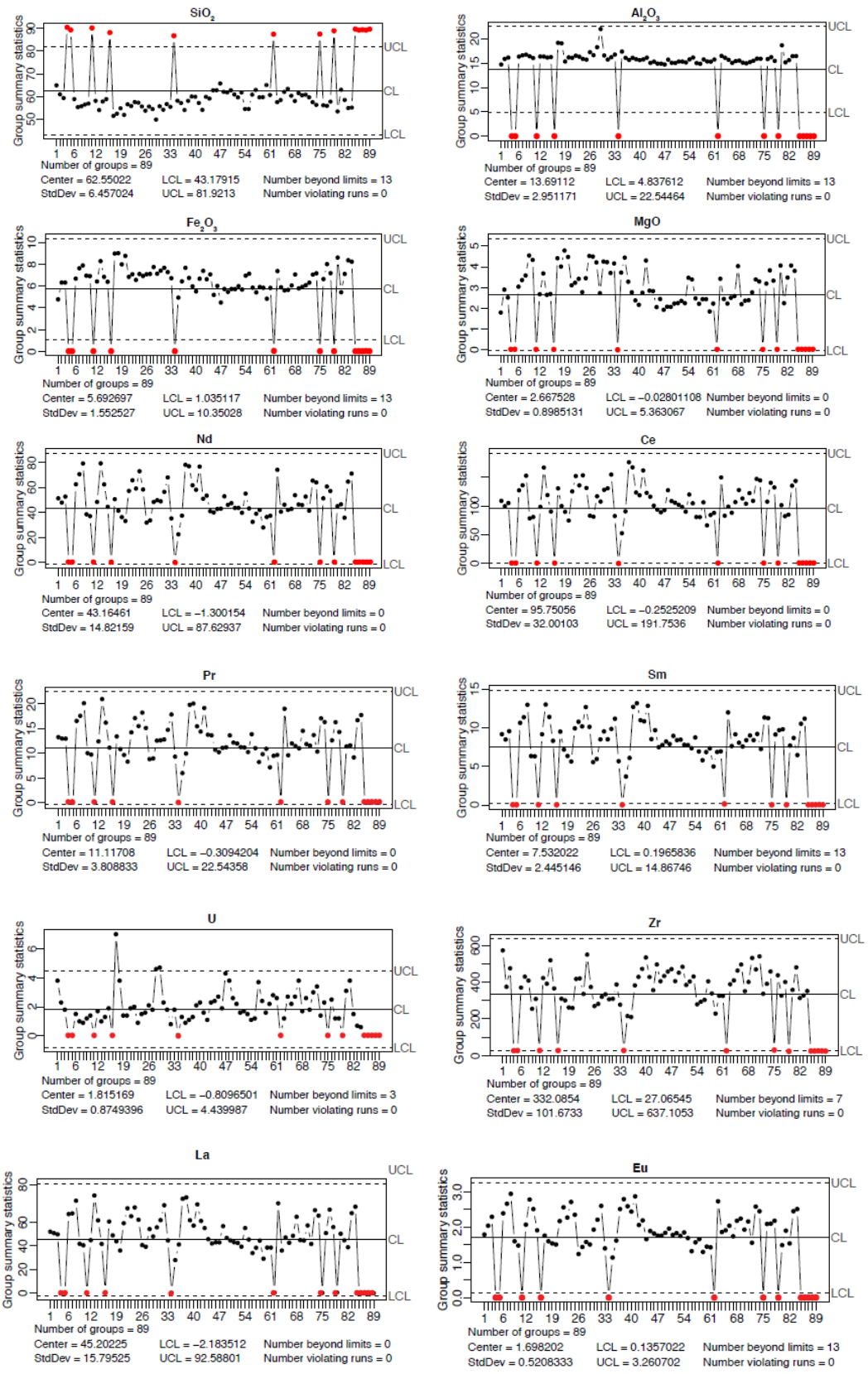

Figure 4.1.1. Shewart control plots for all elements used for geochemical dispersal analysis. Blanks are marked by red circles. The dotted lines represent 2σ from the mean (black line). Results show no carry over or drift for any elements.

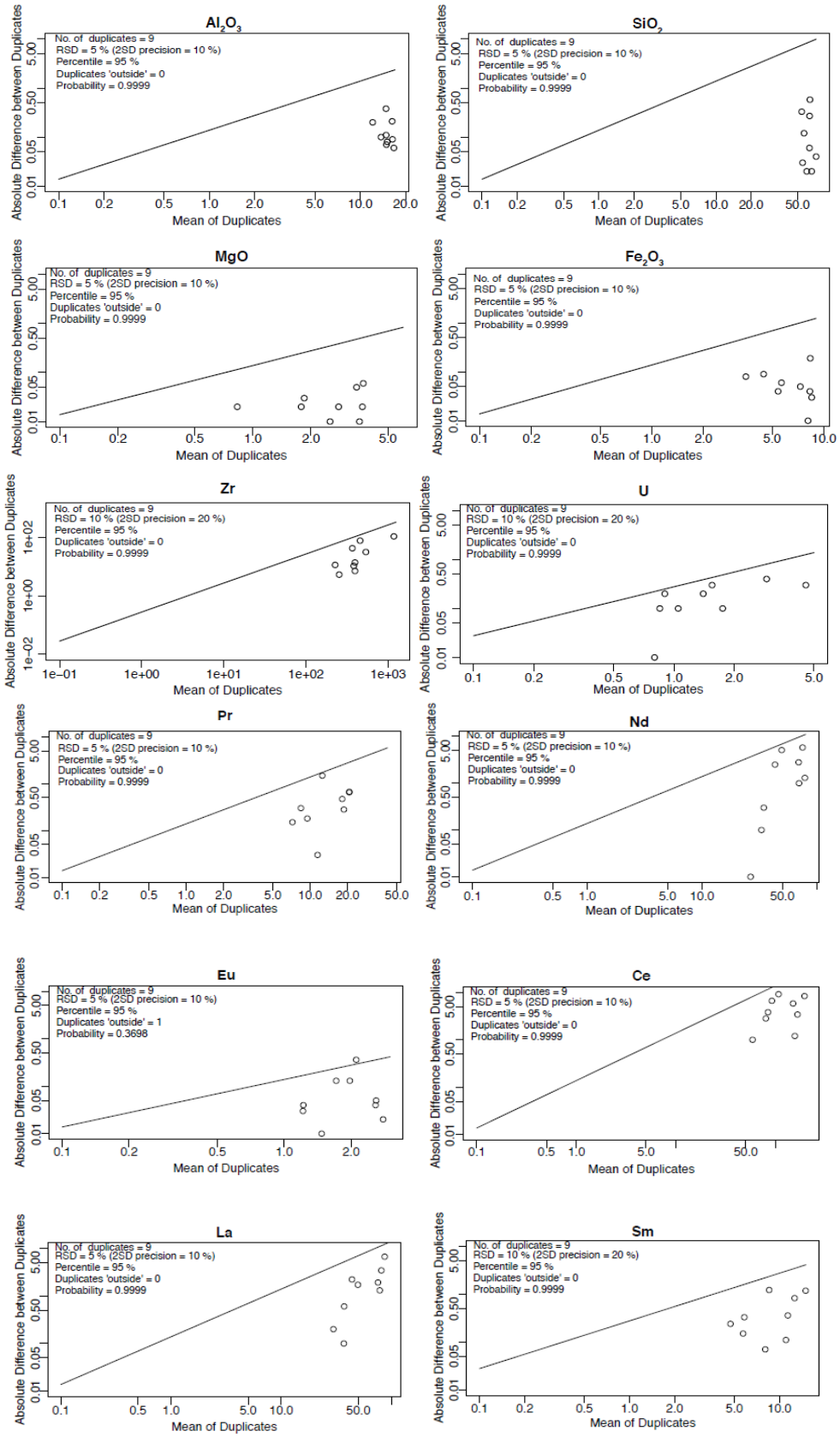

Figure 4.1.2. Thompson-Howarth plots for duplicate analysis for all elements used for geochemical exploration. Results flow all of the duplicates yield better than 95% precision within a 99% confidence level.

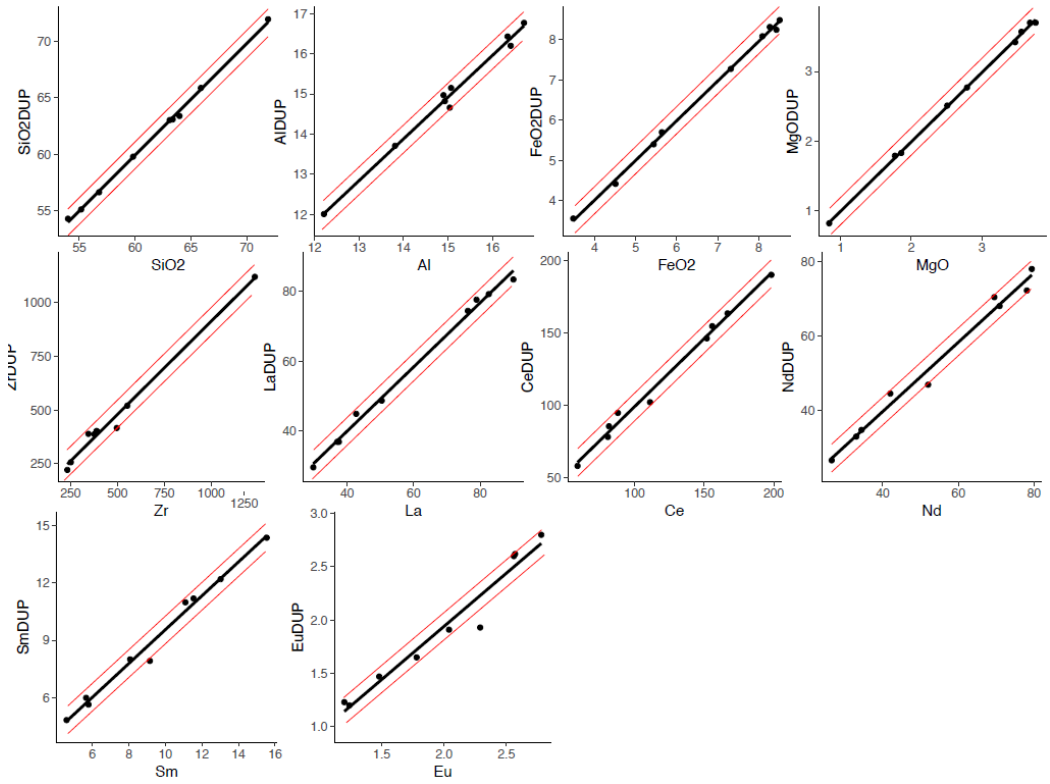

Figure 4.1.3. Scatterplots of duplicate analysis for all elements used for geochemical dispersal. All samples fall within 10% variance except for a single sample of Eu.

References

Croakin, C., and Tobias, P. 2006, NIST/SEMATECH e-Handbook of Statistical Methods, National Institute of Standards and Technology/SEMATECH, (e-book, last updated April 2012): US Commerce Department's Technology Administration.

Dines, G.E., Jusko, T.A., Ho, L.A., Annam, K., Graubard, B.I., Herz-Picciotto, I., Miller, F.W., Gillepsie, B.W., and Weinberg, C.R. 2014. Accommodating Measurements Below a Limit of Detection: A Novel Application of Cox Regression. American Journal of Epidemiology, 179:1018-1024.

Garret, R.G. 1969. The determination of sampling and analytical errors in exploration geochemistry. Economic Geology, 64: 568-569.

Garrett, R.G., and Grunsky, E.C. (2003). S and R functions for the display of Thompson-Howarth plots. Computers and Geosciences, 29: 239-242.

Jenner, G.A. (1996). Trace element geochemistry of igneous rocks: geochemical nomenclature and analytical geochemistry. *In* Wyman, D.A. (ed) Trace Element Geochemistry of Volcanic rocks: Applications for Massive Sulphide Exploration 12, Geological Association of Canada, Short Course notes: 51-77.

Piercey, S.J. (2014). Modern analytical facilities 2. A review of quality assurance and quality control (QA/QC) procedures for lithogeochemical data. Geoscience Canada, 41(1): 75-88.

Plouffe, A., McClenaghan, M.B., Paulen, R.C., McMartin, I., Campbell, J.E., and Spirito, W.A. 2013. Quality assurance and quality control measures applied to indicator mineral studies of glacial sediments at the Geological Survey of Canada. IN: McClenaghan, M.B., Plouffe, A., Layton-Matthews, D., (eds.), Application of indicator mineral methods to mineral exploration. Geological Survey of Canada Open File 7553.

Rice, J.M., McClenaghan, M.B., Paulen, R.C., Pyne, M.D., and Ross, M. 2017. Till geochemical data for the southern Core Zone, Quebec and Newfoundland and Labrador (NTS 23P and 23I): samples collected in 2015 and 2016. Geological Survey of Canada, Open File 8219.

Scrucca, L. 2004. qcc: an R package for quality control charting and statistical process control. R News 4/1, 11-17.

Wickham, H. 2016. Ggplot2: Elegant Graphics for Data Analysis. Springer-Verlag, New York.

Appendix S4.2 Identification of Geochemical indicators from bedrock samples

Appropriate geochemical indicators from each bedrock domain were identified from available bedrock reports (Danis, 1988; Keer et al., 1994; Martelain et al., 1998; Dickson and Kerr, 2007; Collins and Cashin, 2010; Sanborn-Barrie, 2016; Corrigan et al., 2018), previous drift prospecting research (Klassen and Thompson, 1993) and lake geochemistry maps (Clark and Wares, 2004; Amor et al., 2016). To evaluate the average geochemical composition of each bedrock unit, rock geochemistry data for each geological unit was retrieved using the Énergie et Ressources naturelles Systèm d'information géominère of Québec database (http://sigeom.mines.gouv.qc.ca/signet/classes/I1102_indexAccueil?l=a). Only samples with reported bedrock units and analysis through inductive coupling mass spectrometry to a resolution of parts per million (ppm) were utilized for this investigation. Fourteen geochemical results from the Rachel-Laporte (RL) domain, 17 from the George River (GR), and 24 samples from the Mistinibi-Raude (MR) domain were utilized for this analysis (Figure 1).

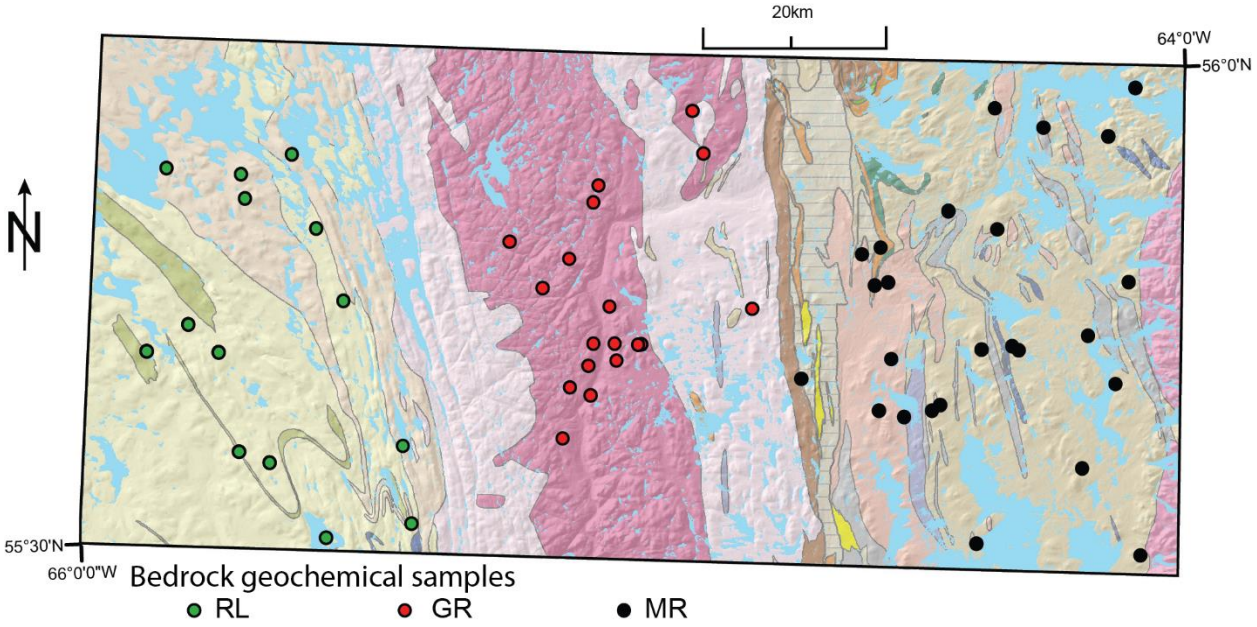

Figure 3. Bedrock geochemistry samples from each domain utilized for establishing baseline geochemical characteristics of each unit.

Each geochemical indicator identified as characteristic of the given bedrock unit (i.e., Ba (ppm) for GR), was evaluated across the study area to assess any other possible major sources. Probability plots

were used to assess the probability distributions of the geochemical values. Natural breaks were used in the data to create 'groups' that were used to create proportional dot maps to assess the geochemical variability of each geochemical indicator across the study area (Figures 2 – 4). If there was significant clustering of elements within a given bedrock unit, it was deemed acceptable for dispersal analysis.

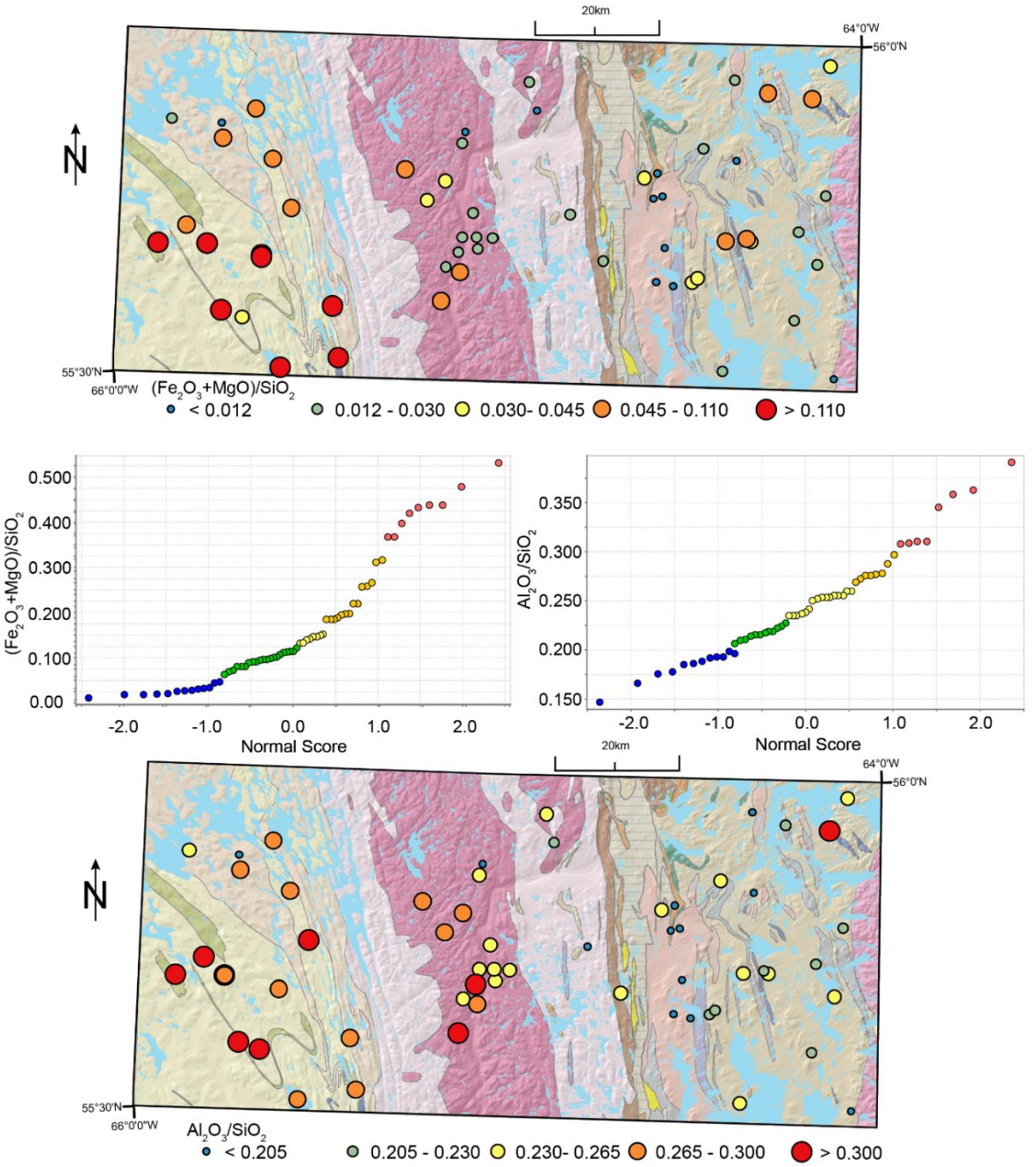

Figure 4. (A) Bedrock geochemistry results for $(Fe_2O_3+MgO)/SiO_2$ (%) across the three bedrock domains, showing elevated abundances in the RL domain. (B) Bedrock geochemistry results for Al_2O_3/SiO_2 (%) across the three bedrock domains, showing elevated abundances in the RL domain.

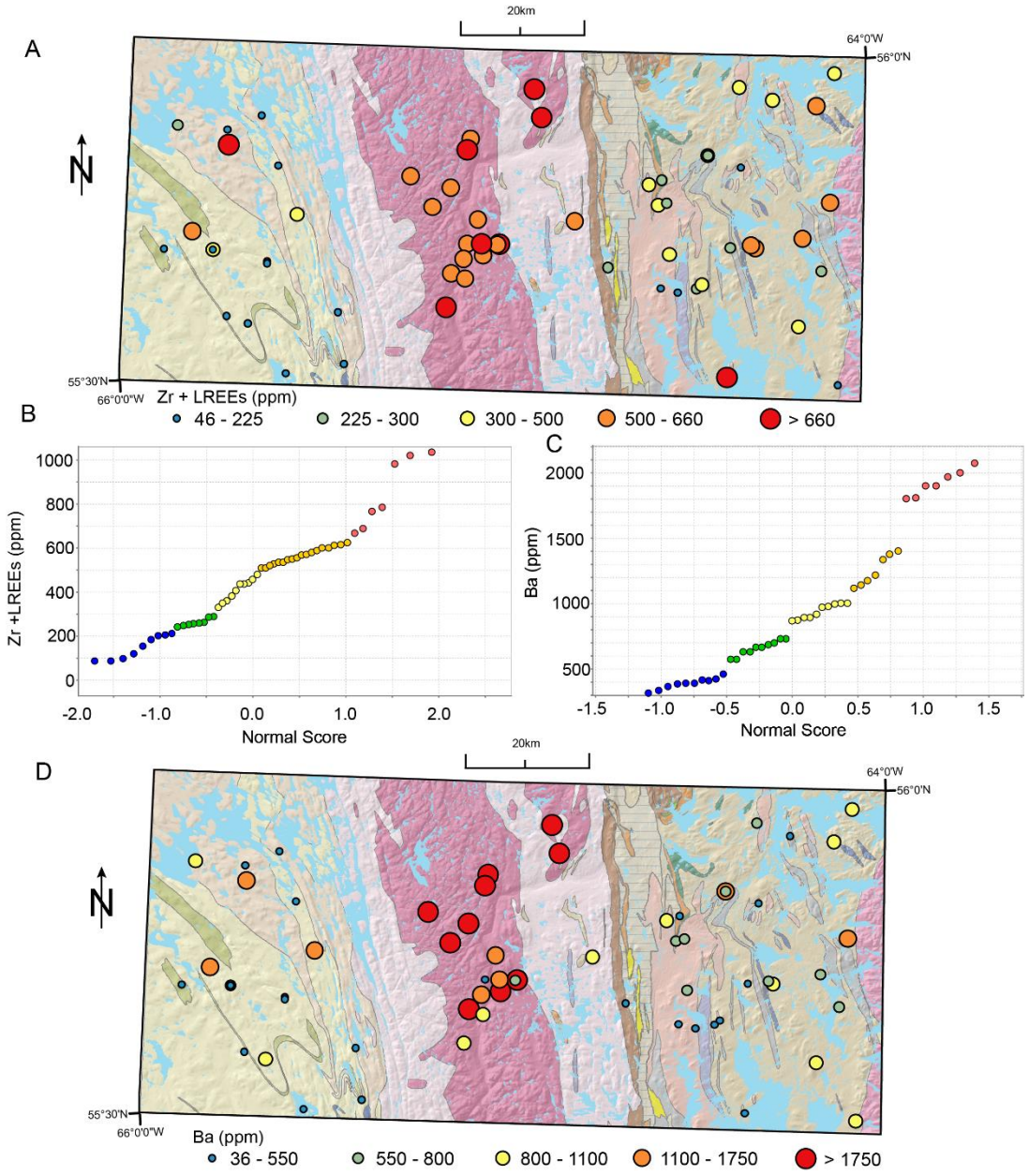

Figure 5. (A) Bedrock geochemistry results for Zr +LREEs (all as ppm) across the three bedrock domains, showing elevated abundances in the GR domain. (B) Bedrock geochemistry results Ba (ppm) across the three bedrock domains, again, showing elevated abundances in the GR domain.

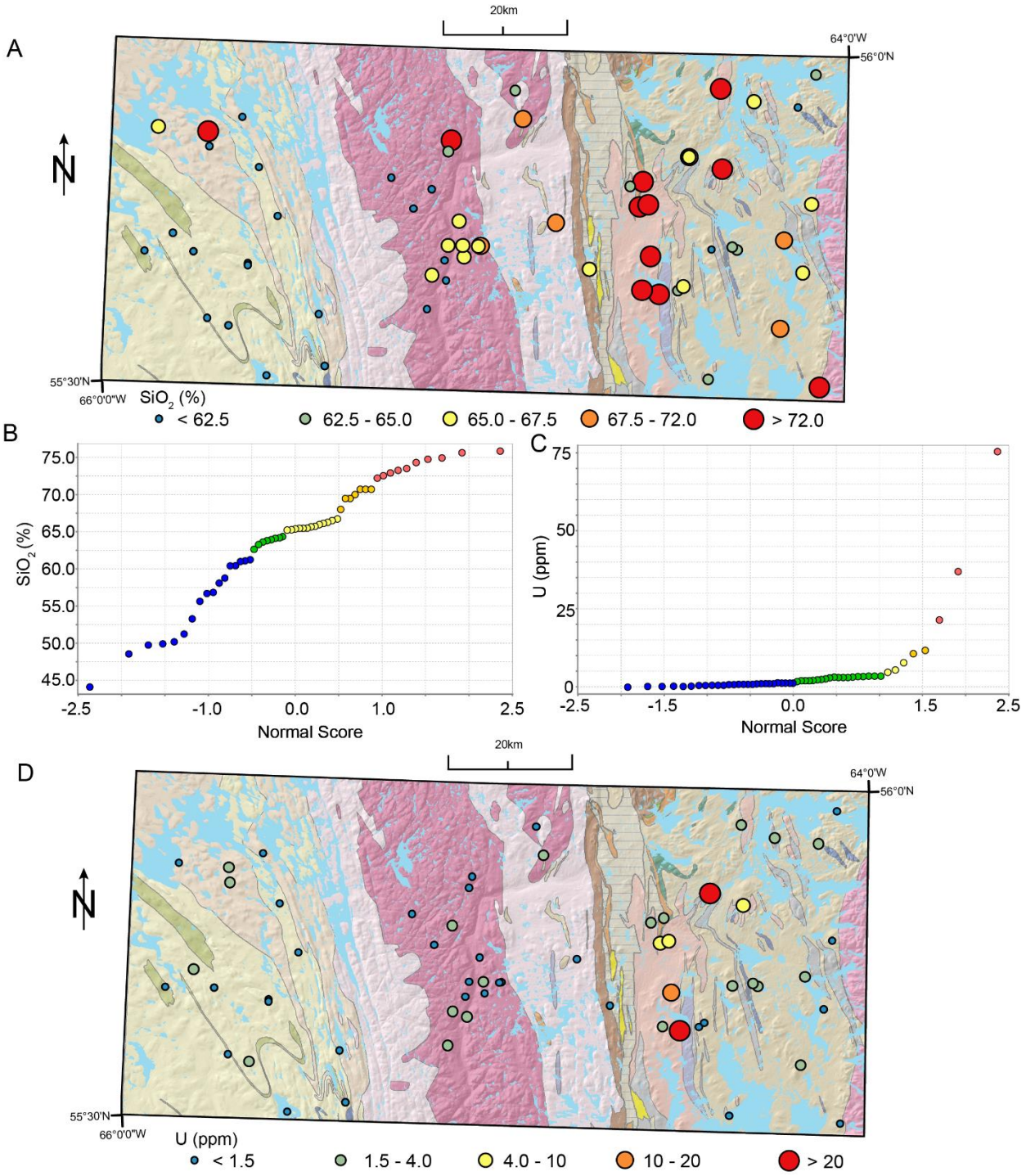

Figure 6. (A) Bedrock geochemistry results for SiO_2 (%) across the three bedrock domains, showing elevated abundances in the MR domain. (B) Bedrock geochemistry results U (ppm) across the three bedrock domains, showing elevated abundances in the MR domain near known U mineralization locations (Collins and Cashin, 2010).

S4.2.1 Separation of classes for till matrix geochemistry

Similar to bedrock samples, till matrix geochemistry samples were assessed using probability plots. Probability plots allow for an easy visual evaluation of how much the data deviates from a normal distribution whereby, a normally distributed dataset would have plotted points along a nearly straight line. By grouping the data based on natural breaks in this slope, groups can help discriminate different tills from different sources and their spatial relationship can be assessed. This process was applied to elements identified through bedrock geochemistry as good indicators for each bedrock domain for till matrix geochemistry. Therefore, probability plots for all elements identified through bedrock geochemical analysis were also constructed for till matrix geochemistry (Figure 6).

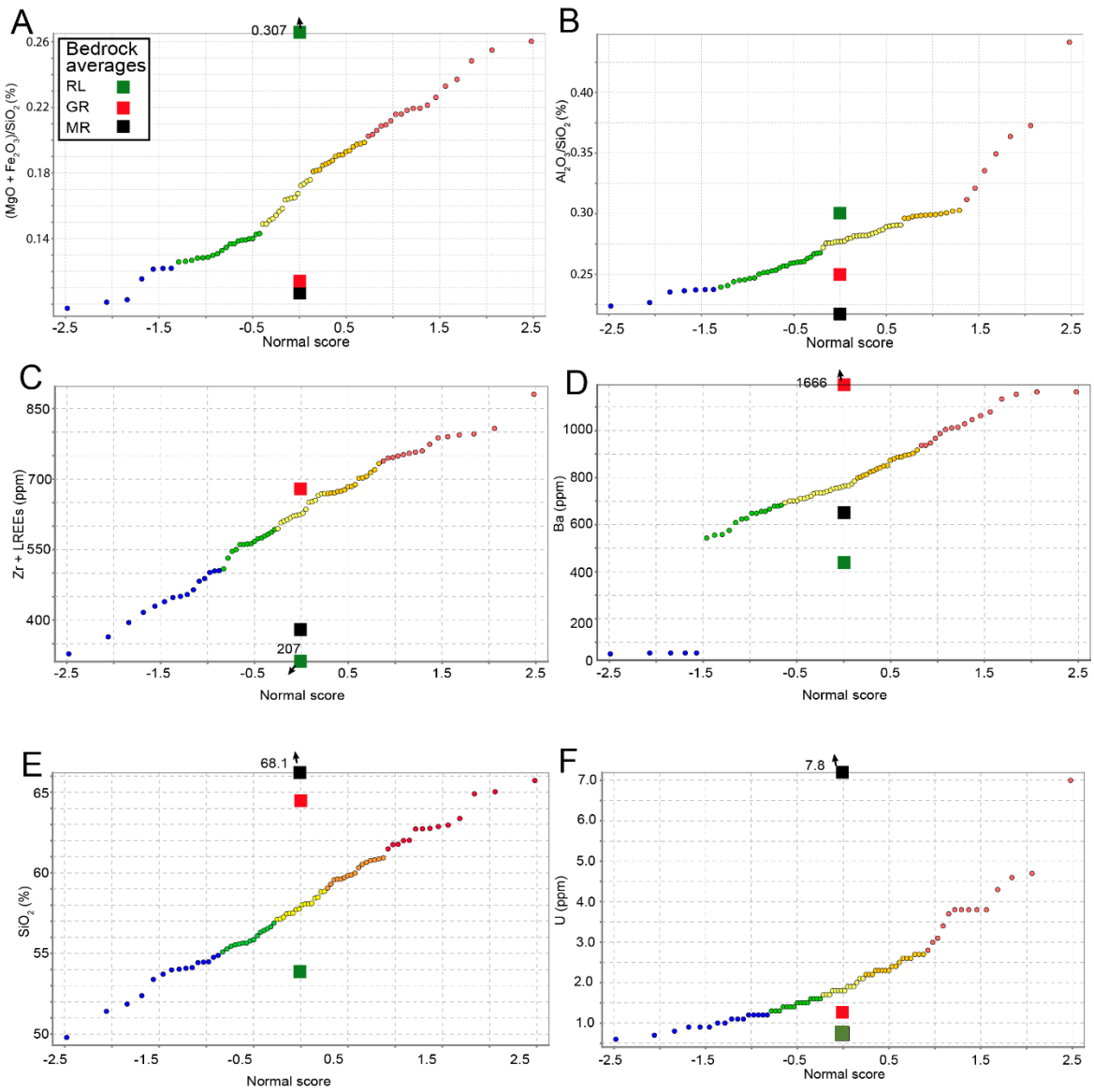

Figure 7. For each probability plot the average bedrock value for each of the three domains is plotted along the normal score. (A). Biplot of $(Fe_2O_3+MgO)/SiO_2$ (all as %) abundances from till samples across the study area, showing the natural breaks used to separate the five classes. (B) Biplot of Al_2O_3/SiO_2 (all as %) abundances from till samples across the study area, showing the natural breaks used to separate the five classes. (C) Biplot of Zr + all LREEs (ppm) abundances from till samples across the study, showing the natural breaks used to separate the five classes. (D) Biplot of Ba (ppm) abundances from till samples across the study area, showing the natural breaks used to separate the five classes. (E) Biplot of SiO_2 (%) abundances from till samples across the study area, showing the natural breaks used to separate the five classes. (F) Biplot of U (ppm) abundances from till samples collected across the study area, showing the natural breaks used to separate the five classes.

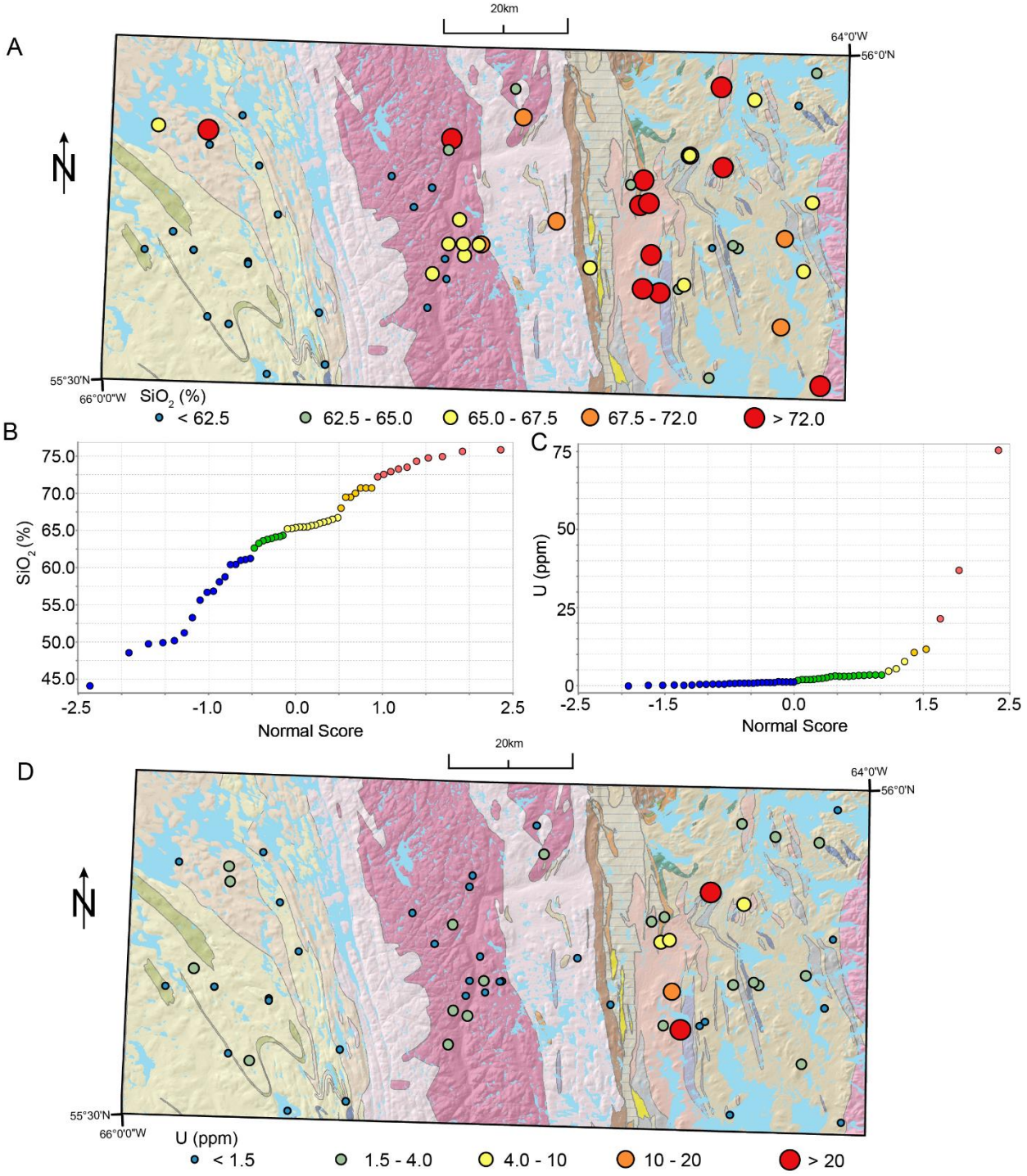

Figure 8. **(A)** Bedrock geochemistry results for SiO_2 (%) across the three bedrock domains, showing elevated abundances in the MR domain. **(B)** Biplot of SiO_2 (%) abundances from till samples across the study, showing the natural breaks used to separate the five classes. **(C)** Biplot of U (ppm) abundances from till samples across the study, showing the natural breaks used to separate the five classes. **(D)** Bedrock geochemistry results U (ppm) across the three bedrock domains, showing elevated abundances in the MR domain near known U mineralization locations (Collins and Cashin, 2010).

S4.2.1 Separation of classes for till matrix geochemistry

Similar to bedrock samples, till matrix geochemistry samples were assessed using probability plots. Probability plots allow for an easy visual evaluation of how much the data deviates from a normal distribution whereby, a normally distributed dataset would have plotted points along a nearly straight line. By grouping the data based on natural breaks in this slope, groups can help discriminate different tills from different sources and their spatial relationship can be assessed. This process was applied to elements identified through bedrock geochemistry as good indicators for each bedrock domain for till matrix geochemistry. Therefore, probability plots for all elements identified through bedrock geochemical analysis were also constructed for till matrix geochemistry (Figure 6).

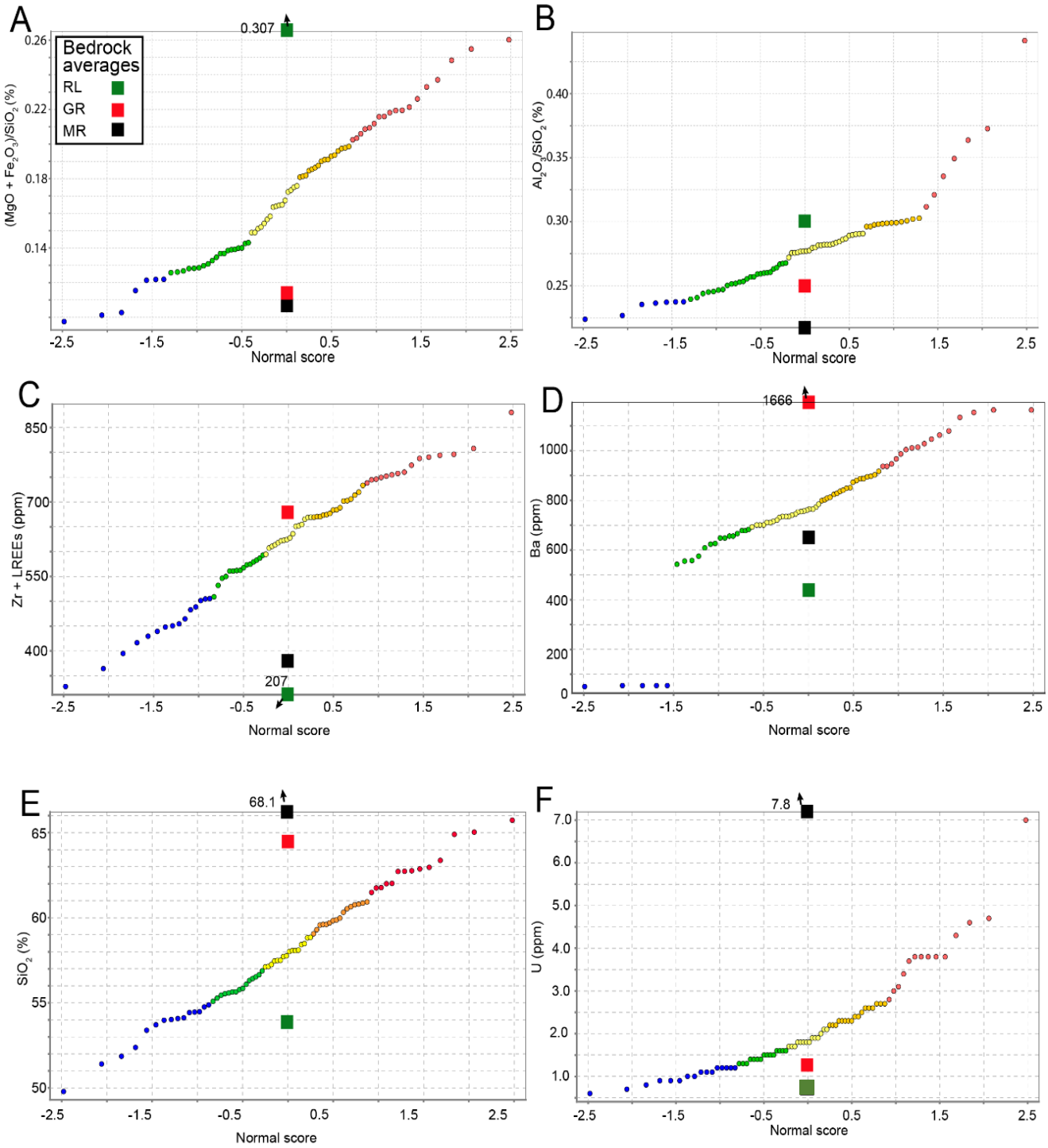

Figure 9. For each probability plot the average bedrock value for each of the three domains is plotted along the normal score. **(A).** Biplot of (Fe_2O_3+MgO)/SiO_2 (all as %) abundances from till samples across the study area, showing the natural breaks used to separate the five classes**. (B)** Biplot of Al_2O_3/SiO_2 (all as %) abundances from till samples across the study area, showing the natural breaks used to separate the five classes. **(C)** Biplot of Zr + all LREEs (ppm) abundances from till samples across the study, showing the natural breaks used to separate the five classes**. (D)** Biplot of Ba (ppm) abundances from till samples across the study area, showing the natural breaks used to separate the five classes**. (E)** Biplot of SiO_2 (%) abundances from till samples across the study area, showing the natural breaks used to separate the five classes**. (F)** Biplot of U (ppm) abundances from till samples collected across the study area, showing the natural breaks used to separate the five classes.

References

Amor, S., McCurdy, M., and Garrett, R. 2018. Creation of an atlas of lake-sediment geochemistry of Western Labrador and Northeastern Québec. Geochemistry: Exploration, Environment, Analysis, 19:339-393. doi 10.1144/geochem2018-061

Collins, C. and Cashin, P.J. 2010. Summary Report on the Mineral exploration Program July to August 2009. Quest Rare Minerals George River Project Nanuk claims NTS area 23P/16. Énergie et Ressources naturelles Québec Report GM 65368. Available online: http://gq.mines.gouv.qc.ca/documents/EXAMINE/GM65368/GM65368.pdf

Corrigan, D., Wodicka, N., McFarlane, C., Lafrance, I., van Rooyen, D., Bandyayera, D., and Bilodeau, C. 2018. Lithotectonic Framework of the Core Zone, Southeastern Churchill Province, Canada. Geoscience Canada, 45: 1-24. doi: 10.12789/geocanj2018.45.128

Clark, T. and Wares, R. 2004. Synthèse lithotectonique et métallogénique de l'Orogène du Nouvequ-Québec (Fosse du Labrador). Ministère des Ressources naturelles et de la Faune, Québec Report MM 2004-01, 182p.

Danis, D. 1988. Géologie de la region du lac Recouet (Territoire-du-Nouveau-Québec). Ministere de l'Énergie et des Ressources Québec; ET 86-11, 60p.

Dickson, W.L. and Kerr, A. 2007. An updated database of historic geochemical data for granitoid plutonic suites of Newfoundland. Newfound and Labrador Geological Survey, Open File NFLD/2957

Kerr, A., James, D.T., and Fryer, B.J. 1994. Nd isotopic and geochemical studies in the Labrador Shield: a progress report and preliminary data from the Churchill (Rae) Province. In Eastern Canadian Shield Onshore- Offshore Transect (ECSCOOT), Wardle, R.J., and Hall, J. (eds.) Report of the transect meeting (Dec. 1994), The University of British Columbia, Lithoprobe Secretrait, Report 45: 51-62.

Martelain, J., Chenevoy, M., and Bélanger, M. 1998. Le Batholite de De Pas, Noveau-Québec: infratstructure composite d'arc magmatique protéroïque. Canadian Journal of Earth Sciences, 35: 1-15.

Figure S2.1. **(Top)** Locations for samples collected for till and bedrock ^{10}Be analysis (red circles). **(A)** Site photos for sample 16-PTA-053. **(B)** Site photos for sample 15-PTA-083. **(C)** Site photos for sample 16-PTA-070. **(D)** Site photos for sample. 16-PTA-058. **(E)** Site photos for samples 15-PTA-081 and 15-PTA-081B.

Figure S2.2

(Top) Sample location map with approximated extents of the two glacial lakes that inundated the study area. **(A)** Sample location photos for sample 16-PTA-052. **(B)** Sample location photos for sample 15-PTA-074. **(C)** Sample location photos for sample 15-PTA-035.

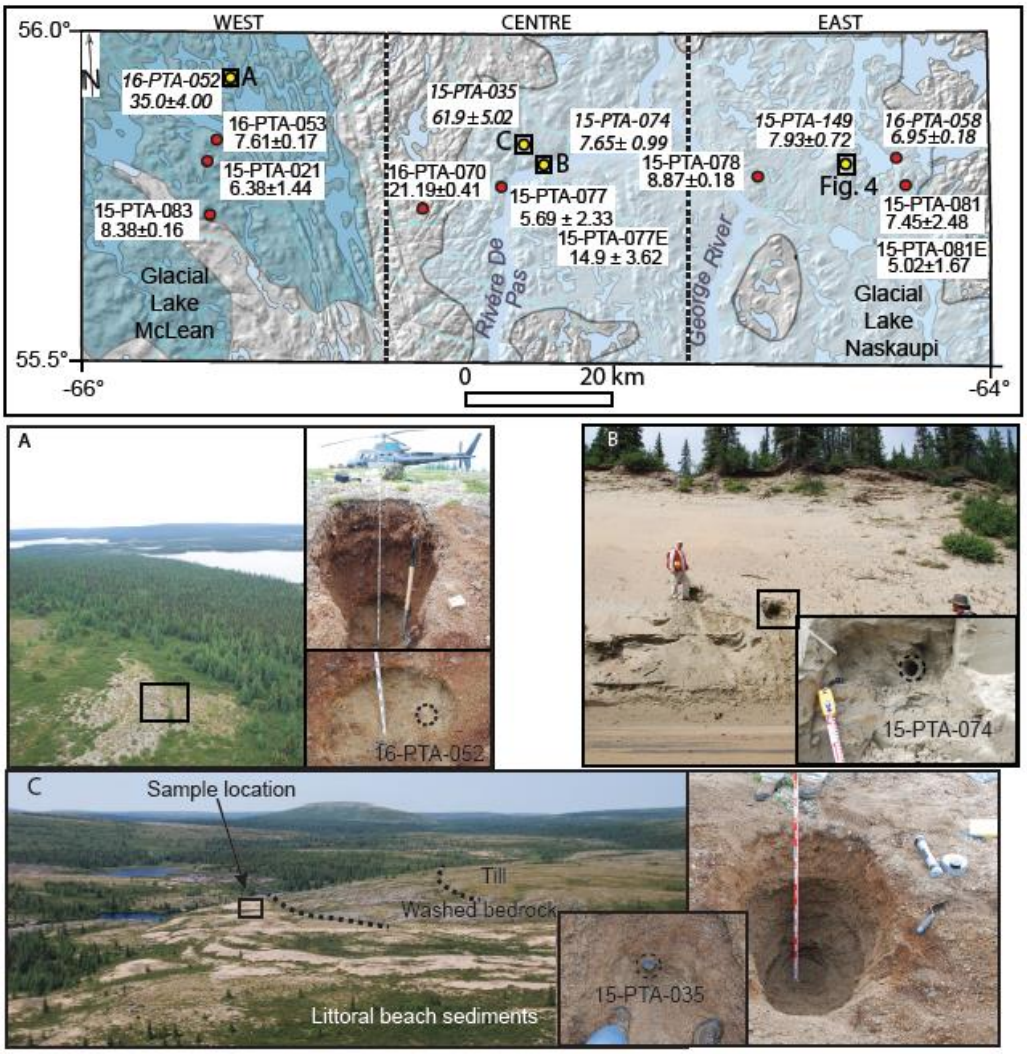

Figure S2.3

Recuperation values, recycling ratios, and D_e distributions for sample 15-PTA-035, 15-PTA-074, 15-PTA-149, and 16-PTA-052. The shaded region on the decay curves marks the initial and final parts of the optical signal used to calculate the D_e value. Optical decay curves and dose response curves (insert).

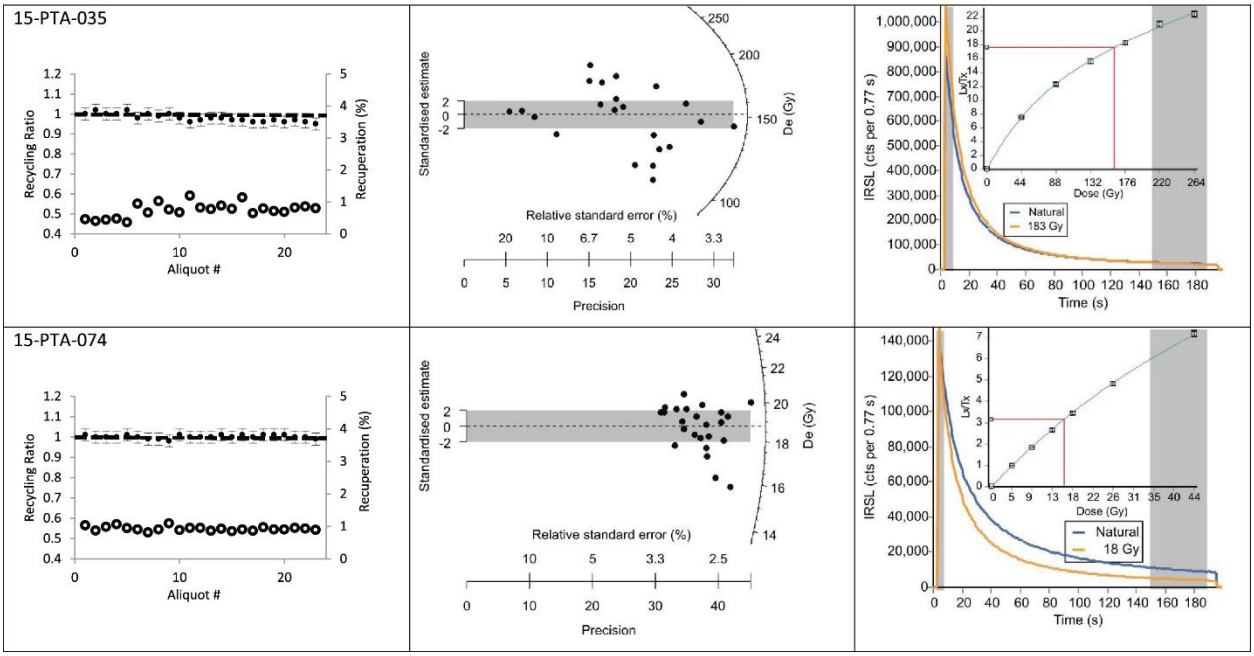

Appendix S4.2

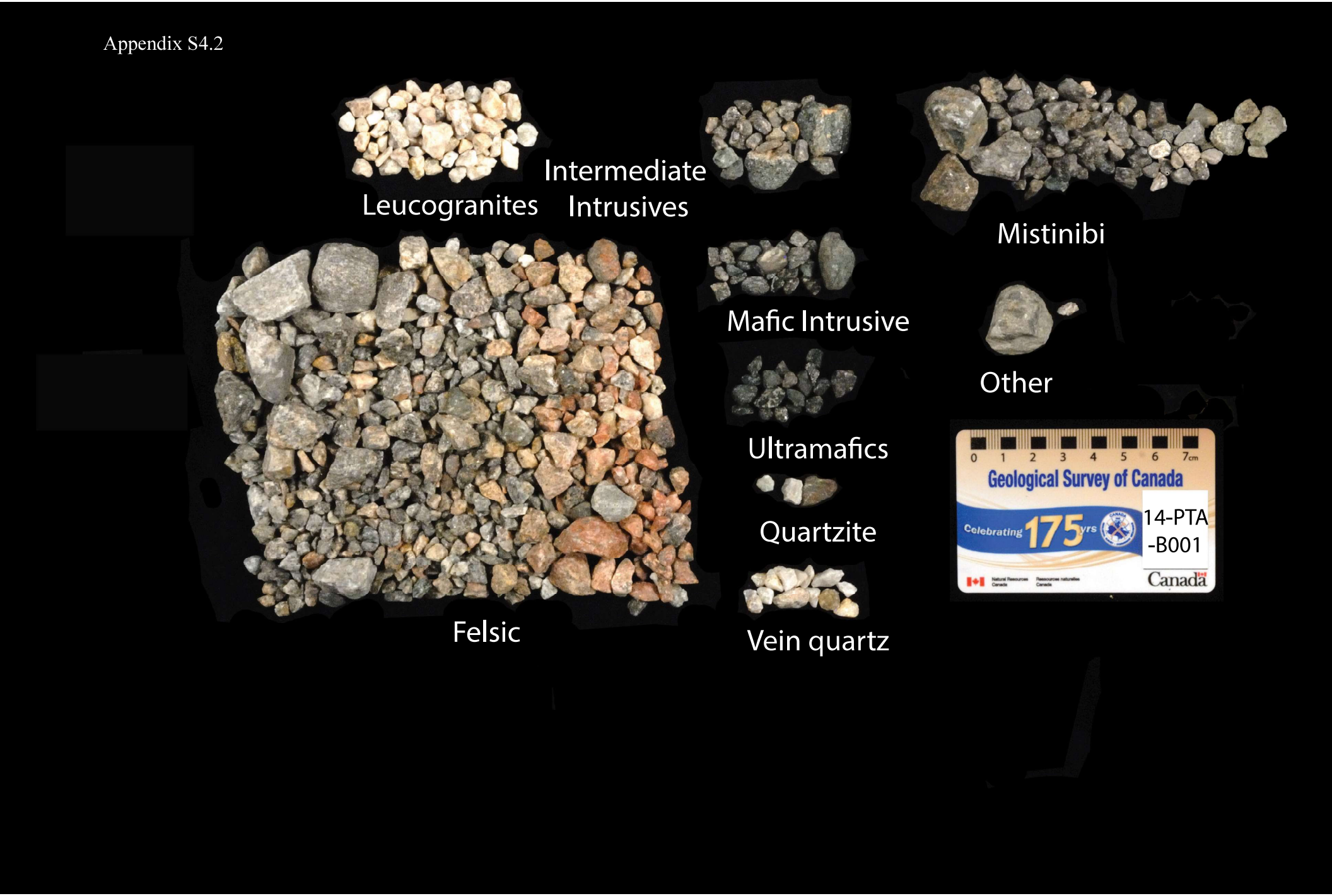

Appendix S4.2

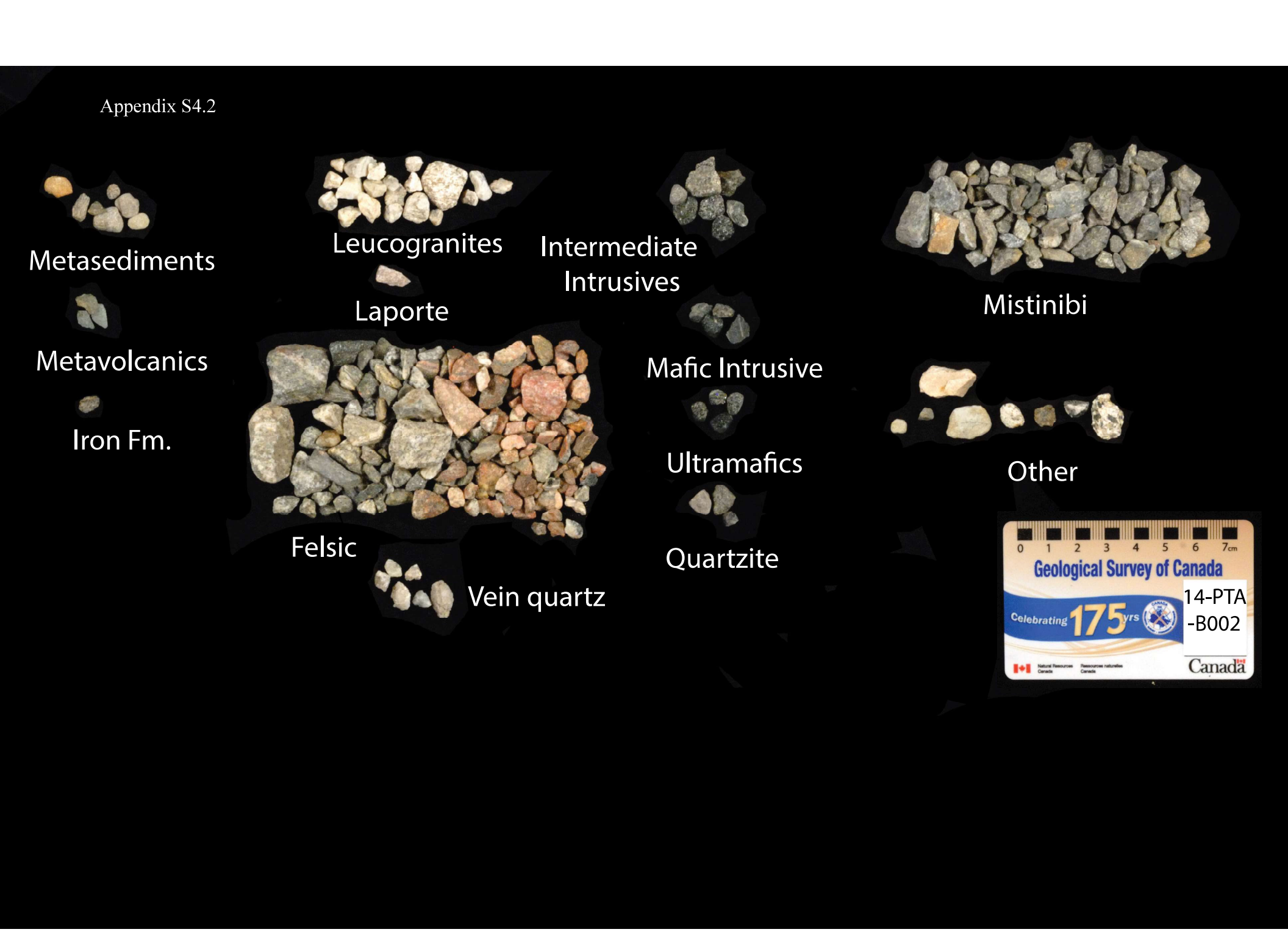

Appendix S4.2

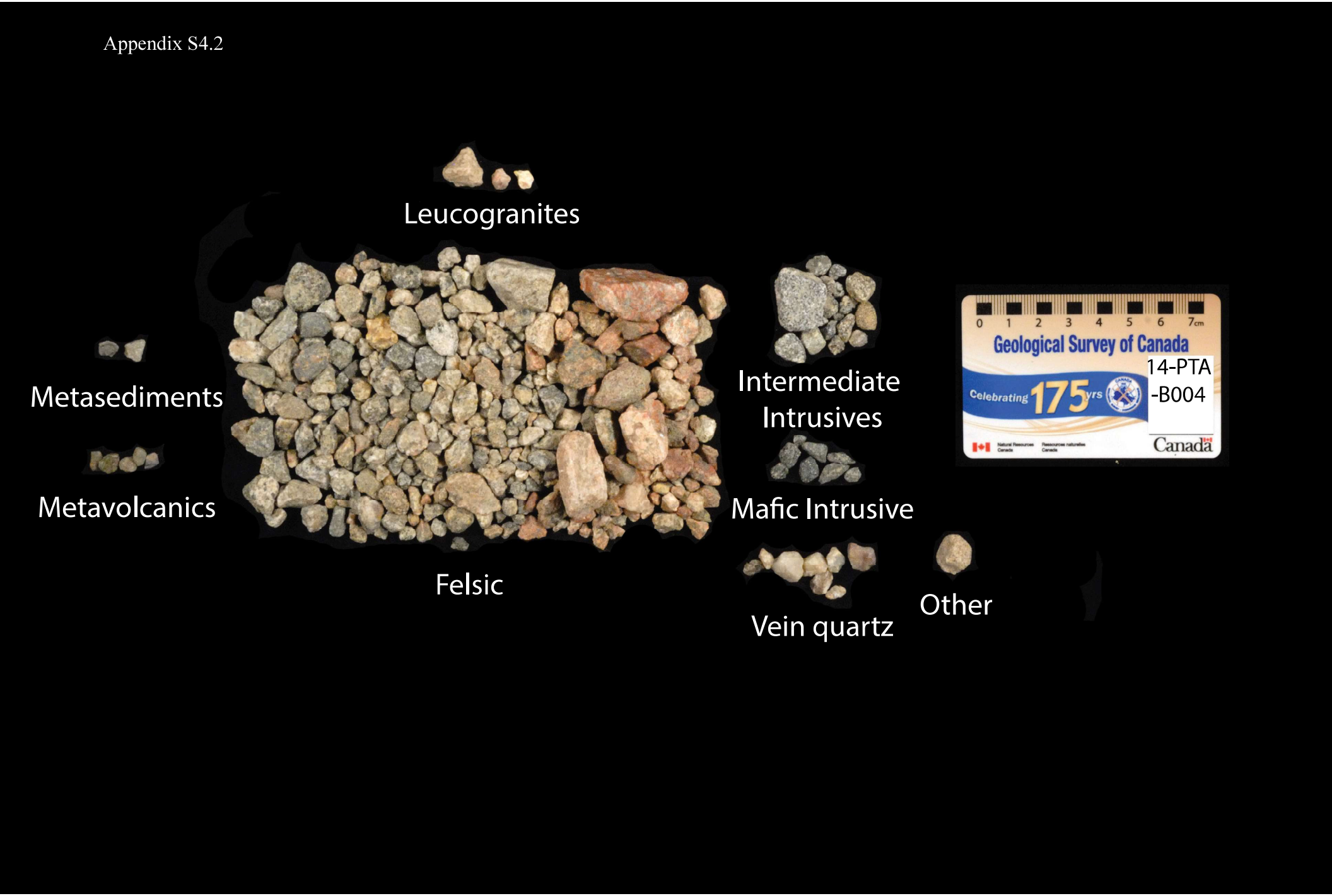

Appendix S4.2

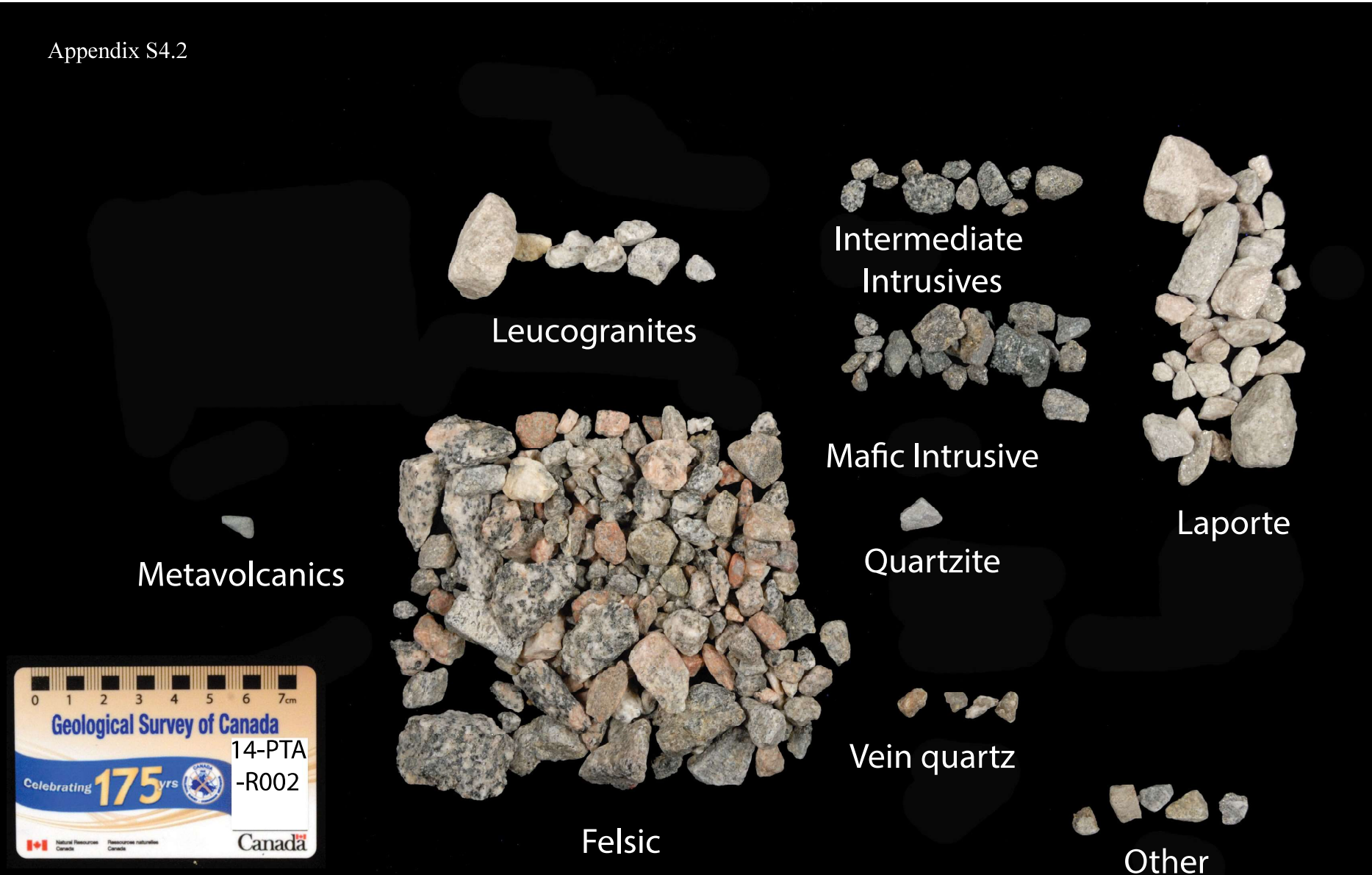

Appendix S4.2

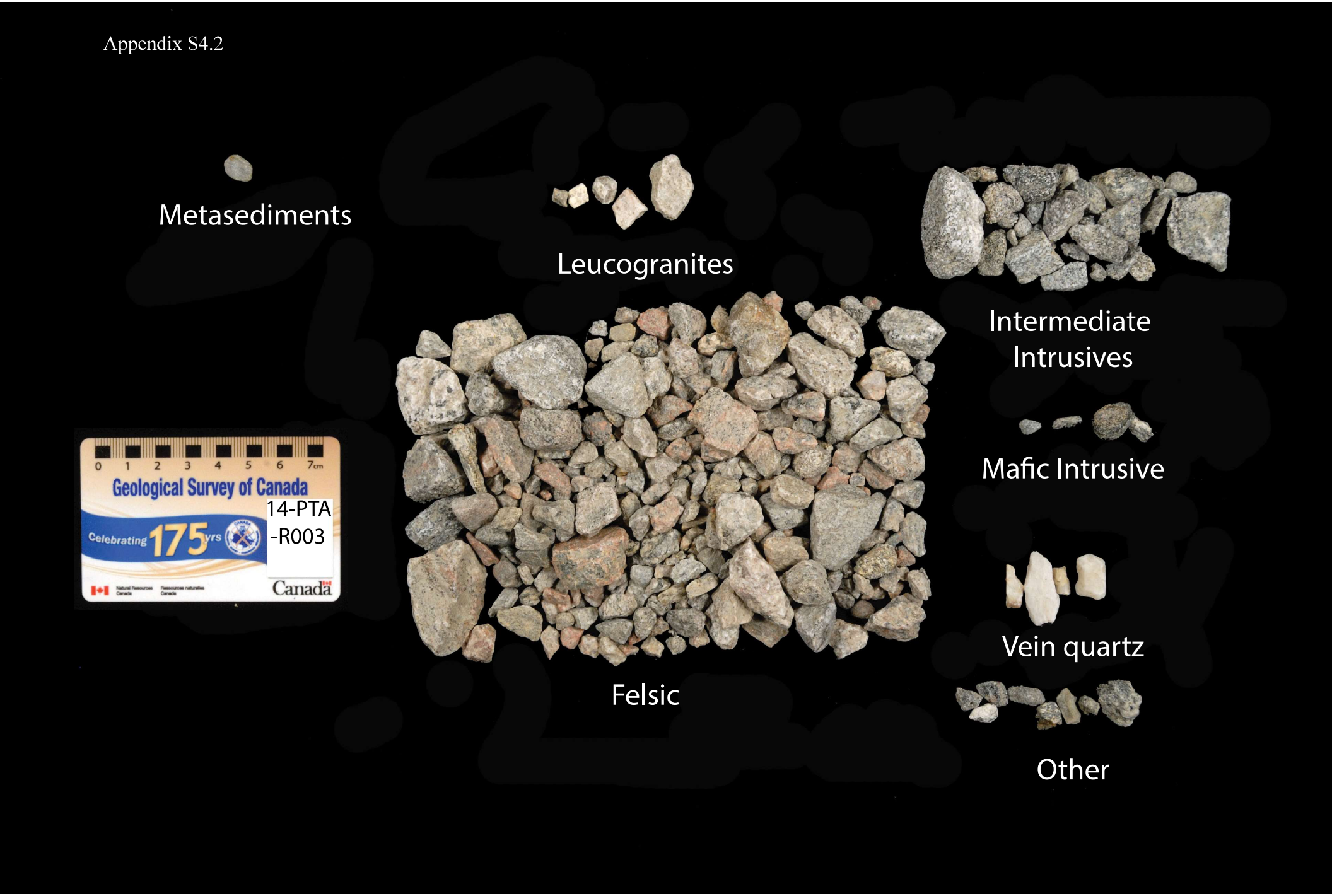

Appendix S4.2

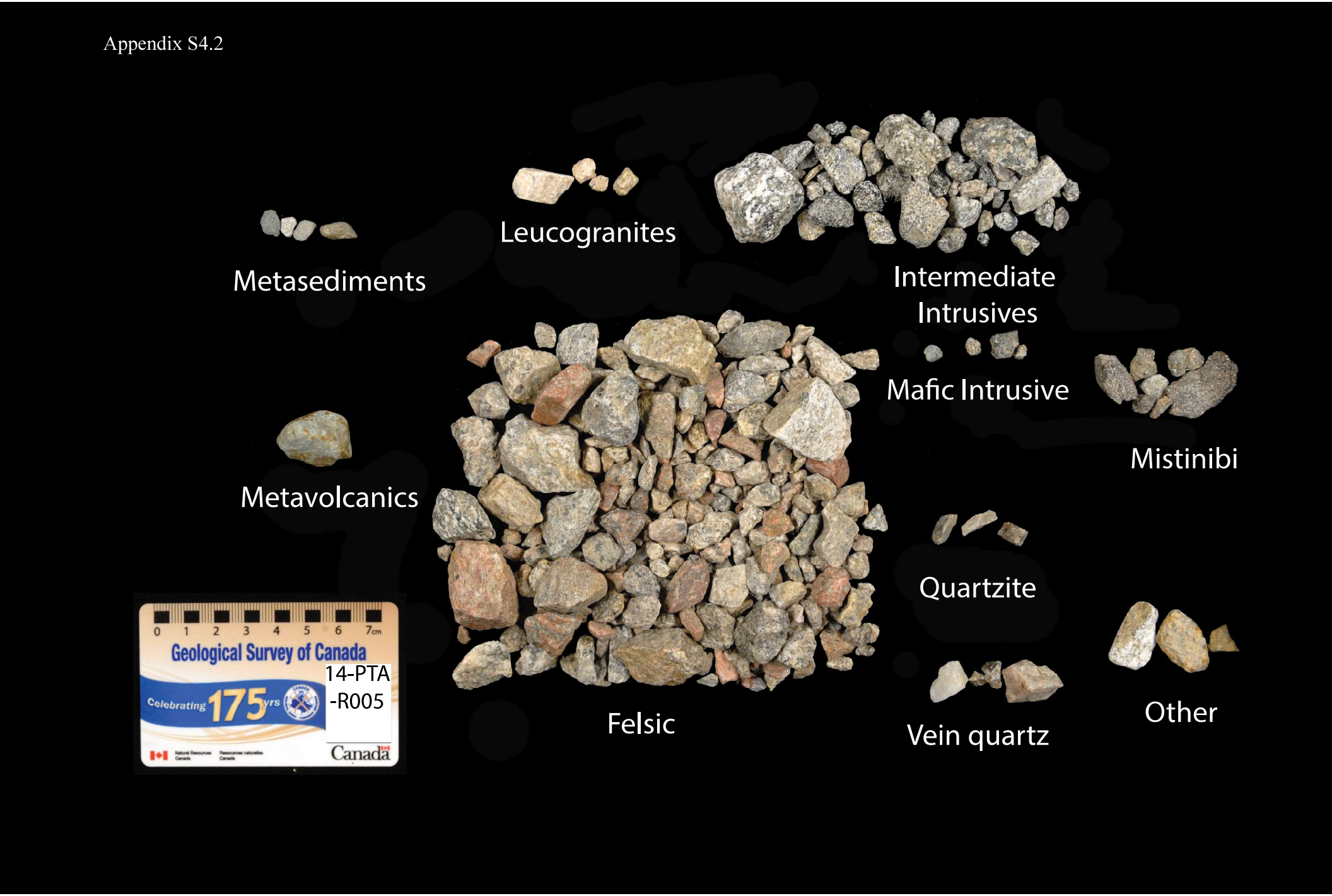

Appendix S4.2

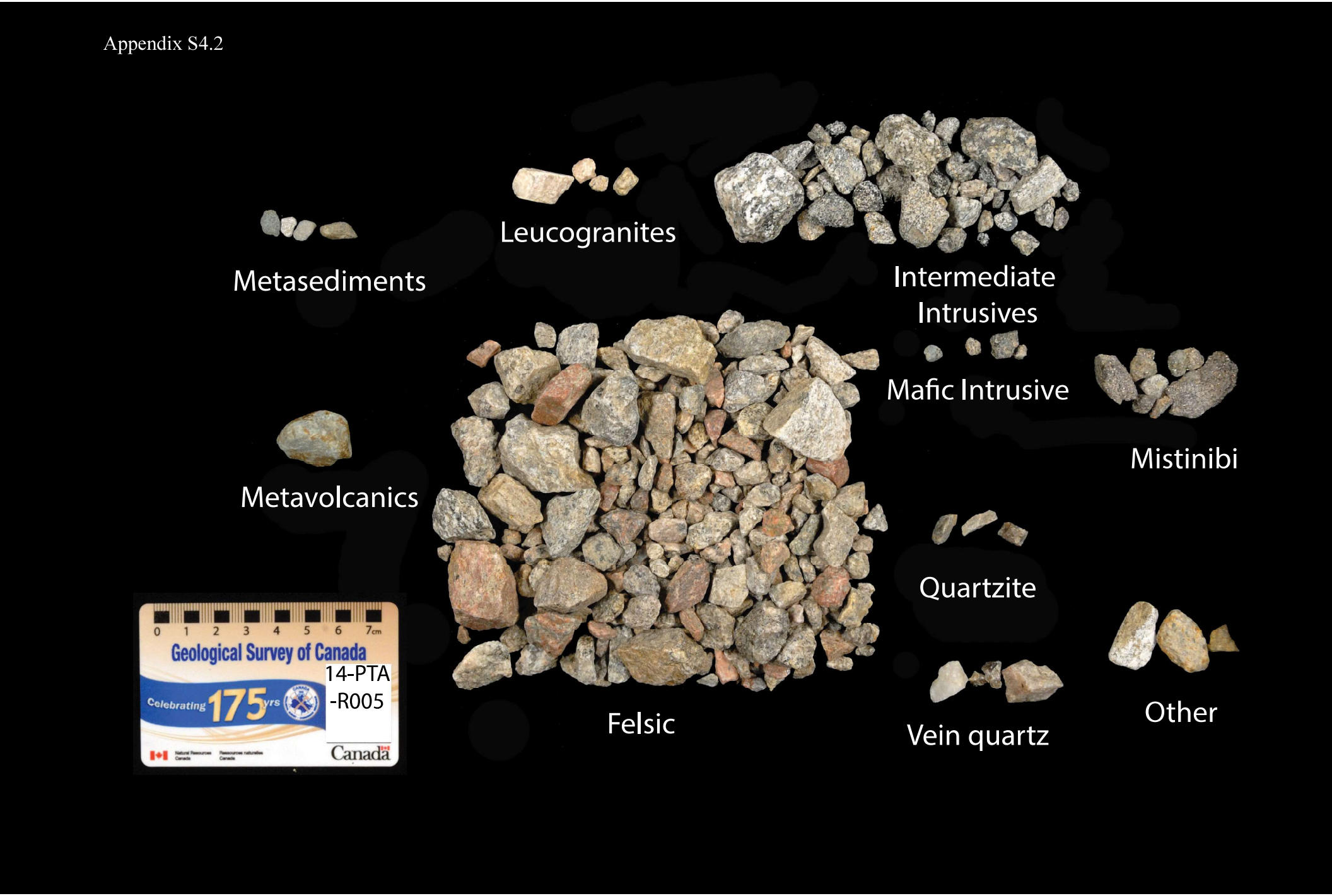

Appendix S4.2

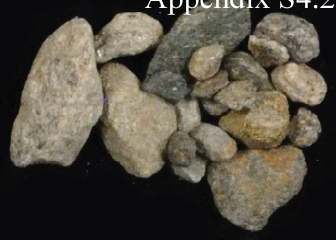

Metasediments

Leucogranites

Intermediate Intrusives

Laporte

Metavolcanics

Felsic

Mafic Intrusive

Other

Iron Fm.

Vein quartz

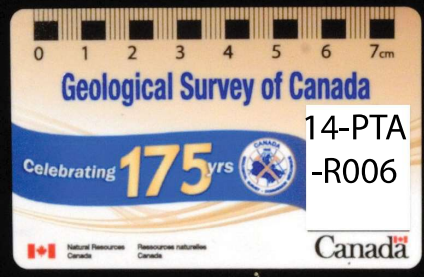

Appendix S4.2

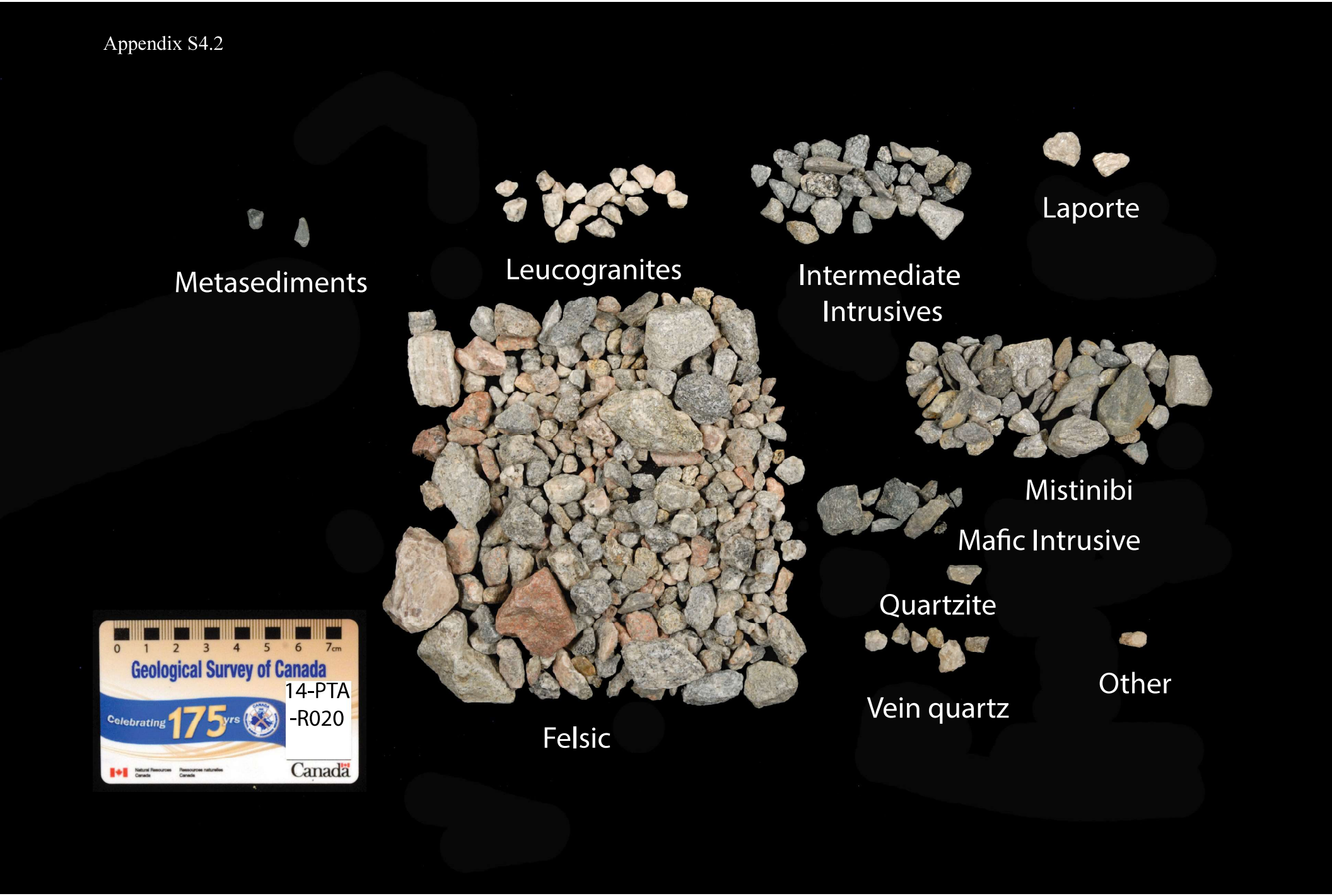

Appendix S4.2

Metasediments

Metavolcanics

Iron Fm.

Felsic

Intermediate Intrusives

Mafic Intrusive

Vein quartz

Other

Laporte

Mistinibi

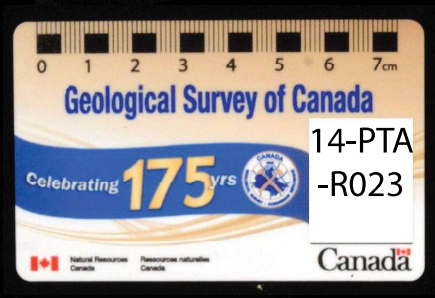

Appendix S4.2

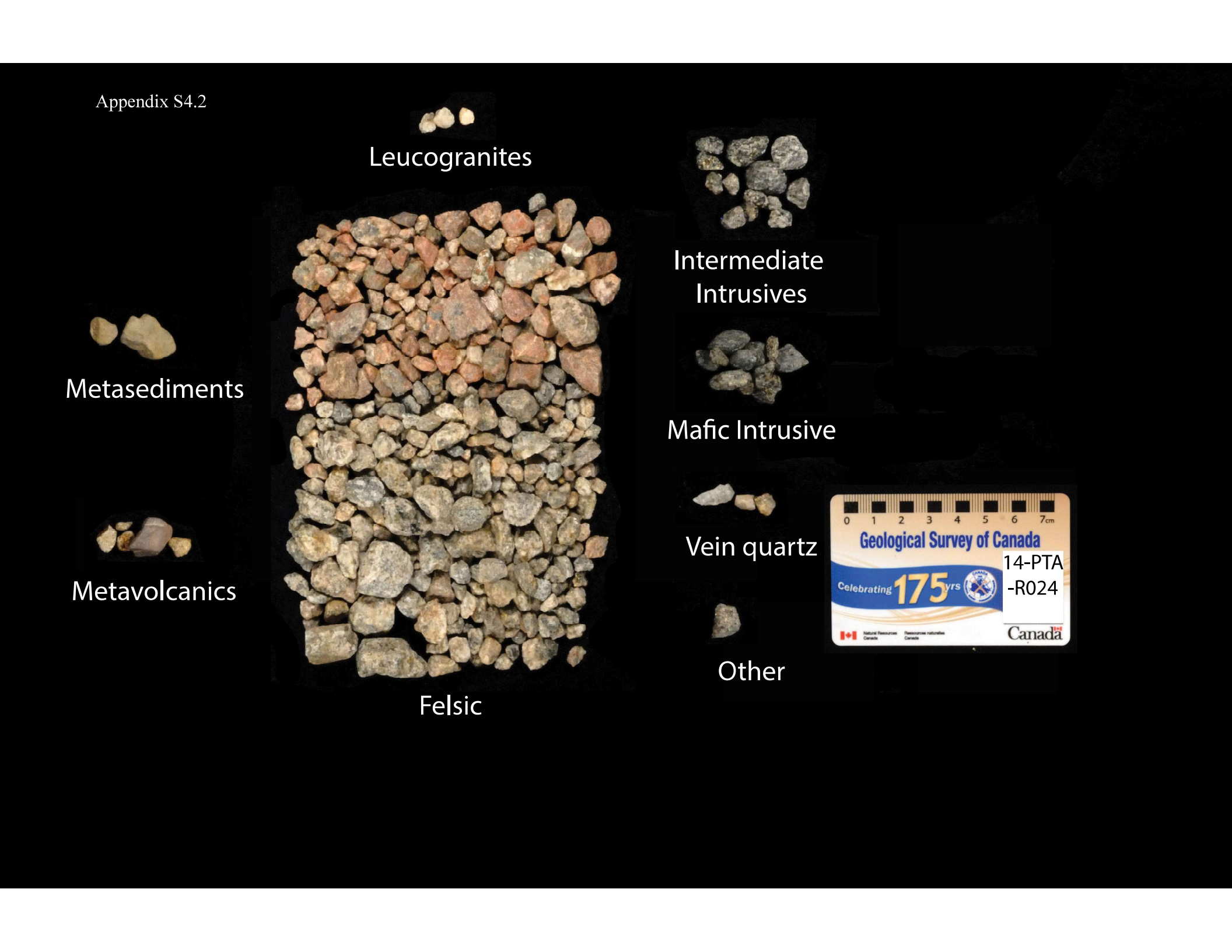

Appendix S4.2

Appendix S4.2

Metasediments

Leucogranites

Intermediate Intrusives

Laporte

Mafic Intrusive

Felsic

Others

Metavolcanics

Vein quartz

Appendix S4.2

Metasediments

Metavolcanics

Leucogranites

Intermediate Intrusives

Juillette Syenite

Felsic

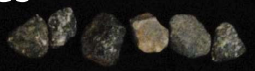

Mafic Intrusive

Ultramafics

Quartzite

Vein quartz

Other

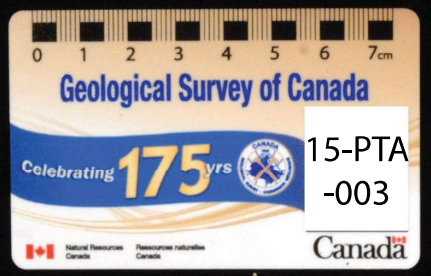

Appendix S4.2

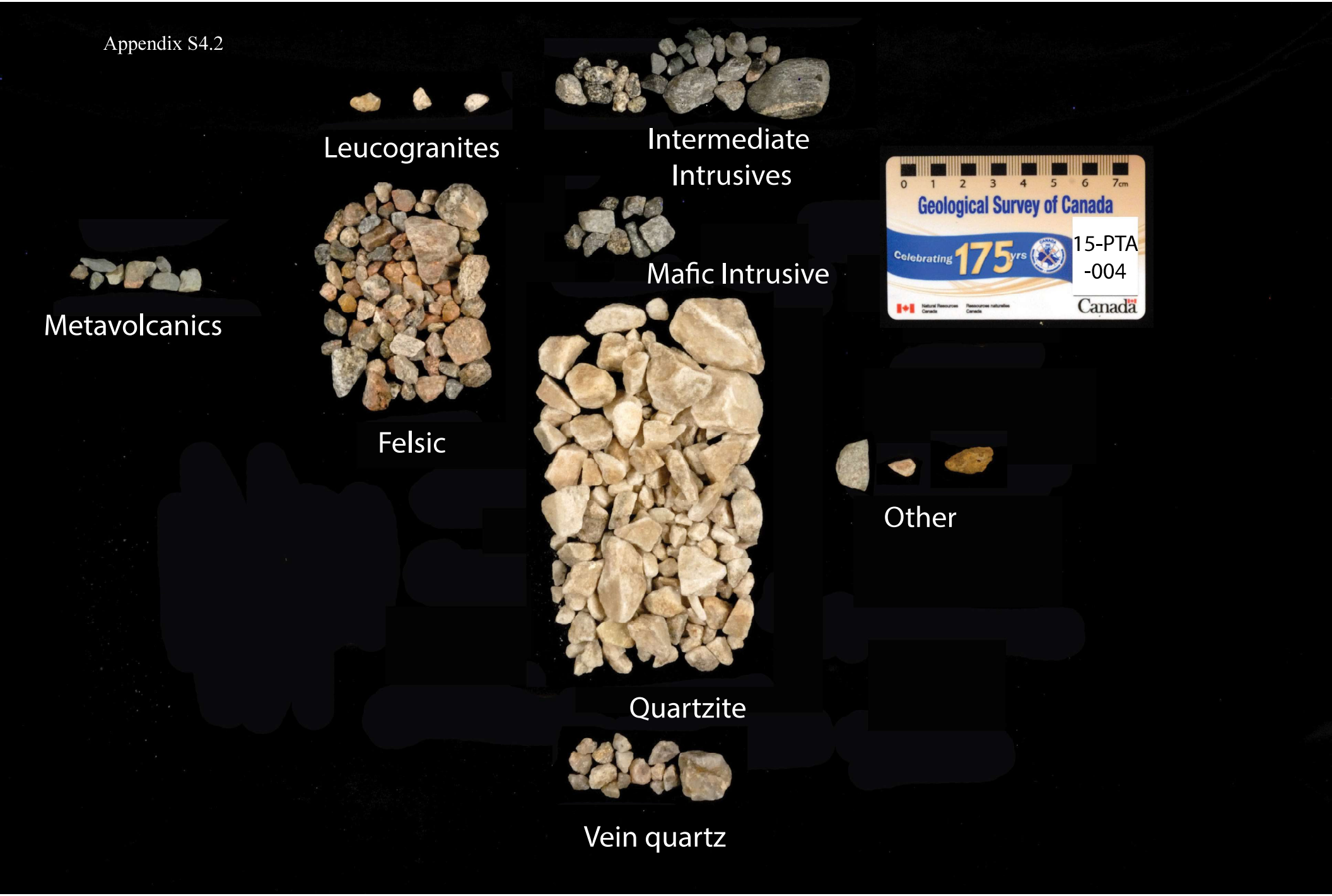

Appendix S4.2

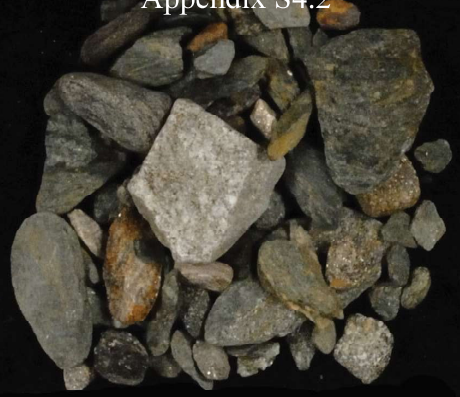

Metasediments

Leucogranites

Felsic

Intermediate Intrusives

Mafic Intrusive

Quartzite

Vein quartz

Other

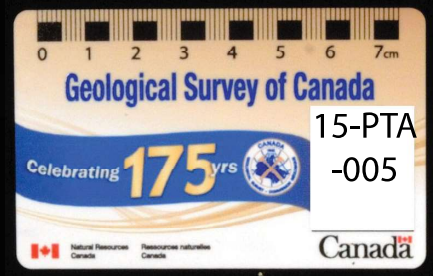

Appendix S4.2

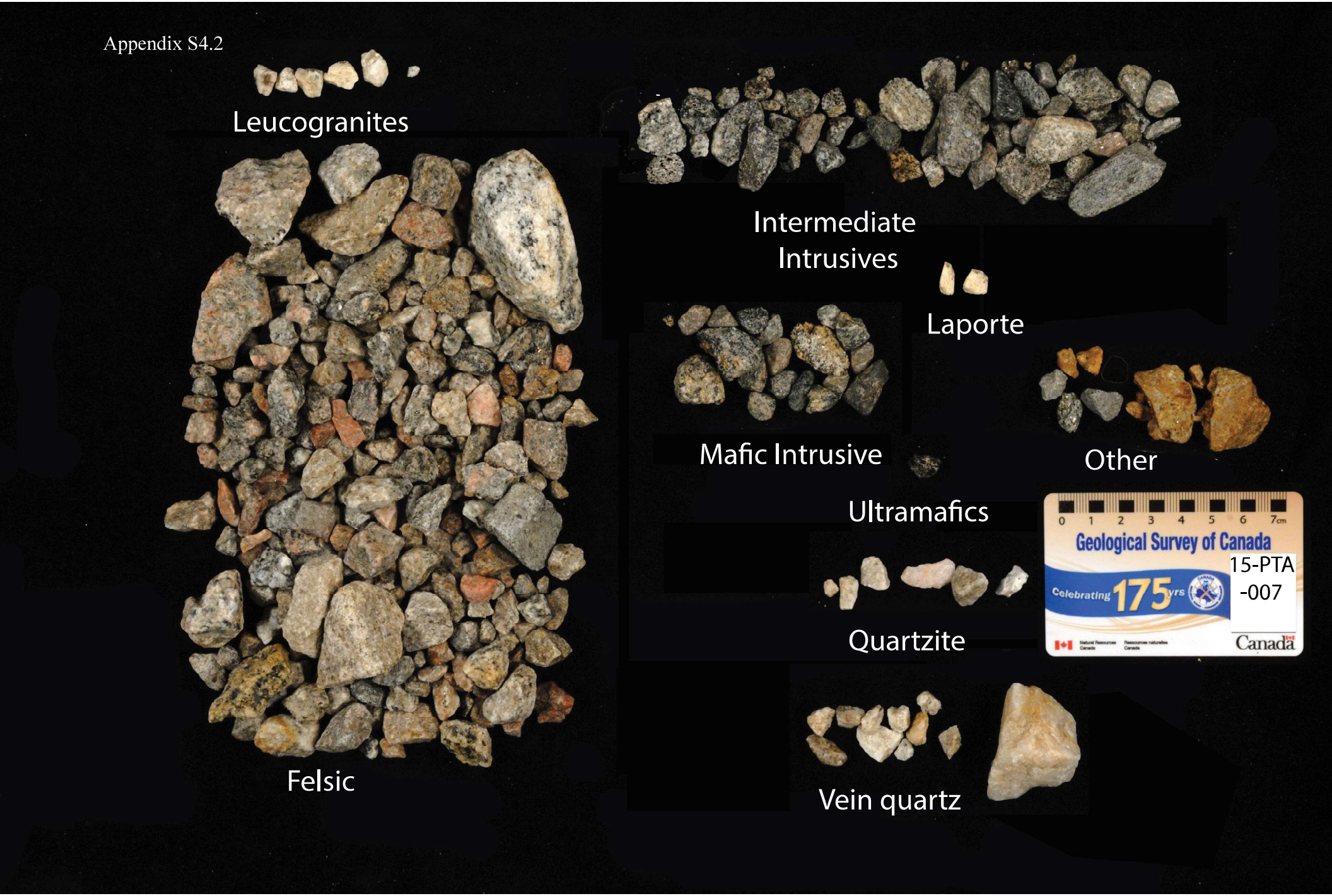

Appendix S4.2

Metasediments

Leucogranites

Intermediate Intrusives

Metavolcanics

Mafic Intrusive

Felsic

Ultramafics

Quartzite

Vein quartz

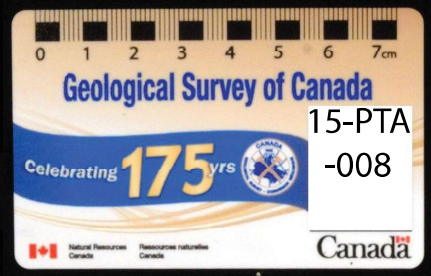

Appendix S4.2

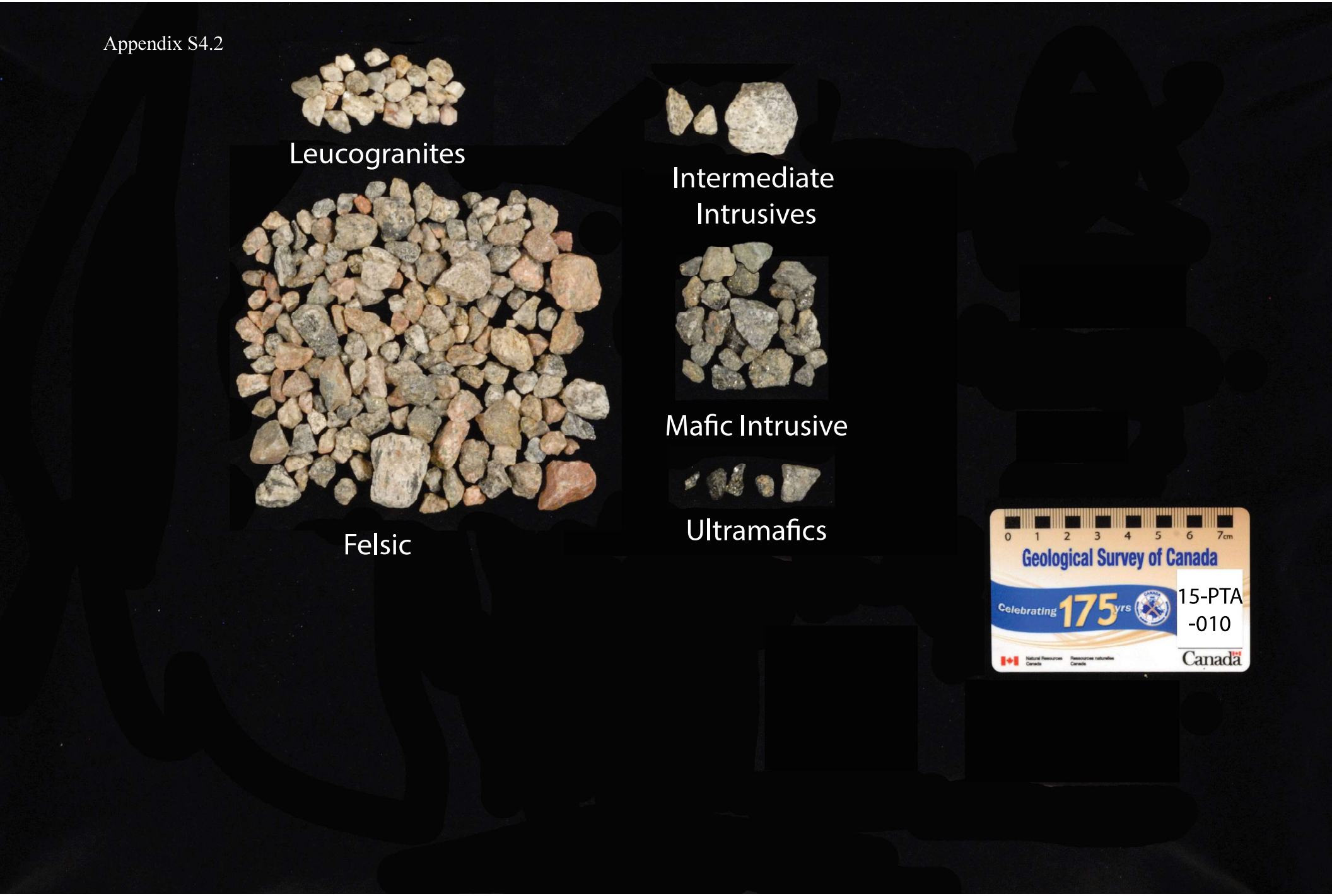

Appendix S4.2

Metasediments

Leucogranites

Intermediate Intrusives

Metavolcanics

Mafic Intrusive

Vein quartz

Other

Felsic

Appendix S4.2

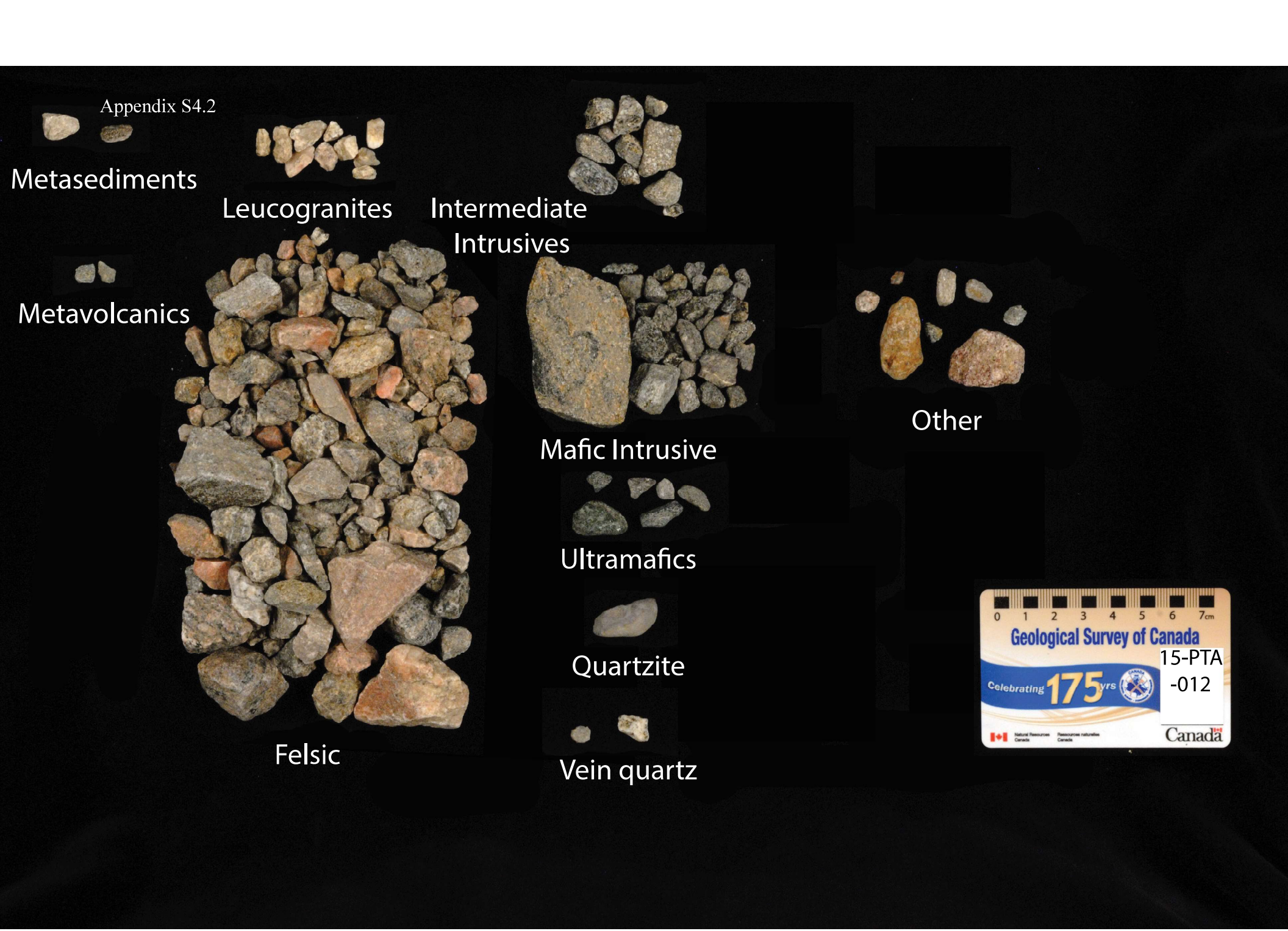

Appendix S4.2

Metasediments

Metavolcanics

Leucogranites

Intermediate Intrusives

Felsic

Mafic Intrusive

Ultramafics

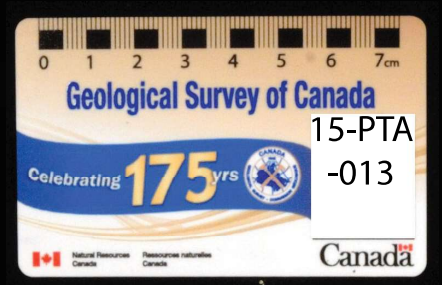

Quartzite

Vein quartz

Appendix S4.2

Metasediments

Leucogranites

Intermediate Intrusives

Felsic

Mafic Intrusive

Metavolcanics

Ultramafics

Quartzite

Vein quartz

Other

Appendix S4.2

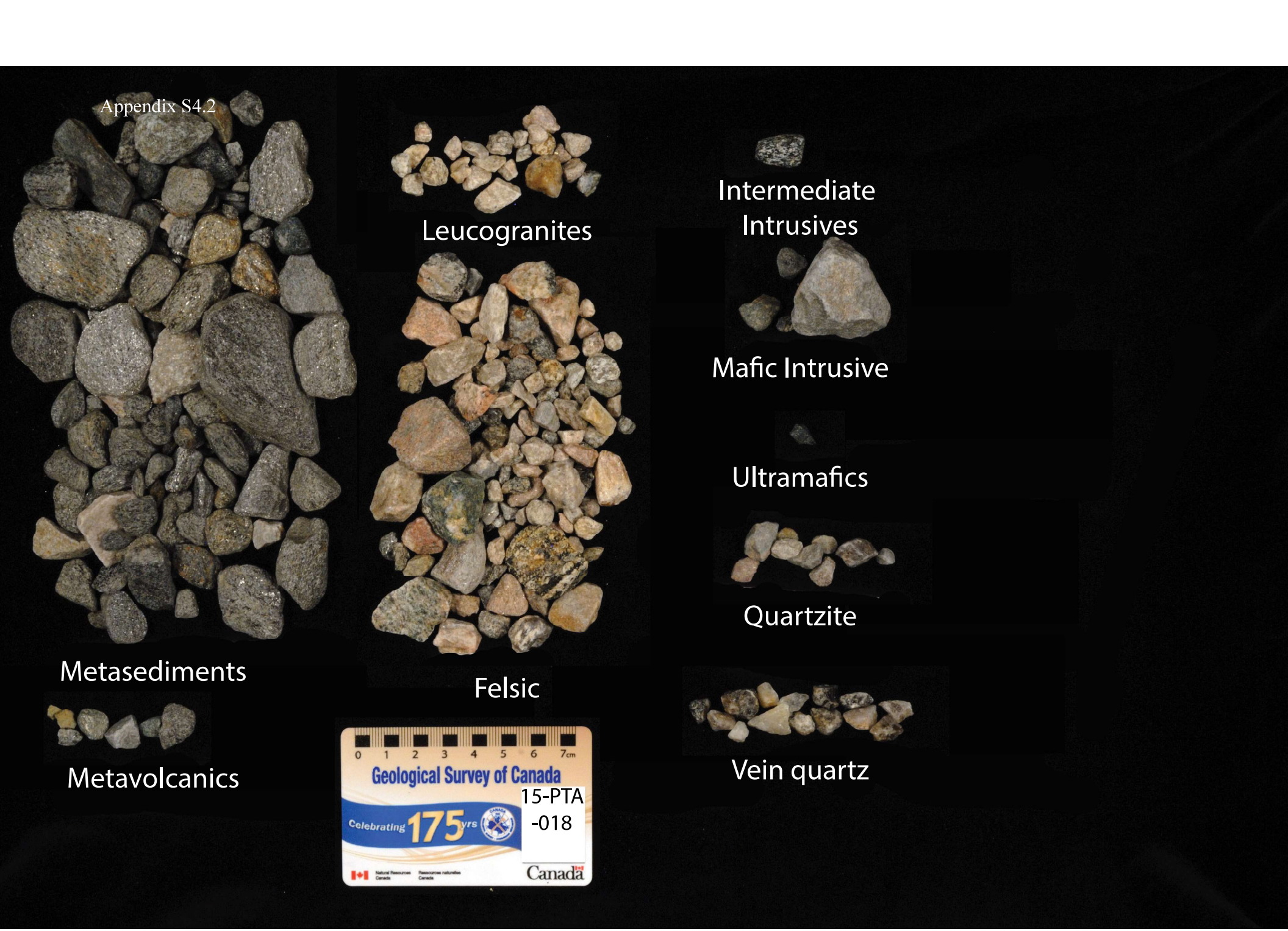

Appendix S4.2

Metasediments

Other

Vein Quartz

Metavolcanics

Appendix S4.2

Metasediments

Leucogranites

Intermediate Intrusives

Other

Mafic Intrusive

Metavolcanics

Felsic

Quartzite

Vein quartz

Appendix S4.2

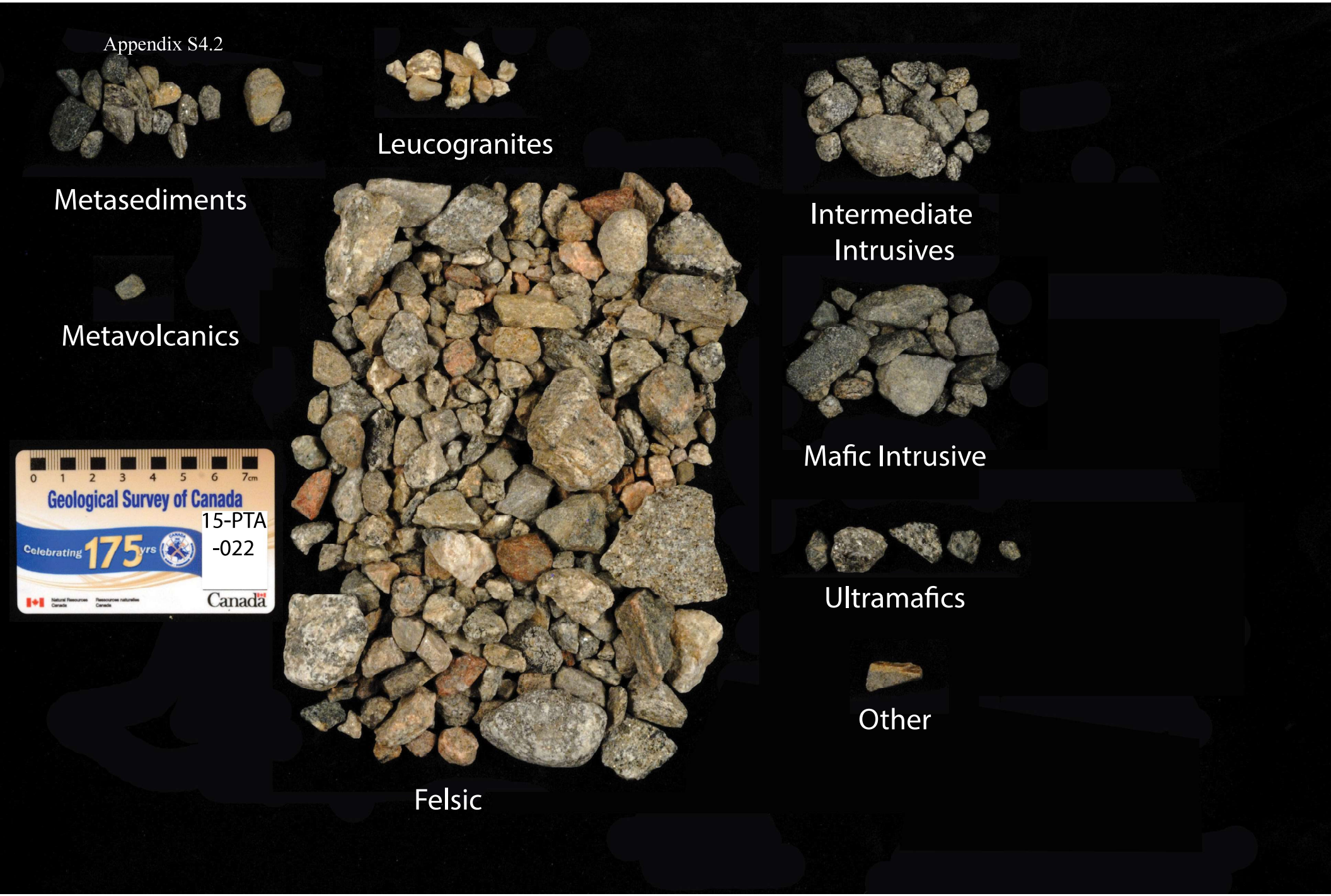

Appendix S4.2

Metasediments

Leucogranites

Intermediate Intrusives

Metavolcanics

Felsic

Mafic Intrusive

Ultramafics

Other

Appendix S4.2

Metasediments

Leucogranites

Felsic

Intermediate Intrusives

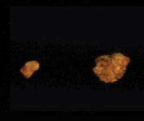

Other

Mafic Intrusive

Quartzite

Vein quartz

Metavolcanics

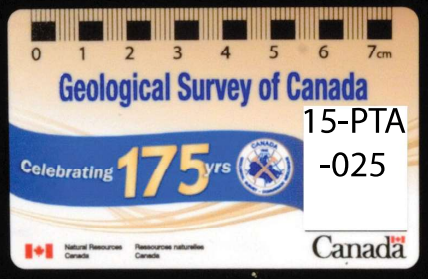

Appendix S4.2

Metasediments

Metavolcanics

Felsic

Intermediate Intrusives

Mafic Intrusive

Vein quartz

Appendix S4.2

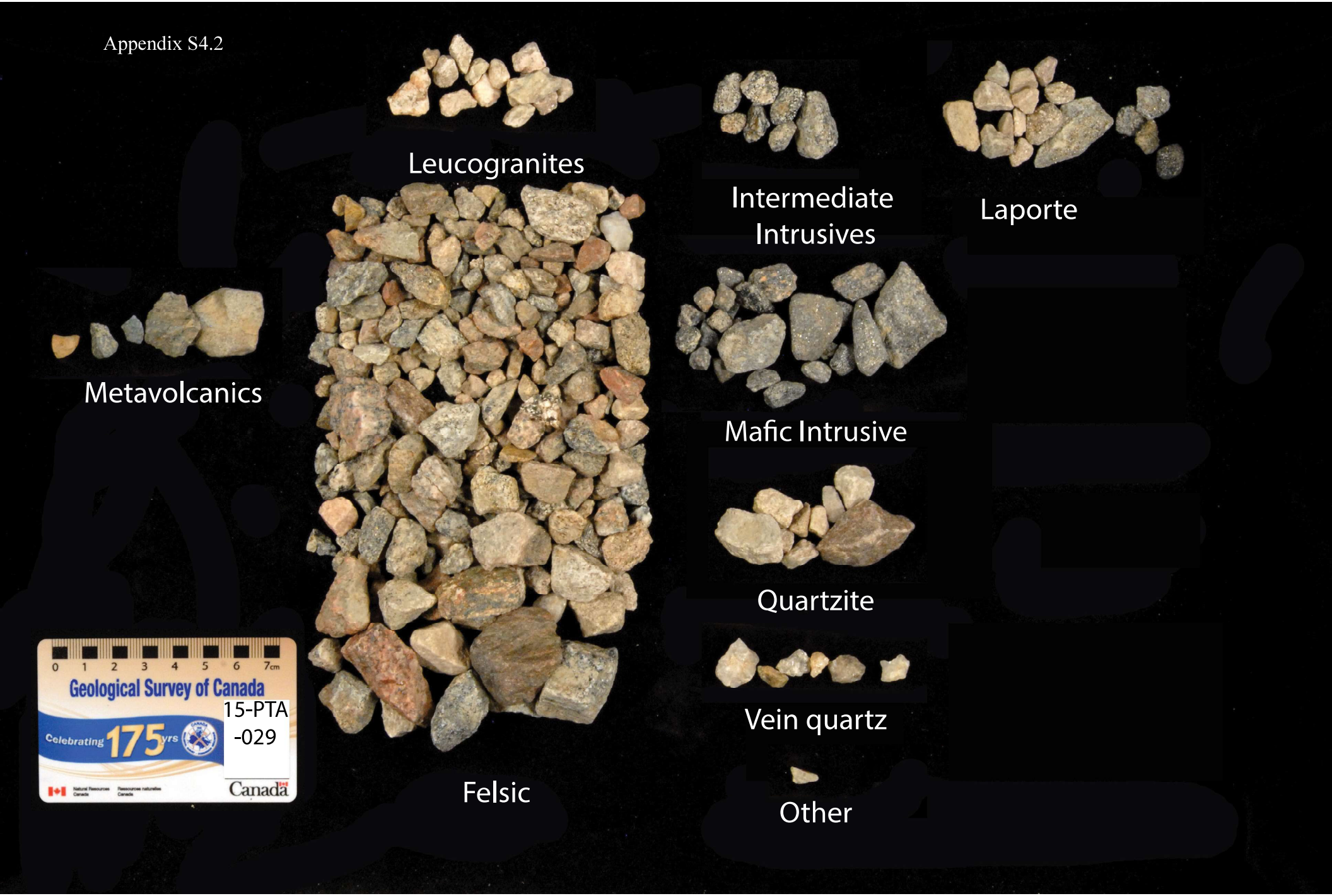

Appendix S4.2

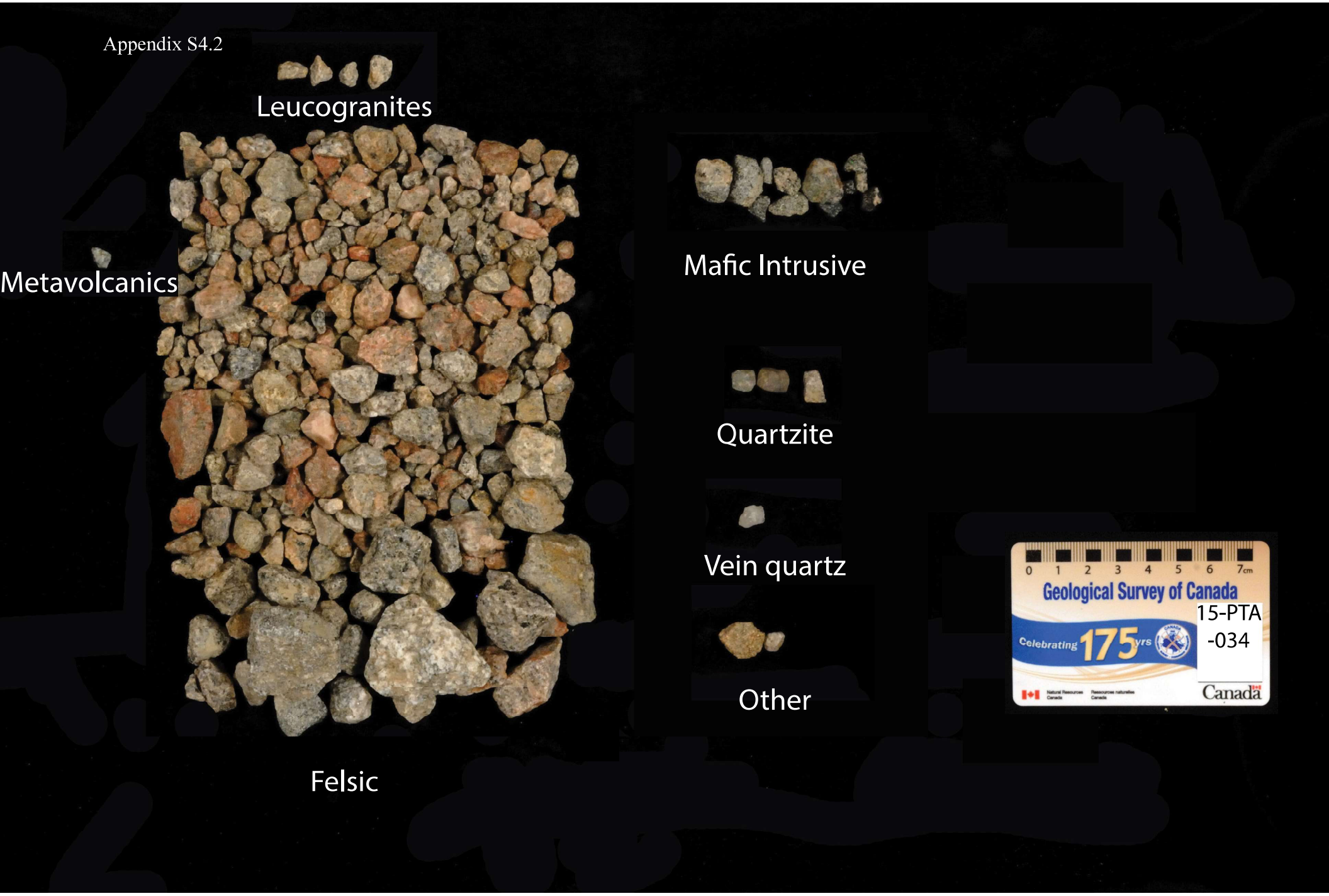

Appendix S4.2

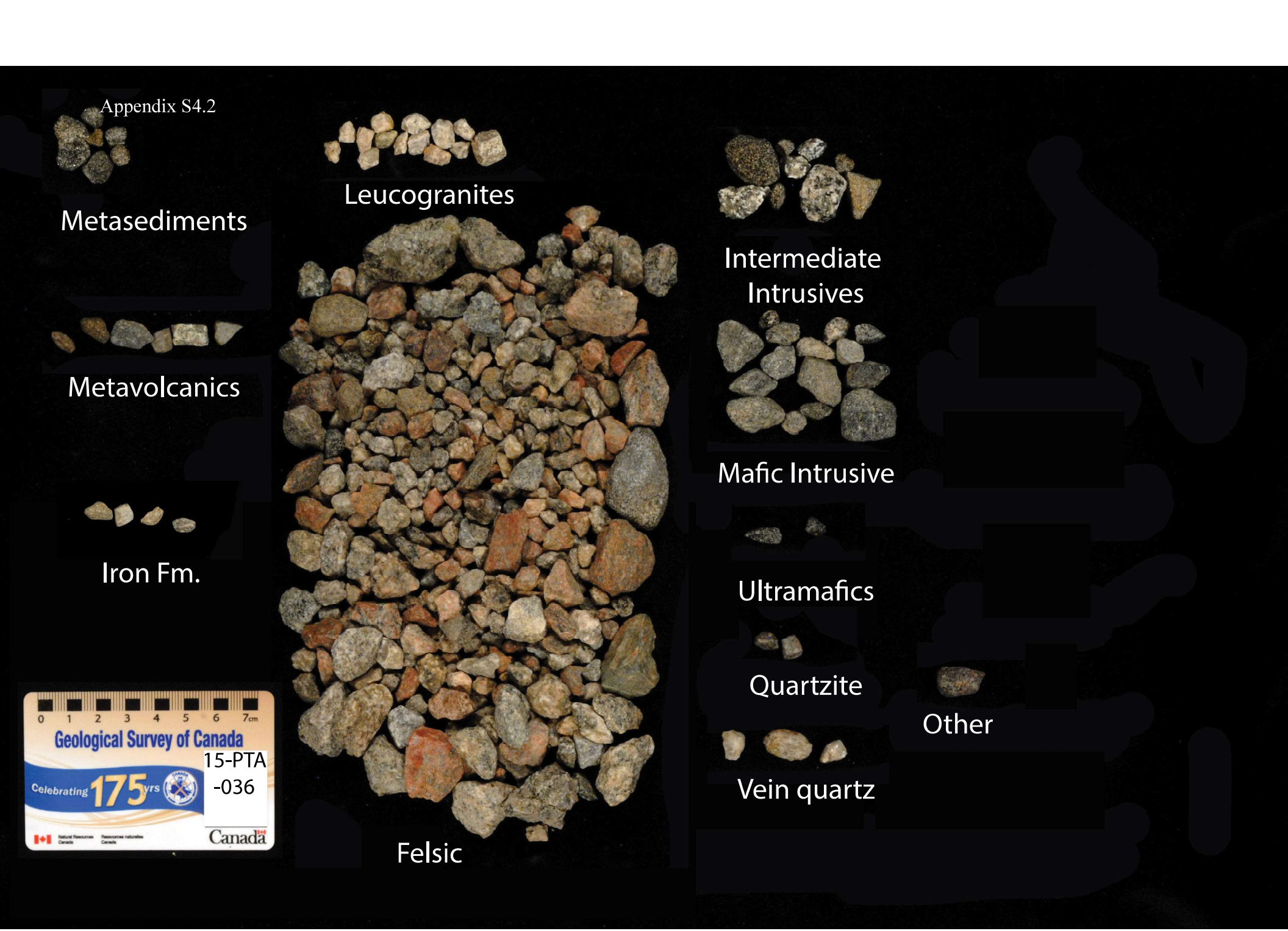

Appendix S4.2

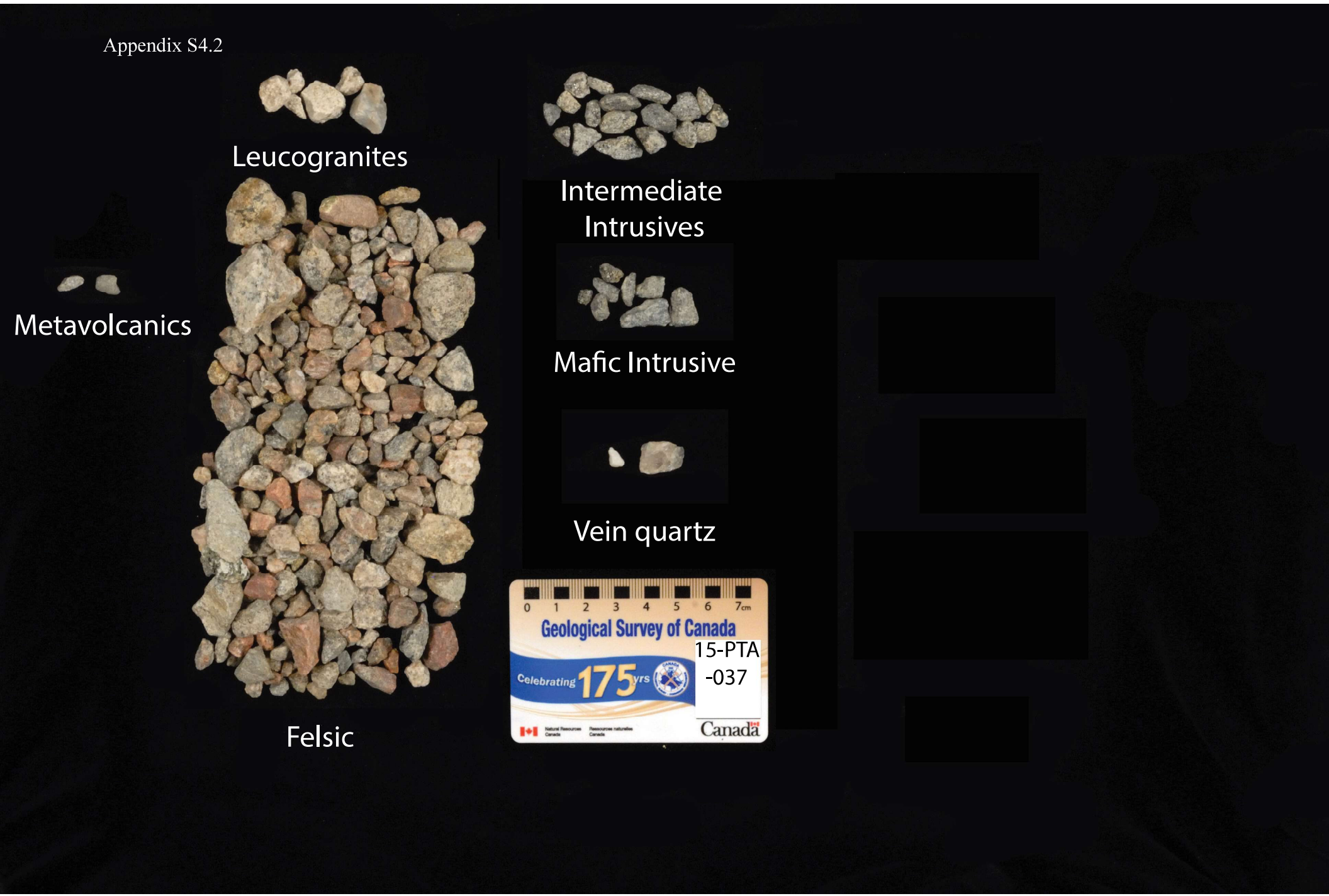

Appendix S4.2

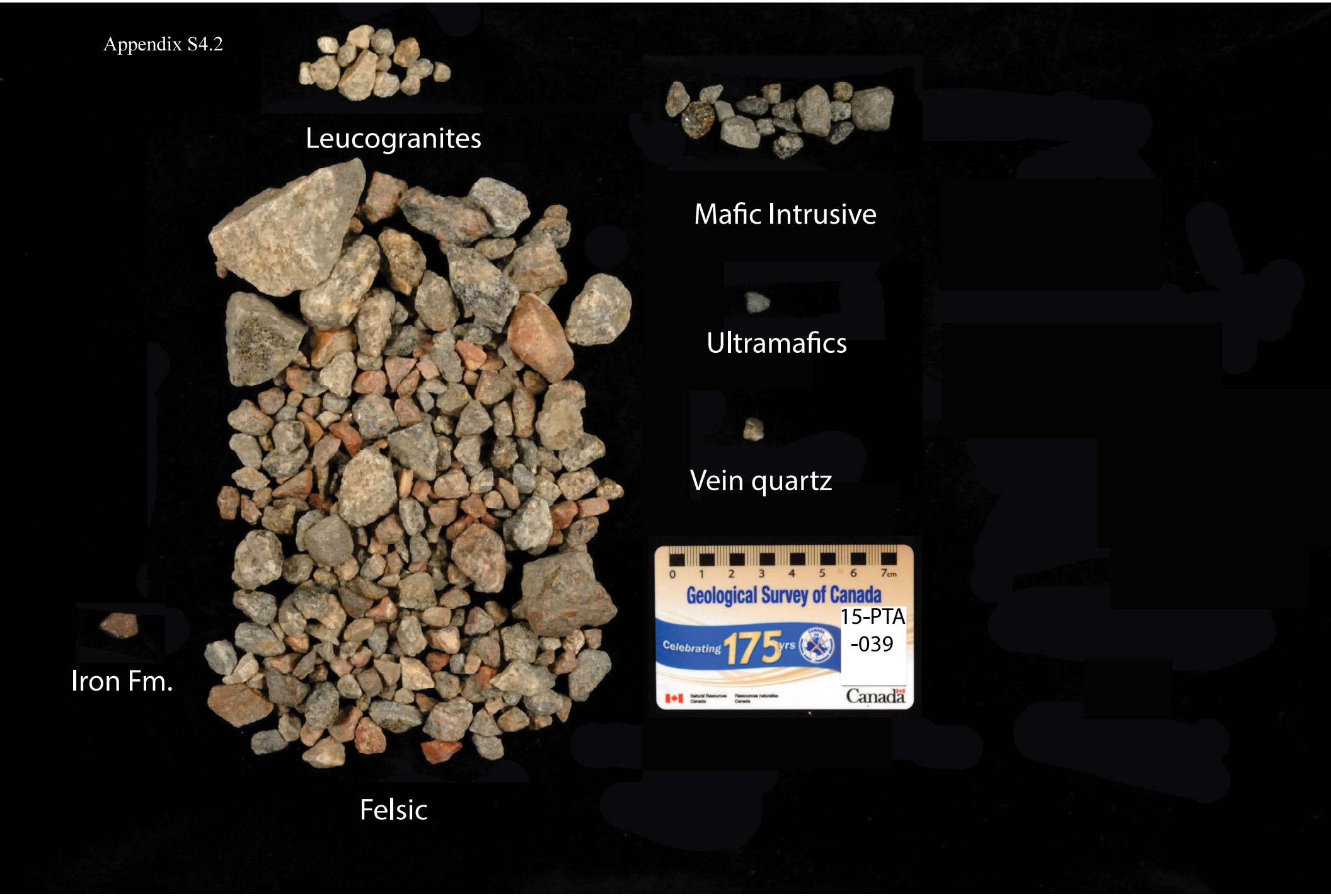

Appendix S4.2

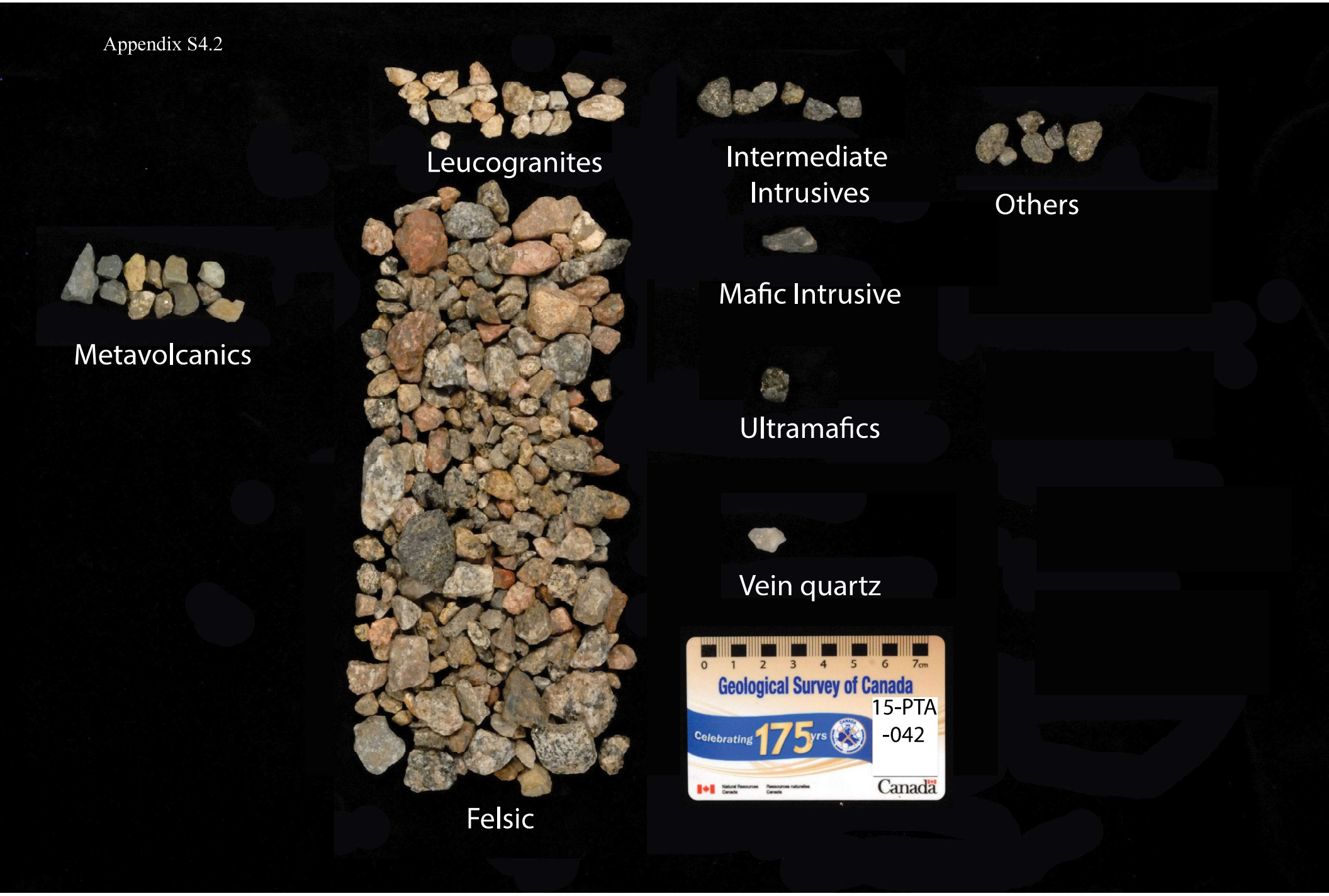

Appendix S4.2

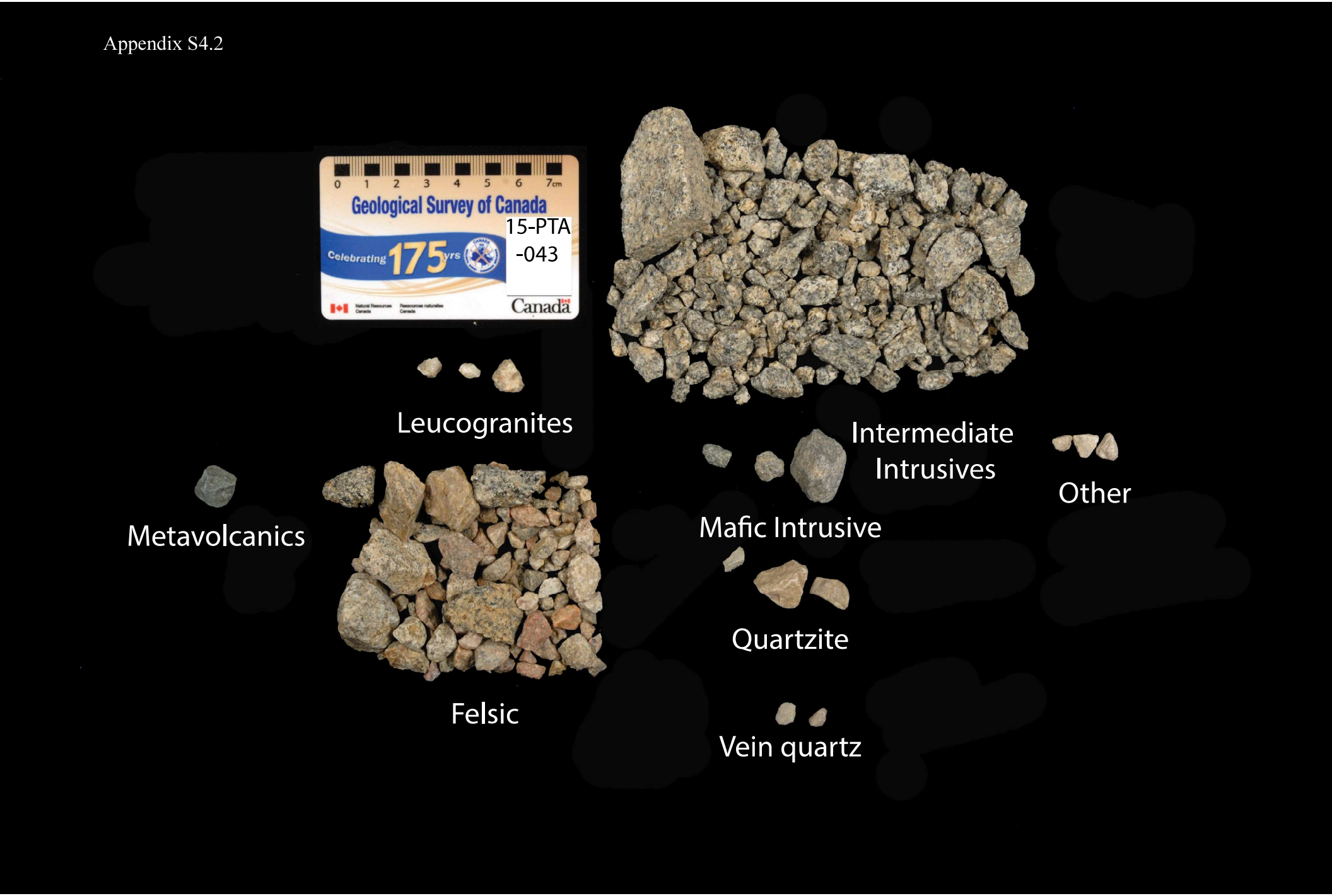

Appendix S4.2

Leucogranites

Intermediate Intrusives

Metavolcanics

Felsic

Mafic Intrusive

Ultramafics

Other

Quartzite

Vein quartz

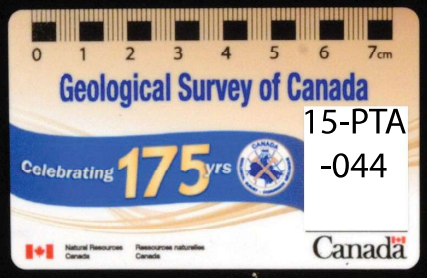

Appendix S4.2

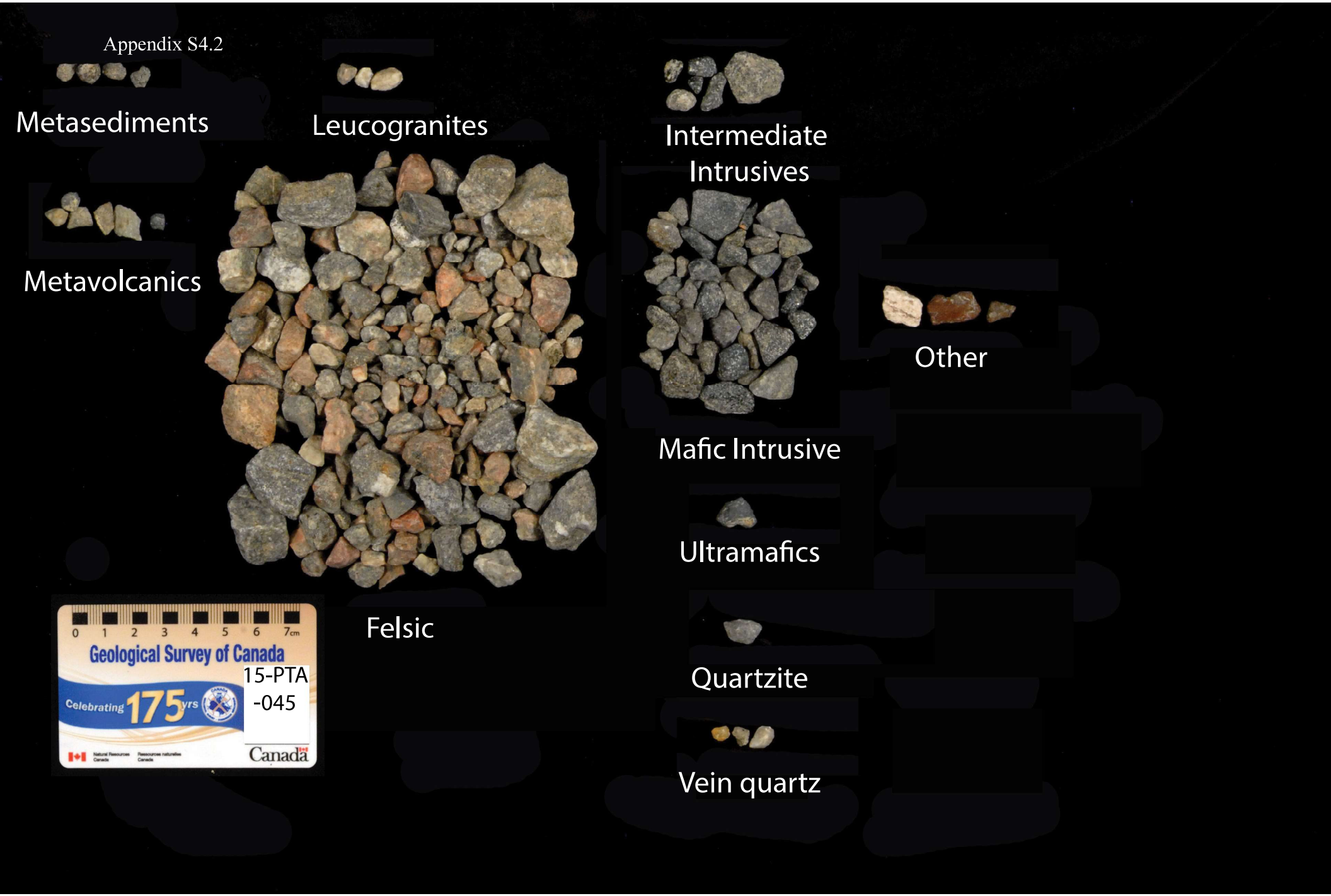

Appendix S4.2

Metasediments

Leucogranites

Intermediate Intrusives

Metavolcanics

Felsic

Mafic Intrusive

Ultramafics

Vein quartz

Appendix S4.2

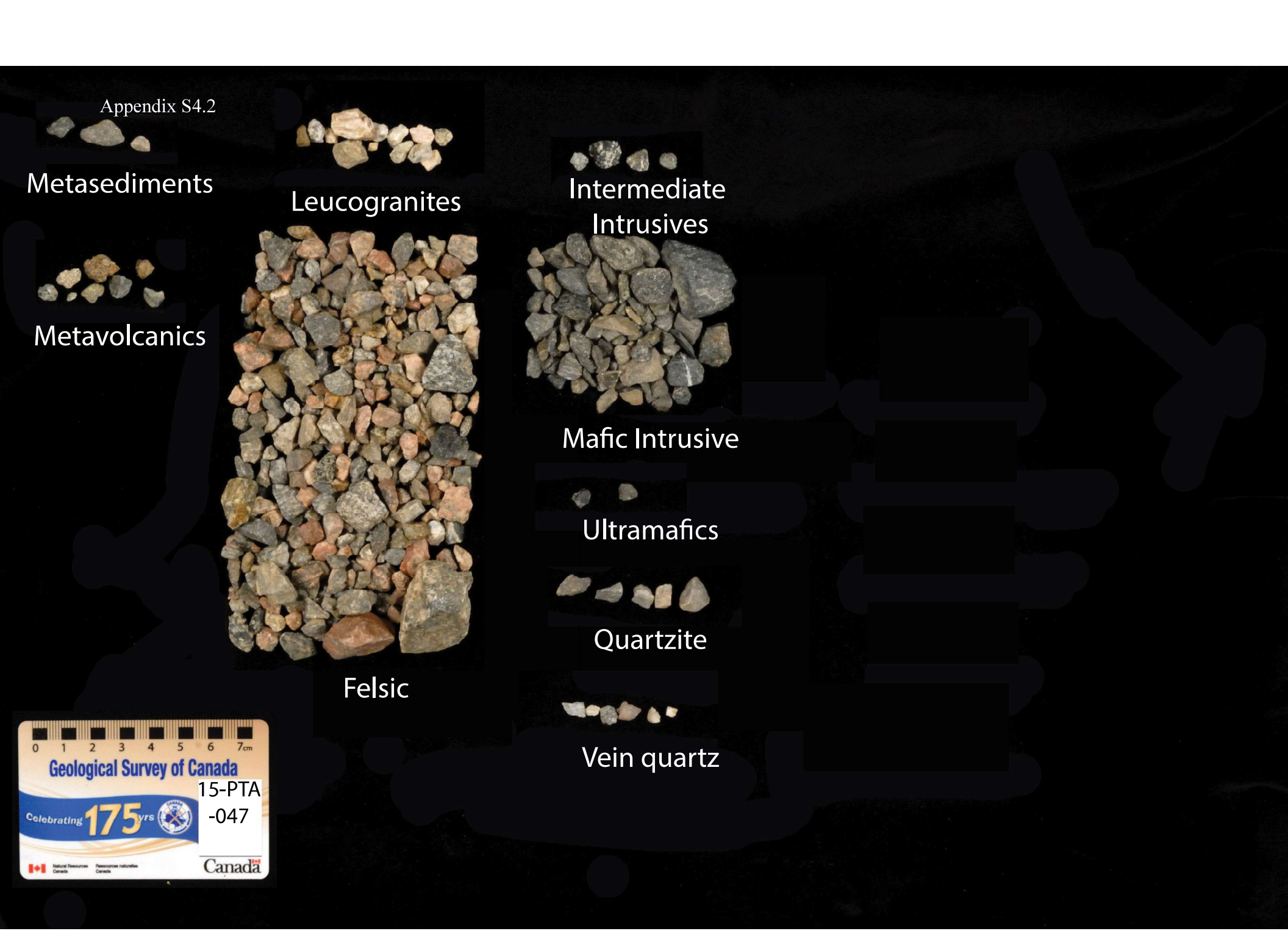

Appendix S4.2

Metasediments

Leucogranites

Intermediate Intrusives

Mafic Intrusive

Metavolcanics

Ultramafics

Quartzite

Iron Fm.

Felsic

Vein quartz

Other

Appendix S4.2

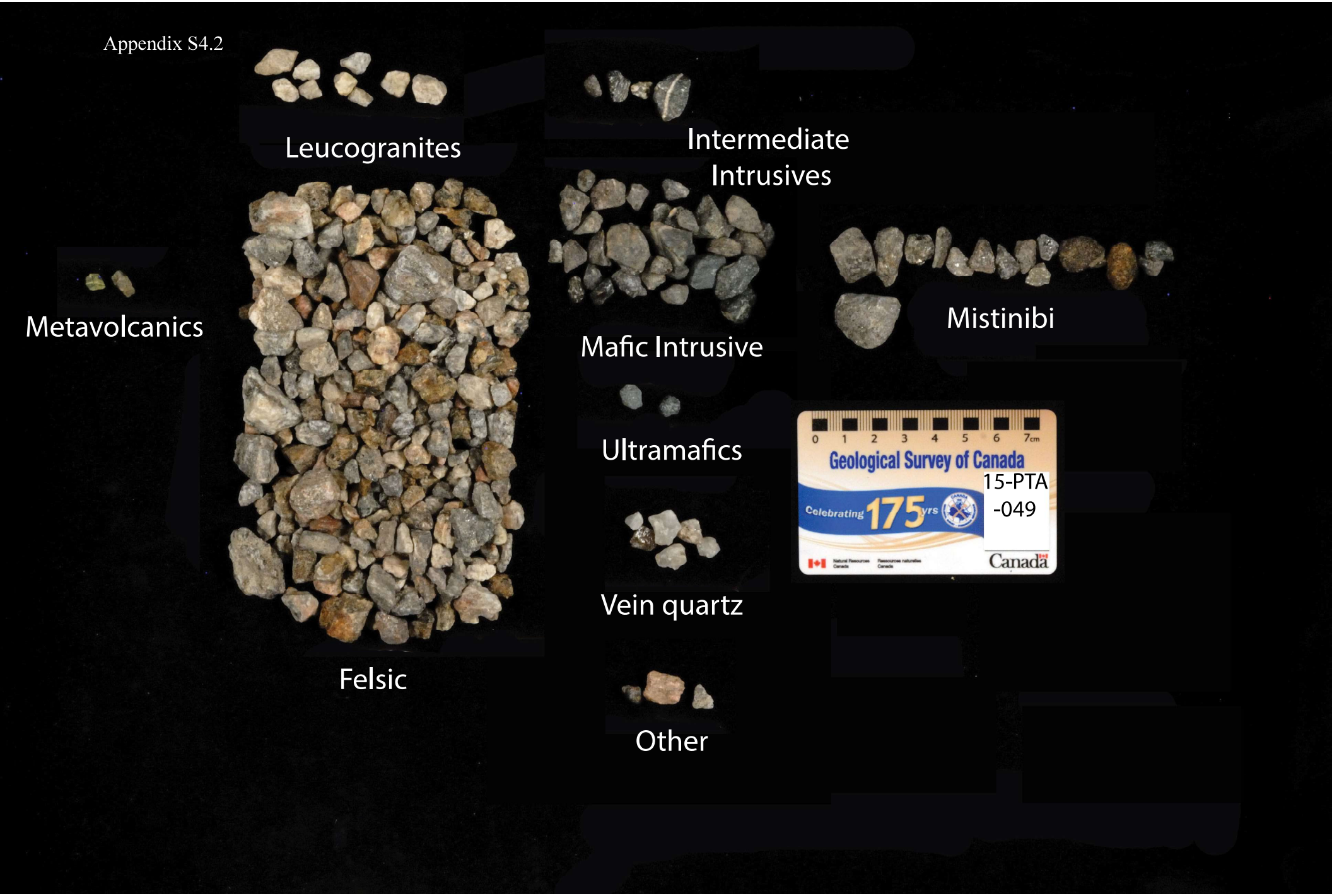

Appendix S4.2

Metasediments

Leucogranites

Intermediate Intrusives

Mafic Intrusive

Felsic

Ultramafics

Quartzite

Vein quartz

Other

Appendix S4.2

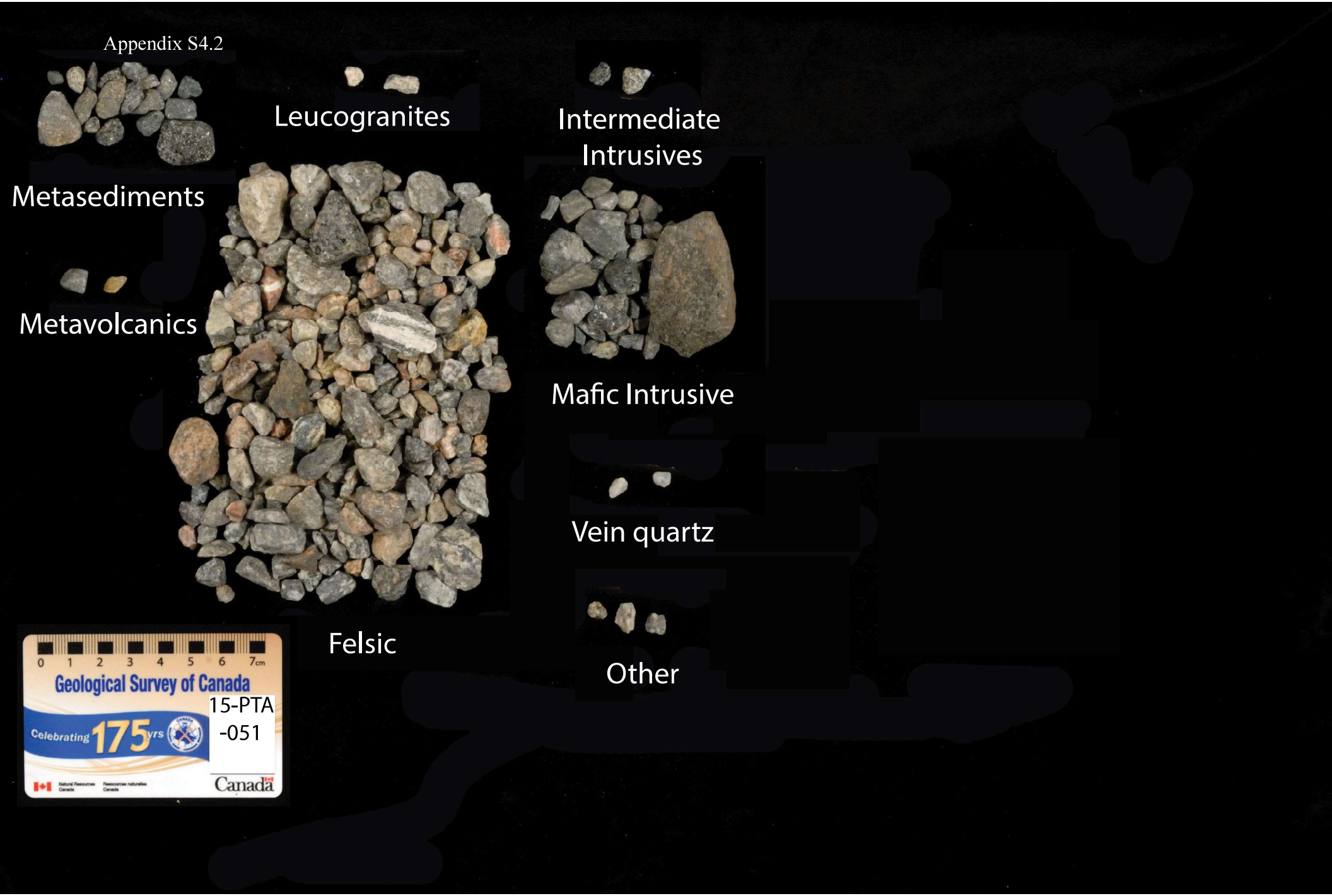

Appendix S4.2

Leucogranites

Intermediate Intrusives

Mistinibi

Felsic

Mafic Intrusive

Quartzite

Vein quartz

Other

Appendix S4.2

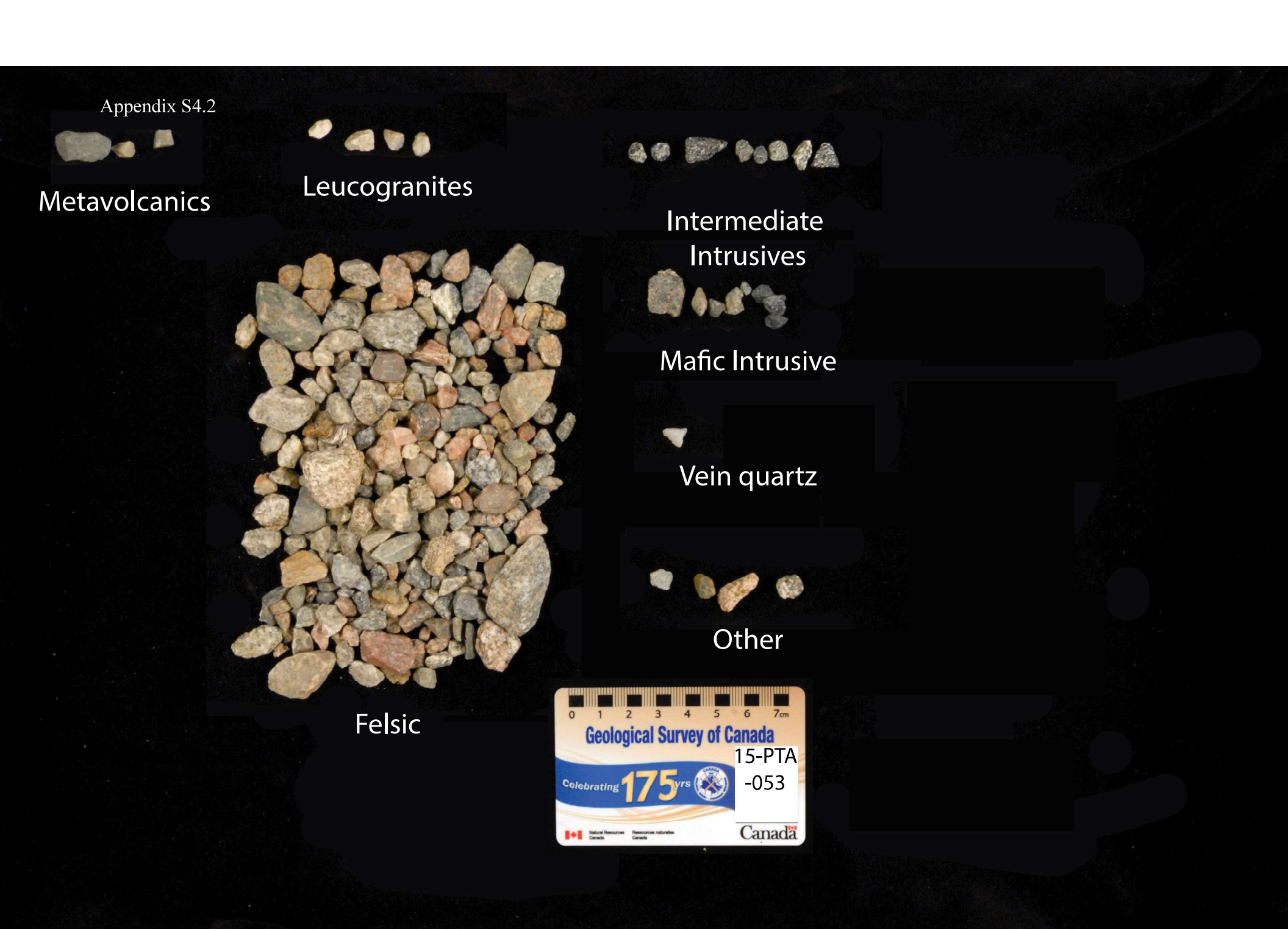

Appendix S4.2

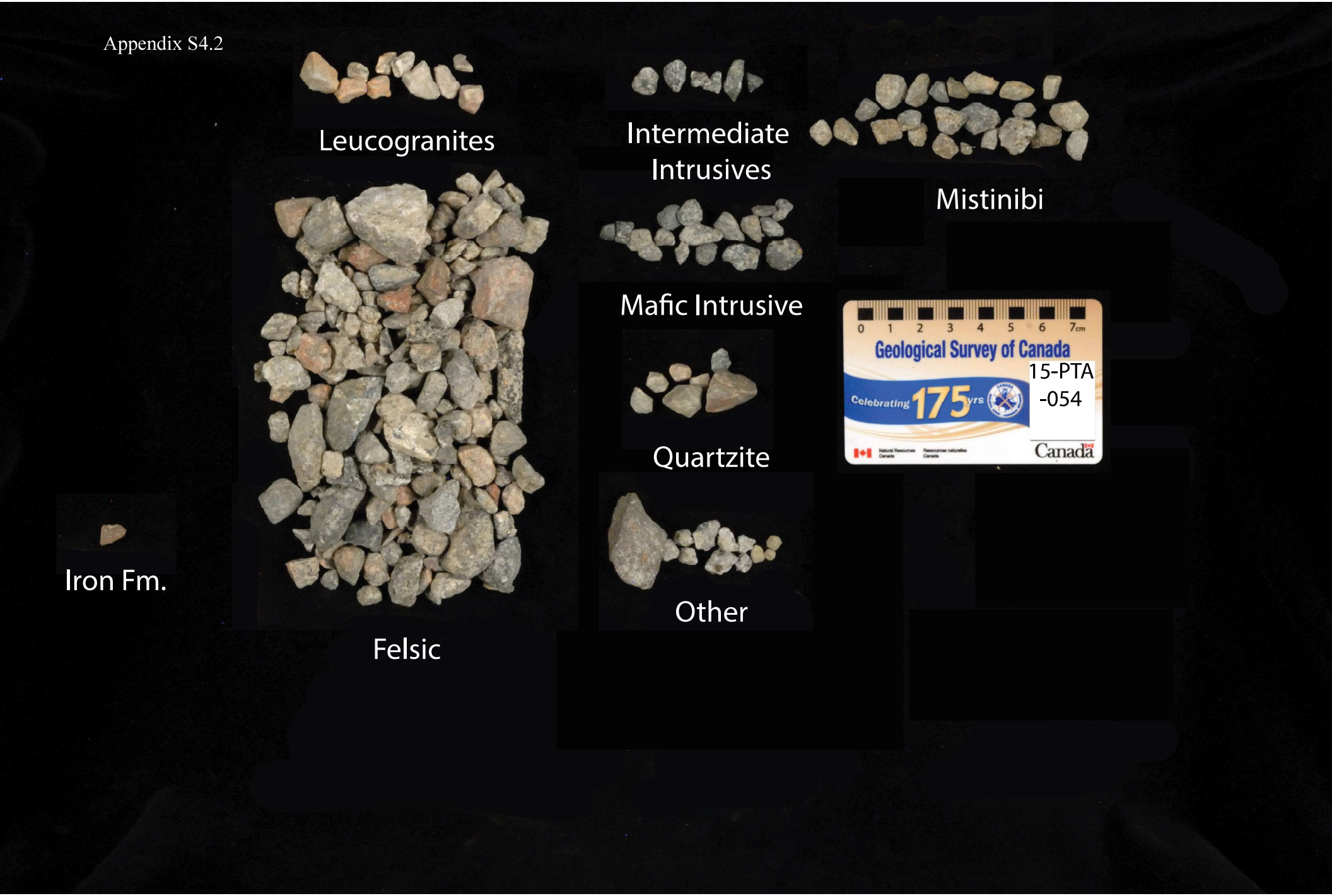

Appendix S4.2

Metasediments

Leucogranites

Intermediate Intrusives

Mafic Intrusive

Metavolcanics

Quartzite

Vein quartz

Other

Felsic

Appendix S4.2

Metasediments

Leucogranites

Intermediate Intrusives

Metavolcanics

Felsic

Mafic Intrusive

Iron Fm.

Quartzite

Vein quartz

Appendix S4.2

Leucogranites

Intermediate Intrusives

Felsic

Mafic Intrusive

Vein quartz

Others

Appendix S4.2

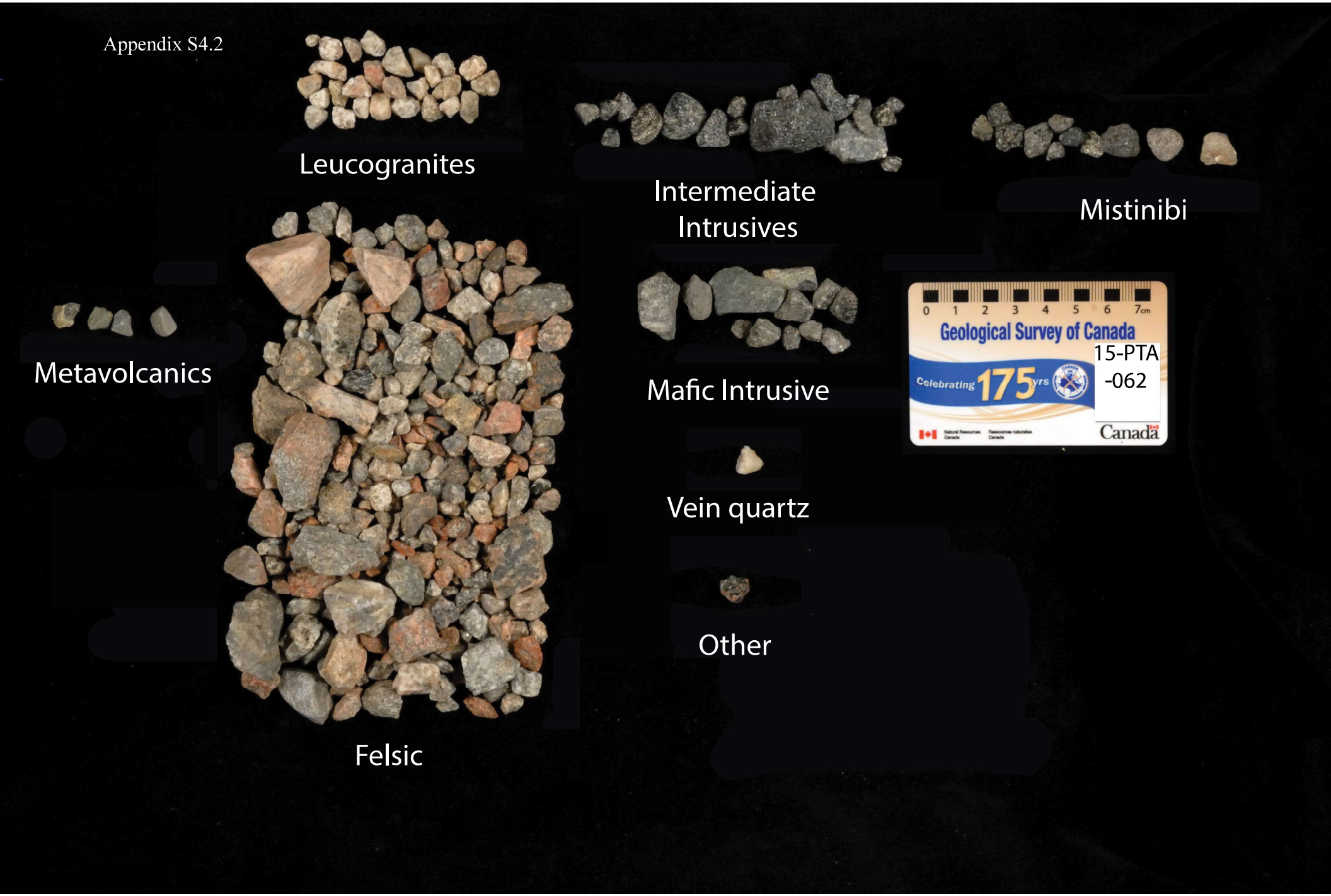

Appendix S4.2

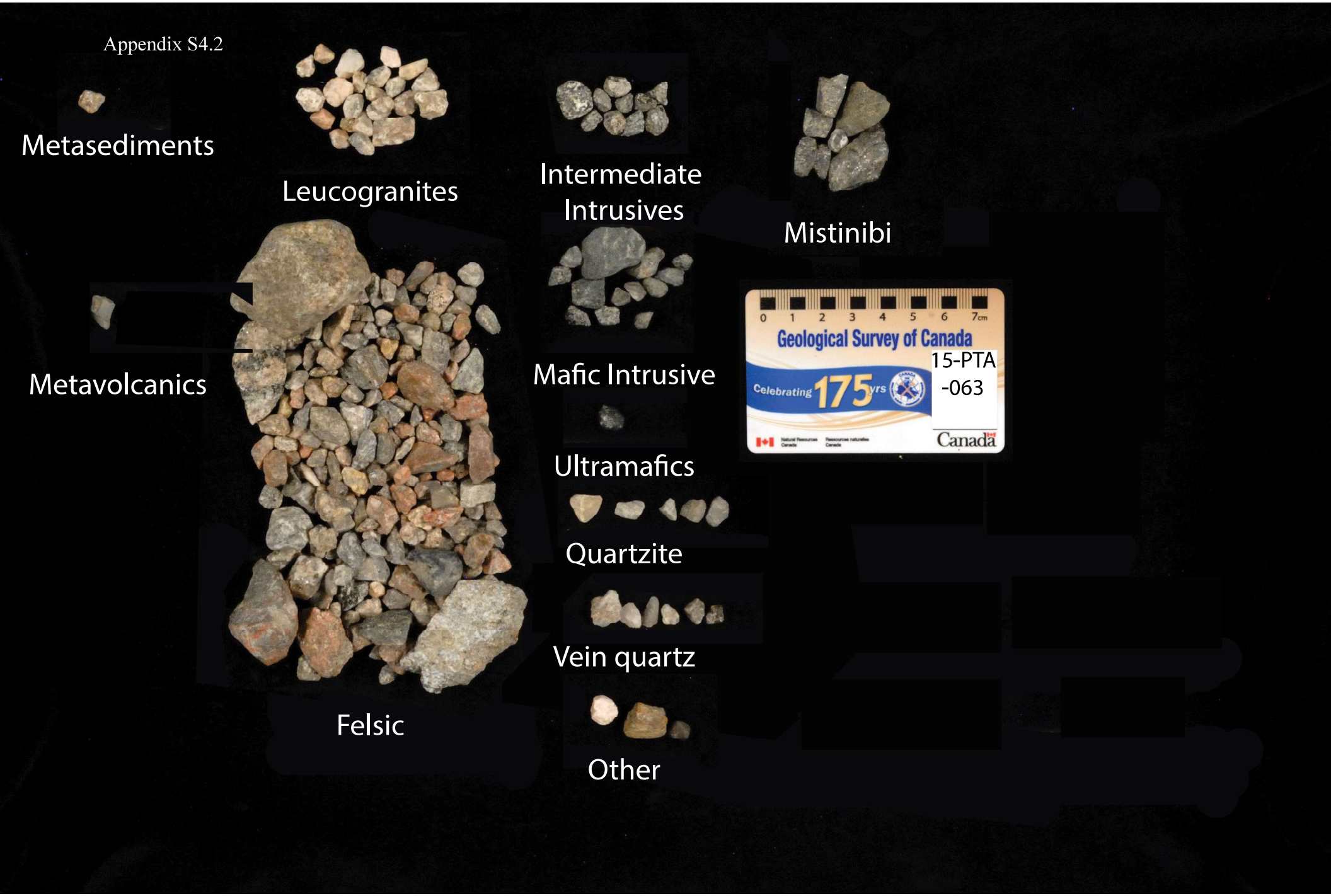

Appendix S4.2

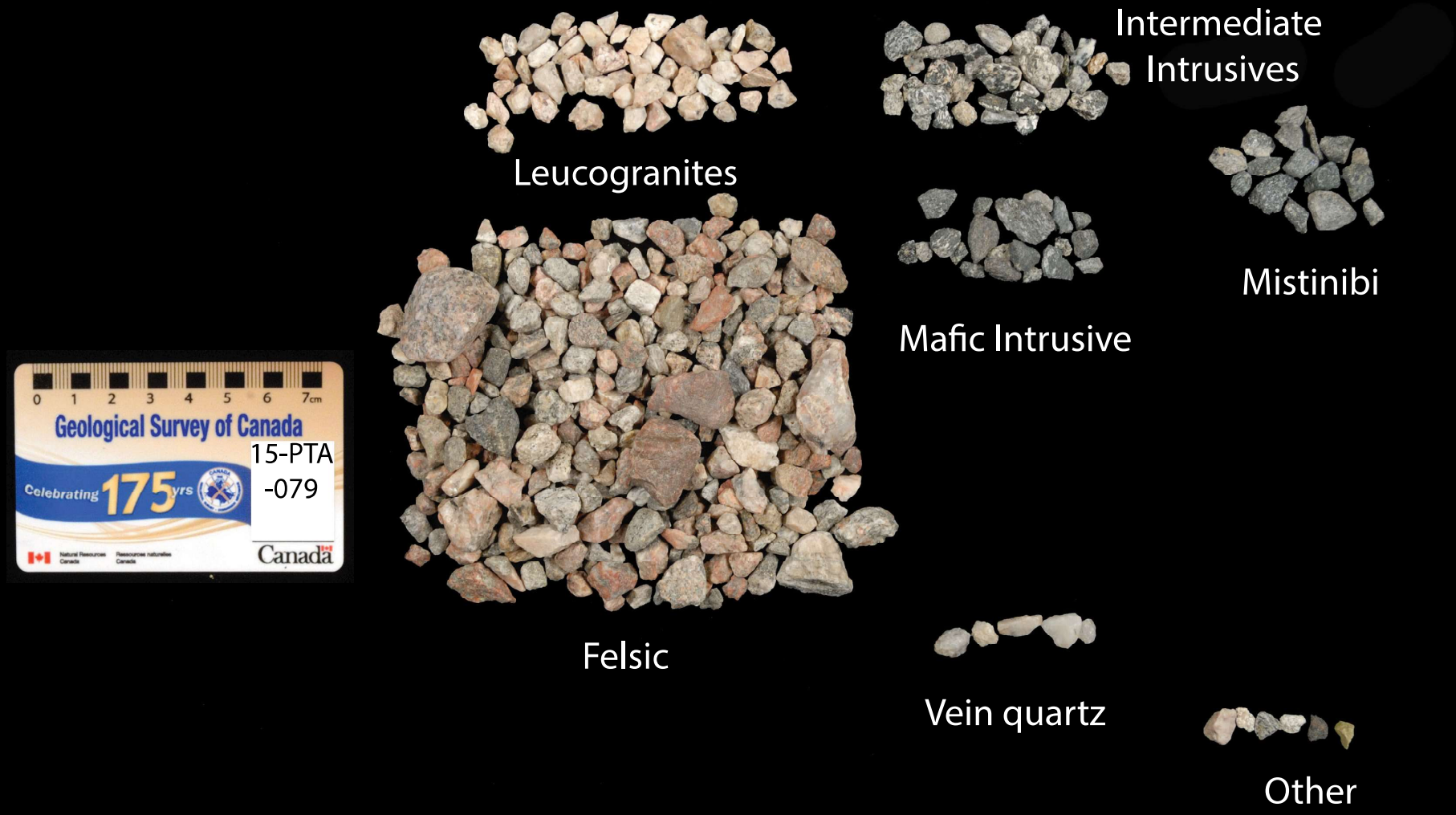

Appendix S4.2

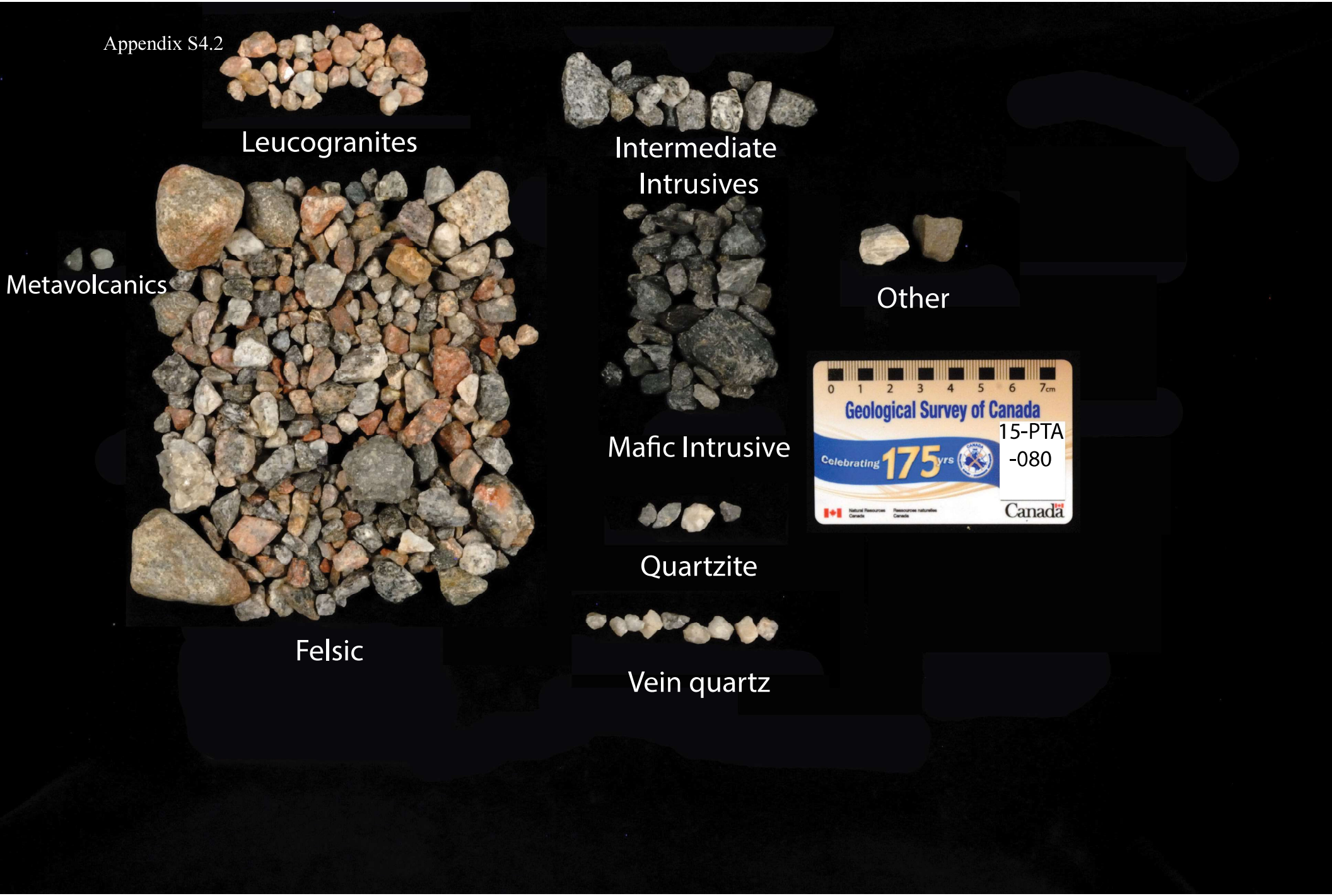

Appendix S4.2

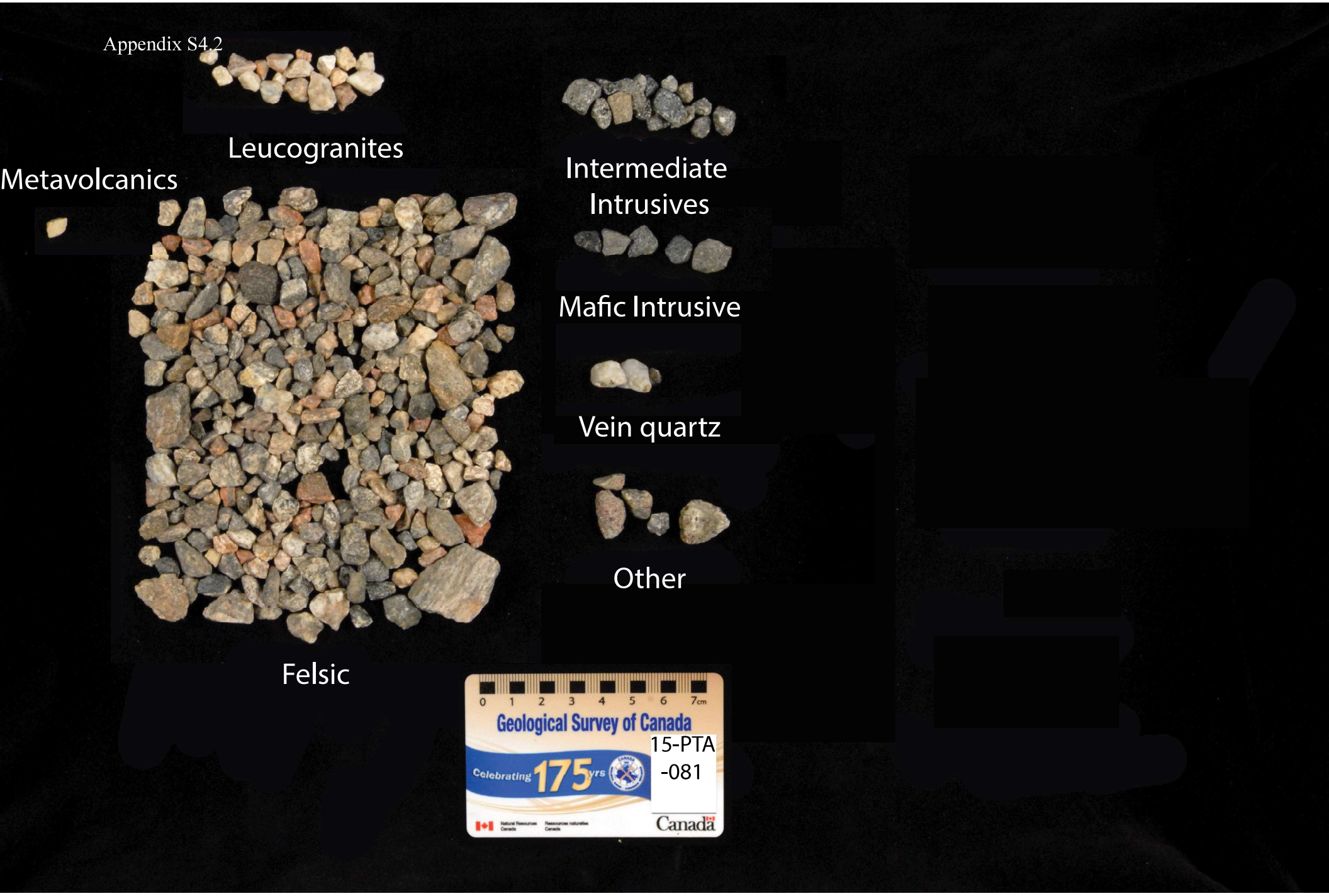

Appendix S4.2

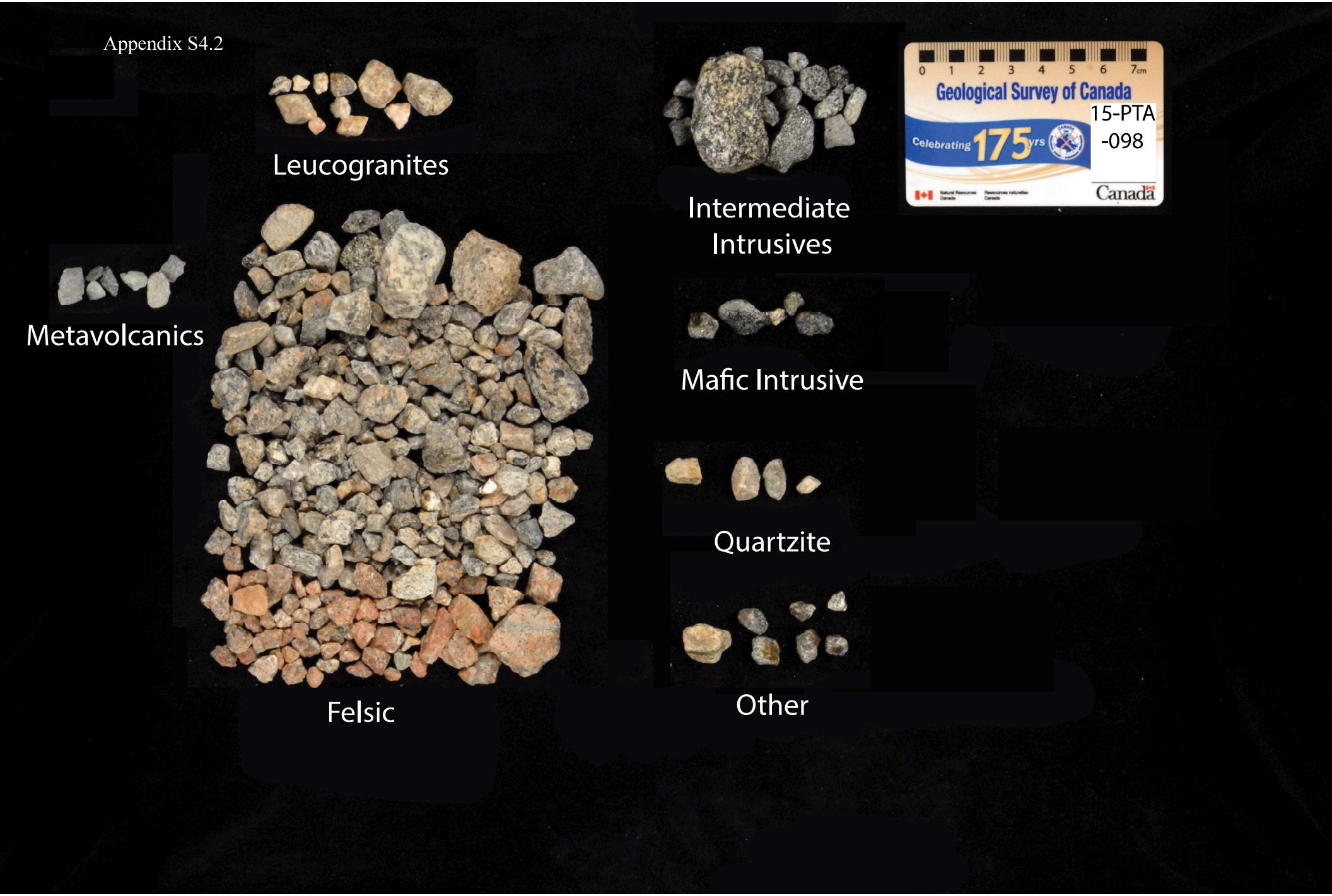

Appendix S4.2

Metasediments

Leucogranites

Intermediate Intrusives

Quartzite

Vein quartz

Other

Felsic

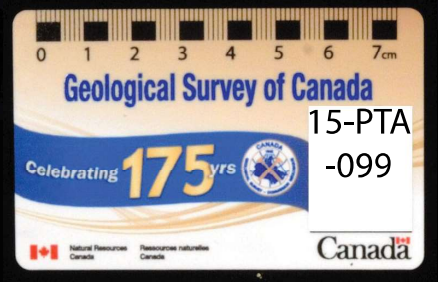

Appendix S4.2

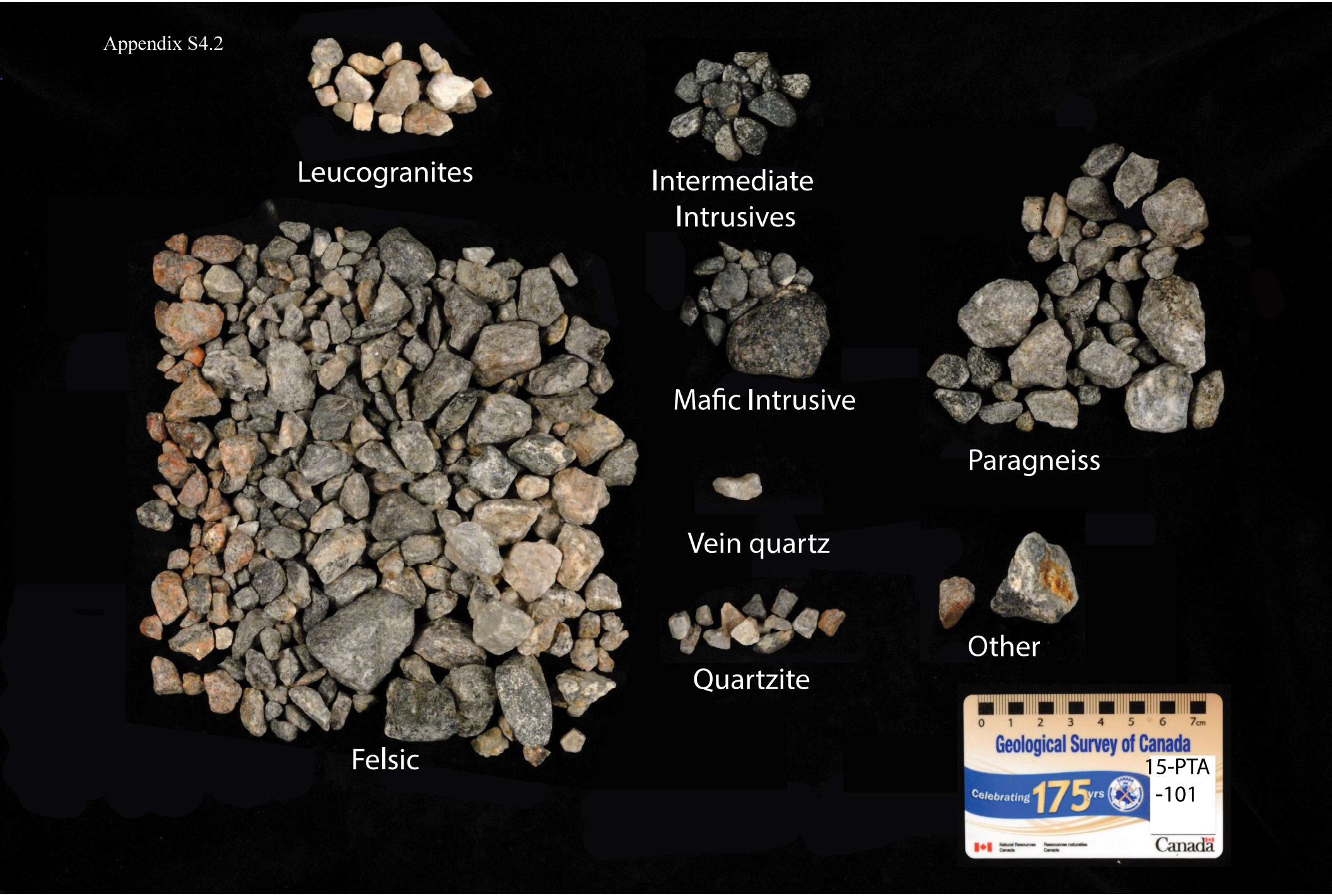

Appendix S4.2

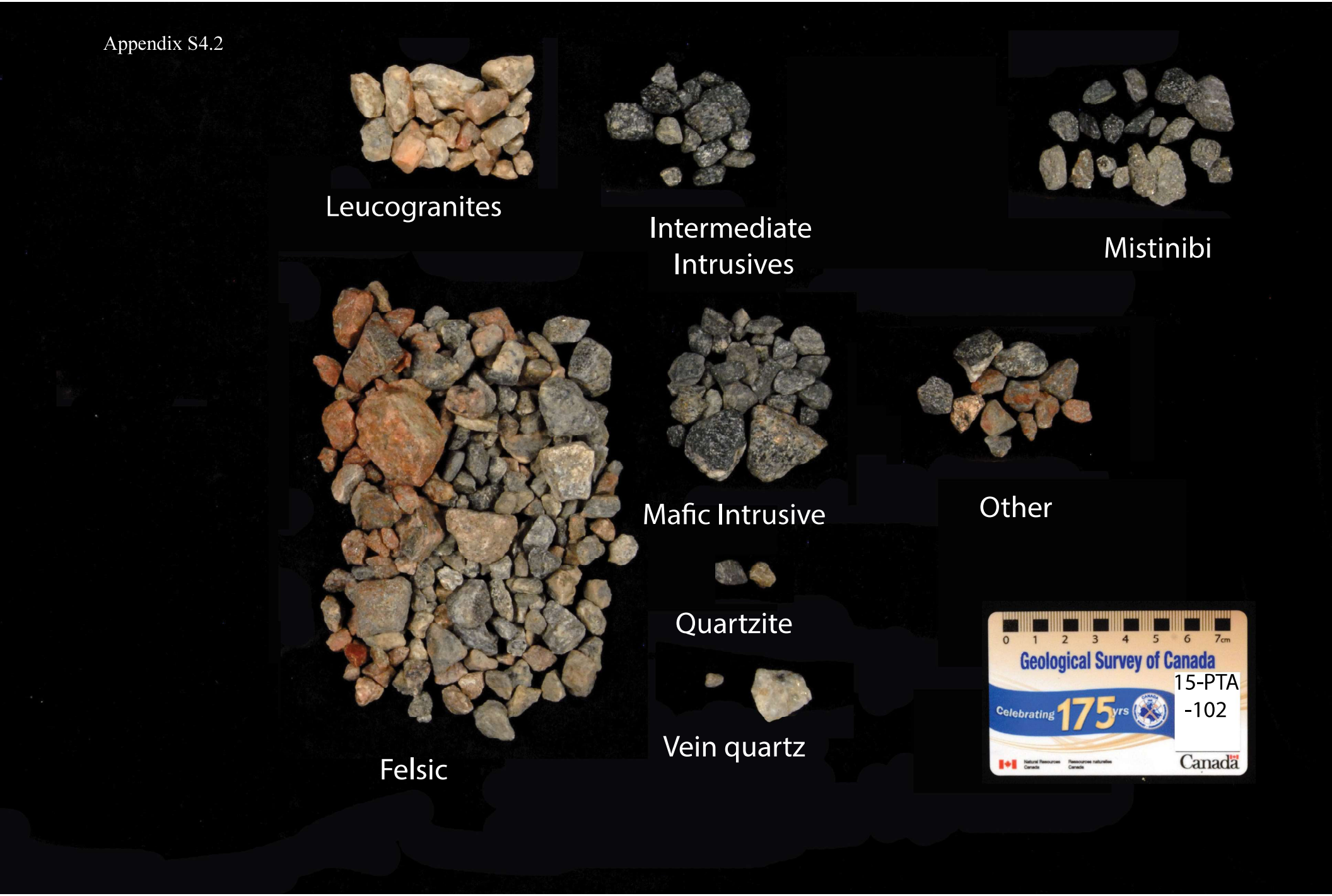

Appendix S4.2

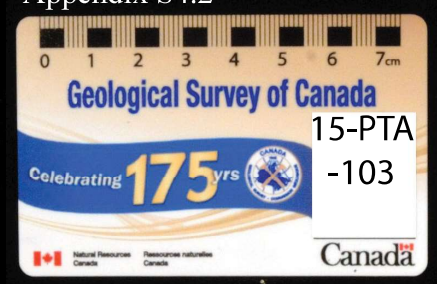

Leucogranites

Intermediate Intrusives

Felsic

Mafic Intrusive

Metavolcanics

Quartzite

Vein quartz

Other

Appendix S4.2

Metasediments

Leucogranites

Intermediate Intrusives

Laporte

Metavolcanics

Mafic Intrusive

Iron Fm.

Felsic

Vein quartz

Others

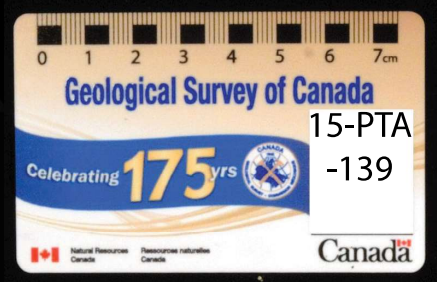

Appendix S4.2

Leucogranites

Intermediate Intrusives

Mistinibi

Felsic

Mafic Intrusive

Laporte

Vein quartz

Others

Appendix S4.2

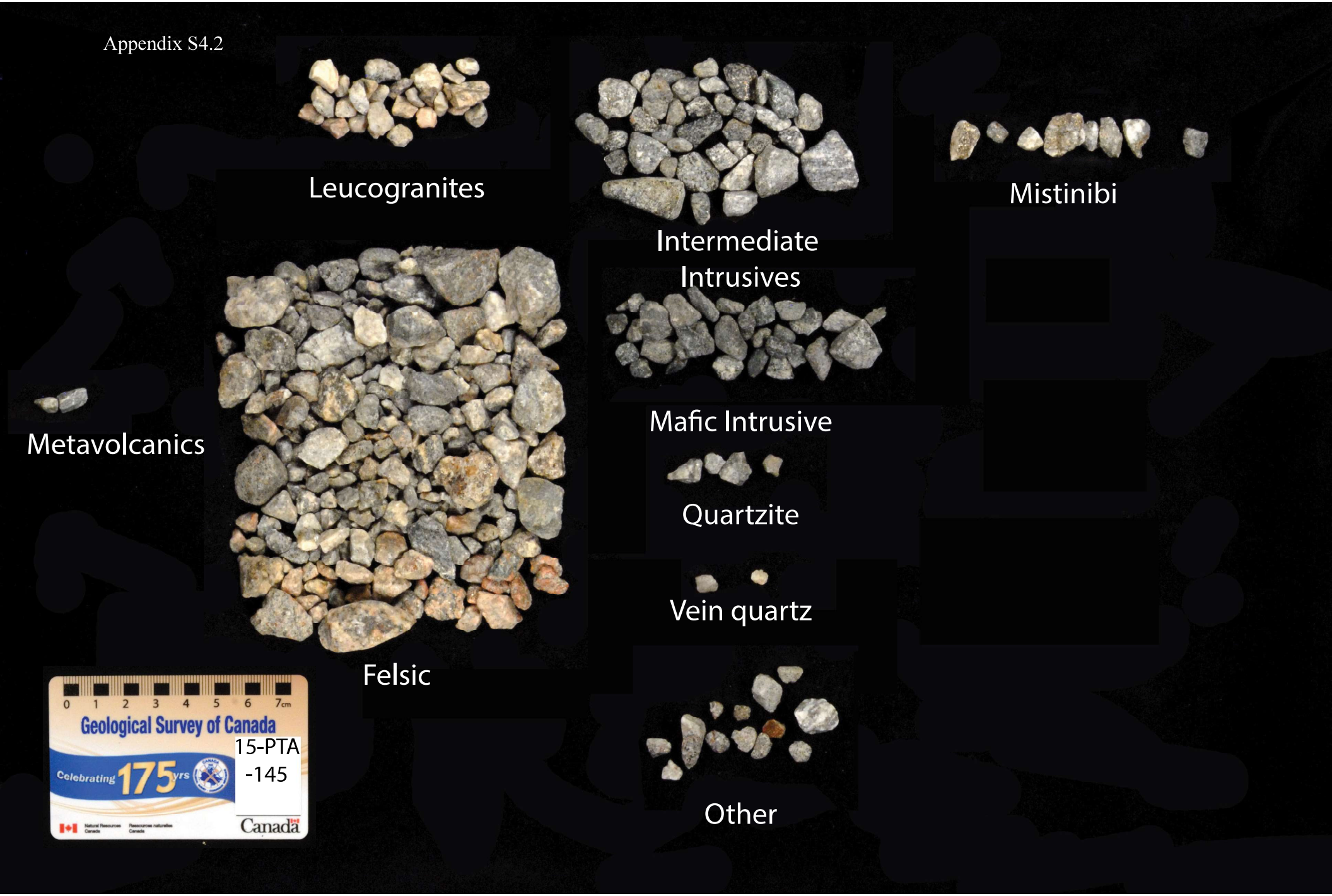

Appendix S4.2

Leucogranites

Intermediate Intrusives

Mistinibi

Mafic Intrusive

Metavolcanics

Felsic

Vein quartz

Other

Appendix S4.2

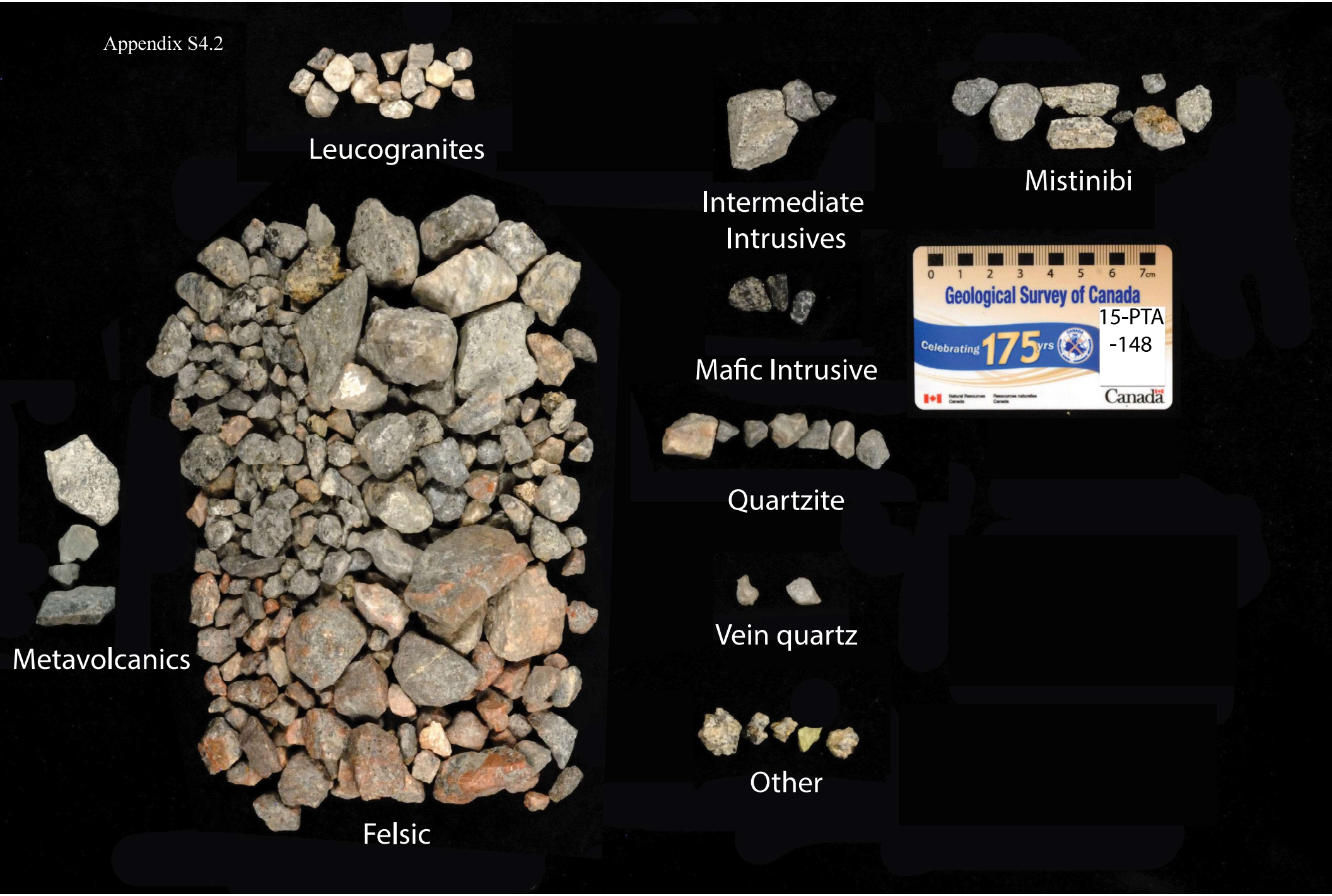

Appendix S4.2

Metasediments

Leucogranites

Intermediate Intrusives

Laporte

Mafic Intrusive

Felsic

Quartzite

Metavolcanics

Vein quartz

Iron Fm.

Other

Appendix S4.2

Metasediments

Leucogranites

Intermediate Intrusives

Laporte

Metavolcanics

Felsic

Mafic Intrusive

Vein quartz

Other

Appendix S4.2

Metasediments

Leucogranites

Intermediate Intrusives

Mistinibi

Metavolcanics

Felsic

Mafic Intrusive

Laporte

Quartzite

Vein quartz

Other

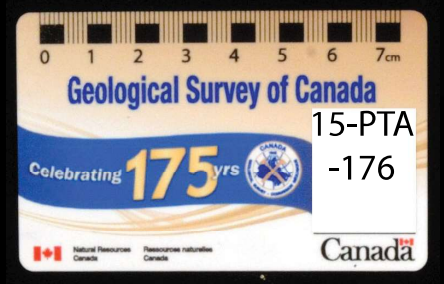

Appendix S4.2

Metasediments

Leucogranites

Intermediate Intrusives

Laporte

Felsic

Mafic Intrusive

Metavolcanics

Quartzite

Vein quartz

Iron Fm.

Others

Appendix S4.2

Metasediments

Leucogranites

Felsic

Intermediate Intrusives

Laporte

Mafic Intrusive

Others

Quartzite

Vein quartz

Others

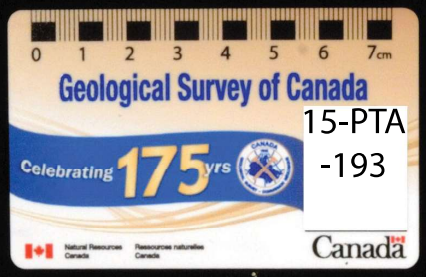

Table S2.1 Isostatic Rebound corrections

Time (ka)	Elevation of cell (m)	Topographic difference (m)	Uplift (m)	
8	951.7	517.6	-517.6	
7.5	206.5	-151	151	<- isostatic rebound begins
7	231.5	-146	146	
6.5	253.6	-129.8	129.8	
6	274.3	-109.2	109.2	
5.5	291.1	-92.4	92.4	
5	305.8	-77.8	77.8	
4.5	318.5	-65.2	65.2	
4	329.6	-54.2	54.2	
3.5	339.5	-44.3	44.3	
3	348.3	-35.5	35.5	
2.5	356.1	-27.8	27.8	
2	362.9	-21	21	
1.5	369	-14.9	14.9	
1	374.6	-9.4	9.4	
0.5	379.5	-4.4	4.4	
0	384	0	0	
		Average uplift =	61	

Data source: http://www.atmosp.physics.utoronto.ca/~peltier/data.php

Cell: Lat 55.5 Long. 295.5

Table S2.2 Striation data

Sample	Lat	Long	Dir'n (°)	Age	Sample	Lat	Long	Dir'n (°)	Age
14PTA-B001	54.1601	-64.0398	21	1	15PTA045	55.7900	-64.4560	63	1
14PTA-B001	54.7638	-64.0552	57	1	15PTA046	55.7514	-64.2636	52	1
14PTA-B002	54.8766	-64.5323	70	1	15PTA048	55.6812	-64.0625	62	1
14PTA-B003	54.7387	-64.5569	66	1	15PTA049	55.5172	-64.0389	73	1
14PTA-B004	54.9113	-64.8286	85	3	15PTA057	55.0618	-65.7303	300	2
14PTA-B014	55.6966	-64.7133	56	1	15PTA057	55.3603	-65.7508	270	4
14PTA-B015	55.5490	-64.9555	47	1	15PTA058	55.5645	-65.3212	290	2
14PTA-B015	55.7569	-64.9659	63	1	15PTA058	55.8949	-65.3409	235	4
14PTA-B044	55.8267	-64.9241	58	1	15PTA058	55.5582	-65.3209	90	1
14PTA-B046	55.8533	-65.0695	54	1	15PTA058	54.6159	-65.2669	90	3
14PTA-B046	55.8201	-65.0677	90	3	15PTA059	54.9648	-65.1036	70	1
14PTA-B049	55.9428	-64.9543	58	1	15PTA059	54.7258	-65.0912	90	3
14PTA-R007	55.7716	-65.5462	85	3	15PTA060	54.7698	-64.9902	55	1
14PTA-R019	55.9836	-64.7392	50	1	15PTA060	54.7940	-64.9914	80	3
14PTA-R019	55.9166	-64.7362	70	1	15PTA061	55.7013	-64.3318	57	1
14PTA-R021	55.6695	-65.0105	87	3	15PTA062	55.8513	-64.4449	35	1
14PTA-R024	55.6948	-65.0477	85	3	15PTA062	55.9962	-64.4503	57	1
14PTA-R025	55.8043	-65.2455	65	1	15PTA063	55.9694	-64.6055	40	1
14PTA-R025	55.7291	-65.2412	86	3	15PTA063	55.9770	-64.6058	65	1
14PTA-R026	55.9713	-65.3849	286	2	15PTA075	55.8295	-65.2643	253	4
14PTA-R026	54.9289	-65.3228	60	3	15PTA075	55.8023	-65.2627	65	1
14PTA-R043	55.6755	-64.7244	50	1	15PTA077	54.8576	-65.0304	80	3
14PTA-R043	55.6052	-64.7214	65	1	15PTA078	55.6425	-64.5083	70	1
15PTA004	55.7651	-65.7771	305	2	15PTA078	55.8520	-64.5164	35	1
15PTA004	55.2455	-65.7407	245	4	15PTA079	55.9404	-64.3707	40	1
15PTA005	55.9473	-65.9510	304	2	15PTA079	55.9640	-64.3715	53	1
15PTA007	55.7989	-65.9635	300	2	15PTA080	55.9540	-64.2336	34	1
15PTA010	54.0341	-65.4654	50	1	15PTA080	55.9670	-64.2340	58	1
15PTA010	54.0341	-65.4654	291	2	15PTA081	55.8430	-64.1895	55	1
15PTA022	54.7683	-65.4668	85	3	15PTA099	55.7617	-64.7631	55	1
15PTA024	54.3455	-65.0791	258	4	15PTA101	55.6940	-64.1790	28	1
15PTA024	54.6859	-65.0964	85	3	15PTA101	55.6147	-64.1766	75	1
15PTA030	55.4872	-65.2971	55	1	15PTA102	55.5318	-64.3714	45	1
15PTA031	54.0926	-65.1337	235	4	15PTA102	55.5007	-64.3704	55	1
15PTA031	54.5723	-65.1587	83	3	15PTA103	55.3960	-64.4765	25	1
15PTA032	54.4602	-65.0911	85	3	15PTA103	55.8375	-64.4932	55	1
15PTA035	54.5590	-64.9779	85	3	15PTA139	54.9900	-65.1075	73	3
15PTA036	55.3357	-65.2138	72	1	15PTA144	55.8497	-64.2786	65	1
15PTA039	55.2369	-64.7423	60	1	15PTA145	55.8534	-64.1965	45	1
15PTA042	55.6125	-64.8836	55	1	15PTA146	55.6502	-64.3507	40	1
15PTA043	55.6417	-65.1737	58	1	15PTA147	55.5448	-64.4838	45	1
15PTA043	54.6485	-65.1203	85	3	15PTA147	55.3663	-64.4771	60	1
15PTA044	55.7503	-64.5431	55	1	15PTA148	54.7086	-64.2938	55	1

Table S2.2 Striation data

Sample	Lat	Long	Dir'n (°)	Age	Sample	Lat	Long	Dir'n (°)	Age
15PTA045	55.7900	-64.4560	63	1	15PTA150	54.3984	-64.0142	55	1
15PTA046	55.7514	-64.2636	52	1	15PTA151	54.2484	-64.0046	55	1
15PTA048	55.6812	-64.0625	62	1	15PTA152	54.2565	-64.1407	48	1
15PTA049	55.5172	-64.0389	73	1	15PTA155	54.3610	-64.8045	55	1
15PTA057	55.0618	-65.7303	300	2	15PTA156	54.4904	-64.6847	45	1
15PTA057	55.3603	-65.7508	270	4	15PTA159	55.2258	-65.2585	240	4
15PTA058	55.5645	-65.3212	290	2	15PTA159	54.6591	-65.2270	65	1
15PTA058	55.8949	-65.3409	235	4	15PTA159	54.7602	-65.2325	95	3
15PTA058	55.5582	-65.3209	90	1	15PTA160	55.4087	-65.1947	270	4
15PTA058	54.6159	-65.2669	90	3	15PTA160	55.4635	-65.1978	55	1
15PTA059	54.9648	-65.1036	70	1	15PTA161	55.9341	-65.4195	240	4
15PTA059	54.7258	-65.0912	90	3	15PTA161	54.8687	-65.3552	45	1
15PTA060	54.7698	-64.9902	55	1	15PTA161	54.4540	-65.3313	95	3
15PTA060	54.7940	-64.9914	80	3	15PTA163	55.6143	-65.9561	300	2
15PTA061	55.7013	-64.3318	57	1	15PTA164	55.2646	-65.9044	300	2
15PTA062	55.8513	-64.4449	35	1	15PTA174	55.8903	-64.7596	65	1
15PTA062	55.9962	-64.4503	57	1	15PTA175	55.9086	-64.7318	55	1
15PTA063	55.9694	-64.6055	40	1	15PTA176	55.8041	-64.6931	65	1
15PTA063	55.9770	-64.6058	65	1	15PTA191	55.9618	-65.0735	240	4
15PTA075	55.8295	-65.2643	253	4	15PTA191	54.5538	-65.0014	90	3
15PTA075	55.8023	-65.2627	65	1	15PTA192	54.6253	-64.9174	95	3
15PTA077	54.8576	-65.0304	80	3	15PTA201	54.0548	-65.0390	270	4
15PTA078	55.6425	-64.5083	70	1	15PTA201	54.9551	-65.0844	65	1
15PTA078	55.8520	-64.5164	35	1	15PTA203	54.9127	-64.5587	62	1
15PTA079	55.9404	-64.3707	40	1	15PTA203	54.9176	-64.5589	45	1
15PTA079	55.9640	-64.3715	53	1	16-PTA-054	55.7220	-65.7650	317	2
15PTA080	55.9540	-64.2336	34	1	16-PTA-055	55.9119	-65.7392	308	2
15PTA080	55.9670	-64.2340	58	1	16-PTA-055	54.7778	-65.6620	238	4
15PTA081	55.8430	-64.1895	55	1	16-PTA-056	55.0959	-65.9464	309	2
15PTA099	55.7617	-64.7631	55	1	16-PTA-058	54.9430	-64.1798	65	1
15PTA101	55.6940	-64.1790	28	1	16-PTA-059	55.1075	-64.6526	40	1
15PTA101	55.6147	-64.1766	75	1	16-PTA-061	55.0250	-64.5228	56	1
15PTA102	55.5318	-64.3714	45	1	16-PTA-062	54.9734	-64.5286	55	1
15PTA102	55.5007	-64.3704	55	1	16-PTA-063	55.1496	-65.4250	305	2
15PTA103	55.3960	-64.4765	25	1	16-PTA-063	54.8410	-65.4065	70	3
15PTA103	55.8375	-64.4932	55	1	16-PTA-064	54.9481	-65.4186	70	1
15PTA139	54.9900	-65.1075	73	3	16-PTA-065	54.2213	-65.4444	310	2
15PTA144	55.8497	-64.2786	65	1	16-PTA-065	54.9036	-65.4856	85	3
15PTA145	55.8534	-64.1965	45	1	16-PTA-068	54.8304	-65.7828	308	2
15PTA146	55.6502	-64.3507	40	1	16-PTA-068	54.4200	-65.7549	229	4
15PTA147	55.5448	-64.4838	45	1	16-PTA-069	55.0548	-65.1806	305	2
15PTA147	55.3663	-64.4771	60	1	16-PTA-069	54.9259	-65.1736	86	3
15PTA148	54.7086	-64.2938	55	1	16-PTA-069	54.9715	-65.1760	53	3

Table S2.2 Striation data

Sample	Lat	Long	Dir'n (°)	Age
16-PTA-070	54.9817	-65.2054	316	2
16-PTA-070	54.9781	-65.2052	89	3
16-PTA-070	55.0396	-65.2086	52	3
16-PTA-077	54.8798	-64.6920	45	1
16-PTA-146	54.3196	-65.5620	332	2
16-PTA-147	55.0362	-65.5652	117	3
16-PTA-147	54.9063	-65.5569	89	3
16-PTA-147	55.0126	-65.5637	59	3
16-PTA-148	54.2591	-65.6311	316	2
16-PTA-148	54.9427	-65.6756	20	1
16-PTA-148	54.8439	-65.6690	79	3
16-PTA-148	55.2001	-65.6928	140	3
16-PTA-150	54.9208	-65.4175	93	3
16-PTA-150	55.1286	-65.4301	65	3
16-PTA-151	54.9469	-65.3447	94	3
16-PTA-151	55.1605	-65.3572	56	3

Table S2.3 Dosimetry information

Dosimetry information (uncertainties are reported as ±1σ).

Sample	Total dose rate (Gy/ka)	Sample depth (cm)	Water content[1] (Δ^w)	Rb (ppm)	Th (ppm)	U (ppm)	K (%)
15-PTA-035	3.81 ± 0.23	100	0.0088 ± 0.001	52.5 ± 2.77	3.00 ± 0.15	0.39 ± 0.08	2.50 ± 0.13
15-PTA-074	3.05 ± 0.39	370	0.1850 ± 0.019	61.8 ± 3.31	5.50 ± 0.28	2.13 ± 1.69	1.80 ± 0.10
15-PTA-149	4.35 ± 0.25	75	0.0329 ± 0.003	108 ± 5.50	5.50 ± 0.28	1.30 ± 0.11	2.40 ± 0.13
16-PTA-052	5.59 ± 0.30	140	0.021 ± 0.010	80 ± 5	20.6 ± 0.5	1.3 ± 0.1	2.9 ± 0.1

[1] Water contents are “as collected” values and are defined as (mass water)/(mass minerals).

Table S2.4 SAR protocol for OSL samples.

1.	Natural / Regenerative Dose
2.	Preheat (160°C, 10 s)
3.	IR diodes (50°C, 200 s @ 20% power) → L_n, L_x[1]
4.	Test dose (4.3 Gy)
5.	Preheat (160°C, 10 s)
6.	IR diodes (50°C, 200 s @ 20% power)….→ T_n, T_x[1]
7.	Hotwash (180°C, 40 s)
8.	Return to step 1.

[1]Ln = natural signal, Lx = regenerative dose signal, Tn = natural test dose signal, Tx = regenerative test dose signal. A "zero dose" point was measured before the second highest regenerative dose to measure recuperation and build-up of background signal, and a repeat dose point was measured after the highest regenerative dose for the recycling ratio.

Table S2.5 Sample De values

Sample D_e values and ages (uncertainties are reported as ±1σ).

Sample	Grain size fraction (μm)	Total dose rate (Gy/ka)	Number of aliquots dated	Approximate # of grains per aliquot	D_e (CAM) (Gy)	OD (%)	Fading rate[1] (%/decade)	Uncorrected age (ka)	Fading-corrected CAM age[2] (ka)	Fading-corrected MAM age[2,3] (ka)
15-PTA-035	180- 250	3.81 ± 0.23	24	40-60	152 ± 8	23 ± 4	4.37 ± 0.11	40.0 ± 3.2	61.9 ± 5.02	n/a
15-PTA-074	85-180	3.05 ± 0.39	24	70-100	18.8 ± 0.3	7 ± 1	2.46 ± 0.05	6.13 ± 0.79	7.65 ± 0.99	n/a
15-PTA-149	250-300	4.35 ± 0.25	23	10-20	28.7 ± 2.0	33 ± 5	2.09 ± 0.08	6.59 ± 0.60	7.93 ± 0.72	n/a
16-PTA-052	180-250	5.59 ± 0.30	29	40-60	120.8 ± 10.8	48 ± 6	4.88 ± 0.30	21.6 ± 3.6	35.0 ± 4.0	15.5 ± 2.7 (20.5 ± 3.5)

[1] Fading rates were measured using the SAR method of Auclair et al. (2003) and are reported as the weighted mean *g*-value of 8-12 aliquots.
[2] Fading corrections were applied using the method of Huntley and Lamothe (2001). Because the natural signal (Ln/Tn) falls in the non-linear part of the dose response curves of sample 16-PTA-052 (Figure S2.3) this correction method may underestimate the true age by ~15-20% (*c.f.* Mathewes et al., 2015).
[3] MAM age in brackets excludes two lowest outlying D_e values (see Figure S2.3).

Table S3.1

Chemical index of alteration data

Source- Report GM 65368 http://gq.mines.gouv.qc.ca/documents/EXAMINE/GM65368/GM65368.pdf

NUMR_ECHN	ESTN	NORD	Reported abundances				Molar Weights				Molar Percentage				CIA
			AL2O3	CAO	NA2O	K2O	Al2O3	CaO	Na2O	K2O	Al2O3	CaO	Na2O	K2O	
1906001244	410072	6191198	13.59	0.41	3.79	5.15	101.96	56.08	61.98	94.20	0.13	0.01	0.06	0.05	0.52
1906001245	410072	6191199	13.19	0.48	3.26	5.49	101.96	56.08	61.98	94.20	0.13	0.01	0.05	0.06	0.52
1906001246	410073	6191200	13.72	0.36	4.15	5.43	101.96	56.08	61.98	94.20	0.13	0.01	0.07	0.06	0.51
1906001247	410074	6191200	13.16	0.16	3.73	5.62	101.96	56.08	61.98	94.20	0.13	0.00	0.06	0.06	0.51
1906001248	410684	6189630	13.19	1.06	2.65	5.8	101.96	56.08	61.98	94.20	0.13	0.02	0.04	0.06	0.51
1906001249	410683	6189629	14.16	2.13	3.39	3.99	101.96	56.08	61.98	94.20	0.14	0.04	0.05	0.04	0.51
1906001251	410682	6189629	11.64	1.8	4.78	2.45	101.96	56.08	61.98	94.20	0.11	0.03	0.08	0.03	0.46
1906001252	410680	6189628	13.87	1.02	3.16	6.16	101.96	56.08	61.98	94.20	0.14	0.02	0.05	0.07	0.50
1906001253	410678	6189628	15.14	1.59	3.61	6.08	101.96	56.08	61.98	94.20	0.15	0.03	0.06	0.06	0.50
1906001254	410675	6189627	14.31	2.62	3.45	3.92	101.96	56.08	61.98	94.20	0.14	0.05	0.06	0.04	0.49
1906001255	410674	6189626	14.19	1.79	3.33	4.39	101.96	56.08	61.98	94.20	0.14	0.03	0.05	0.05	0.51
1906001256	410671	6189625	14.66	2.26	3.75	3.59	101.96	56.08	61.98	94.20	0.14	0.04	0.06	0.04	0.51
1906001257	410670	6189625	13.41	1.4	3.43	4.54	101.96	56.08	61.98	94.20	0.13	0.02	0.06	0.05	0.51
1906001258	410669	6189625	13.36	1.51	3.07	5.09	101.96	56.08	61.98	94.20	0.13	0.03	0.05	0.05	0.50
1906001259	410668	6189624	14	2.03	3.78	3.46	101.96	56.08	61.98	94.20	0.14	0.04	0.06	0.04	0.51
1906001260	410660	6189621	13.09	2.89	3.73	1.68	101.96	56.08	61.98	94.20	0.13	0.05	0.06	0.02	0.50
1906001261	410659	6189621	14.09	3.96	3.84	1.16	101.96	56.08	61.98	94.20	0.14	0.07	0.06	0.01	0.49
1906001262	410658	6189621	14.96	4.92	3.56	2.38	101.96	56.08	61.98	94.20	0.15	0.09	0.06	0.03	0.46
1906001263	410655	6189620	16.47	1.99	3.8	5.95	101.96	56.08	61.98	94.20	0.16	0.04	0.06	0.06	0.50
1906001265	410649	6189618	13.53	1.7	2.8	5.18	101.96	56.08	61.98	94.20	0.13	0.03	0.05	0.05	0.50
1906001266	410648	6189617	13.11	1.27	3.36	5.43	101.96	56.08	61.98	94.20	0.13	0.02	0.05	0.06	0.49
1906001267	410647	6189617	11.43	0.92	2.61	4.26	101.96	56.08	61.98	94.20	0.11	0.02	0.04	0.05	0.52
1906001268	410646	6189617	14.28	1.25	2.59	6.22	101.96	56.08	61.98	94.20	0.14	0.02	0.04	0.07	0.52
1906001269	410645	6189616	13.29	1.7	3.7	2.43	101.96	56.08	61.98	94.20	0.13	0.03	0.06	0.03	0.53
1906001270	410644	6189616	13.86	1.45	5.97	1.36	101.96	56.08	61.98	94.20	0.14	0.03	0.10	0.01	0.50
1906001271	410643	6189616	13.93	1.25	3.32	4.27	101.96	56.08	61.98	94.20	0.14	0.02	0.05	0.05	0.53
1906001272	410641	6189615	13.12	1.71	3.32	3.11	101.96	56.08	61.98	94.20	0.13	0.03	0.05	0.03	0.52
1906001273	410640	6189614	13.05	1.21	3.91	4.1	101.96	56.08	61.98	94.20	0.13	0.02	0.06	0.04	0.50
1906001278	410627	6189610	13.56	1.58	2.25	5.94	101.96	56.08	61.98	94.20	0.13	0.03	0.04	0.06	0.51
1906001279	410627	6189610	14.58	2.8	3.06	3.47	101.96	56.08	61.98	94.20	0.14	0.05	0.05	0.04	0.51
1906001283	410617	6189607	13.55	1.12	2.61	6.67	101.96	56.08	61.98	94.20	0.13	0.02	0.04	0.07	0.50

Table S3.1

Chemical index of alteration data

Source- Report GM 65368 http://gq.mines.gouv.qc.ca/documents/EXAMINE/GM65368/GM65368.pdf

NUMR_ECHN	ESTN	NORD	Reported abundances				Molar Weights				Molar Percentage				CIA
			AL2O3	CAO	NA2O	K2O	Al2O3	CaO	Na2O	K2O	Al2O3	CaO	Na2O	K2O	
1906001284	410617	6189606	13.34	1.81	3.34	3.98	101.96	56.08	61.98	94.20	0.13	0.03	0.05	0.04	0.50
1906001289	410603	6189602	13.44	2.36	4.03	2.34	101.96	56.08	61.98	94.20	0.13	0.04	0.07	0.02	0.50
1906001303	410588	6189597	14.44	1.74	3.28	5.43	101.96	56.08	61.98	94.20	0.14	0.03	0.05	0.06	0.50
1906001304	410588	6189597	13.62	0.81	2.64	6.85	101.96	56.08	61.98	94.20	0.13	0.01	0.04	0.07	0.51
1906001305	410587	6189596	14.34	1.01	3.04	6.55	101.96	56.08	61.98	94.20	0.14	0.02	0.05	0.07	0.51
1906001306	410586	6189596	13.67	0.36	2.24	8.4	101.96	56.08	61.98	94.20	0.13	0.01	0.04	0.09	0.50
1906001307	410585	6189596	8.99	0.66	1.51	4.61	101.96	56.08	61.98	94.20	0.09	0.01	0.02	0.05	0.51
1906001308	410065	6191192	10.82	1.33	3.45	2.83	101.96	56.08	61.98	94.20	0.11	0.02	0.06	0.03	0.49
1906001309	410066	6191192	11.99	0.74	3.52	4.56	101.96	56.08	61.98	94.20	0.12	0.01	0.06	0.05	0.50
1906001310	410066	6191193	12.28	0.23	2.74	6.33	101.96	56.08	61.98	94.20	0.12	0.00	0.04	0.07	0.51
1906001311	410067	6191194	12.57	0.3	3.08	5.96	101.96	56.08	61.98	94.20	0.12	0.01	0.05	0.06	0.51
1906001312	410068	6191194	13.4	0.76	3.6	5.2	101.96	56.08	61.98	94.20	0.13	0.01	0.06	0.06	0.51
1906001313	410069	6191195	13.69	0.7	3.22	5.84	101.96	56.08	61.98	94.20	0.13	0.01	0.05	0.06	0.52
1906001314	410069	6191196	13.01	0.45	3.06	5.58	101.96	56.08	61.98	94.20	0.13	0.01	0.05	0.06	0.52
1906001315	410070	6191197	13.2	0.53	3.34	5.17	101.96	56.08	61.98	94.20	0.13	0.01	0.05	0.05	0.52
1906001316	410071	6191197	13.36	0.47	3.58	5.51	101.96	56.08	61.98	94.20	0.13	0.01	0.06	0.06	0.51
1906001317	410075	6191201	12.9	0.17	3.37	5.9	101.96	56.08	61.98	94.20	0.13	0.00	0.05	0.06	0.51
1906001318	410076	6191202	13.36	0.21	3.89	5.54	101.96	56.08	61.98	94.20	0.13	0.00	0.06	0.06	0.51
1906001319	410076	6191202	13.9	0.27	3.33	6.85	101.96	56.08	61.98	94.20	0.14	0.00	0.05	0.07	0.51
1906001321	410092	6191218	12.12	1.2	2.79	2.36	101.96	56.08	61.98	94.20	0.12	0.02	0.05	0.03	0.57
1906001322	410093	6191219	14.03	1.66	4.17	1.73	101.96	56.08	61.98	94.20	0.14	0.03	0.07	0.02	0.54
1906001323	410094	6191219	10.3	0.92	3.38	1.37	101.96	56.08	61.98	94.20	0.10	0.02	0.05	0.01	0.54
1906001324	410095	6191220	9.98	0.91	2.89	1.71	101.96	56.08	61.98	94.20	0.10	0.02	0.05	0.02	0.55
1906001326	410095	6191221	12.56	1.16	3.93	3.51	101.96	56.08	61.98	94.20	0.12	0.02	0.06	0.04	0.50
1906001328	410117	6191242	10.67	1.34	3.76	1.4	101.96	56.08	61.98	94.20	0.10	0.02	0.06	0.01	0.51
1906001329	410118	6191243	13.74	0.56	3.04	5.52	101.96	56.08	61.98	94.20	0.13	0.01	0.05	0.06	0.53
1906001330	410118	6191243	13.62	0.34	3.26	5.76	101.96	56.08	61.98	94.20	0.13	0.01	0.05	0.06	0.53
1906001331	410119	6191244	9.23	0.73	1.97	3.39	101.96	56.08	61.98	94.20	0.09	0.01	0.03	0.04	0.53
1906001332	410120	6191244	14.7	1.8	3.75	2.28	101.96	56.08	61.98	94.20	0.14	0.03	0.06	0.02	0.55
1906048137	410023	6191086	13.85	0.24	2.23	8.45	101.96	56.08	61.98	94.20	0.14	0.00	0.04	0.09	0.51
1906048138	410062	6191113	12.97	0.88	2.52	5.65	101.96	56.08	61.98	94.20	0.13	0.02	0.04	0.06	0.52

Table S3.1

Chemical index of alteration data

Source- Report GM 65368 http://gq.mines.gouv.qc.ca/documents/EXAMINE/GM65368/GM65368.pdf

NUMR_ECHN	ESTN	NORD	Reported abundances				Molar Weights				Molar Percentage				CIA
			AL2O3	CAO	NA2O	K2O	Al2O3	CaO	Na2O	K2O	Al2O3	CaO	Na2O	K2O	
1906048139	409989	6191363	13.26	0.72	2.66	6.25	101.96	56.08	61.98	94.20	0.13	0.01	0.04	0.07	0.52
1906048140	409953	6191492	11.26	0.72	4.06	1.73	101.96	56.08	61.98	94.20	0.11	0.01	0.07	0.02	0.53
1906048141	409766	6191676	13.66	1.03	3.02	5.41	101.96	56.08	61.98	94.20	0.13	0.02	0.05	0.06	0.52
1906001280	410624	6189609	12.1	1.09	2.62	5.14	101.96	56.08	61.98	94.20	0.12	0.02	0.04	0.05	0.51
1906001281	410623	6189609	13.55	1.64	3.35	4.62	101.96	56.08	61.98	94.20	0.13	0.03	0.05	0.05	0.50
1906001291	410599	6189600	13.85	1.27	2.77	6.21	101.96	56.08	61.98	94.20	0.14	0.02	0.04	0.07	0.50
1906001292	410598	6189600	14.22	1.6	3.14	5.4	101.96	56.08	61.98	94.20	0.14	0.03	0.05	0.06	0.51
1906001293	410597	6189600	13.31	0.85	2.2	7.38	101.96	56.08	61.98	94.20	0.13	0.02	0.04	0.08	0.50
1906001294	410597	6189600	13.31	2.4	3.31	4.19	101.96	56.08	61.98	94.20	0.13	0.04	0.05	0.04	0.48
1906001295	410596	6189599	14.47	1.13	2.23	7.44	101.96	56.08	61.98	94.20	0.14	0.02	0.04	0.08	0.51
1906001296	410595	6189599	13.78	1.07	2.83	6.2	101.96	56.08	61.98	94.20	0.14	0.02	0.05	0.07	0.51
1906001297	410594	6189599	12.75	1.87	2.44	4.51	101.96	56.08	61.98	94.20	0.13	0.03	0.04	0.05	0.51
1906001298	410593	6189598	13.69	1.18	3.03	5.73	101.96	56.08	61.98	94.20	0.13	0.02	0.05	0.06	0.51
1906001299	410592	6189598	13.89	2.58	2.87	4.69	101.96	56.08	61.98	94.20	0.14	0.05	0.05	0.05	0.49
1906001301	410592	6189598	14.97	3.23	4.32	1.46	101.96	56.08	61.98	94.20	0.15	0.06	0.07	0.02	0.51
													Average CIA		0.51

Supplementary Table 4.1

Analysis: BV LF200			LDL	0.01	0.01	0.04	0.01	0.01	0.01	0.01	0.01	0.01	0.01
Sample	Lat	Long	Datum	SiO2 (%)	Al2O3 (%)	Fe2O3 (%)	MgO (%)	CaO (%)	Na2O (%)	K2O (%)	TiO2 (%)	P2O5 (%)	MnO (%)
14-PTA-B001	55.912	-64.086	NAD 83	64.9	14.71	4.77	1.8	3.84	3.16	2.72	0.78	0.24	0.08
14-PTA-B002	55.969	-64.575	NAD 83	60.93	15.85	6.31	2.9	4.34	3.28	2.62	0.89	0.31	0.09
14-PTA-B004	55.944	-64.877	NAD 83	59.3	16.13	6.31	2.52	4.49	3.58	2.72	0.9	0.43	0.09
14-PTA-R002	55.963	-65.796	NAD 83	58.85	16.33	6.67	3.04	4.49	3.55	2.73	0.88	0.44	0.09
14-PTA-R003	55.958	-65.469	NAD 83	55.28	16.58	7.62	3.36	4.61	3.47	2.67	0.96	0.51	0.1
14-PTA-R004	55.814	-65.261	NAD 83	55.64	16.73	7.88	3.58	5.14	3.59	2.44	1.02	0.58	0.11
14-PTA-R005	55.566	-65.219	NAD 83	56.43	16.4	6.94	4.54	3.5	3.1	2.71	0.77	0.23	0.09
14-PTA-R006	55.626	-65.401	NAD 83	56.88	16.04	6.9	4.33	3.54	3.14	2.71	0.74	0.2	0.09
14-PTA-R020	55.741	-64.730	NAD 83	58.07	16.35	6.41	2.68	4.23	3.35	2.61	0.82	0.37	0.08
14-PTA-R023	55.780	-65.016	NAD 83	53.98	16.34	8.27	3.68	4.75	3.24	2.31	1.07	0.55	0.1
14-PTA-R024	55.925	-65.060	NAD 83	57.76	16.14	6.83	2.65	4.76	3.61	2.73	0.96	0.51	0.1
14-PTA-R043	55.838	-64.732	NAD 83	58.82	16.23	6.38	2.69	4.18	3.35	2.63	0.85	0.35	0.09
15-PTA-002	55.674	-65.914	NAD 83	51.41	19.16	8.97	4.41	2.41	2.39	3.99	0.98	0.25	0.09
15-PTA-003	55.530	-65.914	NAD 83	52.38	19.05	9	4.01	3.38	2.63	3.25	1.05	0.26	0.09
15-PTA-004	55.741	-65.775	NAD 83	54.76	15.32	7.98	4.78	4.94	2.92	1.94	0.85	0.32	0.11
15-PTA-005	55.807	-65.940	NAD 83	51.86	16.16	8.75	4.47	4.64	2.86	1.98	0.99	0.28	0.1
15-PTA-007	55.922	-65.973	NAD 83	56.53	16.08	6.83	3.11	4.85	3.59	2.39	0.86	0.5	0.09
15-PTA-008	55.882	-65.812	NAD 83	55.78	16.52	7.07	3.23	4.82	3.56	2.31	0.88	0.5	0.09
15-PTA-010	55.969	-65.587	NAD 83	57.5	16.31	6.55	3.42	4.41	3.51	2.61	0.83	0.42	0.09
15-PTA-011	55.907	-65.334	NAD 83	57.25	15.86	7.09	2.78	4.97	3.56	2.53	0.97	0.59	0.1
15-PTA-012	55.795	-65.690	NAD 83	55.58	15.71	6.91	3.45	4.98	3.55	2.29	0.83	0.51	0.1
15-PTA-013	55.659	-65.642	NAD 83	53.71	17.24	7.07	4.52	3.12	2.49	3.01	0.79	0.24	0.09
15-PTA-014	55.587	-65.705	NAD 83	55.54	16.61	7.1	4.49	3.21	2.82	3.07	0.83	0.27	0.09
15-PTA-018	55.595	-65.789	NAD 83	54.43	18.26	7.73	4.21	2.3	2.64	4.03	0.9	0.22	0.08
15-PTA-019	55.626	-65.929	NAD 83	49.79	21.98	7.12	2.73	1.26	2.33	5.41	0.9	0.38	0.05
15-PTA-020	55.726	-65.884	NAD 83	55.65	16.56	7.4	4.25	4.12	3.13	2.72	0.9	0.32	0.1
15-PTA-022	55.773	-65.530	NAD 83	54.12	15.72	7.66	4.22	4.77	3.48	2.26	0.88	0.46	0.11
15-PTA-024	55.739	-65.153	NAD 83	56.65	16.2	7.27	3.7	5.11	3.62	2.23	0.95	0.49	0.09
15-PTA-025	55.654	-65.781	NAD 83	55.45	16.75	6.71	4.16	3.15	2.97	3.28	0.78	0.25	0.09
15-PTA-028	55.553	-65.560	NAD 83	58.1	17.36	4.93	3.72	2.48	3.19	3.82	0.57	0.13	0.07
15-PTA-029	55.687	-65.307	NAD 83	57.11	16.08	6.42	4.44	4.28	3.35	2.57	0.72	0.31	0.09
15-PTA-034	55.843	-65.062	NAD 83	54.02	15.65	7.66	3.28	4.65	3.41	2.47	0.97	0.6	0.1

Supplementary Table 4.1

Analysis: BV LF200			LDL	0.01	0.01	0.04	0.01	0.01	0.01	0.01	0.01	0.01	0.01
Sample	Lat	Long	Datum	SiO2 (%)	Al2O3 (%)	Fe2O3 (%)	MgO (%)	CaO (%)	Na2O (%)	K2O (%)	TiO2 (%)	P2O5 (%)	MnO (%)
15-PTA-036	55.984	-65.251	NAD 83	58.07	16.08	6.73	2.77	4.99	3.73	2.75	0.9	0.61	0.09
15-PTA-037	55.964	-64.984	NAD 83	59.98	15.78	5.96	2.38	4.78	3.73	2.67	0.87	0.5	0.09
15-PTA-039	55.975	-64.775	NAD 83	59.87	15.6	5.5	2.17	4.64	3.66	2.46	0.84	0.44	0.08
15-PTA-042	55.809	-64.893	NAD 83	57.14	15.75	6.66	2.75	4.53	3.43	2.5	0.95	0.55	0.08
15-PTA-043	55.633	-65.173	NAD 83	54.08	16.12	7.38	4.3	4.01	3.09	2.33	0.83	0.36	0.09
15-PTA-044	55.852	-64.547	NAD 83	59.83	15.04	6.62	2.85	5.02	3.39	2.32	0.96	0.31	0.11
15-PTA-045	55.939	-64.462	NAD 83	59.06	15.3	7.06	2.83	3.73	2.85	2.69	0.94	0.15	0.1
15-PTA-046	55.965	-64.271	NAD 83	62.72	14.89	5.18	2.06	4.26	3.33	2.35	0.8	0.25	0.08
15-PTA-047	55.953	-64.368	NAD 83	62.76	14.88	6	2.45	4.8	3.53	2.31	0.95	0.29	0.1
15-PTA-048	55.969	-64.070	NAD 83	65.73	14.71	4.48	1.93	4.27	3.48	2.72	0.81	0.29	0.08
15-PTA-049	55.844	-64.048	NAD 83	62.02	15.71	5.72	2.08	3.75	3.07	2.82	0.81	0.24	0.09
15-PTA-050	55.770	-64.038	NAD 83	61.77	15.06	5.46	2.07	4.07	3.16	2.48	0.86	0.25	0.09
15-PTA-051	55.695	-64.034	NAD 83	62.73	15.02	5.72	2.23	4.46	3.39	2.45	0.9	0.31	0.1
15-PTA-052	55.616	-64.036	NAD 83	60.86	15.32	5.71	2.25	4.22	3.31	2.45	0.85	0.3	0.09
15-PTA-053	55.535	-64.056	NAD 83	59.57	15.31	5.98	2.36	4.23	3.32	2.4	0.85	0.28	0.09
15-PTA-054	55.502	-64.230	NAD 83	61.75	15.13	5.67	2.25	4.51	3.51	2.41	0.87	0.31	0.09
15-PTA-056	55.820	-65.568	NAD 83	54.48	15.75	6.94	3.47	4.7	3.42	2.31	0.84	0.47	0.1
15-PTA-057	55.825	-65.784	NAD 83	54.46	16.13	7.12	3.39	4.53	3.3	2.22	0.84	0.39	0.09
15-PTA-061	55.852	-64.337	NAD 83	60.8	14.99	5.84	2.48	3.75	3.19	3.1	0.82	0.27	0.1
15-PTA-062	55.649	-64.437	NAD 83	62.87	14.86	5.41	2.22	4.53	3.54	2.61	0.84	0.28	0.09
15-PTA-063	55.544	-64.588	NAD 83	59.61	15.74	5.9	2.44	4.36	3.57	2.37	0.84	0.31	0.09
15-PTA-079	55.895	-64.369	NAD 83	59.7	15.33	5.83	2.44	3.95	3.29	2.7	0.77	0.23	0.09
15-PTA-080	55.915	-64.232	NAD 83	65.03	15.3	4.83	1.85	3.97	3.38	2.87	0.73	0.24	0.08
15-PTA-081	55.810	-64.189	NAD 83	60.65	15.73	5.82	2.23	3.64	2.93	2.72	0.83	0.21	0.08
15-PTA-098	55.814	-65.398	NAD 83	57.46	16.48	7.36	3.42	5.01	3.76	2.44	0.92	0.54	0.1
15-PTA-099	55.780	-65.083	NAD 83	58.42	16.1	5.88	2.45	4.16	3.48	2.45	0.79	0.37	0.08
15-PTA-101	55.680	-64.179	NAD 83	62	15.67	5.59	2.23	4.27	3.27	2.65	0.89	0.3	0.09
15-PTA-102	55.704	-64.378	NAD 83	63.37	15.04	5.64	2.51	4.79	3.49	2.67	0.89	0.31	0.1
15-PTA-103	55.741	-64.490	NAD 83	60.32	15.4	6.04	2.59	4.05	3.25	2.92	0.82	0.25	0.1
15-PTA-139	55.559	-65.138	NAD 83	58.02	15.51	7.05	4.03	4.2	3.38	2.45	0.86	0.28	0.09
15-PTA-144	55.627	-64.271	NAD 83	61.49	15.09	5.78	2.2	4.55	3.51	2.59	0.85	0.33	0.1
15-PTA-145	55.567	-64.188	NAD 83	60.53	14.95	5.91	2.37	4.36	3.41	2.42	0.87	0.31	0.09

Supplementary Table 4.1

Analysis: BV LF200			LDL	0.01	0.01	0.04	0.01	0.01	0.01	0.01	0.01	0.01	0.01
Sample	Lat	Long	Datum	SiO2 (%)	Al2O3 (%)	Fe2O3 (%)	MgO (%)	CaO (%)	Na2O (%)	K2O (%)	TiO2 (%)	P2O5 (%)	MnO (%)
15-PTA-146	55.527	-64.346	NAD 83	60.76	15.2	6.07	2.39	4.43	3.35	2.74	0.88	0.33	0.1
15-PTA-148	55.789	-64.329	NAD 83	59.61	15.49	6.3	2.77	4.15	3.21	2.79	0.82	0.27	0.1
15-PTA-155	55.654	-64.864	NAD 83	57.49	15.91	7.04	3.39	4.87	3.53	2.36	0.92	0.49	0.09
15-PTA-156	55.591	-64.732	NAD 83	56.32	15.88	7.16	3.29	4.44	3.32	2.35	0.94	0.39	0.09
15-PTA-176	55.629	-64.686	NAD 83	56.09	15.82	6.63	3.19	4.03	3.13	2.26	0.87	0.34	0.09
15-PTA-192	55.524	-64.961	NAD 83	55.85	16.21	8	3.83	4.51	3.34	2.43	0.97	0.41	0.1
15-PTA-193	55.512	-64.852	NAD 83	57.72	15.45	7.17	3.33	5.11	3.62	2.26	0.92	0.49	0.1
16-PTA-056	55.692	-65.991	NAD 84	53.39	18.65	8.6	4.06	2.55	2.72	4.03	0.98	0.26	0.08
16-PTA-058	55.843	-64.207	NAD 85	62.96	15.15	5.42	2.25	4.29	3.26	2.67	0.83	0.27	0.09
16-PTA-060	55.898	-64.611	NAD 86	58.48	15.6	7.1	3.48	4.26	3.17	2.42	0.88	0.26	0.12
16-PTA-069	55.721	-65.218	NAD 83	54.88	16.42	8.35	4.06	4.85	3.32	2.23	0.97	0.49	0.11
16-PTA-070	55.784	-65.251	NAD 83	55.09	16.44	8.22	3.8	4.88	3.4	2.19	0.99	0.5	0.11

Supplementary Table 4.1

0.002	Analysis: BV LF200			LDL	20	1	-5.1	0.01	5	5	1	1	1	1
Cr2O3 (%)	Sample	Lat	Long	Datum	Ni (PPM)	Sc (PPM)	LOI (%)	Sum (%)	Cu (PPM)	Zn (PPM)	Mo (PPM)	Pb (PPM)	Ba (PPM)	Be (PPM)
0.009	14-PTA-B001	55.912	-64.086	NAD 83	22	14	2.7	99.72	23	50	0	23	825	4
0.016	14-PTA-B002	55.969	-64.575	NAD 83	39	17	2.2	99.71	30	72	0	17	884	3
0.011	14-PTA-B004	55.944	-64.877	NAD 83	36	15	3.2	99.66	25	85	2	15	1108	0
0.014	14-PTA-R002	55.963	-65.796	NAD 83	34	16	2.6	99.63	32	86	0	16	1286	0
0.013	14-PTA-R003	55.958	-65.469	NAD 83	37	16	4.4	99.6	32	93	0	16	1351	0
0.015	14-PTA-R004	55.814	-65.261	NAD 83	38	18	2.9	99.57	36	96	0	16	1447	1
0.021	14-PTA-R005	55.566	-65.219	NAD 83	57	17	5	99.71	43	61	0	9	952	2
0.021	14-PTA-R006	55.626	-65.401	NAD 83	57	16	5.1	99.7	40	63	0	12	939	1
0.014	14-PTA-R020	55.741	-64.730	NAD 83	40	15	4.7	99.69	33	78	0	20	958	3
0.015	14-PTA-R023	55.780	-65.016	NAD 83	35	17	5.3	99.57	33	97	0	18	1485	0
0.01	14-PTA-R024	55.925	-65.060	NAD 83	33	16	3.6	99.62	25	90	0	18	1224	2
0.014	14-PTA-R043	55.838	-64.732	NAD 83	39	15	4.1	99.7	36	84	0	19	968	2
0.024	15-PTA-002	55.674	-65.914	NAD 83	81	23	5.6	99.86	126	119	2	18	1006	5
0.028	15-PTA-003	55.530	-65.914	NAD 83	77	25	4.6	99.87	79	117	1	17	918	2
0.031	15-PTA-004	55.741	-65.775	NAD 83	62	22	5.8	99.71	35	74	0	13	802	2
0.024	15-PTA-005	55.807	-65.940	NAD 83	60	22	7.6	99.71	43	82	2	13	804	0
0.015	15-PTA-007	55.922	-65.973	NAD 83	32	17	4.8	99.62	27	68	0	17	1199	3
0.017	15-PTA-008	55.882	-65.812	NAD 83	29	18	4.8	99.6	25	75	0	17	1283	0
0.019	15-PTA-010	55.969	-65.587	NAD 83	38	17	3.9	99.6	28	75	0	18	1329	3
0.012	15-PTA-011	55.907	-65.334	NAD 83	29	17	3.8	99.57	19	86	0	21	1304	1
0.018	15-PTA-012	55.795	-65.690	NAD 83	29	18	5.7	99.64	32	71	1	15	1128	2
0.023	15-PTA-013	55.659	-65.642	NAD 83	66	18	7.4	99.7	47	65	1	14	1132	0
0.025	15-PTA-014	55.587	-65.705	NAD 83	71	17	5.6	99.7	55	68	0	10	941	3
0.023	15-PTA-018	55.595	-65.789	NAD 83	68	22	4.9	99.68	69	93	3	14	1015	3
0.022	15-PTA-019	55.626	-65.929	NAD 83	42	25	7.7	99.69	56	123	3	21	1068	1
0.024	15-PTA-020	55.726	-65.884	NAD 83	58	20	4.5	99.66	45	73	0	14	1070	1
0.02	15-PTA-022	55.773	-65.530	NAD 83	44	19	5.9	99.63	73	90	0	14	1121	2
0.017	15-PTA-024	55.739	-65.153	NAD 83	39	18	3.3	99.6	24	78	0	17	1274	0
0.023	15-PTA-025	55.654	-65.781	NAD 83	56	17	6.1	99.72	39	56	2	9	982	1
0.016	15-PTA-028	55.553	-65.560	NAD 83	47	14	5.4	99.75	39	26	1	6	928	0
0.02	15-PTA-029	55.687	-65.307	NAD 83	65	18	4.3	99.71	35	65	0	11	1002	0
0.015	15-PTA-034	55.843	-65.062	NAD 83	44	17	6.8	99.6	23	84	1	15	1185	0

Supplementary Table 4.1

0.002	Analysis: BV LF200			LDL	20	1	-5.1	0.01	5	5	1	1	1	1
Cr2O3 (%)	Sample	Lat	Long	Datum	Ni (PPM)	Sc (PPM)	LOI (%)	Sum (%)	Cu (PPM)	Zn (PPM)	Mo (PPM)	Pb (PPM)	Ba (PPM)	Be (PPM)
0.011	15-PTA-036	55.984	-65.251	NAD 83	28	16	2.8	99.56	20	82	0	17	1480	3
0.011	15-PTA-037	55.964	-64.984	NAD 83	28	16	2.9	99.62	17	69	0	18	1185	3
0.01	15-PTA-039	55.975	-64.775	NAD 83	31	15	4.4	99.62	16	58	1	16	1116	2
0.013	15-PTA-042	55.809	-64.893	NAD 83	27	16	5.2	99.56	24	79	0	19	1467	2
0.02	15-PTA-043	55.633	-65.173	NAD 83	48	18	7	99.64	35	68	0	12	1159	0
0.014	15-PTA-044	55.852	-64.547	NAD 83	31	20	3.2	99.64	32	64	2	18	895	1
0.017	15-PTA-045	55.939	-64.462	NAD 83	46	19	5	99.69	57	80	0	21	871	2
0.011	15-PTA-046	55.965	-64.271	NAD 83	32	16	3.8	99.69	24	45	0	19	841	4
0.014	15-PTA-047	55.953	-64.368	NAD 83	33	18	1.6	99.71	26	57	0	16	774	3
0.01	15-PTA-048	55.969	-64.070	NAD 83	20	16	1.2	99.73	19	52	0	21	753	1
0.011	15-PTA-049	55.844	-64.048	NAD 83	30	16	3.4	99.71	37	61	0	23	861	3
0.011	15-PTA-050	55.770	-64.038	NAD 83	26	16	4.4	99.72	34	56	0	21	812	2
0.012	15-PTA-051	55.695	-64.034	NAD 83	25	16	2.4	99.7	28	58	0	20	848	3
0.012	15-PTA-052	55.616	-64.036	NAD 83	27	15	4.3	99.71	23	58	0	19	874	2
0.012	15-PTA-053	55.535	-64.056	NAD 83	32	15	5.3	99.7	39	58	0	19	917	4
0.011	15-PTA-054	55.502	-64.230	NAD 83	27	15	3.2	99.72	28	53	0	16	812	3
0.016	15-PTA-056	55.820	-65.568	NAD 83	40	17	7.2	99.66	29	77	0	16	1036	1
0.018	15-PTA-057	55.825	-65.784	NAD 83	41	17	7.2	99.67	147	70	0	13	958	0
0.012	15-PTA-061	55.852	-64.337	NAD 83	33	16	4.4	99.76	32	63	0	22	663	3
0.011	15-PTA-062	55.649	-64.437	NAD 83	28	16	2.5	99.73	16	53	0	17	771	2
0.012	15-PTA-063	55.544	-64.588	NAD 83	33	15	4.5	99.71	32	60	0	16	872	1
0.011	15-PTA-079	55.895	-64.369	NAD 83	31	15	5.4	99.77	31	62	0	16	683	1
0.009	15-PTA-080	55.915	-64.232	NAD 83	26	15	1.5	99.77	25	49	0	19	680	1
0.013	15-PTA-081	55.810	-64.189	NAD 83	29	16	4.9	99.75	39	60	0	18	707	0
0.016	15-PTA-098	55.814	-65.398	NAD 83	39	18	2.1	99.59	28	81	0	16	1374	4
0.013	15-PTA-099	55.780	-65.083	NAD 83	38	14	5.5	99.7	20	68	0	17	918	0
0.012	15-PTA-101	55.680	-64.179	NAD 83	31	16	2.7	99.69	34	61	0	19	909	1
0.014	15-PTA-102	55.704	-64.378	NAD 83	31	18	0.9	99.7	23	62	0	18	885	4
0.012	15-PTA-103	55.741	-64.490	NAD 83	34	16	4	99.72	29	73	0	22	843	3
0.022	15-PTA-139	55.559	-65.138	NAD 83	48	18	3.8	99.65	28	58	0	13	1058	0
0.011	15-PTA-144	55.627	-64.271	NAD 83	25	15	3.2	99.67	20	63	0	23	1020	3
0.014	15-PTA-145	55.567	-64.188	NAD 83	25	15	4.5	99.69	23	58	0	18	948	2

Supplementary Table 4.1

0.002	Analysis: BV LF200			LDL	20	1	-5.1	0.01	5	5	1	1	1	1
Cr2O3 (%)	Sample	Lat	Long	Datum	Ni (PPM)	Sc (PPM)	LOI (%)	Sum (%)	Cu (PPM)	Zn (PPM)	Mo (PPM)	Pb (PPM)	Ba (PPM)	Be (PPM)
0.012	15-PTA-146	55.527	-64.346	NAD 83	28	15	3.4	99.65	22	70	0	23	1053	2
0.014	15-PTA-148	55.789	-64.329	NAD 83	34	16	4.2	99.71	38	73	0	24	901	3
0.017	15-PTA-155	55.654	-64.864	NAD 83	43	17	3.5	99.61	24	67	0	18	1249	0
0.016	15-PTA-156	55.591	-64.732	NAD 83	41	17	5.4	99.61	35	73	0	21	1141	3
0.018	15-PTA-176	55.629	-64.686	NAD 83	44	16	7.2	99.67	30	63	0	18	924	2
0.019	15-PTA-192	55.524	-64.961	NAD 83	47	18	4	99.64	37	84	1	16	1099	0
0.017	15-PTA-193	55.512	-64.852	NAD 83	38	17	3.4	99.65	22	67	0	17	1040	2
0.026	16-PTA-056	55.692	-65.991	NAD 84	80	21	4.3	99.78	99	109	1	18	981	5
0.012	16-PTA-058	55.843	-64.207	NAD 85	30	16	2.5	99.81	22	53	0	20	835	4
0.02	16-PTA-060	55.898	-64.611	NAD 86	60	16	3.9	99.81	47	74	0	16	760	2
0.017	16-PTA-069	55.721	-65.218	NAD 83	1279	47	18	3.9	99.74	48	92	0	15	0
0.019	16-PTA-070	55.784	-65.251	NAD 83	1335	47	18	3.9	99.74	43	96	0	17	0

Supplementary Table 4.1

0.2	Analysis: BV LF200			LDL	0.1	0.5	0.1	0.1	0.1	1	0.5	0.1	0.2
Co (PPM)	Sample	Lat	Long	Datum	Cs (PPM)	Ga (PPM)	Hf (PPM)	Nb (PPM)	Rb (PPM)	Sn (PPM)	Sr (PPM)	Ta (PPM)	Th (PPM)
10.1	14-PTA-B001	55.912	-64.086	NAD 83	1.2	16.7	14.8	15	81.5	2	340.9	1.6	14.8
17.2	14-PTA-B002	55.969	-64.575	NAD 83	2.2	18.9	9.6	13.5	72.7	2	400.5	0.8	10.1
16.9	14-PTA-B004	55.944	-64.877	NAD 83	0.7	18.8	11.7	14.6	69	2	467.1	0.7	11.3
16.4	14-PTA-R002	55.963	-65.796	NAD 83	0.8	20.2	8.8	11	66.2	1	590.6	0.6	8.3
20	14-PTA-R003	55.958	-65.469	NAD 83	0.6	20	10.5	10.7	59.8	1	594.8	0.4	7.5
20.5	14-PTA-R004	55.814	-65.261	NAD 83	0.4	20.8	9.5	9.9	50.4	1	664.9	0.3	6.8
21.3	14-PTA-R005	55.566	-65.219	NAD 83	1.2	19.1	6.7	8.1	71.5	1	320	0.4	6.3
19.8	14-PTA-R006	55.626	-65.401	NAD 83	1.4	18.7	7.9	8	71.1	1	306.6	0.3	8.4
17	14-PTA-R020	55.741	-64.730	NAD 83	2.4	20.7	10.8	12.8	77.8	2	459.4	0.9	10.3
20.4	14-PTA-R023	55.780	-65.016	NAD 83	0.5	20.9	9.4	10.5	54.4	1	664.1	0.3	8.1
16.7	14-PTA-R024	55.925	-65.060	NAD 83	0.5	20.8	12.5	14.5	67.3	2	534.4	0.7	10.2
15.4	14-PTA-R043	55.838	-64.732	NAD 83	4.1	18.9	9.5	12.6	78.7	2	431.5	0.9	8.9
30	15-PTA-002	55.674	-65.914	NAD 83	5.3	25.8	8.6	12	130.9	3	226	0.9	14.6
29.5	15-PTA-003	55.530	-65.914	NAD 83	4.4	24.4	7.9	12	108	3	266	0.8	11.1
26.6	15-PTA-004	55.741	-65.775	NAD 83	0.9	18.6	6.5	7.2	47.3	1	423.6	0.5	6.4
24.4	15-PTA-005	55.807	-65.940	NAD 83	1.4	21.2	6	8.9	52.3	1	394.9	0.4	7.3
17.4	15-PTA-007	55.922	-65.973	NAD 83	0.5	19.8	10.3	9.4	50.5	2	675.1	0.5	9
20.3	15-PTA-008	55.882	-65.812	NAD 83	0.9	20.1	10.1	10.1	51.7	1	701.3	0.3	9.6
19.3	15-PTA-010	55.969	-65.587	NAD 83	0.7	19.5	8.2	9	59.1	2	669.2	0.4	6.7
20	15-PTA-011	55.907	-65.334	NAD 83	0.4	20.2	13.4	12.3	59.7	2	719.9	0.5	8.3
18.5	15-PTA-012	55.795	-65.690	NAD 83	0.8	18.5	9	8.7	48.7	1	632.2	0.5	8.9
22.7	15-PTA-013	55.659	-65.642	NAD 83	1.7	20.6	7.2	8.1	81.6	3	322.3	0.5	10
24	15-PTA-014	55.587	-65.705	NAD 83	2.3	20.6	7.1	8.7	95.1	1	339.5	0.5	9.4
21.2	15-PTA-018	55.595	-65.789	NAD 83	4.7	25.1	8.8	11.2	124.6	2	256.6	0.7	12.5
13	15-PTA-019	55.626	-65.929	NAD 83	8.5	29.5	9.3	14.5	157.6	4	161.4	1	14.4
23.9	15-PTA-020	55.726	-65.884	NAD 83	1.6	21.6	7.9	9	77.2	1	454.6	0.6	10.8
24.9	15-PTA-022	55.773	-65.530	NAD 83	0.6	20.3	7.9	8.1	54.8	1	609.1	0.4	6.2
16.1	15-PTA-024	55.739	-65.153	NAD 83	0.4	19.9	9.3	7.8	46.1	1	748.1	0.3	6.2
19.5	15-PTA-025	55.654	-65.781	NAD 83	1.8	19.1	7.2	8.3	91.4	1	310.8	0.5	8.7
17.3	15-PTA-028	55.553	-65.560	NAD 83	1.3	20.1	5.8	5.2	100.1	0	247.1	0.4	6.4
20.2	15-PTA-029	55.687	-65.307	NAD 83	0.7	18.4	4.9	6.3	65.7	1	476.5	0.3	5.3
17	15-PTA-034	55.843	-65.062	NAD 83	0.4	19.1	9.6	8.9	47.5	0	648.4	0.4	7.8

Supplementary Table 4.1

0.2	Analysis: BV LF200			LDL	0.1	0.5	0.1	0.1	0.1	1	0.5	0.1	0.2
Co (PPM)	Sample	Lat	Long	Datum	Cs (PPM)	Ga (PPM)	Hf (PPM)	Nb (PPM)	Rb (PPM)	Sn (PPM)	Sr (PPM)	Ta (PPM)	Th (PPM)
18.1	15-PTA-036	55.984	-65.251	NAD 83	0.3	19.3	10.6	10.4	56.7	1	764.4	0.4	7.9
15.3	15-PTA-037	55.964	-64.984	NAD 83	0.6	21.2	12.7	13.1	64.5	2	633.1	0.7	9.6
14	15-PTA-039	55.975	-64.775	NAD 83	0.7	19.7	13.8	12.9	56.2	2	593.3	0.7	9
17.3	15-PTA-042	55.809	-64.893	NAD 83	0.8	21.6	10.7	11.1	63.2	1	742.4	0.4	8.9
23.5	15-PTA-043	55.633	-65.173	NAD 83	0.9	22.3	9.2	8.4	64.5	1	544.7	0.4	6.9
18.3	15-PTA-044	55.852	-64.547	NAD 83	2.1	20.5	12.3	16.9	72.4	3	512.2	1.7	8.2
20.7	15-PTA-045	55.939	-64.462	NAD 83	2.7	19.9	10.4	16.5	95.4	3	377.1	1.2	14
12.9	15-PTA-046	55.965	-64.271	NAD 83	1.9	18.9	11.4	14.8	71	2	443.1	1.2	9.3
13.9	15-PTA-047	55.953	-64.368	NAD 83	1.7	18.3	11.7	16.4	61.3	2	434.4	1.2	7.3
10.8	15-PTA-048	55.969	-64.070	NAD 83	1	17.3	12.1	16.1	81.3	2	391.9	1.4	10.7
13.7	15-PTA-049	55.844	-64.048	NAD 83	2.2	19.7	10.5	15.9	92.5	3	361.6	1.1	13.2
12.1	15-PTA-050	55.770	-64.038	NAD 83	1.1	17.5	11.7	15	75.3	2	381.9	1.1	11.5
15.2	15-PTA-051	55.695	-64.034	NAD 83	1.1	18.1	12.4	14.2	65.3	2	425.8	1.1	10.2
11.9	15-PTA-052	55.616	-64.036	NAD 83	1	16.3	9.5	12.5	62.9	2	431.1	0.8	9.9
11.8	15-PTA-053	55.535	-64.056	NAD 83	1.1	16.1	9.8	12	55.6	1	457.4	0.9	8.7
11.6	15-PTA-054	55.502	-64.230	NAD 83	0.6	15.3	10.6	13.3	55.9	1	429.1	0.9	8.6
16.6	15-PTA-056	55.820	-65.568	NAD 83	0.3	18	6.6	7.1	44.2	0	543	0.3	5.8
16	15-PTA-057	55.825	-65.784	NAD 83	0.6	17.5	7.1	8	45.4	0	497.5	0.3	7.9
12.9	15-PTA-061	55.852	-64.337	NAD 83	1.6	15.1	8	15.4	89.1	2	292.2	1.1	14
10.3	15-PTA-062	55.649	-64.437	NAD 83	1.1	14.9	10.7	14.2	69.3	2	389.2	1.1	9.1
11.8	15-PTA-063	55.544	-64.588	NAD 83	1.2	15.5	8.7	11	50.5	1	449.4	0.7	7.6
11.1	15-PTA-079	55.895	-64.369	NAD 83	1.3	14.7	6.3	12.7	72	2	312.1	0.8	9.1
9.1	15-PTA-080	55.915	-64.232	NAD 83	1.3	14.9	8.7	12.8	77.6	2	311.7	1.2	10.2
11.5	15-PTA-081	55.810	-64.189	NAD 83	1.7	15.9	8.8	13.2	77.3	1	299.4	1.1	10.4
19.9	15-PTA-098	55.814	-65.398	NAD 83	0.3	20.9	9.1	9.3	48.9	1	671.1	0.3	6.3
16.3	15-PTA-099	55.780	-65.083	NAD 83	1.9	21	9.8	12.8	66.4	3	482.4	0.8	7.1
14.2	15-PTA-101	55.680	-64.179	NAD 83	1.6	20.1	11.8	17.7	85.1	2	391.7	1	11.2
14.8	15-PTA-102	55.704	-64.378	NAD 83	1.8	19.1	11.7	16.8	86.6	2	415.3	1.3	9.2
15.4	15-PTA-103	55.741	-64.490	NAD 83	1.9	19.9	9.2	17.1	97.4	2	383.3	1.4	15.1
20.6	15-PTA-139	55.559	-65.138	NAD 83	0.8	19	10.5	8.6	59	0	443.1	0.5	9.7
13.9	15-PTA-144	55.627	-64.271	NAD 83	1.4	17.4	13.1	18.7	74	2	487.1	1.3	9.6
13.3	15-PTA-145	55.567	-64.188	NAD 83	1.2	16.5	12.6	15.1	64	2	459.1	1	10

Supplementary Table 4.1

0.2	Analysis: BV LF200			LDL	0.1	0.5	0.1	0.1	0.1	1	0.5	0.1	0.2
Co (PPM)	Sample	Lat	Long	Datum	Cs (PPM)	Ga (PPM)	Hf (PPM)	Nb (PPM)	Rb (PPM)	Sn (PPM)	Sr (PPM)	Ta (PPM)	Th (PPM)
14.7	15-PTA-146	55.527	-64.346	NAD 83	1.7	18.5	13.4	19.4	87.5	2	457.4	1.4	13.9
17.4	15-PTA-148	55.789	-64.329	NAD 83	2.2	18.8	9.1	18.2	98.7	2	401.2	1.3	14.5
18.5	15-PTA-155	55.654	-64.864	NAD 83	0.4	19.2	9.6	9.9	51.9	1	636	0.4	8.3
20.1	15-PTA-156	55.591	-64.732	NAD 83	2.1	21.6	11.9	12.7	62.7	2	577.4	0.9	10.6
16.6	15-PTA-176	55.629	-64.686	NAD 83	2.3	18.7	11.1	12.7	57.7	2	452.4	0.9	9.8
20.5	15-PTA-192	55.524	-64.961	NAD 83	0.8	19	8.7	8.3	54.6	1	537.3	0.4	7.2
17.2	15-PTA-193	55.512	-64.852	NAD 83	0.5	17.4	9.9	8.2	39.3	1	560.8	0.4	6
26.2	16-PTA-056	55.692	-65.991	NAD 84	5.8	22.9	9.8	14.5	121.8	2	244.6	1	10.8
13.6	16-PTA-058	55.843	-64.207	NAD 85	1.5	17.8	12	17	84.5	2	398.6	1.3	11.2
23.7	16-PTA-060	55.898	-64.611	NAD 86	3.1	19.1	8	14.5	76.9	2	380.5	0.9	9.6
25.2	16-PTA-069	55.721	-65.218	NAD 83	0.4	19.4	8.1	8	49.2	0	645	0.4	5.8
25.4	16-PTA-070	55.784	-65.251	NAD 83	0.2	21.1	8.8	9.1	46	0	642.2	0.4	6.4

Supplementary Table 4.1

0.1	8	Analysis: BV LF200			LDL	0.5	0.1	0.1	0.1	0.1	0.02	0.3	0.05	0.02
U (PPM)	V (PPM)	Sample	Lat	Long	Datum	W (PPM)	Zr (PPM)	Y (PPM)	La (PPM)	Ce (PPM)	Pr (PPM)	Nd (PPM)	Sm (PPM)	Eu (PPM)
3.8	88	14-PTA-B001	55.912	-64.086	NAD 83	1.3	573.1	35.2	52	108.8	13.27	51.3	9.18	1.79
2.3	115	14-PTA-B002	55.969	-64.575	NAD 83	0.7	375.1	27.1	50.8	99.4	12.98	47.9	8.49	2.04
1.8	103	14-PTA-B004	55.944	-64.877	NAD 83	0	475.9	25.3	49.8	104.9	12.97	52.7	9.57	2.29
1.5	115	14-PTA-R002	55.963	-65.796	NAD 83	0	370.8	24.7	66.9	127.1	16.58	62.6	10.65	2.39
1	124	14-PTA-R003	55.958	-65.469	NAD 83	0	430.1	22.1	67.5	136	17.61	70.7	11.38	2.66
0.9	139	14-PTA-R004	55.814	-65.261	NAD 83	0	408.8	24.9	78.2	152.5	20.15	79.3	12.99	2.94
1.2	131	14-PTA-R005	55.566	-65.219	NAD 83	0	254.7	18.7	41.8	78.3	10.04	38.5	6.34	1.6
1.4	130	14-PTA-R006	55.626	-65.401	NAD 83	0.6	308.7	19.4	40.5	80.6	9.74	37	6.31	1.48
1.7	111	14-PTA-R020	55.741	-64.730	NAD 83	0.6	422.8	27	44.8	98.3	12.41	48.4	9.17	2.07
1	139	14-PTA-R023	55.780	-65.016	NAD 83	0	391.9	25.1	82.6	166.8	20.99	79.4	13.02	2.78
1.3	111	14-PTA-R024	55.925	-65.060	NAD 83	0	519.6	29.5	61.6	118.9	16.22	62.5	11.42	2.51
1.9	107	14-PTA-R043	55.838	-64.732	NAD 83	1	366.4	24.5	41.7	90.2	11.14	44.5	8.32	1.91
7	168	15-PTA-002	55.674	-65.914	NAD 83	0.6	310	29	60.6	130.5	13.41	50.6	9.51	1.76
3.8	190	15-PTA-003	55.530	-65.914	NAD 83	1.1	301	30	48.9	99.7	10.85	41.4	7.18	1.6
1.4	161	15-PTA-004	55.741	-65.775	NAD 83	0	262.3	18.9	43.9	89.7	9.66	36.2	6.35	1.54
1.4	188	15-PTA-005	55.807	-65.940	NAD 83	0	259.1	18.6	36.1	74.4	8.31	33.1	5.64	1.51
1.9	121	15-PTA-007	55.922	-65.973	NAD 83	0.8	417.8	22.3	59.2	125.2	14.25	57.3	9.93	2.17
2	120	15-PTA-008	55.882	-65.812	NAD 83	0	420.7	24	71.8	152	17.14	65.8	10.79	2.56
0.9	115	15-PTA-010	55.969	-65.587	NAD 83	0	335.8	23.6	65.1	135.8	15.53	59.2	10.19	2.27
1.5	120	15-PTA-011	55.907	-65.334	NAD 83	0	550.5	28.8	72.5	153.3	18.25	73.1	12.7	2.71
1.6	121	15-PTA-012	55.795	-65.690	NAD 83	0	373.9	24	62.1	131.2	15.12	58.4	10.13	2.35
2.1	130	15-PTA-013	55.659	-65.642	NAD 83	0	269.7	16.3	40.7	82.8	8.83	31.8	5.56	1.24
1.8	133	15-PTA-014	55.587	-65.705	NAD 83	0	281.7	18.1	39.3	81.1	8.97	33.6	5.96	1.44
4.6	204	15-PTA-018	55.595	-65.789	NAD 83	0.9	320.5	31.3	54.2	116.7	12.56	48.4	8.51	1.58
4.7	154	15-PTA-019	55.626	-65.929	NAD 83	2.2	334.4	41.8	48	107.5	12.65	49.8	9.54	1.51
2.3	162	15-PTA-020	55.726	-65.884	NAD 83	0	307	23.3	55.7	128	12.81	48.9	8.52	1.93
1.8	133	15-PTA-022	55.773	-65.530	NAD 83	0.9	309.3	23.4	61.8	130.6	14.76	56.5	9.86	2.21
0.8	129	15-PTA-024	55.739	-65.153	NAD 83	0.7	387.6	22.3	74.4	154.6	17.87	68.1	11.18	2.6
1.8	132	15-PTA-025	55.654	-65.781	NAD 83	0.8	277.5	18.1	44.6	82.3	9.32	35.2	5.68	1.4
1.3	104	15-PTA-028	55.553	-65.560	NAD 83	0	215.9	13.9	28	52.4	6	22.4	3.69	1.14
0.9	128	15-PTA-029	55.687	-65.307	NAD 83	0	209.8	18.7	41.2	90.5	9.94	37.4	6.1	1.62
1.1	130	15-PTA-034	55.843	-65.062	NAD 83	44.1	382.7	23.4	79.8	176.1	19.82	78.2	12.72	2.51

Supplementary Table 4.1

0.1	8	Analysis: BV LF200			LDL	0.5	0.1	0.1	0.1	0.1	0.02	0.3	0.05	0.02
U (PPM)	V (PPM)	Sample	Lat	Long	Datum	W (PPM)	Zr (PPM)	Y (PPM)	La (PPM)	Ce (PPM)	Pr (PPM)	Nd (PPM)	Sm (PPM)	Eu (PPM)
1.3	122	15-PTA-036	55.984	-65.251	NAD 83	0	429.1	24.8	81	167.2	20.09	77.1	13.19	2.79
2.1	104	15-PTA-037	55.964	-64.984	NAD 83	0	472.6	27.8	61.7	123.3	15.48	61.8	10.99	2.59
2.3	93	15-PTA-039	55.975	-64.775	NAD 83	0	534.9	28.2	57.2	118.5	14.41	58.2	10.85	2.44
1.6	116	15-PTA-042	55.809	-64.893	NAD 83	0	428.3	27	75.1	161.8	19.18	76.8	12.86	2.87
1.1	146	15-PTA-043	55.633	-65.173	NAD 83	0	356.6	22.3	61.1	122.7	13.77	51	8.54	2.06
2.3	128	15-PTA-044	55.852	-64.547	NAD 83	0.7	496.6	35.2	55.1	116	13.65	53.5	9.7	2.19
2.4	129	15-PTA-045	55.939	-64.462	NAD 83	0.8	405.4	29	45.7	100.4	10.7	41	7.49	1.66
2.7	106	15-PTA-046	55.965	-64.271	NAD 83	1	434	31.7	42.1	93.5	10.24	40	7.77	1.89
1.9	108	15-PTA-047	55.953	-64.368	NAD 83	1.3	458.1	29.9	43.1	88.9	11.1	42.7	8.22	1.82
4.3	88	15-PTA-048	55.969	-64.070	NAD 83	1.5	471.5	32	43	92.7	11.22	43	7.9	1.76
3.8	101	15-PTA-049	55.844	-64.048	NAD 83	1.5	405.8	31.3	56.7	127.3	13.64	52.9	8.96	1.76
2.6	98	15-PTA-050	55.770	-64.038	NAD 83	1	451.8	28.3	46.8	108.4	12.16	46.1	8.41	1.84
2.2	104	15-PTA-051	55.695	-64.034	NAD 83	1.3	483.9	27.8	44.6	105.5	11.98	47.4	8.47	1.96
1.6	103	15-PTA-052	55.616	-64.036	NAD 83	0	385.1	25.4	43.1	102	11.26	43.6	7.8	1.78
1.7	109	15-PTA-053	55.535	-64.056	NAD 83	0.5	404.2	23.1	42.5	98	11.18	43.6	7.76	1.83
1.5	98	15-PTA-054	55.502	-64.230	NAD 83	1.1	431	23.9	39.4	90	10.26	39.7	7.36	1.75
1.1	121	15-PTA-056	55.820	-65.568	NAD 83	0	279.4	19.8	55.1	119.8	13.88	55.1	8.75	1.85
1.2	128	15-PTA-057	55.825	-65.784	NAD 83	0	293.6	17.3	45.4	104.5	11.06	43.2	6.93	1.69
3.7	100	15-PTA-061	55.852	-64.337	NAD 83	0.9	303.5	24.7	34	80.6	8.24	32.4	5.8	1.32
2.4	100	15-PTA-062	55.649	-64.437	NAD 83	1.1	404.6	23.6	38.5	80.5	9.84	38.9	6.86	1.57
1.6	100	15-PTA-063	55.544	-64.588	NAD 83	0.7	338.9	24.5	44.5	106.2	10.91	42	7.34	1.66
2.2	99	15-PTA-079	55.895	-64.369	NAD 83	0.6	229	18.7	29.2	66.1	7.17	27.9	4.99	1.3
2.8	86	15-PTA-080	55.915	-64.232	NAD 83	0.9	326.1	26.3	38.6	84	9.49	36.3	6.87	1.45
2.6	104	15-PTA-081	55.810	-64.189	NAD 83	2.4	325.2	24.5	38.6	87.7	9.67	37.3	6.95	1.43
1.2	129	15-PTA-098	55.814	-65.398	NAD 83	0	389	25.3	76	149.6	19.03	74.2	12	2.73
2.7	93	15-PTA-099	55.780	-65.083	NAD 83	0	410.1	25.5	36.1	82.8	9.62	40.6	7.64	1.86
2.2	102	15-PTA-101	55.680	-64.179	NAD 83	1	463.6	28.5	47.2	98.7	11.99	46.2	9.16	1.91
2.7	107	15-PTA-102	55.704	-64.378	NAD 83	0.7	496.2	31.8	42.7	88	11.47	42	8.07	2.04
3.8	107	15-PTA-103	55.741	-64.490	NAD 83	0.6	351.1	31	48.6	106.6	11.02	42.8	7.58	1.74
1.7	128	15-PTA-139	55.559	-65.138	NAD 83	0	401.5	25.5	64.6	127.6	14.56	53.8	8.4	2.18
2.6	101	15-PTA-144	55.627	-64.271	NAD 83	0.6	532.3	29.5	44.9	112.9	11.88	46.4	9.01	2.24
1.8	104	15-PTA-145	55.567	-64.188	NAD 83	0.8	470	27.9	44.6	103.8	11.56	45.9	8.41	1.93

Supplementary Table 4.1

0.1	8	Analysis: BV LF200			LDL	0.5	0.1	0.1	0.1	0.1	0.02	0.3	0.05	0.02
U (PPM)	V (PPM)	Sample	Lat	Long	Datum	W (PPM)	Zr (PPM)	Y (PPM)	La (PPM)	Ce (PPM)	Pr (PPM)	Nd (PPM)	Sm (PPM)	Eu (PPM)
3	101	15-PTA-146	55.527	-64.346	NAD 83	0.7	540.9	31.8	57.3	122.2	13.7	52.7	9.21	2.16
3.4	107	15-PTA-148	55.789	-64.329	NAD 83	0.6	336.8	25.9	41.7	108.8	10.34	41.4	7.26	1.56
1.4	130	15-PTA-155	55.654	-64.864	NAD 83	0	391.4	26.3	70.2	147	17.08	65.5	11.34	2.58
2.3	124	15-PTA-156	55.591	-64.732	NAD 83	0.7	458.3	30.4	65.6	144.4	16.34	64.1	11.26	2.45
2.5	120	15-PTA-176	55.629	-64.686	NAD 83	0.7	437.9	30.2	50.9	107.4	12.64	51.3	9.14	2.09
1.2	138	15-PTA-192	55.524	-64.961	NAD 83	0	326.6	24	70.7	140.2	16.31	60.8	9.7	2.1
1.2	125	15-PTA-193	55.512	-64.852	NAD 83	0	401.1	23.7	55.9	132.1	14.33	57.2	9.82	2.18
3.1	158	16-PTA-056	55.692	-65.991	NAD 84	1.5	358	34.6	50.3	101.2	11.41	45	7.7	1.49
3.8	100	16-PTA-058	55.843	-64.207	NAD 85	1.3	480.9	31.2	44.7	82.1	11.6	46.5	8.69	1.9
1.5	118	16-PTA-060	55.898	-64.611	NAD 86	1.9	313.7	23.8	38.9	84.7	9.17	35.7	6.47	1.54
0.7	146	16-PTA-069	55.721	-65.218	NAD 83	0	328.1	22	67.7	135.2	16.72	64.7	10.53	2.45
0.6	143	16-PTA-070	55.784	-65.251	NAD 83	0	351.9	23.6	73.1	143.5	17.76	71.2	11.19	2.51

Supplementary Table 4.1

0.05	0.01	Analysis: BV LF200			LDL	0.05	0.02	0.03	0.01	0.05	0.01
Gd (PPM)	Tb (PPM)	Sample	Lat	Long	Datum	Dy (PPM)	Go (PPM)	Er (PPM)	Tm (PPM)	Yb (PPM)	Lu (PPM)
8	1.13	14-PTA-B001	55.912	-64.086	NAD 83	6.78	1.29	3.76	0.51	3.64	0.57
7.66	1.01	14-PTA-B002	55.969	-64.575	NAD 83	5.31	0.94	2.72	0.38	2.54	0.39
7.94	1	14-PTA-B004	55.944	-64.877	NAD 83	5.25	0.98	2.56	0.37	2.27	0.34
7.94	0.99	14-PTA-R002	55.963	-65.796	NAD 83	4.86	0.87	2.4	0.34	2.18	0.34
8.63	0.98	14-PTA-R003	55.958	-65.469	NAD 83	4.96	0.86	2.17	0.33	1.94	0.29
9.84	1.14	14-PTA-R004	55.814	-65.261	NAD 83	5.4	0.93	2.4	0.34	2.07	0.32
5.22	0.68	14-PTA-R005	55.566	-65.219	NAD 83	3.59	0.72	2.05	0.29	1.9	0.29
4.84	0.68	14-PTA-R006	55.626	-65.401	NAD 83	3.66	0.72	1.94	0.29	1.87	0.29
7.24	0.96	14-PTA-R020	55.741	-64.730	NAD 83	5.23	0.97	2.75	0.4	2.63	0.34
9.77	1.11	14-PTA-R023	55.780	-65.016	NAD 83	5.15	0.87	2.26	0.31	1.92	0.31
9.16	1.2	14-PTA-R024	55.925	-65.060	NAD 83	6.22	1.05	3.02	0.41	2.6	0.39
6.79	0.92	14-PTA-R043	55.838	-64.732	NAD 83	5.12	0.99	2.65	0.37	2.36	0.36
7.38	1.07	15-PTA-002	55.674	-65.914	NAD 83	6.11	1.06	3.2	0.46	3.14	0.43
6.49	1.01	15-PTA-003	55.530	-65.914	NAD 83	5.7	1.05	3.19	0.48	3.24	0.47
5.36	0.69	15-PTA-004	55.741	-65.775	NAD 83	3.8	0.72	2.01	0.3	1.74	0.29
4.56	0.67	15-PTA-005	55.807	-65.940	NAD 83	3.66	0.71	1.96	0.29	1.8	0.27
7.06	0.91	15-PTA-007	55.922	-65.973	NAD 83	4.58	0.73	2.16	0.3	2	0.29
8.4	1.02	15-PTA-008	55.882	-65.812	NAD 83	5.05	0.83	2.36	0.3	2.04	0.31
7.2	0.91	15-PTA-010	55.969	-65.587	NAD 83	4.67	0.81	2.12	0.31	1.93	0.29
9.65	1.2	15-PTA-011	55.907	-65.334	NAD 83	6.16	1.06	2.85	0.39	2.54	0.37
7.13	0.94	15-PTA-012	55.795	-65.690	NAD 83	4.59	0.82	2.3	0.33	2.2	0.32
4.1	0.62	15-PTA-013	55.659	-65.642	NAD 83	3.3	0.65	1.82	0.26	1.84	0.29
4.84	0.65	15-PTA-014	55.587	-65.705	NAD 83	3.51	0.62	1.79	0.27	1.72	0.26
6.83	1.03	15-PTA-018	55.595	-65.789	NAD 83	5.48	1.06	3.1	0.48	3.14	0.49
8.45	1.3	15-PTA-019	55.626	-65.929	NAD 83	7.78	1.42	4.32	0.65	4.39	0.63
6.43	0.82	15-PTA-020	55.726	-65.884	NAD 83	4.39	0.74	2.25	0.33	2.32	0.34
7.32	0.95	15-PTA-022	55.773	-65.530	NAD 83	4.77	0.8	2.25	0.31	2.14	0.3
8.28	1.01	15-PTA-024	55.739	-65.153	NAD 83	4.92	0.76	2.16	0.3	1.96	0.27
4.45	0.65	15-PTA-025	55.654	-65.781	NAD 83	3.61	0.61	1.85	0.28	1.81	0.29
3.01	0.46	15-PTA-028	55.553	-65.560	NAD 83	2.75	0.5	1.48	0.2	1.55	0.25
4.81	0.64	15-PTA-029	55.687	-65.307	NAD 83	3.22	0.61	1.71	0.24	1.57	0.23
8.4	1.01	15-PTA-034	55.843	-65.062	NAD 83	5.07	0.83	2.14	0.28	1.89	0.28

Supplementary Table 4.1

0.05	0.01	Analysis: BV LF200			LDL	0.05	0.02	0.03	0.01	0.05	0.01
Gd (PPM)	Tb (PPM)	Sample	Lat	Long	Datum	Dy (PPM)	Go (PPM)	Er (PPM)	Tm (PPM)	Yb (PPM)	Lu (PPM)
8.93	1.1	15-PTA-036	55.984	-65.251	NAD 83	5.56	0.9	2.39	0.33	2.15	0.3
8.57	1.13	15-PTA-037	55.964	-64.984	NAD 83	5.73	0.99	2.58	0.36	2.48	0.35
8.72	1.1	15-PTA-039	55.975	-64.775	NAD 83	6.07	1	2.63	0.38	2.44	0.36
9.49	1.11	15-PTA-042	55.809	-64.893	NAD 83	5.28	0.91	2.71	0.35	2.16	0.33
7.13	0.91	15-PTA-043	55.633	-65.173	NAD 83	4.57	0.71	2.09	0.29	1.84	0.29
8.52	1.22	15-PTA-044	55.852	-64.547	NAD 83	6.73	1.19	3.69	0.54	3.46	0.54
6.39	0.93	15-PTA-045	55.939	-64.462	NAD 83	5.58	0.98	2.76	0.44	2.72	0.44
6.88	1.03	15-PTA-046	55.965	-64.271	NAD 83	6.08	1.12	3.22	0.49	3.08	0.47
7	1.01	15-PTA-047	55.953	-64.368	NAD 83	6.11	1	3.07	0.45	2.91	0.45
7.22	1.03	15-PTA-048	55.969	-64.070	NAD 83	6.13	1.08	2.93	0.46	3.03	0.48
7.42	1.1	15-PTA-049	55.844	-64.048	NAD 83	6.28	1.16	3.25	0.48	3.21	0.49
7.11	0.98	15-PTA-050	55.770	-64.038	NAD 83	5.73	1.01	2.98	0.43	2.82	0.45
7.09	1	15-PTA-051	55.695	-64.034	NAD 83	5.51	1	2.84	0.42	2.74	0.43
6.19	0.88	15-PTA-052	55.616	-64.036	NAD 83	4.99	0.86	2.39	0.37	2.32	0.35
5.83	0.8	15-PTA-053	55.535	-64.056	NAD 83	4.32	0.76	2.27	0.3	2.21	0.31
5.95	0.84	15-PTA-054	55.502	-64.230	NAD 83	4.63	0.86	2.37	0.34	2.5	0.37
6.09	0.79	15-PTA-056	55.820	-65.568	NAD 83	4	0.67	1.73	0.25	1.54	0.23
5.55	0.69	15-PTA-057	55.825	-65.784	NAD 83	3.62	0.61	1.56	0.22	1.54	0.24
5.08	0.79	15-PTA-061	55.852	-64.337	NAD 83	4.57	0.82	2.36	0.36	2.39	0.36
5.8	0.84	15-PTA-062	55.649	-64.437	NAD 83	4.86	0.81	2.46	0.37	2.43	0.38
5.65	0.79	15-PTA-063	55.544	-64.588	NAD 83	4.39	0.83	2.24	0.32	2.05	0.31
4.31	0.65	15-PTA-079	55.895	-64.369	NAD 83	3.82	0.71	2.03	0.3	1.92	0.3
5.24	0.84	15-PTA-080	55.915	-64.232	NAD 83	5.14	0.99	2.74	0.41	2.71	0.41
5.21	0.83	15-PTA-081	55.810	-64.189	NAD 83	4.45	0.89	2.7	0.38	2.48	0.37
8.57	1.05	15-PTA-098	55.814	-65.398	NAD 83	5.24	0.87	2.37	0.32	2.01	0.3
6.46	0.88	15-PTA-099	55.780	-65.083	NAD 83	4.64	0.83	2.49	0.35	2.26	0.33
7.19	1.01	15-PTA-101	55.680	-64.179	NAD 83	5.87	0.98	3.03	0.43	2.83	0.45
6.91	1.02	15-PTA-102	55.704	-64.378	NAD 83	5.53	1.07	3.08	0.51	3	0.48
6.62	1	15-PTA-103	55.741	-64.490	NAD 83	5.41	1.12	3.1	0.45	2.85	0.45
6.97	0.98	15-PTA-139	55.559	-65.138	NAD 83	5.1	0.92	2.67	0.38	2.51	0.39
7.83	1.09	15-PTA-144	55.627	-64.271	NAD 83	5.86	1.13	3.34	0.5	3.13	0.51
6.97	0.99	15-PTA-145	55.567	-64.188	NAD 83	5.39	1.01	2.86	0.39	2.7	0.44

Supplementary Table 4.1

0.05	0.01	Analysis: BV LF200			LDL	0.05	0.02	0.03	0.01	0.05	0.01
Gd (PPM)	Tb (PPM)	Sample	Lat	Long	Datum	Dy (PPM)	Go (PPM)	Er (PPM)	Tm (PPM)	Yb (PPM)	Lu (PPM)
7.82	1.06	15-PTA-146	55.527	-64.346	NAD 83	5.72	1.07	2.95	0.44	2.97	0.44
6.07	0.89	15-PTA-148	55.789	-64.329	NAD 83	5.29	0.96	2.75	0.41	2.86	0.44
8.47	1.09	15-PTA-155	55.654	-64.864	NAD 83	5.06	0.97	2.72	0.33	2.14	0.37
9.3	1.2	15-PTA-156	55.591	-64.732	NAD 83	5.83	1.01	2.83	0.39	2.63	0.41
7.49	1.08	15-PTA-176	55.629	-64.686	NAD 83	5.92	1.08	3.06	0.47	3.2	0.46
7.42	0.93	15-PTA-192	55.524	-64.961	NAD 83	4.71	0.81	2.3	0.33	2.03	0.32
7.25	0.92	15-PTA-193	55.512	-64.852	NAD 83	4.89	0.83	2.48	0.32	2.14	0.31
6.87	1.04	16-PTA-056	55.692	-65.991	NAD 84	6.43	1.31	4.12	0.54	3.63	0.57
7.13	1.04	16-PTA-058	55.843	-64.207	NAD 85	5.86	1.25	3.49	0.49	3.22	0.51
5.75	0.85	16-PTA-060	55.898	-64.611	NAD 86	4.8	0.89	2.63	0.37	2.44	0.39
7.63	0.94	16-PTA-069	55.721	-65.218	NAD 83	4.6	0.83	2.2	0.31	1.88	0.27
8.43	0.99	16-PTA-070	55.784	-65.251	NAD 83	4.67	0.89	2.57	0.3	1.89	0.28

Supplementary Table S4.2

Samples	Location		Number of Visible Gold Grains				Nonmag HMC Weight	Calculated PPB Visible Gold in HMC			
	Lat	Long	Total	Reshaped	Mod.	Pristine	(g)	Total	Reshaped	Mod.	Pristine
14-PTA-B001	55.912	-64.086	0	0	0	0	42.8	0	0	0	0
14-PTA-B002	55.969	-64.575	1	1	0	0	45.2	4	4	0	0
14-PTA-B004	55.944	-64.877	0	0	0	0	36.0	0	0	0	0
14-PTA-R002	55.963	-65.796	0	0	0	0	54.4	0	0	0	0
14-PTA-R003	55.958	-65.469	0	0	0	0	42.4	0	0	0	0
14-PTA-R004	55.814	-65.261	0	0	0	0	48.0	0	0	0	0
14-PTA-R005	55.566	-65.219	0	0	0	0	45.6	0	0	0	0
14-PTA-R006	55.626	-65.401	0	0	0	0	36.4	0	0	0	0
14-PTA-R020	55.741	-64.730	0	0	0	0	36.4	0	0	0	0
14-PTA-R023	55.780	-65.016	0	0	0	0	48.8	0	0	0	0
14-PTA-R024	55.925	-65.060	0	0	0	0	35.2	0	0	0	0
14-PTA-R043	55.838	-64.732	3	3	0	0	32.8	1	1	0	0
15-PTA-002	55.674	-65.914	1	0	1	0	38.8	1	0	<1	0
15-PTA-003	55.530	-65.914	0	0	0	0	41.2	0	0	0	0
15-PTA-004	55.741	-65.775	1	1	0	0	22.4	1	1	0	0
15-PTA-005	55.807	-65.940	0	0	0	0	30.8	0	0	0	0
15-PTA-007	55.922	-65.973	1	1	0	0	36.4	1	1	0	0
15-PTA-008	55.882	-65.812	0	0	0	0	26.4	0	0	0	0
15-PTA-010	55.969	-65.587	0	0	0	0	38.0	0	0	0	0
15-PTA-011	55.907	-65.334	0	0	0	0	40.8	0	0	0	0
15-PTA-012	55.795	-65.690	1	1	0	0	42.0	1	1	0	0
15-PTA-013	55.659	-65.642	1	1	0	0	37.6	4	4	0	0
15PTA-014	55.587	-65.705									
15-PTA-018	55.595	-65.789	0	0	0	0	32.4	0	0	0	0
15-PTA-019	55.626	-65.929	0	0	0	0	22.0	0	0	0	0
15-PTA-020	55.726	-65.884	2	2	0	0	34.4	2	2	0	0
15-PTA-022	55.773	-65.530	1	1	0	0	36.8	1	<1	0	0
15-PTA-024	55.739	-65.153	1	1	0	0	36.4	27	27	0	0

Supplementary Table S4.2

Samples	Location		Number of Visible Gold Grains				Nonmag HMC Weight	Calculated PPB Visible Gold in HMC			
	Lat	Long	Total	Reshaped	Mod.	Pristine	(g)	Total	Reshaped	Mod.	Pristine
15-PTA-025	55.654	-65.781	0	0	0	0	29.2	0	0	0	0
15-PTA-028	55.553	-65.560	0	0	0	0	27.2	0	0	0	0
15-PTA-029	55.687	-65.307	0	0	0	0	35.2	0	0	0	0
15-PTA-034	55.843	-65.062	0	0	0	0	34.0	0	0	0	0
15-PTA-036	55.984	-65.251	0	0	0	0	26.4	0	0	0	0
15-PTA-037	55.964	-64.984	0	0	0	0	34.8	0	0	0	0
15-PTA-039	55.975	-64.775	0	0	0	0	30.0	0	0	0	0
15-PTA-042	55.809	-64.893	0	0	0	0	41.2	0	0	0	0
15-PTA-043	55.633	-65.173	0	0	0	0	34.0	0	0	0	0
15-PTA-044	55.852	-64.547	0	0	0	0	35.6	0	0	0	0
15-PTA-045	55.939	-64.462	1	1	0	0	36.4	10	10	0	0
15-PTA-046	55.965	-64.271	1	1	0	0	35.2	1	<1	0	0
15-PTA-047	55.953	-64.368	0	0	0	0	32.8	0	0	0	0
15-PTA-048	55.969	-64.070	1	0	1	0	33.6	2	0	2	0
15-PTA-049	55.844	-64.048	0	0	0	0	34.0	0	0	0	0
15-PTA-050	55.770	-64.038	0	0	0	0	44.0	0	0	0	0
15-PTA-051	55.695	-64.034	0	0	0	0	41.6	0	0	0	0
15-PTA-052	55.616	-64.036	1	1	0	0	38.8	9	9	0	0
15-PTA-053	55.535	-64.056	1	1	0	0	40.8	1	1	0	0
15-PTA-054	55.502	-64.230	1	1	0	0	36.8	5	5	0	0
15-PTA-056	55.820	-65.568	0	0	0	0	26.8	0	0	0	0
15-PTA-057	55.825	-65.784	0	0	0	0	28.0	0	0	0	0
15-PTA-061	55.852	-64.337	1	1	0	0	32.4	1	1	0	0
15-PTA-062	55.649	-64.437	1	1	0	0	36.0	1	1	0	0
15-PTA-063	55.544	-64.588	0	0	0	0	33.6	0	0	0	0
15-PTA-079	55.895	-64.369	2	2	0	0	38.8	10	10	0	0
15-PTA-080	55.915	-64.232	2	1	1	0	34.0	1	1	<1	0
15-PTA-081	55.810	-64.189	2	2	0	0	37.2	1	<1	0	0

Supplementary Table S4.2

Samples	Location		Number of Visible Gold Grains				Nonmag HMC Weight	Calculated PPB Visible Gold in HMC			
	Lat	Long	Total	Reshaped	Mod.	Pristine	(g)	Total	Reshaped	Mod.	Pristine
15-PTA-098	55.814	-65.398	0	0	0	0	38.4	0	0	0	0
15-PTA-099	55.780	-65.083	0	0	0	0	25.6	0	0	0	0
15-PTA-101	55.680	-64.179	1	1	0	0	40.8	2	2	0	0
15-PTA-102	55.704	-64.378	0	0	0	0	38.4	0	0	0	0
15-PTA-103	55.741	-64.490	0	0	0	0	40.8	0	0	0	0
15-PTA-144	55.627	-64.271	0	0	0	0	30.0	0	0	0	0
15-PTA-145	55.567	-64.188	0	0	0	0	36.0	0	0	0	0
15-PTA-146	55.527	-64.346	0	0	0	0	30.8	0	0	0	0
15-PTA-148	55.789	-64.329	2	2	0	0	25.6	15	15	0	0
15-PTA-155	55.654	-64.864	2	1	1	0	32.8	22	11	11	0
15-PTA-156	55.591	-64.732	0	0	0	0	30.0	0	0	0	0
15-PTA-176	55.629	-64.686	0	0	0	0	29.2	0	0	0	0
15-PTA-192	55.524	-64.961	1	0	1	0	35.2	2	0	2	0
15-PTA-193	55.512	-64.852	1	0	1	0	32.4	1	0	1	0

Supplementary Table S4.2

Samples	Location		Bulk Sample					Clasts (+2.0 mm) Percentage				
	Lat	Long	Bulk Rec'd	Archived Split	Table Split	+2.0 mm Clasts*	Table Feed	Size	V/S	GR	LS	OT**
14-PTA-B001	55.912	-64.086	11.9	0.0	11.9	1.2	10.7	P	0	100	0	0
14-PTA-B002	55.969	-64.575	12.2	0.0	12.2	0.9	11.3	P	0	100	0	0
14-PTA-B004	55.944	-64.877	11.4	0.0	11.4	2.4	9.0	P	0	100	0	1
14-PTA-R002	55.963	-65.796	15.0	0.0	15.0	1.4	13.6	P	1	95	0	5
14-PTA-R003	55.958	-65.469	13.7	0.0	13.7	3.1	10.6	P	1	100	0	0
14-PTA-R004	55.814	-65.261	14.5	0.0	14.5	2.5	12.0	P	1	95	0	5
14-PTA-R005	55.566	-65.219	14.1	0.0	14.1	2.7	11.4	P	5	90	0	5
14-PTA-R006	55.626	-65.401	11.6	0.0	11.6	2.5	9.1	P	5	95	0	1
14-PTA-R020	55.741	-64.730	11.8	0.0	11.8	2.7	9.1	P	5	95	0	0
14-PTA-R023	55.780	-65.016	13.7	0.0	13.7	1.5	12.2	P	1	100	0	0
14-PTA-R024	55.925	-65.060	10.7	0.0	10.7	1.9	8.8	P	1	100	0	1
14-PTA-R043	55.838	-64.732	11.1	0.0	11.1	2.9	8.2	P	1	100	0	0
15-PTA-002	55.674	-65.914	11.2	0.0	11.2	1.5	9.7	P	20	80	0	0
15-PTA-003	55.530	-65.914	11.7	0.0	11.7	1.4	10.3	P	20	80	0	0
15-PTA-004	55.741	-65.775	7.0	0.0	7.0	1.4	5.6	P	1	20	0	80
15-PTA-005	55.807	-65.940	9.2	0.0	9.2	1.5	7.7	P	10	90	0	0
15-PTA-007	55.922	-65.973	10.6	0.0	10.6	1.5	9.1	P	1	100	0	0
15-PTA-008	55.882	-65.812	8.2	0.0	8.2	1.6	6.6	P	1	100	0	0
15-PTA-010	55.969	-65.587	9.9	0.0	9.9	0.4	9.5	P	0	100	0	0
15-PTA-011	55.907	-65.334	11.9	0.0	11.9	1.7	10.2	P	0	100	0	0
15-PTA-012	55.795	-65.690	13.0	0.0	13.0	2.5	10.5	P	0	100	0	0
15-PTA-013	55.659	-65.642	11.2	0.0	11.2	1.8	9.4	P	1	100	0	0
15PTA-014	55.587	-65.705	8.9	0.0	8.9	1.6	7.3	P	0	100	0	0
15-PTA-018	55.595	-65.789	10.6	0.0	10.6	2.5	8.1	P	60	40	0	1
15-PTA-019	55.626	-65.929	7.8	0.0	7.8	2.3	5.5	P	100	1	0	0
15-PTA-020	55.726	-65.884	10.7	0.0	10.7	2.1	8.6	P	20	80	0	0
15-PTA-022	55.773	-65.530	11.6	0.0	11.6	2.4	9.2	P	1	100	0	0
15-PTA-024	55.739	-65.153	9.7	0.0	9.7	0.6	9.1	P	1	100	0	0

Supplementary Table S4.2

Samples	Location		Bulk Sample					Clasts (+2.0 mm) Percentage				
	Lat	Long	Bulk Rec'd	Archived Split	Table Split	+2.0 mm Clasts*	Table Feed	Size	V/S	GR	LS	OT**
15-PTA-025	55.654	-65.781	9.1	0.0	9.1	1.8	7.3	P	10	80	0	10
15-PTA-028	55.553	-65.560	8.8	0.0	8.8	2.0	6.8	P	1	10	0	90
15-PTA-029	55.687	-65.307	10.3	0.0	10.3	1.5	8.8	P	1	100	0	1
15-PTA-034	55.843	-65.062	10.5	0.0	10.5	2.0	8.5	P	1	100	0	0
15-PTA-036	55.984	-65.251	8.9	0.0	8.9	2.3	6.6	P	0	100	0	0
15-PTA-037	55.964	-64.984	10.2	0.0	10.2	1.5	8.7	P	1	100	0	0
15-PTA-039	55.975	-64.775	9.0	0.0	9.0	1.5	7.5	P	1	100	0	0
15-PTA-042	55.809	-64.893	11.2	0.0	11.2	0.9	10.3	P	0	100	0	0
15-PTA-043	55.633	-65.173	9.8	0.0	9.8	1.3	8.5	P	0	100	0	0
15-PTA-044	55.852	-64.547	9.9	0.0	9.9	1.0	8.9	P	5	95	0	0
15-PTA-045	55.939	-64.462	11.0	0.0	11.0	1.9	9.1	P	1	100	0	0
15-PTA-046	55.965	-64.271	10.3	0.0	10.3	1.5	8.8	P	5	95	0	1
15-PTA-047	55.953	-64.368	9.0	0.0	9.0	0.8	8.2	P	5	95	0	0
15-PTA-048	55.969	-64.070	10.0	0.0	10.0	1.6	8.4	P	1	100	0	0
15-PTA-049	55.844	-64.048	9.3	0.0	9.3	0.8	8.5	P	0	100	0	0
15-PTA-050	55.770	-64.038	11.5	0.0	11.5	0.5	11.0	P	1	100	0	0
15-PTA-051	55.695	-64.034	12.0	0.0	12.0	1.6	10.4	P	1	100	0	0
15-PTA-052	55.616	-64.036	11.3	0.0	11.3	1.6	9.7	P	1	100	0	1
15-PTA-053	55.535	-64.056	10.5	0.0	10.5	0.3	10.2	P	1	100	0	0
15-PTA-054	55.502	-64.230	10.0	0.0	10.0	0.8	9.2	P	1	100	0	0
15-PTA-056	55.820	-65.568	7.9	0.0	7.9	1.2	6.7	P	1	100	0	0
15-PTA-057	55.825	-65.784	7.8	0.0	7.8	0.8	7.0	P	0	100	0	0
15-PTA-061	55.852	-64.337	8.8	0.0	8.8	0.7	8.1	P	5	95	0	0
15-PTA-062	55.649	-64.437	9.5	0.0	9.5	0.5	9.0	P	1	100	0	0
15-PTA-063	55.544	-64.588	8.9	0.0	8.9	0.5	8.4	P	5	95	0	0
15-PTA-079	55.895	-64.369	10.9	0.0	10.9	1.2	9.7	P	0	100	0	0
15-PTA-080	55.915	-64.232	9.6	0.0	9.6	1.1	8.5	P	1	100	0	0
15-PTA-081	55.810	-64.189	10.7	0.0	10.7	1.4	9.3	P	1	100	0	0

Supplementary Table S4.2

Samples	Location		Bulk Sample					Clasts (+2.0 mm) Percentage				
	Lat	Long	Bulk Rec'd	Archived Split	Table Split	+2.0 mm Clasts*	Table Feed	Size	V/S	GR	LS	OT**
15-PTA-098	55.814	-65.398	11.0	0.0	11.0	1.4	9.6	P	1	100	0	0
15-PTA-099	55.780	-65.083	8.2	0.0	8.2	1.8	6.4	P	1	100	0	0
15-PTA-101	55.680	-64.179	12.3	0.0	12.3	2.1	10.2	P	10	90	0	0
15-PTA-102	55.704	-64.378	10.3	0.0	10.3	0.7	9.6	P	1	100	0	0
15-PTA-103	55.741	-64.490	11.4	0.0	11.4	1.2	10.2	P	1	100	0	0
15-PTA-144	55.627	-64.271	8.4	0.0	8.4	0.9	7.5	P	1	100	0	0
15-PTA-145	55.567	-64.188	10.2	0.0	10.2	1.2	9.0	P	1	100	0	0
15-PTA-146	55.527	-64.346	8.7	0.0	8.7	1.0	7.7	P	1	100	0	0
15-PTA-148	55.789	-64.329	7.8	0.0	7.8	1.4	6.4	P	1	100	0	0
15-PTA-155	55.654	-64.864	9.7	0.0	9.7	1.5	8.2	P	1	100	0	1
15-PTA-156	55.591	-64.732	7.9	0.0	7.9	0.4	7.5	P	1	100	0	0
15-PTA-176	55.629	-64.686	8.1	0.0	8.1	0.8	7.3	P	5	95	0	1
15-PTA-192	55.524	-64.961	9.7	0.0	9.7	0.9	8.8	P	1	100	0	1
15-PTA-193	55.512	-64.852	10.5	0.0	10.5	2.4	8.1	P	1	100	0	1

Supplementary Table S4.2

Samples	Location		KIM data																				
	Lat	Long	Low-Cr diop	Low-Cr diop	Low-Cr diop	GP	GO	DC	IM	CR*	FO*	GP	GO	DC	IM	CR*	FO*	GP	GO	DC	IM	CR*	FO*	Total (KIMs)
14-PTA-B001	55.912	-64.086	0	0	0	0	0	0	0	0	0	0	0	0	0	0	0	0	0	0	0	0	3	3
14-PTA-B002	55.969	-64.575	0	5	0	0	0	0	0	0	0	0	0	0	0	0	0	0	0	0	0	0	0	0
14-PTA-B004	55.944	-64.877	0	0	0	0	0	0	0	0	0	0	0	0	0	0	0	0	0	0	0	0	0	0
14-PTA-R002	55.963	-65.796	2	8	0	0	0	0	0	0	0	0	0	0	0	0	0	0	0	0	0	0	3	3
14-PTA-R003	55.958	-65.469	2	3	0	0	0	0	0	0	0	0	0	0	0	0	1	0	0	0	0	0	21	22
14-PTA-R004	55.814	-65.261	2	10	0	0	0	0	0	0	0	0	0	0	0	0	0	0	0	0	0	0	4	4
14-PTA-R005	55.566	-65.219	0	4	0	0	0	0	0	0	0	0	0	0	0	0	0	0	0	0	0	0	0	0
14-PTA-R006	55.626	-65.401	0	0	0	0	0	0	0	0	0	0	0	0	0	0	0	0	0	0	0	0	1	1
14-PTA-R020	55.741	-64.730	2	0	0	0	0	0	0	0	0	0	0	0	0	0	0	0	0	0	0	0	0	0
14-PTA-R023	55.780	-65.016	0	2	0	0	0	0	0	0	0	0	0	0	0	0	0	0	0	0	0	0	0	0
14-PTA-R024	55.925	-65.060	0	1	0	0	0	0	0	0	0	0	0	0	0	0	0	0	0	0	0	0	0	0
14-PTA-R043	55.838	-64.732	0	0	0	0	0	0	0	0	0	0	0	0	0	0	0	0	0	0	0	0	3	3
15-PTA-002	55.674	-65.914	0	2	3	0	0	0	0	0	0	0	0	0	0	0	0	0	0	0	0	0	0	0
15-PTA-003	55.530	-65.914	0	0	6	0	0	0	0	0	0	0	0	0	0	0	0	0	0	0	0	0	**2**	**2**
15-PTA-004	55.741	-65.775	0	1	2	0	0	0	0	0	0	0	0	0	0	0	0	0	0	0	0	0	0	0
15-PTA-005	55.807	-65.940	0	0	6	0	0	0	0	0	0	0	0	0	0	**1**	0	0	0	0	0	0	0	**1**
15-PTA-007	55.922	-65.973	0	0	7	0	0	0	0	0	0	0	0	0	0	0	**2**	0	0	0	0	0	0	**2**
15-PTA-008	55.882	-65.812	0	1	6	0	0	0	0	0	0	0	0	0	0	0	0	0	0	0	0	0	0	0
15-PTA-010	55.969	-65.587	0	0	6	0	0	0	0	0	0	0	0	0	0	0	0	0	0	0	0	0	0	0
15-PTA-011	55.907	-65.334	0	1	16	0	0	0	0	0	0	0	0	0	0	0	0	0	0	0	0	0	**5**	**5**
15-PTA-012	55.795	-65.690	0	2	8	0	0	0	0	0	0	0	0	0	0	0	0	0	0	0	0	0	0	0
15-PTA-013	55.659	-65.642	0	0	2	0	0	0	0	0	0	0	0	0	0	0	0	0	0	0	0	0	**1**	**1**
15PTA-014	55.587	-65.705	0	1	4	0	0	0	0	0	0	0	0	0	0	0	0	0	0	0	0	0	**1**	**1**
15-PTA-018	55.595	-65.789	0	1	2	0	0	0	0	0	0	0	0	0	0	0	**1**	0	0	0	0	0	**3**	**4**
15-PTA-019	55.626	-65.929	0	0	0	0	0	0	0	0	0	0	0	0	0	0	0	0	0	0	0	0	0	0
15-PTA-020	55.726	-65.884	0	0	3	0	0	0	0	0	0	0	0	0	0	0	0	0	0	0	0	0	**4**	**4**
15-PTA-022	55.773	-65.530	0	0	14	0	0	0	0	0	0	0	0	0	0	0	0	0	0	0	0	0	**2**	**2**
15-PTA-024	55.739	-65.153	0	2	5	0	0	0	0	0	0	0	0	0	0	0	0	0	0	0	0	0	0	0

Supplementary Table S4.2

Samples	Location		KIM data																				
	Lat	Long	Low-Cr diop	Low-Cr diop	Low-Cr diop	GP	GO	DC	IM	CR*	FO*	GP	GO	DC	IM	CR*	FO*	GP	GO	DC	IM	CR*	FO*	Total (KIMs)
15-PTA-025	55.654	-65.781	0	1	0	0	0	0	0	0	0	0	0	0	0	0	0	0	0	0	0	0	0	0
15-PTA-028	55.553	-65.560	0	0	0	0	0	0	0	0	0	0	0	0	0	0	0	0	0	0	0	0	0	0
15-PTA-029	55.687	-65.307	0	2	3	0	0	0	0	0	0	0	0	0	0	0	0	0	0	0	0	0	0	0
15-PTA-034	55.843	-65.062	0	0	4	0	0	0	0	0	0	0	0	0	0	0	0	0	0	0	0	0	**1**	**1**
15-PTA-036	55.984	-65.251	0	0	3	0	0	0	0	0	0	0	0	0	0	0	0	0	0	0	0	0	**1**	**1**
15-PTA-037	55.964	-64.984	0	0	4	0	0	0	0	0	0	0	0	0	0	0	0	0	0	0	0	0	0	0
15-PTA-039	55.975	-64.775	0	0	1	0	0	0	0	0	0	0	0	0	0	0	0	0	0	0	0	0	0	0
15-PTA-042	55.809	-64.893	0	0	3	0	0	0	0	0	0	0	0	0	0	0	0	0	0	0	0	0	0	0
15-PTA-043	55.633	-65.173	0	0	2	0	0	0	0	0	0	0	0	0	0	0	0	0	0	0	0	0	0	0
15-PTA-044	55.852	-64.547	0	0	2	0	0	0	0	0	0	0	0	0	0	0	0	0	0	0	0	0	0	0
15-PTA-045	55.939	-64.462	0	0	0	0	0	0	0	0	0	0	0	0	0	0	0	0	0	0	0	0	**3**	**3**
15-PTA-046	55.965	-64.271	0	0	1	0	0	0	0	0	0	0	0	0	0	0	0	0	0	0	0	0	**1**	**1**
15-PTA-047	55.953	-64.368	0	0	0	0	0	0	0	0	0	0	0	0	0	0	0	0	0	0	0	0	0	0
15-PTA-048	55.969	-64.070	0	0	0	0	0	0	0	0	0	0	0	0	0	0	0	0	0	0	0	0	0	0
15-PTA-049	55.844	-64.048	1	0	2	0	0	0	0	0	0	0	0	0	0	0	0	0	0	0	0	**1**	0	**1**
15-PTA-050	55.770	-64.038	0	1	1	0	0	0	0	0	0	0	0	0	0	0	0	0	0	0	0	0	0	0
15-PTA-051	55.695	-64.034	0	0	3	0	0	0	0	0	0	0	0	0	0	0	0	0	0	0	0	0	0	0
15-PTA-052	55.616	-64.036	0	0	3	0	0	0	0	0	0	0	0	0	0	0	0	0	0	0	0	0	0	0
15-PTA-053	55.535	-64.056	0	0	1	0	0	0	0	0	0	0	0	0	0	0	0	0	0	0	0	0	0	0
15-PTA-054	55.502	-64.230	0	0	1	0	0	0	0	0	0	0	0	0	0	0	0	0	0	0	0	0	**2**	**2**
15-PTA-056	55.820	-65.568	0	0	6	0	0	0	0	0	0	0	0	0	0	0	0	0	0	0	0	0	**1**	**1**
15-PTA-057	55.825	-65.784	0	1	21	0	0	0	0	0	0	0	0	0	0	**1**	0	0	0	0	0	0	**2**	**3**
15-PTA-061	55.852	-64.337	0	0	1	0	0	0	0	0	0	0	0	0	0	0	0	0	0	0	0	0	0	0
15-PTA-062	55.649	-64.437	0	0	1	0	0	0	0	0	0	0	0	0	0	0	0	0	0	0	0	0	0	0
15-PTA-063	55.544	-64.588	0	0	0	0	0	0	0	0	0	0	0	0	0	0	0	0	0	0	0	0	**7**	**7**
15-PTA-079	55.895	-64.369	0	0	2	0	0	0	0	0	0	0	0	0	0	0	0	0	0	0	0	0	**2**	**2**
15-PTA-080	55.915	-64.232	0	0	1	0	0	0	0	0	0	0	0	0	0	0	0	0	0	0	0	0	**2**	**2**
15-PTA-081	55.810	-64.189	0	0	1	0	0	0	0	0	0	0	0	0	0	0	0	0	0	0	0	0	**2**	**2**

Supplementary Table S4.2

Samples	Location		KIM data																				
	Lat	Long	Low-Cr diop	Low-Cr diop	Low-Cr diop	GP	GO	DC	IM	CR*	FO*	GP	GO	DC	IM	CR*	FO*	GP	GO	DC	IM	CR*	FO*	Total (KIMs)
15-PTA-098	55.814	-65.398	0	0	7	0	0	0	0	0	0	0	0	0	0	0	0	0	0	0	0	0	0	0
15-PTA-099	55.780	-65.083	0	0	0	0	0	0	0	0	0	0	0	0	0	0	0	0	0	0	0	0	**1**	**1**
15-PTA-101	55.680	-64.179	0	0	1	0	0	0	0	0	0	0	0	0	0	0	0	0	0	0	0	0	**2**	**2**
15-PTA-102	55.704	-64.378	0	0	1	0	0	0	0	0	0	0	0	0	0	0	0	0	0	0	0	0	**3**	**3**
15-PTA-103	55.741	-64.490	0	0	1	0	0	0	0	0	0	0	0	0	0	0	0	0	0	0	0	0	0	0
15-PTA-144	55.627	-64.271	0	0	1	0	0	0	0	0	0	0	0	0	0	0	0	0	0	0	0	0	0	0
15-PTA-145	55.567	-64.188	0	0	2	0	0	0	0	0	0	0	0	0	0	0	0	0	0	0	0	0	0	0
15-PTA-146	55.527	-64.346	0	0	0	0	0	0	0	0	0	0	0	0	0	0	0	0	0	0	0	0	0	0
15-PTA-148	55.789	-64.329	0	0	1	0	0	0	0	0	0	0	0	0	0	0	0	0	0	0	0	0	0	0
15-PTA-155	55.654	-64.864	0	0	3	0	0	0	0	0	0	0	0	0	0	0	0	0	0	0	0	0	0	0
15-PTA-156	55.591	-64.732	0	0	1	0	0	0	0	0	0	0	0	0	0	0	0	0	0	0	0	0	0	0
15-PTA-176	55.629	-64.686	0	0	2	0	0	0	0	0	0	0	0	0	0	0	0	0	0	0	0	0	**6**	**6**
15-PTA-192	55.524	-64.961	0	0	6	0	0	0	0	0	0	0	0	0	0	0	0	0	0	0	0	0	**7**	**7**
15-PTA-193	55.512	-64.852	0	1	9	0	0	0	0	0	0	0	0	0	0	0	0	0	0	0	0	0	**50**	**50**

Supplementary Table S4.2

Samples	Location		Grains normalized to 10 kg								
	Lat	Long	Gold	Sperrylite	Chalcopyrite	Pyrite	Mn-epidote	Cr_diopside	Red Rutile	Goethite	Orthopyroxene
14-PTA-B001	55.912	-64.086	0	0	0	0	6	0	0	0	20
14-PTA-B002	55.969	-64.575	1	0	0	0	12	4	2	1	20
14-PTA-B004	55.944	-64.877	0	0	0	0	1	0	0	1	15
14-PTA-R002	55.963	-65.796	0	0	0	0	22	6	6	5	3
14-PTA-R003	55.958	-65.469	0	0	0	0	0	3	2	1	25
14-PTA-R004	55.814	-65.261	0	0	0	0	3	8	3	1	1
14-PTA-R005	55.566	-65.219	0	0	0	0	1754	4	1	1	15
14-PTA-R006	55.626	-65.401	0	0	0	0	3297	0	0	30	1
14-PTA-R020	55.741	-64.730	0	2	0	0	879	0	0	2	0
14-PTA-R023	55.780	-65.016	0	0	0	0	98	2	2	1	10
14-PTA-R024	55.925	-65.060	0	0	0	0	0	1	0	1	10
14-PTA-R043	55.838	-64.732	4	0	0	0	7	0	0	1	5
15-PTA-002	55.674	-65.914	1	0	0	0	258	3	14	1	15
15-PTA-003	55.530	-65.914	0	1	0	0	97	6	39	1	15
15-PTA-004	55.741	-65.775	2	0	0	54	179	4	5	1	20
15-PTA-005	55.807	-65.940	0	0	0	3	130	8	10	1	30
15-PTA-007	55.922	-65.973	1	0	0	0	0	8	13	1	20
15-PTA-008	55.882	-65.812	0	0	0	0	8	9	9	1	25
15-PTA-010	55.969	-65.587	0	0	0	21	1	6	32	1	20
15-PTA-011	55.907	-65.334	0	0	0	1	2	16	2	1	15
15-PTA-012	55.795	-65.690	1	0	0	0	29	8	17	1	20
15-PTA-013	55.659	-65.642	1	0	3	0	319	2	21	1	25
15PTA-014	55.587	-65.705	0	0	0	0	2055	5	11	0	5
15-PTA-018	55.595	-65.789	0	0	0	0	1852	2	49	1	5
15-PTA-019	55.626	-65.929	0	0	0	4	2	0	0	2	0
15-PTA-020	55.726	-65.884	2	0	0	1	1744	3	3	1	1
15-PTA-022	55.773	-65.530	1	0	0	0	0	15	43	1	25
15-PTA-024	55.739	-65.153	1	0	0	0	66	5	7	1	30

Supplementary Table S4.2

Samples	Location		Grains normalized to 10 kg								
	Lat	Long	Gold	Sperrylite	Chalcopyrite	Pyrite	Mn-epidote	Cr_diopside	Red Rutile	Goethite	Orthopyroxene
15-PTA-025	55.654	-65.781	0	1	0	0	1096	0	0	0	10
15-PTA-028	55.553	-65.560	0	0	0	0	7353	0	4	0	15
15-PTA-029	55.687	-65.307	0	0	0	0	568	3	13	0	20
15-PTA-034	55.843	-65.062	0	0	0	1	5	5	5	1	30
15-PTA-036	55.984	-65.251	0	0	0	2	2	5	2	0	30
15-PTA-037	55.964	-64.984	0	0	0	0	10	5	1	1	1
15-PTA-039	55.975	-64.775	0	0	0	1	1	1	0	1	1
15-PTA-042	55.809	-64.893	0	0	0	1	49	3	3	1	20
15-PTA-043	55.633	-65.173	0	0	0	0	118	2	2	1	40
15-PTA-044	55.852	-64.547	0	0	0	2	11	2	0	1	1
15-PTA-045	55.939	-64.462	1	0	0	1	2	0	2	1	1
15-PTA-046	55.965	-64.271	1	0	0	0	19	1	1	1	1
15-PTA-047	55.953	-64.368	0	0	0	18	6	6	0	1	1
15-PTA-048	55.969	-64.070	1	0	0	8	48	0	0	1	1
15-PTA-049	55.844	-64.048	0	0	0	6	9	2	1	1	1
15-PTA-050	55.770	-64.038	0	0	0	14	0	1	1	1	1
15-PTA-051	55.695	-64.034	0	0	0	5	5	3	5	1	1
15-PTA-052	55.616	-64.036	1	0	0	2	4	3	2	1	4
15-PTA-053	55.535	-64.056	1	0	0	3	2	1	0	1	20
15-PTA-054	55.502	-64.230	1	0	0	8	4	1	2	1	1
15-PTA-056	55.820	-65.568	0	0	0	0	9	9	16	1	50
15-PTA-057	55.825	-65.784	0	0	0	3	43	30	4	1	60
15-PTA-061	55.852	-64.337	1	0	0	5	31	1	0	1	5
15-PTA-062	55.649	-64.437	1	0	0	0	0	1	1	1	4
15-PTA-063	55.544	-64.588	0	0	0	0	8	0	5	1	7
15-PTA-079	55.895	-64.369	2	0	0	2	82	2	0	1	1
15-PTA-080	55.915	-64.232	2	0	0	2	13	1	2	1	2
15-PTA-081	55.810	-64.189	2	0	0	0	4	1	0	0	1

Supplementary Table S4.2

Samples	Location		Grains normalized to 10 kg								
	Lat	Long	Gold	Sperrylite	Chalcopyrite	Pyrite	Mn-epidote	Cr_diopside	Red Rutile	Goethite	Orthopyroxene
15-PTA-098	55.814	-65.398	0	0	0	1	7	7	10	1	30
15-PTA-099	55.780	-65.083	0	0	0	0	27	0	0	0	2
15-PTA-101	55.680	-64.179	1	0	0	2	3	1	0	1	1
15-PTA-102	55.704	-64.378	0	0	0	0	6	1	0	0	1
15-PTA-103	55.741	-64.490	0	0	0	0	25	1	1	1	5
15-PTA-144	55.627	-64.271	0	0	0	3	12	0	0	2	1
15-PTA-145	55.567	-64.188	0	1	0	2	4	1	0	1	1
15-PTA-146	55.527	-64.346	0	1	0	0	8	3	5	1	2
15-PTA-148	55.789	-64.329	3	0	0	0	14	0	0	1	1
15-PTA-155	55.654	-64.864	2	0	0	18	5	1	1	1	1
15-PTA-156	55.591	-64.732	0	0	0	0	333	4	0	1	60
15-PTA-176	55.629	-64.686	0	0	0	3	274	3	22	1	25
15-PTA-192	55.524	-64.961	1	0	0	0	114	7	13	0	30
15-PTA-193	55.512	-64.852	1	0	0	9	99	11	49	1	60

Supplementary Table 4.3

Sample	Lat	Long	Raw counts																	
			Meta-seds	Volcs.	Iron Fm.	Lap.	Leuco-granite	Felsic Intr.	Inter. Intr.	Mafic Intr.	Ultra-mafic	Vein Qtz	Quartzite	Mist	Zeni	Other	Syen.	Mich.	Leuco-granite (Mist)	SUM
14-PTA-B001	55.912	-64.086	0	0	0	0	0	722	42	20	4	15	2	77	0	2	0	0	61	945
14-PTA-B002	55.969	-64.575	8	3	0	1	0	199	10	4	4	6	3	101	0	8	0	0	19	366
14-PTA-B004	55.944	-64.877	1	1	0	0	3	406	18	8	0	6	0	0	4	0	0	0	0	447
14-PTA-R002	55.963	-65.796	0	1	0	35	7	234	10	25	0	4	1	0	0	5	0	0	0	322
14-PTA-R003	55.958	-65.469	2	0	0	0	5	381	48	4	0	4	0	0	0	8	0	0	0	452
14-PTA-R004	55.814	-65.261	4	0	0	0	0	318	53	4	0	4	3	9	0	3	0	0	0	398
14-PTA-R005	55.566	-65.219	0	0	0	45	11	245	31	9	1	14	2	0	0	4	0	0	0	362
14-PTA-R006	55.626	-65.401	26	2	0	39	65	222	0	19	0	13	0	0	0	1	0	0	0	387
14-PTA-R020	55.741	-64.730	2	1	0	2	0	382	31	13	0	6	3	9	0	3	0	0	18	470
14-PTA-R023	55.780	-65.016	1	13	2	8	0	454	29	13	0	12	0	2	0	3	0	0	0	537
14-PTA-R024	55.925	-65.060	0	2	4	0	3	380	13	13	0	3	0	0	0	1	0	0	0	419
14-PTA-R043	55.838	-64.732	0	0	4	0	0	150	6	13	0	1	0	171	0	0	0	0	11	356
15-PTA-002	55.674	-65.914	229	4	0	9	16	87	16	13	0	23	0	0	0	17	0	0	0	414
15-PTA-003	55.530	-65.914	233	9	0	0	20	68	17	13	1	25	1	0	0	3	3	0	0	393
15-PTA-004	55.741	-65.775	0	8	0	1	3	81	15	13	0	15	198	0	0	3	0	0	0	337
15-PTA-005	55.807	-65.940	98	0	0	0	6	149	14	13	0	27	5	0	0	8	0	0	0	320
15-PTA-007	55.922	-65.973	0	0	0	2	0	276	58	13	1	11	6	0	0	10	0	0	0	377
15-PTA-008	55.882	-65.812	27	1	0	0	7	302	31	13	3	10	7	0	0	0	0	0	0	401
15-PTA-010	55.969	-65.587	0	3	0	0	23	182	3	13	5	0	0	0	0	0	0	0	0	229
15-PTA-011	55.907	-65.334	0	2	0	0	4	342	16	13	0	4	0	0	0	5	0	0	0	386
15-PTA-012	55.795	-65.690	2	2	0	0	5	229	11	13	6	2	1	0	0	7	0	0	0	278
15-PTA-013	55.659	-65.642	77	2	0	0	50	153	18	13	7	48	52	0	0	2	0	0	0	422
15-PTA-014	55.587	-65.705	4	4	0	105	64	67	48	13	0	13	0	0	0	4	0	0	0	322
15-PTA-018	55.595	-65.789	158	6	0	0	23	111	1	13	1	14	9	0	0	0	0	0	0	336
15-PTA-019	55.626	-65.929	359	6	0	0	0	0	0	13	0	2	0	0	0	3	0	0	0	383
15-PTA-020	55.726	-65.884	60	4	0	40	25	284	23	13	0	19	13	0	0	3	0	0	0	484
15-PTA-022	55.773	-65.530	27	1	0	0	10	259	19	13	0	0	0	0	0	1	0	0	0	330
15-PTA-024	55.739	-65.153	1	4	0	0	0	101	2	13	1	0	0	0	0	1	0	0	0	123
15-PTA-025	55.654	-65.781	20	2	0	131	11	113	19	13	0	18	0	0	0	10	0	0	0	337
15-PTA-028	55.553	-65.560	0	4	0	316	0	65	12	13	0	13	0	0	0	0	0	0	0	423
15-PTA-029	55.687	-65.307	0	5	2	18	16	277	7	13	0	6	0	0	0	1	0	0	0	345

Supplementary Table 4.3

Sample	Lat	Long	Raw counts																	
			Meta-seds	Volcs.	Iron Fm.	Lap.	Leuco-granite	Felsic Intr.	Inter. Intr.	Mafic Intr.	Ultra-mafic	Vein Qtz	Quartzite	Mist	Zeni	Other	Syen.	Mich.	Leuco-granite (Mist)	SUM
15-PTA-034	55.843	-65.062	0	1	0	0	4	345	0	13	0	1	3	0	0	2	0	0	0	369
15-PTA-036	55.984	-65.251	0	3	0	0	14	331	16	13	2	3	1	0	0	1	0	0	0	384
15-PTA-037	55.964	-64.984	0	2	0	0	7	355	19	13	0	2	0	0	0	3	0	0	0	401
15-PTA-039	55.975	-64.775	0	0	2	0	0	339	0	13	1	1	0	0	0	0	0	0	15	371
15-PTA-042	55.809	-64.893	0	11	0	0	20	293	6	13	1	1	0	0	0	7	0	0	0	352
15-PTA-043	55.633	-65.173	5	1	0	3	3	108	234	13	0	2	3	0	0	0	0	0	0	372
15-PTA-044	55.852	-64.547	0	7	0	1	0	316	4	13	1	8	0	22	0	0	0	0	12	384
15-PTA-045	55.939	-64.462	0	6	0	0	0	232	10	13	1	3	1	41	0	4	0	0	4	315
15-PTA-046	55.965	-64.271	0	0	0	2	0	379	5	13	9	3	1	57	0	1	0	0	23	493
15-PTA-047	55.953	-64.368	0	8	0	0	0	309	4	13	2	6	5	55	0	4	0	0	17	423
15-PTA-048	55.969	-64.070	0	2	0	1	0	310	28	13	3	12	4	47	0	3	0	0	20	443
15-PTA-049	55.844	-64.048	0	2	0	0	0	0	4	13	2	6	0	43	0	63	0	0	19	152
15-PTA-050	55.770	-64.038	0	0	0	0	0	0	1	13	3	2	3	27	0	2	0	0	19	70
15-PTA-051	55.695	-64.034	0	2	0	2	0	315	4	13	0	2	0	34	0	3	0	0	0	375
15-PTA-052	55.616	-64.036	0	0	0	0	0	367	27	13	0	1	6	37	0	8	0	0	31	490
15-PTA-053	55.535	-64.056	0	3	0	0	4	246	8	13	0	1	0	0	0	4	0	0	4	283
15-PTA-054	55.502	-64.230	0	0	1	0	0	242	6	13	0	0	7	21	0	12	0	0	10	312
15-PTA-056	55.820	-65.568	7	7	0	4	15	348	19	13	0	4	6	0	0	1	0	0	0	424
15-PTA-057	55.825	-65.784	0	3	1	7	0	261	21	13	0	9	13	0	0	0	0	0	0	328
15-PTA-061	55.852	-64.337	0	0	0	0	0	256	9	13	0	9	0	0	0	3	0	0	24	314
15-PTA-062	55.649	-64.437	0	4	0	0	0	278	20	13	0	1	0	20	0	1	0	0	27	364
15-PTA-063	55.544	-64.588	1	1	0	0	0	191	10	13	1	6	5	5	0	3	0	0	24	260
15-PTA-079	55.895	-64.369	0	0	0	0	0	344	37	13	0	5	0	16	0	6	0	0	54	475
15-PTA-080	55.915	-64.232	0	2	0	0	0	320	14	13	0	9	4	41	0	2	0	0	33	438
15-PTA-081	55.810	-64.189	0	1	0	0	0	390	16	13	0	3	0	0	0	5	0	0	18	446
15-PTA-098	55.814	-65.398	0	3	0	0	12	396	12	13	0	0	4	0	0	7	0	0	0	447
15-PTA-099	55.780	-65.083	1	10	0	0	61	427	73	13	0	7	7	0	0	8	0	0	0	607
15-PTA-101	55.680	-64.179	0	0	0	1	0	344	15	13	0	1	0	26	0	19	0	0	19	438
15-PTA-102	55.704	-64.378	0	0	0	0	0	237	15	13	0	1	2	14	0	12	0	0	27	321
15-PTA-103	55.741	-64.490	0	1	0	0	0	349	10	13	0	5	5	11	0	6	0	0	19	419
15-PTA-139	55.559	-65.138	16	19	1	51	26	177	35	13	0	24	0	0	0	5	0	0	0	367

Supplementary Table 4.3

Sample	Lat	Long	Raw counts																
			Meta-seds	Volcs.	Iron Fm.	Lap.	Leuco-granite	Felsic Intr.	Inter. Intr.	Mafic Intr.	Ultra-mafic	Vein Qtz	Quartzite	Mist	Zeni	Other	Syen.	Mich.	Leuco-granite (Mist)	SUM
15-PTA-144	55.627	-64.271	0	0	0	1	0	0	32	13	0	5	0	17	0	3	0	0	16	87
15-PTA-145	55.567	-64.188	0	2	0	0	0	254	37	13	0	2	4	8	0	13	0	0	26	359
15-PTA-146	55.527	-64.346	0	2	0	0	0	249	16	13	0	9	0	14	0	8	0	0	37	348
15-PTA-148	55.789	-64.329	0	0	0	5	0	259	0	13	1	4	4	11	0	6	0	0	28	331
15-PTA-155	55.654	-64.864	27	8	1	24	30	402	33	13	0	6	4	0	0	5	0	0	0	553
15-PTA-156	55.591	-64.732	21	1	0	3	0	165	23	13	0	3	0	0	0	3	0	0	17	249
15-PTA-176	55.629	-64.686	22	4	0	7	0	169	13	13	0	13	6	20	0	8	0	0	54	329
15-PTA-192	55.524	-64.961	17	8	1	2	11	371	13	13	0	6	3	0	0	6	0	0	0	451
15-PTA-193	55.512	-64.852	7	0	0	13	9	331	41	13	0	1	1	0	0	8	0	0	0	424
15-PTA-204	55.487	-64.496	16	15	0	1	0	354	19	13	0	5	8	0	0	2	0	0	18	451

Supplementary Table 4.3

Sample	Lat	Long	Percentages																
			Meta-seds	Volcs.	Iron Fm.	Lap.	Leuco-granite	Felsic Intr.	Inter. Intr.	Mafic Intr.	Ultra-mafic	Vein Qtz	Quartzite	Mist	Zeni	Other	Syen.	Mich.	Leuco-granite (Mist)	SUM
14-PTA-B001	55.912	-64.086	0.000	0.000	0.000	0.000	0.000	0.764	0.044	0.021	0.004	0.016	0.002	0.081	0.000	0.002	0	0	0.06455	1
14-PTA-B002	55.969	-64.575	0.022	0.008	0.000	0.003	0.000	0.544	0.027	0.011	0.011	0.016	0.008	0.276	0.000	0.022	0.000	0.000	0.052	1
14-PTA-B004	55.944	-64.877	0.002	0.002	0.000	0.000	0.007	0.908	0.040	0.018	0.000	0.013	0.000	0.000	0.009	0.000	0.000	0.000	0.000	1
14-PTA-R002	55.963	-65.796	0.000	0.003	0.000	0.109	0.022	0.727	0.031	0.078	0.000	0.012	0.003	0.000	0.000	0.016	0.000	0.000	0.000	1
14-PTA-R003	55.958	-65.469	0.004	0.000	0.000	0.000	0.011	0.843	0.106	0.009	0.000	0.009	0.000	0.000	0.000	0.018	0.000	0.000	0.000	1
14-PTA-R004	55.814	-65.261	0.010	0.000	0.000	0.000	0.000	0.799	0.133	0.010	0.000	0.010	0.008	0.023	0.000	0.008	0.000	0.000	0.000	1
14-PTA-R005	55.566	-65.219	0.000	0.000	0.000	0.124	0.030	0.677	0.086	0.025	0.003	0.039	0.006	0.000	0.000	0.011	0.000	0.000	0.000	1
14-PTA-R006	55.626	-65.401	0.067	0.005	0.000	0.101	0.168	0.574	0.000	0.049	0.000	0.034	0.000	0.000	0.000	0.003	0.000	0.000	0.000	1
14-PTA-R020	55.741	-64.730	0.004	0.002	0.000	0.004	0.000	0.813	0.066	0.028	0.000	0.013	0.006	0.019	0.000	0.006	0.000	0.000	0.038	1
14-PTA-R023	55.780	-65.016	0.002	0.024	0.004	0.015	0.000	0.845	0.054	0.024	0.000	0.022	0.000	0.004	0.000	0.006	0.000	0.000	0.000	1
14-PTA-R024	55.925	-65.060	0.000	0.005	0.010	0.000	0.007	0.907	0.031	0.031	0.000	0.007	0.000	0.000	0.000	0.002	0.000	0.000	0.000	1
14-PTA-R043	55.838	-64.732	0.000	0.000	0.011	0.000	0.000	0.421	0.017	0.037	0.000	0.003	0.000	0.480	0.000	0.000	0.000	0.000	0.031	1
15-PTA-002	55.674	-65.914	0.553	0.010	0.000	0.022	0.039	0.210	0.039	0.031	0.000	0.056	0.000	0.000	0.000	0.041	0.000	0.000	0.000	1
15-PTA-003	55.530	-65.914	0.593	0.023	0.000	0.000	0.051	0.173	0.043	0.033	0.003	0.064	0.003	0.000	0.000	0.008	0.008	0.000	0.000	1
15-PTA-004	55.741	-65.775	0.000	0.024	0.000	0.003	0.009	0.240	0.045	0.039	0.000	0.045	0.588	0.000	0.000	0.009	0.000	0.000	0.000	1
15-PTA-005	55.807	-65.940	0.306	0.000	0.000	0.000	0.019	0.466	0.044	0.041	0.000	0.084	0.016	0.000	0.000	0.025	0.000	0.000	0.000	1
15-PTA-007	55.922	-65.973	0.000	0.000	0.000	0.005	0.000	0.732	0.154	0.034	0.003	0.029	0.016	0.000	0.000	0.027	0.000	0.000	0.000	1
15-PTA-008	55.882	-65.812	0.067	0.002	0.000	0.000	0.017	0.753	0.077	0.032	0.007	0.025	0.017	0.000	0.000	0.000	0.000	0.000	0.000	1
15-PTA-010	55.969	-65.587	0.000	0.013	0.000	0.000	0.100	0.795	0.013	0.057	0.022	0.000	0.000	0.000	0.000	0.000	0.000	0.000	0.000	1
15-PTA-011	55.907	-65.334	0.000	0.005	0.000	0.000	0.010	0.886	0.041	0.034	0.000	0.010	0.000	0.000	0.000	0.013	0.000	0.000	0.000	1
15-PTA-012	55.795	-65.690	0.007	0.007	0.000	0.000	0.018	0.824	0.040	0.047	0.022	0.007	0.004	0.000	0.000	0.025	0.000	0.000	0.000	1
15-PTA-013	55.659	-65.642	0.182	0.005	0.000	0.000	0.118	0.363	0.043	0.031	0.017	0.114	0.123	0.000	0.000	0.005	0.000	0.000	0.000	1
15-PTA-014	55.587	-65.705	0.012	0.012	0.000	0.326	0.199	0.208	0.149	0.040	0.000	0.040	0.000	0.000	0.000	0.012	0.000	0.000	0.000	1
15-PTA-018	55.595	-65.789	0.470	0.018	0.000	0.000	0.068	0.330	0.003	0.039	0.003	0.042	0.027	0.000	0.000	0.000	0.000	0.000	0.000	1
15-PTA-019	55.626	-65.929	0.937	0.016	0.000	0.000	0.000	0.000	0.000	0.034	0.000	0.005	0.000	0.000	0.000	0.008	0.000	0.000	0.000	1
15-PTA-020	55.726	-65.884	0.124	0.008	0.000	0.083	0.052	0.587	0.048	0.027	0.000	0.039	0.027	0.000	0.000	0.006	0.000	0.000	0.000	1
15-PTA-022	55.773	-65.530	0.082	0.003	0.000	0.000	0.030	0.785	0.058	0.039	0.000	0.000	0.000	0.000	0.000	0.003	0.000	0.000	0.000	1
15-PTA-024	55.739	-65.153	0.008	0.033	0.000	0.000	0.000	0.821	0.016	0.106	0.008	0.000	0.000	0.000	0.000	0.008	0.000	0.000	0.000	1
15-PTA-025	55.654	-65.781	0.059	0.006	0.000	0.389	0.033	0.335	0.056	0.039	0.000	0.053	0.000	0.000	0.000	0.030	0.000	0.000	0.000	1
15-PTA-028	55.553	-65.560	0.000	0.009	0.000	0.747	0.000	0.154	0.028	0.031	0.000	0.031	0.000	0.000	0.000	0.000	0.000	0.000	0.000	1
15-PTA-029	55.687	-65.307	0.000	0.014	0.006	0.052	0.046	0.803	0.020	0.038	0.000	0.017	0.000	0.000	0.000	0.003	0.000	0.000	0.000	1

Supplementary Table 4.3

Sample	Lat	Long	Percentages																
			Meta-seds	Volcs.	Iron Fm.	Lap.	Leuco-granite	Felsic Intr.	Inter. Intr.	Mafic Intr.	Ultra-mafic	Vein Qtz	Quartzite	Mist	Zeni	Other	Syen.	Mich.	Leuco-granite (Mist)	SUM
15-PTA-034	55.843	-65.062	0.000	0.003	0.000	0.000	0.011	0.935	0.000	0.035	0.000	0.003	0.008	0.000	0.000	0.005	0.000	0.000	0.000	1
15-PTA-036	55.984	-65.251	0.000	0.008	0.000	0.000	0.036	0.862	0.042	0.034	0.005	0.008	0.003	0.000	0.000	0.003	0.000	0.000	0.000	1
15-PTA-037	55.964	-64.984	0.000	0.005	0.000	0.000	0.017	0.885	0.047	0.032	0.000	0.005	0.000	0.000	0.000	0.007	0.000	0.000	0.000	1
15-PTA-039	55.975	-64.775	0.000	0.000	0.005	0.000	0.000	0.914	0.000	0.035	0.003	0.003	0.000	0.000	0.000	0.000	0.000	0.000	0.040	1
15-PTA-042	55.809	-64.893	0.000	0.031	0.000	0.000	0.057	0.832	0.017	0.037	0.003	0.003	0.000	0.000	0.000	0.020	0.000	0.000	0.000	1
15-PTA-043	55.633	-65.173	0.013	0.003	0.000	0.008	0.008	0.290	0.629	0.035	0.000	0.005	0.008	0.000	0.000	0.000	0.000	0.000	0.000	1
15-PTA-044	55.852	-64.547	0.000	0.018	0.000	0.003	0.000	0.823	0.010	0.034	0.003	0.021	0.000	0.057	0.000	0.000	0.000	0.000	0.031	1
15-PTA-045	55.939	-64.462	0.000	0.019	0.000	0.000	0.000	0.737	0.032	0.041	0.003	0.010	0.003	0.130	0.000	0.013	0.000	0.000	0.013	1
15-PTA-046	55.965	-64.271	0.000	0.000	0.000	0.004	0.000	0.769	0.010	0.026	0.018	0.006	0.002	0.116	0.000	0.002	0.000	0.000	0.047	1
15-PTA-047	55.953	-64.368	0.000	0.019	0.000	0.000	0.000	0.730	0.009	0.031	0.005	0.014	0.012	0.130	0.000	0.009	0.000	0.000	0.040	1
15-PTA-048	55.969	-64.070	0.000	0.005	0.000	0.002	0.000	0.700	0.063	0.029	0.007	0.027	0.009	0.106	0.000	0.007	0.000	0.000	0.045	1
15-PTA-049	55.844	-64.048	0.000	0.013	0.000	0.000	0.000	0.000	0.026	0.086	0.013	0.039	0.000	0.283	0.000	0.414	0.000	0.000	0.125	1
15-PTA-050	55.770	-64.038	0.000	0.000	0.000	0.000	0.000	0.000	0.014	0.186	0.043	0.029	0.043	0.386	0.000	0.029	0.000	0.000	0.271	1
15-PTA-051	55.695	-64.034	0.000	0.005	0.000	0.005	0.000	0.840	0.011	0.035	0.000	0.005	0.000	0.091	0.000	0.008	0.000	0.000	0.000	1
15-PTA-052	55.616	-64.036	0.000	0.000	0.000	0.000	0.000	0.749	0.055	0.027	0.000	0.002	0.012	0.076	0.000	0.016	0.000	0.000	0.063	1
15-PTA-053	55.535	-64.056	0.000	0.011	0.000	0.000	0.014	0.869	0.028	0.046	0.000	0.004	0.000	0.000	0.000	0.014	0.000	0.000	0.014	1
15-PTA-054	55.502	-64.230	0.000	0.000	0.003	0.000	0.000	0.776	0.019	0.042	0.000	0.000	0.022	0.067	0.000	0.038	0.000	0.000	0.032	1
15-PTA-056	55.820	-65.568	0.017	0.017	0.000	0.009	0.035	0.821	0.045	0.031	0.000	0.009	0.014	0.000	0.000	0.002	0.000	0.000	0.000	1
15-PTA-057	55.825	-65.784	0.000	0.009	0.003	0.021	0.000	0.796	0.064	0.040	0.000	0.027	0.040	0.000	0.000	0.000	0.000	0.000	0.000	1
15-PTA-061	55.852	-64.337	0.000	0.000	0.000	0.000	0.000	0.815	0.029	0.041	0.000	0.029	0.000	0.000	0.000	0.010	0.000	0.000	0.076	1
15-PTA-062	55.649	-64.437	0.000	0.011	0.000	0.000	0.000	0.764	0.055	0.036	0.000	0.003	0.000	0.055	0.000	0.003	0.000	0.000	0.074	1
15-PTA-063	55.544	-64.588	0.004	0.004	0.000	0.000	0.000	0.735	0.038	0.050	0.004	0.023	0.019	0.019	0.000	0.012	0.000	0.000	0.092	1
15-PTA-079	55.895	-64.369	0.000	0.000	0.000	0.000	0.000	0.724	0.078	0.027	0.000	0.011	0.000	0.034	0.000	0.013	0.000	0.000	0.114	1
15-PTA-080	55.915	-64.232	0.000	0.005	0.000	0.000	0.000	0.731	0.032	0.030	0.000	0.021	0.009	0.094	0.000	0.005	0.000	0.000	0.075	1
15-PTA-081	55.810	-64.189	0.000	0.002	0.000	0.000	0.000	0.874	0.036	0.029	0.000	0.007	0.000	0.000	0.000	0.011	0.000	0.000	0.040	1
15-PTA-098	55.814	-65.398	0.000	0.007	0.000	0.000	0.027	0.886	0.027	0.029	0.000	0.000	0.009	0.000	0.000	0.016	0.000	0.000	0.000	1
15-PTA-099	55.780	-65.083	0.002	0.016	0.000	0.000	0.100	0.703	0.120	0.021	0.000	0.012	0.012	0.000	0.000	0.013	0.000	0.000	0.000	1
15-PTA-101	55.680	-64.179	0.000	0.000	0.000	0.002	0.000	0.785	0.034	0.030	0.000	0.002	0.000	0.059	0.000	0.043	0.000	0.000	0.043	1
15-PTA-102	55.704	-64.378	0.000	0.000	0.000	0.000	0.000	0.738	0.047	0.040	0.000	0.003	0.006	0.044	0.000	0.037	0.000	0.000	0.084	1
15-PTA-103	55.741	-64.490	0.000	0.002	0.000	0.000	0.000	0.833	0.024	0.031	0.000	0.012	0.012	0.026	0.000	0.014	0.000	0.000	0.045	1
15-PTA-139	55.559	-65.138	0.044	0.052	0.003	0.139	0.071	0.482	0.095	0.035	0.000	0.065	0.000	0.000	0.000	0.014	0.000	0.000	0.000	1

Supplementary Table 4.3

Sample	Lat	Long	Percentages																
			Meta-seds	Volcs.	Iron Fm.	Lap.	Leuco-granite	Felsic Intr.	Inter. Intr.	Mafic Intr.	Ultra-mafic	Vein Qtz	Quartzite	Mist	Zeni	Other	Syen.	Mich.	Leuco-granite (Mist)	SUM
15-PTA-144	55.627	-64.271	0.000	0.000	0.000	0.011	0.000	0.000	0.368	0.149	0.000	0.057	0.000	0.195	0.000	0.034	0.000	0.000	0.184	1
15-PTA-145	55.567	-64.188	0.000	0.006	0.000	0.000	0.000	0.708	0.103	0.036	0.000	0.006	0.011	0.022	0.000	0.036	0.000	0.000	0.072	1
15-PTA-146	55.527	-64.346	0.000	0.006	0.000	0.000	0.000	0.716	0.046	0.037	0.000	0.026	0.000	0.040	0.000	0.023	0.000	0.000	0.106	1
15-PTA-148	55.789	-64.329	0.000	0.000	0.000	0.015	0.000	0.782	0.000	0.039	0.003	0.012	0.012	0.033	0.000	0.018	0.000	0.000	0.085	1
15-PTA-155	55.654	-64.864	0.049	0.014	0.002	0.043	0.054	0.727	0.060	0.024	0.000	0.011	0.007	0.000	0.000	0.009	0.000	0.000	0.000	1
15-PTA-156	55.591	-64.732	0.084	0.004	0.000	0.012	0.000	0.663	0.092	0.052	0.000	0.012	0.000	0.000	0.000	0.012	0.000	0.000	0.068	1
15-PTA-176	55.629	-64.686	0.067	0.012	0.000	0.021	0.000	0.514	0.040	0.040	0.000	0.040	0.018	0.061	0.000	0.024	0.000	0.000	0.164	1
15-PTA-192	55.524	-64.961	0.038	0.018	0.002	0.004	0.024	0.823	0.029	0.029	0.000	0.013	0.007	0.000	0.000	0.013	0.000	0.000	0.000	1
15-PTA-193	55.512	-64.852	0.017	0.000	0.000	0.031	0.021	0.781	0.097	0.031	0.000	0.002	0.002	0.000	0.000	0.019	0.000	0.000	0.000	1
15-PTA-204	55.487	-64.496	0.035	0.033	0.000	0.002	0.000	0.785	0.042	0.029	0.000	0.011	0.018	0.000	0.000	0.004	0.000	0.000	0.040	1

Supplementary Table 4.3

Sample	Lat	Long	Simplified for Bedrock Units					
			Laporte	De Pas	Mistanibi	Lab Trough	Other	Sum
14-PTA-B001	55.912	-64.086	0.00	0.78	0.22	0.00	0.00	1.00
14-PTA-B002	55.969	-64.575	0.03	0.56	0.38	0.01	0.02	1.00
14-PTA-B004	55.944	-64.877	0.01	0.92	0.07	0.00	0.00	1.00
14-PTA-R002	55.963	-65.796	0.13	0.74	0.11	0.00	0.02	1.00
14-PTA-R003	55.958	-65.469	0.02	0.85	0.12	0.00	0.02	1.00
14-PTA-R004	55.814	-65.261	0.02	0.81	0.17	0.00	0.01	1.00
14-PTA-R005	55.566	-65.219	0.16	0.72	0.11	0.00	0.01	1.00
14-PTA-R006	55.626	-65.401	0.34	0.61	0.05	0.01	0.00	1.00
14-PTA-R020	55.741	-64.730	0.01	0.83	0.15	0.00	0.01	1.00
14-PTA-R023	55.780	-65.016	0.02	0.87	0.08	0.03	0.01	1.00
14-PTA-R024	55.925	-65.060	0.01	0.91	0.06	0.01	0.00	1.00
14-PTA-R043	55.838	-64.732	0.00	0.42	0.56	0.01	0.00	1.00
15-PTA-002	55.674	-65.914	0.61	0.27	0.07	0.01	0.04	1.00
15-PTA-003	55.530	-65.914	0.65	0.24	0.09	0.02	0.01	1.00
15-PTA-004	55.741	-65.775	0.60	0.28	0.08	0.02	0.01	1.00
15-PTA-005	55.807	-65.940	0.34	0.55	0.08	0.00	0.03	1.00
15-PTA-007	55.922	-65.973	0.02	0.76	0.19	0.00	0.03	1.00
15-PTA-008	55.882	-65.812	0.10	0.78	0.12	0.00	0.00	1.00
15-PTA-010	55.969	-65.587	0.10	0.79	0.09	0.01	0.00	1.00
15-PTA-011	55.907	-65.334	0.01	0.90	0.08	0.01	0.01	1.00
15-PTA-012	55.795	-65.690	0.03	0.83	0.11	0.01	0.03	1.00
15-PTA-013	55.659	-65.642	0.42	0.48	0.09	0.00	0.00	1.00
15-PTA-014	55.587	-65.705	0.54	0.25	0.19	0.01	0.01	1.00
15-PTA-018	55.595	-65.789	0.57	0.37	0.04	0.02	0.00	1.00
15-PTA-019	55.626	-65.929	0.94	0.01	0.03	0.02	0.01	1.00
15-PTA-020	55.726	-65.884	0.29	0.63	0.07	0.01	0.01	1.00
15-PTA-022	55.773	-65.530	0.11	0.78	0.10	0.00	0.00	1.00
15-PTA-024	55.739	-65.153	0.01	0.82	0.13	0.03	0.01	1.00
15-PTA-025	55.654	-65.781	0.48	0.39	0.09	0.01	0.03	1.00
15-PTA-028	55.553	-65.560	0.75	0.18	0.06	0.01	0.00	1.00
15-PTA-029	55.687	-65.307	0.10	0.82	0.06	0.02	0.00	1.00

Supplementary Table 4.3

Sample	Lat	Long	Simplified for Bedrock Units					
			Laporte	De Pas	Mistanibi	Lab Trough	Other	Sum
15-PTA-034	55.843	-65.062	0.02	0.94	0.04	0.00	0.01	1.00
15-PTA-036	55.984	-65.251	0.04	0.87	0.08	0.01	0.00	1.00
15-PTA-037	55.964	-64.984	0.02	0.89	0.08	0.00	0.01	1.00
15-PTA-039	55.975	-64.775	0.00	0.92	0.08	0.01	0.00	1.00
15-PTA-042	55.809	-64.893	0.06	0.84	0.06	0.03	0.02	1.00
15-PTA-043	55.633	-65.173	0.04	0.30	0.66	0.00	0.00	1.00
15-PTA-044	55.852	-64.547	0.00	0.84	0.14	0.02	0.00	1.00
15-PTA-045	55.939	-64.462	0.00	0.75	0.22	0.02	0.01	1.00
15-PTA-046	55.965	-64.271	0.01	0.77	0.22	0.00	0.00	1.00
15-PTA-047	55.953	-64.368	0.01	0.74	0.22	0.02	0.01	1.00
15-PTA-048	55.969	-64.070	0.01	0.73	0.25	0.00	0.01	1.00
15-PTA-049	55.844	-64.048	0.00	0.04	0.53	0.01	0.41	1.00
15-PTA-050	55.770	-64.038	0.04	0.03	0.90	0.00	0.03	1.00
15-PTA-051	55.695	-64.034	0.01	0.85	0.14	0.01	0.01	1.00
15-PTA-052	55.616	-64.036	0.01	0.75	0.22	0.00	0.02	1.00
15-PTA-053	55.535	-64.056	0.01	0.87	0.09	0.01	0.01	1.00
15-PTA-054	55.502	-64.230	0.02	0.78	0.16	0.00	0.04	1.00
15-PTA-056	55.820	-65.568	0.08	0.83	0.08	0.02	0.00	1.00
15-PTA-057	55.825	-65.784	0.06	0.82	0.10	0.01	0.00	1.00
15-PTA-061	55.852	-64.337	0.00	0.84	0.15	0.00	0.01	1.00
15-PTA-062	55.649	-64.437	0.00	0.77	0.22	0.01	0.00	1.00
15-PTA-063	55.544	-64.588	0.02	0.76	0.20	0.00	0.01	1.00
15-PTA-079	55.895	-64.369	0.00	0.73	0.25	0.00	0.01	1.00
15-PTA-080	55.915	-64.232	0.01	0.75	0.23	0.00	0.00	1.00
15-PTA-081	55.810	-64.189	0.00	0.88	0.11	0.00	0.01	1.00
15-PTA-098	55.814	-65.398	0.04	0.89	0.06	0.01	0.02	1.00
15-PTA-099	55.780	-65.083	0.11	0.71	0.14	0.02	0.01	1.00
15-PTA-101	55.680	-64.179	0.00	0.79	0.17	0.00	0.04	1.00
15-PTA-102	55.704	-64.378	0.01	0.74	0.21	0.00	0.04	1.00
15-PTA-103	55.741	-64.490	0.01	0.84	0.13	0.00	0.01	1.00
15-PTA-139	55.559	-65.138	0.25	0.55	0.13	0.05	0.01	1.00

Supplementary Table 4.3

Sample	Lat	Long	Simplified for Bedrock Units					
			Laporte	De Pas	Mistanibi	Lab Trough	Other	Sum
15-PTA-144	55.627	-64.271	0.01	0.06	0.90	0.00	0.03	1.00
15-PTA-145	55.567	-64.188	0.01	0.71	0.23	0.01	0.04	1.00
15-PTA-146	55.527	-64.346	0.00	0.74	0.23	0.01	0.02	1.00
15-PTA-148	55.789	-64.329	0.03	0.79	0.16	0.00	0.02	1.00
15-PTA-155	55.654	-64.864	0.15	0.74	0.08	0.02	0.01	1.00
15-PTA-156	55.591	-64.732	0.10	0.67	0.21	0.00	0.01	1.00
15-PTA-176	55.629	-64.686	0.11	0.55	0.30	0.01	0.02	1.00
15-PTA-192	55.524	-64.961	0.07	0.84	0.06	0.02	0.01	1.00
15-PTA-193	55.512	-64.852	0.07	0.78	0.13	0.00	0.02	1.00
15-PTA-204	55.487	-64.496	0.06	0.80	0.11	0.03	0.00	1.00

Supplementary Table 4.4

Sample	Lat	Long	Sand <0.2 mm (%)	Silt 0.2 - 0.063 mm (%)	Clay <0.063 mm(%)	Total C (±0.1%)	Inorganic C (±0.1%)	Organic C (±0.2%)	Loss on Ignition (%)	Munsell Colour	Description
14-PTA-B001	55.912	-64.086	0.419	0.554	0.026	0.6	0	0.6	1.9	2.5Y 6/2	light brownish grey
14-PTA-B002	55.969	-64.575	0.482	0.499	0.019	0.1	0	<0.2	1.2	2.5Y 6/2	light brownish grey
14-PTA-B004	55.944	-64.877	0.683	0.290	0.027	0.4	0	0.4	2.2	5Y 6/2	light olive gray
14-PTA-R002	55.963	-65.796	0.436	0.464	0.101	0	0	0	1.4	2.5Y 6/2	light brownish grey
14-PTA-R003	55.958	-65.469	0.651	0.316	0.033	0.6	0	0.6	2.9	2.5Y 6/3	light yellowish brown
14-PTA-R004	55.814	-65.261	0.565	0.391	0.044	0.3	0	0.3	2.8	2.5Y 6/3	light yellowish brown
14-PTA-R005	55.566	-65.219	0.552	0.415	0.033	0.6	0	0.6	3.6	2.5Y 6/3	light yellowish brown
14-PTA-R006	55.626	-65.401	0.632	0.349	0.019	0.8	0	0.8	3.5	2.5Y 6/3	light yellowish brown
14-PTA-R020	55.741	-64.730	0.589	0.387	0.024	0.9	0	0.9	2.7	5Y 5/3	olive
14-PTA-R023	55.780	-65.016	0.512	0.439	0.049	0.7	0	0.7	3.1	2.5Y 6/3	light yellowish brown
14-PTA-R024	55.925	-65.060	0.625	0.342	0.033	0.5	0	0.5	2.1	2.5Y 6/2	light brownish grey
14-PTA-R043	55.838	-64.732	0.604	0.353	0.044	0.6	0	0.6	2.4	2.5Y 6/2	light brownish grey
15-PTA-002	55.674	-65.914	0.568	0.299	0.133	0.7	0.2	0.5	3.5	5Y 6/2	light olive grey
15-PTA-003	55.530	-65.914	0.550	0.437	0.014	0.4	0.2	0.2	2.5	5Y 6/2	light olive grey
15-PTA-004	55.741	-65.775	0.779	0.213	0.008	1.1	0	1.1	4.6	2.5Y 6/3	light yellowish brown
15-PTA-005	55.807	-65.940	0.524	0.461	0.015	1.3	0	1.2	5.4	2.5Y 5/3	light olive brown
15-PTA-007	55.837	-65.890	0.607	0.360	0.033	0.8	0	0.8	3.1	2.5Y 6/3	light yellowish brown
15-PTA-008	55.922	-65.973	0.634	0.330	0.036	0.5	0	0.5	2.8	2.5Y 6/3	light yellowish brown
15-PTA-010	55.969	-65.587	0.406	0.549	0.044	0.4	0	0.4	2	2.5Y 6/2	light brownish grey
15-PTA-011	55.907	-65.334	0.662	0.303	0.035	0.4	0	0.4	2.1	5Y 6/2	light olive grey
15-PTA-012	55.795	-65.690	0.608	0.372	0.020	1	0	1	3.7	2.5Y 5/3	light olive brown
15-PTA-013	55.659	-65.642	0.652	0.339	0.009	1	0	1	4.5	2.5Y 5/3	light olive brown
15-PTA-014	55.587	-65.705	0.651	0.338	0.011	0.6	0	0.6	3.4	2.5Y 6/3	light yellowish brown
15-PTA-018	55.595	-65.789	0.537	0.435	0.028	0.3	0.2	<0.2	1.8	5Y 6/2	light olive grey
15-PTA-019	55.626	-65.929	0.707	0.293	0.000	1.6	0.2	1.4	4.7	2.5Y 5/3	light olive brown
15-PTA-020	55.726	-65.884	0.587	0.377	0.036	0.4	0.2	0.2	2.2	5Y 6/2	light olive grey
15-PTA-022	55.773	-65.530	0.535	0.434	0.031	0.9	0	0.9	3.9	2.5Y 6/3	light yellowish brown
15-PTA-024	55.739	-65.153	0.401	0.570	0.029	0.2	0	<0.2	1.8	2.5Y 6/3	light yellowish brown
15-PTA-025	55.654	-65.781	0.594	0.389	0.017	0.6	0	0.5	2.9	5Y 6/2	light olive grey
15-PTA-028	55.553	-65.560	0.638	0.355	0.007	0.6	0	0.6	2.6	2.5Y 6/2	light brownish grey
15-PTA-029	55.687	-65.307	0.644	0.347	0.009	0.5	0	0.5	2.3	2.5Y 6/2	light brownish grey

Supplementary Table 4.4

Sample	Lat	Long	Sand <0.2 mm (%)	Silt 0.2 - 0.063 mm (%)	Clay <0.063 mm(%)	Total C (±0.1%)	Inorganic C (±0.1%)	Organic C (±0.2%)	Loss on Ignition (%)	Munsell Colour	Description
15-PTA-034	55.843	-65.062	0.587	0.386	0.027	1.3	0	1.3	4.7	2.5Y 6/3	light yellowish brown
15-PTA-036	55.984	-65.251	0.620	0.360	0.020	0.2	0	<0.2	1.2	2.5Y 6/2	light brownish grey
15-PTA-037	55.964	-64.984	0.627	0.346	0.027	0.2	0	0.2	1.2	10YR 6/2	light brownish grey
15-PTA-039	55.975	-64.775	0.413	0.539	0.048	0.7	0	0.7	2.6	2.5Y 6/2	light brownish grey
15-PTA-042	55.809	-64.893	0.455	0.497	0.048	0.9	0	0.9	3.3	2.5Y 6/3	light yellowish brown
15-PTA-043	55.633	-65.173	0.396	0.566	0.037	1	0	0.9	4.4	2.5Y 6/3	light yellowish brown
15-PTA-044	55.852	-64.547	0.444	0.517	0.040	0.3	0	0.3	1.7	5Y 6/2	light olive grey
15-PTA-045	55.939	-64.462	0.441	0.495	0.065	0.6	0	0.6	2.7	2.5Y 6/2	light brownish grey
15-PTA-046	55.965	-64.271	0.587	0.400	0.013	0.7	0	0.7	2.6	2.5Y 6/2	light brownish grey
15-PTA-047	55.953	-64.368	0.483	0.498	0.019	0.2	0	0.2	1.2	5Y 6/2	light olive grey
15-PTA-048	55.969	-64.070	0.496	0.495	0.008	0.2	0	<0.2	0.7	GLEY1 6/1	greenish grey
15-PTA-049	55.844	-64.048	0.438	0.519	0.043	0.5	0	0.5	2.1	2.5Y 6/2	light brownish grey
15-PTA-050	55.770	-64.038	0.421	0.541	0.038	0.9	0	0.9	2.8	2.5Y 6/2	light brownish grey
15-PTA-051	55.695	-64.034	0.523	0.433	0.044	0.2	0	0.2	1.2	2.5Y 6/2	light brownish grey
15-PTA-052	55.616	-64.036	0.458	0.473	0.070	0.7	0	0.7	2.8	2.5Y 6/2	light brownish grey
15-PTA-053	55.535	-64.056	0.394	0.552	0.054	1.1	0	1.1	3.3	2.5Y 6/3	light yellowish brown
15-PTA-054	55.502	-64.230	0.459	0.517	0.024	0.5	0	0.5	2.3	5Y 6/2	light olive grey
15-PTA-056	55.820	-65.568	0.597	0.362	0.041	0.3	0	0.3	1.9	5Y 6/2	light olive grey
15-PTA-057	55.825	-65.784	0.486	0.453	0.061	1.3	0	1.3	4.8	2.5Y 6/3	light yellowish brown
15-PTA-061	55.852	-64.337	0.367	0.561	0.072	0.8	0	0.8	2.7	2.5Y 6/2	light brownish grey
15-PTA-062	55.649	-64.437	0.499	0.471	0.030	0.4	0	0.4	1.6	2.5Y 6/2	light brownish grey
15-PTA-063	55.544	-64.588	0.473	0.466	0.061	0.7	0	0.7	3.1	2.5Y 6/2	light brownish grey
15-PTA-079	55.895	-64.369	0.466	0.463	0.071	1.1	0	1.1	3.9	2.5Y 6/3	light yellowish brown
15-PTA-080	55.915	-64.232	0.493	0.451	0.056	0.2	0	<0.2	1.2	5Y 7/1	light grey
15-PTA-081	55.810	-64.189	0.453	0.505	0.042	1	0	1	3.5	2.5Y 6/3	light yellowish brown
15-PTA-098	55.814	-65.398	0.659	0.312	0.029	0.1	0	<0.2	1.6	5Y 5/2	olive grey
15-PTA-099	55.780	-65.083	0.665	0.326	0.009	1	0	1	4	5Y 5/3	olive
15-PTA-101	55.680	-64.179	0.481	0.457	0.062	0.4	0	0.4	1.9	2.5Y 6/2	light brownish grey
15-PTA-102	55.704	-64.378	0.417	0.547	0.035	0.1	0	<0.2	1.2	5Y 6/2	light olive grey
15-PTA-103	55.741	-64.490	0.479	0.457	0.063	0.5	0	0.5	2.5	5Y 6/2	light olive grey
15-PTA-139	55.559	-65.138	0.304	0.677	0.019	0.6	0	0.6	2.3	2.5Y 6/3	light yellowish brown

Supplementary Table 4.4

Sample	Lat	Long	Sand <0.2 mm (%)	Silt 0.2 - 0.063 mm (%)	Clay <0.063 mm(%)	Total C (±0.1%)	Inorganic C (±0.1%)	Organic C (±0.2%)	Loss on Ignition (%)	Munsell Colour	Description
15-PTA-144	55.627	-64.271	0.535	0.411	0.054	0.3	0	0.3	1.4	2.5Y 6/2	light brownish grey
15-PTA-145	55.567	-64.188	0.528	0.439	0.033	0.8	0	0.8	2.7	5Y 6/2	light olive grey
15-PTA-146	55.527	-64.346	0.349	0.599	0.052	0.5	0	0.5	2.4	5Y 6/2	light olive grey
15-PTA-148	55.789	-64.329	0.588	0.377	0.035	0.3	0	0.3	2.3	2.5Y 6/2	light brownish grey
15-PTA-155	55.654	-64.864	0.515	0.460	0.026	0.5	0	0.5	2.2	2.5Y 6/3	light yellowish brown
15-PTA-156	55.591	-64.732	0.352	0.601	0.047	1	0	1	3.6	2.5Y 6/3	light yellowish brown
15-PTA-176	55.629	-64.686	0.473	0.508	0.019	1.8	0	1.8	6.2	2.5Y 6/3	light yellowish brown
15-PTA-192	55.524	-64.961	0.500	0.464	0.036	0.6	0	0.6	2.9	2.5Y 6/3	light yellowish brown
15-PTA-193	55.512	-64.852	0.709	0.278	0.013	0.7	0	0.7	2.5	2.5Y 5/3	light olive brown
16-PTA-056	55.692	-65.991	0.629	0.349	0.021	0.7	0.3	0.4	2.3	5Y 6/2	light olive gray
16-PTA-058	55.843	-64.207	0.554	0.397	0.049	0.6	<0.1	0.5	2.2	2.5Y 5/2	grayish brown
16-PTA-060	55.898	-64.611	0.682	0.280	0.037	0.4	<0.1	0.4	2.9	5Y 6/2	light olive gray
16-PTA-069	55.721	-65.218	0.604	0.344	0.052	0.5	<0.1	0.5	2.8	2.5Y 6/3	light yellowish brown
16-PTA-070	55.784	-65.251	0.602	0.342	0.056	0.6	<0.1	0.6	2.8	2.5Y 6/3	light yellowish brown